B. K. HODGE

ALTERNATIVE ENERGY SYSTEMS AND APPLICATIONS

SECOND EDITION

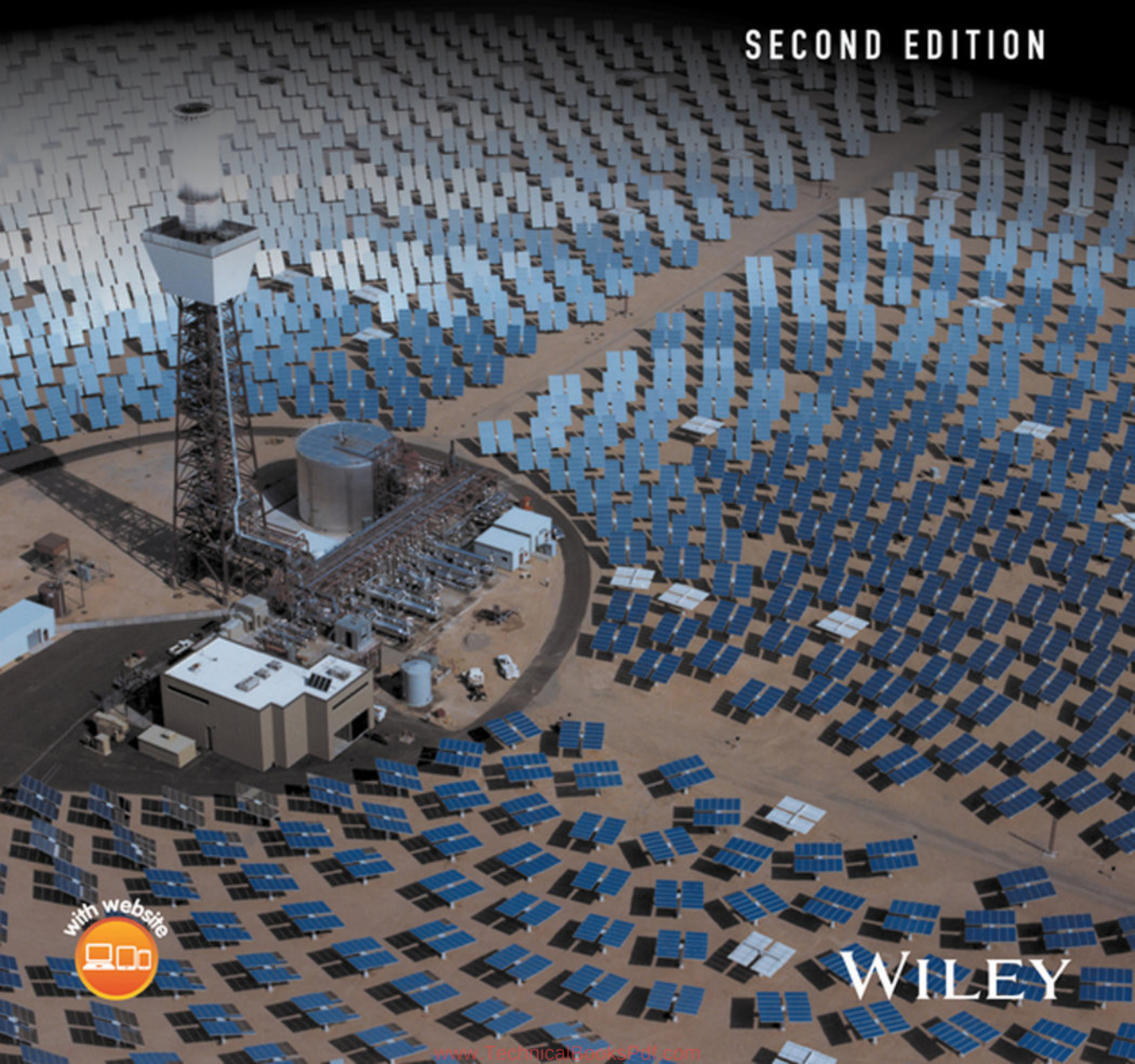

WILEY

Alternative Energy Systems and Applications

Alternative Energy Systems and Applications

B. K. Hodge
Mississippi State University, USA

Second Edition

WILEY

This edition first published 2017

Registered Offices
John Wiley & Sons, Inc., 111 River Street, Hoboken, NJ 07030, USA
John Wiley & Sons Ltd, The Atrium, Southern Gate, Chichester, West Sussex, PO19 8SQ, UK

Editorial Office
The Atrium, Southern Gate, Chichester, West Sussex, PO19 8SQ, UK

For details of our global editorial offices, customer services, and more information about Wiley products visit us at www.wiley.com.

Wiley also publishes its books in a variety of electronic formats and by print-on-demand. Some content that appears in standard print versions of this book may not be available in other formats.

Library of Congress Cataloging-in-Publication Data

Names: Hodge, B. K., author.
Title: Alternative energy systems and applications / B. K Hodge.
Description: Second edition. | Hoboken, NJ : John Wiley & Sons, 2017. | Includes index.
Identifiers: LCCN 2016049895| ISBN 9781119109211 (pbk.) | ISBN 9781119109228 (epdf) | ISBN 9781119109235 (epub)
Subjects: LCSH: Renewable energy sources. | Power resources. | Electric power systems.
Classification: LCC TJ808 .H63 2017 | DDC 333.79/4–dc23 LC record available at https://lccn.loc.gov/2016049895

Cover Image: Courtesy of NREL/DOE
Cover Design: Wiley

Set in 10/12pt WarnockPro-Regular by Thomson Digital, Noida, India

10 9 8 7 6 5 4 3 2 1

To Gayle, my wife
And best friend

For our family:

Lauren (Hodge) and Adam Sims

Selena and Ben Hodge
Liam Finn Hodge
Noah Townshend Hodge

Table of Contents

Preface to the Second Edition

Since the first edition was written (2007–2009), many changes in the energy posture of the USA as well as the rest of the world have taken place. The second edition has been significantly influenced by these changes. Two chapters have been added: one addressing electric and hybrid vehicles (Chapter 16) and one examining enhanced oil and gas recovery (via hydraulic fracturing) and its ramifications (Chapter 17). All of the chapters have been revised and modernized and have had, in many instances, substantial additions. When possible, quantitative information has been updated to the current data available. These data include documented energy usages, energy resource/usages projections, and energy systems' and components' performance metrics and availability. The number of web sites cited in the second edition is substantially greater than in the first edition. All cited web sites were active as of December 2016. However, web sites are updated (and renamed) frequently, but using a search engine with a reasonably complete descriptor will usually redirect to an appropriate site. Since the first edition, useful quantitative information in many company and government agency web sites has been reduced in favor of more words, pictures and illustrations. If sufficient quantitative information is not available on a company/agency web site, queries to that company/agency will often result in securing such metrics.

The theme of the first edition, namely alternative energy sources and the alternative use of existing energy sources, has been continued in the second. Chapter 16, Transportation and Hybrid and Electric Vehicles, was added because electric and hybrid vehicles offer alternatives and efficiency enhancements to conventional internal combustion engine powered vehicles. Chapter 17, Hydraulic Fracturing, Oil, Natural Gas, and the New Reality, was added because enhanced oil and gas recovery has dramatically shifted the energy posture/outlook of many countries. Every topic has been impacted by advances in technology and changes in emphasis. Examples include consideration of new installed hydroelectric capacity, significant increase in wind energy installed capacity, backlog for combustion turbine orders, growth in solar thermal usage, recognition of passive solar advantages, decreasing photovoltaic cell cost per kilowatt enhancing economic attractiveness, advances in fuel cell commercialization, combined heat and power industrial/commercial market penetration, biofuels focus areas diversity, geothermal energy successes and advances, ocean energy potential recognition, renewed interest in nuclear power, hybrid/electric vehicle sales up, and hydraulic fracturing impacts. Since the first edition, the energy concerns of the USA have to some extent diminished, but technically, politically, environmentally, and economically, energy issues, including climate change, have become more divisive. Indeed, in the year 2000 few predicted that the USA would dramatically reduce its energy imports and, perhaps, even become an energy exporting nation.

Enhanced oil and gas recovery has resulted in unexpected increases in domestic fossil fuel production and in the proved reserves of both crude oil and natural gas. However, even if enhanced oil and gas recovery were to provide, in the short term, acceptable energy resources for the USA and the rest of the world, other considerations (greenhouse gas emissions,

environmental effects, climate change, long-term availability, for example) require that alternative energy sources and alternative uses of existing resources be a part of meeting future energy requirements. Hence, the topics of this textbook are very germane for the future. *The identification of additional fossil fuel resources has essentially provided more time to discover, implement, and develop other, more sustainable and more environmentally-friendly energy resources.*

Review questions and exercises, at the end of each chapter in the first edition, are available on the companion web site for this book rather than at the end of each chapter.

I appreciate all the comments, corrections, and suggestions for the first edition received from colleagues. The corrections were implemented and the comments and suggestions considered for the second edition.

Additionally, thanks are due to Professors Tejas S. Pandya, Paul Stewart, Sangaraju Shanmugam, Samuel Sih, Xianchang Li and Alison Subiantoro who reviewed the manuscript; their comments were insightful and helpful.

B.K. Hodge
Mississippi State University
January 2017

Preface to the First Edition

In recent years much has been made of the impact of the myriad energy problems faced not only by the United States, but also the rest of the world. These impacts range from energy security issues (the dependence on imported energy sources) to economic issues (gasoline reached $4.00/gallon in the summer of 2008) to energy sustainability issues (minimum environmental and ecological impacts). Many in the engineering, corporate, and political communities advocate greater reliance on alternative energy sources. Because of the increased interests in such topics, a number of books on subjects ranging from sustainable energy to renewable energy to alternative energy have been offered in recent years. However, many of these books contain mostly qualitative information with little in the way of quantitative information or "engineering" calculations or procedures. Some also advocate specific alternative energy scenarios and some do not present balanced discussions. This textbook was written to address the above concerns.

Alternative Energy Systems and Applications is suitable for use at the senior or beginning graduate level for students in mechanical engineering or in energy-engineering related fields. Familiarity with the basic concepts of fluid mechanics, thermodynamics, and heat transfer is presumed in the development of the topics in the book, but maturity in these subjects is not needed in order to understand the developments.

The title, *Alternative Energy Systems and Applications*, is used to convey the idea that the topics covered encompass both alternative energy sources and alternative uses of existing energy sources. The solution to the current energy dilemma will contain features of both. The breadth of topics proposed for the book is delineated in the chapter headings. Chapter 1 critically examines energy usage in the United States. Although not explicitly subdivided into congruent topical areas, Chapters 2–5 treat turbomachine-based topics (hydro, wind, and combustion turbines), Chapters 6–9 consider solar-based topics (active, passive, and photovoltaic), Chapters 10–11 examine fuel cells and CHP (combined heating and power) applications, and Chapters 12–15 complete the review of alternative energy concepts (biomass, geothermal, ocean, and nuclear).

All chapters except chapter 1 broadly fit into one of two categories—(1) a review of the background information necessary for a topic or (2) an exploration of an alternative energy source or an alternative use of an existing energy source. Chapters 2 and 6, for example, are used to review the backgrounds necessary for turbomachines and solar energy, respectively.

Often alternative energy topics are equated to renewable energy resource discussions. In this book, Chapters 3–4 and 7–9 consider topics usually associated with renewable energy resources.The chapters dealing with renewable energy topics present the physical principles involved in harvesting the renewable, review (in most cases) the amount of the renewable resource available, examine quantitative aspects of the harvesting, point out difficulties with utilizing the renewable resource, discuss limitations and economics aspects, and provide, if applicable, examples of commercial systems for harvesting the renewable. Where appropriate, website addresses are cited.

The chapters addressing alternative uses of existing energy sources are focused on applications. Combustion turbines, fuel cells, and CHP systems represent alternative uses of existing energy sources.The application chapters basically discuss the operation, the thermodynamic aspects, and the expected efficiencies of such systems and provide examples. As with the renewable energy topics, suitable websites are referenced.

All chapters, except Chapter 1, contain worked examples and review questions and exercise problems. The focus is on first-order engineering calculations. Mathcad® is used as the computational software system throughout the book. However, the examples/problems are fundamental, and many other computational systems (MATLAB®, EES, Mathematica®) could be readily adopted for use with little effort. The intent of the book is to provide students with a quantitative approach to alternative energy sources and alternate applications of existing energy sources. Since this is a survey textbook, it does not attempt to provide detailed engineering information on the topics discussed, but references are provided that do contain detailed engineering information.

This textbook is the outgrowth of several years of teaching ME 4353/6353 Alternate Energy Sources in the Bagley College of Engineering at Mississippi State University. The discretionary funds provided to me as holder of the Tennessee Valley Authority Professorship in Energy Systems and the Environment at Mississippi State University were very helpful in this endeavor and are acknowledged. Additionally, thanks are due to Professors Francis Kulacki, James Mathias, and David Ruzic who reviewed the manuscript.Their comments and insights were quite useful.

B. K. Hodge
Mississippi State University
January 2009

About the Companion Website

Alternative Energy Systems and Applications Second Edition is accompanied by a companion website:

www.wiley.com\go\Hodge\AESystemsandApplications2E

The website includes:

- Solutions manual

1

Energy Usage in the USA and the World

1.1 Energy and Power

A review of the customary units used for energy and power is appropriate to initiate a study of alternative energy sources and applications. Although much of the world uses the SI system (Le Système International d'Unités), the USA, in addition to the SI system, also uses the English Engineering and the British Gravitational systems of units. The unit of energy in the SI system is the newton meter (N m) which is defined as the joule (J). Energy in the English Engineering system is defined as the British thermal unit (Btu), or alternately, the foot-pound force (ft lbf); the conversion factor is 1 Btu = 778.16 ft lbf. Power is the rate of energy usage or transfer, in joules per second, British thermal units per second, or foot-pound force per second. Power expressed in joules per second is defined as the watt (W). The most frequently used power unit is 1000 W or 1 kW. In the USA, power is sometimes expressed in terms of horsepower (hp), where 1 hp is 550 ft lbf/s or 0.7457 kW. The kilowatt-hour (kW h) is a frequently used unit of energy and represents an energy rate (kilowatts) times a time (hour). The conversion is 3412.14 Btu = 1 kW h. Anyone engaged in an energy engineering activity needs to remember the conversion between British thermal units and kilowatt-hours; in most instances 3412 Btu = 1 kW h is used.

Tester *et al.* (2012) provide a sampling of power expended for various activities. Some of their results are reproduced as Table 1.1.

The range of power expended is astonishing, about nine orders of magnitude. The entries of Table 1.1 indicate various levels of power expended referenced to everyday experiences and can be used to establish a sense of numeracy for power magnitudes.

1.2 Energy Usage and Standard of Living

An irrefutable fact is that developed countries (e.g., USA, Japan, UK) use more energy per capita than less-developed countries (e.g., Mexico, Indonesia). Figure 1.1 graphically presents the HDI (Human Development Index) as a function of the kilograms of oil equivalent (kgoe) per capita per year. The HDI is a measure of the standard of living, and the kilograms of oil equivalent per capita per year is indicative of the energy consumption. The industrialized nations have HDI values in excess of 0.9, while many of the developing countries' HDI values are dramatically less. The correlation between HDI and kilowatt-hour usage is functionally very strong. However, once a threshold of about 3000 kgoe per capita is reached, further increases in electricity usage do not produce a higher HDI. Iceland has the highest HDI, followed by the USA. Some countries with the higher kilowatt-hour usage have large infrastructure length scales and traditions of abundant energy. One of the main themes from Golemberg and Johansson (2004) is that the only way to increase the HDI in developing nations is to increase their energy usage.

Alternative Energy Systems and Applications, Second Edition. B. K. Hodge.

Companion website: www.wiley.com\go\Hodge\AESystemsandApplications2E

Table 1.1 Power expended for various activities.

Activity	Power expended
Pumping human heart	$1.5\ \text{W} = 1.5 \times 10^{-3}\ \text{kW}$
Household light bulb	$100\ \text{W} = 0.1\ \text{kW}$
Human, hard work	0.1 kW
Draft horse	1 kW
Portable floor heater	1.5 kW
Compact automobile	100 kW
SUV	160 kW
Combustion turbine	$5000\ \text{kW} = 5\ \text{MW}$
Large ocean liner	$200\,000\ \text{kW} = 200\ \text{MW} = 0.2\ \text{GW}$
Boeing 747 at cruise	$250\,000\ \text{kW} = 250\ \text{MW} = 0.25\ \text{GW}$
Coal-fired power plant	$1 \times 10^6\ \text{kW} = 1000\ \text{MW} = 1\ \text{GW}$
Niagara Falls hydroelectric plant	$2 \times 10^6\ \text{kW} = 2000\ \text{MW} = 2\ \text{GW}$

An alternative approach is to examine the gross national product (GNP) per capita as a function of the energy consumption per capita. Figure 1.2a was developed using World Bank information from 1992. Figure 1.2b was developed from more recent World Bank data. The more recent data were mostly from 2012–2013, although data from some developing countries were less recent.

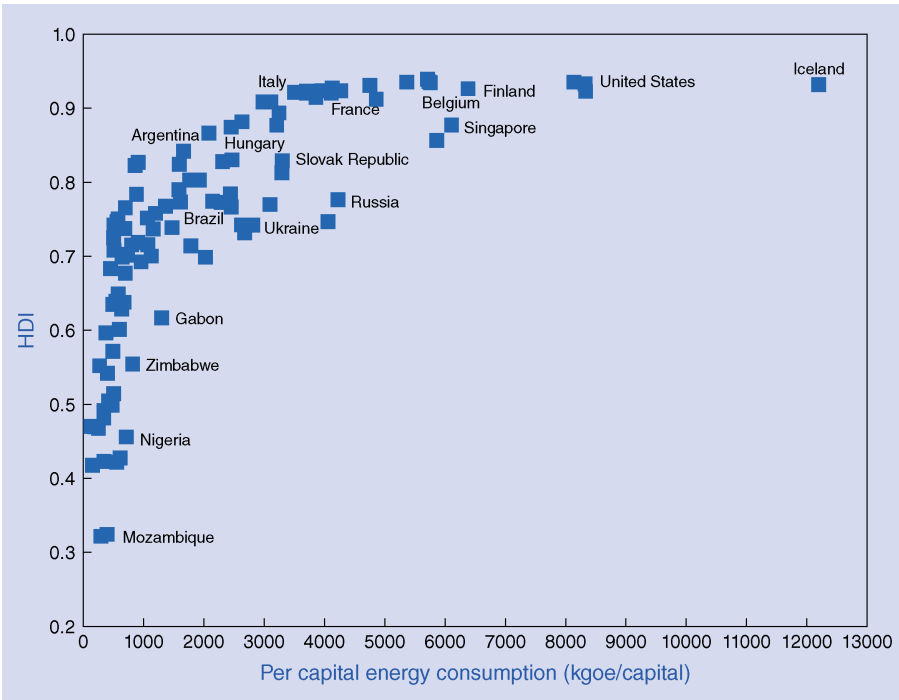

Figure 1.1 Human Development Index (HDI) as a function of per capita kilowatt-hour consumption. *Source:* Golemberg and Johansson (2004). Reproduced with permission of UNDP.

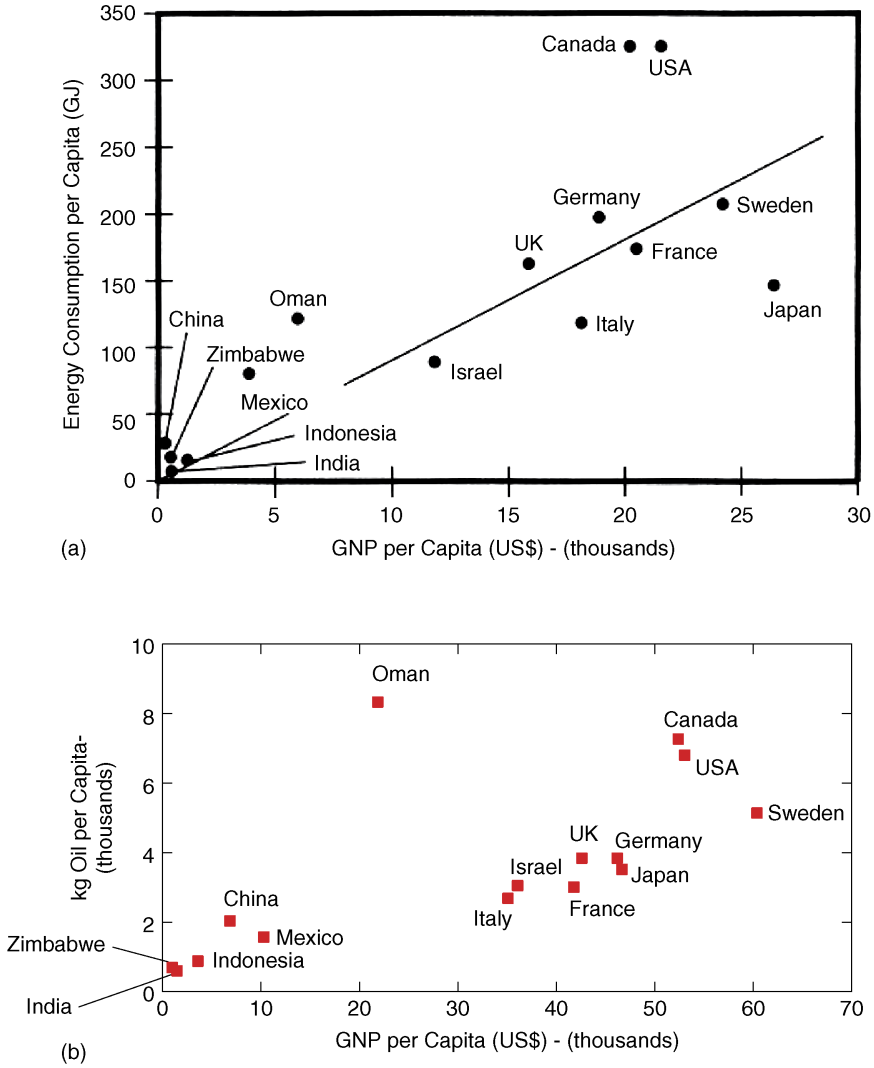

Figure 1.2 Per capita energy consumption versus GNP per capita for a number of countries. (a) 1992 World Bank data. *Source:* Tester *et al.* (2005). (b) Recent World Bank data (www.worldbank.org, 2012–2013).

The energy usage per capita information from the World Bank is presented in kilograms of oil equivalent per capita; hence, the ordinates for Figure 1.2a and b are in different energy units and the abscissas, in dollars, are not adjusted for inflation. A comparison of Figure 1.2a and b reveals no significant differences in relative positions for the developed countries, but China has made real gains in GNP per capita since the 1992 data, and, as expected, the energy use per capita has increased relative to other developing countries since 1992. In Figures 1.1 and 1.2, the USA exhibits per capita kilowatt-hours and energy usages that are large even for developed countries. A number of reasons exist for the high energy consumption per capita in the USA; among them are (1) historically cheap energy, (2) low population density, (3) large area (large infrastructure length scale), and (4) historically an abundance of domestic energy.

Starting with the first "energy crisis" of the late 1970s, low energy costs and domestic energy abundance seemingly vanished from the USA. From the 1970s through to about 2005, the USA required increasing energy imports (chiefly in the form of petroleum) and nearly

monotonic energy cost price escalations. The dependence on energy imports dramatically affected both the economy and the foreign policy posture of the USA. Indeed, the basis of the first edition of this textbook was the need to consider both alternative energy sources and alternative (read more efficient utilization) energy applications to address the energy problems faced in the USA. Since about 2005, increased domestic production of fossil fuels (by enhanced oil recovery via "hydraulic fracturing") and identification of heretofore undiscovered natural gas reserves have altered the expected increases in both energy imports and energy prices. In effect, the US energy economy is being given another chance to reduce energy cost economic impacts via enhanced energy efficiency of existing resources. Chapter 17 examines this topic.

The energy problems in the USA are exacerbated by the demand and expectation of countries (e.g., India and China) to increase the standard of living for their citizens. World energy consumption is rising faster than energy consumption in the USA. Section 1.5 examines world energy consumption patterns.

1.3 A Historical Perspective of Energy Usage in the USA

The Energy Information Administration (EIA) of the US Department of Energy provides a readily accessible and up-to-date source of energy statistics. The EIA web site is www.eia.doe.gov. The EIA provides on a timely basis monthly and yearly energy statistics for the USA. These monthly energy statistics are available in the *Monthly Energy Review* (MER), and a yearly energy summary appears in the *Annual Energy Review* (AER) about 8 months after the end of the calendar year and can be accessed from www.eia.doe.gov/aer. As of 2012, the AER has been suspended because of budget concerns. The suspension of the AER is quite unfortunate as it was arguably the most useful of the EIA periodic documents. The basis for the information contained herein is from the MERs available online at www.eia.gov/totalenergy/data/monthly/.

Figure 1.3, a mosaic of satellite photographs at night of the USA, is a rather dramatic illustration of the population density and dispersion of the population of the USA as well as the energy intensity distribution of night lighting (primarily electricity usage).

Figure 1.3 Mosaic of night satellite photographs of the USA. *Source:* EIA.

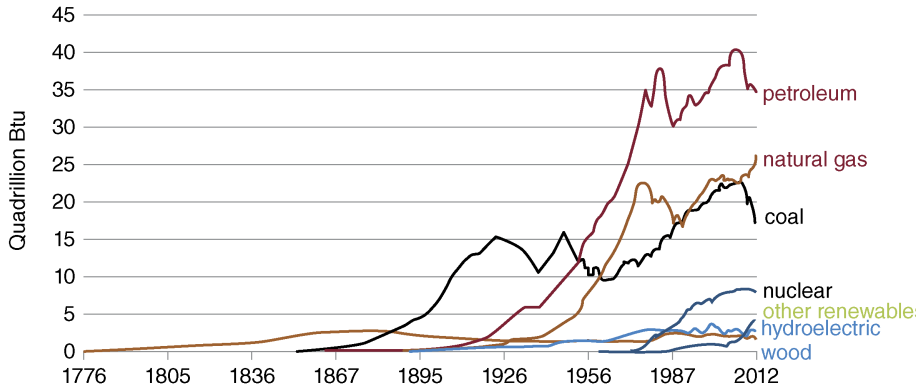

Figure 1.4 Historical energy utilization in the USA (1775–2012). *Source:* EIA.

Consider how the USA arrived at its current energy economy. Figure 1.4, taken from the EIA data, presents a graphical representation of the historical energy utilization. The energy usage unit used is the quad (quadrillion Btu is 10^{15} Btu). Until the mid-1800s, energy utilization was mostly wood, with coal becoming increasingly important after 1850. By 1900, coal usage was much greater than wood, and petroleum was becoming more important as an energy source. And in 1950, petroleum usage exceeded coal usage, and natural gas usage was dramatically rising. At the millennium, petroleum provided the most energy, with natural gas and coal vying for second and third place. Nuclear power was in fourth place, with hydroelectric and renewable energy (including wood) sources making the smallest contributions. Details of the energy utilization in 2014 will be explored in Section 1.4.

The genesis of the energy problem is illustrated in Figure 1.5. Until about 1950, the USA had little dependence on energy imports. However, with the post-World War II prosperity, energy exports began to increase since consumption increased faster than domestic production. From the 1980s to the early 2000s, domestic production increased, but at a rate slower than consumption increased. The result has been a steady increase in energy imports. However, starting about 2005, as demonstrated in Figure 1.6, the result of enhanced domestic production has resulted in a significant decrease in energy-related imports. Much of the increased

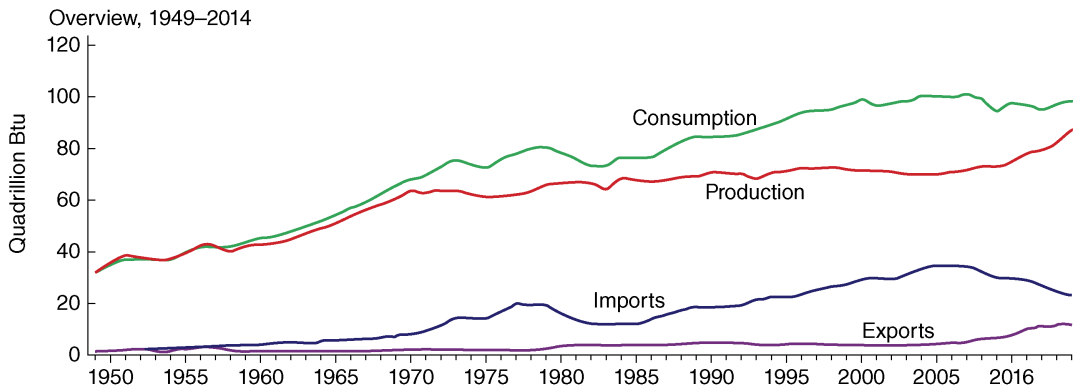

Figure 1.5 Energy consumption, imports, and exports for the USA. *Source:* EIA.

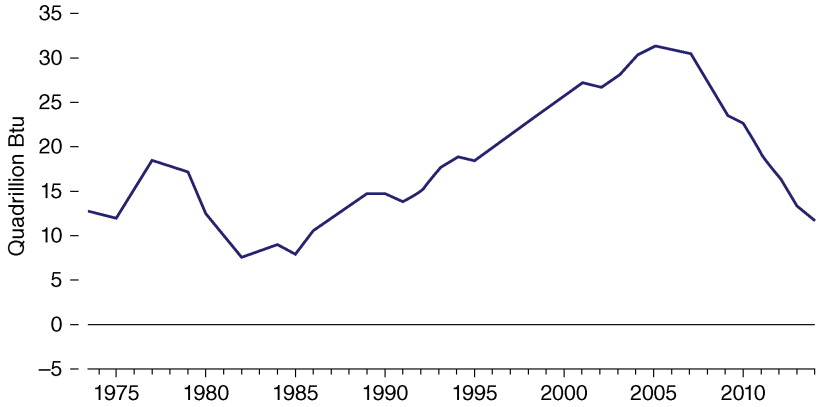

Figure 1.6 Energy imports since 1975. *Source:* EIA.

production has resulted from enhanced oil production from existing oil fields using hydraulic fracturing techniques (see Chapter 17).

Further understanding of how the USA arrived at the current energy consumption is provided in Figures 1.7 and 1.8. Figure 1.7 tracks the per capita energy consumption. Per capita energy consumption reached 344×10^6 Btu/person in 1980, decreased until 1985, and reached a peak at 346×10^6 Btu/person in 1995. Much of the behavior during the 1970s and 1980s was the response to the first "energy crisis." Since 2005, the energy usage per capita has decreased, with the result that in 2014 the per capita energy consumption was 309×10^6 Btu/person. The 1970s energy crisis resulted in no dramatic decrease in per capita energy consumption in the USA; these results explain, in part, the current energy dilemma of the USA. In short, the USA failed to understand and heed the warnings of the first energy crisis. The energy usage per dollar of gross domestic product (GDP) is presented in Figure 1.8. Since the 1980s, the energy consumed per dollar of GDP has meaningfully declined from near 12 000 Btu/$GDP to the current value of 6120 Btu/$GDP (per chained 2009 dollar). Chained dollars are dollars that are adjusted to reflect inflation, "chained" to a base year (2009 in this case). This decline is attributed to increased energy efficiency, especially in manufacturing, and to structural changes (the migration of much energy-intensive industry to other countries) in the economy.

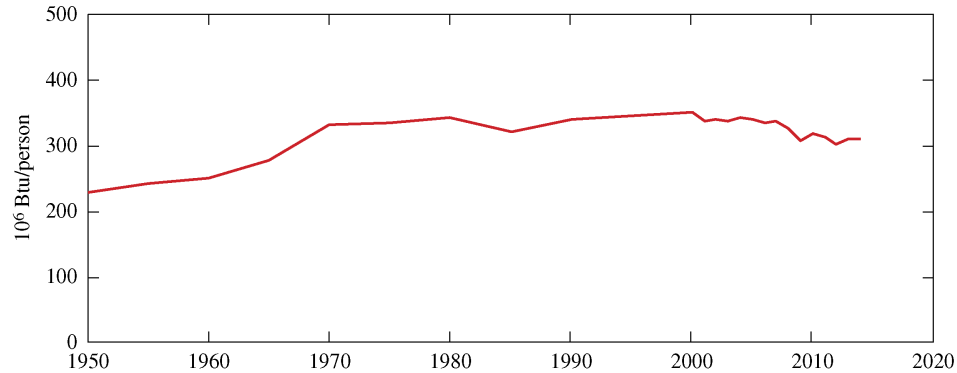

Figure 1.7 Historical per capita energy consumption in the USA. *Source:* EIA.

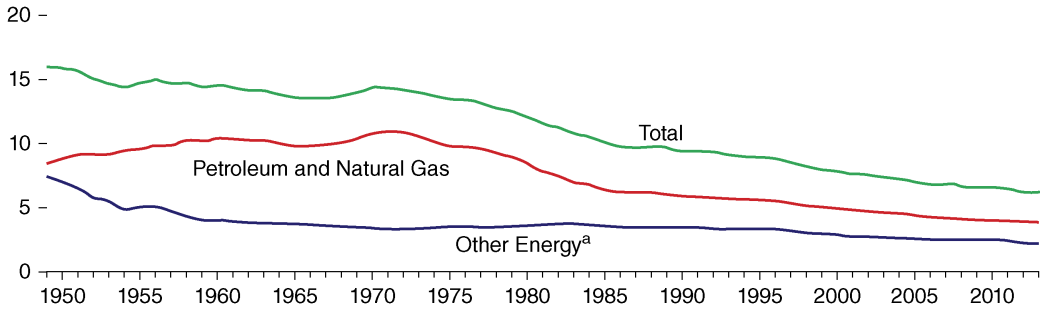

Figure 1.8 Energy consumption per real dollar of GDP. *Source:* EIA.

1.4 US Energy Usage in 2014

The EIA energy flow diagram for 2014, from the EIA Total Energy (EIA, 2015), is arguably the most informative graphical representation provided by the EIA and is reproduced as Figure 1.9. In this figure, all energy usages are in quads (10^{15} Btu). Energy sources are delineated on the left-hand side of the diagram (e.g., coal at 20.26 quad). The sources are then summed and expressed as domestic production (87.04 quad) and imports (23.31 quad). The total supply is 110.55 quad with exports of 12.22 quad, which yields 98.32 quad for consumption. The end-point energy usages (categorized as residential, commercial, industrial, and transportation) are shown on the right-hand side of the figure. Thus, in 2014, the US energy economy was 98.32 quad of which 23.31 quad was imported. A different perspective of the energy flow diagram is presented in Figure 1.10, which delineates the connection between energy sources and end-point energy usages expressed in two different ways: in Figure 1.10a as "transportation," "industrial," "residential and commercial," and "electric power," and in Figure 1.10b as the more conventional four, "transportation," "industrial," "residential," and "commercial." The conventional four end-point energy usages are displayed on a pie chart in Figure 1.11b. Industrial usage accounts for 32% of the total energy used, followed by 28% for transportation. The remainder is almost evenly split between residential and commercial. Since the energy used by no end-use sector is dominant, alternative sources and applications are needed for all end-use sectors if significant reductions in energy uses are to be forthcoming. Figure 1.10a is especially interesting since it directly connects, with percentages indicated, energy sources and end-point energy usages. Mastery of the information in Figures 1.9 and 1.10 is necessary if energy usage in the USA is to be completely understood.

In 2014, renewable energy from all sources contributed about 10% of the total energy utilized in the USA. Figure 1.11 itemizes the percentage contribution of renewable energy sources in the USA for 2014. Perhaps the most amazing statistic is that wood and conventional hydroelectric power accounted for 49% of the total renewable energy that year! Solar and wind contributed 22% of the total renewable energy (or about 2% of the total energy consumption) in 2014. Hence, in spite of much interest and media hype, the penetration of solar and wind energy into the energy mix has not made much progress.

Renewable energy sources have increased in recent years. Figure 1.12 illustrates the contributions of various renewable energy sources since 2000. Hydropower has fluctuated, while biomass and geothermal have exhibited slight increases. But since 2000 wind power has dramatically increased and is now the second largest renewable source after hydropower. Solar has also grown, but not nearly at the rate of wind power. Wind power and hydropower combined to contribute about 87% of the total renewable energy production (excluding

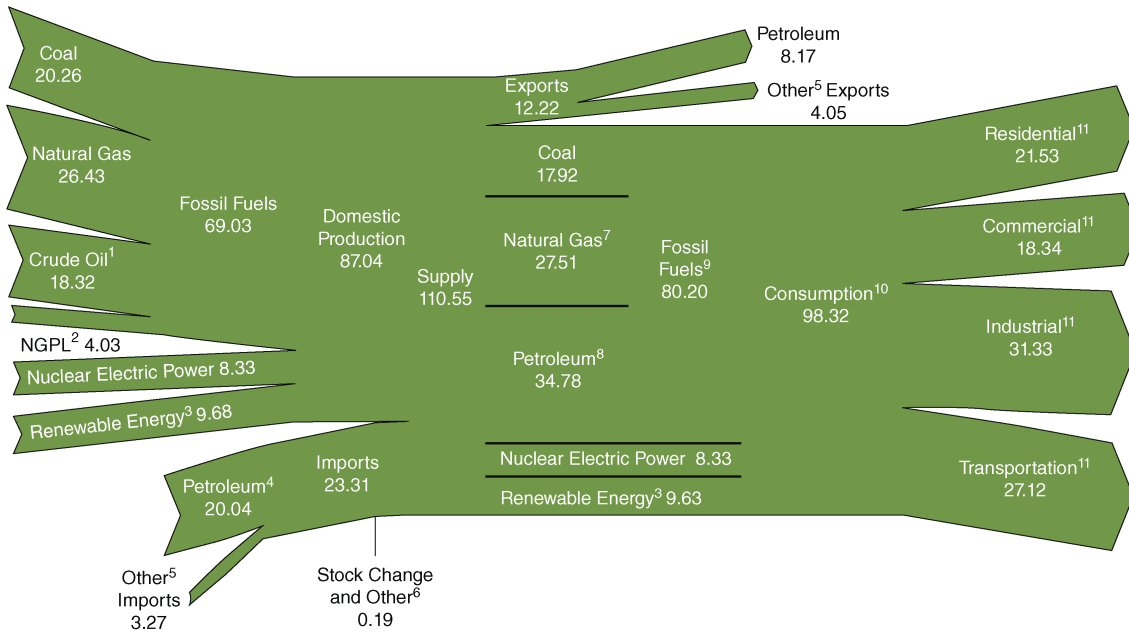

[1] Includes lease condensate.
[2] Natural gas plant liquids.
[3] Conventional hydroelectric power, biomass, geothermal, solar/photovoltaic, and wind.
[4] Crude oil and petroleum products. Includes imports into the Strategic Petroleum Reserve.
[5] Natural gas, coal, coal coke, biofuels, and electricity.
[6] Adjustments, losses, and unaccounted for.
[7] Natural gas only; excludes supplemental gaseous fuels.
[8] Petroleum products, including natural gas plant liquids, and crude oil burned as fuel.
[9] Includes –0.02 quadrillion Btu of coal coke net imports.
[10] Includes 0.16 quadrillion Btu of electricity net imports.
[11] Total energy consumption, which is the sum of primary energy consumption, electricity retail sales, and electrical system energy losses. Losses are allocated to the end-use sectors in proportion to each sector's share of total electricity retail sales. See Note 1. "Electrical Systems Energy Losses," at the end of U.S. Energy Information Administration, *Monthly Energy Review* (March 2015), Section 2.

Notes: • Data are preliminary. • Values are derived from source data prior to rounding for publication. • Totals may not equal sum of components due to independent rounding.

Sources: U.S. Energy Information Administration. *Monthly Energy Review* (March 2015), Tables 1.1, 1.2, 1.3, 1.4a, 1.4b, and 2.1.

Figure 1.9 US energy flow diagram (quadrillion Btu) for 2014. *Source:* EIA.

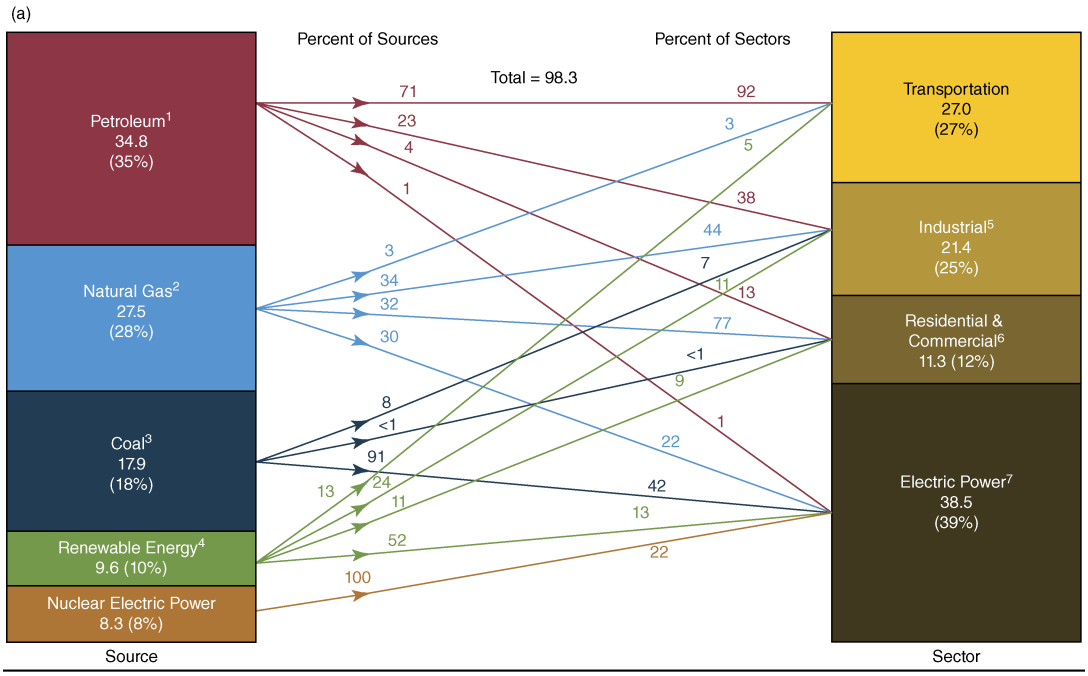

[1]Does not include biofuels that have been blended with petroleum—biofuels are included in "Renewable Energy."
[2]Excludes supplemental gaseous fuels.
[3]Includes less than –0.1 quadrillion Btu of coal coke net imports.
[4]Conventional hydroelectric power, geothermal, solar/photovoltaic, wind, and biomass.
[5]Includes industrial combined-heat-and-power (CHP) and industrial electricity-only plants.
[6]Includes commercial combined-heat-and-power (CHP) and commercial electricity-only plants.
[7]Electricity-only and combined-heat-and-power (CHP) plants whose primary business is to sell electricity, or electricity and heat, to the public. Includes 0.2 quadrillion Btu of electricity net imports not shown under "Source."

Notes: Primary energy in the form that it is first accounted for in a statistical energy balance, before any transformation to secondary or tertiary forms of energy (for example, coal is used to generate electricity). • Sum of components may not equal total due to independent rounding.

Sources: U.S. Energy Information Administration, Monthly Energy Review (March 2015), Tables 1.3, 2.1-2.6.

Figure 1.10 End-use energy utilizations in 2014. *Source:* EIA. (a) End-point energy usages (quadrillion Btu) with electric power separate. (b) End-point energy usages with electric power included in the primary four.

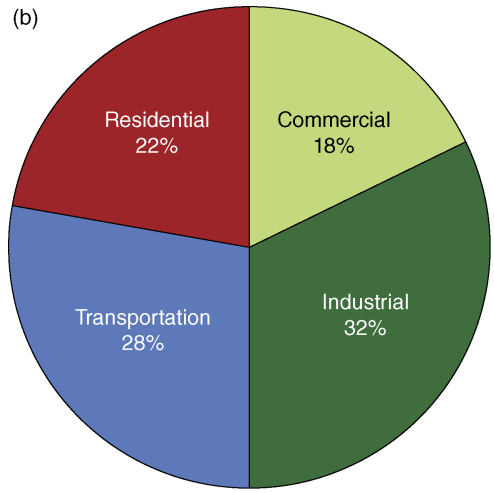

Figure 1.10 (*Continued*)

biomass) in 2014. Subsequent chapters of this book will examine in more detail hydropower, wind power, solar/photovoltaic, biomass, geothermal, and municipal solid waste as well as ocean energy, combined heat and power, and nuclear (not an alternative or renewable energy, but one that must be considered because of its potential). A very comprehensive study of electricity generated from renewable resources was developed by the National Academy of Sciences *et al.* (2010). The title of the study is *Electricity from Renewable Resources: Status, Prospects, and*

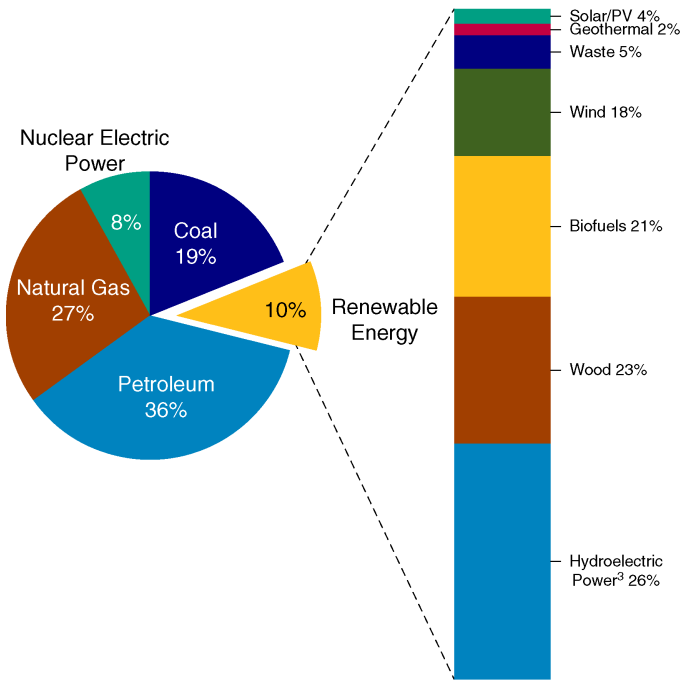

Figure 1.11 Percentage contributions of renewable energy sources in 2014. *Source:* EIA.

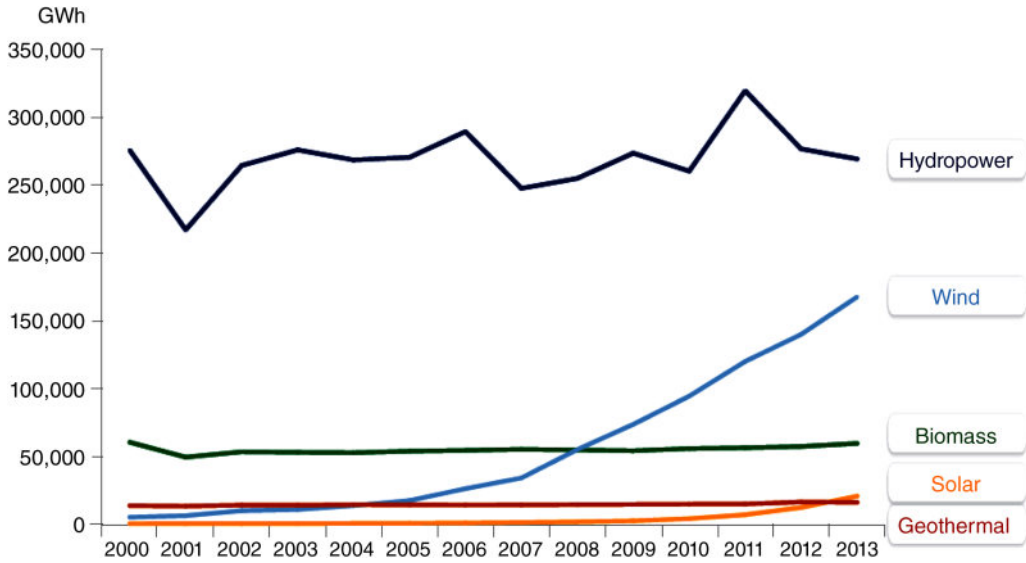

Figure 1.12 Contributions of various renewable energy resources since 2000. *Source:* Esterly and Gelman (2014).

Impediments. The report provides assessments and findings (technical, economic, environmental) for various technologies.

Every year, the Business Center for Sustainable Energy releases the Bloomberg New Energy Finance Study that contains some materials presented from federal sources, typically the EIA, but it also assesses the effects of current events and technologies on the energy scenario. This document is a complimentary, congruent source beyond the EIA. The 2016 edition is *2016 Factbook Sustainable Energy in America* and is available at http://www.bcse.org/sustainableenergyfactbook.html.

Prentiss (2015) argues that, through infrastructure changes and energy usage alternatives, the USA could develop a sustainable energy economy not based on petroleum. She recommends the use of hybrid and electric vehicles (see Chapter 16) for personal transportation and suggests that biomass (see Chapter 12) be used as source of jet fuel for aviation. Such an energy economy would be vastly different from the energy economy of 2015.

Figure 1.13 is a diagram of petroleum flow in the USA for 2014. The format of the figure is similar that of Figure 1.9 except that the numbers in the petroleum flow diagram are in millions of barrels per day (MMBD). Starting at the left-hand side, domestic crude oil production is a little less than that of the crude oil imported. The refinery output is cast in terms of motor gasoline, distillate fuel oil, liquefied petroleum, jet fuel, residual fuel oil, and "other." Motor gasoline, at 8.92 MMBD, accounted for nearly one-half of the total utilization of petroleum products in USA in 2014. The right-hand side of the petroleum flow diagram expresses the end-point petroleum energy usages. Transportation accounts for 71% of the total petroleum. Industrial usage is about 24%, with residential, commercial, and electric power generation responsible for the remaining 5%.

Transportation, the dominant end-point petroleum energy usage, warrants more examination. Much insight can be gained by tracking the cost of a gallon of motor gasoline in terms of "real" and "nominal" dollars. Real dollars are the chained dollars based on the dollar in 2000, while nominal dollars are the actual cost during a given year. Real dollars thus account for

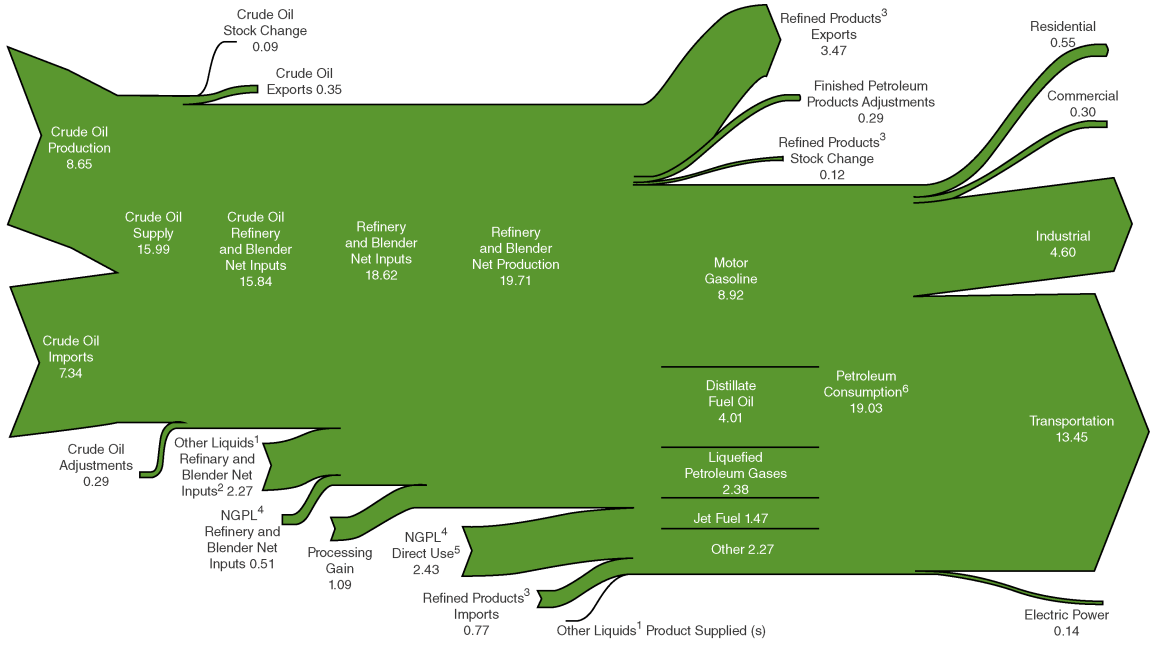

[1]Unfinished oils, hydrogen/oxygenates/renewables/other hydrocarbons, and motor gasoline and aviation gasoline blending components.
[2]Renewable fuels and oxygenate plant net production (1.071), net imports (0.752) and adjustments (0.503) minus stock change (0.059) and product supplied (–0.002).
[3]Finished petroleum products, liquefied petroleum gases, and pentanes plus.
[4]Natural gas plant liquids.
[5]Field production (2.964) and renewable fuels and oxygenate plant net production (–.020) minus refinery and blender net inputs (0.511).
[6]Petroleum products supplied.
(s)=Less than 0.005 and greater than –0.005.
Notes: • Data are preliminary. • Values are derived from source data prior to rounding for publication. • Totals may not equal sum of components due to independent rounding.
Sources: U.S. Energy Information Administration (EIA), *Monthly Energy Review* (March 2015), Tables 3.1, 3.2, 3.3b, 3.4, 3.7a-3.7c; and EIA. *Petroleum Supply Monthly* (February 2015). Table 4.

Figure 1.13 US petroleum flow diagram (million barrels per day) for 2014. *Source:* EIA.

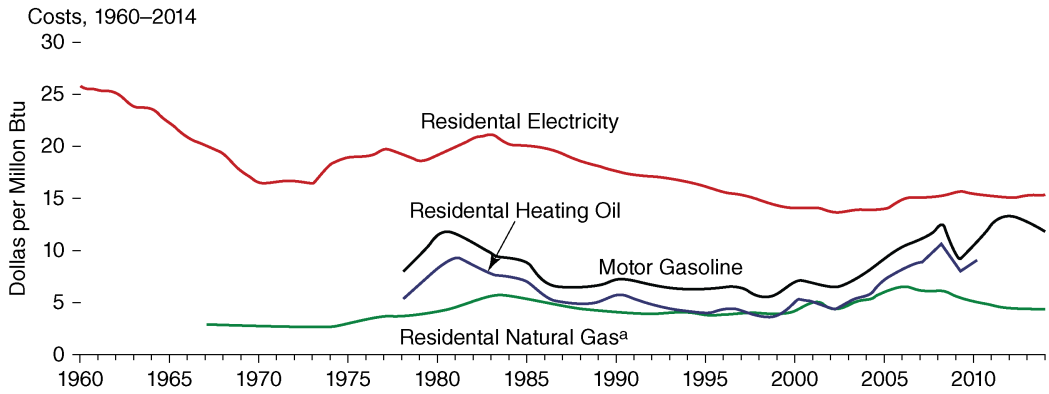

Figure 1.14 Cost of fuels in real (1982–1984) dollars. *Source:* EIA.

inflation. Figure 1.14 shows the real cost in dollars per million British thermal units of motor gasoline from 1978 to 2014. In real dollars gasoline was about $\$12/10^6$ Btu in 1980, a price not reached again until 2008. The rapid increase in gasoline prices, exceeding the inflation rate, after the year 2000 resulted in severe economic strain on the US economy in general. In recent years, the increase in domestic petroleum has reduced the price of gasoline in real dollars. During the prosperous years of the 1980s and 1990s, relative to inflation, gasoline prices declined! No wonder that conservation, higher gas mileage vehicles, and alternative sources possessed little appeal or aroused much interest in the public.

The natural gas flow for 2014 is presented in Figure 1.15. Natural gas usage in this figure is expressed in trillions of cubic feet. As with the other energy flow diagrams (Figures 1.9 and 1.13), information proceeds from the left-hand side (sources) to the right-hand side (end-point usages). Imports account for about 10% of the total consumption. Industrial usage and electric power generation account for 65% of the total natural gas utilization, with the remainder split between residential, commercial, and transportation.

The coal flow for 2014 is illustrated in Figure 1.16 and is expressed in millions of short tons. In a fashion similar to the other energy flow diagrams (Figures 1.9, 1.13, and 1.15), information proceeds from the left-hand side (sources) to the right-hand side (end-point usages). All coal is produced domestically, with a small amount exported. Virtually all of the coal usage (93%) in the USA is for the generation of electricity, with about 7% industrial end-point usage. Coal is the one energy source that does not have to be imported. However, the extensive use of coal for electric generation poses significant environmental issues. The last few years' environmental regulations pertaining to coal usage have become an important political issue in the USA. As a result, coal production and usage have declined.

Although an end-point energy use rather than an energy source, an examination of the electricity flow in the USA is appropriate. Figure 1.17 presents the electricity flow diagram for 2014; the numbers in the figure are in quads. The left-hand side delineates the input energy, including nuclear electric power. Coal is the dominant fossil fuel (64%) source of energy for electricity generation in the USA. The right-hand side of the diagram breaks down the end-point energy usages including transmission and distributions losses (about 9%). With 39.44 quad consumed to generate 14.78 quad of electricity, the overall thermal efficiency of electricity generation is 37%. Hence, of the 39.44 quad of energy used to generate electricity in the USA in 2014, 24.66 quad represents conversion losses. Hence, saving 1 kW h of electricity through conservation and energy efficiency efforts saves nearly 3 kW h equivalents of fuel! Conservation

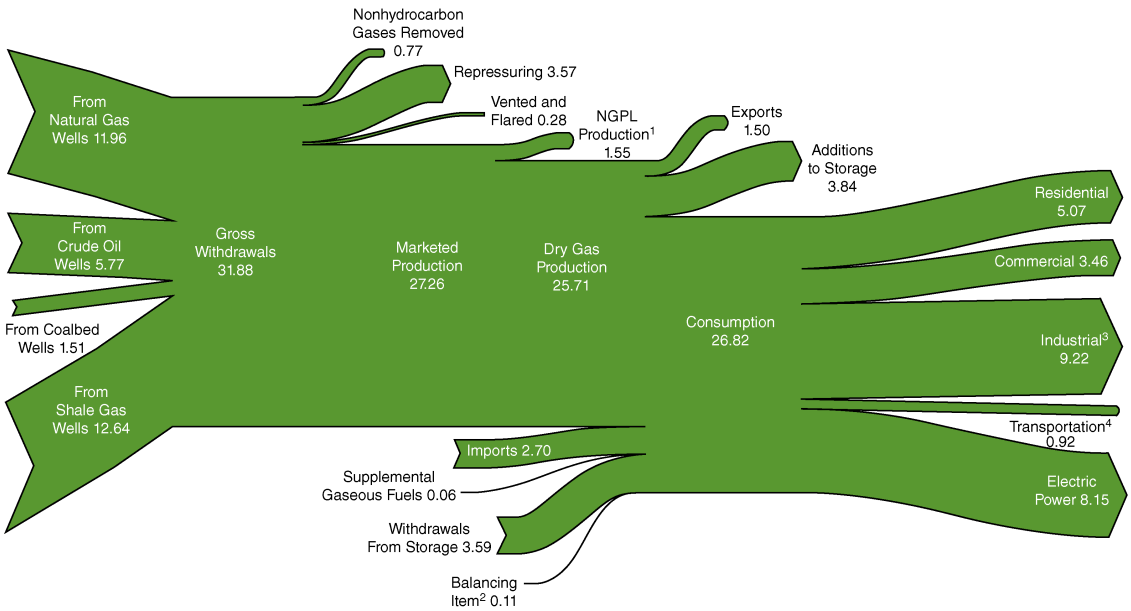

[1]Natural gas plant liquids production (NGPL), gaseous equivalent.
[2]Quantities lost and imbalances in data due to differences among data sources. Excludes transit shipments that cross the U.S.-Canada border (i.e., natural gas delivered to its destination via the other country).
[3]Lease and plant fuel, and other industrial.
[4]Natural gas consumed in the operation of pipelines (primarity in compressors) and as fuel in the delivery of natural gas to consumers, plus a small quantity used as vehicle fuel.

Notes: • Data are preliminary. • Values are derived from source data prior to rounding for publication. • Totals may not equal sum of components due to independent rounding.

Sources: U.S. Energy Information Administration (EIA). *Monthly Energy Review* (March 2015). Tables 4.1, 4.3, and 4.4; and EIA estimates based on previous year's data.

Figure 1.15 US natural gas flow diagram (trillion cubic feet) for 2014. *Source:* EIA.

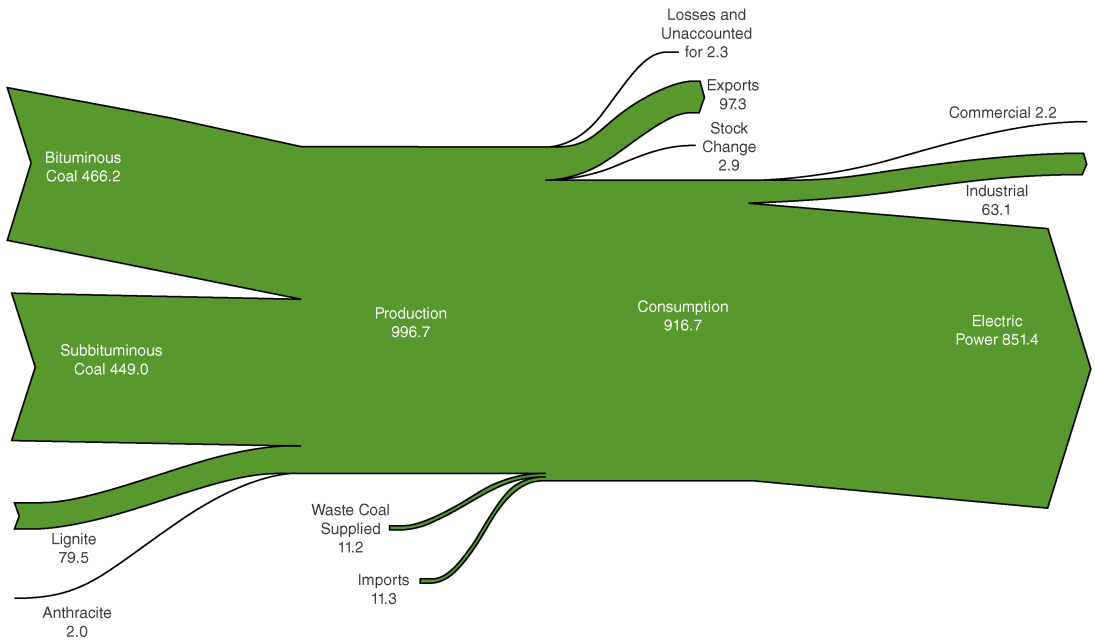

Notes: • Production categories are estimated; all data are preliminary. • Values are derived from source data prior to rounding for publication. • Totals may not equal sum of components due to independent rounding.

Sources: U.S. Energy Information Administration (EIA), *Monthly Energy Review* (March 2015). Tables 6.1 and 6.2; and EIA estimates based on U.S. Department of Labor. Mine Safety and Health Administration. Form 7000-2, "Quarterly Mine Employment and Coal Production Report."

Figure 1.16 US coal flow diagram (million short tons) for 2014. *Source:* EIA.

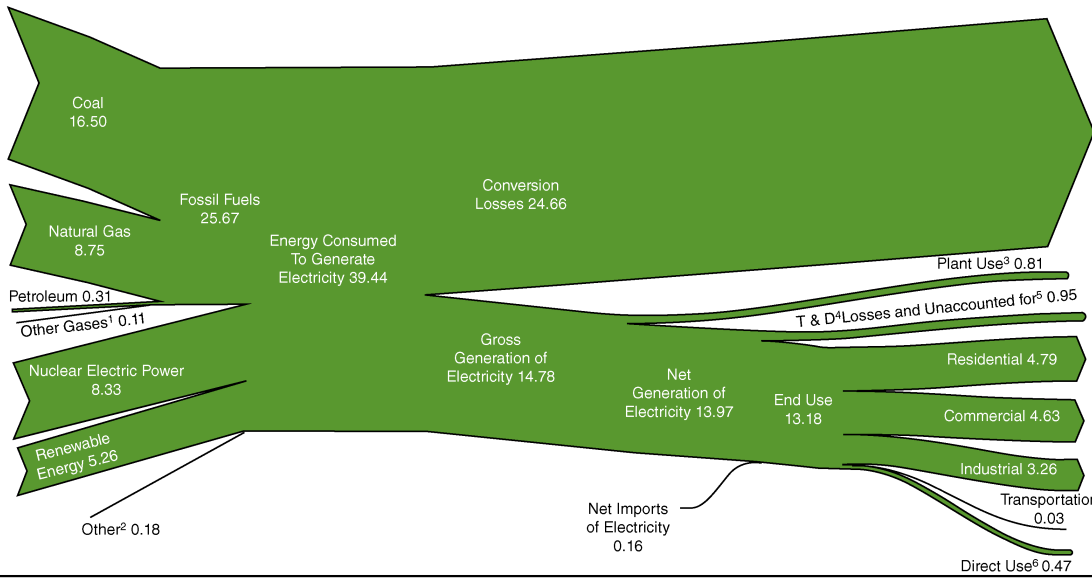

[1]Blast furnace gas and other manufactured and waste gases derived from fossil fuels.
[2]Batteries, chemicals, hydrogen, pitch, purchased steam, sulfur, miscellaneous technologies, and non-renewable waste (municipal solid waste from non-biogenic sources, and tire-derived fuels).
[3]Electric energy used in the operation of power plants.
[4]Transmission and distribution losses (electricity losses that occur between the point of generation and delivery to the customer).
[5]Data collection frame differences and nonsampling error.
[6]Use of electricity that is 1) self-generated. 2) produced by either the same entity that consumes the power or an affiliate, and 3) used in direct support of a service of industrial process located within the same facility or group of facilities that house the generating equipment. Direct use is exclusive of station use.

Notes: • Data are preliminary. • See Note 1. "Electrical System Energy Losses" at the end of EIA, *Monthly Energy Review* (March 2015), Section 2. • Net generation of electricity includes pumped storage facility production minus energy used for pumping. • Values are derived from source that prior to rounding for publication. • Totals may not equal sum of components due to independent rounding.

Sources: U.S. Energy Information Administration, *Monthly Energy Review* (March 2015). Tables 7.1, 7.2a, 7.3a, 7.6, and A6; and EIA Form EIA-923, "Power Plant Operaions Report."

Figure 1.17 US electricity flow diagram (quadrillion Btu) for 2014. *Source:* EIA.

Table 1.2 Percentage of electricity generation by energy source.

Source	Percentage
Coal	39
Natural gas	27
Nuclear	19
Hydropower	6
Other renewables	7
Biomass	1.7
Geothermal	0.4
Solar	0.4
Wind	4.4
Petroleum	1
Other gases	<1

and energy efficiency are the most cost-effective and energy-effective actions, and should always be considered first in any efforts to reduce energy costs and energy usages.

In 2015 the EIA (https://www.eia.gov/tools/faqs/faq.cfm?id=427&t=3) reported the 2014 percentage generation of electricity by energy source. As shown in Table 1.2, coal, natural gas, and nuclear were responsible for 85% of the generation.

In addition to motor gasoline prices, Figure 1.14 also tracks the real cost of electricity in dollars per million British thermal units from 1960 until 2014. Real dollars are the chained cents based on the dollar in 1982–1984. Indeed, except for a few years in the 1980s, the real cost of electricity has been less than in 1960. From 1984 until 2003, the real cost of electricity monotonically declined. As with motor gasoline, the declining real cost of electricity during the prosperous years of the 1990s, relative to inflation, provided no economic impetus for conservation or alternative sources. Now with increasing domestic production of petroleum and identification of massive natural gas reserves, the question is whether the USA can take advantage of these opportunities to increase energy efficiency and enhance use of renewable energy options and applications or whether the lessons of the 1990s will be forgotten.

1.5 Worldwide energy use

Although this chapter has concentrated on the energy scenario in the USA, an examination of energy usage on a worldwide basis will enhance understanding of the global nature of the energy problem. Figure 1.18 shows the energy utilization of the world and the counties with the most energy consumption from 1994 to 2007. Until the *Annual Energy Review 2007*, the AER contained a section on international energy usages. However, starting with the year 2008, that section was omitted. Since the AER is currently suspended, updates from this source are moot. But the 2007 information is still useful since the relative growth of the major energy-using economies is illustrated. All data are presented in quads. The increases in energy use worldwide and by China are evident in the figure. The energy usage in Russia declined slightly, and the energy used by the USA increased, but not as rapidly as the energy use by China. The energy

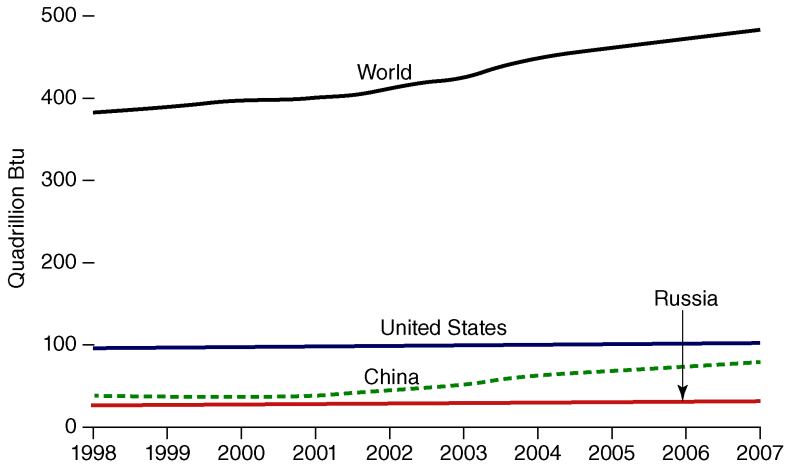

Figure 1.18 World energy utilization from 1994 to 2007. *Source:* EIA.

problems of the USA are exacerbated by the increasing demand for energy worldwide, especially in countries with rapidly expanding economies.

A good annual source of many world energy use statistics is provided by British Petroleum (BP) in the form of its *Statistical Review of World Energy* that is released in June of most years. The data presented in this chapter are from the June 2014 release. Figure 1.19 provides a convenient summary of world consumption from 1988 to 2013 broken into sources (oil, natural gas, nuclear, hydroelectric, renewable, and coal). The unit is tonnes equivalent, with each tonne representing 7.33 barrels or 307.86 gallons. Overall, the figure demonstrates the same world trend of increasing energy usage as Figure 1.18. The only decrease occurs in 2008 as a result of the economic recession; however, by 2009 the trend of increasing usage is reestablished with growth in all sources. Figure 1.20 delineates world energy consumption by region from 1988 through 2013. This figure is far more revealing than Figure 1.19 in understanding the energy usage pattern changes in the world. While North America and Europe and Eurasia demonstrate

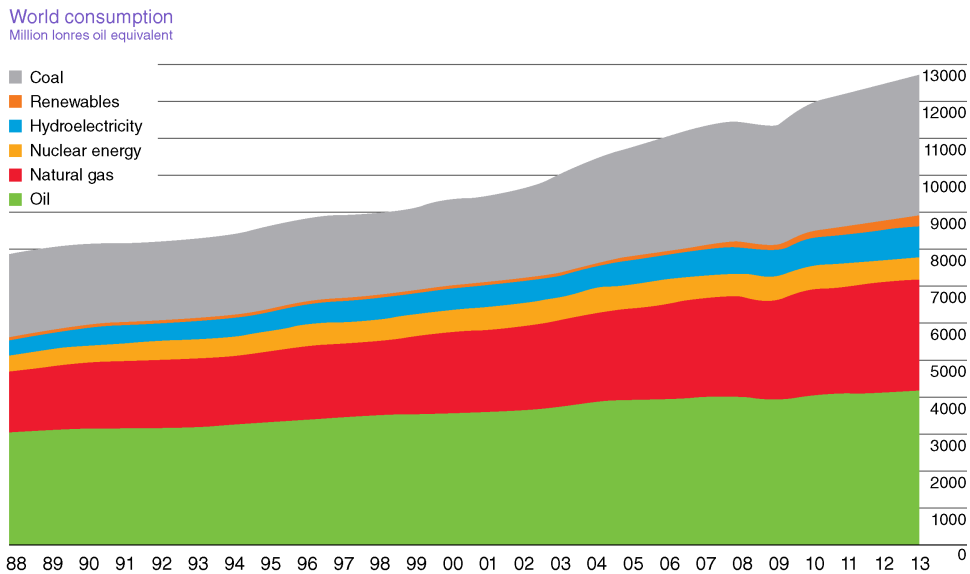

Figure 1.19 World energy consumption from 1988 to 2013. *Source:* British Petroleum (2014) *British Petroleum Statistical Review of World Energy June 2014.*

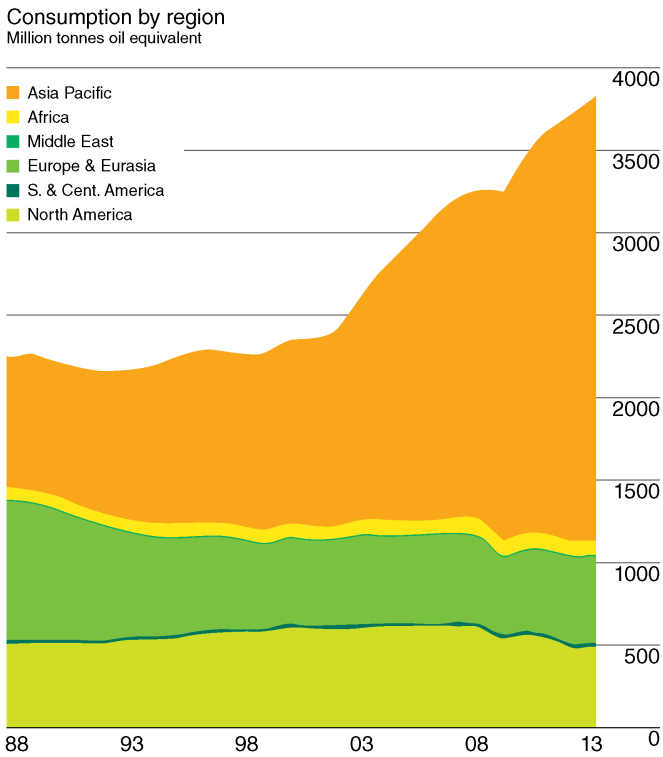

Figure 1.20 World energy consumption by region from 1988 to 2013. *Source:* British Petroleum (2014) *British Petroleum Statistical Review of World Energy June 2014*.

slight declines during the years approaching 2013, Asia Pacific usage effectively doubled from 2005 to 2013! Continued increases in energy consumption of this magnitude will place severe strain on the world oil supply. Indeed, if not for enhanced oil recovery and the discovery of significant additional natural gas reserves in the USA, fossil fuel prices would greatly exceed the current pricing structure. The implication for carbon dioxide production is even more troubling. North America uses about 25% of the world's energy, but because of environmental concerns produces much less than 25% of the world's CO_2. The Asia Pacific region, as evidenced by Figure 1.20, will in the near future consume significantly more energy than North America, but the CO_2 will dwarf the CO_2 output of North America because of more lax environmental regulations in the Asia Pacific region. Muller (2012) presents an interesting discussion of this issue.

1.6 Efficiencies

The usual definition of the thermal efficiency of a heat engine is

$$\eta = \frac{\text{Power}_{\text{out}}}{\text{Power}_{\text{in}}} \tag{1.1}$$

The following three consequences of the second law of thermodynamics are useful for providing limits to the efficiency of a heat engine:

1) No heat engine can be more efficient than an externally reversible engine operating between the same temperature limits.

2) All externally reversible heat engines operating between the same temperature limits have the same efficiency.
3) The efficiency of any externally reversible heat engine operating between temperatures of T_H (high temperature) and T_L (low temperature) is given by the Carnot efficiency

$$\eta_{Carnot} = \frac{T_H - T_L}{T_H} = 1 - \frac{T_L}{T_H} \tag{1.2}$$

The Carnot efficiency η_{Carnot} thus provides a bound on the maximum efficiency that could be obtained by any heat engine.

Tester *et al.* (2012) provide a useful summary of typical efficiencies for a number of components and devices associated with energy use. Table 1.3, adapted from Tester *et al.* (2012), presents the efficiency ranges for a number of energy system components, lighting

Table 1.3 Efficiencies of selected components and biological systems.

Component	Energy conversion path[a)]	Efficiency (%)
Large electric generators	m → e	98–99
Large power plant boilers	c → t	90–98
Large electric motors	e → m	90–97
Home natural gas furnaces	c → t	90–96
Dry-cell batteries	c → e	85–95
Waterwheels (overshot)	m → m	60–85
Small electric motors	e → m	60–75
Large steam turbines	t → m	40–45
Wood stoves	c → t	25–45
Large gas turbines	c → m	35–40
Diesel engines	c → m	30–35
Photovoltaic cells	r → e	20–30
Large steam engines	c → m	20–25
Internal combustion engines	c → m	15–25
Steam locomotives	c → m	3–6
Light sources		
High-pressure sodium lamps	e → r	15–20
Fluorescent lights	e → r	10–12
Incandescent light bulbs	e → r	2–5
Paraffin candles	c → r	1–2
Biological systems		
Milk production	c → c	15–20
Broiler production	c → c	10–15
Beef production	c → c	5–10
Local photosynthesis	r → c	4–5
Global photosynthesis	r → c	0.3

a) c: chemical; e: electrical; m: mechanical; r: radiant; t: thermal.

sources, and biological systems. Additionally, Table 1.3 also indicates the energy conversion path for each entry. For example, for large gas turbines the energy conversion path is chemical to mechanical (c → m) and the nominal efficiency range is 35–40%. Some large components possess efficiencies above 90%, but many widely used components (e.g., internal combustion engines) have efficiencies less than 30%. From a historical perspective, the reason for the demise of the steam locomotive is also evident.

Much of the electricity generated is used for lighting. As the data in Table 1.3 demonstrate, even the most efficient lighting source, high-pressure sodium, is only 15–20% efficient. Incandescent lighting is a woeful 2–5% efficient. Biological systems used for food production, milk or beef, for example, also exhibit low efficiencies. Locally, photosynthesis does not exceed 5% efficiency of the incident sunlight, but the global mean is much smaller.

What Table 1.3 ultimately indicates is that much engineering effort is needed to reduce energy utilization by improving efficiencies of various components.

1.7 Closure

The information contained in this chapter brings us to the purpose of this book. If we are to meet the increasing US and world energy demands, then the use of alternative energy sources and the alternative use of existing energy sources must be considered, even in light of recent changes in the US domestic energy outlook. The remaining chapters of this book examine fundamental principles and facts about a wide variety of alternative energy sources and alternative energy utilization. The level of material covered about each topic is, in most instances, fundamental. To do detailed engineering work on most topics represented in this book, additional technical information will be needed. However, the material presented herein provides an introduction and overview for the many alternative energy scenarios possible.

References

British Petroleum (2014) *British Petroleum Statistical Review of World Energy June 2014*. http://www.bp.com/content/dam/bp-country/de_de/PDFs/brochures/BP-statistical-review-of-world-energy-2014-full-report.pdf (accessed October 3, 2016).

EIA (2015) *Monthly Energy Review June 2015*. US Department of Energy, Washington, DC.

Esterly, S. and Gelman, R. (2014) *2013 Renewable Energy Data Book*, Haas, K. (ed.). US Department of Energy, Energy Efficiency and Renewable Energy, Washington, DC.

Golemberg, J. and Johansson, T.B. (eds) (2004) *World Energy Assessment: Overview 2004 Update*. United Nations Development Program, New York.

Muller, R.A. (2012) *Energy for Future Presidents: The Science behind the Headlines*, Norton, New York.

National Academy of Sciences, National Academy of Engineering, and National Research Council of the National Academies (2010) *Electricity from Renewable Resources: Status, Prospects, and Impediments*, The National Academies Press, Washington, DC. http://www.nap.edu/openbook.php?record_id=12619 (accessed October 3, 2016).

Prentiss, M. (2015) *Energy Revolution: The Physics and the Promise of Efficient Technology*. Harvard University Press, Cambridge, MA.

Tester, J.W., Drake, E.M., Driscoll, M.J., *et al.* (2005) *Sustainable Energy: Choosing among Options*. MIT Press, Cambridge, MA.

Tester, J.W., Drake, E.M., Driscoll, M.J., *et al.* (2012) *Sustainable Energy: Choosing among Options*, 2nd edn. MIT Press, Cambridge, MA.

2

Fundamentals of Turbomachinery

2.1 Definition of a turbomachine

Two of the important categories of renewable, alternative energy sources are wind energy and hydroelectric energy, and one frequently used alternative application for fossil fuels is the gas or combustion turbine. All of these devices are classed as turbomachines, and the operating principle of each is similar. The purpose of this chapter is to develop a basis understanding of and nomenclature for turbomachines. The definition of a turbomachine is a good place to start:

Turbomachine – a device in which *energy is transferred* either to, or from, a *continuously-flowing fluid* by the *action* of one or more *moving blade rows*.

The italicized words in the definition are important. Energy transfer, not energy transformation, takes place in a turbomachine. Since the fluid is continuously flowing, a turbomachine is not a positive-displacement device. The energy transfer that takes place is caused by the action of moving blade rows.

2.2 Turbomachine classifications

Turbomachines are often classified as compressors (or pumps or fans) and turbines. A compressor or pump or fan is a turbomachine in which energy is added by the fluid as the fluid traverses the rotor. In a turbine, energy is extracted from the fluid as the fluid traverses the rotor.

Another classification is based on the path of the fluid as it traverses the rotor. A turbomachine can be a radial device, an axial device, or a mixed device. As the names imply, in a radial device, the path of the fluid is in the radial direction. In an axial device, the path of the fluid is in the axial direction. And in a mixed device, the fluid path has both radial and axial components. Figure 2.1 illustrates some common turbomachines exhibiting radial, axial, or mixed characteristics. In the radial device, Figure 2.1a, the flow traverses the rotor in a predominantly radial direction; in the mixed device, Figure 2.1b, the flow traverses enters the rotor with both radial and axial components of velocity; and in the axial device, Figure 2.1c, a propeller-type turbine, axial flow is exhibited, and the flow both enters and leaves the rotor with axial velocity but little radial velocity.

2.3 Turbomachine analysis

Figure 2.2 is the control volume that will be used to develop fundamental relations for a turbomachine. The control volume is rotating at an angular velocity ω about the shaft. Face 1

Alternative Energy Systems and Applications, Second Edition. B. K. Hodge.

Companion website: www.wiley.com\go\Hodge\AESystemsandApplications2E

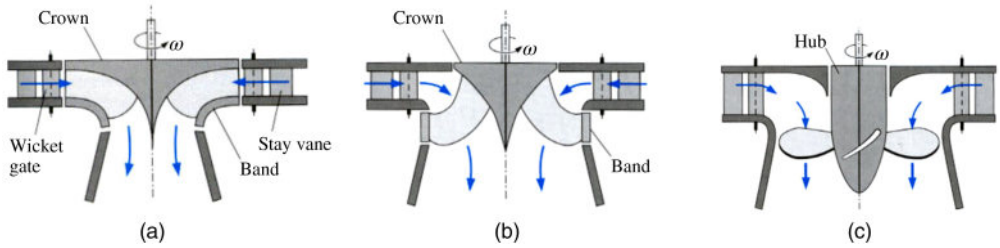

Figure 2.1 Types of turbomachines according to the fluid path: (a) radial flow; (b) mixed flow; (c) axial flow. *Source:* Cengel and Cimbala (2013). Reproduced with permission of McGraw-Hill.

represents the inlet control surface, and face 2 represents the control surface at the exit. At an arbitrary location on the inlet control surface the absolute velocity vector $\mathbf{V}_1$ is shown. $\mathbf{V}_2$ represents the absolute velocity at the exit. In this context, the absolute velocity is measured with respect to a stationary observer. The arbitrary points are located radial distances r_1 and r_2 from the axis of rotation. Three mutually perpendicular velocity components are defined: (1) V_a, the axial component, (2) V_u, the tangential component, and (3) V_m, the radial (or meridional) component. These components completely resolve the absolute velocity vectors. The components' names are also descriptive of their directions; that is, V_a is in the axial direction and is collinear with the axis of rotation. Turbomachinery analysis is greatly facilitated by using the velocity components.

Conservation of angular momentum is the fundamental principle used in analyzing a turbomachine. For a control volume, conservation of angular momentum appears as

$$\sum \mathbf{M} = \frac{\partial}{\partial t}\int_{CV} \rho(\mathbf{r}\times\mathbf{V})\,\mathrm{dVol} + \int_{CS} \rho(\mathbf{r}\times\mathbf{V})\mathbf{V}\cdot\mathbf{dA} \tag{2.1}$$

In words, Equation 2.1 states that the vector sum of moments acting on the control volume is equal to the time rate of change of angular momentum within the control volume plus the net efflux of angular momentum across the control surface. However, what is of interest for a

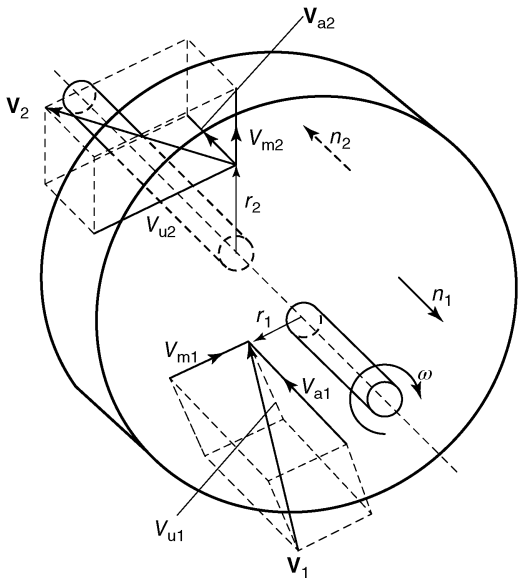

Figure 2.2 Control volume for turbomachinery analysis. *Source:* Hodge and Taylor (1999). Reproduced with permission of Pearson.

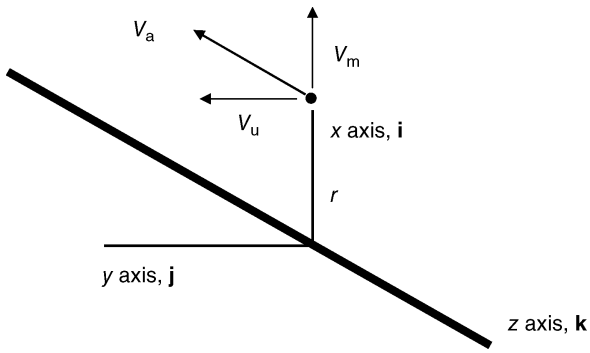

Figure 2.3 Schematic representation of the velocity components at a point.

turbomachine is the moment about the axis of rotation. Consider, as in Figure 2.3, a schematic representation of the velocity components at an arbitrary point located a distance r from the axis of rotation. The x, y, and z axes as well as the unit vectors **i**, **j**, and **k** are indicated on the figure.

The vectors **r** and **V** then become

$$\mathbf{r} = r\,\mathbf{i} \tag{2.2}$$

$$\mathbf{V} = V_m\mathbf{i} + V_u\mathbf{j} + V_a\,\mathbf{k} \tag{2.3}$$

and the cross product $\mathbf{r} \times \mathbf{V}$ is defined as

$$\mathbf{r} \times \mathbf{V} = \begin{vmatrix} \mathbf{i} & \mathbf{j} & \mathbf{k} \\ r & 0 & 0 \\ V_m & V_u & V_a \end{vmatrix} = rV_u\mathbf{k} - rV_a\mathbf{j} \tag{2.4}$$

The moment or torque of interest is that about the z-axis, the axis of rotation. As Equation 2.4 indicates the only component of the cross product that produces angular momentum about the z-axis is rV_u. Using τ as the summation of moments about the axis of rotation and invoking the steady state, conservation of angular momentum reduces to

$$\tau = \int_{CS} \rho\, rV_u \mathbf{V} \cdot \mathbf{dA} \tag{2.5}$$

For a control volume, as in Figure 2.2, with an inlet and an exit, Equation 2.5 becomes

$$\tau = -\int_{inlet} \rho\, rV_u V_a\, dA + \int_{exit} \rho\, rV_u V_a\, dA \tag{2.6}$$

Since n_1, the unit outward normal for the inlet (as indicated on Figure 2.2), is collinear with the z-axis, $\mathbf{V} \cdot \mathbf{dA}$ is equal to $-V_a\, dA$. The mean value of rV_u is defined as $\overline{rV_u}$ such that

$$\int \rho rV_u V_a\, dA = \overline{rV_u} \int \rho V_a\, dA = \dot{m}\,\overline{rV_u} \tag{2.7}$$

If the assertion is made that no flow rate bypasses the rotor, then the mass flow rates entering and leaving the rotor are the same; that is, $\dot{m} = \dot{m}_1 = \dot{m}_2$. The expression for torque about the axis of rotation takes the form

$$\tau = -\dot{m}\left(\overline{rV_u}\right)_1 + \dot{m}\left(\overline{rV_u}\right)_2 = \dot{m}\left[\left(\overline{rV_u}\right)_2 - \left(\overline{rV_u}\right)_1\right] \tag{2.8}$$

For many turbomachines, either rV_u is constant across a control surface or r and V_u are constant and the "bar" notation is dropped, so that

$$\tau = \dot{m}(r_2 V_u - r_1 V_u) \tag{2.9}$$

Equation 2.9 is called the Euler turbine (or pump) equation and is the fundamental application of conservation of angular momentum for a turbomachine. If $r_2 V_{u2} > r_1 V_{u1}$, then angular momentum is added to the flow and the device is called a pump, fan, or compressor. If $r_2 V_{u2} < r_1 V_{u1}$, then angular momentum is extracted from the flow, and the device is called a turbine. The traditional turbomachine sign convention is for torque to be positive for a turbine and negative for a pump. Thus, the usual form of Equation 2.9 becomes

$$\tau = \dot{m}(r_1 V_{u1} - r_2 V_{u2}) \tag{2.10}$$

The power is the torque times the rotation rate:

$$\text{Power} = \tau\omega = \dot{m}(\omega\, r_1 V_u - \omega\, r_2 V_{u2}) \tag{2.11}$$

But $r\omega$ is the tangential velocity of the rotor at a radius r and is assigned the symbol U in turbomachinery notation. The power is expressed as

$$\text{Power} = \dot{m}(U_1 V_{u1} - U_2 V_{u2}) \tag{2.12}$$

The "head" change is the power per unit mass flow rate or

$$\frac{\text{Power}}{\dot{m}} = H = U_1 V_{u1} - U_2 V_{u2} \tag{2.13}$$

Equation 2.13 follows the turbomachinery protocol of defining head as the energy per unit mass (or power per unit mass flow rate).

Two velocities have been introduced, the absolute velocity **V** and the tangential rotor velocity **U**. The relative velocity $\mathbf{V}_r$ is defined by the vector equation

$$\mathbf{V} = \mathbf{U} + \mathbf{V}_r \tag{2.14}$$

The graphical interpretation of Equation 2.14, the velocity triangle, is provided in Figure 2.4. Since V_u is the tangential component of the absolute velocity, V_u is identified as the projection of **V** in the direction of **U**; that is, **V**cosα.

The angle **V** makes with **U**, α, is often called the "nozzle angle." The angle $\mathbf{V}_r$ makes with **U**, β, is the blade angle since $\mathbf{V}_r$ represents the velocity with respect to the rotor.

The law of cosines for the inlet and exit velocity triangles can be written as

$$V_{r_1}^2 = U_1^2 + V_1^2 - 2U_1 V_1 \cos(\alpha_1) = U_1^2 + V_1^2 - 2U_1 V_{u_1} \tag{2.15}$$

$$V_{r_2}^2 = U_2^2 + V_2^2 - 2U_2 V_2 \cos(\alpha_2) = U_2^2 + V_2^2 - 2U_2 V_{u_2} \tag{2.16}$$

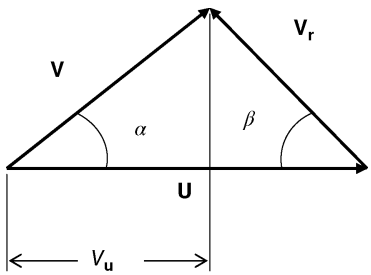

Figure 2.4 Velocity triangle.

Subtracting Equation 2.16 from Equation 2.15 and dividing by 2 yields

$$U_1 V_{u_1} - U_2 V_{u_2} = \frac{1}{2}\left[(V_1^2 - V_2^2) + (U_1^2 - U_2^2) + (V_{r_2}^2 - V_{r_1}^2)\right] = H \tag{2.17}$$

which represents the change in head across a turbomachine expressed in terms of the absolute, relative, and rotor velocities – the components of the velocity triangle.

An examination of each of the terms in the expression between the equal signs in Equation 2.17 yields some insight into energy transfer in turbomachines. Consider the following:

$$\frac{1}{2}[\underbrace{(V_1^2 - V_2^2)}_{\text{dynamic}} + \underbrace{\underbrace{(U_1^2 - U_2^2)}_{\text{centrifugal}} + \underbrace{(V_{r_2}^2 - V_{r_1}^2)}_{\text{relative}}}_{\text{static}}]$$

The first term represents the change in absolute velocity and is called the dynamic effect. The remaining two terms, the centrifugal and the relative, form the static effect. The total change in head is the sum of the static and dynamic effects. Some useful physics can be deduced from Equation 2.17 and the classification of dynamic, centrifugal, and relative. In a radial device the centrifugal effect is often dominant. For a radial-flow compressor, the head H is negative; thus, the centrifugal effects aid the energy transfer process if $U_2 > U_1$ – meaning the exit radius should be greater than the inlet radius. A turbine is just the opposite, as the centrifugal effects should be positive, meaning that the inlet radius should be larger than the exit. This principle is explored in Example 3.3.

The ratio of the static effect to the total change in head is called the reaction and is defined as

$$R = \frac{(U_1^2 - U_2^2) + (V_{r2}^2 - V_{r1}^2)}{(V_1^2 - V_2^2) + (U_1^2 - U_2^2) + (V_{r2}^2 - V_{r1}^2)} = \frac{\frac{1}{2}\left[(U_1^2 - U_2^2) + (V_{r2}^2 - V_{r1}^2)\right]}{U_1 V_{u1} - U_2 V_{u2}} \tag{2.18}$$

If the reaction R is zero, then the change in head is just due to the dynamic effect – the change in absolute velocity across the rotor. Hence, the static change in head is zero, and the rotor can be open (no casing needed). $R = 0$ devices are often referred to as impulse machines since the total head change is due only to the dynamic effect.

Axial-flow turbomachines are devices in which the fluid motion as it traverses the rotor is predominantly in the axial direction. A schematic of an axial flow compressor is shown in Figure 2.5. In an axial turbomachine with stages, rotating blade rows (rotors) are followed by stators, stationary blade rows in which energy transformation, not energy transfer, takes place. The stationary blades ahead of the first rotor are often called inlet guide vanes. For a given rotor or stator, the inlet and exit radii are essentially equal so that $r = r_1 = r_2$, $U = U_1 = U_2$, and

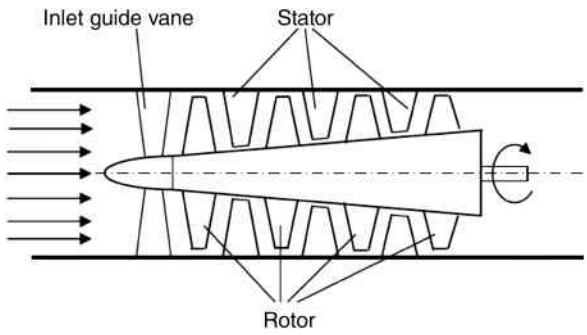

Figure 2.5 Staged axial-flow device schematic. *Source:* Logan (1993). Reproduced with permission of Pearson.

$V_a = V_{a1} = V_{a2}$. For axial flow, the expressions for torque, power, head, and reaction reduce to the following:

$$\tau = \dot{m}\, r(V_{u1} - V_{u2}) \tag{2.19}$$

$$\text{Power} = \dot{m}\, U(V_{u1} - V_{u2}) \tag{2.20}$$

$$H = U(V_{u1} - V_{u2}) \tag{2.21}$$

$$R = \frac{(V_{r2}^2 - V_{r1}^2)}{(V_1^2 - V_2^2) + (V_{r2}^2 - V_{r1}^2)} = \frac{\frac{1}{2}(V_{r2}^2 - V_{r1}^2)}{U(V_{u1} - V_{u2})} \tag{2.22}$$

2.4 Example problems

Some examples exercising the concept developed about turbomachines are in order.

Example 2.1
An axial-flow turbomachine possesses symmetrical velocity triangles as in Figure 2.6. For these conditions answer the following questions.

a) How are the velocity components related?
b) What is the reaction?
c) Is this device a turbine or a compressor? Explain.

Solution The velocity triangles in Figure 2.6 can be envisioned as appropriate for the rotor arrangement of Figure 2.2. In an axial-flow device, the radial component of velocity is by definition zero, and the planes of the velocity triangles are collinear with the axial direction. The axial velocity is then the projection of the absolute velocity perpendicular to the tangential direction. For symmetrical velocity triangles, $V_1 = V_{r2}$ and $V_{r1} = V_2$. Substituting these relations into Equation 2.22 results in

$$R = \frac{V_1^2 - V_2^2}{(V_1^2 - V_2^2) + (V_1^2 - V_2^2)} = \frac{1}{2}$$

Symmetrical velocity triangles in a axial-flow turbomachine result in a $R = 0.5$. For many gas turbines or combustion turbines with staged axial-flow compressors or turbines, a design condition is frequently $R = 0.5$.

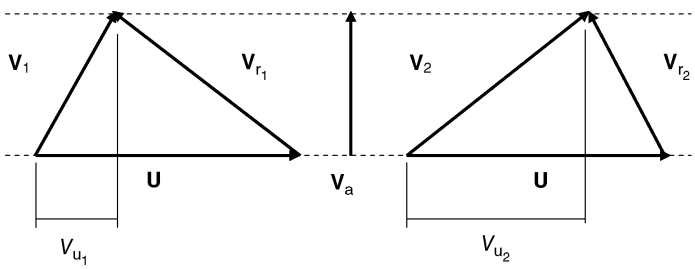

Figure 2.6 Velocity triangles for Example 2.1.

Since $r_2 V_{u2} \geq r_1 V_{u1}$ the device is a compressor (or pump) because the angular momentum is increased as the fluid traverses the rotor; that is, energy is added to the fluid.

Although given as part of the problem statement, the first step in solving any turbomachinery problem is to construct the velocity triangles. We consider a more complex problem next.

Example 2.2

A centrifugal-flow turbomachine has the relative velocity components as indicated in Figure 2.7. Additionally, the following are specified:

$$U_1 = r_1 \omega = 3.75 \text{ m/s}$$

$$U_2 = r_2 \omega = 7.50 \text{ m/s}$$

$$\dot{m} = 57 \text{ kg/s}$$

Determine the power, classify the device as a turbine or compressor, and find the reaction.

Solution The first step is to complete the velocity triangles. Consider the inlet velocity triangle. The values of U_1 and V_{r1}, as well as that V_{r1} is radial, are known. Three pieces of information must be known in order to uniquely specify a velocity triangle. The inlet velocity triangle is a right triangle, and is, thus, completely specified by the angle and the two velocity components. Likewise, two velocity components (U_2 and V_{r2}) as well as an angle are known about the exit velocity triangle. Since $V_{r2} \cos(30.45) = 7.5 \text{ m/s} = U_2$, the exit velocity triangle is also a right triangle. The velocity triangles appear as in Figure 2.8.

The velocity triangles must obey the vector expression $\mathbf{V} = \mathbf{U} + \mathbf{V}_r$. Since V_2 is perpendicular to U_2, $V_{u2} = 0$; and with V_{r1} perpendicular to U_1, $V_{u1} = U_1$. The power can be computed as

$$\text{Power} = \dot{m}(U_1 V_{u1} - U_2 V_{u2}) = \dot{m}(U_1 U_1 - U_2 \times 0) = \dot{m}\, U_1^2$$

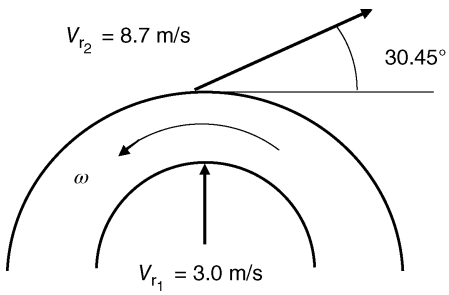

Figure 2.7 Schematic for Example 5.2.

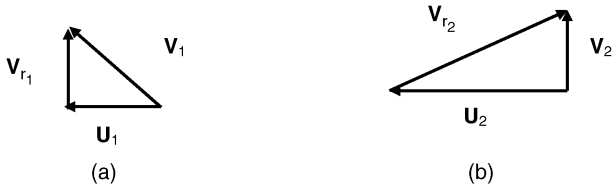

Figure 2.8 Velocity triangles for Example 2.2: (a) inlet; (b) exit.

With numbers and units included, the power becomes

$$\text{Power} = 57\frac{\text{kg}}{\text{s}}\left(3.75\frac{\text{m}}{\text{s}}\right)^2 = 802\frac{\text{kg m}^2}{\text{s}^3}\frac{\text{N s}^2}{\text{kg m}} = 802\frac{\text{N m}}{\text{s}} = 802\frac{\text{J}}{\text{s}} = 802\ \text{W}$$

The device is a turbine since $r_1 \cdot V_{u1} > r_2 \cdot V_{u2}$. With U and V_r known for both velocity triangles, the absolute velocities can be computed and are $V_1 = 4.80$ m/s and $V_2 = 4.41$ m/s. An alternative, but illuminating, approach to computing the power is use an extension of Equation 2.17 for the power:

$$\text{Power} = \dot{m}H = \frac{\dot{m}}{2}\left[(V_1^2 - V_2^2) + (U_1^2 - U_2^2) + (V_{r2}^2 - V_{r1}^2)\right]$$

which becomes for the example

$$\begin{aligned}\text{Power} &= \dot{m}H = \frac{57}{2}\frac{\text{kg}}{\text{s}}\left[(4.8^2 - 4.41^2) + (3.75^2 - 7.5^2) + (8.7^2 - 3^2)\right]\frac{\text{m}^2}{\text{s}^2} \\ &= 28.5(3.59 - 42.2 + 66.7)\text{W} = 802\ \text{W}\end{aligned}$$

Since the power from a turbine is positive, the dynamic contribution and the relative velocity contribution are positive, but the centrifugal effect is negative and reduces the power extracted from the fluid. This device is a radial outflow turbine that must overcome the negative contribution of the centrifugal effect in order to extract power. As discussed earlier, a radial inflow turbine would take advantage of the centrifugal effect.

With the velocity components known, the reaction R can be calculated directly as

$$\begin{aligned}R &= \frac{(U_1^2 - U_2^2) + (V_{r2}^2 - V_{r1}^2)}{(V_1^2 - V_2^2) + (U_1^2 - U_2^2) + (V_{r2}^2 - V_{r1}^2)} \\ &= \frac{(3.75^2 - 7.5^2) + (8.7^2 - 3^2)}{(4.8^2 - 4.41^2) + (3.75^2 - 7.5^2) + (8.7^2 - 3^2)} = 0.87\end{aligned}$$

With little change in the absolute velocity, the dynamics effect is small. This value of R shows that in spite of the relative and centrifugal effects acting opposite, the static change is the dominant effect in this device.

Example 2.3

A schematic of a radial flow turbomachine is illustrated in Figure 2.9.

The inlet velocity, $V_1 = 18$ m/s, makes a 30° angle with the tangential, and the exit velocity V_2 makes a 90° angle with the tangential. The blade (rotor) width is constant at 90 mm. The rotor is rotating at 764 rpm. Rotation is counterclockwise.

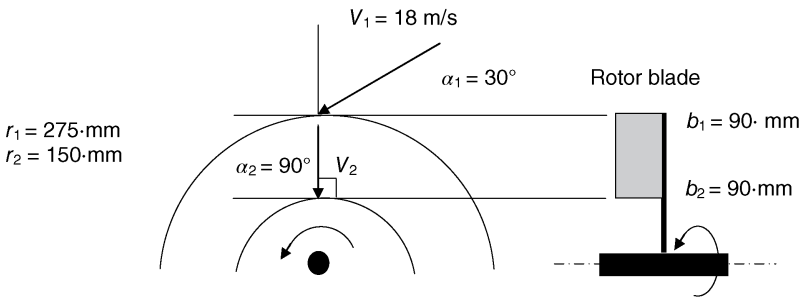

Figure 2.9 Radial turbomachine schematic.

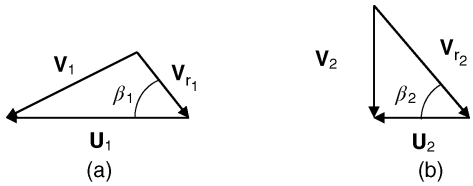

Figure 2.10 Velocity triangles for Example 2.3: (a) inlet; (b) outlet.

a) Sketch and label the velocity triangles for this situation.
b) Find V_2, V_{r1}, and V_{r2}.
c) What is the change in head across this device?
d) Is the device a pump or a turbine? Explain
e) Find the contributions due to the dynamic, centrifugal, and relative effects.
f) What is the reaction?
g) What are the blade angles β_1 and β_2?

Solution The velocity triangles for this situation are presented in Figure 2.10.

The rotor speeds U_1 and U_2 are

$$\omega = 764\frac{\text{rev}}{\text{min}} \times \frac{2\pi}{\text{rev}} \times \frac{\text{min}}{60\,\text{s}} = 80.01\frac{1}{\text{s}}$$

$$U_1 = r_1\omega = 275\,\text{mm} \times 80.01\frac{1}{\text{s}} = 22.002\frac{\text{m}}{\text{s}}$$

$$U_2 = r_2\omega = 150\,\text{mm} \times 80.01\frac{1}{\text{s}} = 12.001\frac{\text{m}}{\text{s}}$$

The value of V_2 can be calculated by using conservation of mass for the turbomachine:

$$\dot{m}_1 = \dot{m}_2$$

$$\rho V_{\text{m1}} \pi D_l\, b_1 = \rho V_{\text{m2}} \pi D_2 b_2$$

$$V_2 = V_1 \sin(30°)\frac{r_1}{r_2} = 9\frac{\text{m}}{\text{s}} \times \frac{275\,\text{mm}}{150\,\text{mm}} = 16.5\frac{\text{m}}{\text{s}}$$

With V_1 and V_2 known, the law of cosines can be used to find the two relative velocity components:

$$V_{\text{r1}} = \sqrt{U_1^2 + V_1^2 - 2\,U_1 V_1 \cos(\alpha_1)}$$

$$= \sqrt{22.002^2 + 18^2 - 2 \times 22.002 \times 18\cos(30°)} = 11.051\frac{\text{m}}{\text{s}}$$

$$V_{\text{r2}} = \sqrt{U_2^2 + V_2^2 - 2\,U_2 V_2 \cos(\alpha_2)}$$

$$= \sqrt{12.001^2 + 16.5^2 - 2 \times 12.001 \times 16.5\cos(90°)} = 20.403\frac{\text{m}}{\text{s}}$$

The head becomes

$$H = U_1 V_{\text{u1}} - U_2 V_{\text{u2}}$$

$$= 22.002 \times 18\cos(30°) - 12.001 \times 16.5\cos(90°)$$

$$= 342.97\frac{\text{m}^2}{\text{s}^2} = 342.97\frac{\text{N m}}{\text{kg}}$$

Since angular momentum is extracted ($U_2 V_{\text{u2}} < U_1 V_{\text{u1}}$), the device is a turbine.

The velocity components permit the contributions of the dynamic, centrifugal, and relative effects to be calculated:

$$\text{dynamic} = \frac{1}{2}(V_1^2 - V_2^2) = \frac{1}{2}(18^2 - 16.5^2) = 25.88\,\frac{\text{m}^2}{\text{s}^2}$$

$$\text{centrifugal} = \frac{1}{2}(U_1^2 - U_2^2) = \frac{1}{2}(22.002^2 - 12.001^2) = 170.03\,\frac{\text{m}^2}{\text{s}^2}$$

$$\text{relative} = \frac{1}{2}(V_{r2}^2 - V_{r1}^2) = \frac{1}{2}(20.402^2 - 11.051^2) = 147.07\,\frac{\text{m}^2}{\text{s}^2}$$

The centrifugal effect is the largest and contributes nearly 50% of the total change in head; the dynamic effect is the smallest with a very modest contribution. Since the inlet radius is larger than the exit, the centrifugal effect sign is positive, indicating a positive contribution to the overall energy transfer process. Hence, for a radial flow turbine, the inlet at a larger radius than the exit takes advantage of the centrifugal effect. Many radial turbines are, thus, *inflow* ($r_1 > r_2$) turbines.

The reaction is the ratio of the static contributions (centrifugal and relative) to the total. For this device the reaction is

$$R = \frac{\text{static}}{\text{total}} = \frac{\text{centrifugal} + \text{relative}}{\text{total}} = \frac{170.03 + 147.07}{342.97} = 0.925$$

In keeping with the observation that the centrifugal and relative effects were much larger than the dynamic contribution, the reaction is near unity.

The two blade angles are found using the arctangent function and the velocity triangles:

$$\beta_1 = \arctan\left(\frac{V_{m1}}{U_1 - V_{u1}}\right) = \arctan\left[\frac{18\sin(30^\circ)}{22.002 - 15.59}\right] = 54.53^\circ$$

$$\beta_2 = \arctan\left(\frac{V_{m2}}{U_2}\right) = \arctan\left(\frac{16.5}{12.001}\right) = 53.97^\circ$$

Using the blade angles, the general shape of the rotor can be defined. Figure 2.11 illustrates how the rotor blades would appear. With the two blade angles within a fraction of a degree, the rotor blades have little camber or curvature. Note: the above is a first-order analysis, and many effects (viscous, circulation, and bypass, for example) have been neglected; nonetheless, the first-order analysis captures the most important nuances of the energy transfer process.

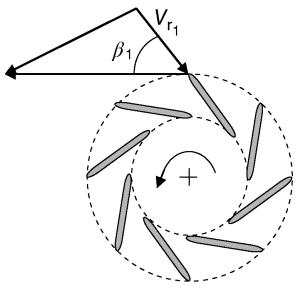

Figure 2.11 Rotor blade orientation.

2.5 Closure

The introductions into turbomachinery analysis and nomenclature are sufficient for the purposes of this book. For additional information, consult the Further reading section for this chapter. The next three chapters treat hydroelectric power, wind energy, and combustion turbines, all topics for which a fundamental understanding of turbomachinery is needed.

References

Cengel, Y.A. and Cimbala, J.M. (2013) *Fluid Mechanics Fundamentals and Applications*, 3rd edn. McGraw-Hill, New York.

Hodge, B.K. and Taylor, R.P. (1999) *Analysis and Design of Energy Systems*, 3rd edn. Prentice Hall, Upper Saddle River, NJ.

Logan, E. (1993) *Turbomachinery*, 2nd edn. Dekker, New York.

Further reading

Dixon, S.L. and Hall, C.A. (2014) *Fluid Mechanics and Thermodynamics of Turbomachinery*, 7th edn. Elsevier.

Hibbler, R.C. (2014) *Fluid Mechanics*. Prentice-Hall, Upper Saddle River, NJ.

Shepherd, D.G. (1956) *Principles of Turbomachinery*. MacMillian, New York. (This is the classic turbomachinery textbook.).

Wright, T. and Gerhart, P. (2009) *Fluid Machinery: Application, Selection, and Design*, 2nd edn. CRC Press, Boca Raton, FL.

3

Hydropower

3.1 Introduction

Hydroelectric dams are among the best known and largest of man-made structures. Such dams have a long and successful history in the USA. In the early decades of the 1900s, many hydroelectric dams were constructed. By the 1930s, the USA was generating about 40% of its electricity by hydropower. In 2014, as delineated in Figures 1.11 and 1.12, that number declined to about 3%. Norway, Nepal, New Zealand, and Canada generate more than 50% of their electricity by hydropower.

For years, hydroelectric power has been viewed as the most environmentally friendly of all electricity power sources. However, in recent years the environmental impacts of hydroelectric power have been viewed as less benign and more intrusive. The books by Leslie (2005) and Scudder (2005) address environmental problems associated with large dams; and Spilsbury (2011) examines pros and cons of large dams using recent examples. Kumar *et al.* (2011) present a reasonable assessment of the future of hydropower and conclude that continued development of hydropower can provide additional renewable energy, but that environmental and social impacts will need to be carefully managed.

Large hydroelectric dams require large capital investments and a timescale of years to build and complete. Figure 3.1, developed from EIA data for 2002, 2009, and 2012, provides a comparison of the total, fuel, maintenance, and operating costs of electricity generated from various sources during these years. Hydroelectric power has the lowest cost per kilowatt-hour of any electricity source. Although the operating and maintenance costs for hydroelectric are higher than for both fossil fuel steam and gas turbine, no fuel is required so the total cost per kilowatt-hour is the smallest of the four sources. Nuclear and hydroelectric monotonically increased during the time span, but both fossil fuel steam and gas turbine had higher costs in 2009 than in 2012 because fuel prices in 2009 were significantly higher than in 2012. Although a few exceptions exist, most hydroelectric dams have long lifetimes and permit electrical generating output to be quickly varied. The USA has about 2400 power-producing dams.

3.2 Examples of Hydroelectric Dams

Perhaps the most famous dam in the USA is the Hoover Dam on the Colorado River (Table 3.1). At 726 ft (221 m) high and 1244 ft (379 m) long, it is one of the world's largest dams and was built between 1931 and 1936. Hoover Dam is a major supplier of hydroelectric power and provides for flood control and improved navigation. The electricity is distributed to California (56%), Nevada (25%), and Arizona (19%). Lake Mead, the largest reservoir in the USA, is impounded by the dam.

Alternative Energy Systems and Applications, Second Edition. B. K. Hodge.

Companion website: www.wiley.com\go\Hodge\AESystemsandApplications2E

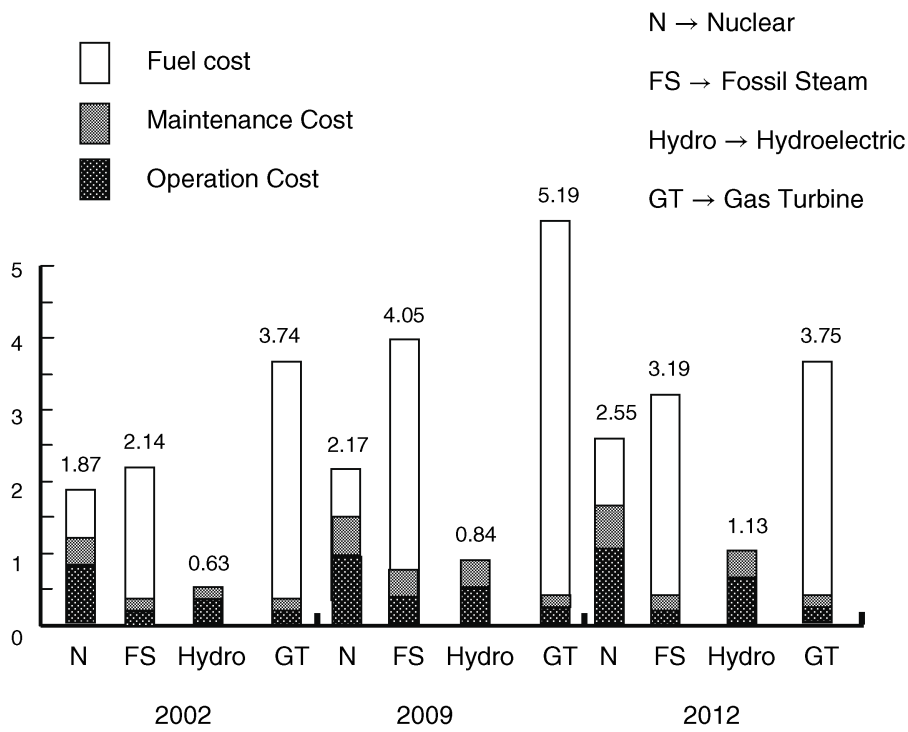

Figure 3.1 Cost components of generating electricity from various energy sources (generated from EIA data).

Figure 3.2 is a reproduction of an original planform for Hoover Dam and is included here for historical interest. Figure 3.3 presents a view of the dam from the tailrace looking upstream at the main structure.

The Itaipú hydroelectric power plant on the Parana River in South America is among the largest operating hydroelectric dams in the world. Built from 1975 to 1991, the 18 generating units add up to a total production capacity of 12 600 MW (18 generating units of 700 MW each) and a reliable output of 75 TW h a year. In 2014, the Itaipú Dam produced 87.8 TW h. This output, in a single powerhouse, is enough to power most of California. The Itaipú Dam contributes 25% of the energy supply in Brazil and 78% in Paraguay.

Table 3.1 Hoover Dam statistics.

726.4 ft (221 m) high
1244 ft (379 m) wide
660 ft (203 m) thick at the base
45 ft (13 m) thick at the top
4.5 years to build
4.4×10^6 cubic yards of concrete used for construction
March 1931 construction started
17 generators
$>4 \times 10^9$ kW h produced each year

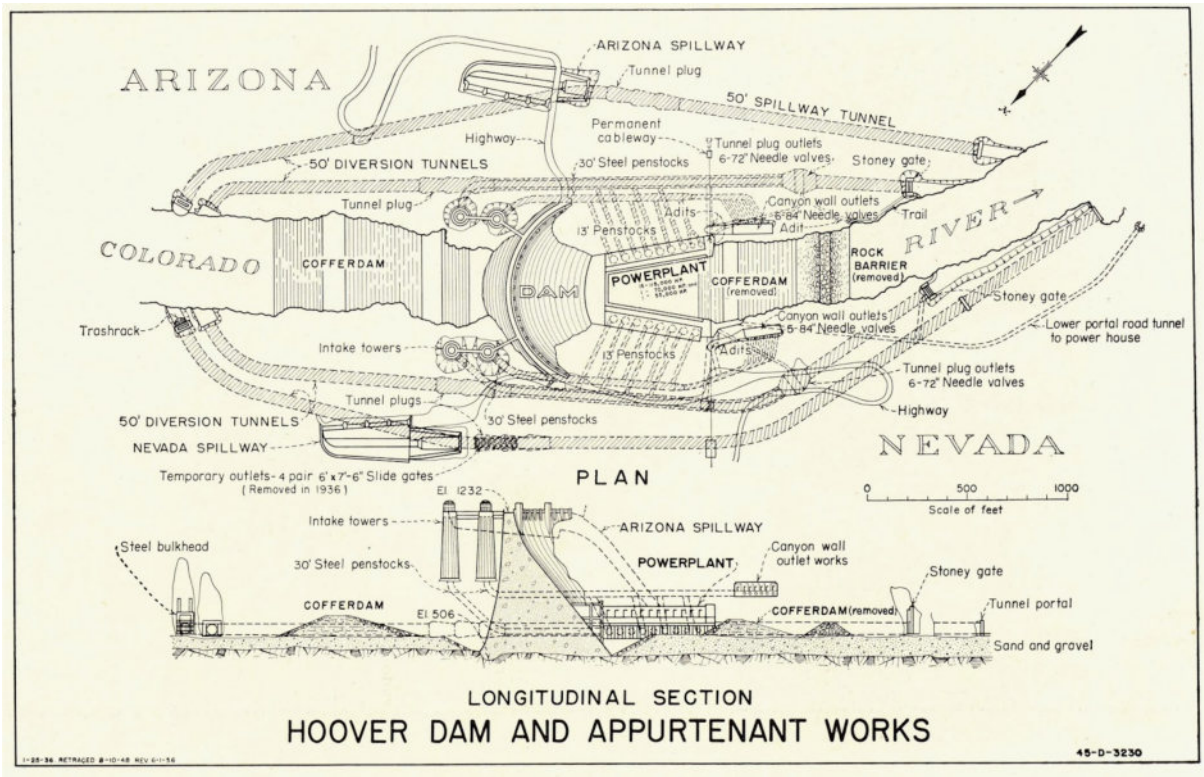

Figure 3.2 Reproduction of a planform drawing of Hoover Dam. *Source:* US Bureau of Reclamation.

Figure 3.3 View of Hoover Dam. *Source:* US Bureau of Reclamation.

The materials list required to construct the Itaipú Dam is impressive. The volume of iron and steel would be enough to build 380 Eiffel Towers, and the volume of concrete used represents 15 times the volume utilized to build the Channel Tunnel between France and England. Figure 3.4 provides an overview of the dam and reservoir.

Perhaps the most famous contemporary dam in the world is the Three Gorges Dam in the Republic of China. Table 3.2 contains some statistics of the Three Gorges Dam. Preliminary work started in 1993, and the dam was completed in 2014. In 2014, the Three Gorges Dam produced 98.9 TW h, making it then the world's largest producer of hydroelectric power. Because of the number of people that had to be relocated and the area of land flooded to form the reservoir, the Three Gorges Dam generated much worldwide controversy. Nonetheless, the government of China completed construction. An idea of the size of the Three Gorges dam is provided in Figure 3.5. Wang et al. (2014) provide an assessment of large dams, including the Three Gorges Dam, on the people and environment in China.

Figure 3.4 Aerial view of the Itaipú hydroelectric power plant.

Table 3.2 Three Gorges Dam statistics.

607 ft (185 m) high
7661 ft (2335 m) wide
666 ft (203 m) thick at the base
1993–2014 construction period
36×10^6 cubic yards of concrete used
22 500 MW of installed capacity
32 generating unit, 700 MW each
2 auxiliary generating units, 50 MW each
100 TWh is expected to be produced each year

Figure 3.5 Three Gorges Dam. *Source: Power Engineering International* (November 17, 2014).

The following web sites are recommended for additional information on hydroelectric dams:

http://www.hydropower.org/
http://www.hydro.org/
http://water.usgs.gov/edu/wuhy.html
http://energy.gov/eere/water/hydropower-research-development
http://www.tva.gov/power/hydro.htm
http://www.nap.edu/openbook.php?record_id=12619
http://www.pbs.org/wgbh/buildingbig/wonder/structure/three_gorges.html
http://www.c1b.com/dam2.jpg

3.3 Hydraulic Analysis

A quantitative understanding of the hydroelectric dams involves two components: (1) a hydraulic analysis of the penstock, the fluid's path between the upper and lower water levels,

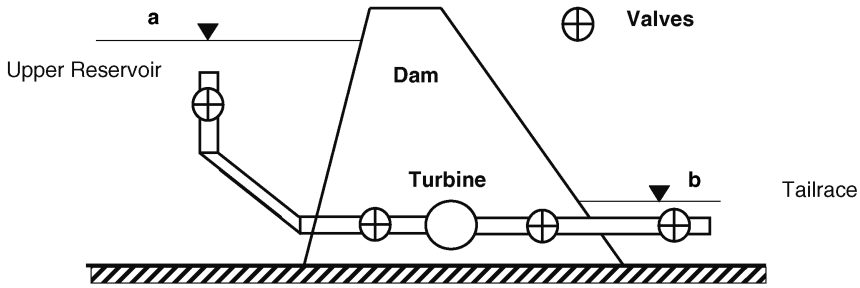

Figure 3.6 Dam schematic arrangement for hydraulic analysis.

and (2) an overview of the characteristics of turbines suitable for different combinations of flow rate and elevation difference. This section develops the hydraulic analysis of the penstock flow, and Section 3.4 examines the different types of turbines suitable for use in hydroelectric installations.

Figure 3.2 illustrates the penstock arrangement of Hoover Dam. The intake towers feed the primary penstocks, each 30 ft in diameter. The primary penstock then branches into several parallel penstocks that feed the turbines located in the power plant. The water traverses the turbines and is then discharged downstream of the dam. The flow arrangement thus contains an inlet, lengths of penstock, a turbine, and an exit. A general arrangement is shown schematically in Figure 3.6. The arrangement shows several valves, several fittings, the turbine, and penstock lengths.

The hydraulic analysis starts with the application of the conservation of energy equation, generally just called the energy equation, to the system. The general energy equation from station "a" to station "b" appears as

$$\frac{P_a}{\gamma}+\frac{V_a^2}{2g}+Z_a=\frac{P_b}{\gamma}+\frac{V_b^2}{2g}+Z_b+\sum_{n=1}^{N}\frac{V_n^2}{2g}\left(f_n\frac{L_n}{D_n}+K_n+C_nf_{T_n}\right)+W_t\frac{g_c}{g} \tag{3.1}$$

where P is pressure, V is velocity, Z is elevation, γ is specific weight, f is friction factor, L is pipe length, D is diameter, K is minor loss, C is minor loss, f_T is the fully rough friction factor, W_t is the change in head across the turbine, and N is number of pipe segments; g_c is used when the English Engineering System is employed and is defined as

$$g_c=32.174\frac{\text{ft lbm}}{\text{lbf s}^2}=1\frac{\text{m kg}}{\text{N s}^2} \tag{3.2}$$

g_c can be used with the SI, but it is an identity just defining the newton (N). In Equation 3.1, the units of the change in head of the turbines are in energy per unit mass (N m/kg or ft lbf/lbm) in conformance with turbomachinery practice.

The first questions to be answered are where to initiate application of the energy equation and where to terminate application of the energy equation. For the case of a hydroelectric dam as illustrated in Figure 3.6, the free surfaces of the water levels (a and b in the figure) upstream and downstream are taken as the range of application of the energy equation. Since both surfaces are at atmospheric pressure, $P_a = P_b$, and since the velocities of the surfaces of the upstream and downstream reservoir are small, $V_a = V_b = 0$. The change in head across the turbine becomes

$$W_t\frac{g_c}{g}=Z_a-Z_b-\sum_{n=1}^{N}\frac{V_n^2}{2g}\left(f_n\frac{L_n}{D_n}+K_n+C_nf_{T_n}\right) \tag{3.3}$$

The change in head across the turbine is the difference in elevation minus the major and minor losses. A more useful expression results if the velocity is expressed in terms of the flow rate as

$$\frac{V^2}{2g} = \left(\frac{Q}{A}\right)^2 \frac{1}{2g} = \left(Q\frac{4}{\pi D^2}\right)^2 \frac{1}{2g} = \frac{8Q^2}{g\pi^2 D^4} \tag{3.4}$$

so that Equation 3.3 becomes

$$W_t \frac{g_c}{g} = Z_a - Z_b - \sum_{n=1}^{N} \frac{8Q^2}{g\pi^2 D_n^4}\left(f_n \frac{L_n}{D_n} + K_n + C_n f_{T_n}\right) \tag{3.5}$$

The power extracted from the fluid by the turbine is

$$\text{Power}_{\text{extracted}} = \rho Q W_t \tag{3.6}$$

In Equation 3.5, expressions for the friction factor and fully rough friction factor are needed. In introductory fluid mechanics courses, the Moody diagram (Hodge and Taylor, 1999) is often used to present the functional dependence of friction factor f on the Reynolds number $Re_D = \rho VD/\mu$, and the relative roughness ε/D. However, the Moody diagram is unhandy for computer-based solutions, and a closed-form expression is desired. In the laminar regime, the usual expression (Hodge and Taylor, 1999) is

$$f = \frac{64}{Re_D} \tag{3.7}$$

Several different representations are available for turbulent flow. In this textbook the Haaland equation (Haaland, 1983) is used:

$$f = \frac{0.3086}{\{\log[(\varepsilon/3.7D)^{1.11} + (6.9/Re_D)]\}^2} \tag{3.8}$$

Minor loss terms are sometimes expressed as equivalent lengths using the fully rough friction factor f_T, the asymptotic value of the friction factor for a given relative roughness. From the Haaland equation, the fully rough friction factor becomes

$$f_T = \frac{0.3086}{\{\log[(\varepsilon/3.7D)^{1.11}]\}^2} \tag{3.9}$$

With the aforementioned as the basis for piping system problem solution formulation, some examples of the unified approach will be examined and discussed.

The minor loss representations, K and C in Equation 3.5, are available in virtually any textbook on fluid mechanics and in specialized textbooks such as Hodge and Taylor (1999) and Cengel and Cimbala (2013). The Crane Company Technical Report 410 (Crane Engineering Department, 1957) is frequently cited as a consistent source of major and minor loss information.

Consider the following example.

Example 3.1

A proposed design for a hydroelectric project is based on a discharge of 0.25 m^3/s through the penstock and turbine as in Figure 3.7. The minor losses are inlet, $K = 0.78$, $K = 1$ for the exit loss and $C = 32$ for two 45° elbows (Hodge and Taylor, 1999).

a) Determine the power in kilowatts that can be expected from the facility, if the turbine efficiency is 0.85.
b) Show that the type of turbine to be installed is a Francis turbine if the desired rotational speed is 1200 rpm.

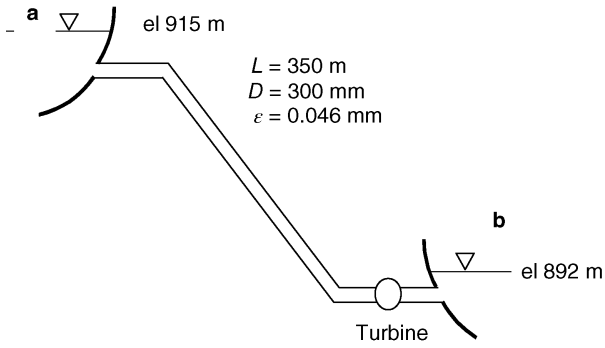

Figure 3.7 Schematic for Example 3.1.

Solution Application of the general energy equation would yield Equation 3.5 minor losses are not zero. In the classification of fluid mechanics hydraulics problems this would be a Category I problem since the flow rate is given and the head change is to be determined. Any fluid mechanics textbook has extensive information on the solution technique for such problems as this one. In this textbook, Mathcad will be used as the arithmetic engine and is used for the solution of Example 3.1. Figure 3.8 contains the Mathcad worksheet with the solution to this problem.

The first part of the worksheet defines the systems with inputs such as pressures, lengths, diameters, minor losses, and physical properties. The Mathcad solve block procedure is used to secure the solution. The solve block is initiated by the *Given* statement and ends with the *Find* command, in which the unknown is specified. The result is that 23 kW is delivered from the turbine.

With some modifications, the procedure of Example 3.1, as illustrated in Figure 3.8, can be used for virtually any penstock problem. Additional details are available in Hodge and Taylor (1999) and Hodge (2006).

The fluid mechanics of dams, as in Figure 3.6, are interesting. Consider the two bounding cases of interest for turbine operation. The first case occurs when the change in head across the turbine is equal to the elevation difference between the upper reservoir and the tailrace. If $W_t = Z_a - Z_b$, then the flow rate must be zero as no head is available for flow. The other bounding condition is if the change in head across the turbine is zero, in which case the flow rate Q_{max} is the maximum possible in the absence of a pump. Since the power extracted from the fluid is $\rho Q W_t$, the power extracted from the fluid is zero for both the bounding cases. However, for the flow rate range $0 < Q < Q_{max}$ the power extracted has nonzero values. Furthermore, as the flow rate increases, the change in head across the turbine decreases. Such circumstances lead to the power extracted being a double-valued function that possesses a maximum value of power extracted. For the conditions of Example 3.1, the maximum available head is 23 N m/kg and the maximum flow rate for $W_t = 0$ is 0.365 m^3/s. If a parametric study is performed with the flow rate as the independent variable and the power extracted as the dependent variable, Figure 3.9 results. The double valuedness of flow rate and power extracted is evident, as is the existence of a maximum value of power extracted. Thus, for a given system definition, a specific combination of flow rate and head change across the turbine provides for maximum power extraction. The solution to Example 3.1 is indicated on the figure. A flow rate of 0.205 m^3/s, not 0.25 m^3/s as in the problem statement, yields the maximum power extracted.

Input the pipe geometry:

Diameter in mm: $D := 0.3 \cdot m$

Length in m: $L := 350 \cdot m$

Roughness in mm: $\varepsilon := 0.046 \cdot mm$ (commercial pipe)

Input the system boundary (initial and end) conditions:

Pressures in Pa: $\begin{pmatrix} P_a \\ P_b \end{pmatrix} := \begin{pmatrix} 0 \\ 0 \end{pmatrix} \cdot Pa$

Elevations in m: $\begin{pmatrix} Z_a \\ Z_b \end{pmatrix} := \begin{pmatrix} 915 \\ 892 \end{pmatrix} \cdot m$

Input the loss coefficients:

K factor: $K := 1.78$

Equivalent length: $C := 32$

Input the fluid properties:

Density in kg/m^3: $\rho := 1000 \frac{kg}{m^3}$

Kinematic Viscosity in m^2/s: $\nu := 1.14 \cdot 10^{-6} \cdot \frac{m^2}{sec}$

Input the flow rate in cms: $Q := 0.25 \cdot \frac{m^3}{sec}$ Flow rate.

Initial guess on turbine decrease in head: $W_t := 15 \cdot newton \cdot \frac{m}{kg}$

Define constants and adjust units for consistency:

$g := 9.806 \frac{m}{sec^2}$

$g_c := 1 \cdot \frac{m \cdot kg}{newton \cdot sec^2}$

Define the functions for Reynolds number, fully-rough friction factor, and friction factor:

$$Re(q,d) := \frac{4 \cdot q}{\pi \cdot d \cdot \nu}$$

$$f_T(d,\varepsilon) := \frac{0.3086}{\log\left[\left(\frac{\varepsilon}{3.7 \cdot d}\right)^{1.11}\right]^2}$$

$$f(q,d,\varepsilon) := \begin{cases} \dfrac{0.3086}{\log\left[\dfrac{6.9}{Re(q,d)} + \left(\dfrac{\varepsilon}{3.7 \cdot d}\right)^{1.11}\right]^2} & \text{if } Re(q,d) > 2300 \\ \dfrac{64}{Re(q,d)} & \text{otherwise} \end{cases}$$

The generalized energy equation is:

Given

$$W_t \cdot \frac{g_c}{g} = \frac{P_a - P_b}{\rho \cdot g} \cdot g_c + Z_a - Z_b - \frac{8}{\pi^2} \cdot \frac{Q^2}{D^4 \cdot g} \cdot \left(f(Q,D,\varepsilon) \cdot \frac{L}{D} + K + C \cdot f_T(D,\varepsilon)\right)$$

$W_t := \text{Find}(W_t)$

$W_t = 108.823 s^{-2} \cdot m^2$

$W_t = 108.823 newton \cdot \frac{m}{kg}$

The head decrease at the turbine can be used to find the power generated.

$Power := Q \cdot \rho \cdot W_t$ $\quad Power = 27.206 kW$

$Power_{gen} := 0.85 \cdot Power$ $\quad Power_{gen} = 23.125 kW$

Figure 3.8 Mathcad worksheet for Example 3.1.

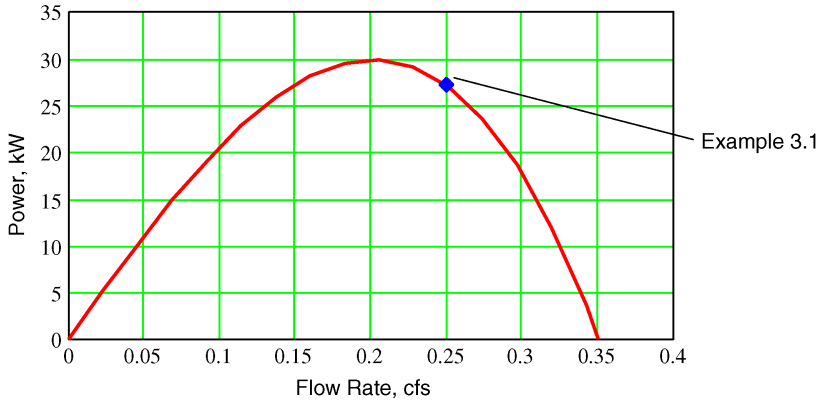

Figure 3.9 Power extracted as a function of flow rate for Example 3.1.

3.4 Turbine Specific Speed Considerations

The hydraulic solution addressed in Section 3.3 does not deal with the details of energy transfer in the turbine or with any details of turbine specification. Realizing the wide range of elevation differences and flow rates associated with hydropower, additional information related to turbines is needed.

The starting point for more detailed considerations of turbines suitable for hydroelectric application is dimensional analysis. A complete set of dimensional variables for a turbomachine is presented in Table 3.3.

With ω, ρ, and D as repeating variables, the complete set of dimensionless parameters is as follows:

$$\text{Power coefficient} \quad C_W = \frac{W}{\rho\omega^3 D^5} \tag{3.10}$$

$$\text{Pressure coefficient} \quad C_P = \frac{\Delta P}{\rho\omega^2 D^2} \tag{3.11}$$

$$\text{Flow coefficient} \quad C_Q = \frac{Q}{\omega D^3} \tag{3.12}$$

$$\text{Reynolds number} \quad Re = \frac{\rho\omega D^2}{\mu} \tag{3.13}$$

Table 3.3 Turbomachine dimensionless analysis parameters.

Parameter	Symbol	Dimensions
Power	W	ML^2/T^3
Speed	ω	$1/T$
Rotor diameter	D	L
Flow rate (volumetric)	Q	L^3/T
Pressure change	ΔP	M/LT^2
Density	ρ	M/L^3
Viscosity	μ	M/LT
Efficiency	η	—

If $\Delta P = \gamma H$, then

$$\text{Head coefficient} \quad C_H = \frac{gH}{\omega^2 D^2} \tag{3.14}$$

By eliminating D and evaluating the resulting dimensionless parameter at the point of maximum efficiency, the specific speed results. Since the specific speed is derived from dimensionless products by eliminating the diameter, the specific speed is also dimensionless. General usage is to define the specific speed for a pump in terms of the flow rate and increase in head; for a turbine, the usual is to define its specific speed in terms of the power and the available head. Thus, the specific speeds of the two devices differ. The traditional definitions are as follows:

$$\text{Pump} \quad N_{SP} = \frac{\omega\sqrt{Q}}{(gH)^{3/4}} \quad \text{at maximum efficiency} \tag{3.15}$$

$$\text{Turbine} \quad N_{SP} = \frac{\omega\sqrt{W/\rho}}{(gH)^{5/4}} \quad \text{at maximum efficiency} \tag{3.16}$$

The customary procedure in the USA is not to involve the density ρ and the acceleration due to gravity g and to express the specific speeds using the following units:

$$\omega \equiv \text{rpm} \quad Q \equiv \text{gal/min or gpm} \quad H \equiv \text{ft} \quad W \equiv \text{hp}$$

A result of these practices is that the specific speed values are no longer dimensionless, but contain dimensions. The customary *dimensional* versions of the specific speeds become

$$\text{Pump} \quad N'_{SP} = \frac{\omega\sqrt{Q}}{H^{3/4}} \tag{3.17}$$

$$\text{Turbine} \quad N'_{SP} = \frac{\omega\sqrt{W}}{H^{5/4}} \tag{3.18}$$

The utility of using the specific speeds is illustrated in the following composite graphs. When expressed at the maximum efficiency operating point, the specific speeds for the pump and the turbine define global machine geometries for optimum operating conditions. In both of these plots, the customary dimensional versions of the specific speeds are used. Although this chapter is primarily treating turbines as used in hydropower, the pump specific speed information is included for completeness and because in some hydropower the system is pumped hydroelectric which uses pumps as well as turbines.

Figure 3.10 demonstrates why the specific speed for a pump is so useful in classifying turbomachines such as pumps. The specific speed in this figure is based on the traditional US procedure and uses Equation 3.17. Below the abscissa on which the pump specific speed is indicated are cross-section schematics illustrating the salient features of pumps as a function of specific speed. At low value of N'_{SP} the flow rates are low and the increases in heads are high – leading to centrifugal (radial) flow pumps in which the centrifugal effect is dominant and the inlet area relatively small. As the specific speed increases, the centrifugal effects diminish and the inlet areas increase – with the result that the pump geometry progresses from radial to mixed to axial (propeller). Hence, the specific speed defines the general geometry of a pump for a given speed, flow rate, and increase in head across the pump. Also presented in Figure 3.10 are the nominal efficiencies expected from a well-designed pump as a function of flow rate and specific speed. Generally, as the size of a pump increases, the efficiencies increase since larger pumps are associated with large flow rates. The reason is that viscous effects become more important as the pump size (and, hence, flow rate) is decreased and as more of the flow is affected by viscous effects near surfaces (or walls).

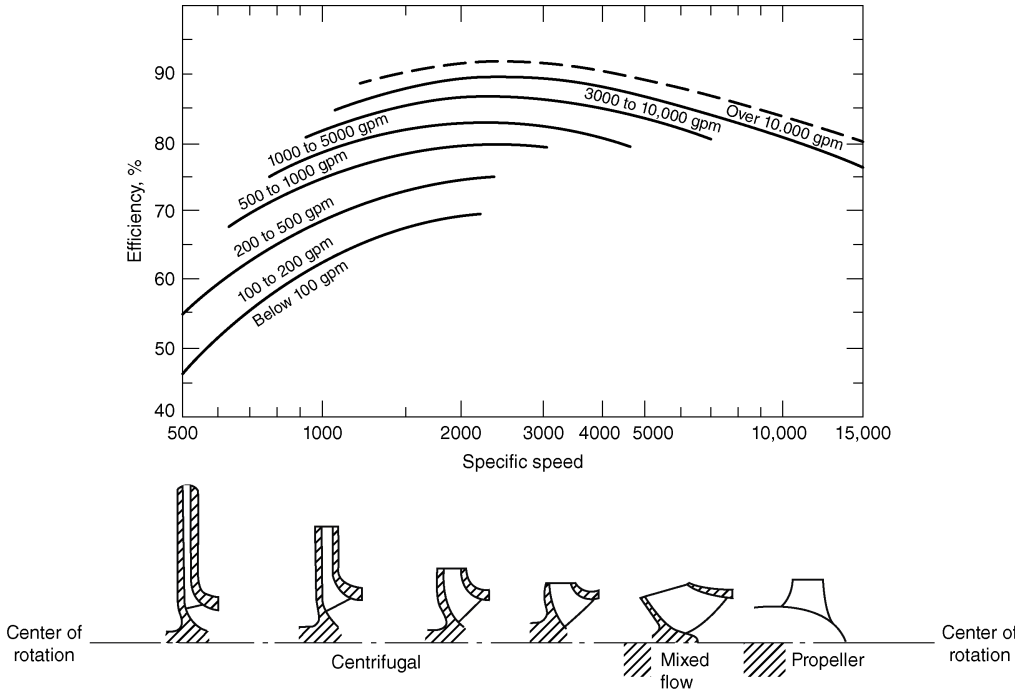

Figure 3.10 Pump specific speed relationship.

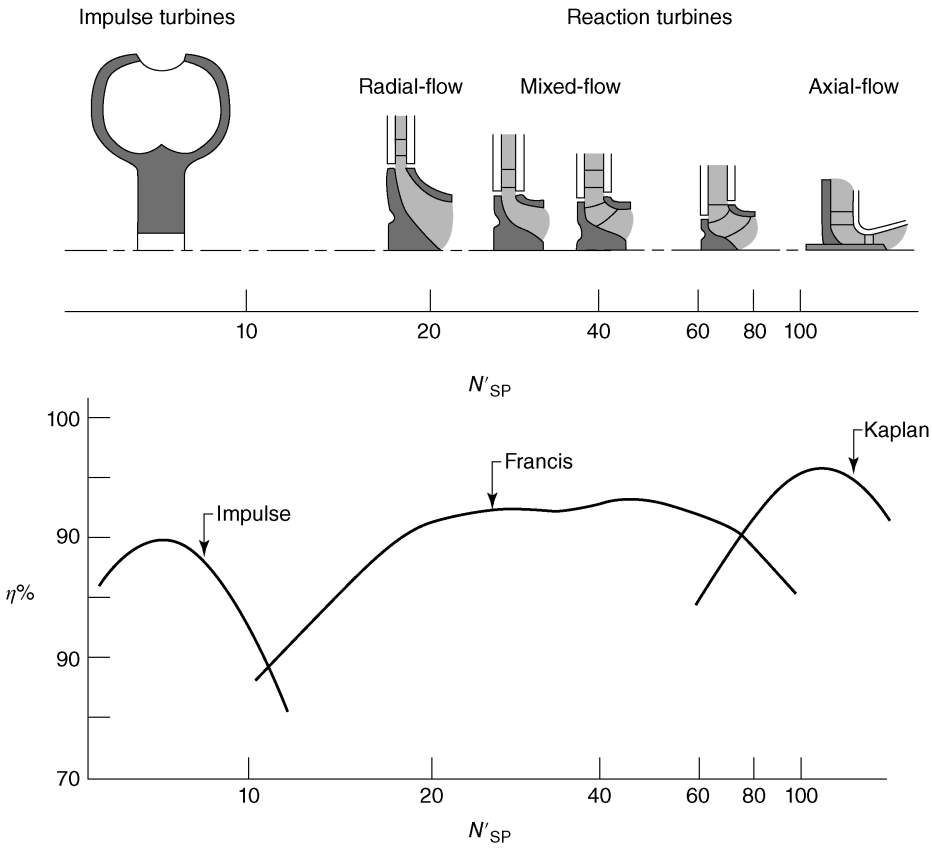

Figure 3.11 Turbine specific speed relationship.

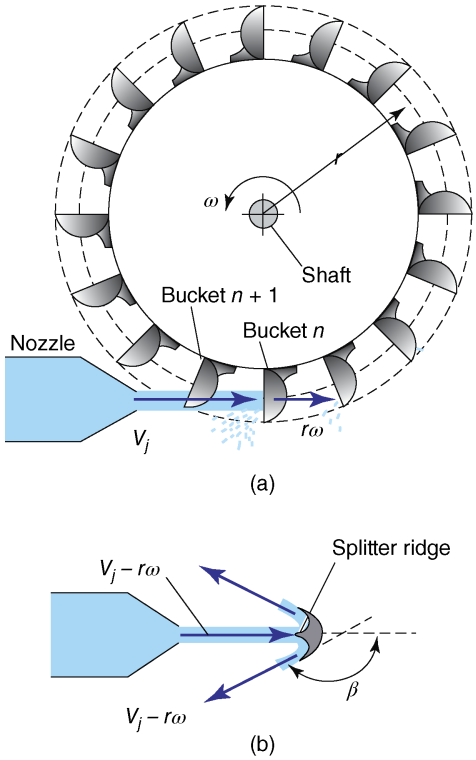

Figure 3.12 Pelton wheel schematic.

Figure 3.11 is the turbine version of the specific speed relationship. For hydroelectric applications, three types of turbines are in common use: the impulse turbine (or Pelton wheel) for low values of the turbine specific speed, the Francis turbine for moderate specific speeds, and the Kaplan turbine for high specific speeds. The general cross-sectional shapes of each type of device as well as expected efficiencies are included in the figure. Figure 3.12 contains a schematic of a Pelton wheel as well as details of the splitter ridge in the "bucket." Flow is accelerated through a nozzle and impacts the moving buckets, the moving blade row, along the periphery of the Pelton wheel. Angular momentum is extracted at the splitter ridge, and the fluid is discharged. Figure 3.13 presents schematics of a radial flow Francis turbine and a Kaplan turbine. Additional information on these different types of turbines will be examined in Section 3.5.

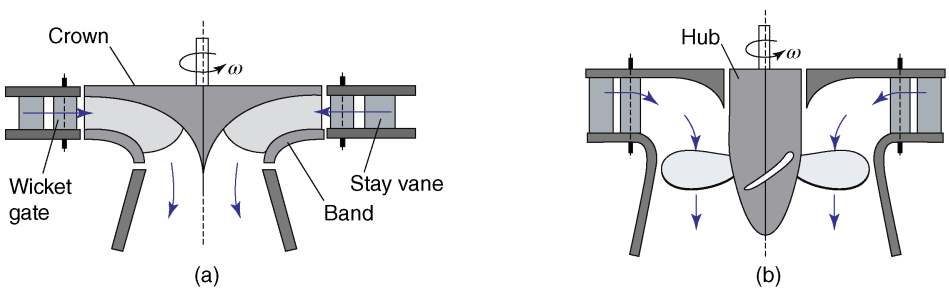

Figure 3.13 (a) Francis turbine and (b) Kaplan turbine schematics.

$$\omega := 1200 \cdot \frac{2 \cdot \pi}{\text{min}}$$

$$N_s := \omega \cdot \frac{\left(\frac{\text{Power}_{gen}}{\rho}\right)^{0.5}}{\left[g \cdot (Z_a - Z_b)\right]^{\frac{5}{4}}} \qquad N_s = 0.691 \qquad \text{(This is the dimensionless version.)}$$

$$N_{cus} := \frac{\omega}{2 \cdot \frac{\pi}{\text{min}}} \cdot \frac{\left(\frac{\text{Power}_{gen}}{\text{hp}}\right)^{0.5}}{\left[\frac{(Z_a - Z_b)}{\text{ft}}\right]^{\frac{5}{4}}} \qquad N_{cus} = 30.047 \qquad \text{(This is the customary version.)}$$

Figure 3.14 Mathcad solution for Example 3.2.

Example 3.2
For the conditions of Example 3.1, determine the type of turbine to be installed if the desired rotational speed in 1200 rpm.

Solution The specific speed will be calculated using the US customary approach with Equation 3.18. The Mathcad solution is reproduced in Figure 3.14. Mathcad is chosen because it easily handles units. In Figure 3.14, N_S is the dimensionless version of the specific speed, and the results are shown as unitless (dimensionless) in Mathcad. Using the customary definition, with the units of rpm, hp, and ft, the specific speed is computed to be 30.047. In Mathcad, dividing a variable by a set of units results in a unitless (nondimensional) number. So using customary units with Equation 3.18 yields the appropriate results N_{CUS}. With a customary value of 30.047, an examination of Figure 3.11 shows that the appropriate turbine type for this application is a Francis turbine and that an efficiency of 0.85 is reasonable.

3.5 Energy Transfer in Turbines

Section 3.4 introduced the turbine specific speed and discussed its importance in classifying the type of turbine required for specific applications. This section examines some details of energy transfer in various turbines. The Pelton wheel will be examined first.

Pelton wheels are appropriate for low values of the turbine specific speed. Low values of the turbine specific speed are associated with large head (elevation difference) availability and relatively small flow rates. Figure 3.15 is a photograph of a large, commercial Pelton wheel in

Figure 3.15 Photograph of a commercial Pelton wheel. *Source:* Voith Hydro.

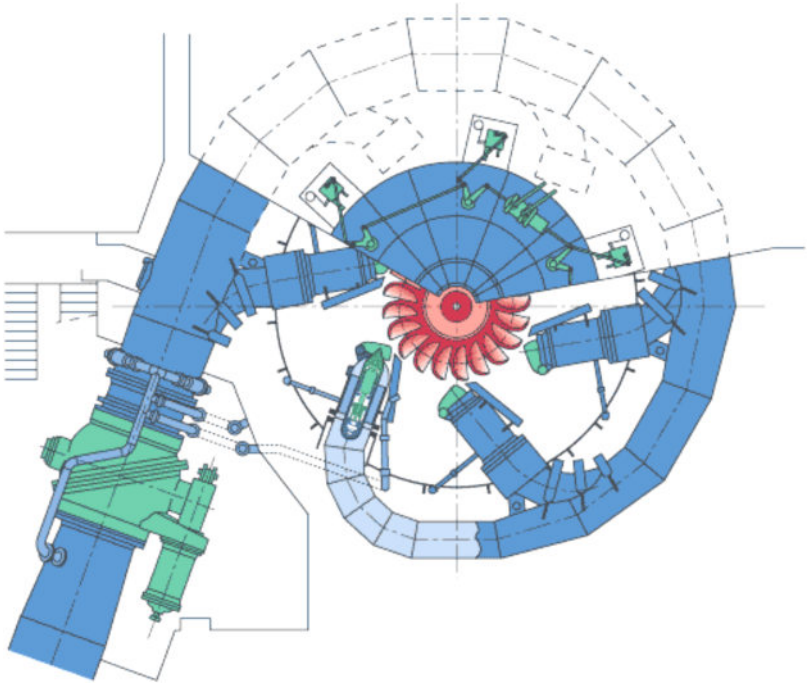

Figure 3.16 A Pelton wheel with six nozzles. *Source:* Voith Hydro.

which the buckets and splitter ridges can be observed. In reality, a Pelton wheel is more complex than the stylized schematic of Figure 3.12.

The water jet to the splitter ridge is supplied from a nozzle. In large Pelton wheels more than a single nozzle may be used. Use of multiple nozzles permits the wheel to be smaller for the same amount of power extracted, but multiple nozzles complicate the physical arrangement. Voith Hydro markets a Pelton wheel with six nozzles. The complexity of a six-nozzle arrangement is illustrated in Figure 3.16. In this figure, four nozzles are drawn and two are indicated by dashes.

The analysis of a Pelton wheel is initiated by defining the velocity triangles. Figure 3.17 illustrates the splitter ridge and the inlet and outlet velocity triangles for a Pelton wheel. Since

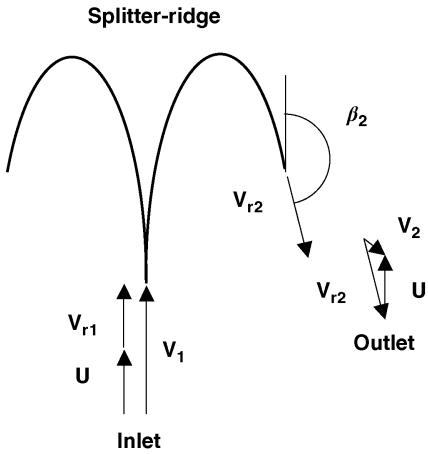

Figure 3.17 Splitter-ridge schematic with velocity triangles.

the jet enters and leaves the splitter ridge at the same radial location, $U_1 = U_2 = U$. A Pelton wheel is an impulse device with no casing; therefore, the reaction is zero. For an impulse device with $U_1 = U_2 = U$, Equation 2.18 requires that $V_{r1} = V_{r2}$. The velocity triangles appear as in Figure 3.16 with the inlet velocity V_1 in the tangential direction, and, thus, collinear with the wheel speed U. The relative velocity component V_{r1} completes the inlet velocity triangle. The exit splitter ridge makes an angle β_2 (<180°) with respect to V_1 so the fluid can exit the splitter ridge without interfering with the incoming stream. With V_{r2} and U known, the exit velocity triangle is defined.

The power extracted from the fluid becomes

$$\text{Power} = \dot{m}(U_1 V_{u1} - U_2 V_{u2}) = \dot{m}U(V_{u1} - V_{u2}) \tag{3.19}$$

And from the velocity triangles

$$\begin{aligned} V_{u1} &= V_1 = U + V_{r1} \\ V_{u2} &= U + V_{r2}\cos(\beta_2) \end{aligned} \tag{3.20}$$

Substituting the equations in Equation 3.20 into Equation 3.19 with $V_{r1} = V_{r2}$ yields

$$\begin{aligned} P &= \dot{m}U[U + V_{r1} - U - V_{r2}\cos(\beta_2)] \\ &= \dot{m}U\{V_{r1}[1 - \cos(\beta_2)]\} = \dot{m}U(V_1 - U)[1 - \cos(\beta_2)] \end{aligned} \tag{3.21}$$

The value of the wheel speed U for the maximum power extracted is obtained by

$$\begin{aligned} \frac{dP}{dU} &= 0 = \dot{m}(V_1 - U)[1 - \cos(\beta_2)] - \dot{m}U_1[1 - \cos(\beta_2)] \\ &= \dot{m}[1 - \cos(\beta_2)][(V_1 - U) - U_1] = V_1 - 2U \end{aligned} \tag{3.22}$$

Equation 3.22 yields the important result that, for maximum power extraction from a Pelton wheel, $U = V_1/2$. The maximum power extracted can be cast as

$$\begin{aligned} P_{max} &= \dot{m}\frac{V_1}{2}\left(V_1 - \frac{V_1}{2}\right)\left[1 - \cos(\beta_2)\right] \\ &= \dot{m}\left(\frac{V_1^2}{4}\right)\left[1 - \cos(\beta_2)\right] \end{aligned} \tag{3.23}$$

Since β_2 is typically very near 180°, $1 - \cos(\beta_2)$ is very close to 2 and

$$P_{max} = \dot{m}\frac{V_1^2}{2} \tag{3.24}$$

Equation 3.24 is a simple expression, but it contains many implications for Pelton turbines. Implicit in the expression is the relationship between the velocity available at the exit of the nozzle, the inlet velocity, and the wheel speed. Also, the relationship between power and the inlet velocity is quadratic. The inlet velocity depends on the elevation difference available; the larger the difference, the higher the velocity. High inlet velocities can arise only because of large elevation differences; thus the stipulation that Pelton wheels are appropriate for dams with high available heads. An example will prove useful.

Example 3.3

What power in kilowatts can be developed by the Pelton wheel shown in Figure 3.18 if the generator efficiency is 85%? The total minor losses are given as $K = 5.25$ and $C = 1500$. What will be the angular speed of the wheel for maximum power extracted? What is the power specific speed? What is the torque?

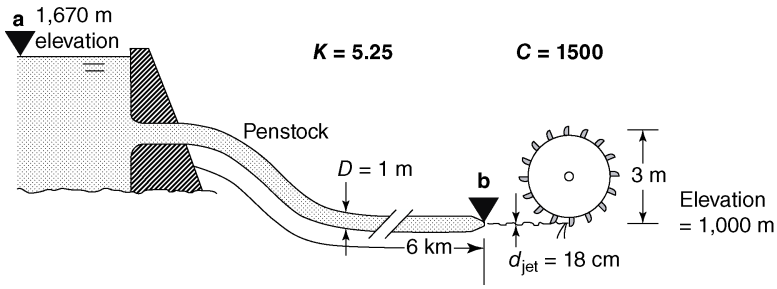

Figure 3.18 Schematic for Example 3.3.

Solution For an arrangement such as in Figure 3.18, the energy equation must be applied between the free surface of the upper reservoir (a) and the exit plane of the nozzle (b) that feeds the Pelton turbine. The energy equation becomes

$$\frac{P_a}{\gamma}+\frac{V_a^2}{2g}+Z_a=\frac{P_b}{\gamma}+\frac{V_b^2}{2g}+Z_b+\frac{V^2}{2g}\left(f\frac{L}{D}+K+Cf_T\right)$$

As with the earlier hydraulic example, $P_a = P_b$ and $V_a = 0$. Unlike Example 3.1, V_b is not zero, but the nozzle exit velocity V_{noz}, and since the Pelton turbine is downstream of b, no energy is extracted from the turbine between a and b. The reduced form of the energy equation becomes

$$Z_a=\frac{V_b^2}{2g}+Z_b+\frac{V^2}{2g}\left(f\frac{L}{D}+K+Cf_T\right)$$

or

$$\frac{V_b^2}{2g}=Z_a-Z_b-\frac{V^2}{2g}\left(f\frac{L}{D}+K+Cf_T\right)$$

This equation is interesting in that it states that the kinetic energy available for the Pelton turbine is equal to the elevation difference (potential energy) minus the major and minor losses. However, a more useful expression for solving the problem is obtained if the velocities are cast in terms of the flow rate using Equation 3.4; the result is

$$\frac{8Q^2}{g\pi^2D_B^4}=Z_a-Z_b-\frac{8Q^2}{g\pi^2D^4}\left(f\frac{L}{D}+K+Cf_T\right)$$

If placed in the form of Example 3.1, the equation becomes

$$0=Z_a-Z_b-\frac{8Q^2}{g\pi^2D_B^4}-\frac{8Q^2}{g\pi^2D^4}\left(f\frac{L}{D}+K+Cf_T\right)$$

The Mathcad worksheet used to solve Example 3.1 was modified for the solution to this problem. The solution is presented in Figure 3.19. The first part of the worksheet presents the solution for the flow rate. The flow rate solution is a Category II pipe-flow problem, and the result is 2.79 m^3/s. The remainder of the worksheet is concerned with the Pelton turbine computations. The power extracted, 16 780 kW, is computed using Equation 3.23, and the wheel rotational speed, 349 rpm, is calculated as $V_1/2$.

The power specific speed is 3.207. An examination of Figure 3.11 confirms that the power specific speed is in the range expected for a Pelton turbine and that the specified efficiency is appropriate for this device.

ORIGIN ≡ 1 Set origin for counters to 1 from the default value of 0.

Input the pipe geometry:

Diameter in m: $D := 1 \cdot m$

Length in m: $L := 6000 \cdot m$

Roughness in mm: $\varepsilon := 0.046 \cdot mm$ (commercial pipe)

Nozzle Diameter: $D_{noz} := 18 \cdot cm$

Input the system boundary (initial and end) conditions:

Pressures in Pa: $\begin{pmatrix} P_a \\ P_b \end{pmatrix} := \begin{pmatrix} 0 \\ 0 \end{pmatrix} \cdot Pa$

Elevations in m: $\begin{pmatrix} Z_a \\ Z_b \end{pmatrix} := \begin{pmatrix} 1670 \\ 1000 \end{pmatrix} \cdot m$

Input the loss coefficients:

K factor: $K := 5.25$

Equivalent length: $C := 1500$

Input the fluid properties:

Density in kg/m^3: $\rho := 1000 \cdot \frac{kg}{m^3}$

Kinematic viscosity in m^2/s: $\nu := 1.14 \cdot 10^{-6} \cdot \frac{m^2}{sec}$

Input the flow rate in cms:

$Q := 1 \cdot \frac{m^3}{sec}$ Initial guess on flow rate.

Define the functions for Reynolds number, fully-rough friction factor, and friction factor:

$$Re(q, d) := \frac{4 \cdot q}{\pi \cdot d \cdot \nu}$$

$$f_T(d, \varepsilon) := \frac{0.3086}{\log\left[\left(\frac{\varepsilon}{3.7 \cdot d}\right)^{1.11}\right]^2}$$

$$f(q, d, \varepsilon) := \begin{cases} \dfrac{0.3086}{\log\left[\dfrac{6.9}{Re(q,d)} + \left(\dfrac{\varepsilon}{3.7 \cdot d}\right)^{1.11}\right]^2} & \text{if } Re(q,d) > 2300 \\ \dfrac{64}{Re(q,d)} & \text{otherwise} \end{cases}$$

Figure 3.19 Mathcad solution for Example 3.3.

For moderate values of the turbine specific speed, the Francis turbine is the preferred type. Figure 3.20 is an illustration of a Francis turbine installation.

Francis turbines are the most frequently used of the three types. With the advent of large dams, Francis turbines have grown in size. In Figure 3.21, Voith Hydro documented the increase in size and output of the Francis turbines they have manufactured over the years.

The Kaplan turbine is the other type of device frequently used in hydropower applications. Figure 3.22 is a reproduction of a Voith Hydro Kaplan turbine, and Figure 3.23 schematically illustrates a typical installation.

Both Francis and Kaplan turbines are reaction, rather than impulse, devices. The general approach to solve problems concerned with Francis or Kaplan turbines is to construct the velocity triangles and apply the Euler equation. The next example is typical of the approach used for these devices.

The generalized energy equation is:

Given

$$0\cdot m = Z_a - Z_b - \left(\frac{8}{\pi^2}\cdot\frac{Q^2}{D_{noz}^4\cdot g}\right) - \left[\frac{8}{\pi^2}\cdot\frac{Q^2}{D^4\cdot g}\cdot\left(f(Q,D,\varepsilon)\cdot\frac{L}{D} + K + C\cdot f_T(D,\varepsilon)\right)\right]$$

$q := \text{Find}(Q)$

$q = 2.79 m^3\cdot s^{-1}$ $\quad q = 1.674\times 10^5 \frac{liter}{min}$ $\quad q = 737.167\frac{gal}{sec}$

The jet velocity is:

$$V_{jet} := \frac{q}{0.25\cdot\pi\cdot D_{noz}^2} \qquad V_{jet} = 109.659 m\cdot s^{-1}$$

The kinetic energy available for the Pelton wheel is 0.5 V_{jet}^2; the available power is the available kinetic energy times flow rate. This assumes (1 + cos β_2 = 2).

$$Power := q\cdot\rho\cdot\frac{V_{jet}^2}{2} \qquad Power = 1.678\times 10^4 kW$$

$Power_{gen} := 0.85\cdot Power$ $\quad Power_{gen} = 1.426\times 10^4 kW$

For maximum efficiency of a Pelton wheel, the blade speed is 0.5 of the jet speed.

$U := 0.5\cdot V_{jet}$ $\quad U = 54.83 m\cdot s^{-1}$ $\quad RPM := \frac{2\cdot\pi\cdot rad}{min}$

$D_{wheel} := 3.0\cdot m$ $\quad \omega := \frac{U}{0.5\cdot D_{wheel}}$ $\quad \omega = 36.553 s^{-1}$

$Torque := \frac{Power_{gen}}{\omega}$ $\quad Torque = 3.902\times 10^5 newton\cdot m$ $\quad \omega = 349.056 RPM$

The power specific speed for this example is

$$N_{cus} := \frac{\omega}{RPM}\cdot\frac{\left(\frac{Power_{gen}}{hp}\right)^{0.5}}{\left(\frac{Z_a - Z_b}{ft}\right)^{\frac{5}{4}}} \qquad N_{cus} = 3.207$$ This is the customary version.

Figure 3.19 (*Continued*).

Example 3.4

A 90% efficient radial-flow Francis turbine produces 111 MW at a speed of 167 rpm. The blade height is 0.732 m, and the inlet radius is 5.52 m. The flow exits the turbine in a radial direction.

a) If the angle between the radial direction and the absolute velocity at the inlet is 30°, determine the volume flow rate.
b) What is the change in head across the turbine?

Solution This turbine has flow in the radial plane at the inlet and radial flow at the exit; thus, the flow is radial (no axial velocity component) throughout the turbine. Figure 3.24 illustrates the general arrangement and the velocity triangles. Figure 3.25 shows a side view with the blade geometry defined.

The inlet radius and the speed of the rotor permit U_1 to be computed directly as

$$U_1 = r_1\omega = 5.52\,\text{m}\times 167\frac{\text{rev}}{\text{min}}\frac{2\pi}{\text{rev}}\frac{\text{min}}{60\,\text{s}} = 96.53\frac{\text{m}}{\text{s}}$$

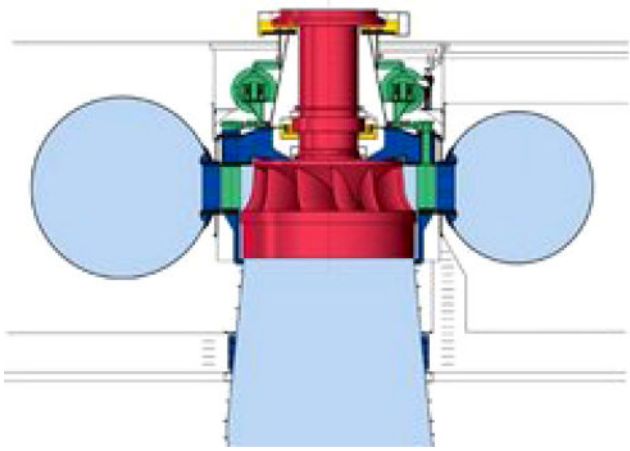

Figure 3.20 Francis turbine installation. *Source:* Voith Hydro.

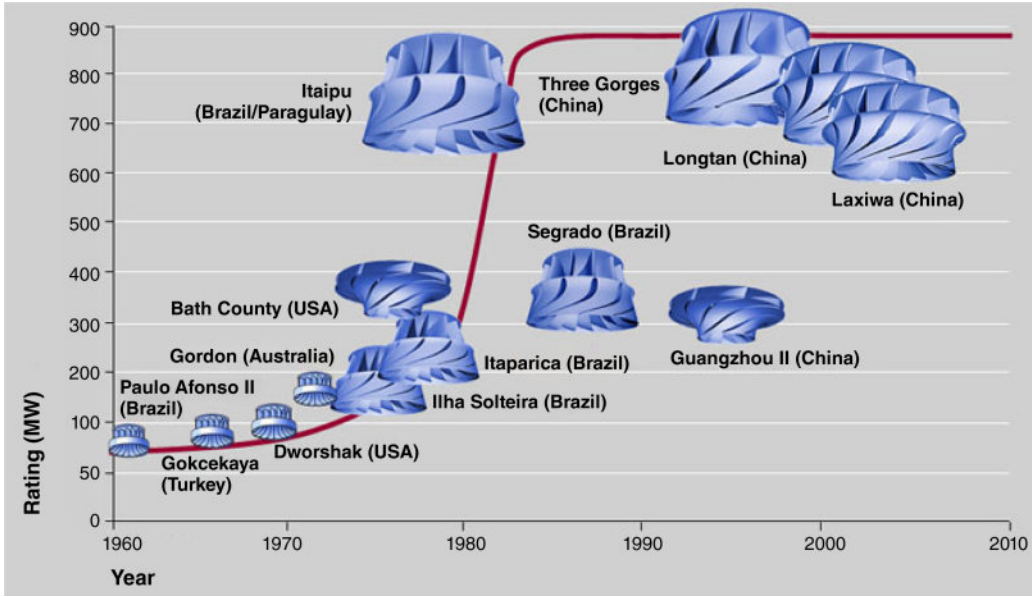

Figure 3.21 Increase in size of Voith Hydro Francis turbines since 1960. *Source:* Voith Hydro.

The power extracted from the fluid is the same as the power input to the turbine and can be expressed as

$$\text{Power}_{\text{in}} = \frac{\text{Power}_{\text{out}}}{\eta} = \frac{111\ \text{MW}}{0.9} = 123.33\ \text{MW}$$

Since V_2 is radial, $V_{u2} = 0$ and the expression for the power becomes

$$\text{Power}_{\text{in}} = \dot{m} U_1 V_{u1}$$

Figure 3.22 Kaplan turbine. *Source:* Voith Hydro.

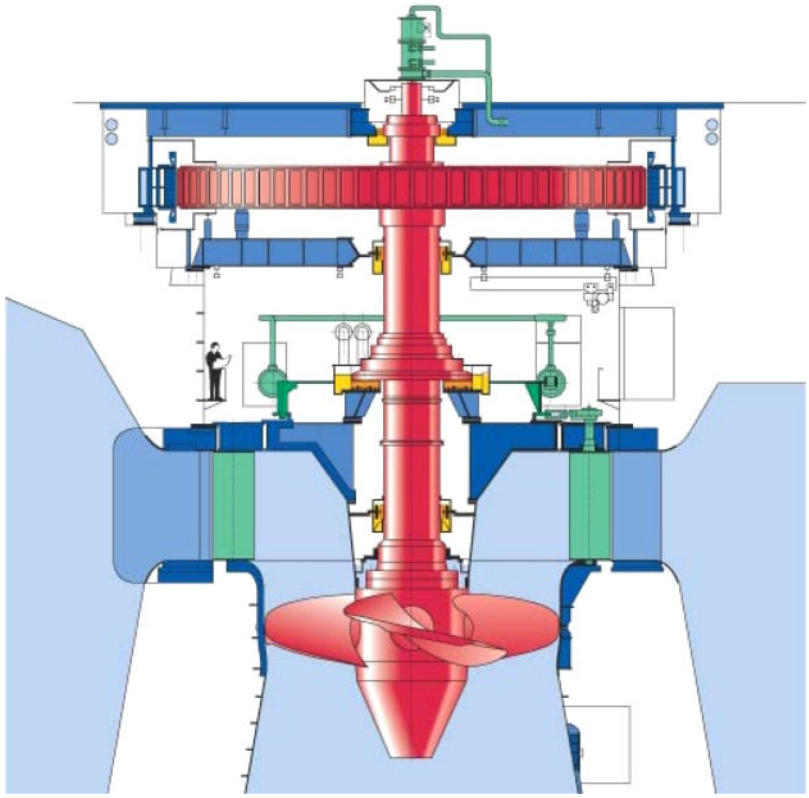

Figure 3.23 Kaplan turbine installation. *Source:* Voith Hydro.

The flow rate into the turbine is the radial velocity times the free flow, or

$$Q = 2\pi r_1 h_1 V_{m1} = 2\pi \times 5.52\,\text{m} \times 0.732\,\text{m} \times V_{m1} = 25.39\,\text{m}^2 \times V_{m1}$$

Combining the previous two expression yields

$$\text{Power}_{in} = 123.33\,\text{MW} = \rho \times 25.39\,\text{m}^2 \times V_{m1} U_1 V_{u1} \tag{3.25}$$

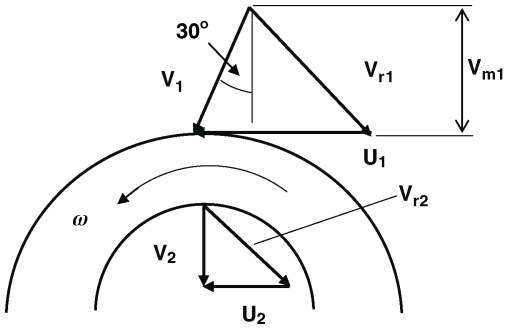

Figure 3.24 Schematic and velocity triangles for Example 3.4.

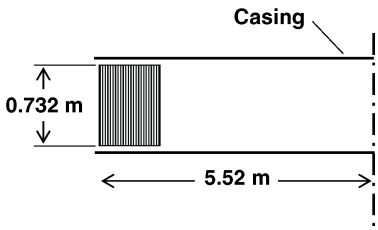

Figure 3.25 Turbine blade details.

But from the inlet velocity triangle, $V_{m1} = V_{u1}\cot(30°)$; so

$$\begin{aligned} 123.33\,\text{MW} &= \rho \times 25.39\,\text{m}^2 \times V_{m1} U_1 V_{u1} \\ &= 1000\frac{\text{kg}}{\text{m}^3} \times 25.39\,\text{m}^2 \times V_{u1}\cot(30°) \times 96.53\,\frac{\text{m}}{\text{s}} \times V_{u1} \\ &= 4.245 \times 10^6\,\frac{\text{kg}}{\text{s}} \times V_{u1}^2 \end{aligned} \tag{3.26}$$

From which we conclude $V_{u1} = 5.39\,\text{m/s}$ and

$$\begin{aligned} V_{m1} &= 5.39\frac{\text{m}}{\text{s}}\cot(30°) = 9.336\frac{\text{m}}{\text{s}} \\ Q &= 25.39\,\text{m}^2 \times 9.336\frac{\text{m}}{\text{s}} = 237\frac{\text{m}^3}{\text{s}} = 3.757 \times 10^6\,\frac{\text{gal}}{\text{min}} \end{aligned} \tag{3.27}$$

As might be expected from a Francis turbine that delivers 111 MW, the flow rate is large: 237 m^3/s or 3.757×10^6 gal/min!

The change in head across the Francis turbine can be computed directly from the relationship between power, mass flow rate, and change in head:

$$\text{Power} = Q\Delta P = Q\rho g\Delta h$$

$$\Delta h = \frac{\text{Power}_{in}}{Q\rho g} = \frac{123.33\,\text{MW}\,\frac{10^6\,\text{W}}{\text{MW}}\,\frac{\text{J}}{\text{s W}}\,\frac{\text{N m}}{\text{J}}\,\frac{\text{kg m}}{\text{N s}^2}}{237\frac{\text{m}^3}{\text{s}} \times 1000\frac{\text{kg}}{\text{m}^3} \times 9.807\frac{\text{m}}{\text{s}^2}}$$

$$= 53.06\,\text{m}$$

Thus, the change in head across the Francis turbine is 53.06 m.

Example 3.4 is typical of the process used to work problems associated with turbomachinery devices. Much of the basis for the solution was developed in Chapter 2.

Hydroelectric power generation brings to mind massive dam and penstock systems, such as in Figures 3.3, 3.4 and 3.5, that drive turbines (as examined in this chapter) and discharge the water in the tailrace below the dam. A different kind of hydroelectric system is the pumped storage configuration in which pumps are used when electricity rates are low (typically at night) to pump water into a reservoir which is discharged to drive turbines when the electrical grid demands are high and electricity is expensive (during peak grid demand periods). Pumped storage systems thus contain both pumps and turbines. Hydrodynamic losses are incurred when pumping as well as when generating in such systems; additionally, the pumps, turbines, and generators all have inefficiencies. The net result is that more energy is consumed in pumping than in generating, so a pumped storage system is a net user of electricity, but from a utility's standpoint such systems can be brought on line quickly and provide electrical energy cheaper than can be purchased from an external source when the electrical demand is high. The Tennessee Valley Authority's Raccoon Mountain Pumped-storage Plant is a good example of a modern pumped storage facility; information is available at https://www.tva.gov/Energy/Our-Power-System/Hydroelectric/Raccoon-Mountain and http://www.energystorageexchange.org/projects/216. In 2015, the EIA reported 42 pumped storage systems, ranging in capacity from 1 to 3000 MW in the USA, with a total capacity of 22 GW. Pumped storage generated 23×10^6 kW h, but consumed 29×10^6 kW h in pumping – an overall efficiency of 79%. Pumped storage in 2015 provided 97% of the utility-size electricity storage capacity. Exercise 3.20 is an exercise structured about a pumped storage system.

3.6 Closure

This chapter has explored hydropower by examining some large hydroelectric sites, developing and utilizing the concept of specific speed, considering how a Pelton turbine (impulse device) works, and demonstrating how to use velocity triangles to solve turbine problems.

As pointed out in Section 3.1, hydroelectric power, while a renewable energy source, does present economic and environmental issues. A recent study by Kao *et al.* (2014), sponsored by Oak Ridge National Laboratory, assessed the potential for hydroelectric power in the USA through 2040. The results are presented in summary form by Bowman in Figure 3.26, taken

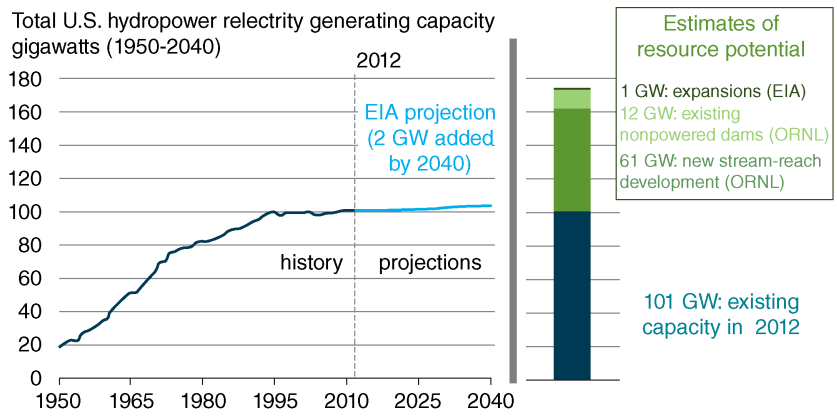

Figure 3.26 Prediction of hydroelectric growth in the USA through 2040. *Source:* EIA (http://www.eia.gov/todayinenergy/detail.cfm?id=17051).

from the EIA *Today in Energy* for July 14, 2014. The study identified the installed hydroelectric capacity as 101 GW in 2012, but projected only an additional 2 GW to be added by 2040 out of a potential about 60 GW. These results basically concur with a 2010 study sponsored by the National Academy of Sciences *et al.* (2010). Both studies acknowledged that economic issues and environmental concerns are the primary reason that little additional hydroelectric capacity is likely to be added in the USA.

Each year the Energy Information Administration releases an Annual Energy Outlook (AEO) that contains 25-year projections on energy resources and consumptions. These projections are built around a reference case and various energy scenarios. The AEO 2016 (EIA, 2016), which projects a 0.1% hydropower growth through 2040, is in substantial agreement with Bowman (2014) and the National Academy of Sciences *et al.* (2010) study findings for hydropower growth. For a number of years the projections on hydropower have predicted little significant growth. For example, AEO 1998 (EIA, 1997) projected only a 0.1% growth out to 2020, the same growth rate as AEO 2016.

The issue of hydropower growth was considered settled until July 2016 when the Wind and Water Power Technologies Office within the US Department of Energy Office of Energy Efficiency and Renewable Energy (EERE, 2016) issued the report, "HydroPower Vision: A New Chapter for America's 1st Renewable Electricity Source." The Wind and Water Power Technologies Office supports the development, deployment, and commercialization of wind and water power technologies. This report, which postulated that a hydropower growth scenario

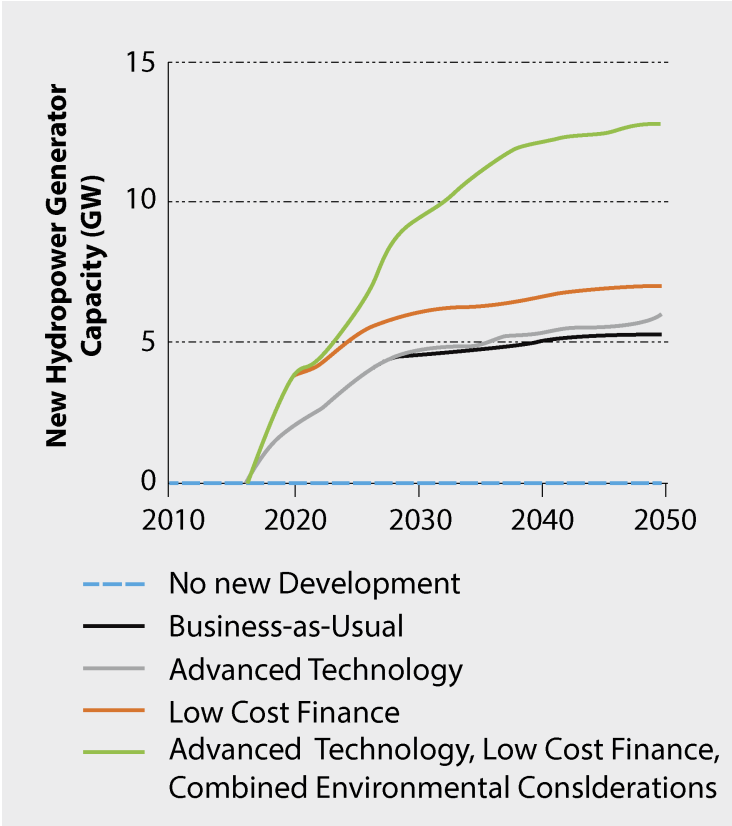

Figure 3.27 HydroPower Vision conventional hydro summary projections from 2016 to 2050. *Source:* http://energy.gov/eere/water/new-vision-united-states-hydropower.

different from low growth was possible, was based on collaboration of experts from more than 150 entities, including federal, state, and local government agencies, as well as industry trade associations, manufacturers, environmental organizations, utilities, and research organizations. The majority of participants were from federal agencies. HydroPower Vision finds, in summary form:

> . . . that U. S. hydropower could grow from 101 GW of capacity to nearly 150 GW by 2050. Growth under this modeled scenario would result from a combination of 13 GW of new hydropower generation capacity (upgrades to existing plants, adding power at existing dams and canals, and limited development of new stream-reaches), and 36 GW of new pumped storage capacity . . .

These findings stand in contrast to the here-to-fore accepted projections of scant hydropower growth. HydroPower Vision examines several alternative scenarios for conventional hydropower: (1) no new development, (2) business as usual, (3) advanced technology, (4) low-cost finance, and (5) advanced technology, low-cost finance, and combined environmental considerations. Figure 3.27, taken from HydroPower Vision, provides an excellent summary of the different scenarios and outcomes for conventional hydroelectric power. No new development results in no increase in capacity (gigawatts), while business as usual adds about 5 GW through 2050. Advanced technology is projected to add about 5 GW, while low-cost finance would secure an additional about 7 GW. However, if advanced technology and low-cost finance are

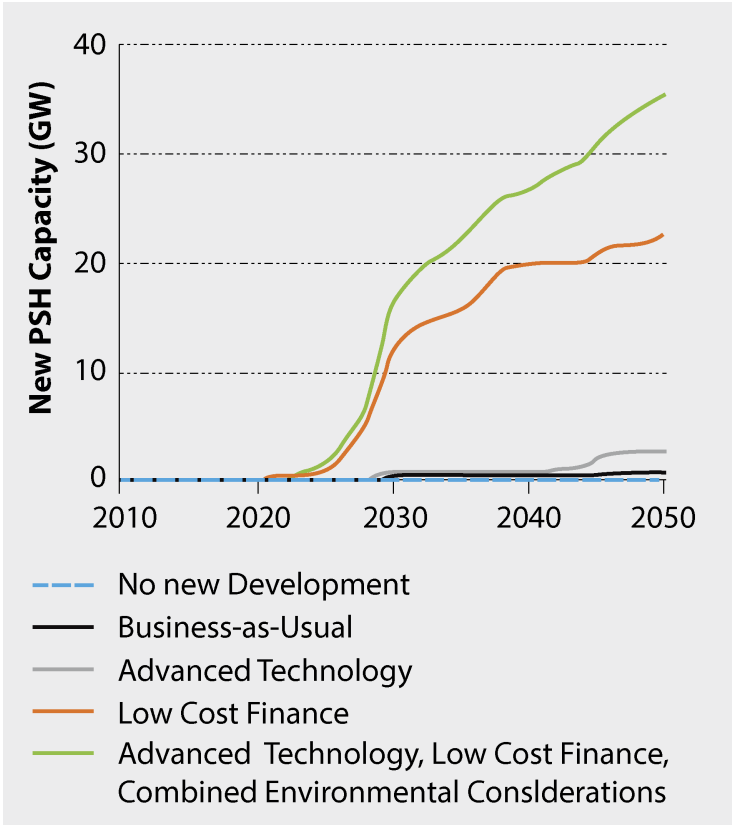

Figure 3.28 HydroPower Vision pumped storage summary projections from 2016 to 2050. *Source:* http://energy.gov/eere/water/new-vision-united-states-hydropower.

coupled with environmental considerations, the increase in conventional hydroelectric generation capacity is about 13 GW by 2050.

In addition to conventional hydropower capacity growth (13 GW), HydroPower Vision considers added pumped storage capacity (36 GW). The pumped storage scenarios are the same as for conventional hydro, and the projections for pumped storage are displayed in Figure 3.28. Pumped storage exhibits little growth from advanced technology, but benefits from low-cost finance much more than conventional hydro. As with conventional hydroelectric power, the combination of advanced technology and low-cost finance coupled with environmental considerations demonstrates the most increase in projected capacity. Indeed, for pumped storage, low-cost finance is more important than environmental considerations. HydroPower Vision points out that pumped storage could become a dominant source of stored electricity energy capacity by 2050.

Which of these hydropower scenarios (traditional or HydroPower Vision) or what combination of the two will occur by 2050 cannot be known in 2016. Upgrades of existing hydroelectric facilities are certainly possible, and the addition of significant pumped storage capacity offers enhanced flexibility for grid management strategies. The HydroPower study does add to the feasible energy mix and must be considered.

References

Bowman, M. (2014) EIA projections show hydro growth limited by economics not resources. *Today in Energy*, EIA, July 14.

Cengel, Y.A. and Cimbala, J.M. (2013) *Fluid Mechanics: Fundamentals and Applications*, 3rd edn. McGraw-Hill, New York.

Crane Engineering Department (1957) Flow of fluids through valves, fittings, and pipe. Technical Paper 410, 4th printing. Crane Company, Chicago, IL.

EERE (2016) HydroPower Vision: A New Chapter for America's 1st Renewable Electricity Source. DOE/GO-102016-4869, July.

EIA (1997) *Annual Energy Outlook 1998: With Projections to 2020*. DOE/EIA-0383(98). http://www.greatchange.org/bb-moredinoblood-aeo98.pdf (accessed October 14, 2016).

EIA (2016) *Annual Energy Outlook 2016*. https://www.eia.gov/forecasts/aeo/tables_ref.cfm (accessed October 14, 2016).

Haaland, S.E. (1983) Simple and explicit formulas for the friction factor in turbulent flow. *Transactions of the ASME, Journal of Fluids Engineering*, **103** (5): 89–90.

Hodge, B.K. (2006) A unified approach to piping system problems. *ASEE Computers in Education Journal*, **16** (2): 68–79.

Hodge, B.K. and Taylor, R.P. (1999) *Analysis and Design of Energy Systems*, 3rd edn. Prentice-Hall, Upper Saddle River, NJ.

Kao, S.C., McManamay, R.A., Stewart, K.M., *et al.* (2014) New Stream-reach Development: A Comprehensive Assessment of Hydropower Energy Potential in the United States. Contract DE-AC05-00OR22725, Oak Ridge National Laboratory, GPO DOE/EE-1063.

Kumar, A., Schei, T., Ahenkora, A., *et al.* (2011) Hydropower. In *Renewable Energy Sources and Climate Change Mitigation*, Edenhofer, O., Pichs-Madruga, Y., Sokona, K., *et al.* (eds). Cambridge University Press, New York.

Leslie, J. (2005) *Deep Water: The Epic Struggle over Dams, Displaced People, and the Environment*. Farrar, Straus and Giroux, New York.

National Academy of Sciences, National Academy of Engineering, and National Research Council of the National Academies (2010) *Electricity from Renewable Resources: Status, Prospects, and*

Impediments, The National Academies Press, Washington, DC. http://www.nap.edu/openbook.php?record_id=12619 (accessed October 3, 2016).
Scudder, T. (2005) *The Future of Large Dams: Dealing with Social, Environmental, Institutional, and Political Costs*. Earthscan, London.
Spilsbury, L. (2011) *Dams and Hydropower: Development or Destruction*. Rosen Publishing Group.
Wang, P., Dong, S., and Lassoie, J. (2014) *The Large Dam Dilemma: An Exploration of the Impacts of Hydro Projects on People and the Environment in China*. Springer Netherlands, Dordrecht.

Further Reading

Munson, B.R., Rothmayer, A.P., Okishii, T.H., and Huebsch, W.W. (2012) *Fundamentals of Fluid Mechanics*, 7th edn. John Wiley & Sons, Inc., Hoboken, NJ.

4

Wind Energy

4.1 Introduction

Wind energy, like solar energy, has captured much media attention recently. Indeed, wind energy has exhibited the most rapid growth of all renewable energy sources in the last few years. As shown in Figure 1.11, wind energy accounted for 18% of the renewable energy used in the USA in 2014, up from 4% in 2007. Figure 1.12 illustrates the rapidity of the increase in installed wind energy capacity in the USA from 2000 to 2013. Wind energy is also an increasingly important component of the energy mix in western Europe. The purposes of this chapter are to develop the fundamental principles of wind energy and to impart a quantitative understanding of wind energy.

Devices to harvest wind energy are available in many different configurations. A number of possible configurations are illustrated in Figures 4.1 and 4.2. Fundamental designations of a wind energy device include the HAWT shown in Figure 4.1 and the VAWT in Figure 4.2. The designation depends simply on the axis of rotation of a wind machine: HAWT devices rotate in the horizontal plane and VAWT devices rotate in the vertical plane. HAWT devices are more common than VAWTs, but horizontal devices must have a mechanism – a yaw control – to keep them pointed into the wind. VAWTs, on the other hand, do not need a yaw control.

Many of the wind energy devices illustrated in Figures 4.1 and 4.2 are speculative; they have little or no demonstrated functionality and are not available commercially. The most common configurations for the HAWT are the two- and three-bladed, the windmill, and the sail wing. The two- and three-bladed wind turbines can be either upwind or downwind, with upwind being the most common. In terms of installed kilowatts, the total capacity of the HAWTs greatly exceeds that of the VAWTs. Figure 4.3 presents photographs of HAWTs and VAWTs; Figure 4.3a shows a large HAWT, suitable for commercial power generation, and the turbine in Figure 4.3b is a much smaller device, suitable for a residence. A detailed examination of characteristics of commercially available horizontal wind turbines will be provided later in this chapter.

The Savonius and the Darrieus are the most common versions of the VAWT, with most of the remaining vertical configurations either in the experimental/developmental or speculative stage. However, even the Savonius and the Darrieus configurations have not been extensively commercialized. VAWTs are generally classified as drag or lift devices, based on their operating principle. The Savonius rotor is a drag device, since the drag of the wind on the "cups" generates the torque on the axis. The Darrieus is classified as a lift device since the shaft torque results primarily from lift on the blades. One indication of the dominance of the horizontal configuration wind turbines is that on the National Renewable Energy Laboratory (NREL) web site only one photograph (depicting a Darrieus) of a VAWT is presented in the renewable-energy photographic section. Figure 4.3c is reproduced from the NREL web site and is a photograph of a

Alternative Energy Systems and Applications, Second Edition. B. K. Hodge.

Companion website: www.wiley.com\go\Hodge\AESystemsandApplications2E

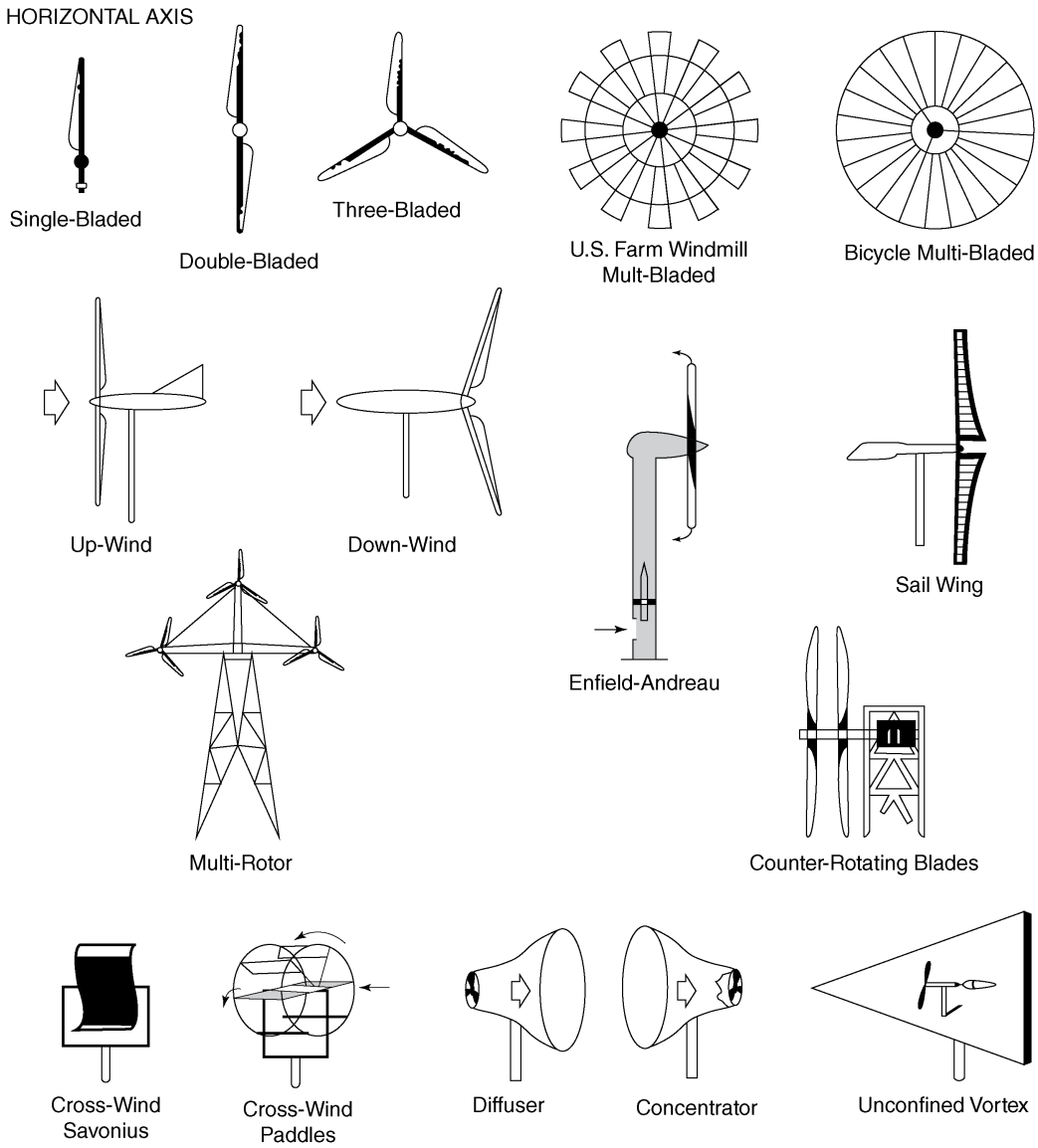

Figure 4.1 Horizontal-axis wind turbine (HAWT) taxonomy. *Source*: Kreith and West (1997). Reproduced with permission of Taylor and Francis.

Darrieus wind turbine, a FloWind Corporation 17 EHD, taken in 1995. Figure 4.3d shows an example of a modern VAWT installed in Martigny, Switzerland.

4.2 Fundamental Concepts

As a prelude to discussing wind turbine operation, some details of the components of a wind turbine are needed. Figure 4.4 is a schematic illustrating the important parts of a typical

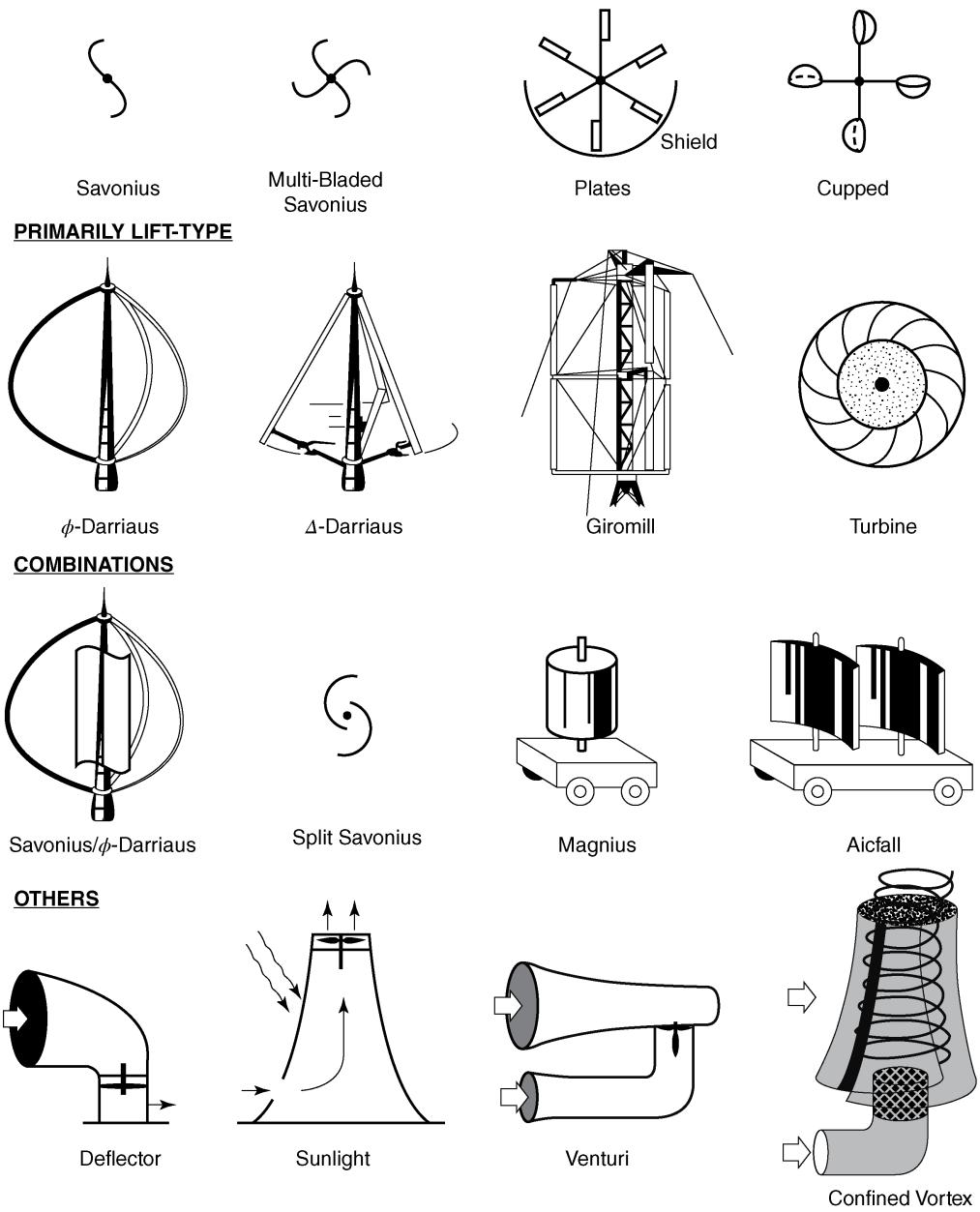

Figure 4.2 Vertical-axis wind turbine (VAWT) taxonomy. *Source*: Kreith and West (1997). Reproduced with permission of Taylor and Francis.

HAWT. The tower is mounted to a base, and on top of the tower is the nacelle, which contains the gearbox, controls, and generator subsystems. The rotor is attached to the gearbox and generator by a shaft. The rotor diameter and the swept area of the blades are indicated, as is the hub height.

Figure 4.3 Examples of wind turbines. (a) HAWT (600 kW Mitsubishi); (b) HAWT (1.5 kW Bergey); (c) VAWT (FloWind Corporation 17 EHD); (d) Martigny wind turbine. *Source*: NREL.

The power available from a wind of speed V with a mass flow rate $\dot{m}$ sweeping an area A is

$$\text{Power} = \frac{1}{2}\dot{m}V^2 \tag{4.1}$$

but the mass flow rate is $\dot{m} = \rho AV$, so the power available becomes

$$\text{Power} = \frac{1}{2}\rho AV^3 \tag{4.2}$$

Equation 4.2 is very important, as it demonstrates that the power available from the wind is proportional to the area swept by a wind turbine and the cube of the wind speed. With a cubic

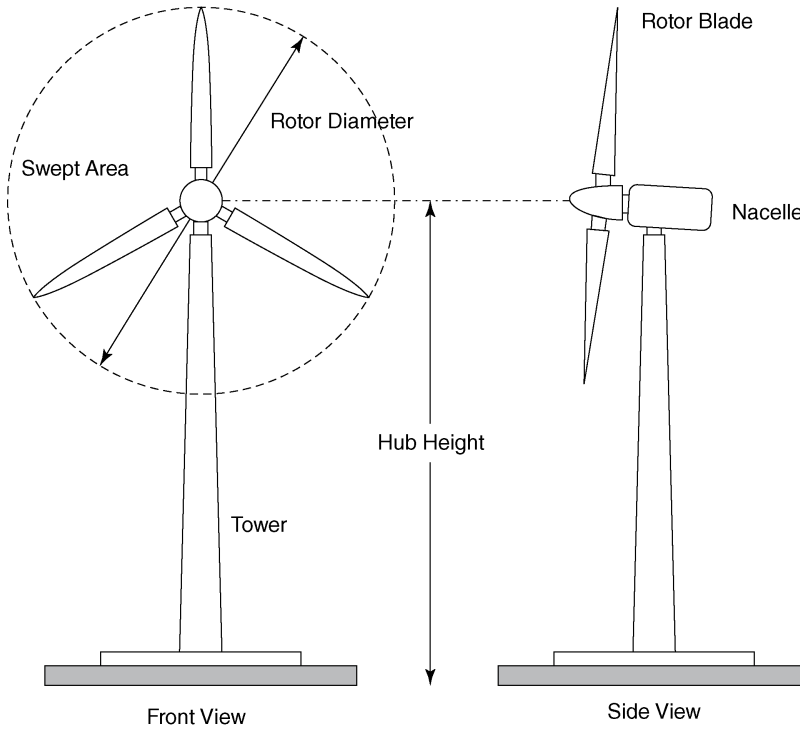

Figure 4.4 HAWT schematic and nomenclature.

power-available relationship, it is not surprising that the ideal location for wind turbines is where wind speeds are high. Wind resource information will be examined in Section 4.3. The most fundamental question relating to Equation 4.2 is how much of the available power can be extracted from the wind. The analysis of Betz is the traditional approach used to answer the question.The Betz analysis uses an actuator disk approach. In actuator theory, all energy transfer takes place in the plane of the actuator, and only energy transformation takes place upstream and downstream of the actuator. Actuator disk analysis is illustrated in Figure 4.5. The figure depicts three distributions: pressure, velocity, and cross-sectional flow area. Each will be examined in turn. The actuator disk is represented by the blades in the pressure and velocity distributions and by a solid line in the cross-sectional area distribution. The actuator area, the area swept by the blades, is $A = \pi D^2/4$, where D is the rotor diameter. Far upstream from the actuator, at the point denoted as (e), for entrance, in Figure 4.5c, the velocity is the wind velocity – c in this analysis. At the actuator disk, the velocity has been reduced to $c(1 - a)$, and at the outlet, indicated as (o), the velocity is $c(1 - b)$. As the velocity is reduced from c to $c(1 - a)$ upstream of the actuator, the static pressure increases from P_e to P_1. When energy is extracted from the flow at the actuator, the pressure discontinuously decreases to P_2. Downstream of the actuator, as the velocity continues to decrease, the pressure increases from P_2 to P_o. Far downstream of the actuator, atmospheric pressure is recovered, so that $P_o = P_e$, the atmospheric pressure. Since the velocity decreases from the entrance to the outlet, the cross-sectional flow area must increase. Cast in terms of the variables in the figure, the power available, Equation 4.2, becomes

$$\text{Power}_{\text{avail}} = \frac{1}{2}\rho A c^3 \tag{4.3}$$

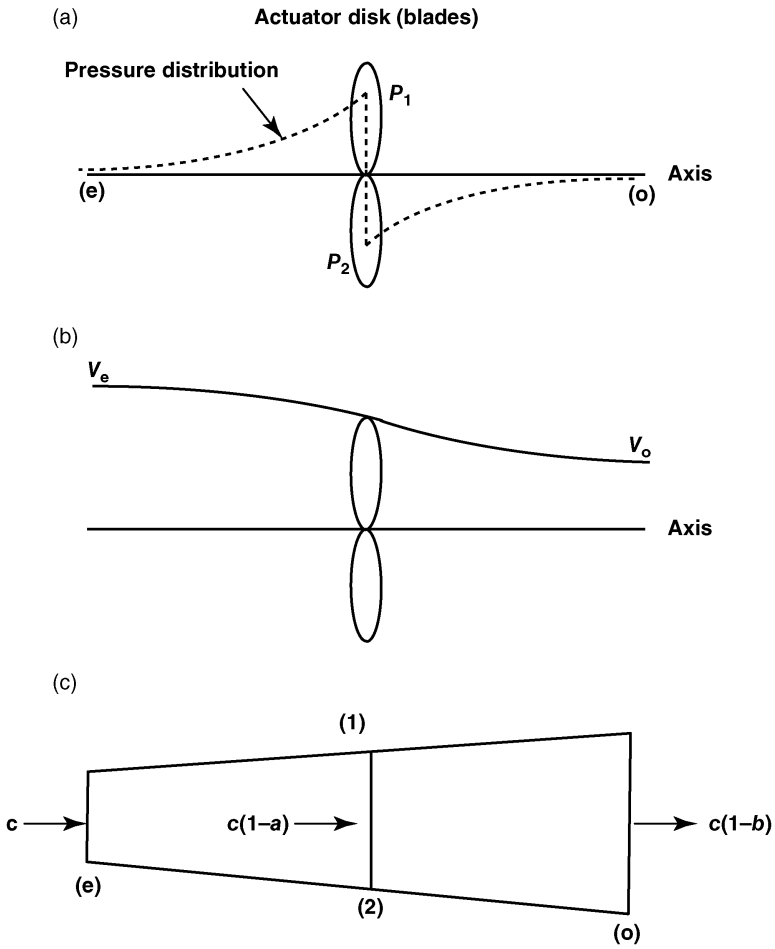

Figure 4.5 Actuator disk schematic with pressure, velocity, and area distributions illustrated: (a) static pressure distribution; (b) velocity distribution; (c) cross-sectional flow area distribution.

Upstream and downstream of the actuator, the incompressible flow Bernoulli equation applies and can be written as

$$P_e + \frac{1}{2}\rho c^2 = P_1 + \frac{1}{2}\rho c^2(1-a)^2$$
$$P_2 + \frac{1}{2}\rho c^2(1-a)^2 = P_o + \frac{1}{2}\rho c^2(1-b)^2 \tag{4.4}$$

Solving for the pressure differences yields

$$\frac{P_e - P_1}{\rho} = \frac{1}{2}c^2\left[(1-a)^2 - 1\right]$$
$$\frac{P_2 - P_o}{\rho} = \frac{1}{2}c^2\left[(1-b)^2 - (1-a)^2\right] \tag{4.5}$$

Adding the two expressions and using $P_e = P_o$, the expression for the change in pressure across the actuator becomes

$$\begin{aligned}\frac{P_2 - P_o + P_e - P_1}{\rho} &= \frac{P_2 - P_1}{\rho} = \frac{1}{2}c^2\left[(1-b)^2 - (1-a)^2 + (1-a)^2 - 1\right] \\ &= \frac{1}{2}c^2\left[(1-b)^2 - 1\right]\end{aligned} \tag{4.6}$$

The change in pressure, $P_1 - P_2$, is thus

$$P_1 - P_2 = \frac{1}{2}\rho c^2\left[1 - (1-b)^2\right] \tag{4.7}$$

The axial thrust on the actuator is

$$T = (P_1 - P_2)A = \frac{1}{2}\rho A\, c^3\left[1 - (1-b)^2\right] \tag{4.8}$$

But the axial thrust is equal to the change in axial momentum

$$T = \dot{m}[c - c(1-b)] = \rho A\, c(1-a)[c - c(1-b)] = \rho A\, c^2(1-a)b \tag{4.9}$$

Equating Equations 4.8 and 4.9 and solving yields

$$\begin{aligned}&\frac{1}{2}\rho A\, c^3\left[1 - (1-b)^2\right] = \rho A\, c^2(1-a)b \\ &a = \frac{b}{2}\end{aligned} \tag{4.10}$$

Equation 4.10 demonstrates that the change in velocity upstream of the actuator plane is equal to the change in velocity downstream of the actuator plane. In many actuator disk analyses, the velocity at the actuator plane is taken as the average of the far upstream velocity c and far downstream velocity $c(1-b)$ – an equivalent result.

The rate of kinetic energy change, expressed in terms of c and a, is

$$E_k = \frac{1}{2}\rho A\, c(1-a)\left[c^2 - (1-b)^2\right] = \frac{1}{2}\rho A\, c(1-a)\left[c^2 - (1-2a)^2\right] \tag{4.11}$$

The maximum rate of change of kinetic energy, the maximum power extracted, will occur when the derivative of E_k with respect to a is set equal to zero, or

$$\begin{aligned}&\frac{dE_k}{da} = 0 = (1)(1-a)^2 + a2(1-a)(-1) \\ &a = \frac{1}{3}\end{aligned} \tag{4.12}$$

Then, using $a = 1/3$ in Equation 4.11 yields the expression for maximum power extracted:

$$\text{Power}_{max} = \frac{8}{27}\rho A\, c^3 \tag{4.13}$$

The power coefficient is defined as the power extracted divided by the available power of the wind stream or

$$\text{Cp} = \frac{\text{Power}_{ext}}{\frac{1}{2}\rho A\, V_{wind}^3} \tag{4.14}$$

The maximum value of the power coefficient, the Betz limit, then becomes

$$\mathrm{Cp}_{\max} = \frac{\frac{8}{27}\rho A\, c^3}{\frac{1}{2}\rho A\, c^3} = \frac{16}{27} = 0.5926 \tag{4.15}$$

The Betz limit represents the maximum value of the power coefficient and defines the maximum power that can be extracted from a given wind stream. The power coefficient is perhaps the most important single metric used in characterizing a wind turbine. Equation 4.14 is usually rewritten to specify the power extracted in terms of the power coefficient:

$$\mathrm{Power}_{\mathrm{ext}} = \frac{1}{2}\mathrm{Cp}\rho A\, V_{\mathrm{wind}}^3 \tag{4.16}$$

If the power coefficient is the most important metric for wind turbines, then Figure 4.6 is arguably the most referenced figure in wind turbine engineering. This figure presents the expected range of power coefficients for well-designed wind turbines of different configurations. The abscissa, the x-axis, is the advance ratio, which is the rotor tip speed divided by the wind speed, or

$$\Omega = \frac{r\omega}{V_{\mathrm{wind}}} \tag{4.17}$$

where r is the rotor radius and ω is the rotor rotation rate.

The Betz limit is shown on the figure. The Glauert ideal Cp is the result of a more detailed analysis that explicitly involves the advance ratio. Lying below and to the right of the Glauert ideal are the expected Cp values for different wind turbine configurations. The American multi-blade and the Dutch windmill possess the lowest Cp values. In many recent publications, the

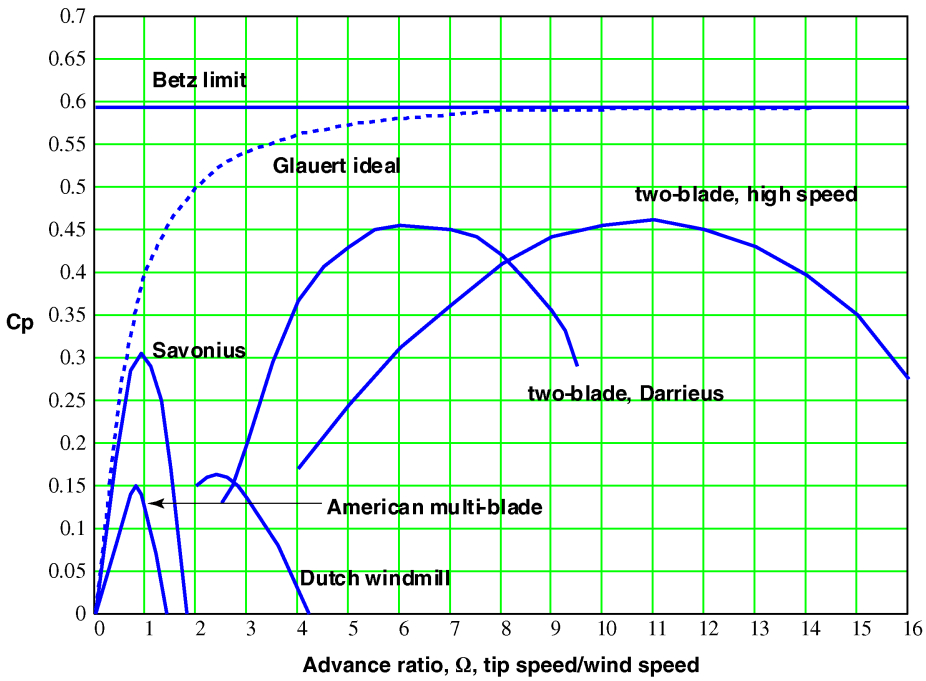

Figure 4.6 Power coefficient versus advance ratio for different wind turbine configurations.

labels for the American multi-blade and the Savonius configurations have been interchanged, with the result that the Savonius Cp values are smaller than those for the American multi-blade. The values presented in Figure 4.6 are correct. This interchange of configurations designations has had detrimental effects on considerations of Savonius devices, as the implication is that a Savonius rotor would not be as efficient as the American multi-blade. As pointed out by Johnson (2001), such an error will take years to correct. In addition to the Savonius and the American multi-blade, typical power coefficient values for the Darrieus and the modern, high-speed two-blade HAWT are presented. The HAWT shows relatively high Cp values over a rather wide range of advance ratios.

Example 4.1
A 27 mph wind at 14.7 psia and 70 °F enters a two-bladed wind turbine with a diameter of 36 ft. Calculate (a) the power of the incoming wind, (b) the theoretical maximum power that could be extracted, (c) a reasonable attainable power, (d) the rotor speed in rpm required for part (c), and (e) the torque for part (c).

Solution The power of the incoming wind is defined by Equation 4.2:

$$\text{Power} = \frac{1}{2}\rho A V^3$$

The thermal equation of state is

$$P = \rho R T$$

where R is the gas constant for air and, in English Engineering and SI units, has the values

$$R = 53.35\frac{\text{ft lbf}}{\text{lbm °R}} = 287\frac{\text{J}}{\text{kg K}}$$

The absolute temperature is required for use in the equation of state:

$$70\,^\circ\text{F} = (460 + 70)^\circ\text{R} = 530\,^\circ\text{R}$$

Using the thermal equation of state, the density becomes

$$\rho = \frac{P}{RT} = 14.7\frac{\text{lbf}}{\text{in}^2}144\frac{\text{in}^2}{\text{ft}^2}\frac{\text{lbm °R}}{53.35\ \text{ft lbf}}\frac{1}{530\,^\circ\text{R}} = 0.075\ \frac{\text{lbm}}{\text{ft}^3}$$

The area swept by the rotor is

$$A = \frac{\pi}{4}D^2 = \frac{\pi}{4}(36\ \text{ft})^2 = 1018\ \text{ft}^2$$

The power available from the wind is thus

$$\begin{aligned}\text{Power}_{\text{avail}} &= \frac{1}{2}\rho A V^3 = \frac{1}{2}0.075\ \frac{\text{lbm}}{\text{ft}^3}1018\ \text{ft}^2\left(27\frac{\text{mi}}{\text{h}}\frac{5280\ \text{ft}}{\text{mi}}\frac{\text{h}}{3600\ \text{s}}\right)^3 \\ &= 2.371\times10^6\ \frac{\text{lbm ft}^2}{\text{s}^3}\frac{\text{lbf s}^2}{32.174\ \text{ft lbm}} = 73\,693\frac{\text{ft lbf}}{\text{s}}\frac{\text{s hp}}{550\ \text{ft lbf}} \\ &= 134\ \text{hp} = 100\ \text{kW}\end{aligned}$$

The power available is 134 hp or 100 kW. The theoretical maximum power that could be extracted is the Betz limit, or

$$\text{Power}_{\text{max}} = 0.5926 \times \text{Power}_{\text{avail}} = 0.5926 \times 134\ \text{hp} = 79.4\ \text{hp} = 59.3\ \text{kW}$$

For a two-bladed HAWT, Figure 4.6 suggests Cp = 0.45 for an advance ratio, $\Omega = r\omega/V_{\text{wind}}$, of 11. A reasonable attainable power from such a wind turbine is

$$\text{Power}_{\text{act}} = 0.45 \times 134\,\text{hp} = 60.3\,\text{hp} = 45\,\text{kW}$$

Using the definition of advance ratio, the rotor speed can be cast as

$$\omega = \frac{\Omega V_{\text{wind}}}{0.5D} = 11 \times 39.6\,\frac{\text{ft}}{\text{s}}\frac{1}{0.5 \times 36\,\text{ft}} = 24.2\,\frac{1}{\text{s}} = 24.2\,\text{Hz}$$
$$= 24.2\,\frac{1}{\text{s}}\frac{\text{rev}}{2\pi}\frac{60\,\text{s}}{\text{min}} = 231\,\text{rpm}$$

In order to attain a Cp value of 0.45, a speed of 231 rpm is needed. From Equation 2.11, the torque becomes

$$\tau = \frac{\text{Power}_{\text{act}}}{\omega} = 60.3\,\text{hp}\,\frac{550\,\text{ft lbf}}{\text{s hp}}\frac{\text{s}}{24.2} = 1370\,\text{ft lbf}$$

4.3 Wind Energy Resources

Section 4.2 treated wind turbine performance in terms of a specified wind speed and pointed out the cubic relationship between speed and power from the wind. Since the wind is variable in terms of the speed, direction, and altitude, the results of the previous section need to be extended to account for site-specific wind conditions. Extensive wind data are available at the NREL web site, www.nrel.gov. The primary wind resources document is the *Wind Energy Resource Atlas of the United States* (http://rredc.nrel.gov/wind/pubs/atlas/). This atlas contains annual average wind resource data as well as regional summaries and extensive explanations and references for the statistics of wind. A unique feature is as assessment of the "certainty" of the wind data. The wind data are rated from 1 (lowest degree) to 4 (the highest degree of certainty).

The wind power density distribution across the USA is very useful for first-order evaluations of candidate locations to determine if wind energy harvesting is feasible. The wind power density is the available average wind power per square meter of wind turbine area. The basis of the distribution classification are the wind power density classes. The wind power density is measured from class 1 (lowest) to class 7 (highest) and is specified at nominal 10 m and 50 m elevations. Table 4.1 presents the wind power density classes and their associated wind speeds.

Table 4.1 Wind power density classes.

Wind power class	10 m (33 ft)		50 m (164 ft)	
	Wind power density (W/m^2)	Speed (m/s [mph])	Wind power density (W/m^2)	Speed (m/s [mph])
1	0	0	0	0
2	100	4.4 [9.8]	200	5.6 [12.5]
3	150	5.1 [11.5]	300	6.4 [14.3]
4	200	5.6 [12.5]	400	7.0 [15.7]
5	250	6.0 [13.4]	500	7.5 [16.8]
6	300	6.4 [14.3]	600	8.0 [17.9]
7	400	7.0 [15.7]	800	8.8 [19.7]
	1000	9.4 [21.1]	2000	11.9 [26.6]

Each wind class is bounded by a minimum wind power density and a maximum wind power density. The wind speeds in meters per second and miles per hour corresponding to the minimum and maximum wind power density values are also indicated in Table 4.1. For example, class 4 is defined as a wind power density between 200 and 250 W/m^2 or wind speed range between 5.6 and 6.0 m/s, all at 10 m elevation. At a 50 m elevation, the wind power classes are defined using different power density values than at 10 m elevation.

The most useful summary figure from the *Wind Energy Resource Atlas of the United States* is the annual average wind power density distribution, reproduced as Figure 4.7a. In this figure, the darker the color, the higher the wind class. Much of the Midwest is assessed as wind class 3 or 4, with isolated portions of the mountain west containing embedded regions of class 5 or 6. Except for areas near the coast, the Southeast region is not generally suitable for wind energy production. NREL states that wind energy is appropriate only for wind class 3 and above. A newer NREL-derived figure is provided as Figure 4.7b: the average annual wind speed at an elevation of 80 m. Figure 4.7b is likely the more useful of the two as it demonstrates that the US

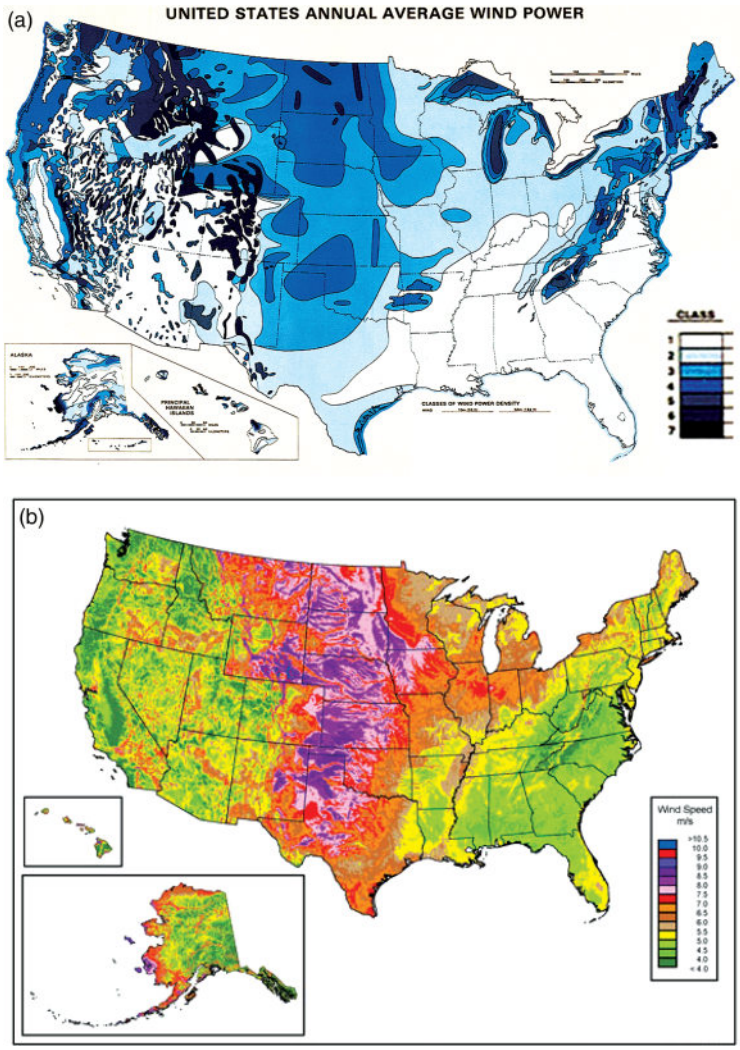

Figure 4.7 US annual average wind resources: (a) wind power density; (b) wind speed at 80 m. *Source*: NREL.

Midwest region is a prime location for high wind speeds at an elevation of 80 m –a good height for large wind turbines.

The wind power density as illustrated in Figure 4.7 accounts for the yearly variation in wind speed at given locations. In order to understand the basis of development of information such as is contained in Figure 4.7, the statistics of wind energy need to be explored.

The probability of occurrence of a given wind speed v is expressed by the Weibull distribution:

$$h(v,k,c) = \frac{k}{c}\left(\frac{v}{c}\right)^{k-1} \exp\left[-\left(\frac{v}{c}\right)^{k}\right] \tag{4.18}$$

In the Weibull distribution, c is the scale parameter and k is the shape parameter. The shape parameter controls the shape of the distribution; the larger the shape factor, the closer the distribution comes to being Gaussian. The scale parameter controls the value of the mode (the most probable speed). The larger the scale parameter, the higher the mode, and the lower the probability of a given speed less than the mode. The shape parameter is dimensionless, and the scale parameter must have the same units as the speed. For wind distributions, the shape parameter value is usually near 2 (Patel, 2005).

Figure 4.8 presents the probability distribution, expressed in percent, for shape parameters of 1, 2, and 3 for a constant value of $c = 10$ mph. A shape parameter of 1 yields an exponential distribution that has the highest percentage of hours at zero speed, and a shape parameter of 2 results in a distribution skewed toward a higher percentage of occurrence at the lower speeds. A shape parameter of 3 yields a more symmetrical distribution and starts to resemble the Gaussian. A shape factor of $k = 2$ provides a generally acceptable match for the wind speed distribution at most sites.

Figure 4.9 illustrates the probability distribution, expressed in hours per year per mile per hour, for scale parameters values of 10, 15, and 20 mph for a constant value of $k = 2$. The smaller the value of the scale parameter, the more hours at lower wind speeds. As the value of c increases, the mode wind speed values increase and the number of hours per year at wind speeds greater than the mode increases.

Figures 4.8 and 4.9 provide a visual interpretation of the behavior of the Weibull distribution. Figure 4.10 was generated from wind data and shows an overlay of a Weibull distribution for $k = 2$. Although not an exact match, the results do demonstrate that the Weibull distribution is

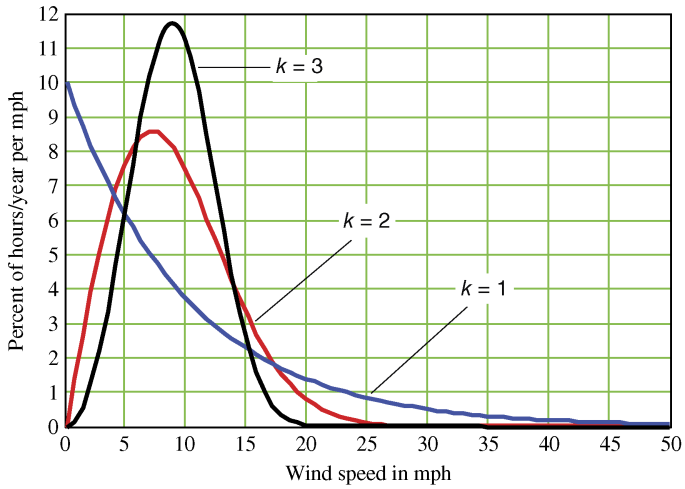

Figure 4.8 Weibull distribution for $c = 10$ mph and various k values.

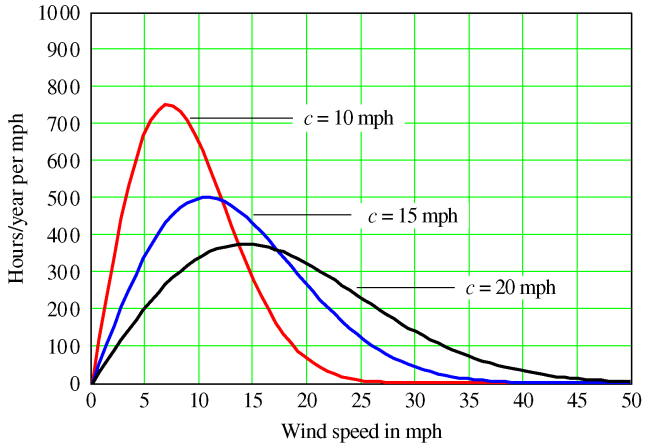

Figure 4.9 Weibull distribution for various c values and $k = 2$.

reasonable, especially when considering the actual energy content for low wind speeds (<2 m/s) is small and contributes little to power generation. This is explored in Examples 4.2 and 4.3.

However, the real question is how the Weibull distribution relates to assessing the metrics of wind energy. The mode speed is the most probable speed in a distribution. The mean speed is defined as

$$V_{\text{mean}} = \int_0^\infty h(v,k,c)v \, \mathrm{d}v \tag{4.19}$$

Since the wind power is proportional to the cube of the wind speed, the average power density available for collection over a year per unit area of swept area is

$$\text{Power}_{\text{avail}} = \int_0^\infty \frac{1}{2}\rho h(v,k,c)v^3 \, \mathrm{d}v \tag{4.20}$$

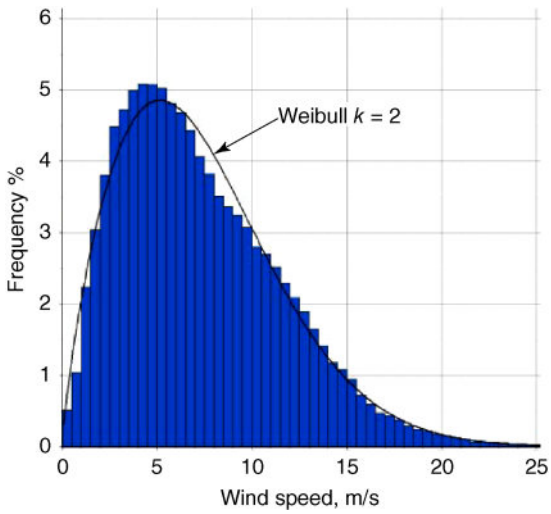

Figure 4.10 Wind speed data and a Weibull distribution $k = 2$. *Source*: http://projects-web.engr.colostate.edu/ALP/ALP_78_Walsenburg_South.htm. Reproduced with permission of Colorado State University.

Thus, the speed of interest for wind energy is the root-mean-cube (rmc) speed

$$V_{\text{rmc}} = \sqrt[3]{\int_0^\infty h(v,k,c)v^3\,\mathrm{d}v} \tag{4.21}$$

and the annual average power density available becomes

$$\text{Power}_{\text{avail}} = \frac{1}{2}\rho V_{\text{rmc}}^3 \tag{4.22}$$

Based on the results of Figure 4.6, a reasonable value of the power coefficient for a modern, well-designed wind turbine is 0.5. The annual average extraction power density can be cast as

$$\text{Power}_{\text{ext}} = \frac{1}{4}\rho V_{\text{rmc}}^3 \tag{4.23}$$

The total energy that can extracted per year (8760 h/year) for a given distribution is the integral of Equation 4.23 for each velocity over all possible velocities, or

$$\text{Energy}_{\text{rmc}} = 0.25\rho \int_0^\infty h(v,k,c) \times 8760v^3\,\mathrm{d}v \tag{4.24}$$

The best way to assimilate the aforementioned is an example problem.

Example 4.2

Find V_{mode}, V_{mean}, V_{rmc}, the power density available distribution, and the power extracted per square meter for a wind turbine at a site which possesses a Weibull wind distribution with $c = 9$ m/s and $k = 2.0$. The density is 1.225 kg/m^3. The choice of $c = 9$ m/s is consistent with locations favorable for wind energy in Figure 4.7b.

Solution A graphical representation of the Weibull distribution for $k = 2.0$ and $c = 9$ m/s is presented in Figure 4.11.

The mode, the most probable wind speed, occurs at 6.36 m/s. The mean wind speed and the rmc speed are defined in Equations 4.19 and 4.21 respectively. The arithmetic for this example is accomplished in Mathcad, and the Mathcad worksheet is reproduced in Figure 4.12.

At the start of the worksheet, mph and kW are defined in Mathcad variables and the density (specified in the problem statement) is indicated. Functions are defined for the Weibull distribution $h(v,k,c)$ and the power density PowerDen(V). The shape and scale parameters from the problem statement are inserted in the worksheet. The mode speed is

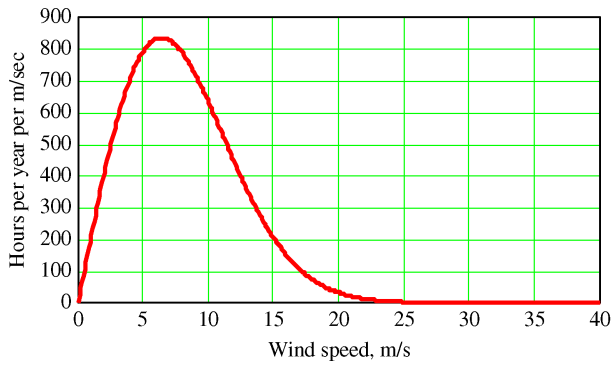

Figure 4.11 Weibull distribution for $k = 2.0$ and $c = 9$ m/s.

$\rho := 1.225 \cdot \frac{kg}{m^3}$ density $mph := \frac{mi}{hr}$ define mph $kW := 1000 \cdot watt$ define kW

$c := 9 \cdot \frac{m}{sec}$ $k := 2.0$ specify values of the scale parameter and shape parameter

$h(v,k,c) := \frac{k}{c} \cdot \left(\frac{v}{c}\right)^{k-1} \cdot e^{-\left(\frac{v}{c}\right)^k}$ Weibull distribution function definition.

$PowerDen(V) := 0.5 \cdot \rho \cdot V^3$ Power density definition.

Generate distribution plot for specified parameters:

Find V_{mode}.

$vm := 10 \cdot \frac{m}{s}$

Given

$$\frac{d}{dvm}\left[\frac{k}{c} \cdot \left(\frac{vm}{c}\right)^{k-1} \cdot e^{-\left(\frac{vm}{c}\right)^k}\right] = 0$$

$V_{mode} := Find(vm)$

$V_{mode} = 6.364 \frac{m}{s}$ $PowerDen(V_{mode}) = 157.866 \frac{watt}{m^2}$

$$V_{mean} := \int_{0 \cdot \frac{m}{sec}}^{\infty \cdot \frac{m}{sec}} \frac{k}{c} \cdot \left(\frac{v}{c}\right)^{k-1} \cdot e^{-\left(\frac{v}{c}\right)^k} \cdot v \, dv$$

$V_{mean} = 7.976 \frac{m}{sec}$ $PowerDen(V_{mean}) = 310.791 \frac{watt}{m^2}$

$$V_{rmc} := \sqrt[3]{\int_{0 \cdot \frac{m}{sec}}^{\infty \cdot \frac{m}{sec}} \frac{k}{c} \cdot \left(\frac{v}{c}\right)^{k-1} \cdot e^{-\left(\frac{v}{c}\right)^k} \cdot v^3 \, dv}$$

$V_{rmc} = 9.896 \frac{m}{sec}$ $PowerDen(V_{rmc}) = 593.567 \frac{watt}{m^2}$

$Power(v) := 0.5 \cdot \rho \cdot h(v,k,c) \cdot v^3$ Power density available with Cp = 1.0.

$PowerCp(v) := 0.25 \cdot \rho \cdot h(v,k,c) \cdot v^3$ Power density available with Cp = 0.5.

$$Energy := \int_{0 \cdot \frac{m}{sec}}^{100 \cdot \frac{m}{sec}} 0.25 \cdot \rho \cdot \left[\frac{k}{c} \cdot \left(\frac{v}{c}\right)^{k-1} \cdot e^{-\left(\frac{v}{c}\right)^k}\right] \cdot 8760 \frac{hr}{yr} \cdot v^3 \, dv$$

$Energy = 2.6 \times 10^3 \cdot kW \cdot \frac{hr}{yr \cdot m^2}$

Figure 4.12 Mathcad solution for Example 4.2.

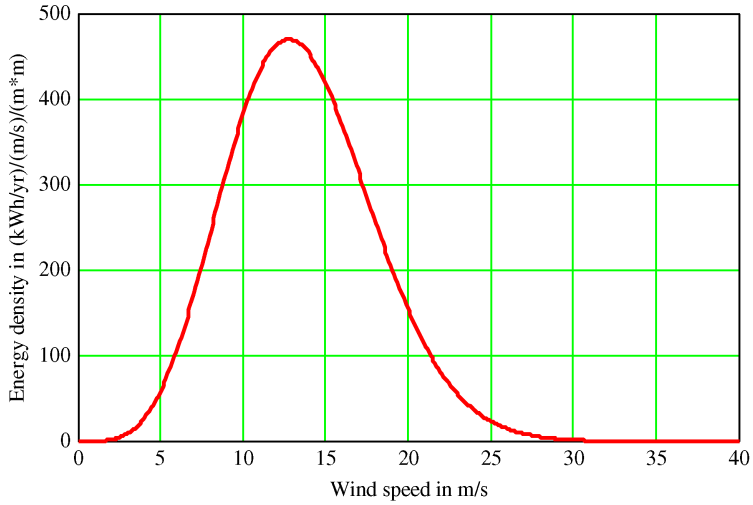

Figure 4.13 Annual energy available distribution for Example 4.2.

6.36 m/s, and the power density is calculated as 158 W/m^2. The mean speed is computed using Equation 4.19 to be 7.98 m/s with a power density of 311 W/m^2. This value is congruent with what might be expected from a location suitable for wind energy extraction; see Figure 4.7b. The rmc speed is 9.90 m/s (using Equation 4.21), and the power density at the rmc speed is 594 W/m^2. The use of Mathcad, and its ability to carry units in computations, simplifies the arithmetic in this example. Since the cubic power of the wind speed is specified in the average power density expression, care should always be exercised to differentiate between the mode, mean, and rmc speeds as the power density manifests significant variation depending on which value is used.

The energy density available for collection over a year per unit area of wind turbine is specified in Equation 4.24, since $h(v, k, c) \times 8760$ represents the hours per year at a given wind speed from the distribution. Figure 4.13 presents the energy density per year per square meter per meter per second for the wind speed distribution specified in the problem statement. The mode for the annual energy density available is near 13 m/s. Although the hours per year at 13 m/s are small (far from the mode, as illustrated in Figure 4.11), the product of this wind speed and the hours per year is a maximum for the distribution because of the cubic functional dependence on wind speed.

An estimate of the annual energy extracted for a Cp = 0.5 for a given wind speed distribution is provided by Equation 4.24. Under the assumption of a Cp = 0.5, the annual energy extracted for this distribution is 2600 kW h/(year/m^2).

Section 4.2 delineated the performance characteristics of wind turbines at specified speeds. This section has described the wind speed distribution description and the statistics of the wind speed distribution. Section 4.4 assimilates the material in Sections 4.2 and 4.3 and addresses the operation and control of wind turbines as a function of wind speed.

4.4 Wind Turbine Operation

What should the operating strategy be for a wind turbine as a function of wind speed? The answer is *not* to always operate the wind turbine at the maximum power coefficient. Why not operate the wind turbine at the maximum Cp? Operation at the maximum Cp for all wind

speeds would maximize the energy extracted, but factors such as generator capacity, structural requirements, and safety preclude such operation. The maximum speed-range will occur for only a few hours for a given wind speed distribution. Thus, sizing a generator for an input corresponding to the maximum-speed range would result in an oversized generator that would operate at maximum output only a few hours per year. And if the maximum Cp were specified, the advance ratio Ω would have to be maintained constant. As the wind speed increased, the rotor rotation rate would have to increase to maintain a constant Cp. Since the radial stresses in a rotor are proportional to the rotation speed, operating at high wind speeds and a constant Ω would require a structurally robust wind turbine. Additionally, as the wind speed increases, safety issues and structural integrity become of increasing concern.

But, no matter what operating strategy is used, a wind turbine must contain a controller to implement the strategy and mechanical elements to respond to the controller. Figure 4.14, from the NREL web site, graphically illustrates typical HAWT features. The cutaway of the nacelle shows the gearbox and generator as well as other elements needed for operation. The blades and tower are also shown. The yaw motor and yaw drive are used to keep the plane of the blade oriented into the wind. The pitch mechanism on the blades adjusts the angle of the blades (the pitch) with respect to the wind direction in order to control the power extracted from the wind. The purpose of the brake is to slow down or completely stop the rotor. All of these element are needed to implement a control strategy.

The ultimate purpose of a wind turbine control strategy is to regulate the power output of the turbine as a function of wind speed and direction. Additionally, the control protocol must ensure safe operation over all wind conditions. Patel (2005) suggests that the power output versus wind speed characteristic of a wind turbine can be viewed as being composed of several regions. Figure 4.15, adapted from Patel (2005), illustrates a typical power output as a function of wind speed and delineates the various operating regimes and conditions. The ordinate variable is the percentage of generator output.

The first condition is the cut-in speed of the system. Below the cut-in wind speed, the system component efficiencies are so low that running the system is not worthwhile. Once the cut-in speed is reached, the system is operated in a constant-Cp region. In the constant-Cp region, the

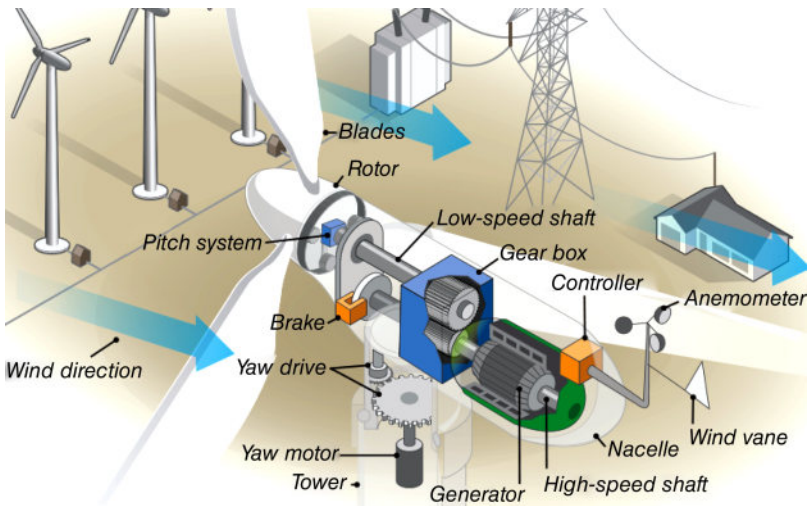

Figure 4.14 HAWT nacelle components and features. *Source*: http://www.energy.gov/eere/wind/inside-wind-turbine-0 (NREL).

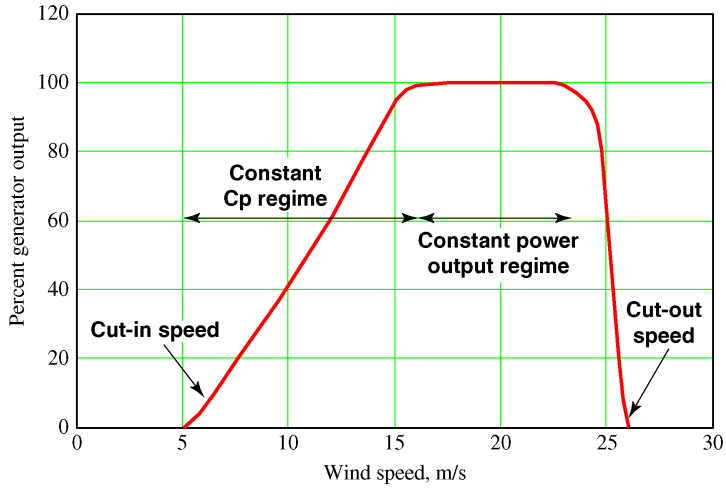

Figure 4.15 Typical regimes of turbine speed control.

turbine extracts the maximum power from the wind, but the power extracted is less than the rated input to the generator. The rotor speed is varied so that the advance ratio is maintained near the maximum Cp value. When the wind speed is sufficiently high, the power extracted by the rotor can exceed the rated input of the generator. In this regime, the constant power output regime, the system is made to produce the rated output of the generator by operating the turbine at a Cp lower than the maximum Cp. The cut-out speed is the wind speed beyond which operation would damage the system. For speed in excess of the cut-out, the rotor pitch is set to unload the rotor, and the rotor is locked with the brake. The total energy that can be extracted from a given wind distribution is reduced by the rated input of the generator and the cut-in and cut-out speeds. Example 4.2 will be extended to illustrate these effects.

Example 4.3

The system described in Example 4.2 is specified to have a cut-in speed of 5 m/s, a cut-out speed of 35 m/s, and a rated generator input of 0.8 kW/m^2. The maximum power coefficient Cp is 0.45. Determine and plot the following for both the system with no controls and the system controlled to meet the constraints: (a) the power density of the system, (b) the Cp versus wind speed required, (c) energy extraction, and (d) the total energy extracted by the system.

Solution Much of the information requested for the "no controls" part of this problem was accomplished in Example 4.2. However, since the results are more meaningful if both the "no controls" and the controlled versions are compared, both will be examined in the solution. Mathcad will be utilized for all the calculations. The Mathcad worksheet for the solution to this problem is given in Figure 4.16.

The conditions and constraints defined in the problem statement are entered in the worksheet. The range of wind speed is designated by a Mathcad range variable, $v := 0, 0.1, \ldots,$ 40 m/s. This range variable specifies that the velocity v is to range from 0 to 40 m/s. Any time v is specified, all of the values in the range are automatically included. The power density function for the speed range specified is

$$\text{PowerDen}(v) = 0.5\text{Cp}_{\text{nom}}\rho v^3 \tag{4.25}$$

$v := 0 \cdot \frac{m}{sec}, 0.1 \cdot \frac{m}{sec} .. 40 \cdot \frac{m}{sec}$

$Cp_{nom} := 0.45$ Power coefficient.

$Powerin_{max} := 0.80 \cdot \frac{kW}{m^2}$ Generator input

$V_{cutin} := 5 \cdot \frac{m}{sec}$ Cut-in speed

$V_{cutout} := 35 \cdot \frac{m}{sec}$ Cut-out speed

$PowerDen(v) := 0.5 \cdot Cp_{nom} \cdot \rho \cdot v^3$ Power density available with specified Cp.

$$PowerDenCon(v) := \begin{cases} 0 \cdot \frac{kW}{m^2} & \text{if } v < V_{cutin} \\ Powerin_{max} & \text{if } PowerDen(v) > Powerin_{max} \\ 0 \cdot \frac{kW}{m^2} & \text{if } v > V_{cutout} \\ PowerDen(v) & \text{otherwise} \end{cases}$$

Piece-wise continuous function defined to implement the cut-in, cut-out, and rated power constraints.

$CpV(v) := \frac{PowerDenCon(v) \cdot Cp_{nom}}{PowerDen(v)}$ Power coefficient as a function of speed.

$Energy(v) := PowerDen(v)\, h(v, k, c) \cdot 8760\,hr$ Energy density available with nominal Cp.

$EnergyCon(v) := PowerDenCon(v) \cdot h(v, k, c) \cdot 8760\,hr$ Energy density with controls.

$$EnergyCon := \int_{0 \cdot \frac{m}{sec}}^{1000 \cdot \frac{m}{sec}} EnergyCon(v) \cdot \frac{1}{yr}\, dv$$

$EnergyCon = 1.912 \times 10^3 \cdot kW \cdot \frac{hr}{yr \cdot m^2}$

Energy extracted per year per m^2 for system with controls.

$$Energy_{max} := \int_{0 \cdot \frac{m}{sec}}^{1000 \cdot \frac{m}{sec}} Energy(v) \cdot \frac{1}{yr}\, dv$$

$Energy_{max} = 2.34 \times 10^3 \cdot kW \cdot \frac{hr}{yr \cdot m^2}$

Energy extracted per year per m^2 with no controls.

$CaptureRatio := \frac{EnergyCon}{Energy_{max}}$ $CaptureRatio = 0.817$

Figure 4.16 Mathcad worksheet for Example 4.3.

The PowerDenCon(v) function is a piecewise continuous function in Mathcad that calculates the power density subject to the cut-in speed, the cut-out speed, and the rated input power of the generator. The first line sets the power density to zero for wind speeds less than the cut-in speed; the second line constrains the power extracted not to exceed the generator input power. The third line implements the cut-out speed constraint, and the last line ensures the constant-Cp regime results. Figure 4.17 presents the power densities for the controlled (constrained) and uncontrolled conditions. The power coefficient Cp as a function of velocity can be expressed as

$$Cp(v) = \frac{PowerDenCon(v)}{PowerDen(v)} \times Cp_{nom} \tag{4.26}$$

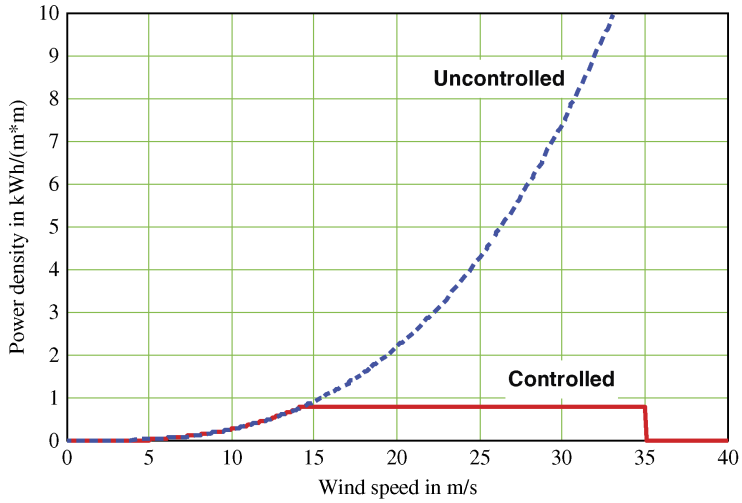

Figure 4.17 Power densities as a function of wind speed and constraints.

and is graphically illustrated in Figure 4.18. The Cp is zero until the cut-in speed is reached and zero for speed larger than the cut-out speed. The constant-Cp regime is present, as is the variable-Cp regime.

The power densities multiplied by the wind speed probability distribution $h(v, k, c)$ and the number of hours in a year, 8760, yield the energy densities. Figure 4.19 is a representation of the energy densities for the controlled and uncontrolled conditions. This figure is perhaps the most revealing in the solution. The effects of the cut-out speed and the generator input restriction are quite evident in the presentation. Since the areas under the curve are the total energy extracted, the effects of the control constraints are evident, especially at the higher wind speeds.

The energy densities integrated over all the speeds yield the total energy extracted. For the case of no control, the total energy extracted is 2340 kW h/(year/m^2) (slightly different from the result in Example 4.2 since the Cp for Example 4.3 is 0.45). The actual energy extracted corresponds to the case with controls implemented and is 1912 kW h/(year/m^2). The capture ratio is defined as the ratio of the actual energy extracted divided by the maximum possible (no controls) for a given wind speed distribution. For the conditions of this problem, the capture ratio is 0.817; that is, 82% of the available energy can be extracted. The only ways to significantly change the capture ratio are to increase the rated input power of the generator

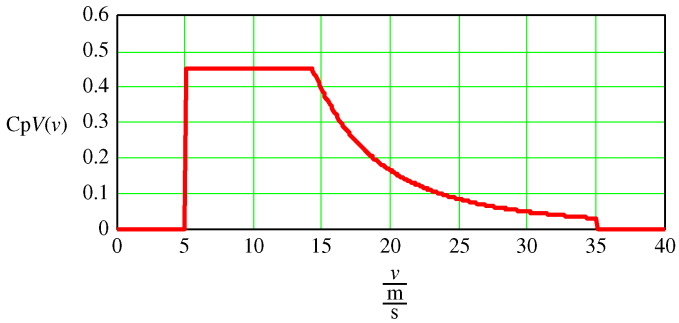

Figure 4.18 Cp as function of wind speed.

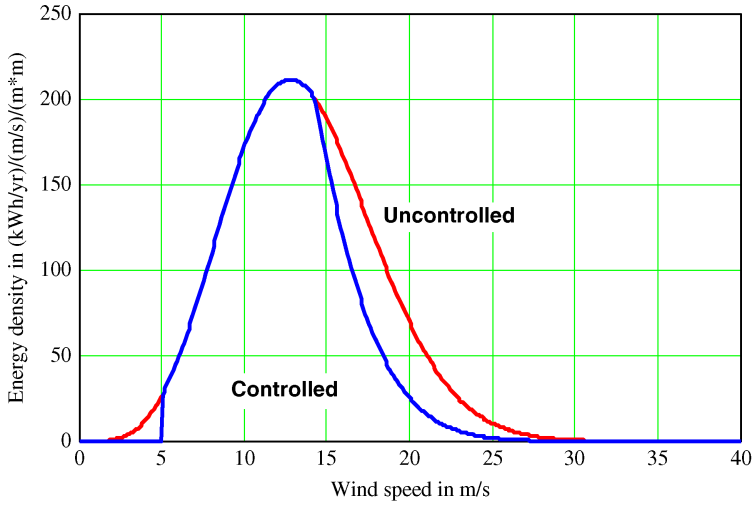

Figure 4.19 Energy densities as a function of wind speed.

and to increase the cut-out speed. For the stated conditions of this example problem, neither of these strategies for increasing the capture ratio is appropriate. Increasing the rated input power would be more expensive and would mean more generator operation at less than the rated input. For example, doubling the rated input of the generator to1.6 kW/m^2 would result in a capture ratio of 0.941, an increase of only 15% in actual energy extracted. Increasing the cut-off speed to a value much greater than 35 m/s would require enhanced structural integrity of the tower, nacelle, and blades.

Vestas Wind Systems, a leading manufacturer, of large (megawatt range) wind turbines, presents an interesting demonstration of the effectiveness of their control strategy for a Vestas V52 850 kW wind turbine. Figure 4.20 illustrates the response of the generator output for a V52 wind turbine subject to variations in wind speed.

The random nature of the wind speed variation is shown in Figure 4.20a. The purpose of the control protocol is to maintain the generator output at a constant value, 850 kW. In order to do this the blade pitch and the generator speed are modulated. Figure 4.20b and c illustrates the required modulations in pitch angle and generator speed. The generator output is tracked in Figure 4.20d. The success of the control protocol in maintaining a constant generator output is evident.

Thus far, this section has addressed the operation of a single wind turbine. However, wind turbine "farms," employing arrays of turbines, are common for utility applications. For wind turbines employed in arrays, the recommended space is 2–4 rotor diameters facing the prevailing wind and 8–12 rotor diameters parallel to the prevailing wind. For more than a single row of wind turbines in an array, the turbine locations in the succeeding rows are staggered. Figure 4.21 provides a schematic illustration of the recommended spacing of wind turbines on wind farms.

4.5 Commercial Wind Turbine Examples

This section contains some information and technical data on a sampling of wind turbines that are commercially available. The American Wind Energy Association provides a list of US manufacturers of small wind turbines at www.awea.org. A list of manufacturers worldwide for

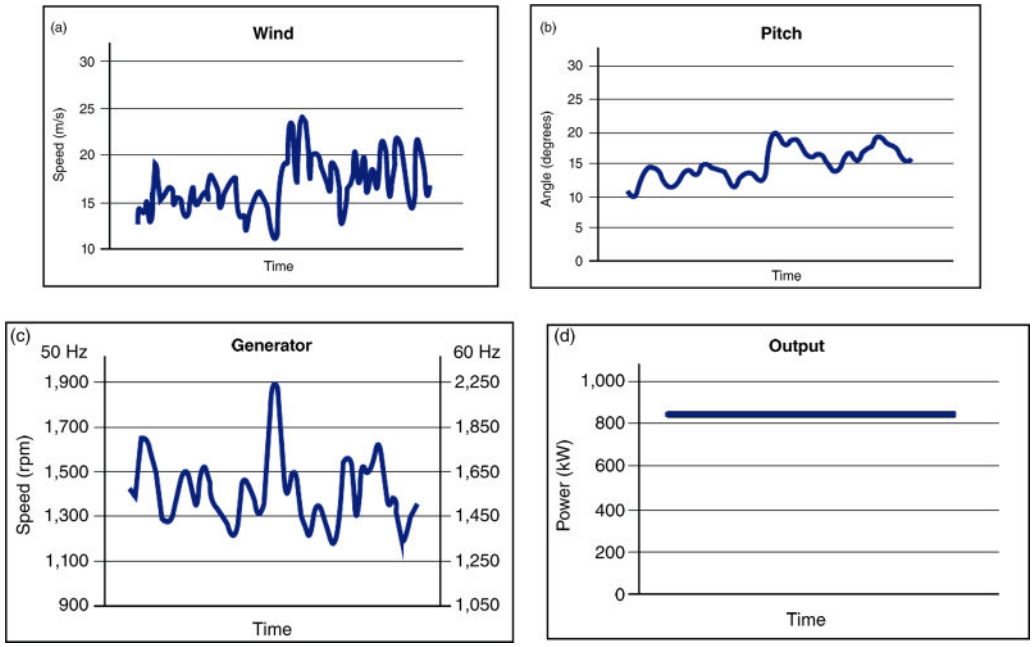

Figure 4.20 Vestas V52 850 kW wind turbine generator output response to: (a) wind speed variation; (b) pitch angle variation; (c) generator speed variation; (d) generator output. *Source*: Vestas web site.

large wind turbines is available under the heading of "large wind turbine manufacturers" at www.ecobusinesslinks.com. The information in this section was obtained from the various company web sites and literature and from the NREL database. Additional technical data and price information can be obtained by contacting the individual companies. Examples included herein are for a GE Energy 1.5 MW wind turbine, a Vestas V52 850 kW wind turbine, and a Bergey 10 kW Excel wind turbine. Almost all of the companies contained in the small and large wind turbine manufacturers list have web sites.

- *GE Energy 1.5 MW* GE Energy (https://www.gerenewableenergy.com/wind-energy.html and https://www.gepower.com/) manufacturers large wind turbines; in 2015 their wind turbines

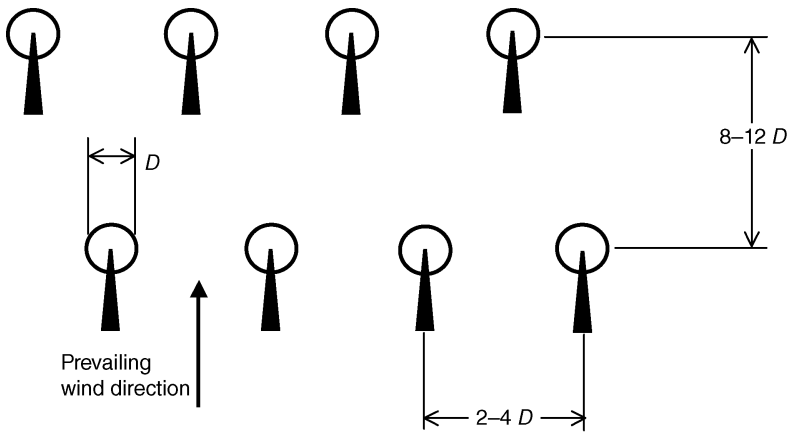

Figure 4.21 Wind turbine arrangement for wind farms.

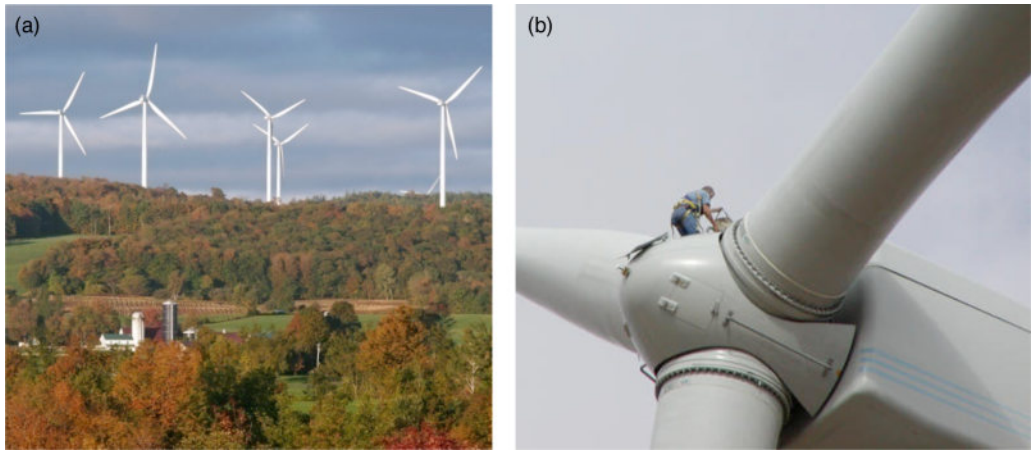

Figure 4.22 GE Energy 1.5 MW wind turbine: (a) wind farm example; (b) nacelle with person. *Source*: NREL.

had nominal outputs ranging from 1.7 to 3.2 MW. Although no longer manufactured, the GE family of 1.5 MW devices will be examined since they were very popular, with more than 12 000 sold by 2009. Figure 4.22 contains pictures of a GE Energy 1.5 MW wind turbines. Figure 4.22a shows the 1.5 MW turbines in a wind farm (see the discussion at the end of Section 4.4) arrangement. Figure 4.22b, a view of the nacelle and blade arrangement with a person, is included because it conveys some idea of the size of a 1.5 MW wind turbine.

The technical information for the turbine is presented in Table 4.2. The power curve is available in the GEA14954C 1.5 MW brochure, which can be downloaded from the internet.

- *Vestas V52 850 kW* The Vestas Wind Systems V52 has a rated output of 850 kW and is a popular wind turbine worldwide. The Vestas web site address is www.vestas.com. Vestas reported that in 2005 the company averaged more than 50 installations per week for the year. The effectiveness of the control system for the V52 was discussed in Section 4.4. Technical information on the V52 850 kW wind turbine is presented in Table 4.3, and a photograph is provided in Figure 4.23. The power output–wind speed performance characteristics are contained in Figure 4.24. The performance characteristics in the figure are parameterized in terms of the sound level.
- *Bergey 10 kW Excel* The previous examples were for relatively large wind turbines used for commercial power generation. The Bergey Wind Power Company (www.bergey.com)

Table 4.2 GE Power 1.5 MW specifications.

	1.5 s	1.5 se	1.5 sl	1.5 sle	1.5xle
Rated capacity (kW)	1500	1500	1500	1500	1500
Cut-in speed (m/s)	4	4	3.5	3.5	3.5
Cut-out speed (m/s)	25	25	20	25	20
Rated wind speed (m/s)	13	13	14	14	12.5
Rotor diameter (m)	70.5	70.5	77	77	82.5
Swept area (m^2)	3904	3904	4657	4657	5346
Rotor speed (rpm)	12–22.2	12–22.2	11–20.4	11–20.4	10.1–18.7

Table 4.3 Vestas V52 850 kW specifications.

Rated capacity (kW)	850
Cut-in speed (m/s)	4
Cut-out speed (m/s)	25
Rated wind speed (m/s)	16
Rotor diameter (m)	52
Swept area (m^2)	224
Rotor speed (rpm)	14–31.4

manufactures small wind turbines suitable for use in residential and small commercial applications.

Technical information on the Bergey 10 kW Excel wind turbine is presented in Table 4.4, and a photograph is shown in Figure 4.25. The power output–wind speed performance characteristics are contained in Figure 4.26.

Prices, for a complete system including a voltage regulator and a line-commutated inverter, ranged in 2014 from $23 000 to $29 000, depending on options.

The BWC Excel is most often installed on a guyed or self-supporting lattice tower, of height 60 ft with prices ranging from $9000 to $12 000. Other tower heights are also available. Thus, the cost per installed kilowatt is from $3600/kW to $4600/kW, again depending on the options chosen. These prices were obtained from dealers via the web as the Bergey web site contains no cost information.

The three examples presented here are a relatively small sample of commercially available wind turbines. No recommendation or endorsement of the manufacturers is implied by the

Figure 4.23 Vestas V52 850 kW wind turbine. *Source*: http://images.nrel.gov/viewphoto.php?imageId=6311986.

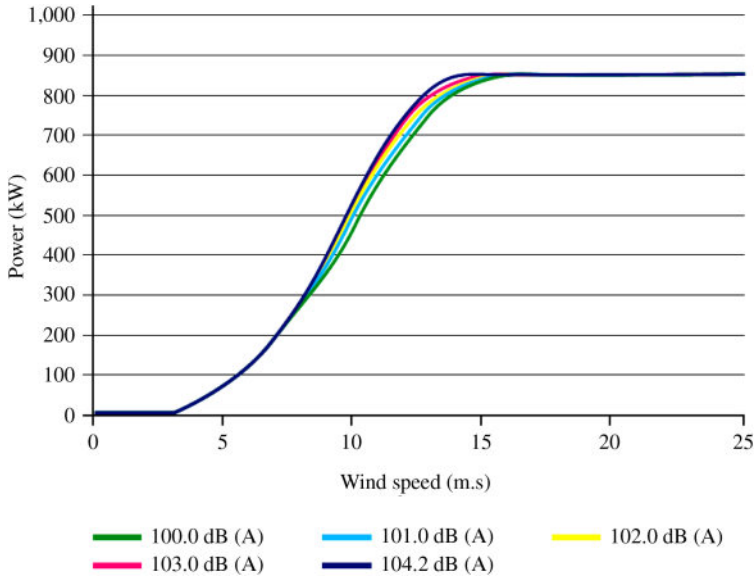

Figure 4.24 Power versus wind speed for a Vestas V52 850 kW wind turbine. *Source*: Vestas.

Table 4.4 Bergey 10 kW Excel specifications.

Rated capacity (kW)	8.9
Cut-in speed (m/s)	2.2
Cut-out speed (m/s)	None (furled at 16–18 m/s)
Rated wind speed (m/s)	11
Rotor diameter (m)	7
Swept area (m^2)	38.5
Rotor speed (rpm)	0–400

Figure 4.25 Bergey 10 kW Excel wind turbine. *Source*: Bergey.

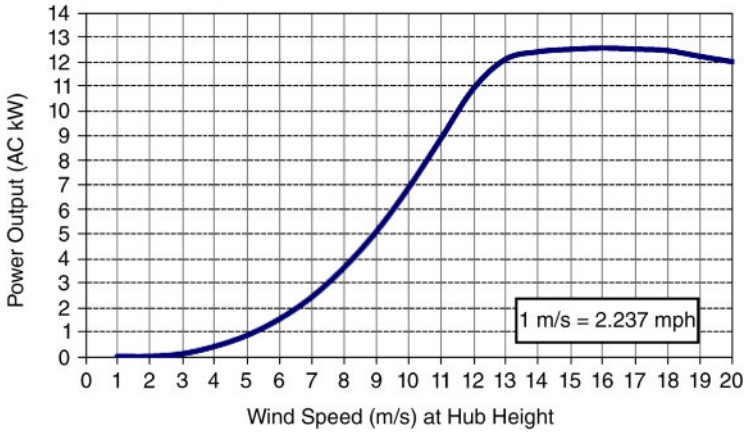

Figure 4.26 Power versus wind speed for a Bergey 10 kW Excel wind turbine. *Source*: Bergey Excel 10 Owner's Manual.

inclusion of the examples in this section; they are merely presented as samples of commercially available wind turbines.

4.6 Growth in Wind Power Capacity

In the twenty-first century, wind energy has exhibited the most increase in capacity of all renewable energy sources, both in the USA and in the world. Figure 1.12 shows the growth in various renewable energy resources in the USA from 2000 to 2013; the growth in wind energy is by far the most impressive. A dramatic indication of the magnitude of the increase in installed wind generating capacity since 1999 is provided by comparing Figure 4.27a and b. Figure 4.27a presents the installed capacity in 1999 (end of year), while Figure 4.27b shows the installed capacity as of September 2014. In 1999, the installed capacity was 2472 MW, which increased to 62 300 MW by September 2014 – an increase of 2400%!

The rate of increase is expected to remain nearly constant. Recent projections by the EIA are contained in Figure 4.28. An additional 14 GW of capacity is anticipated by the end of 2015, bringing the total installed wind generating capacity in the USA to 76 GW. Comparing the wind class from Figure 4.7a and the average wind speed from Figure 4.7b with the installed capacity in 2014 from Figure 4.27b and the projected installations from Figure 4.28, the region of highest activity, the "sweet" spot, in the USA is the Midwest. Although the mountain west offers higher wind power classes, terrain and population demographics favor the Midwest.

One of the reasons for the continued rapid expansion of installed wind generating capacity has been the favorable tax envirnoment. The wind federal production tax credit, enacted in 1992, and continued more or less to the present, allowed eligible wind generators to take an inflation-adjusted tax credit in 2014 of 2.3¢/kW h. This tax advantage is permitted for the first 10 years of operation of a commercial wind installation. Congress in December 2014 extended the tax credit.

A number of companies, in the USA and worldwide, are engaged in the manufacture, installation, operation, and maintenance of wind turbines. Figure 4.29 presents a breakdown of

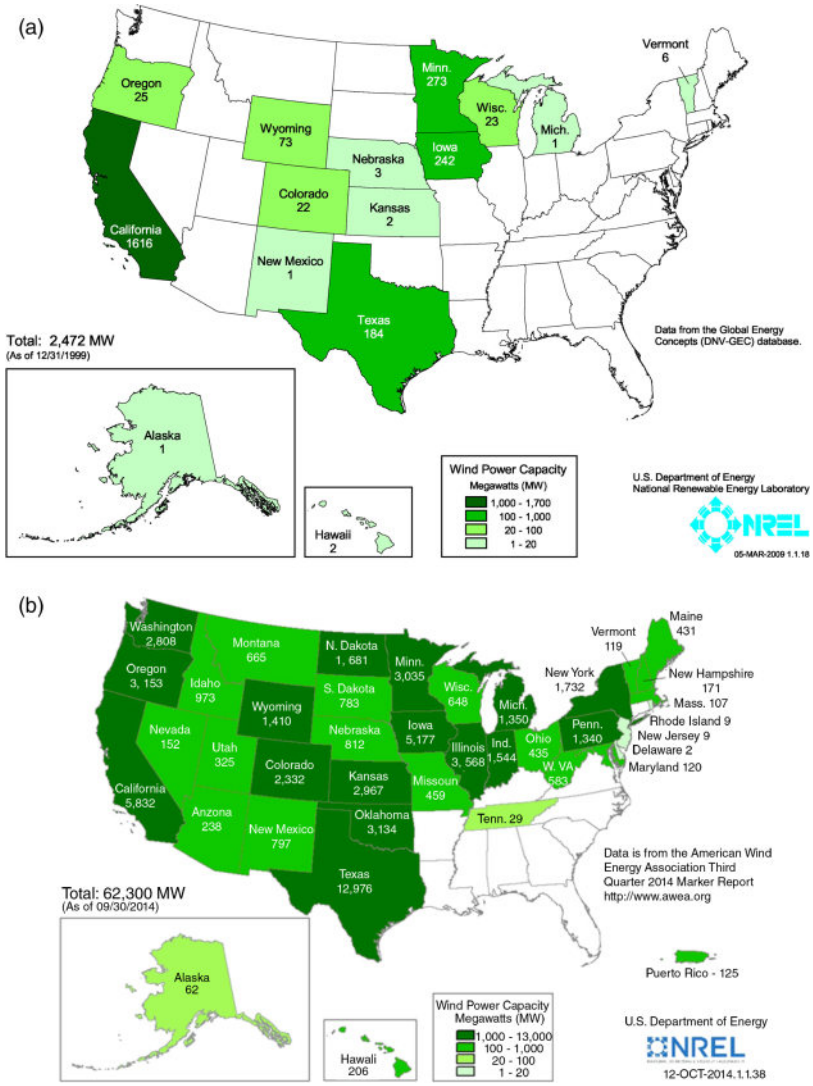

Figure 4.27 Growth in installed wind generating capacity (MW): (a) December 1999; (b) September 2014. *Source*: NREL.

companies (in terms of market share) that were involved in the installation of wind turbines in the USA in 2012. At 38%, GE Wind captured nearly twice the market share of Siemens and three times the market share of Vestas. The figure also serves as a good source of information on wind turbines via company web sites.

The wind energy growth in the world is similar. Figure 4.30 graphically confirms the trend. The European Union (EU) has long pursued an aggressive commitment to wind energy. Figure 4.31 provides a comparison, in 2012, of the EU share of the world's wind energy generating capacity. Considering the size and population of the EU member counties, these results are impressive and confirm the EU stance on renewable energy.

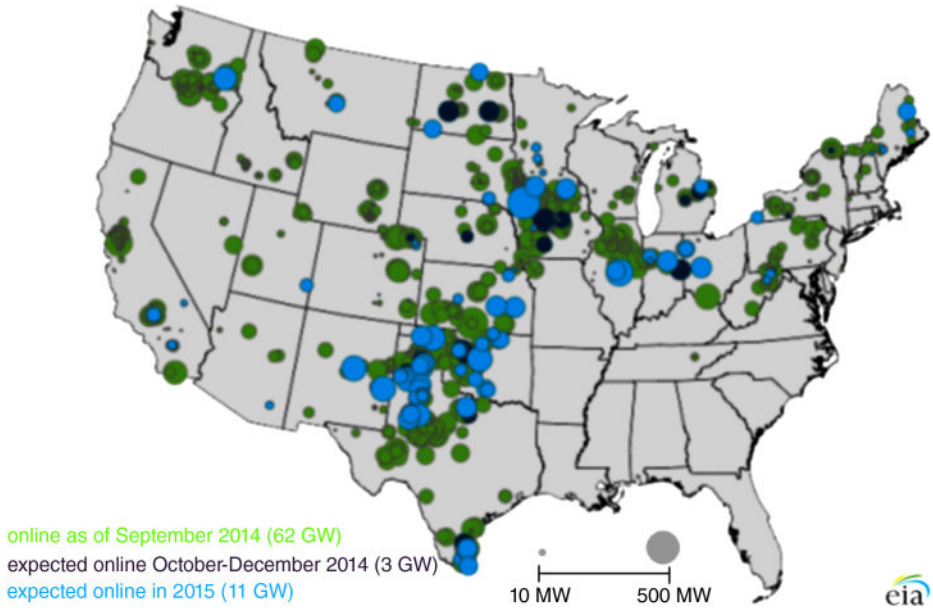

Figure 4.28 Growth in installed wind generating capacity through 2015. *Source*: EIA.

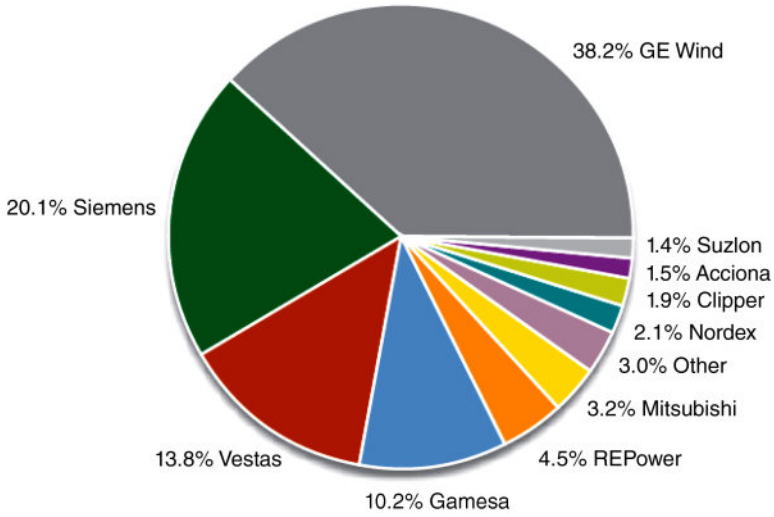

Figure 4.29 Company market share of wind turbine installations in 2012.

4.7 Closure

This chapter has explored wind power by developing the operating principles for wind turbines, exploring how the wind speed distribution can be used, considering how a wind turbine must be controlled, and examining some commercially available wind turbines.

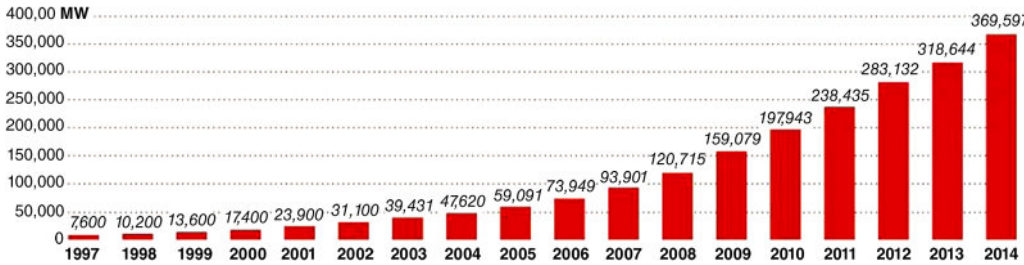

Figure 4.30 World growth (1997–2014) in installed wind generating capacity. *Source*: Reproduced with permission of GWEC.

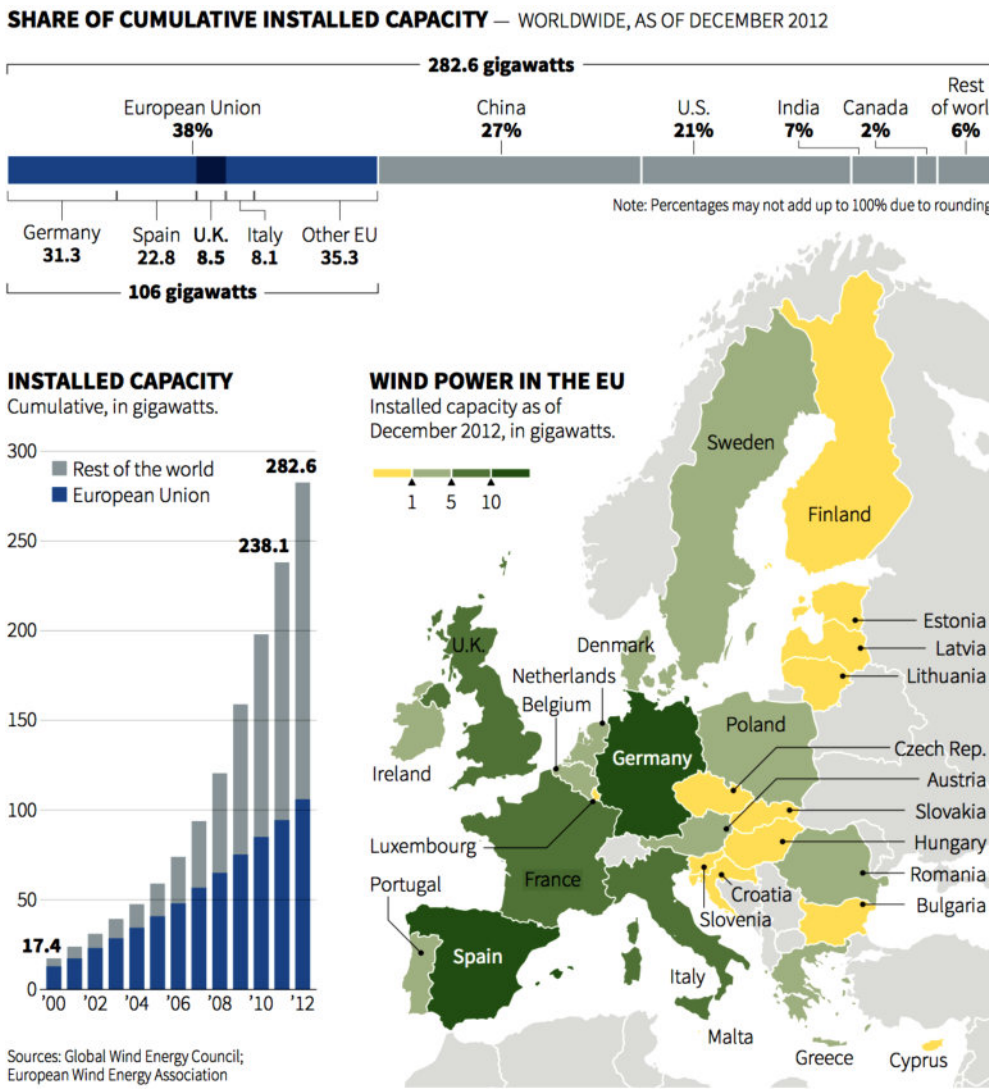

Figure 4.31 EU wind generating capacity comparison, 2012.

References

Johnson, G.L. (2001) Wind turbine power, energy, and torque. In *Wind Energy Systems,* pp. 4–1–4–54. http://www.ece.k-state.edu/people/faculty/gjohnson/files/Windbook.pdf (accessed October 15, 2016).

Kreith, F. and West, R.E. (1997) *CRC Handbook of Energy Efficiency*. CRC Press, Boca Raton, FL.

Patel, M.R. (2005) *Wind and Solar Power Systems*, 2nd edn. Taylor & Francis, New York.

Further Reading

Logan, E. (1993) *Turbomachinery*, 2nd edn. Marcel Dekker, New York.

5

Combustion Turbines

5.1 Introduction

Gas turbines were developed for aeronautical applications prior to and during World War II. Wilson (1983) provides an excellent historical account of the engineering aspects of the development of gas turbine engines. Frank Whittle in the UK and Hans von Ohain in Germany are credited with essentially simultaneously producing the first useful, flightworthy gas turbine engines. In the decades following World War II, the gas turbine engine became the preferred propulsion system for most aircraft. At the same time, the inherent simplicity (compared with other prime movers) and operational characteristics of the gas turbine engine resulted in its adaptation for a variety of uses, including power generation and marine propulsion. When used for electric power generation, gas turbines are often called combustion turbines to distinguish them from steam turbines, a long-time mainstay of the electric power industry.

Combustion turbines are used for peaking, base-load, backup/emergency, and grid-independent power generation as well as power sources for remote or isolated facilities such as offshore drilling platforms. When used for electric power generation, combustion turbines are operated in two modes: (1) electric power generation with no heat recovery and (2) electric power generation with heat recovery. The latter is called combined heat and power (CHP) and is the subject of Chapter 11. CHP is often referred to as cogeneration – the recovery and use of thermal energy in conjunction with the decentralized generation of electricity. This chapter develops the principles for combustion turbines.

5.2 The Combustion Turbine

Figure 5.1 is a schematic of a combustion turbine showing the primary components: the compressor, the combustor, and the turbine. Air is compressed as it passes through the compressor. The work required to drive the compressor is provided by the turbine. Fuel is burned in the combustor, and the temperature of the air and combustion products mixture is increased by the combustion process. As the mixture expands through the turbine, the power extracted by the turbine is used to power the compressor. In the combustion turbine, the additional energy extracted by the "power" turbine is available as output power from the engine. The combustion turbine output power is typically used to drive a generator for the production of electricity. In many combustion turbines, only a single turbine section is present; part of the power extracted is used to drive the compressor, and the remainder is the output power.

The Brayton cycle is often used as a representation of the gas turbine. The Brayton cycle is composed of isentropic compression and expansion processes and constant-pressure heat addition and rejection processes. P–v (pressure–specific volume) and T–s (temperature–

Alternative Energy Systems and Applications, Second Edition. B. K. Hodge.

Companion website: www.wiley.com\go\Hodge\AESystemsandApplications2E

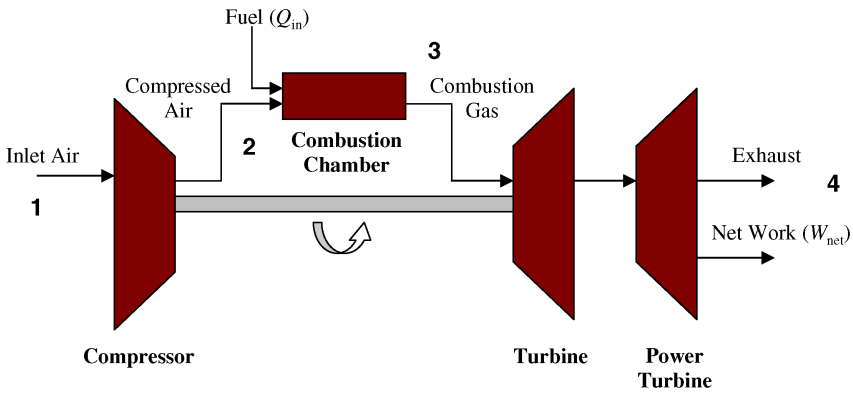

Figure 5.1 Combustion turbine schematic.

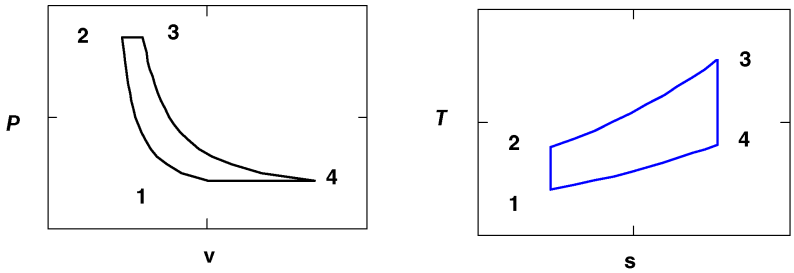

Figure 5.2 *P–v* and *T–s* diagrams for a Brayton gas turbine cycle.

entropy) diagrams are provided in Figure 5.2 for a Brayton cycle gas turbine. State 1 is the inlet state to the compressor, state 2 is the exit from the compressor and inlet to the combustor, state 3 is the exit from the combustor and inlet to the turbine, and state 4 is the exit from the turbine. The four states are indicated in Figures 5.1 and 5.2.

Most first-order gas turbine analysis procedures use an air-standard analysis. Air standard means that the working fluid is air that is treated as an ideal gas. A cold air-standard analysis means that the working fluid is treated as air with all properties at their room-temperature values. Thermodynamic properties for air and combustion products are thus needed for an air-standard analysis. A thermally perfect gas is described by the thermal equation of state

$$P = \rho RT \tag{5.1}$$

where the gas constant is

$$R = 287\frac{\text{J}}{\text{kg K}} = 53.35\frac{\text{ft lbf}}{\text{lbm °R}}$$

A calorically perfect gas is a gas for which the specific heat at constant volume c_v and the specific heat at constant pressure c_p are constant. A gas that is both thermally perfect and calorically perfect is labeled a perfect gas. The ratio of specific heats is defined as $k = c_p/c_v$.

For a thermally perfect gas

$$R = c_p - c_v \quad \text{and} \quad R = \frac{k-1}{k}c_p \tag{5.2}$$

The isentropic relations are expressed as

$$\frac{T_a}{T_b} = \left(\frac{P_a}{P_b}\right)^{(k-1)/k} = \left(\frac{\rho_a}{\rho_b}\right)^{k-1} = \left(\frac{v_b}{v_a}\right)^{k-1} \tag{5.3}$$

For air and combustion products, the accepted values of the thermodynamic constants are as follows:

Air	Combustion products
$c_p = 1.004 \frac{\text{kJ}}{\text{kg K}} = 0.24 \frac{\text{Btu}}{\text{lbm °R}}$	$c'_p = 1.148 \frac{\text{kJ}}{\text{kg K}} = 0.2744 \frac{\text{Btu}}{\text{lbm °R}}$
$k = 1.40$	$k = 1.33$

In a gas turbine, the combustion products cause the properties at the exit of the combustor to be different from those of air. However, in virtually all gas turbines the fuel-to-air ratio is less than 0.02, so the actual deviations in combustor exit properties from those of air at the same temperature and pressure are small. A reasonable estimate is that the thermodynamic constants in the heat addition (combustion) process are the average of the air and combustion products:

$$c''_p = 1.076 \frac{\text{kJ}}{\text{kg K}} = 0.2572 \frac{\text{Btu}}{\text{lbm °R}}$$

$$k = 1.367$$

5.3 The Air-Standard Brayton Cycle

The cold air-standard Brayton cycle is the simplest model of a gas turbine. For the cold air-standard Brayton cycle, the compressor work (per unit mass) W_c and the expansion work W_e are

$$\begin{aligned} W_c &= h_1 - h_2 \\ W_e &= h_3 - h_4 \end{aligned} \tag{5.4}$$

where h represents the enthalpy, which for a thermally perfect gas can be cast as $h = c_p T$. And the heat supplied is

$$Q_s = h_3 - h_2 \tag{5.5}$$

The net work out of the turbine is the difference between the turbine work and the compressor work. In the Brayton cycle, combustion is replaced by heat addition, so the mass flow rates through all components are the same. The thermal efficiency is defined as the net work divided by the heat supplied. Hence, for the cold air-standard analysis

$$\begin{aligned} \eta_t &= \frac{\sum W}{Q_s} = \frac{h_1 - h_2 + h_3 - h_4}{h_3 - h_2} \\ &= \frac{c_p(T_1 - T_2) + c_p(T_3 - T_4)}{c_p(T_3 - T_2)} = \frac{T_1 - T_2 + T_3 - T_4}{T_3 - T_2} \\ &= \frac{T_3 - T_2 + T_1 - T_4}{T_3 - T_2} = 1 + \frac{T_1 - T_4}{T_3 - T_2} = 1 - \frac{T_1\left(\frac{T_4}{T_1} - 1\right)}{T_2\left(\frac{T_3}{T_2} - 1\right)} \end{aligned} \tag{5.6}$$

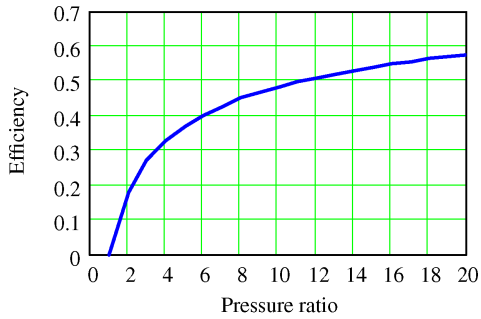

Figure 5.3 Cold air-standard Brayton cycle thermal efficiency.

But since the processes are either isentropic or constant pressure, the following can be verified:

$$\frac{T_4}{T_1} = \frac{T_3}{T_2} \tag{5.7}$$

So that the thermal efficiency η_t becomes

$$\eta_t = 1 - \frac{T_1}{T_2} = 1 - \frac{1}{T_2/T_1} = 1 - \frac{1}{(P_2/P_1)^{k-1/k}} \tag{5.8}$$

Thus, for a cold air-standard Brayton cycle, the thermal efficiency is only a function of the pressure ratio. A plot of the thermal efficiency as a function of pressure ratio is presented in Figure 5.3. A pressure ratio of 20 represents a reasonable upper limit for the pressure ratios expected for typical gas turbines. The figure also demonstrates that, even for high pressure ratios, the thermal efficiency is not likely to exceed 60%. The cold air-standard Brayton cycle thermal efficiency also represents an effective upper bound for gas turbine engine performance expectations.

5.4 Actual Gas Turbine Cycle Analysis

The cold air-standard Brayton cycle is useful for quickly establishing limits and understanding the working principles of a gas turbine engine, but irreversibilities (inefficiencies) must be included in the component models for more realistic analyses. The usual irreversibilities considered are losses in the compression and expansion processes and a pressure drop in the heat addition process. Each will be examined in turn.

Consider the compression process with irreversibilities. Figure 5.4 illustrates a T–s diagram with an isentropic compression from P_1 to P_2 and a compression process, also from P_1 to P_2, with losses. The actual process is from state 1 to state 2, and the isentropic process is from state 1 to state 2s. The isentropic compression efficiency η_c is defined as the ratio of the work required in the isentropic process to the work required by the actual process, or

$$\eta_c = \frac{h_1 - h_{2s}}{h_1 - h_2} = \frac{c_p(T_1 - T_{2s})}{c_p(T_1 - T_2)} = \frac{T_1 - T_{2s}}{T_1 - T_2} = \frac{(T_{2s}/T_1) - 1}{(T_2/T_1) - 1} \tag{5.9}$$

But the process from 1 to 2s is isentropic, so that

$$\frac{T_{2s}}{T_1} = \left(\frac{P_2}{P_1}\right)^{(k-1)/k} \tag{5.10}$$

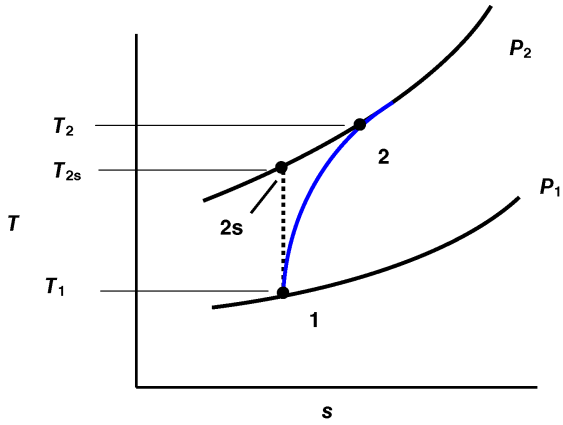

Figure 5.4 *T–s* diagram for compression processes.

The isentropic compression efficiency cast in terms of the compressor pressure ratio and the actual exit temperature is

$$\eta_c = \frac{(P_2/P_1)^{(k-1)/k} - 1}{(T_2/T_1) - 1} \tag{5.11}$$

The work of compression is

$$W_c = c_p(T_1 - T_2) = c_p T_1 \left(1 - \frac{T_2}{T_1}\right) \tag{5.12}$$

Substituting Equation 5.11 into Equation 5.12 results in

$$W_c = \frac{c_p T_1}{\eta_c}\left[1 - \left(\frac{P_2}{P_1}\right)^{(k-1)/k}\right] \tag{5.13}$$

Equation 5.13 provides some insight into the thermodynamics of the compression process in gas turbines. The higher the inlet temperature T_1, the more work (per unit mass) required to compress a gas through a given pressure ratio. Not surprisingly, the lower the isentropic compression efficiency, the more compressor work required. Solving Equation 5.11 for the actual compressor exit temperature yields

$$T_2 = T_1\left\{1 + \frac{1}{\eta_c}\left[\left(\frac{P_2}{P_1}\right)^{(k-1)/k} - 1\right]\right\} \tag{5.14}$$

Equations 5.11, 5.13, and 5.14 are the "working" expressions needed for the compression process in a gas turbine. Equation 5.11 provides the isentropic compression efficiency given the inlet conditions (P_1 and T_1) and the actual exit (P_2 and T_2) conditions. Given the pressure ratio, inlet temperature, and isentropic compression efficiency, Equation 5.13 can be used to compute the work required to drive the compressor. Given the pressure ratio, the inlet temperature, and the isentropic compression efficiency, Equation 5.14 yields the actual compressor exit temperature. The isentropic compression efficiency is defined using the actual process and a reference

isentropic process and is not defined as a work out and work in relationship. The isentropic efficiency concept is exercised in Example 5.1.

Example 5.1
Air enters the compressor of a gas turbine engine at 100 kPa (absolute) and 300 K. If the compressor pressure ratio is 8 and the isentropic compression efficiency is 0.87, find the following:

a) the exit temperature and pressure of the air from the compressor;
b) the work (per unit mass) added to the air by the compressor;
c) the exit temperature of the air if the compression process were isentropic.

Solution The process path on the T–s diagram is as indicated in Figure 5.4. From the problem statement:

$$T_1 = 300\ \text{K}$$

$$P_1 = 100\ \text{kPa}$$

$$\frac{P_2}{P_1} = 8$$

Since the working fluid is air, $k = 1.4$ and $c_p = 1.004\ \text{kJ/(kg K)}$. The actual exit temperature can be calculated using Equation 5.14:

$$T_2 = T_1\left\{1 + \frac{1}{\eta_c}\left[\left(\frac{P_2}{P_1}\right)^{(k-1)/k} - 1\right]\right\} = 300\ \text{K}\left\{1 + \frac{1}{0.87}\left[8^{(1.4-1)/1.4} - 1\right]\right\} = 580\ \text{K}$$

And the exit pressure is

$$P_2 = \frac{P_2}{P_1}P_1 = 8 \times 100\ \text{kPa} = 800\ \text{kPa}$$

The work imparted to the air is

$$W_c = c_p(T_1 - T_2) = 1.004\frac{\text{kJ}}{\text{kg K}}(300 - 580)\text{K} = -281\frac{\text{kJ}}{\text{kg}}$$

The negative sign indicates that work is done on the air. If the compression process were isentropic, then the exit temperature would correspond to that of an isentropic compression, or

$$T_{2s} = T_1\left(\frac{P_2}{P_1}\right)^{(k-1)/k} = 300\ \text{K}(8)^{(1.4-1)/1.4} = 543\ \text{K}$$

The work for the isentropic compression would be

$$W_{\text{isen}} = \eta_c W_c = 0.87\left(-281\frac{\text{kJ}}{\text{kg}}\right) = -244\frac{\text{kJ}}{\text{kg}}$$

A similar approach is used in defining the isentropic expansion efficiency. The T–s diagram for the expansion process is shown in Figure 5.5. The actual process is from state 3 to state 4, and the isentropic process is from state 3 to state 4s. The isentropic expansion efficiency η_e is defined as the ratio of the actual work extracted in the expansion process to the work that would be extracted if the process were isentropic, or

$$\eta_e = \frac{h_3 - h_4}{h_3 - h_{4s}} = \frac{c_p(T_3 - T_4)}{c_p(T_3 - T_{4s})} = \frac{T_3 - T_4}{T_3 - T_{4s}} = \frac{1 - (T_4/T_3)}{1 - (T_{4s}/T_3)} \tag{5.15}$$

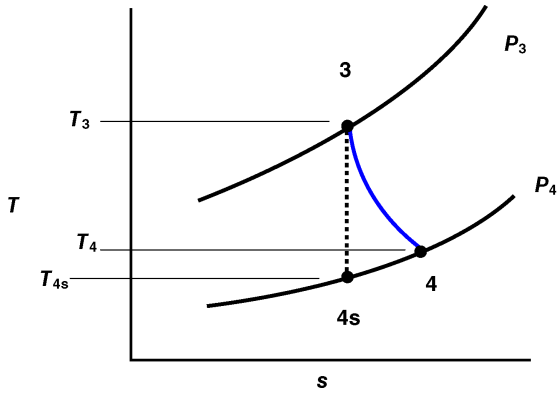

Figure 5.5 *T–s* diagram for expansion processes.

But the process from 3 to 4s is isentropic, so

$$\frac{T_{4s}}{T_3} = \left(\frac{P_4}{P_3}\right)^{(k-1)/k} \tag{5.16}$$

The isentropic expansion efficiency cast in terms of the turbine pressure ratio and the actual turbine exit temperature is

$$\eta_e = \frac{1 - (T_4/T_3)}{1 - (P_4/P_3)^{(k-1)/k}} \tag{5.17}$$

The work (per unit mass) extracted by the turbine is

$$W_e = c_p(T_3 - T_4) = c_p T_3 \left(1 - \frac{T_4}{T_3}\right) \tag{5.18}$$

Substituting Equation 5.17 into Equation 5.18 yields

$$W_e = \eta_e c_p T_3 \left[1 - \left(\frac{P_4}{P_3}\right)^{(k-1)/k}\right] \tag{5.19}$$

Guidance for the expansion process is contained in Equation 5.19. The higher the turbine inlet temperature T_3, the more work (per unit mass) can be extracted from a turbine for a given pressure ratio. This dependence on the turbine inlet temperature has been the driving impetus for the quest for seeking materials that can tolerate higher temperatures in the turbine section. And the lower the isentropic expansion efficiency, the less work can be extracted. Solving Equation 5.19 for the actual turbine exit temperature yields

$$T_4 = T_3 \left\{1 - \eta_e \left[1 - \left(\frac{P_4}{P_3}\right)^{(k-1)/k}\right]\right\} \tag{5.20}$$

Equations 5.17, 5.19, and 5.20 for the turbine (expansion process) are used in a fashion similar to Equations 5.11, 5.13, and 5.14 for the compressor. The isentropic expansion efficiency, similar to the isentropic compression efficiency, is defined using the actual process and a reference isentropic process, and is not defined as a work in and work out relationship. The isentropic expansion concept is demonstrated in Example 5.2.

Example 5.2
The inlet and outlet absolute pressures for the turbine section of a gas turbine engine are 550 kPa and 100 kPa respectively. If the turbine inlet temperature is 1000 K and the isentropic expansion efficiency is 0.91, compute the following:

a) the turbine exit temperature;
b) the work (per unit mass) extracted by the turbine.

Solution The process path on the T–s diagram is as indicated in Figure 5.5. From the problem statement:

$$T_3 = 1000\ \text{K}$$

$$P_3 = 550\ \text{kPa}$$

$$\frac{P_4}{P_3} = \frac{100\ \text{kPa}}{550\ \text{kPa}} = 0.182$$

Since the working fluid is the combustion product, $k = 1.334$ and $c_p = 1.148\ \text{kJ/(kg K)}$. The exit temperature can be calculated using Equation 5.20:

$$T_4 = T_3\left\{1 - \eta_e\left[1 - \left(\frac{P_4}{P_3}\right)^{(k-1)/k}\right]\right\} = 1000\ \text{K}\left\{1 - 0.91\left[1 - 0.182^{(1.33-1)/1.33}\right]\right\} = 686\ \text{K}$$

The work extracted by the turbine is

$$W_T = c_p(T_3 - T_4) = 1.148\frac{\text{kJ}}{\text{kg K}}(1000 - 686)\text{K} = 360\frac{\text{kJ}}{\text{kg}}$$

Some considerations of the combustor are appropriate. For first-order estimates, modeling the combustion process as a heat addition process does not introduce unacceptable errors. For the air-standard Brayton cycle analysis, $P_2 = P_3$; that is, no pressure change across the combustor. In actual gas turbine combustors, P_3 is less than P_2; that is, a pressure drop is experienced in the combustor. The pressure drop is caused by two effects: (1) friction and mixing losses in the combustor and (2) the Rayleigh effect ("simple" heat addition in an open system results in a loss in pressure) (Hodge and Koenig, 1995). For well-designed combustors, the drop in pressure is small, typically less than 5% of the pressure at the inlet of the combustor.

The heat of reaction per unit mass resulting from the complete combustion of a fuel is defined as the fuel heating value. Heating values are specified either as the lower heating value (LHV) or the higher heating value (HHV). The HHV means that the water in the combustion products is in liquid form – that is, the water vapor has been condensed. The LHV value means that the water in the combustion products is in a gaseous state. For most gas turbines, the LHV is used since the temperatures are above the condensing temperature of the water vapor. Table 5.1 provides a compilation of the nominal heating values of typical gas turbine fuels.

A simple model of the combustor equates the rate of energy release by the combustion process to the rate of heating of the air, or

$$\dot{m}_{\text{fuel}}H_v = \dot{m}_{\text{air}}c_p''(T_3 - T_2) \tag{5.21}$$

where c_p'' is the specific heat for the heat addition process, so that the fuel-to-air ratio f/a becomes

$$\frac{f}{a} = \frac{\dot{m}_{\text{fuel}}}{\dot{m}_{\text{air}}} = \frac{c_p''(T_3 - T_2)}{H_v} \tag{5.22}$$

Table 5.1 Heating values of selected fuels.

Fuel	Heating value H_v	
	Btu/lbm	MJ/kg
Jet A	18 400	42.8
Jet B/JP4	18 400	42.8
JP5	18 315	42.6
Natural gas	19 800	46.1
Propane	19 807	46.1
Ethanol	11 500	26.7

The fuel-to-air ratio in a gas turbine is small because the amount of fuel that can be added is constrained by the high-temperature-limit mechanical properties of the materials used in the combustor and the turbine. Example 5.3 illustrates the concept.

Example 5.3
A combustion turbine utilizing natural gas as a fuel has a combustor exit temperature of 1500 K and a compressor exit temperature of 690 K. Estimate the fuel-to-air ratio.

Solution Using the simple model for the combustor:

$$\frac{f}{a} = \frac{\dot{m}_{\text{fuel}}}{\dot{m}_{\text{air}}} = \frac{c_p''(T_3 - T_2)}{H_v} = \frac{1.076\ \text{kJ/(kg K)} \times (1500\ \text{K} - 690\ \text{K})}{46.1\ \text{MJ/kg}} = 0.019$$

The numbers in this example are typical for gas turbines. The fuel-to-air ratio is 0.019, which verifies that the fuel flow rate is low compared with the air flow rate.

The thermal efficiency of an actual gas turbine, neglecting the effects of the fuel flow rate, is defined as in Equation 5.5:

$$\eta_t = \frac{\sum W}{Q_s} = \frac{W_{\text{net}}}{Q_s} = \frac{c_p(T_1 - T_2) + c_p'(T_3 - T_4)}{c_p''(T_3 - T_2)} \tag{5.23}$$

where c_p' is the specific heat for the turbine process.

For a combustion turbine that is producing electricity with no heat recovery, the most important metric is the heat rate, the input energy per kilowatt-hour output. The smaller the heat rate, the better. Thus:

$$\text{Heat rate} = \frac{\text{Energy in}}{\text{Energy out}} = \frac{Q_s}{W_{\text{net}}} = \frac{c_p''(T_3 - T_2)}{c_p(T_1 - T_2) + c_p'(T_3 - T_4)} = \frac{1}{\eta_t} \tag{5.24}$$

The heat rate from Equation 5.24 is based on the shaft power available from the operation of the turbine. If the generator (including any mechanical loses) has an efficiency of η_{gen}, then the dimensionless heat rate can be expressed as

$$\text{Heat rate} = \frac{1}{\eta_t \eta_{\text{gen}}}$$

However, the heat rate, especially for electrical generation, is usually expressed in the units of kilojoules per kilowatt-hour or British thermal units per kilowatt-hour. A more convenient representation of the heat rate thus becomes

$$\text{Heat rate} = \frac{1}{\eta_t \eta_{gen}} \times 3412 \frac{\text{Btu}}{\text{kW h}} = \frac{3412}{\eta_t \eta_{gen}} \frac{\text{Btu}}{\text{kW h}} = \frac{3600}{\eta_t \eta_{gen}} \frac{\text{kJ}}{\text{kW h}} \tag{5.25}$$

where 1 kW h = 3412 Btu is the conversion factor. In many instances, the generator efficiency η_{gen} is taken as unity. Many companies specify the heat rates of their combustion turbines in both British thermal units per kilowatt-hour and kilojoules per kilowatt-hour. Consider Example 5.4.

Example 5.4
A combustion turbine possesses a thermal efficiency η_t of 31% and a generator efficiency of 0.98. What is the heat rate?

Solution The heat rate can be calculated directly from Equation 5.25:

$$\text{Heat rate} = \frac{3412}{\eta_t \eta_{gen}} \frac{\text{Btu}}{\text{kW h}} = \frac{3412}{0.31 \times 0.98} \frac{\text{Btu}}{\text{kW h}} = 11\,231 \frac{\text{Btu}}{\text{kW h}} = 11.850 \frac{\text{kJ}}{\text{kW h}}$$

The heat rate states that for every 11 231 Btu of input energy, 1 kW h of electricity is produced by the combustion turbine.

A more comprehensive example is in order.

Example 5.5
A combustion turbine possesses the following characteristics:

Compressor
- 97 kPa (abs) and 30 °C, inlet conditions
- pressure ratio of 5.5
- isentropic compression efficiency of 0.84

Combustor
- outlet temperature of 1000 °C
- pressure loss of 3%
- the fuel is natural gas

Turbine
- exit pressure of 100 kPa (abs)
- isentropic expansion efficiency of 0.88

Generator
- generator efficiency of 0.98.

Determine the overall thermal efficiency and the heat rate, and sketch the T–s diagram. Is the fuel flow rate small compared with the air flow rate?

Solution If the fuel flow rate is small compared with the air flow rate, the thermal efficiency is described by Equation 5.22. T_1, T_2, T_3, and T_4 are needed in order to calculate the thermal efficiency. The inlet temperature T_1 is given as 30 °C, or 303 K. The compressor exit temperature T_2 can be calculated as

$$T_2 = T_1 \left\{ 1 + \frac{1}{\eta_c} \left[\left(\frac{P_2}{P_1} \right)^{(k-1)/k} - 1 \right] \right\} = 303\ \text{K} \left\{ 1 + \frac{1}{0.84} \left[5.5^{(1.4-1)/1.4} - 1 \right] \right\} = 529\ \text{K}$$

The compressor exit pressure is $5.5 \times 97\,\text{kPa} = 533.5\,\text{kPa}$. The combustor exit temperature T_3 is specified as 1000 °C, or 1273 K, and the combustor exit pressure is

$$P_3 = (1 - 0.03)P_2 = 0.97 \times 533.5\,\text{kPa} = 517.5\,\text{kPa}$$

The turbine expands the flow from 517.5 kPa to 100 kPa, or

$$\frac{P_4}{P_3} = \frac{100\,\text{kPa}}{517.5\,\text{kPa}} = 0.193$$

The turbine exit temperature T_4 becomes for these conditions

$$T_4 = T_3\left\{1 - \eta_\text{T}\left[1 - \left(\frac{P_4}{P_3}\right)^{(k-1)/k}\right]\right\} = 1273\,\text{K}\left\{1 - 0.88\left[1 - 0.193^{(1.33-1)/1.33}\right]\right\} = 898\,\text{K}$$

The thermal efficiency can now be computed as

$$\eta_t = \frac{c_p(T_1 - T_2) + c'_p(T_3 - T_4)}{c''_p(T_3 - T_2)}$$

$$= \frac{1.004\,\frac{\text{kJ}}{\text{kg K}}(303\,\text{K} - 529\,\text{K}) + 1.148\,\frac{\text{kJ}}{\text{kg K}}(1273\,\text{K} - 898\,\text{K})}{1.076\,\frac{\text{kJ}}{\text{kg K}}(1273\,\text{K} - 529\,\text{K})} = 0.256$$

The heat rate becomes

$$\text{Heat rate} = \frac{3412}{\eta_\text{t}\eta_\text{gen}}\frac{\text{Btu}}{\text{kW h}} = \frac{3412}{0.256 \times 0.98}\frac{\text{Btu}}{\text{kW h}} = 13\,600\frac{\text{Btu}}{\text{kW h}} = 14\,349\frac{\text{kJ}}{\text{kW h}}$$

The fuel-to-air ratio is calculated using the simple combustor model:

$$\frac{f}{a} = \frac{\dot{m}_\text{fuel}}{\dot{m}_\text{air}} = \frac{c''_p(T_3 - T_2)}{H_\text{v}} = \frac{1.076\frac{\text{kJ}}{\text{kg K}}(1273\,\text{K} - 529\,\text{K})}{46.1\frac{\text{MJ}}{\text{kg}}} = 0.017$$

Thus, the fuel flow rate is small compared with the air flow rate.

Taking into account the states (1, 2, 3, and 4) of the combustion turbine, the T–s diagram appears as in Figure 5.6.

Most of the development to this point has been based on the assertion that the fuel flow rate is small in comparison with the air flow rate. Equation 5.23 for the thermal efficiency of a gas turbine was formulated based on this assertion. The thermal efficiency of a gas turbine including the effects of fuel flow rate can be developed by considering the power required by the compressor and extracted by the turbine, or

$$\begin{aligned}\dot{W}_\text{c} &= \dot{m}_\text{air}c_p(T_1 - T_2)\\ \dot{W}_\text{e} &= (\dot{m}_\text{air} + \dot{m}_\text{fuel})c'_p(T_3 - T_4)\end{aligned} \tag{5.26}$$

And the rate at which heat supplied in the combustor is

$$\dot{Q}_\text{s} = (\dot{m}_\text{air} + \dot{m}_\text{fuel})c''_p(T_3 - T_4) \tag{5.27}$$

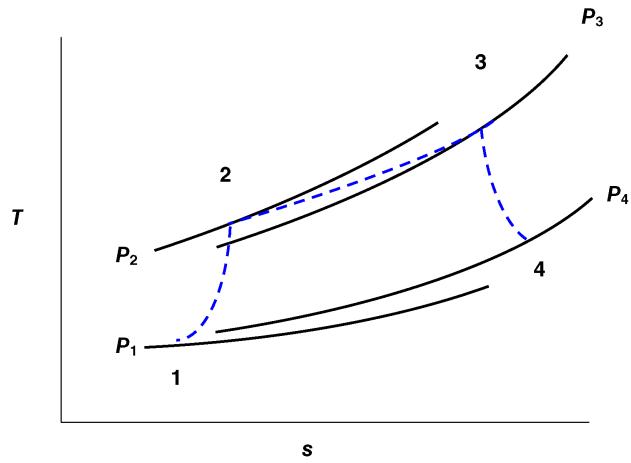

Figure 5.6 *T–s* diagram for Example 5.5.

The thermal efficiency can be cast as

$$\eta_t = \frac{\sum \dot{W}}{\dot{Q}_s} = \frac{\dot{m}_{air} c_p (T_1 - T_2) + (\dot{m}_{air} + \dot{m}_{fuel}) c'_p (T_3 - T_4)}{(\dot{m}_{air} + \dot{m}_{fuel}) c''_p (T_3 - T_2)}$$
$$= \frac{c_p (T_1 - T_2) + [1 + (f/a)] c'_p (T_3 - T_4)}{[1 + (f/a)] c''_p (T_3 - T_2)} \tag{5.28}$$

where f/a is the fuel-to-air ratio. Thus, to account for the effect of the fuel mass flow rate, the thermal efficiency expression with the fuel mass flow rate included is very similar to the thermal efficiency expression, except that the factor $1 + (f/a)$ appears in the turbine work and heat addition terms. Cohen *et al.* (1972) point out that in many gas turbines, 1 or 2% of the compressed air is bled from the compressor and that the fuel flow rate is 1 or 2% the air flow rate. Hence, the two essentially cancel out, and, as a result, the mass flow rates through the compressor and turbine tend to be equal.

5.5 Combustion Turbine Cycle Variations

Figure 5.1 and most of this chapter has been devoted to aspects of Brayton-cycle-like gas turbines. However, as fuel prices continue to be a significant cost and as the electrical utility grid becomes more stressed, more thermally efficient combustion turbines are becoming increasingly attractive. Although there are many variations of the basic combustion turbine cycle, two are especially effective: (1) the addition of a recuperator (regenerator) and (2) the addition of a compressor intercooler.

As the example problems demonstrate, turbine exhaust temperatures are well above ambient conditions and offer the *potential* for heat recovery. A recuperator is a heat exchanger that uses the turbine exhaust gases to preheat the air exiting the compressor before the air enters the combustor. Increasing the temperature of the air entering the combustor reduces the amount of fuel necessary for a given combustor exit temperature. A decrease in Q_s, the denominator term in the thermal efficiency expression (Equation 5.23), results in an increased thermal efficiency. The schematic of a combustion turbine with a regenerator is provided in Figure 5.7.

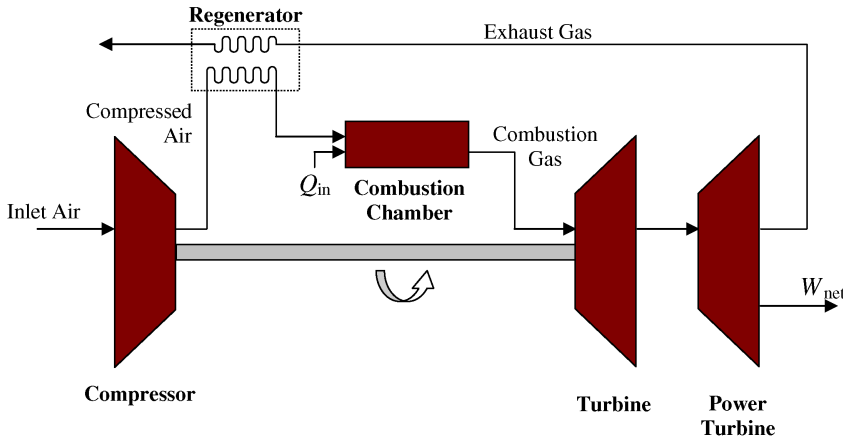

Figure 5.7 Gas turbine with regenerator.

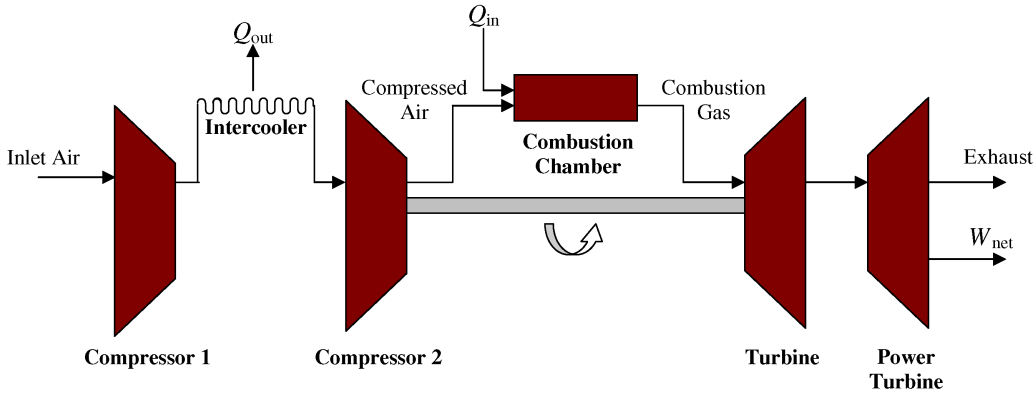

Figure 5.8 Gas turbine with intercooler and two-compression stages.

The other common variation of the basic combustion turbine cycle is produced with the addition of an intercooler. As Equation 5.13 indicates, the compressor work required to achieve a given pressure ratio is directly proportional to the inlet temperature. Thus, if the compression process is broken into two or more stages, the heat removed from an upstream stage results in a reduction in the inlet temperature of the downstream stage, reducing the compressor work required for the latter compression stage. Figure 5.8 illustrates a combustion turbine with an intercooler between the low-pressure and high-pressure compressor sections.

For ground-based gas turbines, such as combustion turbines, the added weight and volume of a regenerator or intercooler are not problems. The inclusion of a regenerator or intercooler decreases the heat rate and increases the overall cycle thermal efficiency.

5.6 Examples of Commercially Available Combustion Turbines

Combustion turbines are commercially available in an electrical power output range from 30 kW (micro) to 250 MW. The term "microturbine" is applied to combustion turbines with electrical outputs less than 60–200 kW. Industrial turbines typically have electrical outputs of

0.5–250 MW. The internet is a ready source of general information on commercially available combustion turbines.

In the USA, industrial combustion turbines are available from a number of companies, including Solar Turbines, Siemens-Westinghouse, United Technologies Corporation (Pratt & Whitney Division), Rolls-Royce (North America), and General Electric (GE) Energy. The examples presented here are a relatively small sample of commercially available combustion turbines. No recommendation or endorsement of the manufacturers is implied by the inclusion of the examples in this section; the examples are merely samples of what is commercially available.

5.6.1 Solar Turbines

Solar Turbines Incorporated, a subsidiary of Caterpillar Incorporated, manufactures a line of combustion turbines with electrical output in the range 1–22 MW. More than 15 000 Solar Turbines units have been installed worldwide. Solar Turbines offers combustion turbines systems for (1) the oil-and-gas industry and (2) the power generation industry. Table 5.2 lists the family of turbines available for the generally severe requirements of the oil-and-gas sector along with their nominal outputs (kilowatts and horsepower) and the ISO-rated heat rates (British thermal units per kilowatt-hour, kilojoules per kilowatt-hour, and British thermal units per horsepower per hour). Table 5.3 tabulates the family of turbines available for the power generation industry along with their nominal outputs (kilowatts) and the ISO-rated heat rates (British thermal units per kilowatt-hour and kilojoules per kilowatt-hour). In common in the power generation industry, the output is usually expressed in kilowatts and the heat rates in kilojoules per kilowatt-hour or British thermal units per kilowatt-hour. The two tables demonstrate only slight differences in the performance metrics between the oil-and-gas and the power generation sectors. Information for the tables was obtained from the Solar Turbines product specifications on their web site.

For the Solar Turbines family of combustion turbines, the effect of size is interesting, as the heat rate is essentially monotonic with electrical output – the heat rate decreases with increasing output – except for the Mars and Mercury turbines.

Table 5.2 Solar Turbines family of combustion turbines (oil and gas).

	Nominal output		Heat rate		
Name	kW	hp	Btu/kW h	kJ/kW h	Btu/hp h
Saturn 20	1.185	1 590	13 910	14 670	10 370
Centaur 40	3.5	4 700	12 240	12 905	9 125
Centaur 50	4.57	6 130	11 400	12 030	8 500
Taurus 60	5.74	7 700	10 680	11 265	7 965
Taurus 70	8.14	10 915	9 662	10 195	7 205
Mars 90	9.86	13 220	10 270	10 830	7 655
Mars 100	11.86	15 900	9 917	10 465	7 395
Titan 130	15.29	20 500	9 421	9 940	7 025
Titan 250	22.37	30 000	8 529	9 000	6 360

Table 5.3 Solar Turbines family of combustion turbines (power generation).

		Heat rate	
Name	**Nominal output (kW)**	**Btu/kW h**	**kJ/kW h**
Saturn 20	1.21	14 020	14 795
Centaur 40	3.515	12 240	12 910
Centaur 50	4.60	11 630	12 270
Mercury 50	4.60	8 865	9 350
Taurus 60	5.67	10 830	11 430
Taurus 70	7.965	9 955	10 505
Mars 100	11.40	10 365	10 935
Titan 130	15.00	9 695	10 230
Titan 250	21.745	8 775	9 260

The Solar Turbines web site (https://mysolar.cat.com/en_US/products/gas-turbine-overview.html) contains detailed specifications of their oil-and-gas product line. A popular Solar turbine is the Mars 100 combustion turbine with an ISO nominal rating of 11 860 kW. The nominal ISO performance is for 15 °C at sea level with 60% relative humidity. The Mars 100 data sheet is available at https://mysolar.cat.com/en_US/products/oil-and-gas/gas-turbine-packages/compressor-sets/mars-100.html. As with all combustion turbines, the inlet air temperature has a significant impact on the electrical output and the heat rate for the Mars 100. Decreasing output as the inlet temperature increases is a characteristic of gas turbines. At the ISO rating conditions, the Mars 100 electrical output is 11.86 MW with a heat rate of 9919 Btu/(kW h) and an exhaust flow rate of 337 900 lbm/h at 905 °F. The electrical outputs and heat rates vary from about 13.7 MW and 9810 Btu/(kW h) at −22 °F to about 10 MW and 10 300 Btu/(kW h) at 100 °F in a monotonic fashion.

5.6.2 GE Energy

GE Energy is a major provider of a variety of energy systems in the USA. The company offers combustion turbines via two end-use designations: (1) oil and gas and (2) power and water. Table 5.4 contains a partial listing of GE Energy gas turbines used for power generation, although most of the turbines in the list are also available with mechanical power output instead of power generation. Their combustion turbines are denoted as aeroderivative or heavy duty. Details are available on the GE Energy web site (www.gepower.com) and can be accessed as either "oil and gas" or "power and water."

The GE Energy aeroderivative combustion turbines are based on their very successful line of aircraft engines. The company's aeroderivative line of gas turbines provides an output range of 11–100 MW as well as the ability to utilize a variety of fuels. In addition to power generation, the GE Energy aeroderivative gas turbines have been used for marine applications and a variety of oil-and-gas sector applications. Included are the LMS100, the LM6000, the GE10, and the PGT family (with the compressors from the LM1600, the LM2000, or the LM2500 gas turbines). Details are available on each of the gas turbines on the GE Energy web site. The LM2500, perhaps the most successful and long-lived of the GE family of combustion turbines, offers different electrical output energy rating, different applications (including marine), and different cycle features. GE Energy offers many variations on their line of gas turbines; the values in

Table 5.4 Examples of GE Power combustion turbines.

Name	Nominal output (MW)	Heat rate		Comment
		Btu/kW h	kJ/kW h	
GE10-1	11.25	10 890	11 489	Aeroderivative
PGT16 (LM1600)[a)]	13.72	9 758	10 295	Aeroderivative
PGT20 (LM2000)[a)]	17.46	9 704	10 238	Aeroderivative
PGT25 (LM2500)[a)]	22.40	9 402	9 919	Aeroderivative
PGT25+G4	33.06	8 575	9 047	Aeroderivative
LM2500PE	23.30	9 315	9 827	Aeroderivative
LM6000	42.26	8 329	8 787	Aeroderivative
LMS100	98.20	7 580	7 997	Aeroderivative
MS5001	26.83	12 026	12 687	
MS5002E	31.10	9 749	10 285	
MS6001B	42.10	10 645	11 230	
MS7001EA	85.40	10 417	10 990	
MS9001E	126.10	10 095	10 650	
7F.05	227	8 680	9 157	Simple cycle
2x1 7F.05	688	5 740	6 056	Combined cycle
7HA.02	330	8 240	8 693	Simple cycle
2x1 7HA.02	976	5 570	5 876	Combined cycle
9F.05	299	8 810	9 295	Simple cycle
9HA.02	470	8 220	8 672	Simple cycle

Source: Adapted from *Gas Turbine World* (2014) and GE Oil & Gas (2011).

a) Denotes compressor source.

Table 5.4 are representative and are only a sample of available systems. The LM2500 was derived from the CF6 aircraft engine used on large commercial and military aircraft. The LM2500 and the LMS100 will be examined in more detail later in this section.

The heavy-duty gas turbines are available with electrical outputs ranging from 26 to 470 MW (in simple cycle configuration) and were specifically developed for utility and industrial applications. The 7F and 9F configurations have steadily evolved and offer the highest outputs of the GE Energy gas turbines. In combined cycle operation, the heavy duty 7F and 9F possess impressive output magnitudes (up to 976 MW) and heat rates (as low as 5570 Btu/(kW h)).

Considering the range of outputs (11–976 MW), the number and variations available, the output options (power generation or mechanical power extraction), and the number of units in service, GE Energy is a dominant player in the combustion turbine arena.

Figure 5.9 shows a cutaway drawing of the LM2500. Table 5.4 presents a summary of the LM2500 gas turbine performance, and Figure 5.10 illustrates the electrical output and heat rate as a function of the inlet temperature.

The LMS100 is an advanced aeroderivative combustion turbine that utilizes intercooling between the low- and high-pressure compressor stages. A unique feature of the LMS100 is that the intercooler heat exchanger is not adjacent to the engine package but is located away from the engine installation. Discharge air from the low-pressure compressor section is ducted to the

Figure 5.9 LM2500 cutaway drawing. *Source:* Reproduced with permission of GE Power & Water.

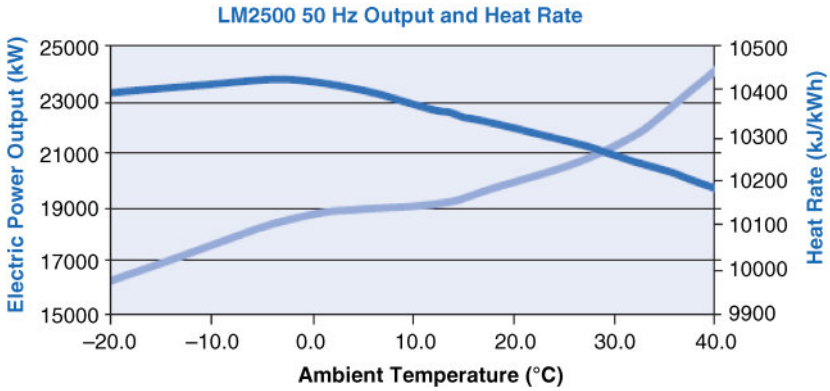

Figure 5.10 LM2500 output and heat rate. *Source:* Reproduced with permission of GE Power & Water.

intercooler heat exchanger, cooled, and returned to the inlet of the high-pressure compressor section. Such an arrangement provides significant flexibility in the choice of an intercooler heat exchanger design. A cutaway drawing of the LMS100 is presented in Figure 5.11. The intercooler collection and discharge scrolls are indicated on the figure. A detailed discussion of the LMS100 is given by Reale (2004) and is available on the GE Power web site.

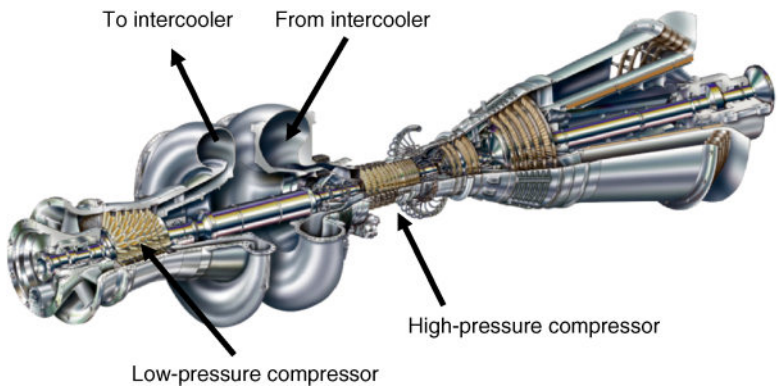

Figure 5.11 LMS100 cutaway drawing. *Source:* Reproduced with permission of GE Power & Water.

Table 5.5 LMS100 nominal performance summary.

Model	ISO base rating (kW)	Heat rate (Btu/kW h)	Efficiency (%)	Mass flow (lb/s)	Turbine speed (rpm)	Exhaust temperature (°F)
LMS100PB	97 718	7 592	45.0	453	3 600	783
LMS100PB	97 878	7 579	45.0	453	3 600	784
LMS100PA	102 795	7 287	46.8	472	3 600	747
LMS100PA	102 833	7 285	46.8	472	3 600	749
LMS100PA	103 112	7 773	43.9	469	3 600	770
LMS100PA	103 162	7 769	43.9	469	3 600	767
LMS100PA STIG	112 166	6 845	49.9	438	3 600	729

Source: GE Energy.

Nominal performance characteristics at ISO standard rating conditions for different versions of the LMS100 are delineated in Table 5.5. The LMS100 output as a function of inlet temperature is illustrated in Figure 5.12, and Figure 5.13 provides the heat rate as a function of inlet temperature for the LMS100 STIG (steam injected gas turbine) version.

5.6.3 Capstone Turbines

Capstone Turbines manufactures microturbines in the 30–200 kW range and is arguably the best known of the microturbine manufacturers in the USA. Capstone offers a nominal 30 kW unit, the C30, a nominal 65 kW unit, the C65, and a nominal 200 kW, the C200. The Capstone turbines are offered in versions that utilize different fuels and offer a number of options for exhaust stream heat recovery. The basic, natural-gas fueled, C30 will be previewed herein. The C30 is 70 in high, 30 in wide, and 60 in deep and weighs 891 lb. Table 5.6 presents the performance specifications at ISO conditions. Additional information is available on the Capstone web site (www.capstoneturbine.com).

A cutaway view of the basic C30 is provided in Figure 5.14. The compact C30 layout is much different from layouts of the much higher output combustion turbines previously examined herein. Natural-gas-fired microturbines without recuperators produce electricity at efficiencies

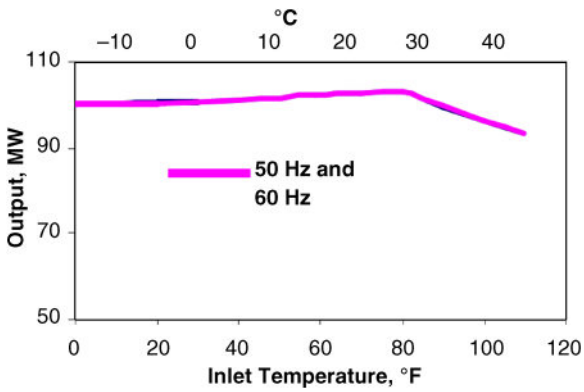

Figure 5.12 LMS100 output as a function of inlet temperature. *Source:* Reproduced with permission of GE Power & Water.

Table 5.6 Capstone C30 performance specifications.

Power output	30 kW
Heat rate	13 100 Btu/kW h
Electrical efficiency (LHV)	26%
Exhaust temperature	530 °F
Mass flow rate	0.68 lb/s
Exhaust gas energy	310 000 Btu/h

Source: Capstone Turbines.

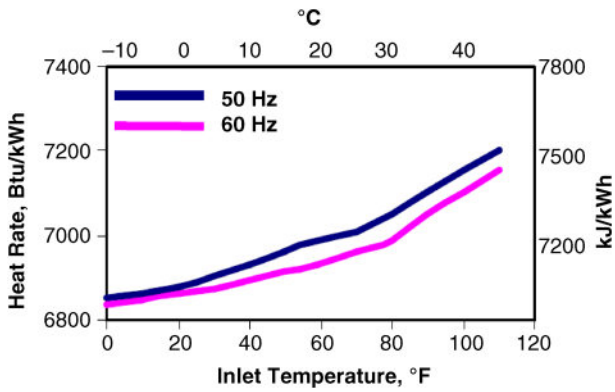

Figure 5.13 LMS100 STIG heat rate as a function of inlet temperature. *Source:* Reproduced with permission of GE Power & Water.

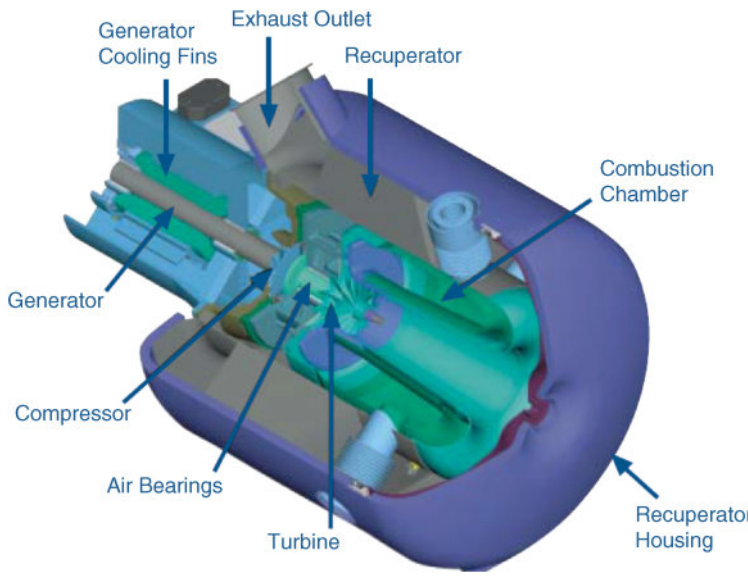

Figure 5.14 Capstone Turbines C30 cutaway view. *Source:* Capstone Turbines.

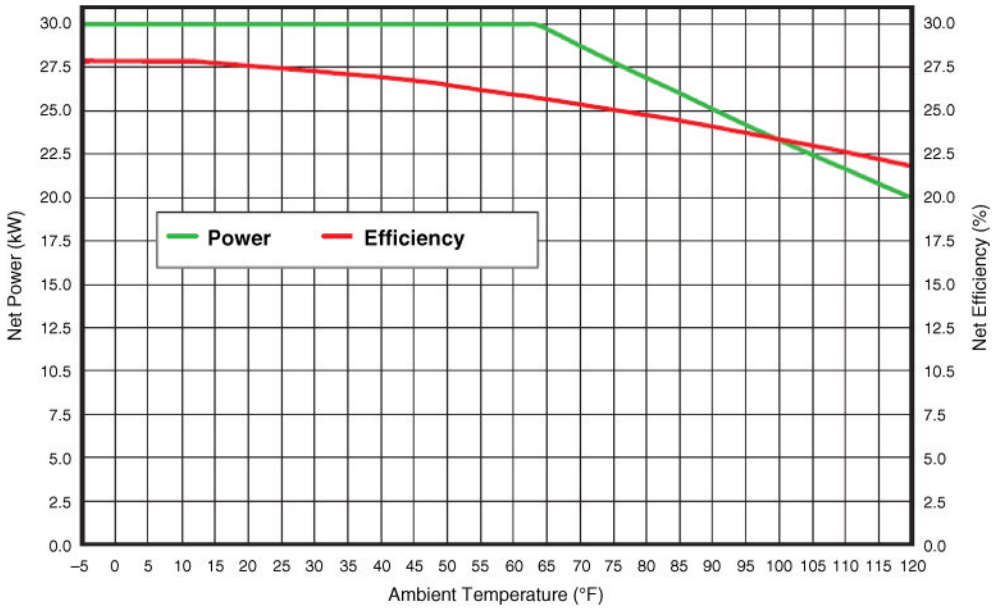

Figure 5.15 Power output and efficiency for the C30. *Source:* Capstone Turbines.

around 15%. Thus, most microturbines are equipped with recuperators that result in electrical generation efficiencies from 20% to 30%. Recuperated microturbines yield 30–40% fuel savings by preheating the incoming combustion air. The C30 recuperator is indicated, as is the casing for the recuperator. The rotating components are attached to a single shaft and are supported by air bearings. The air bearings permit rotational speeds as high as 96 000 rpm. Because the generator is cooled by the inlet air flow and air bearings are utilized, no oil, lubricants, or coolants are required.

The output electrical power and the electrical efficiency as a function of input temperature are illustrated in Figure 5.15. In a fashion similar to the large power output combustion turbines, the performance of the C30 decreases as the ambient temperature is increased.

Combustion turbines are relatively inexpensive compared with most decentralized power generation systems. The basic cost of combustion turbines ranges from $300/kW to $1000/kW and generally decreases with increasing power output. Combustion turbines cost more than internal combustion engines with smaller power output but cost less than larger power output internal combustion engines. Installation costs and the cost of other required components, plus other owner or miscellaneous costs, increase the initial capital costs by 30–50%. A natural-gas compressor is an example of a component that is required in sequence, since natural-gas compressors are needed to meet the high gas pressure requirements of combustion turbines. Natural-gas compressors increase the costs of a combustion turbine system by 5–10%. Also, if heat recovery capability is added, the capital cost increases by $100–$200 per kilowatt. Fully installed, the typical installed cost of a combustion turbine with a heat recovery is in the $1000/kW to $1200/kW range.

5.6.4 Other Gas Turbine Suppliers

In addition to Solar Turbines, GE Energy, and Capstone, other notable companies offering gas turbines for power applications include Dresser Rand (http://www.dresser-rand.com/products-solutions/), Pratt & Whitney (http://www.pwps.com/), and Siemens (http://www.energy

.siemens.com/hq/en/fossil-power-generation/gas-turbines/). In addition to Capstone, Ingersoll Rand offers a nominal 250 kW gas turbine (http://www.ingersollrandproducts.com/ap-en/solutions/microturbine-energy-solutions/chp-combined-heat-and-power).

5.7 Closure

The essentials of combustion turbines have been developed in this chapter, and some typical commercially available combustion turbines have been examined. In this chapter the focus has been on combustion turbines uses for the generation of electricity only. However, as is evident from the exhaust temperatures of the examples, the potential for significant thermal energy recovery exists. Chapter 11 examines the concept of CHP or the decentralized generation of electricity coupled with the recovery and use of exhaust thermal energy as from a combustion turbine.

References

Cohen, H., Rogers, G.F.C., and Saravanamuttoo, H.I.H. (1972) *Gas Turbine Theory*, 2nd edn. Longman, London.

Gas Turbine World (2014) **44** (1). http://www.gasturbineworld.com/assets/14–jan-feb-t-of-c.pdf (accessed November 1, 2016).

GE Oil & Gas (2011) *Gas Turbines*. https://www.geoilandgas.com/sites/geog.dev.local/files/ge-oil-and-gas-turbines-product-information.pdf (accessed November 1, 2016).

Hodge, B.K. and Koenig, K. (1995) *Compressible Fluid Dynamics with Personal Computer Applications*. Prentice-Hall, Englewood Cliffs, NJ.

Reale, M.J. (2004) *New High Efficiency Simple Cycle Gas Turbine – GE's LMS100*. General Electric Company, GER 4222A. https://powergen.gepower.com/content/dam/gepower-pgdp/global/en_US/documents/technical/ger/ger-4222a-new-high-efficiency-simple-cycle-gas-turbine-lms100.pdf (accessed October 17, 2016).

Wilson, D.G. (1984) *The Design of High-efficiency Turbomachinery and Gas Turbines*. MIT Press, Cambridge, MA.

Further Reading

Bathie, W.W. (1984) *Fundamentals of Gas Turbines*. John Wiley & Sons, Inc., New York.

Harman, R.T.C. (1981) *Gas Turbine Engineering*. John Wiley& Sons, Inc./Halsted Press, New York.

6

Solar Energy Fundamentals

6.1 Introduction

This chapter and Chapters 7, 8, and 9 will examine solar energy. The purposes of this chapter are to review radiation heat transfer and to present fundamental solar energy information necessary to understand the applications of the next three chapters.

6.2 Radiation Heat Transfer Review

An understanding of solar energy must be based on the spectral nature of solar radiation from the sun. This section reviews the fundamental radiation heat transfer information needed for solar energy engineering processes.

From a solar energy standpoint, two areas of interest are the characteristics of energy from the sun and the response of a surface to that energy. The starting point is to consider the characteristics of radiation heat transfer. Thermal radiation may be viewed as the transport of photons or the propagation of an electromagnetic wave. For the propagation of radiation in a medium, the frequency and wavelength are related as

$$\lambda = \frac{c}{\nu} \tag{6.1}$$

where c is the speed of light in the medium, λ is the wavelength, and ν is the frequency. In a vacuum, $c = 2.998 \times 10^8$ m/s.

The electromagnetic continuum is divided into different regimes as a function of the wavelength. The regimes and wavelength ranges are delineated in Table 6.1.

Of interest in solar energy engineering is thermal radiation in the wavelength range $10^{-1} < \lambda < 10^2$ μm. The visible part of the spectrum is in the range $0.4 < \lambda < 0.7$ μm and is bounded by the ultraviolet and the infrared. Part of the ultraviolet and the infrared regimes are also in the thermal radiation regime.

The magnitude of thermal radiation varies with the wavelength and gives rise to the spectral distribution. In addition to the spectral nature of thermal radiation, a key feature is the directional distribution. In order for thermal radiation to be quantified, both the spectral and directional attributes must be examined.

A good starting point is to consider the characteristics of a blackbody.

1) A blackbody absorbs all incident radiation, regardless of wavelength and direction.
2) For a prescribed temperature and wavelength, no surface can emit more energy than a blackbody.
3) The blackbody is a diffuse (independent of direction) emitter.

Alternative Energy Systems and Applications, Second Edition. B. K. Hodge.

Companion website: www.wiley.com\go\Hodge\AESystemsandApplications2E

Table 6.1 The electromagnetic continuum and regimes.

Regime	Range (μm)
Gamma rays	$\lambda < 10^{-4}$
X-rays	$10^{-4} < \lambda < 10^{-2}$
Ultraviolet	$10^{-2} < \lambda < 0.4$
Thermal radiation	$10^{-1} < \lambda < 10^{2}$
Infrared	$0.7 < \lambda < 10^{2}$
Microwave	$\lambda > 10^{2}$

The spectral emissive power density of a blackbody is given by the Planck distribution (Bergman *et al.*, 2011)

$$E_{\lambda,\mathrm{b}}(\lambda, T) = \frac{C_1}{\lambda^5[\exp(C_2/\lambda T) - 1]} \tag{6.2}$$

where $C_1 = 3.742 \times 10^8$ W μm^4/m^2 and $C_2 = 1.439 \times 10^4$ μm K. The spectral emissive power density $E_{\lambda,\mathrm{b}}$ is customarily expressed in the units of watts per micrometer per square meter, which is interpreted as the emissive power per unit area per wavelength. The subscripts λ and b in Equation 6.2 signify that the power density is per wavelength (spectral) and is from a blackbody respectively. The total emissive power density of a blackbody is the integral of the blackbody spectral emissive power density over all wavelengths, or

$$E_{\mathrm{b}}(\lambda T) = \int_0^\infty E_{\lambda,\mathrm{b}}\, \mathrm{d}\lambda = \int_0^\infty \frac{C_1}{\lambda^5[\exp(C_2/\lambda T) - 1]}\, \mathrm{d}\lambda = \sigma T^4 \tag{6.3}$$

where $\sigma = 5.67 \times 10^{-8}$ W/(m^2 K^4) is the Stefan–Boltzmann constant. The T^4 functional dependence of the blackbody emissive power is one of the strongest functional dependencies in physics and emphasizes the importance of temperature is thermal radiation.

Additional examination of Equation 6.2 is warranted. Figure 6.1, plotted in log–log coordinates, presents a graphical study of the blackbody spectral emissive power density for several different temperatures. $T = 5800$ K is one of the temperatures considered because the spectral distribution of thermal radiation from the sun is close to that of a blackbody at 5800 K. The pronounced effect of temperature on the blackbody spectral emissive power is demonstrated by its range: eight orders of magnitude, from 1 W/(μm m^2) to nearly 10^8 W/(μm m^2). Also of interest is the location of the maximum spectral emissive power as a function of surface temperature. For example, at $T = 300$ K, close to room temperature, the maximum occurs near $\lambda = 10$ μm, but as the temperature is increased the maximum shifts to shorter wavelengths; thus, at $T = 5800$ K the maximum is near 0.5 μm. Not surprisingly, $\lambda = 0.5$ μm is the middle of the visible spectrum for which vision on Earth is optimally adapted. The thermal radiation range given in Table 6.1 is congruent with the results of Figure 6.1, as the $10^{-1} < \lambda < 10^2$ μm range of Figure 6.1 contains virtually all the emitted energy for these relevant temperatures. The total blackbody emissive power is the "area under the curve," and the blackbody emissive power at $T = 5800$ K is 140 000 times that at $T = 300$ K.

For many radiation heat transfer considerations, the fraction of energy contained between a wavelength interval is needed. The basis of obtaining such fractions is the blackbody radiation function. Using the Planck distribution, the fraction of thermal energy in the wavelength range

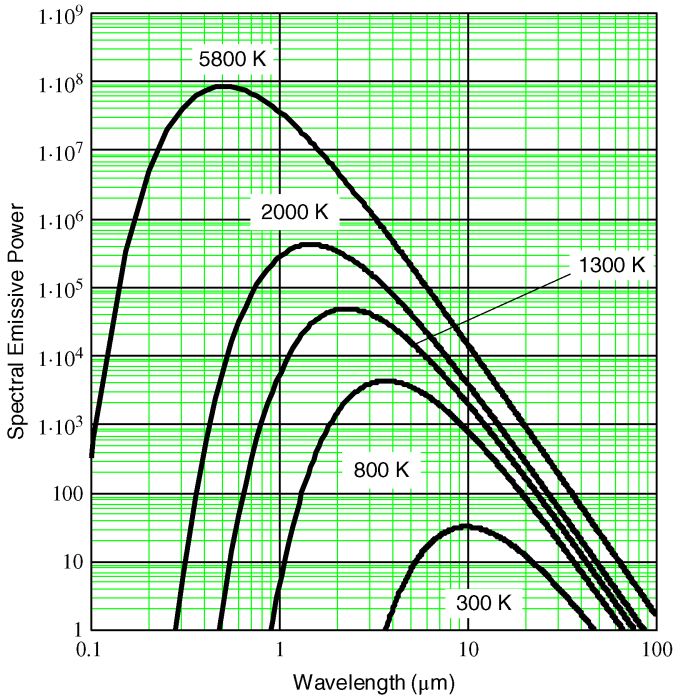

Figure 6.1 Blackbody spectral emissive power density for selected surface temperatures.

zero to λ is cast as follows:

$$F(0-\lambda T)=\frac{\int_0^{\lambda} E_{\lambda,\mathrm{b}}\,\mathrm{d}\lambda}{\int_0^{\infty} E_{\lambda,\mathrm{b}}\,\mathrm{d}\lambda}=\frac{\int_0^{\lambda} E_{\lambda,\mathrm{b}}\,\mathrm{d}\lambda}{\sigma T^4}=\int_0^{\lambda T}\frac{E_{\lambda,\mathrm{b}}}{\sigma T^5}\,\mathrm{d}(\lambda T) \tag{6.4}$$

Figure 6.2 illustrates the concept graphically.

Many heat transfer textbooks contain tabulations of the blackbody radiation function, or Equations 6.2 and 6.4 can be integrated to give the blackbody radiation function values. However, Howell *et al*. (2010) devised a closed-form series that replicates, to within a fraction of a percent, the accepted blackbody radiation function values, but also provides a convenient expression for use in many problem solutions. Their series appears as

$$F(\zeta)=\frac{15}{\pi^4}\sum_{n=1}^{20}\frac{\mathrm{e}^{-n\zeta}}{n}\left(\frac{6}{n^3}+6\frac{\zeta}{n^2}+\zeta^3+3\frac{\zeta^2}{n}\right) \tag{6.5}$$

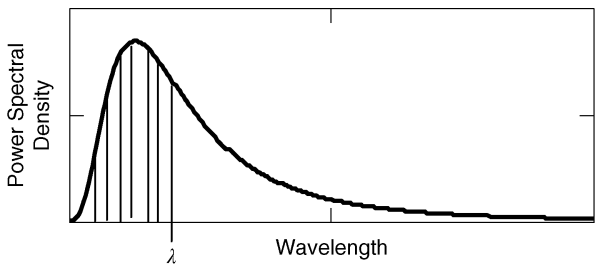

Figure 6.2 Blackbody radiation function illustration.

Table 6.2 Blackbody radiation function tabulation.

λT (μm K)	$F(0-\lambda T)$	λT (μm K)	$F(0-\lambda T)$	λT (μm K)	$F(0-\lambda T)$	λT (μm K)	$F(0-\lambda T)$
200	0	5 200	0.6579				
400	1.8554×10^{-12}	5 400	0.6802				
600	9.263×10^{-8}	5 600	0.7009				
800	1.6396×10^{-5}	5 800	0.72				
1 000	0.0003	6 000	0.7377				
1 200	0.0021	6 200	0.754	10 500	0.9236		
1 400	0.0078	6 400	0.7691	11 000	0.9318		
1 600	0.0197	6 600	0.7831	11 500	0.9389		
1 800	0.0393	6 800	0.796	12 000	0.945		
2 000	0.0.0667	7 000	0.808	12 500	0.9504	25 000	0.9922
2 200	0.1008	7 200	0.8191	13 000	0.9551	30 000	0.9953
2 400	0.1402	7 400	0.8294	13 500	0.9592	35 000	0.997
2 600	0.183	7 600	0.839	14 000	0.9628	40 000	0.9979
2 800	0.2278	7 800	0.8479	14 500	0.9661	45 000	0.9985
3 000	0.2731	8 000	0.8562	15 000	0.9689	50 000	0.9989
3 200	0.318	8 200	0.8639	15 500	0.9715	55 000	0.9992
3 400	0.3616	8 400	0.8711	16 000	0.9738	60 000	0.9993
3 600	0.4035	8 600	0.8778	16 500	0.9758	65 000	0.9995
3 800	0.4433	8 800	0.8841	17 000	0.9776	70 000	0.9996
4 000	0.4808	9 000	0.8899	17 500	0.9793	75 000	0.9997
4 200	0.5159	9 200	0.8954	18 000	0.9808	80 000	0.9997
4 400	0.5487	9 400	0.9006	18 500	0.9822	85 000	0.9998
4 600	0.5792	9 600	0.9054	19 000	0.9834	90 000	0.9998
4 800	0.6074	9 800	0.9099	19 500	0.9845	95 000	0.9998
5 000	0.6336	10 000	0.9141	20 000	0.9855	1×10^5	0.9998

where $\zeta = C_2/\lambda T$. Table 6.2 contains a tabular listing of Equation 6.5 as a function of λT. Table 6.2 and Equation 6.5 will be used in the solution of example problems requiring the use of the blackbody radiation function. Example 6.1 illustrates the use of the blackbody radiation function.

Example 6.1
For a blackbody at 5800 K, what is the percentage of energy contained in the visible part of the spectrum? Contrast this with the percentage of energy contained in the visible spectrum for a blackbody at 3000 K.

Solution Two different approaches for obtaining the solution will be presented and discussed: (1) the use of Table 6.2 and (2) the use of Equation 6.5 and Mathcad. The visible spectrum spans the wavelength range $0.4 \le \lambda \le 0.7$ μm. Figure 6.3, with $\lambda_1 = 0.4$ μm and

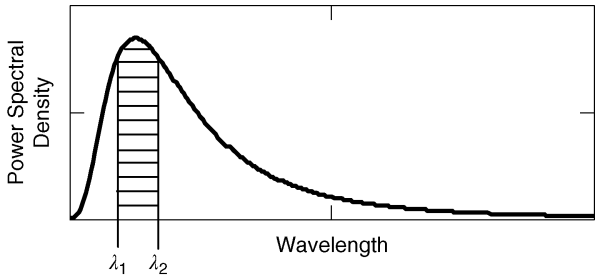

Figure 6.3 Visible spectrum range for a 5800 K blackbody.

$\lambda_2 = 0.7$ μm, illustrates the range of interest for the 5800 K blackbody. $F(0 - \lambda_2 T)$ provides the fraction of radiant energy from 0 to λ_2, and $F(0 - \lambda_1 T)$ provides the fraction from 0 to λ_2. The fraction of radiant energy contained between λ_1 and λ_2 can be expressed as the difference, or

$$F(\lambda_2 T - \lambda_1 T) = F(0 - \lambda_2 T) - F(0 - \lambda_1 T) \tag{6.6}$$

Equation 6.6 is the fundamental radiation function algebra relationship.

The Table 6.2 approach will be illustrated first. For the blackbody at 5800 K we have

$$\lambda_1 T = 0.4\ \mu\text{m} \times 5800\ \text{K} = 2320\ \mu\text{m K}$$
$$\lambda_2 T = 0.7\ \mu\text{m} \times 5800\ \text{K} = 4060\ \mu\text{m K}$$

Interpolating between the entries in Table 6.2 yields

$$F(2320\ \mu\text{m K}) = 0.1244$$
$$F(4060\ \mu\text{m K}) = 0.4913$$

So that the fractional radiant energy contained between $\lambda_1 = 0.4$ μm and $\lambda_2 = 0.7$ μm becomes

$$F(\lambda_2 T - \lambda_1 T) = 0.4913 - 0.1244 = 0.3669$$

Thus, for a 5800 K blackbody, 37% of the radiant energy is contained in the visible part of the spectrum.

The same procedure is applied for the 3000 K blackbody, except that the temperature used is 3000 K, not 5800 K. The results can be summarized as

$$\lambda_1 T = 0.4\ \mu\text{m} \times 3000\ \text{K} = 1200\ \mu\text{m K}$$
$$\lambda_2 T = 0.7\ \mu\text{m} \times 3000\ \text{K} = 2100\ \mu\text{m K}$$

$$F(1200\ \mu\text{m K}) = 0.0021$$
$$F(2100\ \mu\text{m K}) = 0.0838$$

$$F(\lambda_2 T - \lambda_1 T) = 0.0830 - 0.0021 = 0.0817$$

Hence, for the 3000 K blackbody only 8% of the total radiant energy is in the visible range.

Figure 6.4 presents the solution using Equation 6.5 and Mathcad. The same procedure is followed, with the only major difference being the use of Equation 6.5 for the blackbody radiation function. The use of the Howell *et al.* (2010) expression is very convenient, as it obviates the need for table lookups and interpolations to solve spectral distribution problems. As the remainder of the section will demonstrate, this ability will be important for a number of thermal radiation problems not limited to blackbody formulations. The results in Figure 6.4 are more accurate than using Table 6.2 since no interpolation is required, but the differences between the two approaches are so negligible that for most purposes either will suffice.

$\sigma := 5.67 \cdot 10^{-8} \cdot \frac{W}{m^2 \cdot K^4}$ $\mu m := \frac{m}{10^6}$ The Stefan—Boltzmann constant and μm.

$C_1 := 3.742 \cdot 10^8 \cdot W \cdot \frac{\mu m^4}{m^2}$ $C_2 := 1.439 \cdot 10^4 \cdot \mu m \cdot K$ C_1 and C_2 for the Planck power spectral density expression.

$F(\zeta) := \frac{15}{\pi^4} \cdot \left[\sum_{n=1}^{20} \frac{e^{-n \cdot \zeta}}{n} \cdot \left(\frac{6}{n^3} + 6 \cdot \frac{\zeta}{n^2} + \zeta^3 + 3 \cdot \frac{\zeta^2}{n} \right) \right]$ $\zeta = \frac{C_2}{\lambda \cdot T}$ Definition of ζ

Blackbody at 5800 K.

$\lambda T_1 := 0.4 \cdot \mu m \cdot 5800 \cdot K$ $F\left(\frac{C_2}{\lambda T_1}\right) = 0.12392$

$\lambda T_2 := 0.7 \cdot \mu m \cdot 5800 \cdot K$ $F\left(\frac{C_2}{\lambda T_2}\right) = 0.49154$

$Fvisible := F\left(\frac{C_2}{\lambda T_2}\right) - F\left(\frac{C_2}{\lambda T_1}\right)$ $Fvisible = 0.36762$

Blackbody at 3000 K:

$\lambda T_1 := 0.4 \cdot \mu m \cdot 3000 \cdot K$ $F\left(\frac{C_2}{\lambda T_1}\right) = 2.13115 \times 10^{-3}$

$\lambda T_2 := 0.7 \cdot \mu m \cdot 3000 \cdot K$ $F\left(\frac{C_2}{\lambda T_2}\right) = 0.083$

$Fvisible := F\left(\frac{C_2}{\lambda T_2}\right) - F\left(\frac{C_2}{\lambda T_1}\right)$ $Fvisible = 0.08087$

Figure 6.4 Mathcad worksheet for the solution to Example 6.1.

The source of solar energy on the Earth is obviously the sun. The sun is located 1.50×10^{11} m from the Earth and has a diameter of 1.39×10^9 m. The solar constant, defined as the flux of solar energy incident on a surface oriented normal to the rays of the sun has a mean value of 1353 W/m^2. However, the solar constant is the flux incident at the outer edge of the atmosphere. For terrestrial applications, what is important is the solar flux incident on the surface of the Earth, after the sun's rays have passed through the atmosphere. Figure 6.5 provides a quantitative assessment of the solar flux. The spectral distribution is illustrated as extraterrestrial (incident on the edge of the atmosphere) and on the Earth's surface. The extraterrestrial solar flux has approximately the spectral distribution of blackbody radiation at 5800 K, *but not the total emissive power of a blackbody* – as a comparison of Figures 6.1 and 6.2 will confirm.

As the solar flux passes through the atmosphere, it is attenuated by the presence of oxygen (O_2), ozone (O_3), water vapor (H_2O), and carbon dioxide (CO_2). As a result, the solar flux at the Earth's surface is significantly less than the extraterrestrial solar flux. As the solar flux traverses the atmosphere, both the magnitude and directional distributions are altered. These alternations are due to absorption and scattering. The innermost plot in Figure 6.5 demonstrates the absorption of radiant energy by the gases in the atmosphere. In the ultraviolet regime, $10^{-2} < \lambda < 0.4\,\mu$m, ozone is responsible for the absorption and results in virtually no solar flux reaching the surface for $\lambda < 0.3\,\mu$m. Part of the concern about

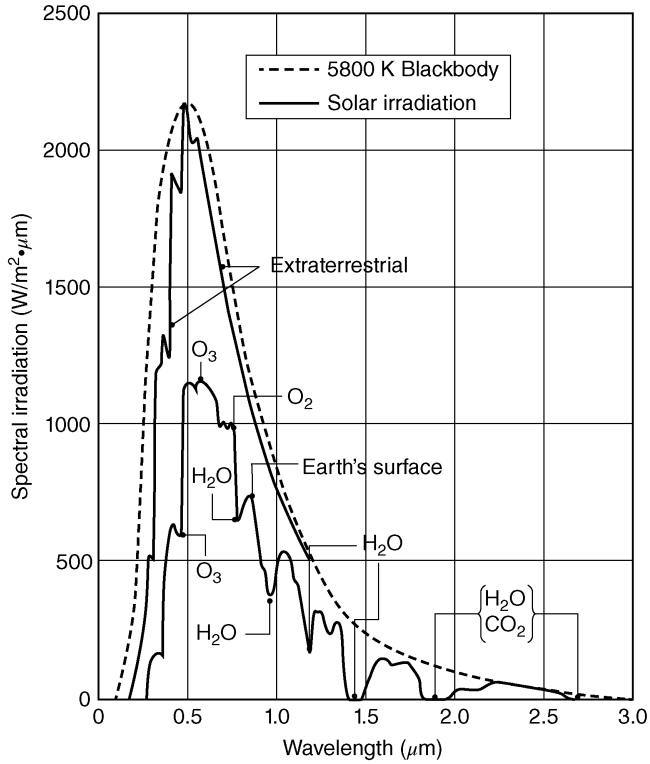

Figure 6.5 Solar irradiation characteristics. *Source*: Bergman *et al*. (2011).

depletion of the ozone layer is that without the ozone much more of the thermal radiation in the ultraviolet regime would reach the surface of the Earth, with long-term, deleterious results. In the infrared regime, the absorption is primarily due to water vapor, although CO_2 also plays a role. For all wavelengths, thermal radiation is also absorbed by the particulates content of the atmosphere.

In addition to absorption, scattering occurs, resulting in the redirection of the sun's rays. Rayleigh scattering, attributable to the gas molecules, provides for virtually uniform scattering of thermal radiation. The uniformity of Rayleigh scattering means that about one-half of the scattered radiation is redirected away from the Earth. At any point on the Earth's surface, the scattered radiation is incident from all directions. Mie scattering by the particulates in the atmosphere does little to reorient the sun's rays. Bergman *et al*. (2011) provide the following cogent summary:

> That portion of the radiation that has penetrated the atmosphere without having been scattered (or absorbed) is in the direction of the zenith angle and is termed the direct radiation. The scattered radiation is incident from all directions, although its intensity is largest for the directions close to that of the direct radiation. However, because the radiation intensity is often assumed to be independent of the direction, the radiation is termed diffuse.

The total thermal radiation reaching the surface is the sum of the direct and the diffuse components. On a clear day, the diffuse may account for only 10% of the total, while on a cloudy day it is essentially 100% of the total.

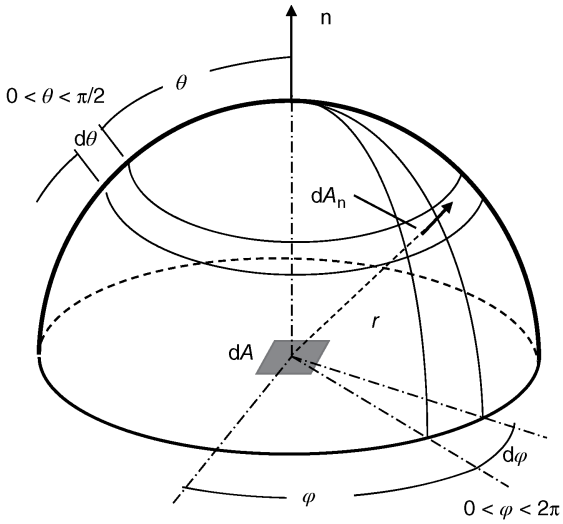

Figure 6.6 Hemisphere surrounding an area emitting thermal radiation.

With the characteristics of thermal radiation from the sun understood, consideration of radiation heat transfer fundamentals for a surface is appropriate. Specific topics include (1) what happens when thermal radiation is incident on a surface and (2) the emission characteristics of a surface. Emission will be examined first.

The emissive characteristics of a blackbody have been established. Emissions from a non-blackbody can have directional and spectral characteristics. Consider, as in Figure 6.6, a hemisphere surrounding an elemental area that is emitting thermal radiation. The hemisphere about the emitting area dA is a convenient mechanism for visualizing the geometry of thermal radiation. The spectral intensity $I_{\lambda,\mathrm{e}}$ of the emitted radiation is defined as the rate at which radiant energy is emitted at the wavelength λ in the (θ, φ) direction per unit area of the emitting surface normal to this direction, per unit solid angle about this direction, and per unit wavelength interval dλ about λ. The normal to the emitting surface area in the (θ, φ) direction is the area $\mathrm{d}A_\mathrm{n}$ in Figure 6.6. If the blackbody surface is used as the basis, the spectral directional emissivity $\varepsilon_{\lambda,\theta}(\lambda, \theta, \varphi, T)$ is defined as the ratio of the emitted radiation intensity in a given direction at a given wavelength divided by the radiation intensity of a blackbody:

$$\varepsilon_{\lambda,\theta}(\lambda, \theta, \varphi, T) = \frac{I_{\lambda,\mathrm{e}}(\lambda, \theta, \varphi, T)}{I_{\lambda,\mathrm{b}}(\lambda, T)} \tag{6.7}$$

Equation 6.7 provides a process for computing the actual emission in reference to that of a blackbody and provides a process for computing the actual emission if $\varepsilon_{\lambda,\theta}(\lambda, \theta, \varphi, T)$ is known. If the spectral directional intensity is integrated over $0 \leq \varphi \leq 2\pi$ and $0 \leq \theta \leq \pi/2$, the spectral hemispherical emissivity $\varepsilon_\lambda(\lambda, T)$ results and is defined as

$$\varepsilon_\lambda(\lambda, T) = \frac{I_{\lambda,\mathrm{e}}(\lambda, T)}{I_{\lambda,\mathrm{b}}(\lambda, T)} = \frac{E_\lambda(\lambda, T)}{E_{\lambda,\mathrm{b}}(\lambda, T)} \tag{6.8}$$

where $E_\lambda(\lambda, T)$ is the spectral hemispherical emissive power and $\varepsilon_\lambda(\lambda, T)$ is the spectral hemispherical emissivity. Since the angular dependences have been integrated out, the word "hemispherical" rather than "directional" is used. The transition from $I_{\lambda,\mathrm{e}}(\lambda, T)$ to $E_\lambda(\lambda, T)$ is seamless since the emission intensity is based on the projected area and the emission is based on the actual area, and they are related as $E_\lambda(\lambda, T) = \pi I_{\lambda,\mathrm{e}}(\lambda, T)$. Details are provided in heat transfer textbooks such as Bergman *et al.* (2011). If the spectral hemispherical emissive power is

integrated over all wavelengths, the total hemispherical emissive power $E(T)$ is recovered and appears as

$$\varepsilon(T) = \frac{E(T)}{E_b(T)} \tag{6.9}$$

where $E(T)$ is the total hemispherical emissive power and $\varepsilon(T)$ is the total hemispherical emissivity, generally referred to as simply the emissivity. The integration sequence is from spectral directional to spectral hemispherical to total hemispherical. Values for the spectral, hemispherical, and total hemispherical emissivities of various materials are available from handbooks and textbooks and on a number of web sites (e.g., http://www.icess.ucsb.edu/modis/EMIS/html/em.html).

Example 6.2

A wall at $T_s = 500\,\text{K}$ has the spectral emissivity illustrated in Figure 6.7. Determine the total emissivity and the emissive power of the surface.

Solution Once the total emissivity is known, Equation 6.9 can be used to calculate the emissive power. The emissive power of the surface is composed of the individual contribution for each wavelength range associated with each spectral hemispherical emissivity, or

$$\varepsilon E_b = \varepsilon_1 \int_0^{\lambda_1} E_{\lambda,b}\,d\lambda + \varepsilon_2 \int_{\lambda_1}^{\lambda_2} E_{\lambda,b}\,d\lambda + \varepsilon_3 \int_{\lambda_2}^{\infty} E_{\lambda,b}\,d\lambda \tag{6.10}$$

which can be expressed as

$$\varepsilon = \varepsilon_1 F(0-\lambda_1 T) + \varepsilon_2[F(0-\lambda_2 T) - F(0-\lambda_1 T)] + \varepsilon_3[1 - F(0-\lambda_2 T)] \tag{6.11}$$

Thus, by using the spectral emissive description of the surface behavior, the blackbody radiation function can be used to make computations for non-blackbody surfaces.

The Mathcad worksheet for this problem is presented in Figure 6.8. The total emissivity is 0.6099, and the total emissive power is $2161\,\text{W/m}^2$. By comparison, if the surface were a blackbody, the total emissive power would have been $3544\,\text{W/m}^2$.

Equations 6.7, 6.8 and 6.9 involve surface emissions of thermal radiation. Radiation incident on surface is called irradiation and is denoted as G, and the spectral irradiation (the irradiation at a given wavelength) is denoted as G_λ. Three things happen to thermal radiation incident on a surface: (1) some is absorbed, (2) some is reflected, and (3) some is transmitted. Figure 6.9 schematically illustrates these processes. Consider each of the possibilities in turn. Irradiation, like

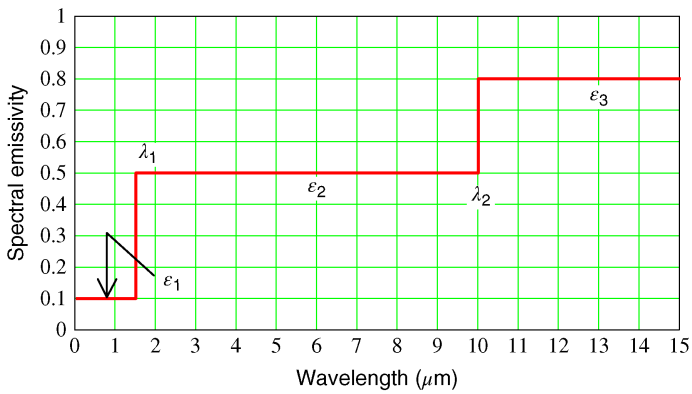

Figure 6.7 Spectral emissivity for Example 6.2.

Evaluation of the total emissivity:

$\lambda T_1 := 1.5 \cdot \mu m \cdot 500 \cdot K$ $\quad F\left(\frac{C_2}{\lambda T_1}\right) = 5.93352 \times 10^{-6}$

$\lambda T_2 := 10 \cdot \mu m \cdot 500 \cdot K$ $\quad F\left(\frac{C_2}{\lambda T_2}\right) = 0.63363$

$$\varepsilon := 0.1 \cdot F\left(\frac{C_2}{\lambda T_1}\right) + 0.5 \cdot \left(F\left(\frac{C_2}{\lambda T_2}\right) - F\left(\frac{C_2}{\lambda T_1}\right)\right) + 0.8 \cdot \left(1 - F\left(\frac{C_2}{\lambda T_2}\right)\right)$$

$\varepsilon = 0.60991$

Compute the total emissive power per unit area:

$T_s := 500 \cdot K$ $\quad E := \varepsilon \cdot \sigma \cdot T_s^4$ $\quad E = 2.16137 \times 10^3 \frac{W}{m^2}$

Blackbody emissive power:

$E_b := \sigma \cdot T_s^4$ $\quad E_b = 3.54375 \times 10^3 \frac{W}{m^2}$

Figure 6.8 Mathcad solution for Example 6.2.

emitted radiation, has a spectral nature; but unlike emitted radiation, whose spectral characteristics are determined by the surface temperature, the spectral characteristics of irradiation are determined by the source of the irradiation. And just like emitted radiation, irradiation has directional attributes. Surface properties associated with irradiation are described by three terms: (1) *absorptivity*, for the absorbed irradiation, (2) *reflectivity*, for the reflected irradiation, and (3) *transmissivity*, for the transmitted irradiation. The same hierarchy of spectral directional to spectral hemispherical to total hemispherical is used. Working definitions are as follows.

Absorptivity:

$$\text{spectral directional} \quad \alpha_{\lambda,\theta}(\lambda,\theta,\varphi) = \frac{I_{\lambda,\text{i,absorbed}}(\lambda,\theta,\varphi)}{I_{\lambda,\text{i}}(\lambda,\theta,\varphi)} \tag{6.12}$$

$$\text{spectral hemispherical} \quad \alpha_{\lambda}(\lambda) = \frac{G_{\lambda,\text{absorbed}}(\lambda)}{G_{\lambda}(\lambda)} \tag{6.13}$$

$$\text{total hemispherical} \quad \alpha = \frac{\int_0^\infty \alpha_\lambda G_\lambda(\lambda)\mathrm{d}\lambda}{\int_0^\infty G_\lambda(\lambda)\mathrm{d}\lambda} \tag{6.14}$$

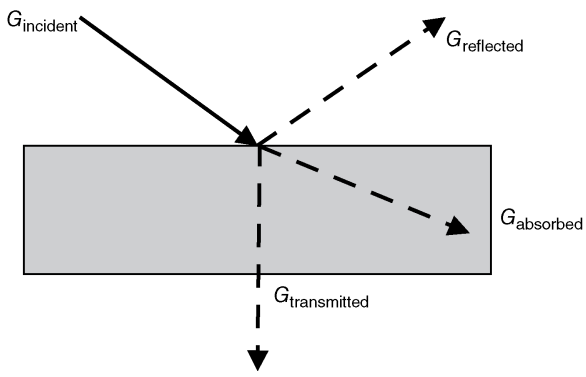

Figure 6.9 Irradiation on a surface.

where $I_{\lambda,\mathrm{i}}$ is the incident irradiation flux and $G_\lambda(\lambda)$ is spectral irradiation. Analogous sequences are also defined for the reflectivity and the transmissivity.

Reflectivity:

$$\text{spectral directional} \quad \rho_{\lambda,\theta}(\lambda,\theta,\varphi) = \frac{I_{\lambda,\mathrm{i,reflected}}(\lambda,\theta,\varphi)}{I_{\lambda,\mathrm{i}}(\lambda,\theta,\varphi)} \tag{6.15}$$

$$\text{spectral hemispherical} \quad \rho_\lambda(\lambda) = \frac{G_{\lambda,\mathrm{reflected}}(\lambda)}{G_\lambda(\lambda)} \tag{6.16}$$

$$\text{total hemispherical} \quad \rho = \frac{\int_0^\infty \rho_\lambda G_\lambda(\lambda)\mathrm{d}\lambda}{\int_0^\infty G_\lambda(\lambda)\mathrm{d}\lambda} \tag{6.17}$$

Transmissivity:

$$\text{spectral directional} \quad \tau_{\lambda,\theta}(\lambda,\theta,\varphi) = \frac{I_{\lambda,\mathrm{i,transmitted}}(\lambda,\theta,\varphi)}{I_{\lambda,\mathrm{i}}(\lambda,\theta,\varphi)} \tag{6.18}$$

$$\text{spectral hemispherical} \quad \tau_\lambda(\lambda) = \frac{G_{\lambda,\mathrm{transmitted}}(\lambda)}{G_\lambda(\lambda)} \tag{6.19}$$

$$\text{total hemispherical} \quad \tau = \frac{\int_0^\infty \tau_\lambda G_\lambda(\lambda)\mathrm{d}\lambda}{\int_0^\infty G_\lambda(\lambda)\mathrm{d}\lambda} \tag{6.20}$$

For an opaque surface, a surface that does not transmit thermal radiation, the transmissivity terms are all zero.

Conservation of energy and the above definitions demand that

$$\begin{aligned} 1 &= \alpha_\lambda + \rho_\lambda + \tau_\lambda \\ 1 &= \alpha + \rho + \tau \end{aligned} \tag{6.21}$$

Example 6.3
If the spectral absorptivity is equal to the spectral emissivity of Example 6.2, $\varepsilon_\lambda = \alpha_\lambda$, and if the irradiation G of 750 W/m^2 has the spectral characteristics of a blackbody at 2000 K, find the total absorptivity, the total reflectivity, and the irradiation absorbed if the surface is opaque.

Solution The spectral absorptivity is known from Example 6.2. Since the irradiation has the spectral characteristics of a blackbody at 2000 K, the blackbody emission function with the temperature of 2000 K can be used to describe the spectral distribution of the irradiation. Since the surface is opaque, the transmissivity is zero. The Mathcad solution is presented in Figure 6.10. The solution follows the general approach of Example 6.2. Several things are of interest in the problem. Because of the spectral characteristics of the surface, $\alpha \neq \varepsilon$, which is an assumption sometimes made for problems such as this. The irradiation is not that of a blackbody, but the irradiation has the spectral characteristics of a blackbody at 2000 K.

In the problem statement for Example 6.3, $\varepsilon_\lambda = \alpha_\lambda$: under what conditions is this a viable assertion? When is $\alpha = \varepsilon$ acceptable? Most heat transfer textbooks address these issues. The usual question to ask is, when is $\varepsilon_{\lambda,\theta} = \alpha_{\lambda,\theta}$? This is always true, since $\varepsilon_{\lambda,\theta}$ and $\alpha_{\lambda,\theta}$ are properties of the surface and are independent of the emission or irradiation. The spectral hemispherical emissivity and absorptivity are equal under two conditions: (1) when the irradiation is diffuse or (2) when the surface is diffuse. For many problems of interest, one of these conditions is often approximated. Moving up the hierarchy, when is $\alpha = \varepsilon$? The total absorptivity is equal to the total emissivity under two circumstances: (1) when the irradiation

$\mu m := \frac{m}{10^6}$ The definition of μm.

$C_1 := 3.742 \cdot 10^8 \cdot W \cdot \frac{\mu m^4}{m^2}$ $C_2 := 1.439 \cdot 10^4 \cdot \mu m \cdot K$ C_1 and C_2 for the Planck power spectral density expression.

$F(\zeta) := \frac{15}{\pi^4} \cdot \left[\sum_{n=1}^{20} \frac{e^{-n \cdot \zeta}}{n} \cdot \left(\frac{6}{n^3} + 6 \cdot \frac{\zeta}{n^2} + \zeta^3 + 3 \cdot \frac{\zeta^2}{n} \right) \right]$ $\zeta = \frac{C_2}{\lambda \cdot T}$ Definition of ζ

$G := 750 \frac{W}{m^2}$ Irradiation.

$\lambda T_1 := 1.5 \cdot \mu m \cdot 2000 \cdot K$ $F\left(\frac{C_2}{\lambda T_1}\right) = 0.27312$

The radiation function for the absorptivity must be calculated using the spectral characteristics of the source of the irradiation.

$\lambda T_2 := 10 \cdot \mu m \cdot 2000 \cdot K$ $F\left(\frac{C_2}{\lambda T_2}\right) = 0.98555$

$\alpha := 0.1 \cdot F\left(\frac{C_2}{\lambda T_1}\right) + 0.5 \cdot \left(F\left(\frac{C_2}{\lambda T_2}\right) - F\left(\frac{C_2}{\lambda T_1}\right) \right) + 0.8 \cdot \left(1 - F\left(\frac{C_2}{\lambda T_2}\right) \right)$

$\alpha = 0.39509$

$\rho := 1 - \alpha$ $\rho = 0.60491$ Reflectivity

$G_{absorbed} := \alpha \cdot G$ $G_{absorbed} = 296.31455 \frac{W}{m^2}$

Irradiation absorbed by surface

Figure 6.10 Mathcad solution of Example 6.3.

corresponds to that of blackbody or (2) when the surface is gray. A gray surface is a surface for which $\varepsilon_\lambda = \alpha_\lambda$ for all λ (in the ranges of interest). Many spectrally selective surfaces, such as the one in Examples 6.2 and 6.3, are *not* gray surfaces, and $\alpha \neq \varepsilon$.

Table 6.3 presents the emissivity and solar absorptivity for selected surfaces. The ratio α/ε of the absorptivity for solar irradiation and the emissivity is a useful solar engineering parameter, as small values reject heat and large values absorb solar energy.

The foregoing review of radiation heat transfer is sufficient for the needs of this book. The next section will explore the motion of the sun with respect to the Earth.

6.3 Sun Path Description and Calculation

An understanding of the position of the sun relative to the Earth is important for solar engineering topics. Perhaps the most effective tool for explaining and understanding the position of the sun is the sun path – the path of the sun in relation to a location on the surface of the Earth. A number of textbooks, reference books, and web sites contain discussions, descriptions, tables, and illustrations of sun paths for various locations. However, few describe how to calculate sun paths or contain software elements to aid in their computation. The purpose of this section is to provide a procedure for calculating and understanding sun path lines.

Table 6.3 Solar absorptivity, emissivity, and their ratio for selected surfaces.

Surface	Solar absorptivity α	Emissivity ε	α/ε
Aluminum			
evaporated film	0.09	0.03	3.00
hard anodized	0.03	0.80	0.04
White paint	0.21	0.96	0.22
Black paint	0.97	0.97	1.00
Black chrome	0.95	0.15	6.33
Red brick	0.63	0.93	0.68
Snow	0.28	0.97	0.29
Teflon	0.12	0.85	0.14
Vegetation (corn)	0.76	0.97	0.78

Consider the Earth–sun geometric relationship. As illustrated in Figure 6.11, the Earth rotates at an angle of 23.45° with respect to the ecliptic orbital plane. This rotation angle is responsible for the seasons (and for much of the difficulty in computing sun paths). Although the Earth moves around the sun, the simplest way to understand the motion of the Earth is to adopt a Ptolemaic view – to consider the Earth as stationary and the sun as being in motion. In the Ptolemaic view, the sun's relation to a point on the surface of the Earth is described by the solar altitude angle α and the solar azimuth angle a_s. These angles are shown in Figure 6.12. The altitude angle is the angle between a line collinear with the sun and the horizontal plane. The azimuth angle is the angle between a due-south line and the projection of the site-to-sun line on the horizontal plane. The sun path for June 21 for Mississippi State University (MSU), 33.455°N latitude, is illustrated in Figure 6.13. In addition to the relation between the azimuth and altitude angles, the solar time is shown in the figure. At MSU, June 21 has almost 14 h of

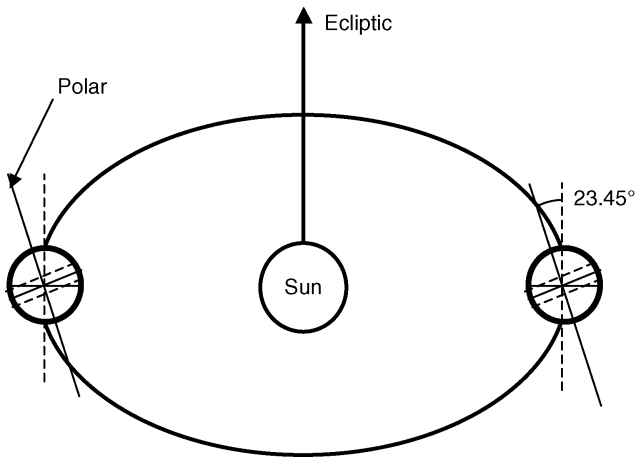

Figure 6.11 Motion of the Earth about the sun.

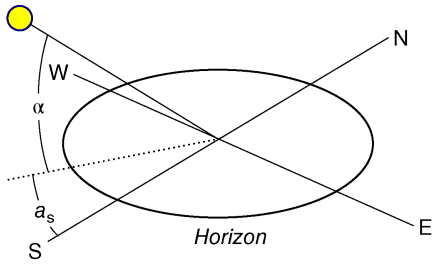

Figure 6.12 Solar azimuth angle and solar altitude angle definitions.

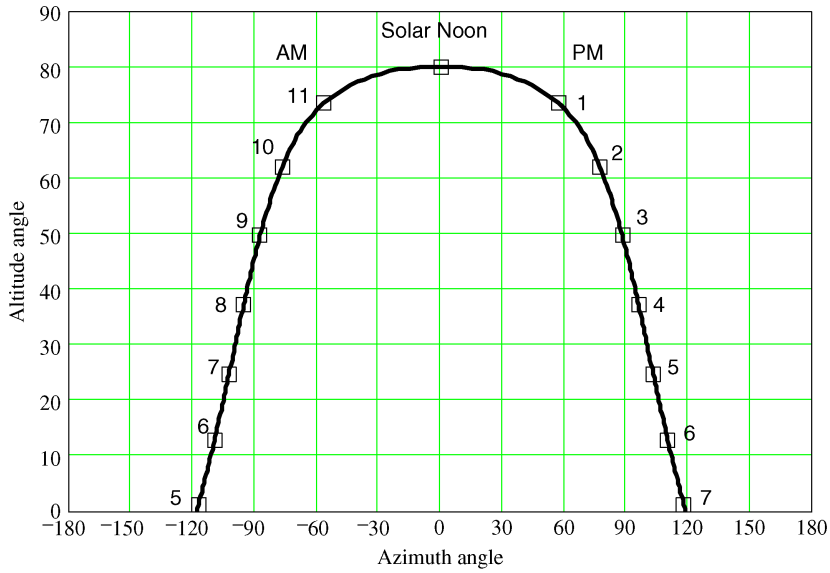

Figure 6.13 Sun path line for June 21 for MSU.

daylight, and at solar noon the sun is nearly vertical ($\alpha \approx 80°$). The sun rises almost 30° north of east ($a_s \approx -120°$) and sets almost 30° north of west ($a_s \approx +120°$). An interesting aspect of this sun path line is the rapidity of movement of the sun between 11:00 am and 1:00 pm. During this time, the sun traverses a total azimuth angle of nearly 120° – almost one-half of the total azimuth angle traverse of 240°. The motion of the sun is also symmetrical about solar noon, with the difference between morning and afternoon being just the sign of the azimuth angle.

However, as Goswami *et al.* (2000) point out, the altitude and azimuth angles are not fundamental but are functions of the location (the latitude), the time (the solar hour angle), and the solar declination. (As an aside, longitudes and latitudes for locations, as well as an overhead image, in the USA and many parts of the world can be found at http://www.latlong.net/.) Many other web sites provide similar information, including Google map locations or Google Earth images.

The solar declination δ_s varies between −23.45° and +23.45° and has the same numerical value as the latitude at which the sun is directly overhead at solar noon on a given day. The solar declination can be approximated as

$$\delta_s = 23.45° \sin\left[\frac{360(284 + n)}{365}\right] \tag{6.22}$$

where n is the ordinal day, many times called, or confused with, the Julian day number (JDN). The ordinal day is the number of the day measured sequentially from January 1 (ordinal day 1) to December 31 (ordinal day 365 for a non-leap year or 366 for a leap year). A convenient ordinal date table is located at http://www.atmos.anl.gov/ANLMET/OrdinalDay.txt. The Julian date (JDN) is a count of the number of days starting January 1, 4713 BC. Strictly interpreted, the number of the day from January 1 is the ordinal day, but in many solar engineering applications the Julian day is taken as the ordinal day. http://aa.usno.navy.mil/data/docs/JulianDate.php is a convenient web site for determining the Julian day and Julian date. For example, the Julian day for June 30, 2015, is 2 457 203, and the Julian date for noon on June 30, 2015, is 2 457 203.500 000.

The solar declination as a function of the ordinal day is illustrated in Figure 6.14.

The solar hour angle h_s is based on the 24 h required for the sun to move 360° around the Earth. The motion is 15° per hour with $-180° \leq h_s \leq +180°$. The solar hour angle at solar noon (the time when the azimuth angle is zero and the sun altitude angle is a maximum for a given day) is defined as zero, with values east of south (morning) being negative and values west of south (afternoon) being positive.

The solar altitude angle α is related to the declination δ_s, the latitude L, and the solar hour h_s angles as

$$\sin(\alpha) = \sin(L)\sin(\delta_s) + \cos(L)\cos(\delta_s)\cos(h_s) \tag{6.23}$$

The solar azimuth angle a_s is given as

$$\sin(a_s) = \frac{\cos(\delta_s)\sin(h_s)}{\cos(\alpha)} \tag{6.24}$$

For a given day, the generation of a sun path line using Equations 6.23 and 6.24 is straightforward for a latitude greater than the solar declination. Care must be taken for solar azimuth angles greater than +90° for the afternoon or less than −90° for the morning. Since the principal angle range for the arcsin function is +90° to −90°, for azimuth angles greater/less than ±90°, logic must be included to ensure that a value greater/less than 90° is obtained. One way to accomplish this is to determine the hour angle hlimit that corresponds to $a_s = \pm 90°$ (the sun position due west/east). Then, for all hour angles greater/less than ±hlimit, the azimuth angle must be greater/less than ±90°. Goswami *et al.* (2002) provide the following expression for hlimit:

$$\cos(\text{hlimit}) = \pm\frac{\tan(\delta_s)}{\tan(L)} \tag{6.25}$$

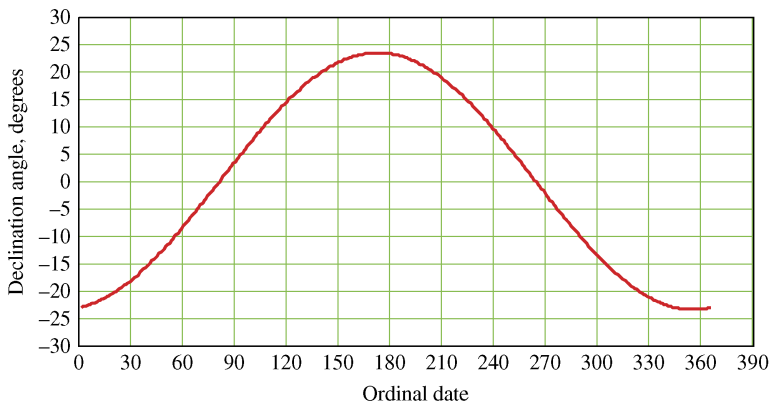

Figure 6.14 Declination angle as a function of ordinal day.

Table 6.4 Standard longitudes for US time zones.

75° for Eastern
90° for Central
105° for Mountain
12° for Pacific

When the hour angle is greater/less than ±hlimit, the azimuth angle is evaluated as $\pm\{\pi - \arcsin[\sin(a_s)]\}$, properly preserving $|a_s| > 90°$ for hour angles greater/less than ±hlimit.

The relation between standard time and local time must be incorporated if the sun path times are to be cast as local or "clock" times. The relationship between solar time and local (clock) time is presented in the following expressions:

$$\text{SolarTime} = \text{ST} + 4(\text{SL}-\text{LL})(\text{min}) + E(\text{min}) \tag{6.26}$$

$$\text{ST} + 1\,\text{h} = \text{DST} \tag{6.27}$$

where SolarTime is the solar time, ST is the standard time, SL is the standard longitude, LL is the local longitude, DST is daylight savings time, and E is the correction in minutes provided by the equation of time. The equation of time is

$$E = 9.87\sin(2B_n) - 7.53\cos(B_n) - 1.5\sin(B_n) \tag{6.28}$$

with

$$B_n = \frac{360(n-81)\pi}{364 \times 180} \tag{6.29}$$

and n the ordinal day (the day number during the year, with January 1 being 1). Table 6.4 provides the standard longitudes for US time zones.

The equation of time is plotted as a function of the ordinal day in Figure 6.15.

Using Equations 6.26–6.28 or Equations 6.26 and 6.27 and Figure 6.15, the solar time can be related to the standard time at any longitude and ordinal day. In this context, standard time is the local time or the time indicated by a clock.

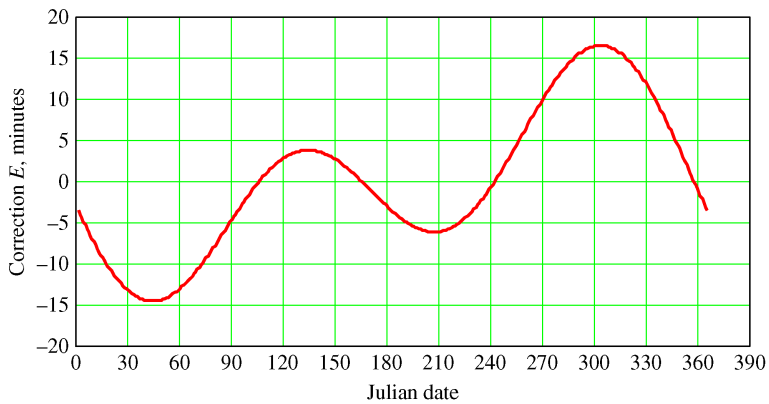

Figure 6.15 The equation of time as a function of Julian day.

Example 6.4
What is the standard time corresponding to 1:00 pm solar time on August 20 at MSU?

Solution MSU is located in the Central time zone at latitude 33.455°N and longitude 88.789°W. The ordinal day for August 20 is 232. Daylight savings time is observed. Inserting Equation 6.27 into Equation 6.26 and solving for the standard time yields

$$\mathrm{DST} = \mathrm{SolarTime} + 1\,\mathrm{h} - 4(\mathrm{SL}-\mathrm{LL})\mathrm{min} - E\,\mathrm{min} \tag{6.30}$$

The equation of time correction can be read from Figure 6.15 or calculated for day 232 using Equation 6.28 with the result of −2.946 min. Inserting the values into Equation 6.30, the local standard daylight saving time becomes

$$\begin{aligned}\mathrm{DST} &= 1:00\,\mathrm{pm} + 1\,\mathrm{h} - 4(90-88.789)\mathrm{min} - (-2.95\,\mathrm{min}) \\ &= 1:58.10\,\mathrm{pm}\end{aligned}$$

6.4 Sun Path Development Using Mathcad

A number of web-based aids discuss all or some aspects of sun path computations. The University of Oregon web site at http://solardat.uoregon.edu/SunChartProgram.html is convenient and generates a pdf file of the sun path at a specified latitude and longitude location. The United States Naval Observatory web site at http://www.usno.navy.mil/USNO provides a wide range of data and computations capabilities. The National Oceanic and Atmospheric Administration (NOAA) web site at www.srrb.noaa.gov/highlights/sunrise/azel.html possesses an online sun position calculator as well as some explanation of the approach. Additionally, www.susdesign.com/sunangle/presents an online sun position calculator, but with no explanation as to the method(s) used.

Software to compute solar positions and sun paths are also available. For example, the Florida Solar Energy Center (Cocoa, FL) provides SUNPATH 3.2 at http://www.fsec.ucf.edu/en/research/buildings/fenestration/software.htm#Software for computing sun path lines. This web site also offers other software elements related to solar energy applications. sunPATH™ is available from http://www.sunpathonline.com/csStore/and is designed for determining lighting issues associated with filming/photography, but sunPATH can also be used to generate conventional sun paths. The out-of-print book by Petherbridge (1996) presents sun paths and overlays for heat gain calculations.

With the ordinal day and the latitude known, Equations 6.23–6.29 are sufficient to construct the sun path line for corresponding day and location (latitude). Figure 6.13, the sun path line for June 21 for MSU, was generated from these equations using the Mathcad software element, as described next.

Figure 6.16 shows the complete Mathcad worksheet needed to compute and plot the sun path for June 21 at MSU (Figure 6.13). Only the date and latitude need be changed to generate and plot the sun path line for another day or location. Since the worksheet represents the kernel needed to construct sun path lines, an examination of the procedure is warranted.

The ordinal day is used to compute the declination from Equation 6.22. The latitude is entered, and the hour angle, hss, is specified to range from solar noon (0°) to solar midnight (180°). Equation 6.23 is used to calculate the solar altitude angle for every hour angle for the specified day and latitude. Equation 6.24 provides the corresponding solar azimuth angles. Logic is provided to determine solar altitude angles greater than 90°. "hlimit" is the hour angle for which the azimuth angle is equal to ±90° and is determined using Equation 6.25. The sun path can then be plotted, or values of the altitude and azimuth angles printed, as a function of hour angle. The initial computational results cover solar noon to solar midnight. However, since only

The generation of the sun path line for a given day as a function of latitude.

$n := 1..365$ The days of the year.

Declination Angle

$$\delta_n := 23.45 \sin\left[360 \cdot \frac{(n + 284)\cdot\pi}{365 \cdot 180}\right]$$

The declination angle is the angle between the sun's rays and the zenith (overhead) direction at solar noon on the equator. The declination is dependent on the Earth's position in its orbit around the sun.

Declination for specific day (use Julian date). For June 21, the Julian date is 172.

$\delta D := \delta_{172}$ $\delta D = 23.45$ 21 June Declination angle in degrees for use in sun path generation.

Input the latitude (in degrees):

$L := 33.455$ Location of Mississippi State University

Establish range variables for days and hours. Degrees to radian conversion:

$hss := 0..180$ $hsp_{hss} := hss$ Hours $dr := \frac{\pi}{180}$

Calculation of sun path angles following Goswami *et* al. (2000)

$$\sin\alpha_{hss} := \sin(L\cdot dr)\cdot\sin(\delta D\cdot dr) + \cos(L\cdot dr)\cdot\cos(\delta D\cdot dr)\cdot\cos(hsp_{hss}\cdot dr)$$ Altitude angle

$$\alpha_{hss} := \operatorname{asin}(\sin\alpha_{hss})$$ $$ang_{hss} := \frac{\alpha_{hss}}{dr}$$ Altitude angle in degrees

$$sinas_{hss} := \cos(\delta D\cdot dr)\cdot\frac{\sin(hsp_{hss}\cdot dr)}{\cos(\alpha_{hss})}$$ Azimuth angle

Test for azimuth angle > 90 degrees.

Since the principal values of the arcsin are defined for -90 degrees < angle < 90 degrees, logic is needed for any azimuth angle greater than 90 degrees.

$$hlimit := \begin{cases} \left(\operatorname{acos}\left(\frac{\tan(\delta D\cdot dr)}{\tan(L\cdot dr)}\right)\right)\cdot\frac{1}{dr} & \text{if } L > \delta D \\ 0 \quad \text{otherwise} \end{cases}$$

$hlimit = 48.968$ Hour angle at 90-degree azimuth for given day.

Definition of arcsin function to include azimuth angles > 90 degrees.

$$as_{hss} := \begin{cases} \left(\pi - \operatorname{asin}(sinas_{hss})\right) & \text{if } hsp_{hss} > hlimit \\ \operatorname{asin}(sinas_{hss}) & \text{otherwise} \end{cases}$$

Change all angles from radians to degrees $\alpha_{hss} := \frac{\alpha_{hss}}{dr}$ $as_{hss} := \frac{as_{hss}}{dr}$

Plot the sun path taking advantage of the symmetry of the morning and afternoon segments.

Figure 6.16 Sun path Mathcad worksheet for single day.

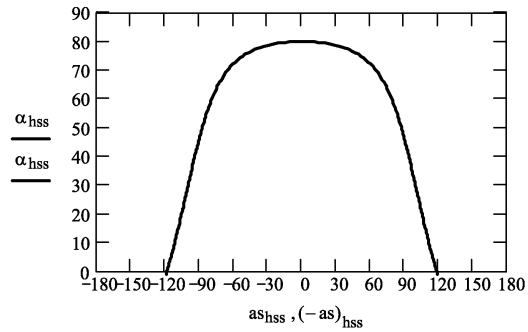

Establish the lines of constant solar time (hour angle) on the sun path. Each solar hour corresponds to 15 degrees of hour angle. Thus, 1 pm solar time is 15 degrees from solar noon.

$solar_1 := \alpha_{15}$ $azi_1 := as_{15}$ $solar_2 := \alpha_{30}$ $azi_2 := as_{30}$

$solar_3 := \alpha_{45}$ $azi_3 := as_{45}$ $solar_4 := \alpha_{60}$ $azi_4 := as_{60}$

$solar_5 := \alpha_{75}$ $azi_5 := as_{75}$ $solar_6 := \alpha_{90}$ $azi_6 := as_{90}$

$solar_7 := \alpha_{105}$ $azi_7 := as_{105}$ $solar_8 := \alpha_{120}$ $azi_8 := as_{120}$

$solar_9 := \alpha_{135}$ $azi_9 := as_{135}$ $solar_{10} := \alpha_{150}$ $azi_{10} := as_{150}$

$solar_{11} := \alpha_{165}$ $azi_{11} := as_{165}$ $solar_{12} := \alpha_{180}$ $azi_{12} := as_{180}$

$solar_0 := \alpha_0$ $azi_0 := as_0$ Solar noon

Add the solar time to the sun path plot taking advantage of the symmetry.

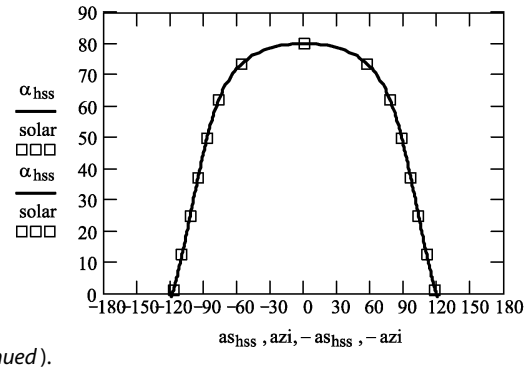

Figure 6.16 (*Continued*).

the sign of the azimuth angles differs for morning, the complete day's sun path can be generated simply by plotting $-a_s$ for the morning hours.

The solar times corresponding to the azimuth and altitude angles are then extracted for every solar hour (hss = 0, 15, 30, . . . , 180) from the azimuth and altitude angles. The solar times are added to the sun path plot to complete the presentation in Figure 6.13.

Although the sun path for one day is useful for that particular day, a complete understanding of the sun's yearly path at a given location is also needed. Figure 6.17 shows the sun path lines

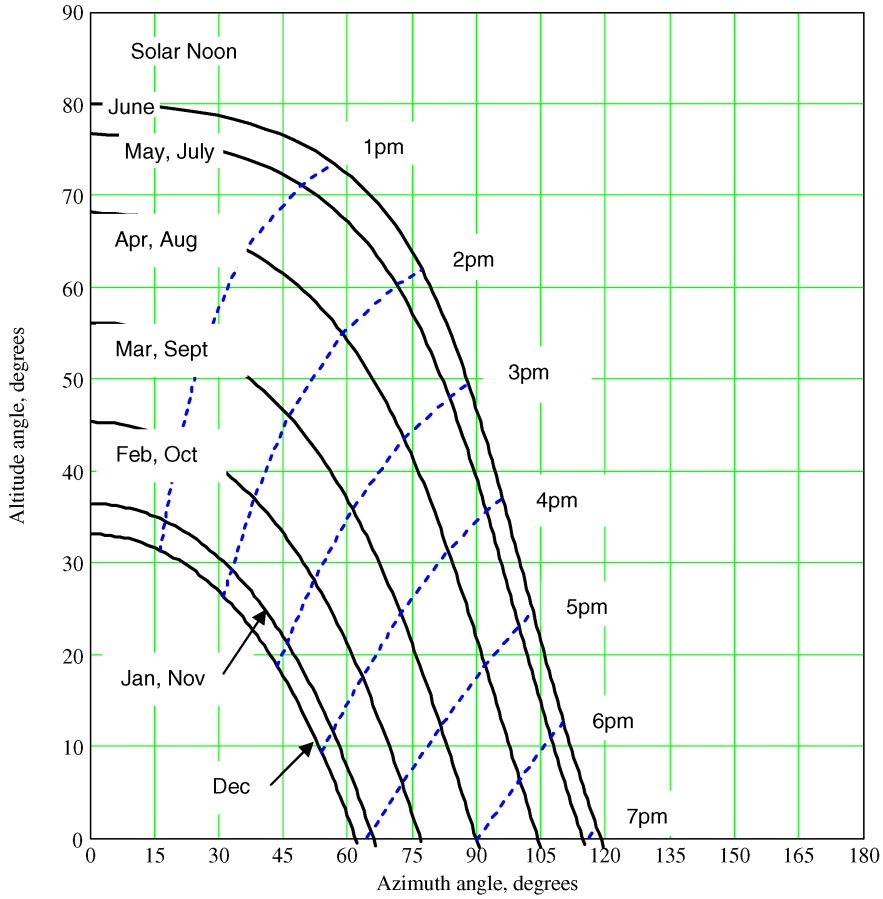

Figure 6.17 Sun path lines for the 21st day of every month for MSU.

and solar times for the seven days spanning the year for MSU. Figure 6.18 illustrates the Mathcad worksheet that is used to generate the sun path for different days of the year. For this example, the 21st of each month was chosen. Because of symmetry, the sun paths for May 21 and July 21, April 21 and August 21, March 21 and September 21, February 21 and October 21, and January 21 and November 21 are the same. Only June 21 and December 21 are lacking symmetry months. On the multiday sun paths, to avoid cluttered presentations, only the afternoon portions are presented, since symmetry provides the mornings. The seven sun path lines representing the 21st day of each month, provide a relatively complete picture of the variations of the sun's path (Ptolemaic view) over the year for a given location. The variations in length of day, in solar azimuth sunset (and sunrise) angles, and in solar altitude angle at noon are evident on inspection of the figure. Additionally, the azimuth angles swept per hour can determined.

An examination of Figure 6.18 is appropriate. The solar declinations are computed for each of the seven days, and the altitude and azimuth angles are generated for each solar hour angle for each day. The same logic as used in Figure 6.16 for the single day is used in Figure 6.18 for each day. Thus, the altitude and azimuth angles are arrays rather than vectors (in the nomenclature of Mathcad).

Obviously, sun path lines could be presented for a wide range of latitudes. In particular, a sun path at a higher latitude is worth examining. Consider Figure 6.19, which is for a latitude above the Arctic Circle. Such latitudes are characterized by the phenomenon "the sun never sets"

during some summer months. The figure, for latitude 80°N, illustrates that the sun does not set from April through August. Even in the summer, the maximum solar altitude angle is only 33.45°, which is relatively low on the horizon. However, if the sun never sets during some summer months, the sun never rises during some winter months. For the latitude of 80°N the sun barely rises (has a positive solar altitude angle) during March and September, and, as the sun path lines indicate, the sun does not rise during October through February. All in all, Figure 6.19 portrays the sun's path at this high latitude as skirting the horizon in the summer and sinking below the horizon during the winter.

Additional information and details on the Mathcad procedure describe herein can be found in Hodge (2003).

The generation of the sun path chart as a function of latitude.

$n := 1..365$ The days of the year.

Declination Angle

$\delta_n := 23.45 \cdot \sin\left[360 \cdot \frac{(n+284)\cdot\pi}{365\cdot 180}\right]$

The declination angle is the angle between the sun's rays and the zenith (overhead) direction at solar noon on the equator. The declination is dependent on the Earth's position in its orbit around the sun.

Declination for specific days

$\delta D_0 := \delta_{355}$ 21 Dec $\delta D_1 := \delta_{21}$ 21 Jan $\delta D_2 := \delta_{52}$ 21 Feb $\delta D_3 := \delta_{80}$ 21 March

$\delta D_4 := \delta_{111}$ 21 April $\delta D_5 := \delta_{141}$ 21 May $\delta D_6 := \delta_{172}$ 21 June

$$\delta D = \begin{pmatrix} -23.45 \\ -20.138 \\ -11.226 \\ -0.404 \\ 11.579 \\ 20.138 \\ 23.45 \end{pmatrix}$$

Declination angle in degrees for use in sun path generation.

Input the latitude (in degrees):

$L := 33.455$ Latitude of Mississippi State University

Establish range variables for days and hours.

$i := 0..6$ Days of interest Hours

$hss := 0..180$ $hsp_{hss} := hss$

Degrees to radian conversion:

$dr := \frac{\pi}{180}$

Calculation of sun path angles following Goswami, *et al*. (2000)

$\sin\alpha_{hss,i} := \sin(L\cdot dr)\cdot\sin(\delta D_i\cdot dr) + \cos(L\cdot dr)\cdot\cos(\delta D_i\cdot dr)\cdot\cos(hsp_{hss}\cdot dr)$ Altitude angle

$\alpha_{hss,i} := \operatorname{asin}(\sin\alpha_{hss,i})$ $ang_{hss} := \frac{\alpha_{hss,6}}{dr}$ Altitude angle in degrees

$\sin as_{hss,i} := \cos(\delta D_i\cdot dr)\cdot\frac{\sin(hsp_{hss}\cdot dr)}{\cos(\alpha_{hss,i})}$ Azimuth angle

Figure 6.18 Mathcad worksheet for the sun path for MSU.

Test for azimuth angle > 90 degrees.

Since the principal values of the arcsin are defined for -90 degrees < angle < 90 degrees, logic is needed for any azimuth angle greater than 90 degrees.

$$hlimit_i := \frac{1}{dr}\,acos\left(\frac{\tan(\delta D_i \cdot dr)}{\tan(L \cdot dr)}\right)$$

$$hlimit^T = (131.032 \quad 123.709 \quad 107.481 \quad 90.611 \quad 71.936 \quad 56.291 \quad 48.968)$$

Hour angles at a 90-degree azimuth for a given latitude.

Definition of arcsin function to include azimuth angles > 90 degrees.

$$as_{hss,i} := \begin{cases} (\pi - asin(sinas_{hss,i})) & \text{if } hsp_{hss} > hlimit \\ asin(sinas_{hss,i}) & \text{otherwise} \end{cases}$$

Change all angles from radians to degrees $\alpha_{hss,i} := \frac{\alpha_{hss,i}}{dr}$ $as_{hss,i} := \frac{as_{hss,i}}{dr}$

Redefine $\alpha_{hss,i}$ and $as_{hss,i}$ as Y_i and X_i, respectively. $X_i := as^{\langle i \rangle}$ $Y_i := \alpha^{\langle i \rangle}$

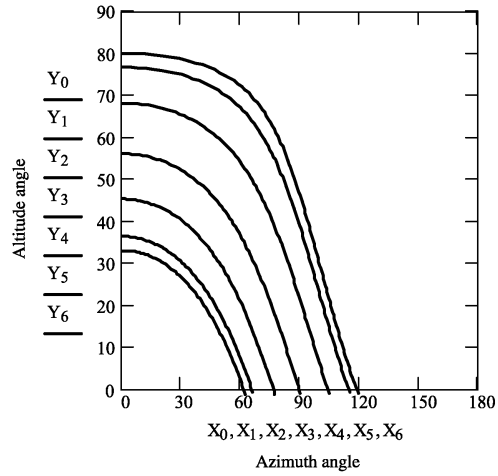

Establish the lines of constant solar time (hour angle) on the sun path. Each solar hour corresponds to 15 degrees of hour angle. Thus, 1 pm solar time is 15 degrees from solar noon.

Figure 6.18 (*Continued*).

$solar1_i := \alpha_{15,i}$ $azi1_i := as_{15,i}$ $solar2_i := \alpha_{30,i}$ $azi2_i := as_{30,i}$

$solar3_i := \alpha_{45,i}$ $azi3_i := as_{45,i}$ $solar4_i := \alpha_{60,i}$ $azi4_i := as_{60,i}$

$solar5_i := \alpha_{75,i}$ $azi5_i := as_{75,i}$ $solar6_i := \alpha_{90,i}$ $azi6_i := as_{90,i}$

$solar7_i := \alpha_{105,i}$ $azi7_i := as_{105,i}$ $solar8_i := \alpha_{120,i}$ $azi8_i := as_{120,i}$

$solar9_i := \alpha_{135,i}$ $azi9_i := as_{135,i}$ $solar10_i := \alpha_{150,i}$ $azi10_i := as_{150,i}$

$solar11_i := \alpha_{165,i}$ $azi11_i := as_{165,i}$ $solar12_i := \alpha_{180,i}$ $azi12_i := as_{180,i}$

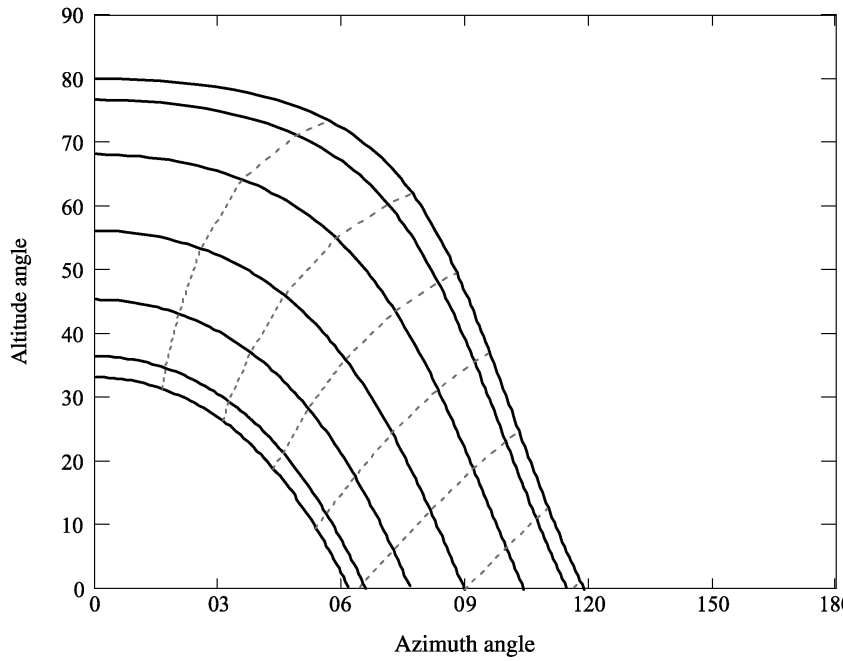

Figure 6.18 (*Continued*).

6.5 The National Solar Energy Database

For any quantitative considerations of solar energy applications, hourly, monthly, and yearly information about the climate, including irradiation (the solar "insolation") is needed. The US Department of Energy National Renewable Energy Laboratory (NREL) at Golden, Colorado, provides an astonishingly wide range of climatic and energy engineering information, much of which is available on their web site (http://www.nrel.gov/rredc/).

The National Solar Radiation Database (NSRDB) contains 30 years (1961–1990) of solar radiation and supplementary meteorological data from 237 National Weather Service sites in the USA, plus sites in Guam and Puerto Rico. Figure 6.20 shows the sites for which 1961–1990 NSRDB data are available.

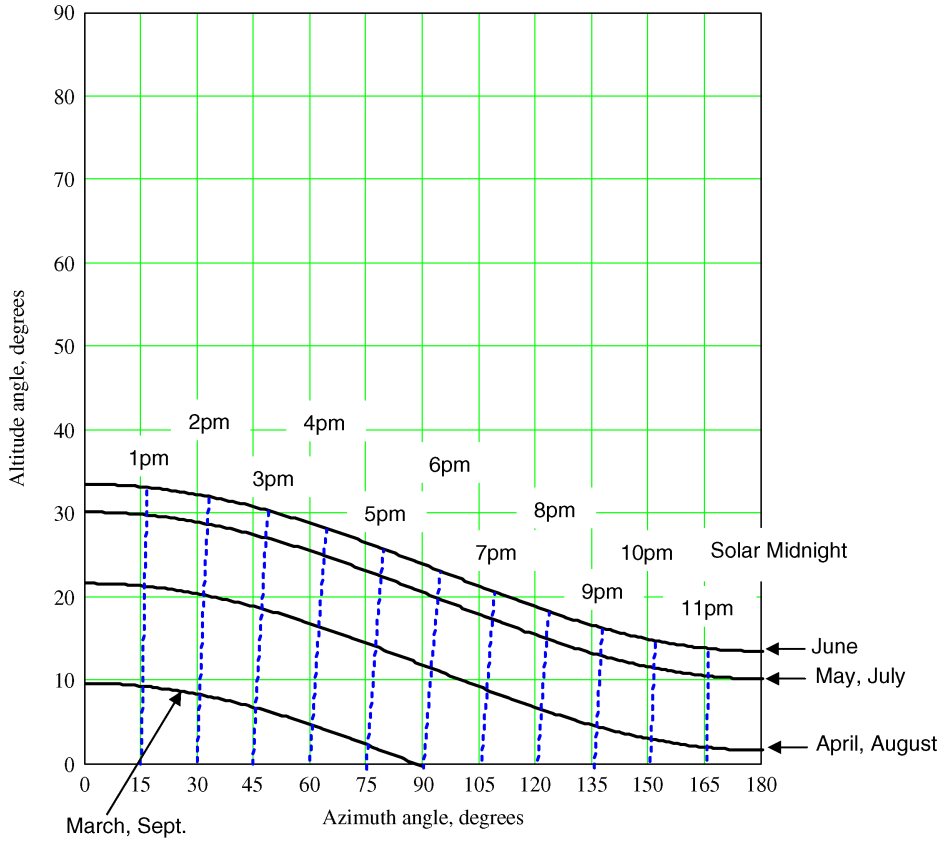

Figure 6.19 Sun path lines for above the Arctic Circle.

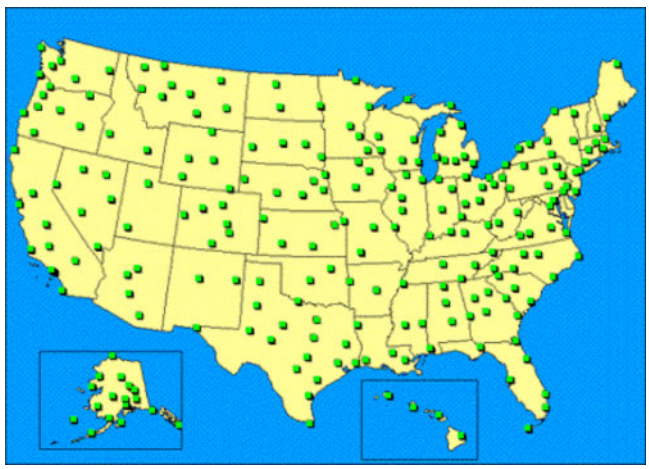

Figure 6.20 National Weather Service sites for which 1961–1990 NSRDB data are available. *Source*: http://rredc.nrel.gov/solar/old_data/nsrdb/1961-1990/gifs/NSRDBmap.gif.

The following data products are included in the 1961–1990 NSRDB on the NREL web site:

1) daily statistics files (monthly averages of daily totals);
2) hourly data files;
3) *Solar Radiation Data Manual for Buildings* – 30-year (1961–1990) average of solar radiation and illuminance for each month;
4) *Solar Radiation Data Manual for Flat-plate and Concentrating Collectors*:
   a) averages of solar radiation for each of the 360 months from 1961–1990
   b) 30-year (1961–1990) average of solar radiation for each month.

Extensive use of the 1961–1990 NSRDB is made in Chapters 7–9.

The NREL web site also contains updates and additions to the 1961–1990 NSRDB. These include:

1) *NSRDB 1991–2010 Update* The updated 1991–2010 NSRDB holds solar and meteorological data for 1454 locations in the USA and its territories. Specific to each of these locations are
   a) hourly solar data
   b) statistical summaries
      daily statistics files
      hourly statistics files
      threshold files

   The web site is http://rredc.nrel.gov/solar/old_data/nsrdb/1991-2010/.

   These data are more extensive than in the original, contain more variables, address in greater detail uncertainties, and more clearly distinguish between measured data and modeled data. A user's manual is available at http://www.nrel.gov/docs/fy12osti/54824.pdf.
2) *NSRDB 2005–2012 Update* The 2005–2010 NSRDB update comprises 30-minute solar and meteorological data for approximately 1.4 million (0.038° latitude by 0.038° longitude) surface pixels (nominally 4 km^2). The area covered is bordered by longitudes −25°E on the eastern side and −175°E on the west; and by latitudes 5°N on the south and 60°N on the northern edge.
3) *Typical Meteorological Year 3* (*TMY3*) Since the initial Typical Meteorological Year (TMY) database release about 1980, the TMY files have become the accepted weather input to virtually all building simulation programs. The original TMY was formed from data collected between 1949 and 1980 in 229 locations in the USA. TMY2 data were based on 239 locations using 1961–1990 data. TMY3, first released in 2005, represents 1020 locations. The updated TMY3 files are available on the NREL TMY3 web site at http://rredc.nrel.gov/solar/old_data/nsrdb/1991-2005/tmy3.

   The TMY3s are data sets of hourly values of solar radiation and meteorological elements for a 1 year period. Their intended use is for computer simulations of solar energy conversion systems and building systems to facilitate performance comparisons of different system types, configurations, and locations in the USA and its territories. Since TMY3s represent typical rather than extreme conditions, they are not suited for designing systems to meet the worst-case scenarios occurring at a location.
4) *US solar radiation resource maps* The NREL web site also provides a useful assessment of the potential for solar energy in the USA. Figure 6.21 shows the average daily direct solar energy incident on a perpendicular surface tracking the sun path for the USA. The desert southwest consistently receives 6.5–8.5 kW h/(m^2 day), while the southeast, because of cloud cover and humidity effects, receives about 4.0 kW h/(m^2 day). Much of the northeast solar energy reception is 3.0 kW h/(m^2 day) or less. Even though the southwest is the most favored region, solar energy systems are viable in other parts of the USA. NREL provides a wide range of maps of various solar and weather details.

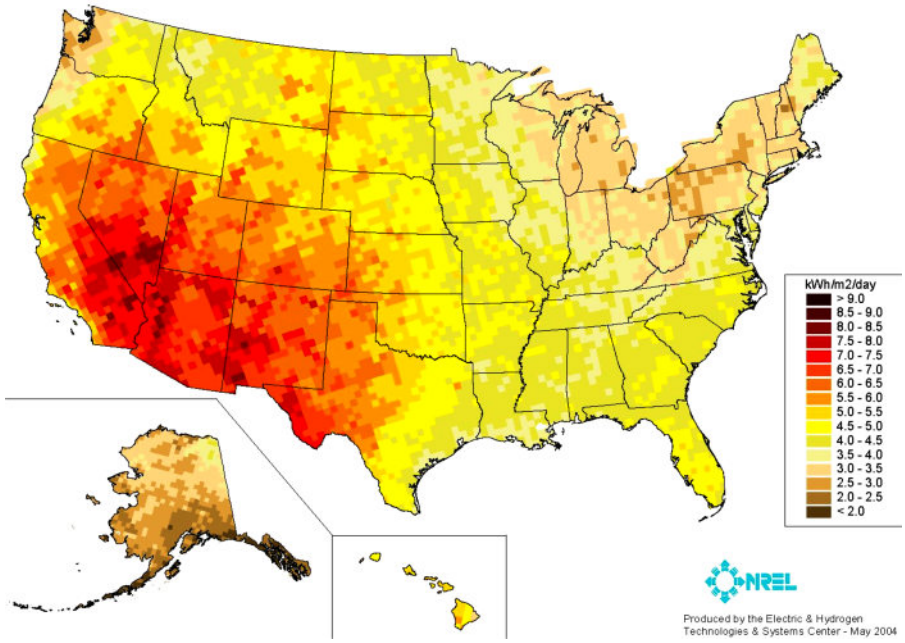

Figure 6.21 Solar potential for the USA. *Source*: NREL.

The quantity of solar and meteorological data available on the NREL web site has expanded significantly in terms of locations available, variables presented, quality assessments, and usages. Indeed, the era of "big data" has arrived.

In addition to NREL, NOAA collects, analyzes, and dissimilates meteorological data. NOAA is part of the Department of Commerce. For a number of years, the National Climatic Data Center (NCDC) was responsible for weather-related data. Recently, NOAA combined all climate-related data acquisition activities into the National Centers for Environmental Information (NCEI). The NCEI includes the Center for Weather and Climate (formerly NCDC) and the Center for Coasts, Oceans, and Geophysics as well as NOAA Central Library.

6.6 Closure

This chapter has provided a review of radiation heat transfer, examined sun path lines, and indicated sources of solar energy engineering data. With these topics as a basis, solar energy engineering principles can now be considered. Chapters 7, 8, and 9 respectively discuss active solar application, passive solar applications, and photovoltaic solar concepts.

References

Bergman, F.P., Lavine, A.S., Incropera, F.P., and DeWitt, D.P. (2011) *Introduction to Heat Transfer*, 7th edn. John Wiley & Sons, Inc., New York.

Goswami, D.Y., Kreith, F., and Kreider, J.F. (2000) *Principles of Solar Engineering*, 2nd edn. Taylor and Francis, Philadelphia, PA.

Hodge, B.K. (2003) Sunpath lines using Mathcad. *ASEE Computers in Education Journal*, **8** (4): 78–92.

Howell, J.R., Siegel, R., and Menguc, M.P. (2010) *Thermal Radiation Heat Transfer*, 5th edn. CRC Press, New York.

Petherbridge, P. (1966) *Sunpath Diagrams and Overlays for Solar Heat Gain Calculations*. Building Research Station, London.

7

Active Solar Thermal Applications

7.1 Introduction

This is the first of three applications chapters dealing with solar energy. Although not precisely defined, solar energy applications are generally classed as active, passive, or photovoltaic – which are the topics of interest for this chapter and Chapters 8 and 9. Active solar energy applications are usually concerned with harvesting thermal energy through the use of solar collectors that employ "active" mechanical components (such a pumps) to collect and transport heat. Passive systems, typically associated with the built environment, collect and transport heat by nonmechanical means. Photovoltaics utilize solar energy to directly produce electricity. As the title indicates, this chapter deals with active solar thermal systems.

Solar collectors provide ubiquitous images that represent solar energy engineering. The two most common configurations are the flat-plate collector and the parabolic trough. Figure 7.1a shows a typical flat-plate collector, and Figure 7.1b illustrates a typical parabolic-trough collector. Flat-plate collectors are widely used in residences and commercial and industrial buildings for hot water and space conditionings (heating). The example in Figure 7.1a is mounted at a fixed angle on the south-facing roof of a residence. The parabolic-trough collector illustrated in Figure 7.1b possesses the ability to track the altitude angle of the sun. The parabolic-trough collector in this example focuses the sun's rays on a single pipe and provides higher hot-water temperatures than a flat-plate collector. Parabolic-trough collectors are more expensive than flat-plate collectors and, because of the tracking mechanisms, require more maintenance. For these reasons, parabolic-trough collectors are more frequently used by institutional, industrial, and commercial facilities than by residences. Additional configurations for solar collectors include Fresnel reflector, tubular, paraboloids, and compound parabolic.

The heliostat with a central receiver, shown in Figure 7.2, is most impressive and produces temperatures much higher than are possible with the conventional flat-plate or parabolic-trough collector. As illustrated in the figure, heliostats have many reflecting mirrors, with each mirror capable of being oriented so as to reflect the sun's rays onto a central receiver. The mirror field surrounding the central receiver is circular, so that energy can be directed to the receiver throughout the day. Very high temperatures are thus obtainable in the receiver.

Thermal solar collectors, except for heliostat-type systems, are based on five configurations:

1) unglazed collector
2) transpired collector
3) flat-plate collector
4) evacuated-tube collector
5) concentrating collector.

Figure 7.3 presents schematics of each type with brief explanations of the energy-harvesting principle.

Alternative Energy Systems and Applications, Second Edition. B. K. Hodge.

Companion website: www.wiley.com\go\Hodge\AESystemsandApplications2E

(a) (b)

Figure 7.1 Examples of flat-plate and parabolic-trough solar collectors: (a) flat-plate (NREL 09188); (b) parabolic trough (NREL 14087).

The unglazed solar collector is the simplest of the thermal solar collectors since it possesses a receiver plate (high solar absorptivity) through which water flows to absorb the heat. As its name implies, the unglazed solar collector does not have a transparent cover (glazing). The transpired solar collector is simple, with a receiver plate to absorb solar energy and a fan that circulates air through a plenum in the back of the receiver. The air is warmed and used for interior heating. The flat-plate solar collector is similar to the unglazed type, except that the flat-plate collector has a glazing (high solar transmissivity and low transmissivity) to retain long wavelength thermal radiation inside the collector. The evacuated-tube solar collector uses an evacuated cylinder (high solar absorptivity) to absorb solar irradiation. Water flows through a copper tube inside the cylinder and absorbs thermal energy. The last of the thermal solar collector types is the concentrating solar collector. In a concentrating collector, trough or parabolic shaped, solar irradiation is incident on the surface (low solar absorptivity and high solar reflectivity) and is reflected to a receiver where it is absorbed. Concentrating solar collectors provide higher temperatures than the other types. An examination of typical uses for each type of thermal solar collector is appropriate.

Figure 7.2 Heliostat (NREL 00036).

(a)

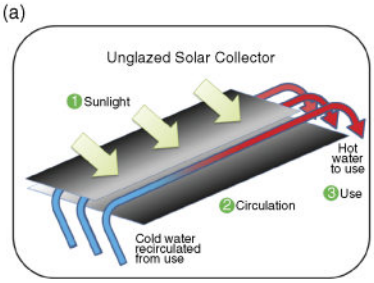

1. Sunlight: Sunlight hits the dark material in the collector, which heats up.
2. Circulation: Cool fluid (water) or air circulates through the collector, absorbing heat.
3. Use: The warmer fluid is used for applications such as pool heating.

(b)

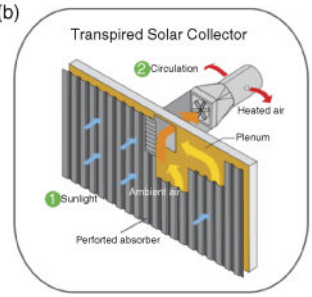

1. Sunlight: Sunlight hits the dark perforated metal cladding, which heats up.
2. Circulation: A circulation fan pulls air through the perforations behind the metal cladding, heating the air, which is then pulled into the building for distribution.

(c)

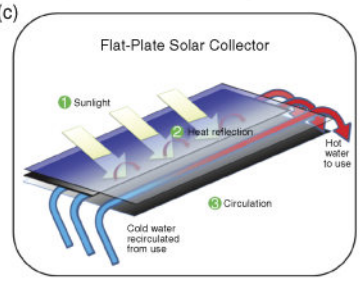

1. Sunlight: Sunlight travels through the glass and hits the dark material inside the collector, which heats up.
2. Heat reflection: A clear glass or plastic casing traps heat that would otherwise radiate out
3. Circulation: Cold water or another fluid circulates through the collector, absorbing heat.

(d)

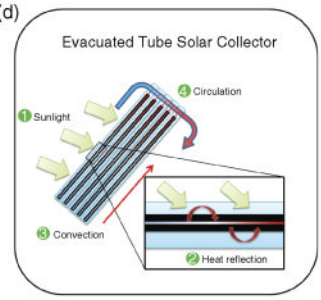

1. **Sunlight:** Sunlight hits a dark cylinder, efficiently heating it from any angle.
2. **Heat reflection:** A clear glass or plastic casing traps heat that would otherwise radiate out.
3. **Convection:** A copper tube running through each cylinder absorbs the cylinder's stored heat, causing fluid inside the tube to heat up and rise to the top of the cylinder
4. **Circulation:** Cold water circulates through the tops of the cylinders, absorbing heat.

(e)

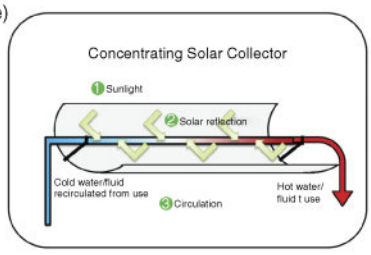

1. Sunlight: Sunlight hits a reflective material, a mirrored surface.
2. Solar reflection: The reflective material redirects the sunlight onto to a single point (for a dish) or a pipe (for a trough).
3. Circulation: Cold water or a special heat transfer fluid circulates through the pipe, absorbing heat.

Figure 7.3 Thermal solar collector types: (a) unglazed solar collector; (b) transpired solar collector; (c) flat-plate solar collector; (d) evacuated-tube solar collector; (e) concentrating solar collector. *Source*: www2.epa.gov/rhc/solar-heating-and-cooling-technologies#Evacuated%20tube%20solar%20collectors.

Figure 7.4 provides a useful delineation of temperature ranges and applications for each of the five types of thermal solar collectors. Unglazed and transpired air devices are used for temperature applications less than 100 °F – typically pool heating and space heating. Flat-plate collectors are suitable for space heating, hot water heating, and pool heating and are limited to temperatures not much in excess of 150 °F. Evacuated tube and concentrating solar collectors can be used for all five applications. Evacuated tube device working temperatures can reach 400 °F. Concentrating solar collectors can reach high temperatures depending on the concentration factor (see Section 7.5). The focus of this chapter will be on flat-plate collectors, since they are arguably the most frequently used solar thermal collector.

Solar thermal collectors can be either tracking or nontracking. Tracking collectors, as their name implies, track the diurnal motion of the sun (discussed in Chapter 6) about single— or dual-axis systems. The azimuth and altitude angles of nontracking collectors are fixed, and a common arrangement is a zero azimuth angle and an altitude angle set equal to the latitude of the collector location. Figure 7.5 illustrates arrangements for nontracking, one-axis tracking, and two-axis tracking flat-plate collectors. Figure 7.6 shows the arrangement for tracking parabolic-trough collectors.

Generally, flat-plate thermal solar collectors are used to heat water for domestic and/or for space heating purposes. A simple flat-plate solar collector system is schematically illustrated in Figure 7.7. The system consists of two flow loops: one from the solar collector to the storage system and one from the storage system to the load. Water circulated through the collector system is heated by the collector and stored in a storage tank. Hot water for the load is drawn from the storage tank and returned at reduced temperature to the storage tank. The auxiliary heater is used when the solar system is providing insufficient hot water for the load. But, the system's primary component is the solar collector. Section 7.2 develops and examines the fundamental principles of operation of a flat-plate solar collector.

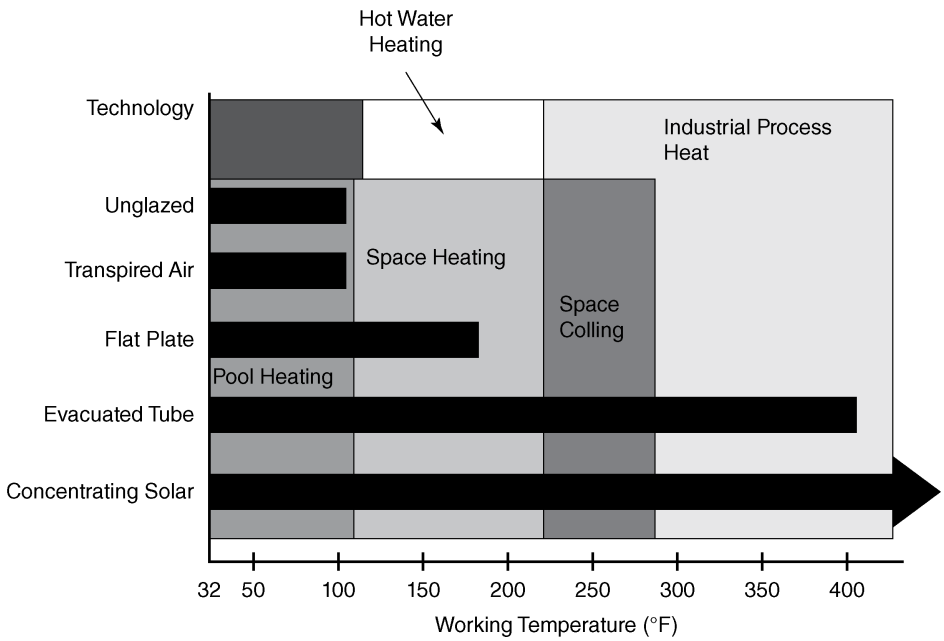

Figure 7.4 Temperature ranges and applications for thermal solar collectors. *Source*: www2.epa.gov/rhc/rhc-technologies-and-applications.

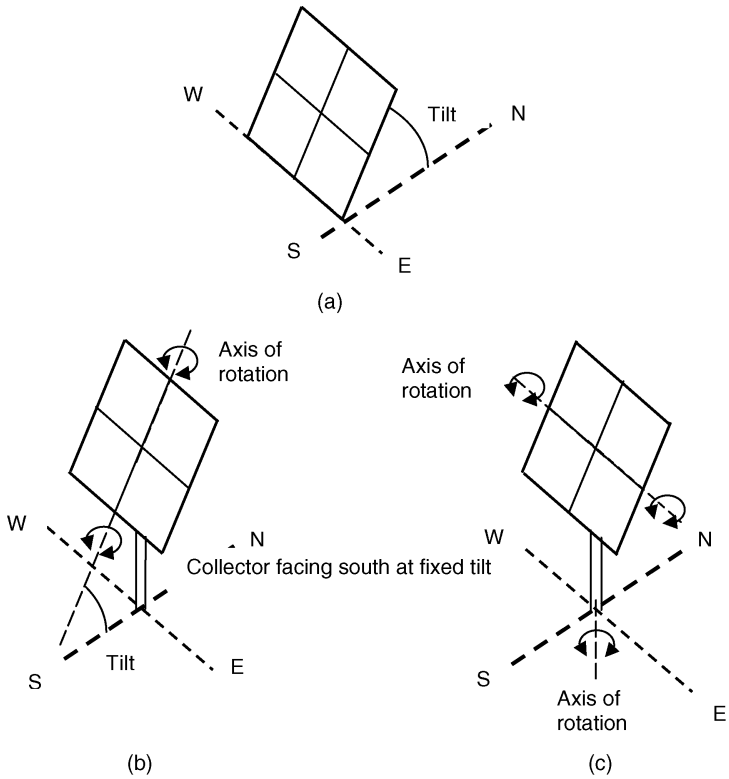

Figure 7.5 Nontracking and tracking flat-plate collector arrangements: (a) fixed tilt; (b) one-axis (N–S), fixed tilt; (c) two-axis tracking.

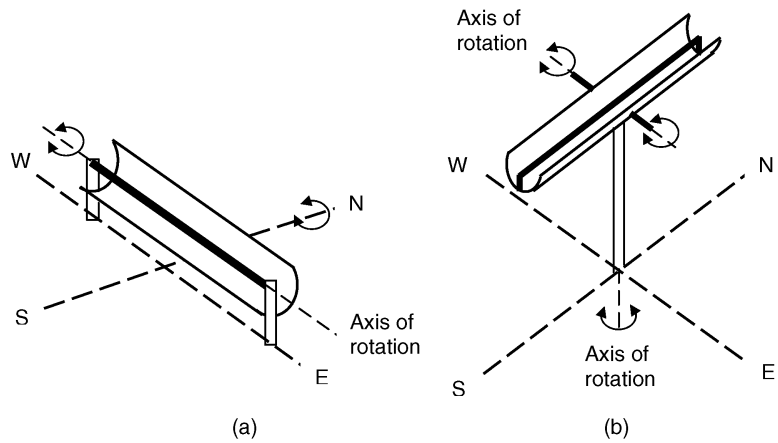

Figure 7.6 Tracking trough collector arrangements: (a) one-axis tracking (E–W) concentrating collector; (b) two-axis tracking concentrating collector.

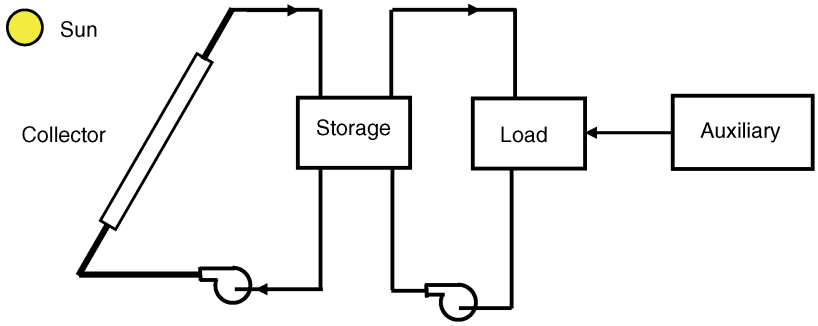

Figure 7.7 Flat-plate solar collector system schematic.

7.2 Flat-Plate Collector Fundamentals

A cut-away view of a flat-plate solar collector is presented in Figure 7.8. The collector components are contained in an enclosure that provides structural support and protection. Glazings are transparent cover sheets (typically made of glass with high solar transmissivities) that provide protection and pass most of the solar irradiation. The absorber plate is made of a material that has a high solar absorptivity and a low emissivity. Water flowing through the tubes is heated by energy from the absorber plate. To minimize heat loss, the collector bottom, which is in contact with the absorber plated, is insulated.

The energy flow for a flat-plate collector is delineated in Figure 7.9. The useful energy q_{useful} available is

$$q_{\text{abs}} - q_{\text{loss}} = q_{\text{useful}} \tag{7.1}$$

where q_{abs} is the solar irradiation absorbed by the collector and q_{loss} are the conduction and radiation losses from the collector to the environment. The irradiation absorbed by the absorber plate (α, absorptivity) must first pass through the glass cover plates (τ, transmissivity) so that

$$q_{\text{abs}} = I_{\text{T}} A_{\text{c}} \alpha\tau \tag{7.2}$$

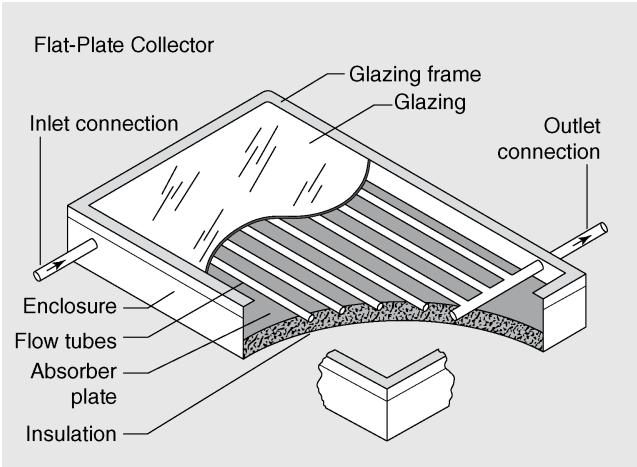

Figure 7.8 Flat-plate collector cutaway (DOE/EERE). *Source*: http://www.nrel.gov/docs/fy04osti/34279.pdf (p. 3).

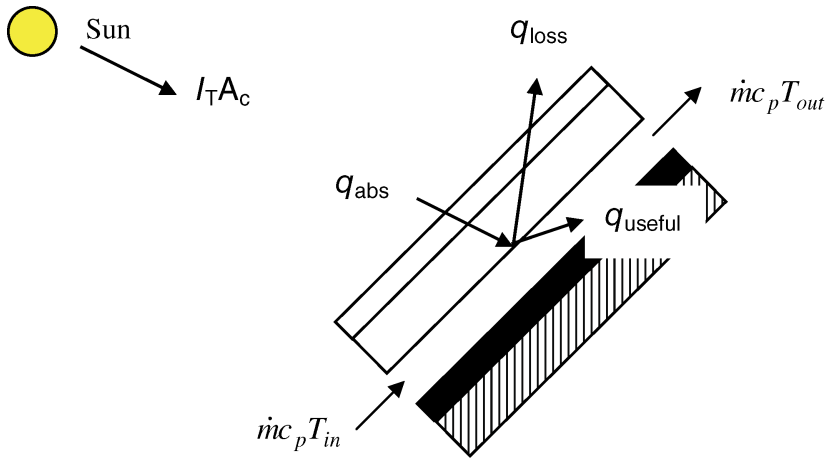

Figure 7.9 Energy flow for a flat-plate collector.

where A_c is the collector surface area and I_T is the irradiation intensity. The losses due to conduction and radiation, expressed in terms of an overall conductance U_L, and temperature difference $T_{ave} - T_a$ can be expressed as

$$q_{losses} = A_c U_L (T_{ave} - T_a) \tag{7.3}$$

where T_{ave} is the average temperature of the collector and T_a is the ambient temperature.

The useful energy then becomes

$$q_{useful} = A_c [I_T \tau\alpha - U_L (T_{ave} - T_a)] = \dot{m} c_p (T_{out} - T_{in}) \tag{7.4}$$

which must also be equal to the change in the working fluid energy. This expression provides some interesting insight on the limiting performance of flat-plate collectors. Consider the case to minimize losses, $T_{ave} = T_a$. But if $T_{ave} = T_a$, the collector and the circulating fluid are at the ambient temperature, and the temperature of the working fluid is so low that the energy is not useful. As the collector temperature increases, the losses increase. The meaningful upper limiting case is for T_{ave} to be so high that $q_{loss} = q_{abs}$, in which case $q_{useful} = 0$. Energy at a high temperature is available, but only at a very low flow rate of the working fluid.

The collector efficiency is defined as the useful energy extracted divided by the total incident irradiation, or

$$\eta_c = \frac{q_{useful}}{I_T A_c} \tag{7.5}$$

which, when q_{useful} is substituted in and the expression simplified, becomes

$$\eta_c = \tau\alpha - U_L \frac{T_{ave} - T_a}{I_T} \tag{7.6}$$

The collector efficiency η_c is thus a linear function of the temperature difference divided by the irradiation I_T, with a slope of $-U_L$. Table 7.1 contains typical values of $\tau\alpha$ and U_L for flat-plate solar collectors (Mitchell, 1983).

The behavior of typical collectors using the values from Table 7.1 is illustrated in Figure 7.10. This simple analysis conveys most of the important aspects of flat-plate solar collector performance and is the basis of the procedure used by solar collector manufacturers to describe the performance of their products.

Table 7.1 Typical flat-plate solar collector properties.

	Black		Selective	
	$\tau\alpha$	U_L	$\tau\alpha$	U_L
No. of covers		(Btu/(h ft^2 °F))		(Btu/(h ft^2 °F))
0	0.95	6.0	0.90	5.0
1	0.90	1.0	0.85	0.5
2	0.85	0.6	0.80	0.3

Even though the $\tau\alpha$ product decreases as the cover configuration changes from unglazed to one cover to two covers, the decreases in the U_L values are even more pronounced, with the net result that, for a given temperature difference, the efficiencies increase as the glazing progresses from unglazed to two covers.

The simple analysis expressed the collector efficiency in terms of the average collector temperature T_{avg}. A more useful expression involves T_{in}, the inlet fluid temperature, which can be cast as

$$\eta = F_R\left(\tau\alpha - U_L\frac{T_{in} - T_a}{I_T}\right) = F_R\tau\alpha - F_R U_L\frac{T_{in} - T_a}{I_T} \tag{7.7}$$

where F_R is the collector heat-removal factor. Equation 7.7 is sometimes called the Hottel–Whillier–Bliss equation and is considered the most important equation associated with flat-plate solar collectors. This approach incorporates the heat exchange process between the absorber plate and the collector heat exchanger. Collector data are usually represented in terms of the intercept $F_R\tau\,\alpha$ and the slope $F_R U_L$. Goswami *et al.* (2000) and Duffie and Beckman (2006) provide excellent discussions of the details of the heat-removal factor.

For more accurate analyses of flat-plate solar collectors, an incident angle modifier $K_{\tau\alpha}$ is often added to Equation 7.7:

$$\eta = F_R\left(K_{\tau\alpha}(\tau\alpha)_n - U_L\frac{T_{in} - T_a}{I_T}\right) = F_R K_{\tau\alpha}(\tau\alpha)_n - F_R U_L\frac{T_{in} - T_a}{I_T} \tag{7.8}$$

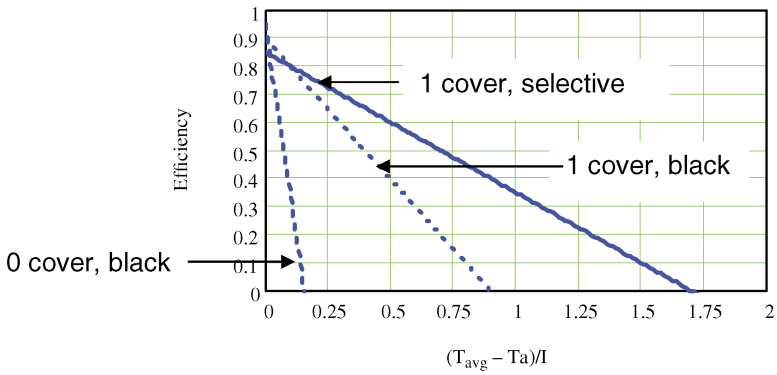

Figure 7.10 Performance characteristics of typical flat-plate solar collectors.

In the Hottel–Whillier–Bliss equation, the product $\tau\alpha$ will change with the angle of incidence of the solar irradiation. But many flat-plate collectors are fixed and the angle of incidence will change throughout the day. The incidence angle modifier accounts for that variation by expressing the value of $\tau\alpha$ as

$$\tau\alpha = K_{\tau\alpha}(\tau\alpha)_{\mathrm{n}} \tag{7.9}$$

where $(\tau\alpha)_{\mathrm{n}}$ is for irradiation normal to the collector. $K_{\tau\alpha}$ is usually cast in the form

$$K_{\tau\alpha} = 1 - b\left[\frac{1}{\cos(i)} - 1\right] \tag{7.10}$$

where i is the incidence angle and $b \approx 0.1$ for single glazing and $b \approx 0.17$ for double glazing. Consider the following example.

Example 7.1

Figure 7.11 provides the results of a performance test for a single-glazed flat-plate collector. The transmissivity τ of the glass is 0.90, and the absorptivity α of the surface is 0.92. For the collector, find:

a) the collector heat-removal factor F_{R};
b) the overall conductance U_{L} in Btu/(h ft^2 °F);
c) the rate at which the collector can deliver useful energy when the irradiation incident on the collector per unit area is 200 Btu/(ft^2 h), the ambient temperature is 30 °F, and the inlet water temperature is 60 °F;
d) the collector temperature when the flow rate is zero ($\eta = 0$).

Solution From Figure 7.11, the intercept (extrapolated) is approximately 0.8. Then

$$0.8 = F_{\mathrm{R}}\tau\alpha = F_{\mathrm{R}}(0.9)(0.92)\ F_{\mathrm{R}} = 0.97$$

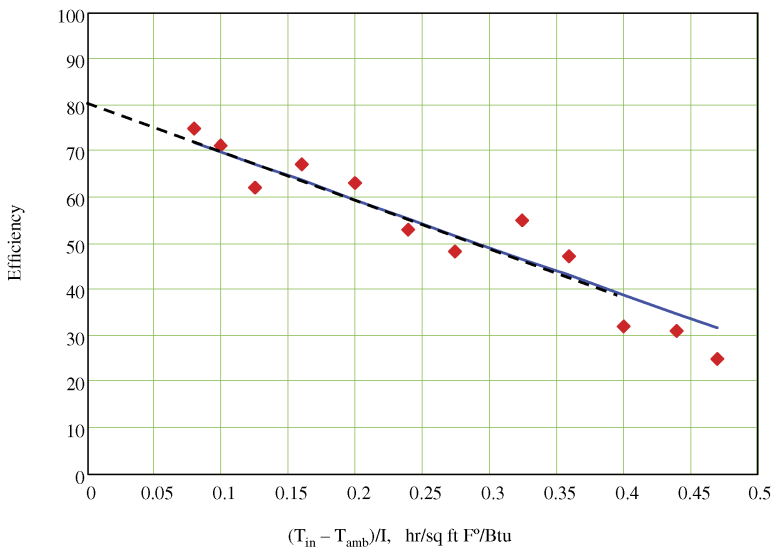

Figure 7.11 Flat-plate solar collector performance data.

From the collector efficiency expression, the slope is $-F_R U_L = \Delta\eta/\Delta X$:

$$-0.97U_L = \frac{(0.5-0.8)\text{Btu}/(\text{h ft}^2\ ^\circ\text{F})}{0.3-0.0} = -1\ \text{Btu}/(\text{h ft}^2\ ^\circ\text{F})$$

From which the overall conductance U_L is found as

$$U_L = 1.03\ \text{Btu}/(\text{h ft}^2\ ^\circ\text{F})$$

The collector efficiency expression is $\eta = 0.8 - 1.0[(T_{in} - T_a)/I_T]$. The efficiency becomes

$$\eta = 0.8 - 1.0\frac{\text{Btu}}{\text{ft}^2\ \text{h}\ ^\circ\text{F}}\frac{(60-30)\ ^\circ\text{F}}{200\ \text{Btu}/(\text{ft}^2\ \text{h})} = 0.65$$

The definition of collector efficiency is $\eta = q_{useful}/(I_T A_c)$, from which

$$\frac{q_{useful}}{A_c} = 0.65 \times 200\frac{\text{Btu}}{\text{ft}^2\ \text{h}} = 130\frac{\text{Btu}}{\text{ft}^2\ \text{h}}$$

When the flow rate is zero, the "stagnation" condition that results in the maximum collector temperature is attained. When the flow rate is zero, no useful energy is removed from the collector by the flowing fluid, and the steady-state temperature of the collector increases until all the incident solar energy is dissipated by convection and radiation. For this condition, $\eta = 0$ and

$$0 = F_R\left(\tau\alpha - U_L\frac{T_{max} - T_a}{I_T}\right) \quad \text{or} \quad \tau\alpha = U_L\frac{T_{max} - T_a}{I_T}$$

$$(0.9)(0.92) = 1.03\frac{\text{Btu}}{\text{ft}^2\ \text{h}\ ^\circ\text{F}}\frac{T_{max} - 30\ ^\circ\text{F}}{200\ \text{Btu}/\text{ft}^2\ \text{h}}$$

$$T_{max} = 191\ ^\circ\text{F}$$

The stagnation temperature T_{max} is 191 °F. Thus, if the flow were stopped, the collector would eventually be heated to 191 °F.

Example 7.1 provides insight into the information needed for flat-plate collector engineering calculations. Slope and intercept data are needed for any flat-plate collector that is to be considered, and solar insolation data, appropriate for specific collector azimuth and altitude angles orientation, are required to assess the performance of a collector. Sources for and examples of flat-plate solar collector data and solar data are considered in Section 7.3.

7.3 Solar Collector and Weather Data

Third-party certification data on specific thermal solar collectors and solar hot water heating systems are available from the Solar Rating and Certification Corporation (SRCC). The SRCC web site, which is well organized and user friendly, is www.solar-rating.org. The SRCC web site provides, in PDF format, online solar collector ratings. When "CERTIFICATION & LISTING DIRECTORY" is selected on the home page, the following list appears:

OG-100 Collector Certifications

- Solar Thermal Collectors (Flat Plate, Tubular, ICS, Thermosiphon, Concentrating)
- Transpired Collectors
- PV Water Heating Collectors

OG-300 System Certifications
Codes and Standards Listings
Directory of Participating Companies

When one of the three solar collector categories is selected, the ratings directory for that type is accessed via http://www.solar-rating.org/certification_listing_directory/index.html. The directory contains all the ratings for a particular type, but the opening page permits selection of specified collectors according to viewer-specified criteria, including specific manufacturers. The "OG-300 System Certifications " leads to an SRCC-developed solar water heating system rating and certification.

The SRCC also maintains an up-to-date list of names (and contact information) of companies that participate in the SRCC certification programs, as well as convenient summary sheets (company name, model number, collector area, absorber coating, slope, intercept, and average daily energy collected for standard conditions) for certified solar collectors. Some examples of SRCC data presentations are in order.

Figure 7.12 reproduces a data sheet from the "glazed solar collector" selection. These data were obtained in accordance with SRCC™ Standard 100-2014-07 Minimum Standard for Solar Thermal Collectors, which references ISO Standard 9806:2013 Solar energy – Solar thermal collectors – Test methods. Administrative information is presented at the top of the data sheet. The "Collector Thermal Performance Rating" section consists of performance metrics in SI and inch–pound (IP) units for three irradiance conditions (clear, mildly cloudy, and cloudy) and five (A–E) temperature categories. The five categories represent different uses that have one-to-one correspondences with the inlet fluid and ambient air temperature differences. Table 7.2 contains information defining categories A–E. "Collector Specifications," "Collector Materials," and "Technical Information" information is delineated under these headings near the middle of the page. Slope and intercept as well as quadratic efficiency equations are listed in both SI and IP units, and incident-angle modifier expressions are given. The lower part of the page is devoted to "Pressure Drop." Thus, sufficient information is provided in the certification-rating sheet to make engineering calculations.

As with most energy systems components, information on flat-plate solar collectors is also available from manufacturers. For example, the Alternate Energy Technologies web site is accessible for information on the AE-21 collector. In addition to referencing the SRCC data sheet, Figure 7.13 is the Alternate Energy Technologies marketing sheet for the AE-21 solar collector. Presentations, such as the one reproduced as Figure 7.13, are typical for solar collector manufacturers.

Table 7.2 Flat-plate collector end-use descriptions.

Category	Temperature difference		Application
A	−5 °C	−9 °F	Swimming pool heating
B	5 °C	9 °F	Liquid collectors (heat pump)
			Space heating, air systems
C	20 °C	36 °F	Service hot water,
			Space heating, air systems
D	50 °C	90 °F	Service hot water
			Space heating, liquid systems
			Air conditioning
E	80 °C	144 °F	Space heating, liquid systems
			Air conditioning, process heating

CERTIFIED SOLAR COLLECTOR

SUPPLIER:
Alternate Energy Technologies
1345 Energy Cove Court
Green Cove Springs, FL 32043 USA
www.aetsolar.com

In Accordance with:
-Please Select-

BRAND:	Alternate Energy
MODEL:	AE-21
COLLECTOR TYPE:	Glazed Flat Plate
CERTIFICATION #:	10001940
Original Certification:	December 12, 2014
Expiration Date:	December 03, 2024

The solar collector listed below has been evaluated by the Solar Rating & Certification Corporation™ (SRCC™), an ISO/IEC 17065 accredited and EPA recognized Certification Body, in accordance with SRCC OG-100, Operating Guidelines and Minimum Standards for Certifying Solar Collectors, and has been certified by the SRCC. This award of certification is subject to all terms and conditions of the Program Agreement and the documents incorporated therein by reference. This document must be reproduced in its entirety.

COLLECTOR THERMAL PERFORMANCE RATING

Kilowatt-hours (thermal) Per Panel Per Day				Thousands of Btu Per Panel Per Day			
Climate -> Category (Ti-Ta)	High Radiation (6.3 kWh/m².day)	Medium Radiation (4.7 kWh/m².day)	Low Radiation (3.1 kWh/m².day)	Climate -> Category (Ti-Ta)	High Radiation (2000 Btu/ft².day)	Medium Radiation (1500 Btu/ft².day)	Low Radiation (1000 Btu/ft².day)
A (-5 °C)	8.8	6.7	4.6	A (-9 °F)	30.1	22.9	15.6
B (5 °C)	7.7	5.6	3.5	B (9 °F)	26.4	19.1	11.9
C (20 °C)	6.1	4.0	2.0	C (36 °F)	20.8	13.7	6.7
D (50 °C)	3.1	1.3	0.0	D (90 °F)	10.5	4.3	0.0
E (80 °C)	0.5	0.0	0.0	E (144 °F)	1.8	0.0	0.0

A- Pool Heating (Warm Climate) B- Pool Heating (Cool Climate) C- Water Heating (Warm Climate)
D- Space & Water Heating (Cool Climate) E- Commercial Hot Water & Cooling

COLLECTOR SPECIFICATIONS					
Gross Area:	1.932 m²	20.80 ft²	Dry Weight:	34 kg	74 lb
Net Aperture Area:	1.783 m²	19.19 ft²	Fluid Capacity:	2.7 liter	0.7 gal
Absorber Area:	1.747 m²	18.80 ft²	Test Pressure:	1103 kPa	160 psi

TECHNICAL INFORMATION							Tested in accordance with: ISO 9806:1994			
ISO Efficiency Equation [NOTE: Based on gross area and (P)=Ti-Ta]										
SI UNITS:	η= 0.740 - 5.18920(P/G) - 0.01910(P²/G)						Y Intercept:	0.749	Slope:	-6.159 W/m².°C
IP UNITS:	η= 0.740 - 0.91456(P/G) - 0.00187(P²/G)						Y Intercept:	0.749	Slope:	-1.086 Btu/hr.ft².°F

Incident Angle Modifier								Test Fluid:	Water	
θ	10	20	30	40	50	60	70	Test Mass Flow Rate:	0.0194 kg/(s m²)	14.29 lb/(hr ft²)
Kτα	1.00	1.00	0.99	0.97	0.93	0.79		Impact Safety Rating: 11		

From page 3 of the AE21 SRCC Certification

PRESSURE DROP				
Flow	ΔP		Flow	ΔP
ml/s	Pa		gpm	in H_2O
20	0		0.32	0.0
50	0		0.79	0.0
80	0		1.27	0.0

Figure 7.12 SRCC sample certification information. *Source*: SRCC.

Solar energy engineering weather and solar irradiance database information was reviewed in Section 6.5. In addition to data available from by NREL, various textbook authors have provided solar data needed for performance estimates of solar energy systems. For example, Goswami *et al.* (2000) presented hourly solar irradiance information useful for hour-by-hour solar collector calculations such as in Example 7.1. Their tabulations are for the 21st day of each month and are provided for 24°N, 32°N, 40°N, 48°N, 56°N, and 64°N latitude. Total solar insolation (Btu/h ft^2) is provided for south-facing surfaces inclined at the latitude angle, at the latitude angle −10°, +10°, and +20°, for vertical (90°) surfaces, and for surfaces normal to the sun. The Goswami *et al.* (2000) solar insolation tables are included as Appendix A.

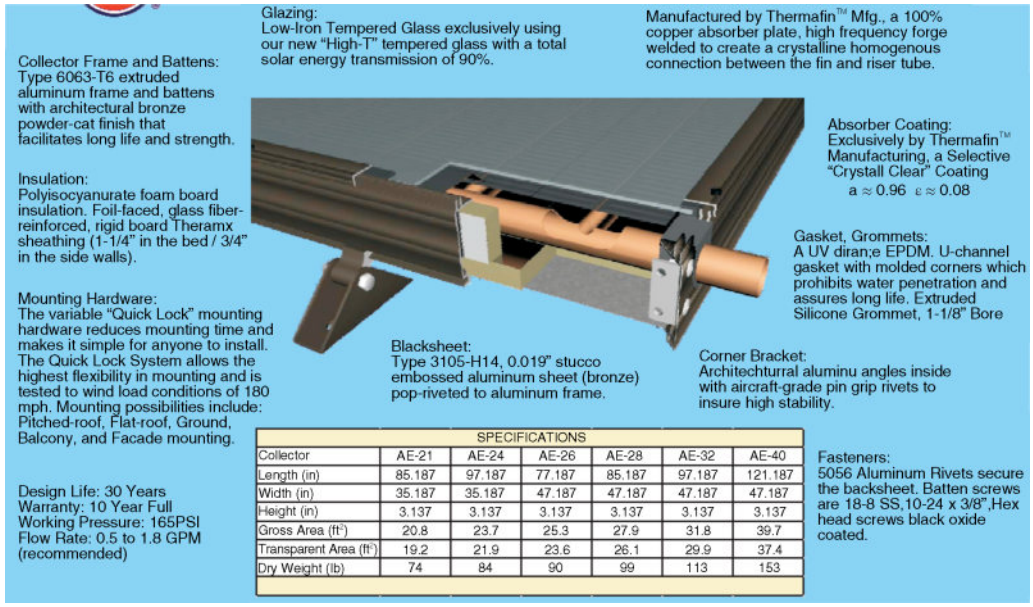

SPECIFICATIONS

Collector	AE-21	AE-24	AE-26	AE-28	AE-32	AE-40
Length (in)	85.187	97.187	77.187	85.187	97.187	121.187
Width (in)	35.187	35.187	47.187	47.187	47.187	47.187
Height (in)	3.137	3.137	3.137	3.137	3.137	3.137
Gross Area (ft^2)	20.8	23.7	25.3	27.9	31.8	39.7
Transparent Area (ft^2)	19.2	21.9	23.6	26.1	29.9	37.4
Dry Weight (lb)	74	84	90	99	113	153

Figure 7.13 Alternate Energy Technologies AE-21 information. *Source*: Alternate Energy Technologies.

For many solar engineering calculations, monthly insolation (irradiance) values for various orientations and tracking protocols are needed. The NREL website (www.nrel.gov) provides solar and meteorological information in a number of different data sets (discussed in Section 6.5). The original National Solar Radiation Database (NSRDB) is the most appropriate of the data sets for use in this textbook. The original NSRDB contains monthly solar and meteorological information based on 30-year averages (1961–1990) for the 239 locations shown in Figure 6.20. The original NSRDB contains the following:

Daily statistics files
Hourly data files
The *Solar Radiation Data Manual for Buildings* (Marion and Wilcox, 1995)

- 30-year averages (1961–1990) of solar radiation and illuminance for each month
- The *Solar Radiation Data Manual for Flat-Plate and Concentrating Collectors* (Marion and Wilcox, 1994)
- averages of the monthly solar radiation and meteorological data for each of the 360 months during the period 1961–1990.

In addition the web site contains other broadband solar radiation data and resource maps in atlas form for buildings and flat-plate and concentrating solar collectors. A number of solar computer codes, algorithms, models, and calculators are also provided and described on the web site. The information contained on the web site, as well as references by SRCC and NREL at the end of this chapter, are logical next resorts for engineering details and procedures beyond the scope of this chapter.

Solar Radiation Data Manual for Flat-Plate and Concentrating Collectors (Marion and Wilcox, 1994) provides the necessary data for the next level of solar system analyses and performance estimates. The data for Meridian, MS, from the manual are reproduced as Figure 7.14. An examination of the contents of this typical file is appropriate. The first series of entries contain location information and specify the site as primary or secondary – secondary

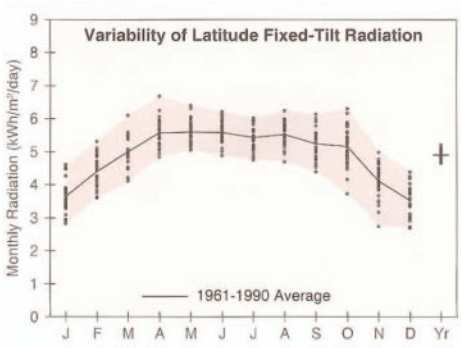

Meridian, MS

WBAN NO. 13865

LATITUDE: 32.33° N
LONGITUDE: 88.75° W
ELEVATION: 94 meters
MEAN PRESSURE: 1007 millibars

STATION TYPE: Secondary

Solar Radiation for Flat-Plate Collectors Facing South at a Fixed Tilt (kWh/m²/day), Uncertainty ±9%

Tilt (°)		Jan	Feb	Mar	Apr	May	June	July	Aug	Sept	Oct	Nov	Dec	Year
0	Average	2.6	3.4	4.4	5.4	5.9	6.2	5.9	5.6	4.8	4.1	2.9	2.4	4.5
	Min/Max	2.2/3.0	3.0/3.9	3.7/5.1	4.8/6.4	5.4/6.8	5.3/6.9	5.2/6.5	4.8/6.3	4.1/5.5	3.2/4.8	2.3/3.4	2.0/2.8	4.2/4.7
Latitude -15	Average	3.2	4.1	4.8	5.7	5.9	6.0	5.8	5.7	5.2	4.8	3.7	3.1	4.8
	Min/Max	2.6/4.0	3.4/4.8	4.1/5.8	4.9/6.8	5.4/6.8	5.2/6.7	5.1/6.4	4.9/6.4	4.4/6.0	3.6/5.8	2.6/4.4	2.5/3.8	4.6/5.1
Latitude	Average	3.6	4.4	5.0	5.6	5.6	5.6	5.4	5.5	5.2	5.2	4.1	3.5	4.9
	Min/Max	2.8/4.6	3.6/5.3	4.1/6.1	4.8/6.7	5.1/6.4	4.9/6.2	4.8/6.0	4.7/6.2	4.4/6.1	3.7/6.3	2.7/5.0	2.7/4.4	4.7/5.2
Latitude +15	Average	3.8	4.5	4.9	5.2	5.0	4.9	4.8	5.0	5.0	5.2	4.3	3.8	4.7
	Min/Max	2.9/5.0	3.6/5.5	4.0/6.0	4.5/6.2	4.5/5.7	4.3/5.4	4.2/5.3	4.3/5.7	4.2/5.9	3.7/6.4	2.8/5.3	2.8/4.8	4.5/5.0
90	Average	3.3	3.5	3.3	2.8	2.2	2.0	2.1	2.6	3.1	3.9	3.6	3.3	3.0
	Min/Max	2.4/4.4	2.8/4.4	2.7/4.0	2.5/3.3	2.1/2.4	1.9/2.1	2.0/2.2	2.3/2.8	2.6/3.7	2.6/4.8	2.2/4.5	2.3/4.3	2.8/3.2

Solar Radiation for 1-Axis Tracking Flat-Plate Collectors with a North-South Axis (kWh/m²/day), Uncertainty ±9%

Axis Tilt (°)		Jan	Feb	Mar	Apr	May	June	July	Aug	Sept	Oct	Nov	Dec	Year
0	Average	3.5	4.6	5.7	7.0	7.5	7.7	7.2	7.0	6.1	5.5	4.0	3.2	5.7
	Min/Max	2.7/4.4	3.6/5.6	4.6/7.1	5.8/8.9	6.5/8.9	6.3/9.0	6.2/8.4	5.6/8.1	4.9/7.3	3.8/6.9	2.6/4.8	2.5/4.0	5.4/6.2
Latitude -15	Average	4.0	5.1	6.1	7.2	7.5	7.6	7.2	7.1	6.5	6.1	4.5	3.8	6.0
	Min/Max	3.0/5.1	4.0/6.3	4.8/7.7	5.9/9.1	6.5/8.9	6.2/8.9	6.1/8.4	5.7/8.2	5.1/7.8	4.1/7.6	2.8/5.6	2.8/4.7	5.6/6.5
Latitude	Average	4.3	5.3	6.2	7.1	7.2	7.3	6.9	7.0	6.5	6.4	4.9	4.1	6.1
	Min/Max	3.1/5.6	4.1/6.7	4.9/7.8	5.9/9.1	6.3/8.6	5.9/8.5	5.9/8.1	5.6/8.1	5.1/7.8	4.3/8.0	3.0/6.1	3.0/5.2	5.7/6.6
Latitude +15	Average	4.4	5.4	6.1	6.8	6.8	6.8	6.5	6.6	6.3	6.4	5.0	4.3	6.0
	Min/Max	3.2/5.9	4.2/6.8	4.8/7.8	5.6/8.7	5.9/8.1	5.5/7.9	5.5/7.6	5.3/7.7	4.9/7.7	4.2/8.1	3.0/6.3	3.0/5.5	5.6/6.5

Solar Radiation for 2-Axis Tracking Flat-Plate Collectors (kWh/m²/day), Uncertainty ±9%

Tracker		Jan	Feb	Mar	Apr	May	June	July	Aug	Sept	Oct	Nov	Dec	Year
2-Axis	Average	4.5	5.4	6.2	7.2	7.6	7.8	7.3	7.1	6.5	6.4	5.1	4.4	6.3
	Min/Max	3.2/6.0	4.2/6.9	4.9/7.9	6.0/9.2	6.6/9.0	6.3/9.1	6.2/8.5	5.7/8.3	5.1/7.9	4.3/8.1	3.0/6.3	3.1/5.6	5.9/6.8

Direct Beam Solar Radiation for Concentrating Collectors (kWh/m²/day), Uncertainty ±8%

Tracker		Jan	Feb	Mar	Apr	May	June	July	Aug	Sept	Oct	Nov	Dec	Year
1-Axis, E-W Horiz Axis	Average	2.5	2.8	2.9	3.3	3.3	3.4	3.1	3.0	2.9	3.4	2.8	2.5	3.0
	Min/Max	1.3/3.7	1.8/4.1	1.9/4.3	2.4/4.9	2.5/4.5	2.3/4.4	2.1/4.0	1.9/3.9	1.9/3.9	1.7/4.7	1.2/3.9	1.4/3.5	2.7/3.4
1-Axis, N-S Horiz Axis	Average	2.1	2.9	3.5	4.4	4.4	4.4	4.0	3.9	3.6	3.6	2.5	2.0	3.4
	Min/Max	1.1/3.2	1.7/4.1	2.3/5.1	3.1/6.5	3.3/6.0	2.9/5.8	2.8/5.3	2.5/5.1	2.3/4.8	1.8/5.1	1.0/3.4	1.0/2.8	3.0/4.0
1-Axis, N-S Tilt=Latitude	Average	2.8	3.5	3.9	4.5	4.2	4.1	3.8	3.9	3.9	4.3	3.2	2.7	3.7
	Min/Max	1.5/4.2	2.2/5.1	2.6/5.7	3.2/6.7	3.1/5.8	2.7/5.4	2.6/5.0	2.5/5.1	2.5/5.2	2.1/6.0	1.3/4.5	1.4/3.8	3.3/4.3
2-Axis	Average	2.9	3.6	3.9	4.5	4.5	4.4	4.0	4.0	3.9	4.3	3.4	2.9	3.9
	Min/Max	1.6/4.5	2.2/5.2	2.6/5.7	3.3/6.8	3.3/6.1	2.9/5.9	2.8/5.4	2.6/5.2	2.5/5.3	2.2/6.1	1.4/4.7	1.6/4.2	3.5/4.5

Average Climatic Conditions

Element	Jan	Feb	Mar	Apr	May	June	July	Aug	Sept	Oct	Nov	Dec	Year
Temperature (°C)	7.2	9.4	13.7	17.8	21.8	25.6	27.2	27.0	24.1	17.8	13.1	9.1	17.8
Daily Minimum Temp	0.8	2.6	6.4	10.5	14.9	18.9	21.1	20.7	17.7	10.3	5.8	2.6	11.0
Daily Maximum Temp	13.6	16.2	20.9	25.2	28.7	32.2	33.4	33.2	30.5	25.4	20.3	15.6	24.6
Record Minimum Temp	-17.8	-13.3	-9.4	-2.2	3.3	5.6	12.8	11.7	1.1	-4.4	-8.9	-16.7	-17.8
Record Maximum Temp	28.3	29.4	32.2	35.0	37.2	40.0	41.7	40.0	40.6	36.1	30.6	27.8	41.7
HDD, Base 18.3°C	349	253	162	55	8	0	0	0	3	68	167	292	1358
CDD, Base 18.3°C	4	3	17	40	117	218	276	269	177	53	9	6	1188
Relative Humidity (%)	74	71	70	71	73	74	77	77	76	75	75	75	74
Wind Speed (m/s)	3.2	3.4	3.5	3.2	2.6	2.3	2.1	2.1	2.4	2.3	2.8	3.2	2.7

Figure 7.14 Average monthly solar data for Meridian, MS.

for the case depicted in the figure. The remaining data are divided into solar-radiation-specific and climatic-condition-specific sections. The solar-radiation-specific data are presented as the incident solar insolation energy per square meter per day (kW h/(m^2 day)) for four solar collector configurations. The solar collector configurations referenced in the data are as follows:

1) Flat-plate collectors facing south at a fixed tilt
   i) 0° tilt (horizontal)
   ii) latitude −15° tilt
   iii) latitude tilt
   iv) latitude +15° tilt
   v) 90° tilt (vertical)
2) One-axis tracking flat-plate collectors with north–south axis
   i) 0° tilt
   ii) latitude −15° tilt
   iii) latitude tilt
   iv) latitude +15° tilt
3) Two-axis tracking flat-plate collectors
4) Direct-beam radiation for concentrating collectors
   i) One-axis, east–west horizontal axis
   ii) One-axis, north–south horizontal axis
   iii) One-axis, north–south tilt at latitude angle
   iv) Two-axis

Monthly average insolation values for each solar collector configuration are given for each month and specified for minimum, average, and maximum irradiation conditions. For example, for June for a fixed-tilt solar collector tilted at the latitude angle, the average insolation on the collector would be 5.6 kW h/(m^2 day). The four solar collector configurations and the orientation options contained within each configuration provide the insolation data needed for most applications.

The last segment of the data presents climatic conditions on a monthly basis. The average, daily minimum, and daily maximum temperatures are listed, as are the record lows and record highs for each month. The heating degree days (HDD, base of 65 °F or 18.3 °C) and the cooling degree days (CDD, base of base of 65 °F or 18.3 °C) are provided along with the average relative humidity and the average wind speed. The HDD and CDD are indicators of the relative need for heating and cooling respectively and will be defined and used in Chapter 8 on passive solar energy.

Example 7.2

Evaluate the performance of an Alternate Energy Technologies AE-21 solar collector on January 21 if the collector is located at 32°N latitude and tilted at an angle of 32°. The water inlet temperature is 58 °F. The ambient temperature varies from 25 °F at 8 am to 45 °F at solar noon to 35 °F at 4 pm. Metrics of interest include the hourly efficiency, the hourly solar energy collected, and the percentage of incident solar energy collected.

Solution Information about the AE-21 is available from the SRCC web site and is reproduced as Figure 7.12. Example 7.1 evaluated the instantaneous performance of a solar collector given the ambient and water inlet temperatures and the incident solar irradiation flux, and it serves as the basis of the solution for this example. The incident solar energy on January 21 at 32°N with a collector tilt angle of 32° is available on an hourly basis from Appendix A. The inlet water temperature is taken as constant, since no information about its variation is

indicated. The ambient temperature is provided at 8 am, solar noon, and 4 pm. From the ambient temperature information, estimates of the ambient temperatures at 9, 10, and 11 am as well as 1, 2, and 3 pm can be made. With hourly ambient temperature, water inlet temperature, and solar irradiation available, the collector performance for every hour of incident sunlight can be evaluated. The daily performance can be generated by summing the hourly performance information. The Mathcad worksheet for the solution is reproduced as Figure 7.15. Information from the AE-21 SRCC data sheet is entered. Consistent with SRCC recommendations, the solar collector area is the gross area, not the aperture area. The hourly input solar irradiation (from Appendix A for 32° latitude and 32° inclination from the horizontal for January 21), water inlet temperature, and ambient temperatures are entered. The solar collector efficiency for each hour is calculated using Equation 7.7. The vector symbol over the efficiency definition is a Mathcad operator indicating that a computation is to be carried out for each nine defined "i" values – the range variable. The hourly energy harvested is computed utilizing the hourly value of the collector efficiency. The last calculations are for the daily energy harvested (expressed in kilowatt-hours) and the fraction of incident solar energy harvested. For the scenario described in the problem statement, the AE-21collector will harvest 7.91 kW h during the day, or 65% of the incident solar energy that day.

Calculations such as those presented in Example 7.2 indicate how to estimate solar collector performance for one day; however, for many engineering applications, the performance over a year is needed. Many simulations programs exist that can accomplish yearly performance estimates on an hour-by-hour basis using TMY3 weather data. Duffie and Beckman (2013) provide an excellent discussion of such programs. However, a viable alternative with accuracy acceptable for preliminary design and analysis purposes is the *f*-chart method, which is covered in Section 7.4.

Enter information about the flat-plate solar collector (obtained from SRCC web site).

$Area := 20.80 \cdot ft^2$ $AreaTot := 1 \cdot Area$ $AreaTot = 20.8 ft^2$

$Intercept := 0.749$ $Slope := -1.086 \cdot \frac{Btu}{hr \cdot ft^2 \cdot F}$

Setup vectors for I (solar irradiation), T_{in}, T_{amb}.

$ORIGIN \equiv 1$ $i := 1 .. 9$

$$I := \begin{pmatrix} 106 \\ 193 \\ 256 \\ 295 \\ 308 \\ 295 \\ 256 \\ 193 \\ 106 \end{pmatrix} \cdot \frac{BtU}{ft^2 \cdot hr} \quad T_{in} := \begin{pmatrix} 58 \\ 58 \\ 58 \\ 58 \\ 58 \\ 58 \\ 58 \\ 58 \\ 58 \end{pmatrix} \cdot F \quad T_{amb} := \begin{pmatrix} 25 \\ 30 \\ 35 \\ 40 \\ 45 \\ 43 \\ 41 \\ 38 \\ 35 \end{pmatrix} \cdot F$$

Figure 7.15 Mathcad solution for Example 7.2.

Calculate the solar collector efficiency.

$$\eta := \overrightarrow{\left[\text{Intercept} + \text{Slope}\cdot\frac{\left(T_{in} - T_{amb}\right)}{I}\right]} \qquad \eta = \begin{pmatrix} 0.411 \\ 0.591 \\ 0.651 \\ 0.683 \\ 0.703 \\ 0.694 \\ 0.677 \\ 0.636 \\ 0.513 \end{pmatrix}$$

Calculate the useful energy harvested.

$$Q_{useful} := \overrightarrow{(\text{AreaTot}\cdot I\cdot\eta)} \qquad Q_{useful} = \begin{pmatrix} 905.965 \\ 2.374\times 10^3 \\ 3.469\times 10^3 \\ 4.189\times 10^3 \\ 4.505\times 10^3 \\ 4.257\times 10^3 \\ 3.604\times 10^3 \\ 2.555\times 10^3 \\ 1.132\times 10^3 \end{pmatrix}\cdot\frac{BtU}{hr}$$

The daily harvested energy is the sum of the hourly-harvested energy.

$$Q_{Total} := \sum_{i=1}^{9} Q_{useful_i}\cdot 1\cdot hr \qquad Q_{Total} = 7.91\,kW\cdot hr$$

Percent of incident solar energy captured.

$$percent := \frac{\sum_{i=1}^{9}\left(Q_{useful_i}\right)}{\sum_{i=1}^{9}\left(\text{AreaTot}\cdot I_i\right)}$$

$$percent = 64.624\,\%$$

Figure 7.15 (*Continued*)

7.4 The *f*-Chart Method

The *f*-chart method is frequently used for estimating the annual thermal performance of an active solar heating system for a building. Duffie and Beckman (2013), as well as Goswami *et al.* (2000), provide much more detail of the development and application of the *f*-chart method than is possible here. The *f*-chart method is a procedure for estimating the fraction *f* of the total monthly heating load (space plus domestic hot water) that can be supplied by an active solar energy system. The procedure is based on a correlation for *f* as a function of two system

parameters. The correlation was derived from the results of a large number of hour-by-hour solar energy system simulations. The two parameters are the ratio of collector losses to heating loads X and the ratio of absorbed solar irradiation to heating loads Y. f-charts have been developed for three system configuration: (1) space and hot water heating using water as the medium, (2) space and hot water heating using air as the medium, and (3) process hot water. Only the first configuration will be presented here. Figure 7.16 is a schematic of the "standard" system configuration using a liquid heat transfer medium. The system consists of a solar collector, three heat exchangers (HX), a main storage tank, a preheat tank, the load, and ancillary components. Energy harvested by the collector is used to heat water for the main storage tank via the collector–storage heat exchanger. Water from the storage tank is used in the load heat exchanger to provide heated air to the house. Potable water is preheated before entering the service hot-water tank. Auxiliary systems are provided for both the house load and the service hot-water tank in case the solar system is unable to meet the required loads.

Detailed simulations of the system illustrated in Figure 7.16 were used to develop the correlation between the two dimensionless variables (X and Y) and f, the monthly fraction of the load carried by solar energy. The first of the two dimensionless parameters is defined as

$$X = \frac{A_c F'_R U_L \Delta t (100 - \overline{T}_a)}{L} \tag{7.11}$$

where X is the ratio of collector losses to load, A_c is the collector area, F'_R is the corrected collector heat removal factor (usually taken as $0.97F_R$), U_L is the collector loss coefficient, $\overline{T}_a$ is the monthly average ambient temperature, Δt is the number of hours in a month, and L is the monthly total heating load (space and water). The expression is dimensionless. The second dimensionless parameter, Y, is the ratio of the absorbed solar to the total heating load and is cast as

$$Y = \frac{A_c F'_R \overline{\tau\alpha} H_T N}{L} \tag{7.12}$$

where $\overline{\tau\alpha}$ is the monthly average $\tau\alpha$ product for the collector (usually taken as $0.96\tau\alpha$), H_T is the monthly average daily radiation incident on the collector surfaced, and N is the number of days in the month.

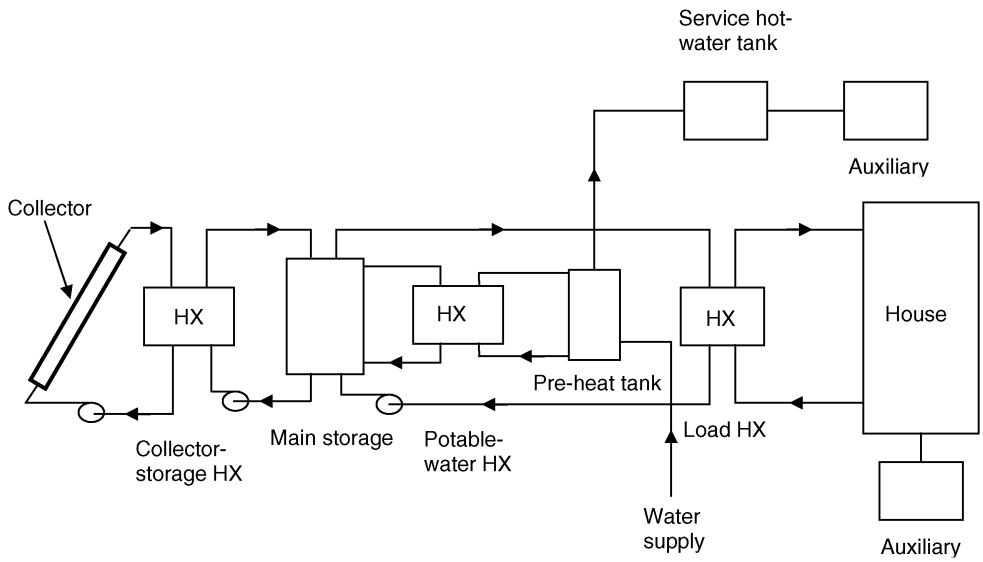

Figure 7.16 "Liquid" solar system schematic.

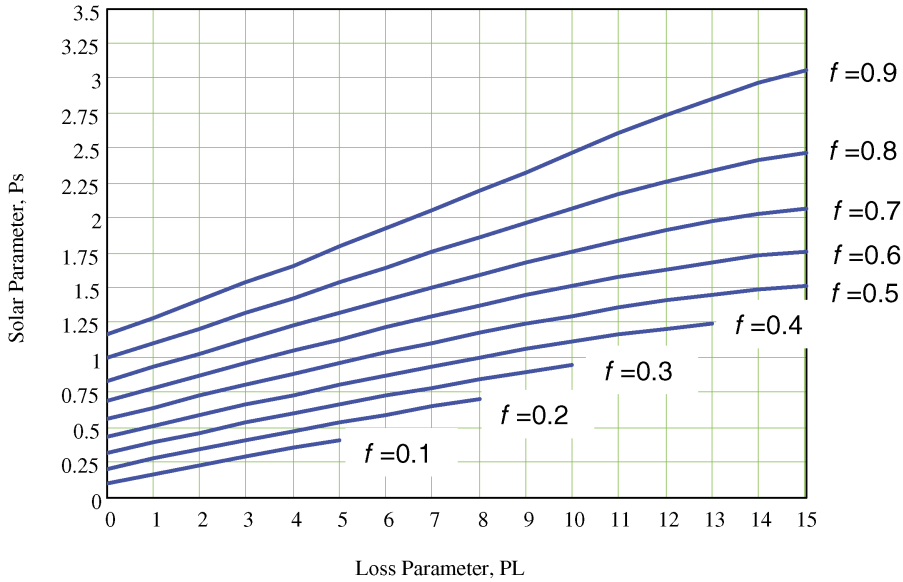

Figure 7.17 The *f*-chart relationship for liquid systems.

The monthly solar fraction f is obtained for the following correlation for "liquid" solar heating systems:

$$f = 1.029Y - 0.065X - 0.245Y^2 + 0.0018X^2 + 0.0215Y^3 \tag{7.13}$$

Figure 7.17 is a parametric representation of this equation.

A similar relationship has also been derived for air heating systems. The monthly solar fraction correlation for air heating systems is

$$f = 1.0409Y - 0.065X - 0.159Y^2 + 0.00187X^2 - 0.0095Y^3 \tag{7.14}$$

Figure 7.18 presents the *f*-chart relationship for air heating systems.

Example 7.3

An office building in Meridian, MS, is to employ Alternate Energy Technologies AE-21 flat-plate solar collectors for space and hot water heating. The collectors will be mounted facing south. The estimated monthly load is provided in the Table 7.3.

The solar energy system is to provide all the hot water heating requirements for the summer months and a yearly solar heating fraction of 60%.

a) How many AE-21 solar collectors are needed to meet the specifications?
b) If natural gas cost \$10 per 10^6 Btu, how much would be saved by the installation of such a solar energy system?

Solution The solution is accomplished in Mathcad. The solution worksheet is contained in Figure 7.19. For ease of use, MJ is defined as megajoules, and the days of the month are entered for use in calculating the *f*-chart parameters X and Y. The average daily irradiation for each month and the average temperature for each month are obtained from the weather data for Meridian, MS. Because the solar heating requirement is much larger in the winter months, latitude+15° was selected as the tilt angle to increase the winter solar energy

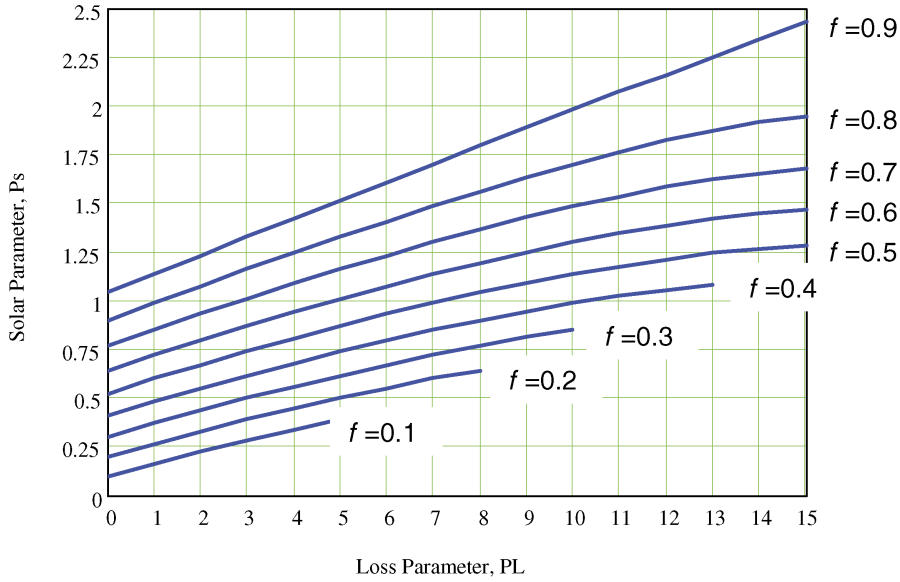

Figure 7.18 The *f*-chart relationship for air systems.

collected. The weather data are taken in Figure 7.14 and were obtained from the Solar Radiation Data Manual for Flat-Plate and Concentrating Collectors database at www.nrel.gov. The slope and intercept information for the AE-21 solar collector were taken from the SRCC data sheet that is reproduced as Figure 7.12. Determining the number of AE-21 collectors needed is an iterative process. The required number of collectors is guessed and the analysis completed to ascertain performance of the guessed number of collectors.

Table 7.3 Monthly heating energy requirements for an office building.

Month	Load (1000 MJ)
January	140
February	120
March	80
April	50
May	28
June	20
July	20
August	20
September	20
October	40
November	80
December	110

***f*-chart example for solar heating in Meridian, MS**

Set up all input parameters on a monthly basis using the range variable i:

ORIGIN ≡ 1 i := 1 .. 12

$MJ := 10^6 \cdot J$

Define month in terms of days.

$$month := \begin{pmatrix} 31 \\ 28 \\ 31 \\ 30 \\ 31 \\ 30 \\ 31 \\ 31 \\ 30 \\ 31 \\ 30 \\ 31 \end{pmatrix} \cdot day \qquad \begin{pmatrix} jan \\ feb \\ mar \\ apr \\ may \\ jun \\ jul \\ aug \\ sep \\ oct \\ nov \\ dec \end{pmatrix}$$

The monthly-average conditions from NREL are used to obtain solar and weather data for the location, Meridian, MS, in this case. The load must come from building information.

$$I := 1 \cdot \frac{kW \cdot hr}{m^2 \cdot day} \qquad I = 3.6 \frac{MJ}{m^2 \cdot day}$$

Irradiation (daily)

$$I := \begin{pmatrix} 3.8 \\ 4.5 \\ 4.9 \\ 5.2 \\ 5.0 \\ 4.9 \\ 4.8 \\ 5.0 \\ 5.0 \\ 5.2 \\ 4.3 \\ 3.8 \end{pmatrix} \cdot \frac{kW \cdot hr}{m^2 \cdot day}$$

Load (monthly)

$$Load := \begin{pmatrix} 140 \\ 120 \\ 80 \\ 50 \\ 28 \\ 20 \\ 20 \\ 20 \\ 20 \\ 40 \\ 80 \\ 110 \end{pmatrix} 1000 \cdot MJ$$

Average Temperature C

$$T_{amb} := \begin{pmatrix} 7.2 \\ 9.4 \\ 13.7 \\ 17.8 \\ 21.8 \\ 25.6 \\ 27.2 \\ 27.0 \\ 24.1 \\ 17.8 \\ 13.1 \\ 9.1 \end{pmatrix} C$$

Figure 7.19 Mathcad solution for Example 7.3.

When the required performance is achieved, the iterative procedure has attained convergence. The parameters, X and Y, are computed for each month, and the value of the solar fraction fall for each month is obtained from the *f*-chart correlation, expressed as Equation 7.13. Both X and Y must be positive, so in the calculation of X the value of the slope of the collector performance curve is taken as positive. Since the required solar fraction for a given month cannot exceed unity, the value of the solar fraction fall for months that exceed unity is set to unity by the piecewise continuous "if" statement.

Insert solar collector characteristics: $Y :=$

$Number := 135$

$FR\tau\alpha := 0.749$ $\quad FRUL := 6.159 \frac{W}{m^2 \cdot C}$ $\quad A := 1.932 Number \cdot m^2$

Implement the *f*-chart analysis using the definitions of X and Y.

Compute *X* and *Y*:

$$X := \left[0.97 FRUL \left(100\,C - T_{amb} \right) \cdot \frac{A \cdot month}{Load} \right] \qquad Y := \left(A \cdot 0.96 \cdot 0.97 FR\tau\alpha \cdot I \cdot \frac{month}{Load} \right)$$

Calculate f (the solar fraction per month) based on the f -chart correlation:

$$fall := \left(1.029 \cdot Y - 0.065 \cdot X - 0.245 \cdot Y^2 + 0.0018 \cdot X^2 + 0.0215 \cdot Y^3 \right)$$

$$f_i := \begin{cases} fall_i & \text{if } fall_i < 1 \\ 1 & \text{otherwise} \end{cases}$$

If solar will more than satisfy the load, set f = 1.

$$X = \begin{pmatrix} 2.766 \\ 2.846 \\ 4.502 \\ 6.64 \\ 11.656 \\ 15.025 \\ 15.191 \\ 15.233 \\ 15.327 \\ 8.576 \\ 4.387 \\ 3.449 \end{pmatrix} \quad Y = \begin{pmatrix} 0.551 \\ 0.688 \\ 1.243 \\ 2.043 \\ 3.625 \\ 4.813 \\ 4.872 \\ 5.075 \\ 4.912 \\ 2.639 \\ 1.056 \\ 0.701 \end{pmatrix} \quad fall = \begin{pmatrix} 0.33 \\ 0.428 \\ 0.686 \\ 0.911 \\ 1.022 \\ 1.104 \\ 1.112 \\ 1.15 \\ 1.118 \\ 0.979 \\ 0.588 \\ 0.406 \end{pmatrix} \quad f = \begin{pmatrix} 0.33 \\ 0.428 \\ 0.686 \\ 0.911 \\ 1 \\ 1 \\ 1 \\ 1 \\ 1 \\ 0.979 \\ 0.588 \\ 0.406 \end{pmatrix}$$

Figure 7.19 (*Continued*)

Values of *X*, *Y*, fall, and *f* (the solar fraction) are tabulated in the worksheet. The solar load for each month is computed. The yearly solar fraction, the total solar energy harvested, and the cost savings are then estimated. When the guessed number of required collectors yields the required solar fraction (60% in the problem statement) and solar fractions of unity during the summer, the solution procedure has converged. In this example, 135 AE-21 collectors are needed to meet the specifications. The savings are $4141/year.

Example 7.3 illustrates how the *f*-chart procedure can be used to assess the performance of a flat-plate solar collector system. The *f*-chart procedure is based on correlating the outputs from a number of TRYNS systems simulations and, as such, is an approximate procedure. However, the *f*-chart procedure is easy to apply and yields solutions that are much better than just an order of magnitude. Indeed, with all the uncertainties in many flat-plate solar collector

Determine the monthly load supplied by solar system.

$$Load_{solar} := \overrightarrow{(f \cdot Load)}$$

$$Load_{solar}^{T} = (4.623 \quad 5.14 \quad 5.487 \quad 4.554 \quad 2.8 \quad 2 \quad 2 \quad 2 \quad 2 \quad 3.918 \quad 4.706 \quad 4.464)\, MJ \cdot 10^4$$

Estimate the yearly solar fraction.

$$percent := \frac{\sum_{i=1}^{12} \left(Load_{solar_i}\right)}{\sum_{i=1}^{12} Load_i} \qquad percent = 60.015\,\%$$

$$TotalSolar := \sum_{i=1}^{12} Load_{solar_i} \qquad TotalSolar = 4.369 \times 10^{11}\, J$$

$$TotalSolar = 4.141 \times 10^{8}\, Btu$$

$$Savings := \frac{TotalSolar}{10^6 \cdot Btu} \cdot 10 \qquad Savings = 4.141 \times 10^3$$

Figure 7.19 (*Continued*)

engineering calculations, an argument can be made that the *f*-chart approach provides sufficient accuracy for most initial assessments of such systems.

7.5 Other Solar Thermal Systems

As is apparent from Figures 7.1 Figures 7.1b and 7.2, solar thermal systems can contain more than flat-plate collectors. Figure 7.1b shows a parabolic trough collector, and Figure 7.2 shows a heliostat. Both devices collect solar energy, but they also concentrate solar energy – that is, they enable higher temperatures to be attained. Since higher output temperatures can be attained by concentrating collectors, the usefulness of the energy collected increases and activities requiring higher working temperatures become possible (refer to Figure 7.4). This section reviews some of the salient features of concentrating collectors.

However, a preliminary review of the fundamentals of concentrating collectors is appropriate. Concentration of incident radiation is achieved by directing (by reflection or refraction) the radiation on an aperture area A_a to a smaller absorber or received area A_r. A geometric concentration factor CR is defined as the ratio of the aperture to receiver area:

$$CR = \frac{A_a}{A_r} \tag{7.15}$$

The energy delivered to the receiver is the incident solar flux I_c at the aperture times the product of the aperture area and the optical efficiency of the aperture to receiver process η_{ar}:

$$q_{del} = \eta_{ar} I_c A_a \tag{7.16}$$

As with the flat-plate collector, the convective losses are expressed as

$$q_{\text{losses}} = U_c A_r (T_{\text{avg}} - T_a) \tag{7.17}$$

The useful energy then becomes

$$q_{\text{useful}} = \eta_{ar} I_c A_a - U_c A_r (T_{\text{avg}} - T_a) \tag{7.18}$$

The collector efficiency is defined to be the useful incident radiation flux divided by the incident irradiation

$$\eta_c = \frac{q_{\text{useful}}}{I_c A_a} = \eta_{ar} - \frac{U_c (T_{\text{avg}} - T_a) A_r}{I_c A_a} \tag{7.19}$$

Recognizing that the geometric concentration factor CR is A_a/A_r, Equation 7.19 becomes

$$\eta_c = \frac{q_{\text{useful}}}{I_c A_a} = \eta_{ar} - \frac{U_c (T_{\text{avg}} - T_a)}{I_c \cdot \text{CR}} \tag{7.20}$$

For concentrating collectors, CR $>$ 1. The loss term in Equation 7.20 is thus smaller for concentrating collectors than for flat-plate collectors (CR~1), and as a result the efficiency for concentrating collectors is higher. For further details see Goswami *et al.* (2000), who present a particularly lucid evaluation of concentrating solar collectors.

Technical and engineering information for flat-plate solar collectors can be obtained from manufacturers' web sites and from the SRCC. Such information for concentrating solar collectors and heliostats is more difficult to find. Most web sites for companies manufacturing concentrating solar collectors contain little technical information.

One interesting question in relation to concentrating collectors is the limit of the receiver temperature. Very high temperatures can be obtained in concentrating collectors such as heliostats (Figure 7.2). The ultimate limit of the receiver temperature is limited by the second law of thermodynamics to be less than the effective temperature of the sun. Indeed, Goswami *et al.* (2000) point out that this conclusion is equivalent to the Clausius statement of the second law.

7.6 Closure

Solar thermal systems have become increasingly popular as the cost of energy continues to rise. The Energy Information Administration monitors the sale of solar collectors. Figure 7.20 presents data on the yearly installed square footage (in millions of square feet) of solar collections from 1975 through 2009 (except for 1985, when no data were collected). Although flat through the last years of the decade of the 1990s, solar collector sales after the millennium dramatically increased during the first part of the decade, but then decreased significantly in the remaining years of the decade. This behavior tracks the relatively constant energy prices (e.g., see Figure 1.14) of the 1990s and the escalating energy prices during the first decade of the twenty-first century. The decreases of the last years of the decade likely represents some loss of luster by solar thermal systems in favor of other renewable energy sources.

The Solar Energy Industries Association, SEIA (www.seia.org) provides an alphabetical listing of manufacturers of solar energy-related items, including solar thermal collectors. The SEIA web site is a good source of addresses and contact information, listing companies manufacturing solar collectors of all types.

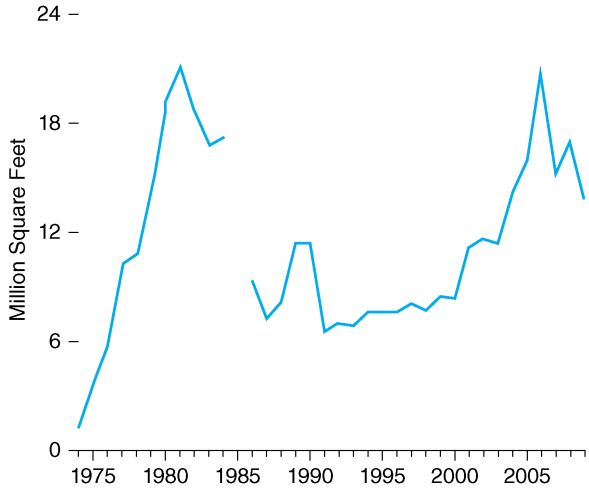

Figure 7.20 Solar collector sales (expressed in square feet) from 1975 through 2009. *Source*: http://www.eia.gov/totalenergy/data/annual/pdf/aer.pdf (p. 292).

References

Duffie, J.A. and Beckman, W.A. (2013) *Solar Engineering of Thermal Processes*, 4th edn. John Wiley & Sons, Inc., New York.

Goswami, Y., Kreith, F., and Kreider, J.F. (2000) *Principles of Solar Engineering*, 2nd edn. Taylor and Francis, New York.

Marion, W. and Wilcox, S. (1994) *Solar Radiation Data Manual for Flat-Plate and Concentrating Collectors*. NREL, Golden, CO.

Marion, W. and Wilcox, S. (1995) *Solar Radiation Data Manual for Buildings*. NREL, Golden, CO.

Mitchell, J.W. (1983) *Energy Engineering*. John Wiley & Sons, Inc., New York.

8

Passive Solar Energy

8.1 Fundamental Concepts of Passive Solar Energy

Passive solar energy is generally defined to include systems in which the flow of solar energy is by passive (or natural) processes such as natural (free) convection. Passive solar concepts have been known and practiced since ancient times. The following statements are attributed to Socrates (~400 BC) and Aristotle (~350 BC) respectively:

> In houses with south aspect, the sun's rays penetrate into the porticos in winter, but in summer the path of the sun is right over our heads and above the roofs so that there is shade.
>
> For well being and health . . . the homestead should be airy in summer and sunny in winter. A homestead promising these quantities would be longer than it is deep and the main front would face south.

In the modern vernacular of modern passive solar practices, these statements mean that a home should be oriented east-to-west with significant southern exposure with overhang such that in the winter sunlight is incident on the southern exposure but in the summer sunlight is blocked.

However, even a first-order examination of passive solar concepts requires a more formal examination of fundamental principles. The book *Passive Solar Buildings* by Balcomb (1992) is regarded as establishing the basis for modern developments in passive building technology, while Duffie and Beckman (2013) and Goswami *et al*. (2000) contain contemporary treatments of passive concepts. The distinction between an active and a passive system is that a passive system uses no mechanical intervention to distribute energy, but relies on radiation and free convection. A passive solar system generally possesses five components:

1) collector (or aperture) arrangement
2) absorber
3) thermal mass
4) distribution protocol
5) control strategy.

Additionally, most passive solar systems also have a backup energy source for use when passive solar features are insufficient for comfort or utility.

Passive collectors consist of windows or a more exotic feature such as a water roof. An absorber is a hard surface with a high absorptivity that is in the direct path of the solar irradiation entering through the collector. The passive thermal storage mass can be provided by external or internal walls, floors, or water walls. These thermal masses receive energy for solar irradiation in

Alternative Energy Systems and Applications, Second Edition. B. K. Hodge.

Companion website: www.wiley.com\go\Hodge\AESystemsandApplications2E

the winter, but are blocked in the summer. The distribution protocol is the method by which the thermal energy is stored, retrieved, and circulated to different areas of the structure. Controls are provided to enhance distribution from the collector/absorber/thermal mass arrangement. In many residences, passive controls include human participation in such tasks as moving panels or opening/closing dampers, as well as passive features such as overhangs.

If a structure has south-facing glazing but no thermal storage mass, the structure is called sun-tempered. The use of extensive south-facing glazing, up to 7% of the floor area, can markedly reduce the heating energy requirement, especially in a cold climate. If the south-facing glazing exceeds roughly 7%, then a thermal storage mass is needed to effectively utilize the solar irradiation incident on the interior of the structure.

Passive solar heating configurations are categorized as direct gain, indirect gain, or isolated gain. As the name implies, in direct-gain solar systems the solar irradiation is directly incident on the interior of a structure. Figure 8.1a is a schematic of a direct gain system, and Figure 8.1b illustrates a direct gain implementation in a residence. The thermal mass thickness should not exceed 6 in, and the thermal mass should not be carpeted. Two well accepted rules of thumb, are that 150 lb of masonry is needed for every square foot of south-facing glazing and that 9 ft^2 of thermal mass storage area is needed for every square foot of south-facing glazing.

Indirect gain systems are characterized by having the thermal mass located between the sun and the interior space. Figure 8.2 presents a schematic and an example of an indirect passive solar system with a Trombe wall. A Trombe wall is a thick wall, usually constructed of masonry, designed to absorb solar irradiation during the day, store it, and radiate heat during the night or on overcast days. A rule of thumb is that 0.2 ft^2 of thermal mass wall is required for every square foot of floor area. The recommended Trombe wall thickness is 12–18 in of concrete or 8–12 in of adobe.

Figure 8.3 illustrates a schematic and an example of an isolated-gain solar system, a sunspace. An isolated-gain system is separate from the main building, but thermal mass is provided for

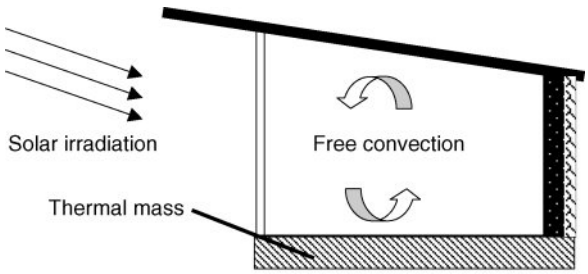

(a)

(b)

Figure 8.1 Direct-gain passive solar system: (a) schematic; (b) implementation example (NREL 08427).

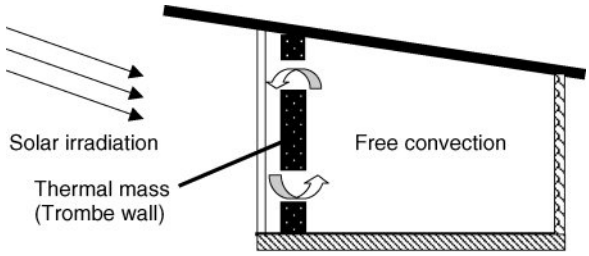

(a)

(b)

Figure 8.2 Indirect-gain solar system with a Trombe wall: (a) schematic (b) implementation example (NREL 02929).

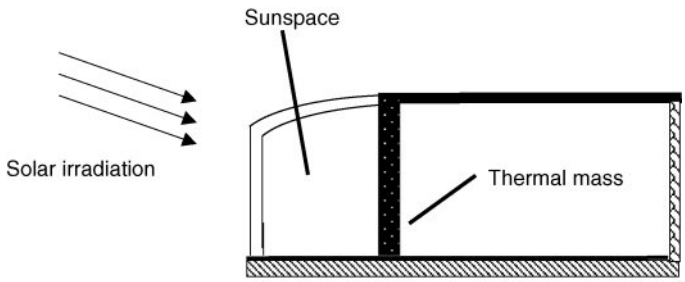

(a)

(b)

Figure 8.3 Isolated solar system (sunspace): (a) schematic (b) implementation example (NREL 08427).

Figure 8.4 Daylighting example (NREL 09536).

energy storage. For a masonry thermal wall the recommended thicknesses are the same as for a Trombe wall, but 0.3 ft^2 of south glazing is needed for every square foot of floor area. Ventilation and shading are generally required during the summer months.

The National Institute of Building Science via their web site http://passivesolar.sustainablesources.com/ contains recommendations and rules of thumb for the passive solar features presented in Figures 8.1, 8.2, and 8.3 Additionally, *Passive Solar Design for the Home* (NREL, 2001) lists recommendations for passive features in residences.

Another important feature often implemented in passive solar is daylighting – the use of radiant energy from the sun for interior illumination so that the need for artificial illumination during daylight hours is reduced. Figure 8.4 illustrates the use of daylighting for the stacks of a library.

Passive solar features can be implemented in virtually any structure, regardless of size. Figure 8.5a and b shows photographs of the NREL Solar Energy Research Facility (SERF) and a residence respectively, illustrating the implementation of many passive (and some active) solar features.

SERF is a state-of-the-art research facility completed in 1993. The facility faces 15° east of due south and is built into the site slope to take advantage of earth sheltering. SERF incorporates a number of energy-saving features, including, daylighting, window shades, evaporative cooling, and heat recovery systems. Annual energy usage and costs are 30–40% lower than for a similar building designed to meet federal standards (1990s era). SERF costs less than one-half of what a typical research facility costs to operate. Photovoltaic arrays, which are not passive solar elements, have been installed on the roof of the east and west wings.

Figures 8.1, 8.2, and 8.3 illustrate the use of south-facing glazing to capture solar irradiation for heating. An equally important passive solar feature, especially in warm climates, is overhang on the south-facing walls to block out solar irradiation in the summer. The residence in Figure 8.5b shows overhang that blocks the sun in summer (high sun altitude angles) but admits solar irradiation in winter (low sun altitude angles).

The preceding schematics and pictures, as well as the accompanying text, establish the fundamentals of passive solar energy but do little to quantify expected performance and energy savings. Sections 8.2–8.4 develop a first-order process and a second-order process to quantify the effects of various passive solar features.

8.2 Quantifying Passive Solar Features

The first- and second-order procedures for estimating or quantifying the effects of various passive solar features are based on the correlated results of a large number of computer

(a)

(b)

Figure 8.5 Passive building examples: (a) NREL's SERF (NREL 01257); (b) residence (NREL 11050).

simulations. The basis of the passive solar estimates is analogous to the *f*-chart procedure explored in Chapter 7. Perhaps the single most referenced document for passive solar energy is the *Passive Solar Design Handbook* (Anderson *et al*., 1980; Balcomb *et al*., 1980; Anderson, 1984). Additional information is available from *The Passive Solar Design and Construction Handbook* (Crosbie, 1997). A common set of definitions used to quantify the performance of passive solar features is examined next.

The most common single-variable method used to express climatological effects on building energy usage is the "degree-day." The degree-day is built around the concept of a no-load (balance point) temperature and an average daily temperature. The no-load temperature is the ambient (outdoor) temperature for which no heating or cooling energy would be required for human comfort in a building. Traditionally, the no-load temperature has been taken to be 65 °F. Thus, heating would be required for ambient temperatures less than 65 °F, and cooling would be required for ambient temperatures greater than 65 °F. The average daily temperature is defined as the average of the minimum and maximum temperature for a given day. The difference between the no-load temperature and the average temperature is defined as the number of degree-days for a given day. Hence, if the average temperature is 45 °F during a particular day, that day has 20 heating degree-days (HDDs). If the average temperature is 85 °F, that day has 20 cooling degree-days (CDDs). The total HDDs for a given location is the sum of the all the daily HDD, and the total CDDs are the sum of the daily CDDs for the location. The total values are a useful metric for estimating energy usage to heat and cool a building since the energy required is essentially proportional to the HDD and CDD. Energy usage estimated from the HDD

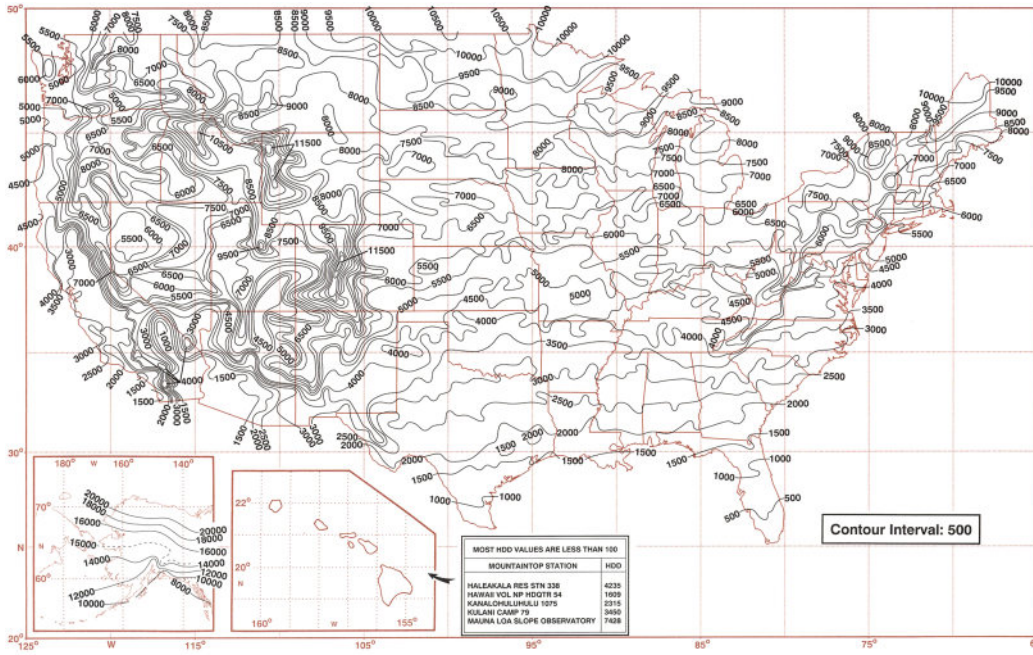

Figure 8.6 Annual F HDDs, based on normal period 1961–1990. *Source*: http://www.ncdc.noaa.gov/img/documentlibrary/clim81supp3/annualheatingDD_hires.jpg

is generally more accurate than energy usage estimated from CDD since cooling degree-days do not consider humidity effects, which can be a significant cooling load in a humid climate.

HDDs and CDDs are available from the National Weather Service and are archived by the National Centers for Environmental Information (NCEI). The *Solar Radiation Data Manual for Flat-Plate and Concentrating Collectors* (Marion and Wilcox, 1994), discussed in Chapter 7, also tabulates the HDD and the CDD values. Figure 7.14 indicates that Meridian, MS, has 1358 Celsius HDDs (C HDD). In the NREL data from Figure 7.14, the Celsius degree-days are referenced to a no-load temperature of 18.3 °C, which is 65 °F. Using this basis, conversion from Celsius degree-days to Fahrenheit degree-days is simple: the conversion factor is 5/9. Care needs to be exercised in using SI units for degree-days since some are tabulated on the basis of 19.0 °C for which the 5/9 conversion factor is slightly off. Additionally, many heating, ventilating, and air conditioning and solar energy engineering textbooks provide tabulations for selected cities as well as maps containing constant HDD and CDD contour lines. For the purposes of this textbook, a contour map will suffice. Figure 8.6 presents a contour of Fahrenheit HDDs (F HDDs) for the USA.

The higher the HDD, the more severe is the winter. In Figure 8.6, the HDDs in the north are much larger than in the south. The HDD values in the mountains of the west show the effects of elevation and latitude. More detailed contour maps are available from the NCEI (www.ncei.noaa.gov).

Figure 8.7 shows a contour map of the F CDDs for the USA. As demonstrated in Figure 8.7, the CDDs in the north are smaller than in the south.

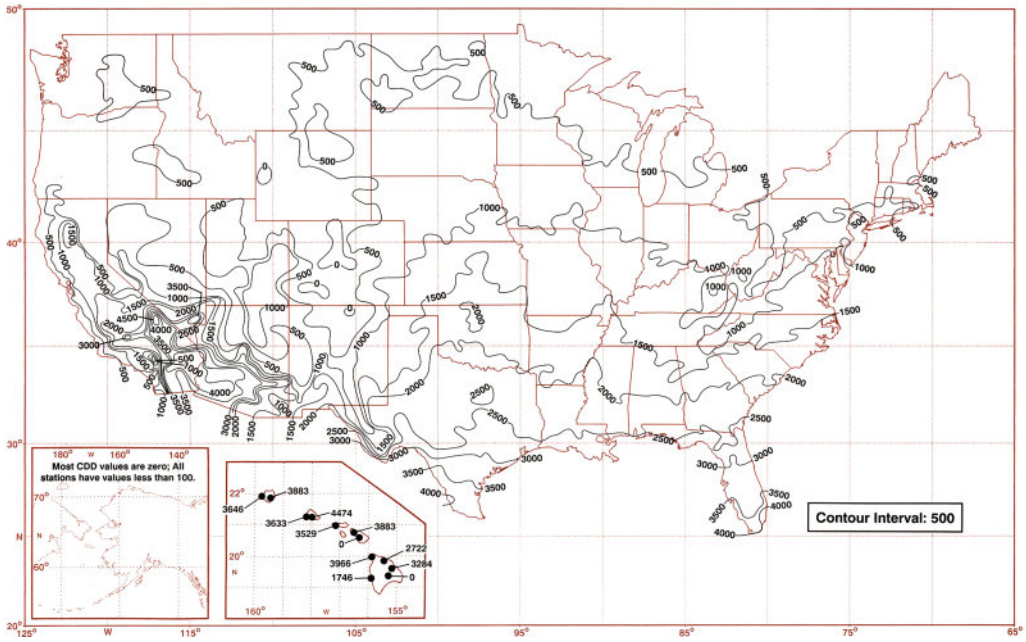

Figure 8.7 Annual F CDDs, based on normal period 1961–1990. *Source*: http://www.ncdc.noaa.gov/img/documentlibrary/clim81supp3/annualcoolingDD_hires.jpg.

In addition to the degree-days concept, many passive solar energy applications utilize a common nomenclature. Consider the following terms:

A_p	vertically projected net south-facing solar glazing (ft^2 or m^2)
NLC	net building load coefficient; the net heating load of the non-solar portion of the structure per HDD (kJ/C HDD or Btu/F HDD)
Q_{net}	net heating load; Q_{net} = NLC × HDD (kWh or Btu)
Q_{solar}	heating load provided by solar energy (kWh or Btu)
Q_{aux}	heating load not provided by solar (kWh or Btu)
LCR	load collector ratio; LCR = NLC/A_p (kJ/(m^2 C HDD) or Btu/(ft^2 F HDD)
SSF	solar savings fraction; the fraction of the total heating energy provided by solar, Q_{solar}/Q_{net}

The net heating energy required is the sum of the solar contribution and the auxiliary:

$$Q_{net} = Q_{solar} + Q_{aux} \tag{8.1}$$

Dividing by Q_{net} and solving for Q_{solar}/Q_{net}, the solar savings fraction (SSF) is

$$\frac{Q_{solar}}{Q_{net}} = SSF = 1 - \frac{Q_{aux}}{Q_{net}} \tag{8.2}$$

from which the auxiliary heating energy is found as

$$Q_{aux} = (1 - SSF) \times NLC \times HDD \tag{8.3}$$

The preceding definitions are used in the two most common procedures for quantifying the effects of passive solar features. These two methods (Anderson *et al.*, 1980; Balcomb *et al.*, 1980; Anderson, 1984; Kreith and West, 1997; Goswami *et al.*, 2000) are the first-level method (or rules of thumb) and the second-level method (or LCR method). Each method's procedures will be examined in the following two sections.

8.3 The First-Level Method (Rules of Thumb)

The first-level method is based on the observation that residences that effectively incorporate passive solar features have similar NLC values per floor area and climate-dependent SSF values. The NLC per square foot of floor area in conventional buildings with energy conserving features are typically in the range 120–160 kJ/(C HDD m^2) or 6–8 Btu/(F HDD ft^2). These values (Anderson *et al.*, 1980; Balcomb *et al.*, 1980; Anderson, 1984; Kreith and West, 1997; Goswami *et al.*, 2000) are reduced by 20% when passive solar features are added, resulting in NLC/floor area values of 100–130 kJ/(C HDD m^2) or 4.8–6.4 Btu/(F HDD ft^2). If climate-dependent, cost-based optimum passive solar features are used, the expected SSF for the US can be found in Figure 8.8.

For well-designed passive solar features, the expected LCR values are climate dependent and are defined (Anderson *et al.*, 1980; Balcomb *et al.*, 1980; Anderson, 1984; Kreith and West, 1997; Goswami *et al.*, 2000) as follows:

	Warm climate	Cold climate
LCR, kJ/(C HDD m^2) [Btu/(F HDD ft^2)]	610 [30]	410 [20]

When the thermal mass directly absorbs the solar irradiation, sufficient thermal mass to store 613 kJ/(°C m^2) or 30 Btu(°F ft^2) per unit area of glazing must be available (Anderson *et al.*, 1980; Balcomb *et al.*, 1980; Anderson, 1984; Kreith and West, 1997; Goswami *et al.*, 2000). If the storage material is heated from room air, then four times as much mass is needed. A reasonable value of the specific heat of typical masonry material is 0.2 Btu/(lbm °F) (837 J/(kg °C)) with a density of 150 lbm/ft^3 (2400 kg/m^3). Consider Example 8.1.

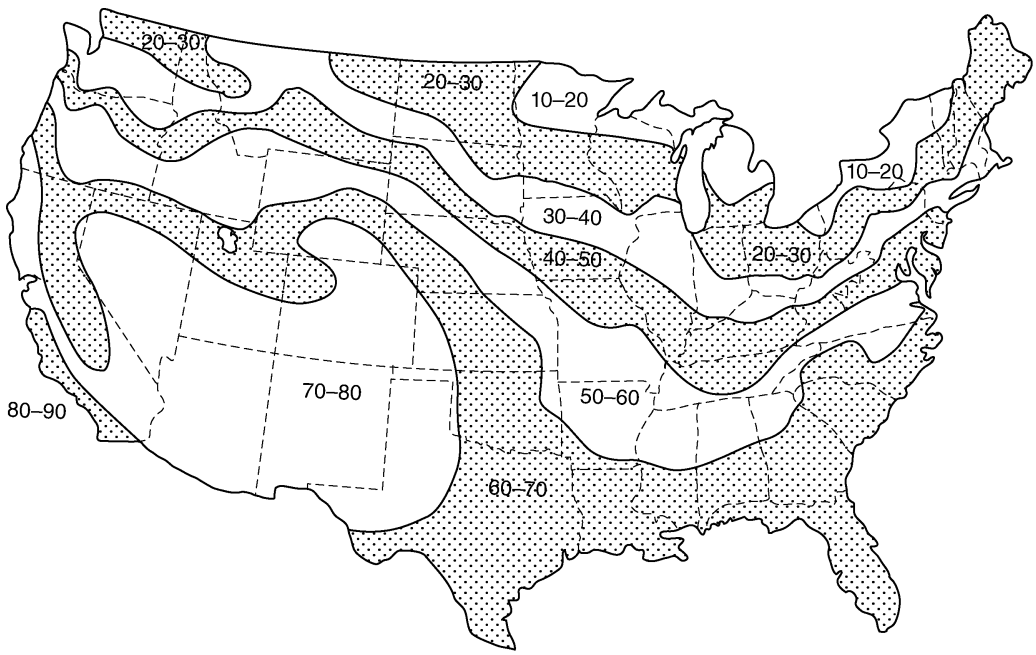

Figure 8.8 Expected SSF values (in percent). *Source*: Anderson (1984).

Example 8.1
A 2500 ft^2 house located in Meridian, MS, has an estimated NLC/ft^2 of floor area of 7.5 Btu/(F HDD ft^2). Estimate the characteristics of an effective passive solar design and the auxiliary heating energy required. Also, estimate the thermal storage mass required.

Solution Figure 7.11 shows that Meridian, MS, has 1358 C HDDs which converts (multiply by 9/5) to 2444 F HDDs. A similar number could be estimated from Figure 8.6. The NLC is thus

$$\text{NLC} = 7.5\frac{\text{Btu}}{\text{F HDD ft}^2} \times 2500\,\text{ft}^2 = 18\,750\frac{\text{Btu}}{\text{F HDD}}$$

The LCR for a warm climate is 30 Btu/(F HDD·ft^2). The projected south-facing glazing is computed as

$$A_p = \frac{\text{NLC}}{\text{LCR}} = 18\,750\frac{\text{Btu}}{\text{F HDD}}\frac{\text{F HDD ft}^2}{30\,\text{Btu}} = 625\,\text{ft}^2$$

The SSF is estimated from Figure 8.8 as 0.6, so Q_{aux} becomes

$$Q_{aux} = (1 - 0.6) \times 18\,750\frac{\text{Btu}}{\text{F HDD}} \times 2444\,\text{F HDD} = 18.3 \times 10^6\,\text{Btu}$$

The thermal mass storage requirement can be estimated by equating the storage requirement per Btu/°F to the product of the mass times the specific heat:

$$30\frac{\text{Btu}}{\text{ft}^2\,^\circ\text{F}} \times 625\,\text{ft}^2 = \text{mass} \times 0.2\frac{\text{Btu}}{\text{lbm}\,^\circ\text{F}}$$

from which the mass storage requirement is found to be 94 750 lbm or about 630 ft^3 with the typical masonry density.

The results of this problem give some indication of the effectiveness of an effective use of passive solar features, but the solution does not indicate any of the details of the solar features. The second-level method incorporates some of the details of the solar features and is examined next.

8.4 The Second-Level Method (the Load Collector Ratio Method)

Instead of rules of thumb, the LCR method is based on extensive computer-based analyses of various passive solar features in a variety of sites (or climates). The LCR method is philosophically similar to the *f*-chart approach for active solar features discussed in Chapter 7. Ninety-four different passive solar systems were analyzed to develop the LCR method (Anderson *et al.*, 1980; Balcomb *et al.*, 1980; Anderson, 1984; Kreith and West, 1997; Goswami *et al.*, 2000). The LCR method is specific to a given structure, in that the NLC and projected solar area A_p are required. From these two quantities, the LCR can be determined by the definition given earlier:

$$\text{LCR} = \frac{\text{NLC}}{A_p} \tag{8.4}$$

Once the LCR is known, the SSF can be found for a given city by matching the LCR with specific passive solar features.

The five different passive solar configurations considered by the LCR method are as follows:

1) direct gain (DG)
2) vented Trombe wall (TW)

3) unvented Trombe wall (TW)
4) waterwall (WW)
5) sunspace (SS).

Within each of these configuration, different values of various feature parameters are used. These parameters include thermal storage capacity, wall thickness, number of glazings, nighttime insulation, ρck value, and sunspace details. The parameter variations for each of the five types leads to the 94 distinct passive solar systems. For a given city, the SSF is tabulated as a function of the LCR. Appendix B, tabulated in Goswami *et al.* (2000) from data in the *Passive Solar Design Handbook* (Anderson *et al.*, 1980; Balcomb *et al.*, 1980; Anderson, 1984), is convenient and useful with LCR method.

Appendix B starts with the common systems descriptions (e.g., masonry density) incorporated into each analysis. Variations of each of the five configuration types are tabulated and assigned a designation – such as TWA1 for the vented Trombe wall system. Tables for Albuquerque, Boston, Madison, Medford, Nashville, and Santa Maria are provided in which LCR values for each system variation are tabulated, and from which the SSF can be estimated. An example is in order.

Example 8.2
A 2000 ft^2 home with passive solar features is located in Nashville. A heating load analysis determines that the NLC is 12 000 Btu/F HDD. The home has 150 ft^2 of direct-gain solar glazing. Characteristics of the direct gain features include double glazing, nighttime insulation, and 30 Btu/(ft^2 °F) thermal storage. Determine the SSF and the auxiliary heating required.

Solution The LCR is first calculated:

$$\text{LCR} = \frac{\text{NLC}}{A_p} = \frac{12\,000 \dfrac{\text{Btu}}{\text{F HDD}}}{150\ \text{ft}^2} = 80 \frac{\text{Btu}}{\text{F HDD ft}^2}$$

The system designation is DGA3 for a direct-gain system with double glazing, nighttime insulation, and 30 Btu/(ft^2 °F) thermal storage. Entering the LCR table (Appendix B) for Nashville with an LCR of 80 Btu/(F HDD ft^2) and the system designator DGA3, an SSF of 0.2 is estimated. The table also provides the F HDD as 3696. The auxiliary heating Q_{aux} is calculated as

$$Q_{aux} = (1 - 0.2) \times 12\,000 \frac{\text{Btu}}{\text{F HDD}} \times 3696\ \text{F HDD} = 35.5 \times 10^6\ \text{Btu}$$

The thermal mass can also be estimated since system DGA3 has a mass area to glazing area ratio of 6 and a thickness of 2 in. Thus:

$$\text{mass} = \text{volume} \times \rho = 6 \times 150\ \text{ft}^2 \times 2\ \text{in} \times \frac{\text{ft}}{12\ \text{in}} \times 150 \frac{\text{lbm}}{\text{ft}^3} = 22\,500\ \text{lbm}$$

The utility of the LCR method is that once a baseline structure is described, the LCR method provides an easy procedure for ascertaining the effects of changing passive solar features within the 94 systems in the original computational base.

8.5 Daylighting

Figure 8.4 demonstrates the effectiveness of daylighting – the use of natural lighting, not artificial lighting (e.g., incandescent or fluorescent) – to illuminate the interior of a structure.

An examination of the salient features of daylighting is appropriate, since significant energy savings are possible for properly designed and effectively integrated daylighting implementations.

Spaces that are occupied during daylight hours have a high potential for daylighting. For a new building, maximizing the use of daylighting will likely mean a higher skin-to-volume ratio than for a conventional building. A standard window produces useful illumination to a depth of 1.5 times the height of the window. Using additional daylighting features, illumination penetration to 2.0 times the window height is possible. The higher the placement of the window, the deeper the penetration. The illumination of daylighting is composed of three components: (1) an exterior reflected component, (2) a direct sun/sky component, and (3) an internal reflected component. The ceiling provides the most important internal reflected component; ceiling reflectivities above 80% are recommended. Wall reflectivities between 50 and 70% and floor reflectivities between 20 and 40% are recommended. The proportions of a room are more important than the dimensions for daylighting considerations.

One method of quantifying the relationship between the visible light and the size of a window (glazing) is the effective-aperture method. The effective aperture is the product of the window-to-wall ratio and the window transmissivity. The window-to-wall ratio is the window area divided by the wall area where the window is located. Effective apertures in the range 0.2 to 0.3 are considered good. Consider an example.

Example 8.3

A south-facing wall has a total area of 300 ft^2 and a window area of 100 ft^2. If the transmissivity of the glass is 0.7, determine the effective aperture. Comment on the appropriateness of this configuration for daylighting.

Solution The effective aperture is calculated as

$$\text{effective apeture} = \frac{A_{\text{window}}}{A_{\text{wall}}}\tau_{\text{window}} = \frac{100\ \text{ft}^2}{300\ \text{ft}^2} \times 0.7 = 0.233$$

Since the effective aperture, 0.233, is between 0.2 and 0.3, the configuration is appropriate for daylighting.

One way to increase the illumination level without increasing the brightness is to utilize light shelves. A light shelf is a horizontal light-reflecting overhang placed above eye level with a transom window above the light shelf. Light is reflected from the light shelf into the interior of the building, and the ceiling is used to distribute the light throughout the room.

The effectiveness of daylighting can be increased by the use of toplighting strategies. Toplighting features include skylights, clerestory windows, roof monitors, and sawtooth roofs. However, some of these features have problems and therefore are sparingly used. Skylights seem a natural for daylighting, but skylights receive the maximum solar gain at solar noon, which can lead to increased cooling loads as well as severe variations in illumination between the morning and afternoon. Clerestory windows are vertical glazings located high on an exterior wall. North- or south-oriented clerestory windows are very effective daylighting features, but east- or west-oriented clerestory windows can lead to high heat gains and major variations in interior illumination. A roof monitor is a flat roof section raised above the adjacent roof line with vertical glazing on all sides. Monitors can result in excessive glazing areas, high heat losses and gains, and interior glare and shading problems during the day. Some older industrial buildings have sawtooth roofs. The sloped surface is opaque, and the vertical surface is glazed. South-facing sawtooth roofs may result in large heat gains during the summer. Thus, taking into account all

these factors, daylighting features must be carefully considered if satisfactory illumination, without large heat gains and losses, is to result.

An important part of any daylighting implementation is control of the electrical lighting within a daylighted area. Light-level sensors are effective in cutting off or dimming electrical lights when illumination for daylighting features reaches the desired level.

A number of computer programs are available to model and predict daylighting illumination levels in a specific building at a specific site.

The Whole Building Design Guide (WBDG) of the National Institute of Building Sciences presents a good description of daylighting concepts on their web site (www.wbdg.org/resources/daylighting.php). Included in the WBDG daylighting discussion are descriptions, applications, operation and maintenance considerations, relevant codes and standards, and additional resources. The Energy Center of Wisconsin (http://www.seventhwave.org/) provides examples and discussions on simple tools and calculations, physical modeling, and computer modeling of daylighting concepts. A number of computer software elements are available for daylighting; a list of the most common includes: Velux Daylight Visualizer (http://viz.velux.com), Radiance (http://www.radiance-online.org/), DAYSIM (http://daysim.ning.com/), DIVA for RHINO (http://diva4rhino.com), DIAL+ (http://www.estia.ch), Evalglare (http://www.ise.fraunhofer.de), and 3DS Max Design (http://www.autodesk.com).

8.6 Passive Solar Simulation Software

There is a plethora of passive solar software elements and programs available to quantify building energy usage. Many of the common energy analysis programs incorporate passive solar features that are more accurate than the methods previewed in this chapter. Indeed, many organizations have web-based passive solar energy software that can be executed from the web site. But in many of the web-based passive solar programs, the assumptions and numerical procedures are not clearly defined or explained, so the user should exercise caution.

In the first edition, Energy-10, then marketed and maintained by the Sustainable Buildings Industry Council, was cited as a program which incorporated many passive solar features. Unfortunately, Energy-10 is no longer supported. A program that is downloadable is EnergyPlus, described by the DOE Building Technologies Office as a building energy simulation program used to model energy consumption, which runs on Windows, Mac OS X, and Linux operating systems. EnergyPlus is a professional, state-of-the-art program for modeling low-energy designs and systems and is the only energy simulation engine provided under a commercial-friendly open-source license. Information and technical support on EnergyPlus are available from the following web sites: https://energyplus.net/ and http://energy.gov/eere/buildings/about-building-energy-modeling. EnergyPlus is comprehensive (and complex) and requires some effort to master, but it represents a path for quantifying the effects of various options on building energy savings.

Figure 8.9, taken from the Energy-10 information, presents a graphical comparison of a conventional building and that same building with extensive energy conservation features, including passive solar components. As is evident from the figure, the energy consumption of the "low-energy" case is about one-third that of the base case.

Computer programs similar in capability to EnergyPlus are necessary for engineering endeavors involving building energy usage. Much of the passive solar information available on the web is qualitative, not quantitative. In reality, building owners/operators and home owners need quantified energy and cost savings information to justify passive solar implementations.

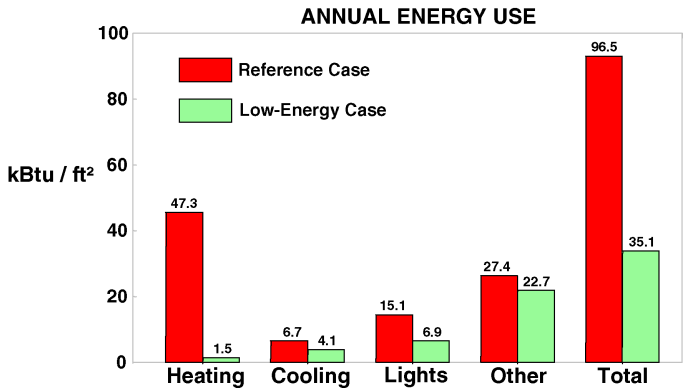

Figure 8.9 Energy-10 output showing end-point energy usage differences. *Source*: image provided courtesy of the Sustainable Buildings Industry Council.

8.7 Closure

This chapter has reviewed the fundamentals of passive solar energy. Many passive solar features can be added with little additional cost for a new construction. Retrofits of passive solar features to existing buildings may be more expensive, but are possible with careful consideration. Additional information is available in the references and on the web. Indeed, a Google search on the web will produce many "hits." As with all web information, care must be exercised in assessing the validity of the information. However, in the case of passive solar energy, the US Department of Energy web sites provide a range of validated information.

References

Anderson, B. (1984) *Passive Solar Design Handbook*. Van Nostrand Reinhold, New York.

Anderson, B., Michal, C., Temple, P., and Lewis, D. (1980) *Passive Solar Design Handbook, Volume 1: Passive Solar Design Concepts*. US DOE Report No. DOE/CS-0127/1. US Department of Energy, Washington, DC.

Balcomb, J.D. (1992) *Passive Solar Buildings*. The MIT Press, Cambridge, MA.

Balcomb, J.E., Barley, C.D., McFarland, R.D., *et al*. (1980) *Passive Solar Design Handbook, Volume 2: Passive Solar Design Analysis*. US DOE Report No. DOE/CS-0127/2. US Department of Energy, Washington, DC.

Crosbie, M.J. (1997) *The Passive Solar Design and Construction Handbook*. John Wiley & Sons, Inc., New York.

Duffie, J.A., and Beckman, W.A. (2013) *Solar Engineering of Thermal Processes*, 4th edn. John Wiley & Sons, Inc., New York.

Goswami, Y., Kreith, F., and Kreider, J.F. (2000) *Principles of Solar Engineering*, 2nd edn. Taylor and Francis, New York.

Kreith, F., and West, R.E. (1997) *CRC Handbook of Energy Efficiency*. CRC Press, Boca Raton, FL.

Marion, W. and Wilcox, S. (1994) *Solar Radiation Data Manual for Flat-Plate and Concentrating Collectors*. NREL, Golden, CO.

NREL (2001) *Passive Solar Design for the Home*. DOE/GO-102001-1105. http://www.nrel.gov/docs/fy01osti/27954.pdf (accessed October 19, 2016).

9

Photovoltaic Systems

9.1 Introduction

"Photovoltaic" refers to the direct generation of electricity by solar irradiation. Duffie and Beckman (2006) and Goswami *et al*. (2000) are classical solar engineering textbooks that include discussions of photovoltaic systems. Patel (2005) examines in detail wind and solar photovoltaic systems, and the handbook by Kreith and West (1997) contains a chapter on photovoltaic energy.Like flat-plate solar collectors for thermal solar systems, discussed in Chapter 7, "solar cells" are well-recognized icons of photovoltaic systems. As an example of a photovoltaic system, Figure 9.1 presents a photograph of an 18 kW, fixed flat-plate photovoltaic array with dual-axis tracking. The system shown in the figure was installed by the Nevada Power Company and is an example of a very sophisticated application of photovoltaics. However, no matter how sophisticated the photovoltaic system, the solar cell is the fundamental building block. Section 9.2 develops the fundamentals of photovoltaic cell operation.

9.2 Photovoltaic Cell Fundamentals

Atomic theory and semiconductor theory are good places to start an examination of the operation of a photovoltaic cell. An atom is composed of a nucleus containing protons and neutrons, with electrons in orbits about the nucleus. In an atom, the number of protons is equal to the number of electrons, and that number is the atomic number of an element. For silicon, a common material extensively used in photovoltaic cells, the atomic number is 14. The electrons are positioned in orbitals or bands about the nucleus. All inner bands must be filled before any band farther out can be partially filled. The energy of an electron is determined by its position in one of the various bands. The number of electrons in the outermost band determines the chemical characteristics of the element. The outermost band an electron can occupy and maintain its association with the atom is called the valence band. In silicon, the valence band is partially filled and contains four electrons; it must contain eight electrons to be filled.

If the valence band is filled, the element is chemically inert. If electrons in an unfilled valence band are lightly bound, they may attach themselves to a neighboring atom, which gives that atom a negative charge, resulting in the donor atom becoming a positively charged ion. The positively and negatively charged ions form an ionic bond. If the electrons in an unfilled valence band are more strongly attached, they configure themselves so that neighboring atoms can share electrons to keep the valence bands filled. Such sharing of electrons results in a covalent bond.

Electrons in the valence band can become so energetic that they jump into a band that is far removed from the nucleus. This remote band is called the conduction band. The difference in the energy between an electron in the valence band and one in the conduction band is called the

Alternative Energy Systems and Applications, Second Edition. B. K. Hodge.

Companion website: www.wiley.com\go\Hodge\AESystemsandApplications2E

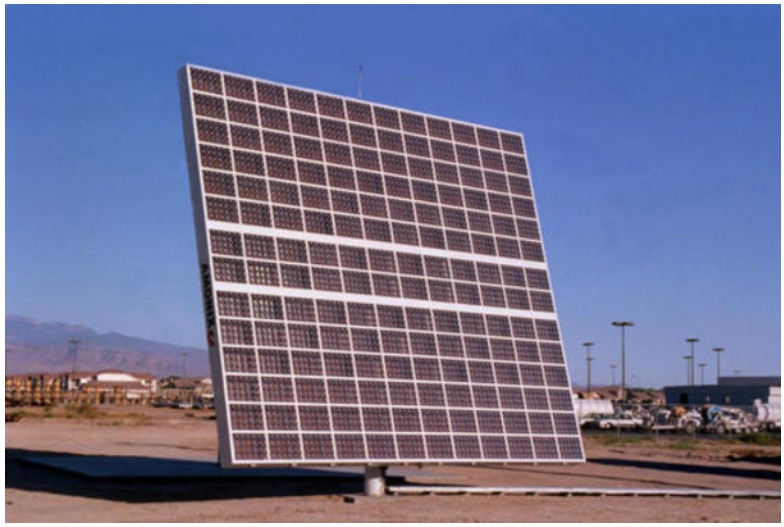

Figure 9.1 Photovoltaic system example. *Source*: NREL 08851.

band gap energy. Electrons in the conduction band require only a small amount of energy to move away from the atom, and this is responsible for heat and electrical conduction. Band gap energies are usually expressed in electron-volts (eV): $1\,\text{eV} = 1.602 \times 10^{-19}$ J. Insulators are materials whose atoms possess full valence bands and have high band gap energies, >3 eV. Conductors are materials whose atoms have relatively empty valence bands. Materials whose atoms have relatively full valence bands are semiconductors with band gap energies <3 eV. Band gap energies for some typical materials used in photovoltaic cells are presented in Table 9.1.

Silicon is an example of a semiconductor (four electrons in the valence band). Pure silicon is called an intrinsic semiconductor, but if a small amount of impurities, usually called the dopant, is combined with the pure silicon, an extrinsic semiconductor results. An n-type of semiconductor results if the dopant has more electrons in the valence band than the base material. An n-type semiconductor seems to have an excess of electrons even though the semiconductor is electrically neutral. A p-type semiconductor results if the dopant has fewer electrons in the valence band than the base material. The p-type semiconductor appears to have a deficit of electrons, or an excess of "holes," although it is electrically neutral. The reason for doping a pure

Table 9.1 Representative photovoltaic material band gap energies.

Material	Band gap energy (eV)
Si, silicon	1.11
CdTe, cadmium telluride	1.44
CdS, cadmium sulfide	2.42
$CuInSe_2$, copper indium diselenide	1.01
GaAs, gallium arsenide	1.40
GaP, gallium phosphide	2.24
InP, indium phosphide	1.27

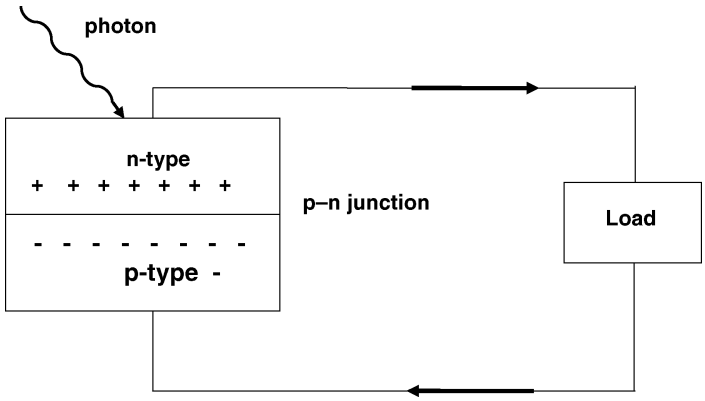

Figure 9.2 Photovoltaic cell schematic.

semiconductor such as silicon is that a junction formed with n-type and p-type semiconductor material enhances the flow of electrons and holes.

Consider the schematic of a photovoltaic cell in Figure 9.2. The PV cell is shown as a p-n junction with an incident photon. An external load is connected. If the incident photon is energetic enough to dislodge a valence electron, the electron will jump to the conduction band and initiate a current flow. For an electron to be forced from the valence band to the conduction band, the photon must possess at least the band gap energy.

The energy of a photon is given by

$$E = h\nu \tag{9.1}$$

with $h = 6.625 \times 10^{-34}$ J s (Planck's constant) and ν the frequency. The frequency, wavelength λ, and speed of light ($c = 2.998 \times 10^8$ m/s) are related as

$$\nu = \frac{c}{\lambda} \tag{9.2}$$

Combining:

$$E = h\frac{c}{\lambda}$$

Example 9.1

Determine the wavelength of light that corresponds to the band gap energy of silicon, 1.11 eV.

Solution Combining Equations 9.1 and 9.2 and solving for the wavelength yields

$$\begin{aligned}\lambda &= \frac{h\,c}{E} \\ &= 6.625 \times 10^{-34}\ \text{J s} \times 2.998 \times 10^8 \frac{\text{m}}{\text{s}} \times \frac{1}{1.11\ \text{eV}} \times \frac{\text{eV}}{1.602 \times 10^{-19}\ \text{J}} \\ &= 1.1169 \times 10^{-6}\ \text{m} = 1.12\ \mu\text{m}\end{aligned}$$

Hence, light with a wavelength of 1.12 μm has sufficient energy to dislodge a valence electron in silicon.

Example 9.1 has important implications for the operation and efficiency of photovoltaic devices. Photons with a wavelength greater than 1.12 μm contain insufficient energy to dislodge a valence electron in silicon; hence, photons with wavelengths greater than 1.12 μm will induce

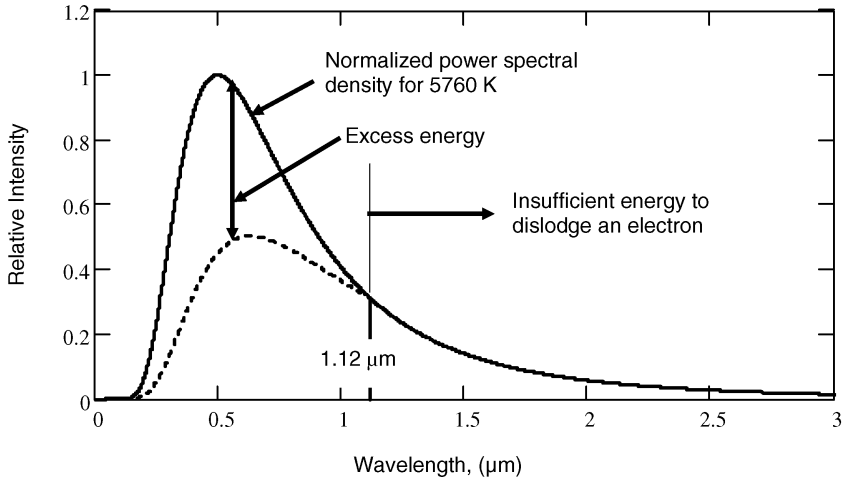

Figure 9.3 Solar irradiation and the band gap of silicon.

no photovoltaic effect in silicon. Photons with wavelength less than 1.12 μm possess more energy than is required to dislodge a valence electron in silicon. However, a single photon can dislodge only a single valence electron, and the difference in the band gap energy and the photon energy is absorbed as heat by the photovoltaic device. The graphical representation Figure 9.3 is useful in delineating the behavior of a photovoltaic device exposed to solar irradiation.

Figure 9.3 was specifically generated for silicon, but the same features would hold for any semiconductor material (or band gap energy) specified. The solid curve represents the power spectral density at 5760 K (the temperature that corresponds to the spectral energy distribution of solar irradiation) normalized by its maximum value. The 1.12 μm wavelength is indicated on the figure. Wavelengths greater than 1.12 μm contain insufficient energy to dislodge a valence electron, while wavelength less than 1.12 μm result in excess energy. If $E_{1.12}$ represents the energy required to dislodge a silicon valence electron, then Equations 9.1 and 9.2 can be converted to ratio form to express that portion of the energy required to dislodge a valence electron for a wavelength lower than 1.12 μm:

$$E_{1.12} = E\frac{\lambda}{\lambda_{1.12}} \tag{9.3}$$

and the excess energy term becomes

$$E - E_{1.12} = E - E\frac{\lambda}{\lambda_{1.12}} = E\left(1 - \frac{\lambda}{\lambda_{1.12}}\right) \tag{9.4}$$

Thus, the smaller the wavelength, the greater the excess energy of the photon. The generally low efficiencies of photovoltaic devices are attributable to this principle and to additional conversion inefficiencies associated with photon wavelengths less than those corresponding to the exact band gap energy.

Table 9.2 contains theoretical and measured efficiencies for common photovoltaic cell materials. The theoretical efficiencies are the generally accepted values (http://www.solarserver.com/knowledge/basic-knowledge/photovoltaics.html) while the measured values were obtained from National Renewable Energy Laboratory (NREL) – as reproduced as Figure 9.4 – and represent laboratory values, not production values. As they are the results of active and aggressive research programs, the measured efficiencies of some materials in the table are subject to change. NREL, for example, sponsored the Thin Film Partnership Program

Table 9.2 Theoretical and measured efficiencies of photovoltaic cells.

Material	Efficiency (%)	
	Theoretical	Measured
Si, silicon	28	25
Si (amorphous)	23	14
CdTe, cadmium telluride	29	22
$CuInSe_2$, copper indium diselenide	27	22
GaAs, gallium arsenide	30	29

(1994 until 2009) focused on amorphous silicon (a-Si), cadmium telluride (CdTe), and copper indium gallium diselenide (CIGS) and its alloys. The partnership program resulted in significant reductions in manufacturing costs with a concurrent 25-fold increase in installed megawatts of thin-film systems. The NREL photovoltaic web site is http://www.nrel.gov/materials-science/thin-film.html.

A summary of long-term gains in photovoltaic cell efficiencies was generated by NREL in 2015 and is reproduced as Figure 9.4. The figure presents general trends of efficiencies of various photovoltaic cells (and the research entities involved). Except for multijunction devices, the general trend is a slow, but steady increase in cell efficiencies with time. One strategy used to overcome the relatively low conversion efficiencies of solar cells is to provide more than a single junction; that is, to fabricate two or more junctions, one above the other. Over the last decade, these multijunction photovoltaic cells have shown impressive increases in conversion efficiencies. Indeed, the 2015 maximum photovoltaic value is 46% for a four-junction concentrator device. However, while multijunction devices exhibit impressive efficiencies, manufacturing costs are high.

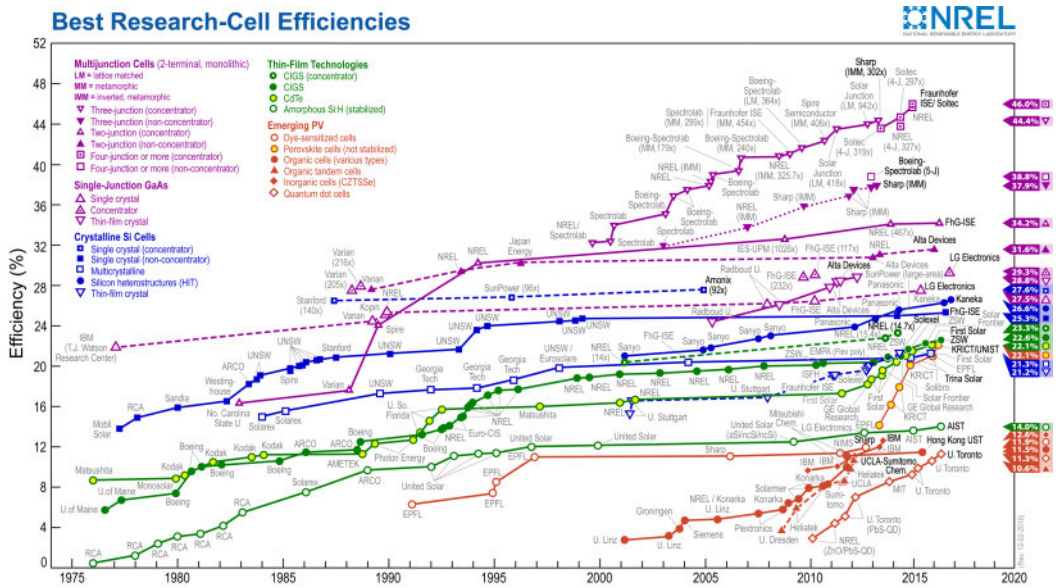

Figure 9.4 History of photovoltaic cell efficiencies. *Source*: http://www.nrel.gov/ncpv/images/efficiency_chart.jpg.

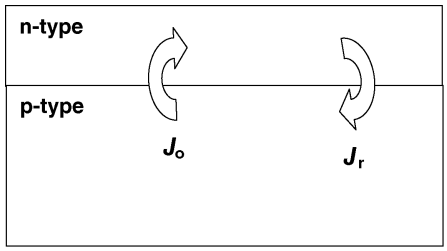

Figure 9.5 Current density at a p–n junction.

Although the detailed physics of a photovoltaic cell are quite complex, simple models are available. Consider, as in Figure 9.5, the current density flow at a p–n junction of a photovoltaic cell. The current density is the current I divided by the surface area A, and is denoted as J.

At the p–n junction, a junction current density J_j is generated. The junction current density is the algebraic sum of the current density from the p-side to the n-side (the dark current or reverse saturation current) J_o, and the current density from the n-side to the p-side (the light-induced recombination current) J_r. In an illuminated photovoltaic cell, the light-induced recombination current density is proportional to the reverse saturation current and is given by

$$J_r = J_o \exp\left(\frac{e_o V}{kT}\right) \tag{9.5}$$

where $e_o = 1.602 \times 10^{-19}$ J/V (the charge of one electron) and $k = 1.381 \times 10^{-23}$ J/K (Boltzmann's constant). The junction current density J_j is

$$\begin{aligned} J_j &= J_r - J_o \\ &= J_o \left[\exp\left(\frac{e_o V}{kT}\right) - 1\right] \end{aligned} \tag{9.6}$$

The equivalent circuit for a photovoltaic cell is shown in Figure 9.6. In the equivalent circuit, the solar cell current output density J_s flows in parallel either through the junction or the load. The load current density J_L can be expressed as

$$J_L = J_s - J_j \tag{9.7}$$

Using Equation 9.6, the load current density can be cast as

$$J_L = J_s - J_o \left[\exp\left(\frac{e_o V}{kT}\right) - 1\right] \tag{9.8}$$

If the cell is short circuited, $R_L = 0$, so that $J_s = J_L$, and Equation 9.8 requires $V = 0$. If the circuit is open, then $J_L = 0$, and the output of the cell is directed through the junction. Under these circumstances, the voltage is called the open-circuit voltage V_{oc}. The performance of a

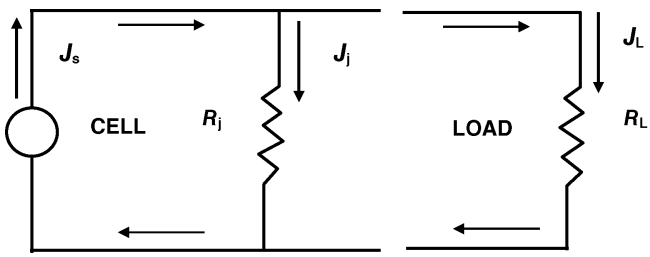

Figure 9.6 Photovoltaic cell equivalent circuit.

photovoltaic cell is typically described using the short circuit current and the open-circuit voltage.

The open-circuit voltage occurs when $J_L = 0$. If the voltage for $J_L = 0$ is denoted as V_{oc}, then Equation 9.8 can be solved for V_{oc} with the results

$$V_{oc} = \frac{kT}{e_o} \ln\left(\frac{J_s}{J_o} + 1\right) \tag{9.9}$$

Given the open-circuit voltage and temperature, Equation 9.9 can be solved for the ratio J_s/J_o. A typical value of V_{oc} is 0.6 V for a single solar cell. The J_s/J_o ratio is quite large. Dividing Equation 9.8 by J_s yields an expression for the load current density to short-circuit current density ratio:

$$\frac{J_L}{J_s} = 1 - \frac{J_o}{J_s}\left[\exp\left(\frac{e_o V}{kT}\right) - 1\right] \tag{9.10}$$

By using Equation 9.10 and a specified value of V_{oc}, the current density versus voltage relationship can be determined. The power delivered to the load is the load current density J_L times the voltage drop across the load times the photovoltaic cell area:

$$\text{Power} = J_L V A \tag{9.11}$$

where A is the photovoltaic cell area. Figure 9.7 presents, for a $V_{oc} = 0.6$ V and $T = 300$ K, the variations of J_L/J_s and the normalized power as a function of the voltage. The power is normalized with the maximum power to the load, which occurs at $V \sim 0.5$ V. The general functional form of both the current density ratio and the power ratio are similar for most photovoltaic cells. The load current density decreases slowly as the voltage increases from zero, but as V_{oc} is approached, the current density rapidly decreases to zero at the open-circuit condition. At the short-circuit condition, the power delivered to the load is zero, and the power delivered to the load is also zero at the open-circuit condition. Between these two extremes, the power reaches a maximum value, usually relatively close to the open-circuit voltage. The voltage and current at maximum power are shown in Figure 9.7 as V_{mp} and I_{mp} respectively.

Not surprisingly, the higher the solar irradiation, the higher the power output of a photovoltaic cell. Consider as in Figure 9.8 the effect of irradiation on the performance of a solar cell.

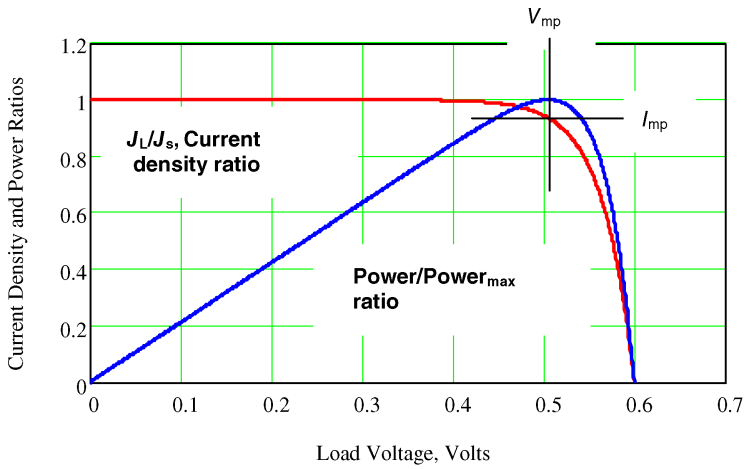

Figure 9.7 Current density ratio and power ratio versus voltage.

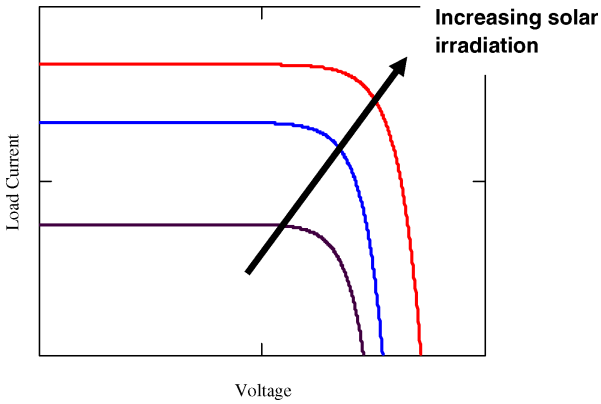

Figure 9.8 Effect of solar irradiation on solar cell performance.

As the solar irradiation increases, the open-circuit voltage increases slightly, but the load current is almost directly proportional to the solar irradiation. *The maximum power to the load is also almost directly proportional to the solar irradiation incident on the cell.*

With the fundamental physics of photovoltaic cells discussed, an examination of actual components and systems is needed, and will be covered in Section 9.3.

9.3 Photovoltaic Components

No matter what kind of photovoltaic systems are examined, the most fundamental element is the individual photovoltaic cell. Individual cells are assimilated into modules; modules are assembled into arrays, which are integrated into systems with a wide range of components. Figure 9.9 schematically illustrates the sequence. The internet is a good source of information on all photovoltaic systems components.

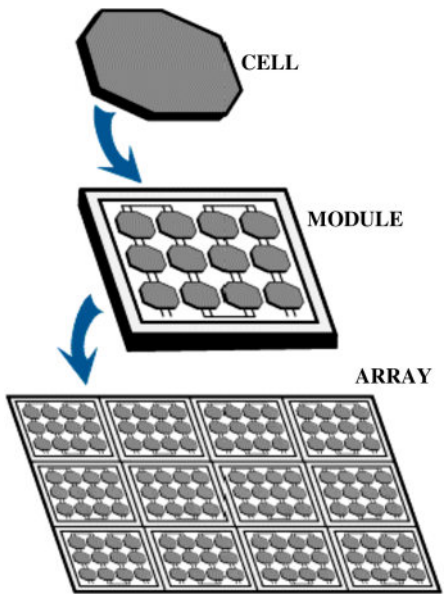

Figure 9.9 Cells, modules, and arrays. *Source*: http://science.nasa.gov/science-news/science-at-nasa/2002/solarcells/.

Monocrystalline silicon solar cell
CT7S20 - 3BB

Mechanical data and design

Dimensions	156 mm x 156 mm +/-0.5 mm
Thickness	200 µm +/- 20 µm
Cell surface	243 cm^2 +/- 3.12 cm^2
Front (-)	Alkaline texture surface with SINx anti-reflective coating 3 BB in 1.5 mm width
Back (+)	BSF 3 BB in 3.5 mm width

Electrical Characteristics (Typical Values)

Voc (Volts)	Isc (Amps)	Efficiency	Fill Factor
0.622	8.624	0.172	0.787
0.622	8.638	0.174	0.794
0.625	8.654	0.176	0.797
0.626	8.663	0.178	0.802
0.624	8.909	0.180	0.794
0.626	8.940	0.182	0.797
0.627	8.950	0.184	0.801
0.627	8.950	0.186	0.811

Figure 9.10 Typical photovoltaic cell specifications (PhotoWatt 6MB). *Source*: http://www.photowatt.com/en/products/cellules.

The basic building block is the individual solar cell. Although the internet contains significant information on individual photovoltaic cells, much of the information is qualitative, not quantitative, and does not provide the full specifications of a given photovoltaic cell. The web site for PhotoWatt International (http://www.photowatt.com/en/products/cellules), a French company, is one that does contain technical specifications of PhotoWatt photovoltaic cells. Figure 9.10 reproduces some of the technical details for the PhotoWatt photovoltaic cell 6MB. The first portion of the figure reproduces a visual image of the cell as well as presenting information on the size and materials used and some construction details. The table in the middle segment of the figure delineates the open-circuit voltage, short-circuit current, efficiency, and fill factor (FF) for a sampling of 6MB cells. The FF is defined as the ratio of the maximum power $V_{mp}I_{mp}$ from the solar cell to the product of V_{oc} and I_{sc}:

$$\text{FF} = \frac{V_{mp}I_{mp}}{V_{oc}I_{sc}}$$

The general irradiation level used for photovoltaic cell testing is 1000 W/m^2. The open-circuit voltage is ~0.62 V, and the short-circuit current is ~8.7 A. An examination of the numbers confirms that if appreciable power and voltage are to be attained, then more than a single cell will be needed. Modules are devised by placing photovoltaic cells in series and parallel arrangements.

Series and parallel configurations of solar cells follow the same rules as series and parallel DC circuits. For identical components placed in a series arrangement, the voltages add at constant current, and for identical components placed in parallel, the currents add at constant voltage. Consider the graphical visualization of placing two identical cells in series and then in parallel in Figure 9.11. For cells in series, Figure 9.11a, the voltages add at constant values of the current; hence, placing cells in series results in increasing the voltage. Cells in parallel, Figure 9.11b, result in increasing the current. Consider Example 9.2.

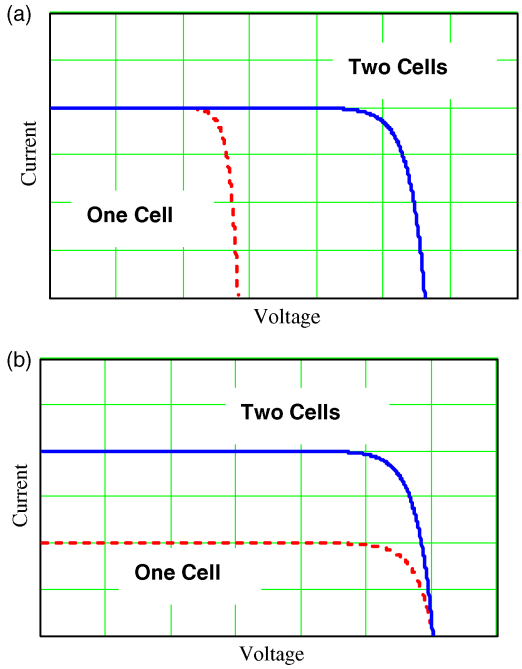

Figure 9.11 Behavior of cells in series and parallel: (a) two identical cells in series; (b) two identical cells in parallel.

Example 9.2

PhotoWatt 6MB photovoltaic cells are to be arranged to provide an output of 12 V and a power of 210 W. Recommend an arrangement that meets the specifications.

Solution From Figure 9.10, representative open-circuit voltage and short-circuit current are 0.622 V and 8.625 A respectively, with an FF of 0.787. The power output for these conditions is

$$\text{Power} = I_{sc} V_{oc} \times \text{FF} = 0.622\,\text{V} \times 8.625\,\text{A} \times 0.787 = 4.22\,\text{W}$$

The number of cells required for 120 W is

$$\text{Number of cells} = \frac{210\,\text{W}}{4.22\,\text{W/cell}} = 49.8\,\text{cells}$$

To provide the correct voltage, 12 V, the number of cells in series must be

$$\text{Cells in series} = \frac{12\,\text{V}}{0.622\,\text{V/cell} \times 0.787} = 24.5\,\text{cells}$$

where the voltage at the maximum power is approximated as $V_{oc} \times \text{FF}$. Round the number of cells in series to 25 cells. Two rows of 25 cells in parallel will require 50 cells with a total power of 211 W. The recommended configuration is sketched in Figure 9.12.

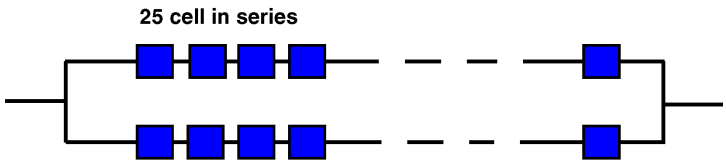

Figure 9.12 Cell configuration for Example 9.2.

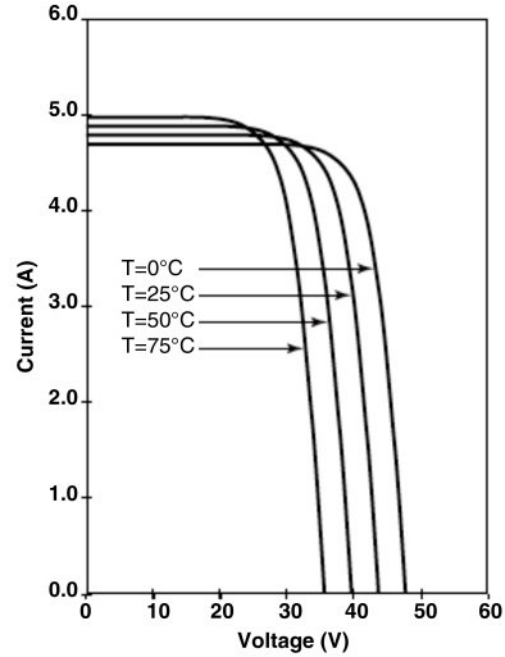

	BP 3160	BP 3150
Maximum power (P_{max})	160W	150W
Voltage at P_{max} (I_{mp})	35.1V	34.5V
Current at P_{max} (I_{mp})	4.55A	4.34A
Warranted minimum P_{max}	150W	140W
Short-circuit current (I_{sc})	4.8A	4.75A
Open-circuit voltage (V_{oc})	44.2V	43.5V
Temperature coefficient of I_{sc}	(0.065±0.015)%/°C	
Temperature coefficient of voltage	-(160±20)mV/°C	
Temperature coefficient of power	-(0.5±0.05)%/°C	
NOCT	47±2°C	

Figure 9.13 Specifications for BP 3160 photovoltaic module. NOCT: normal operating cell temperature. *Source*: BP Solar.

Example 9.2 illustrates how individual solar cells can be arranged to provide specified voltage and power. Such an arrangement is called a module and is the typical product marketed by many photovoltaic manufacturers. Photovoltaic cells are arranged as described to provide certain specifications. However, in order to ensure proper module operation under realistic conditions, such as failure of an individual cell or shading of a portion of a module, in-series elements in arrays are usually provided with blocking diodes to prevent reverse current flow and other inefficiencies.

BP Solar was an important international manufacturer of photovoltaic cells and components until they closed in December 2011. Information on the BP 3160 photovoltaic module is provided in Figure 9.13 and is typical of what is on the market. BP Solar modules are still available from the internet.

The BP 3160 measures 62.8 in by 31.1 in by 1.97 in deep and weights 33.1 lb. The price of the BP 3160 was $719 in 2008 (www.solarhome.org). The price (summer 2015) for 1 kW of BP 3160

modules would be about $5000. A visual image of the module appears in Figure 9.13 next to the I–V curve. The I–V information is parameterized by temperature but conforms to the expected shape. Additional performance details of the module are in the accompanying table. All of Figure 9.13 was abstracted from the BP Solar web site prior to their closing.

The I–V curve and the tabular information are similar to that associated with an individual photovoltaic cell, which is not surprising since series and parallel arrangements of individual solar cells retain the same functional forms. The solar irradiation level corresponding to the performance data for the BP E3160 was 1000 W/m^2. Temperature coefficients α, β, and γ are provided for current, voltage, and power respectively. These permit the effects on module performance of different temperatures to be estimated. The corrections for temperature are as follows:

$$I_{sc} = I_o(1 + \alpha \Delta T) \tag{9.12}$$

$$V_{soc} = V_o(1 + \beta \Delta T) \tag{9.13}$$

$$\text{Power} = \text{Power}_o(1 + \gamma \Delta T) \tag{9.14}$$

where the subscript "o" represents conditions at the reference temperature. An example is in order.

Example 9.3
Estimate the annual kilowatt-hour production of one BP E160 module in Meridian, MS. Examine two cases: (1) constant tilt at the latitude angle and (2) two-axis tracking.

Solution The solution is accomplished in Mathcad. The Mathcad worksheet is reproduced as Figure 9.14. The days in each month are defined. The *Solar Radiation Data Manual for Flat-Plate and Concentrating Collectors* (Marion and Wilcox, 1994) provides the necessary solar data for the performance estimates. The data for Meridian, MS, from the manual are reproduced as Figure 7.12. For part 1 of the problem, the average monthly data for a surface tilted at the latitude angle is used for the solar irradiation incident on the module and is entered in the vector $\mathbf{I}_F$. For part 2, the average monthly data for a surface with two-axis tracking (as in Figure 7.3) is used for the solar irradiation incident on the module and is entered in the vector $\mathbf{I}_T$. The irradiation is given in the units of kilowatt-hours per square meter per day. The nominal power from the module is 160 W at an irradiation of 1000 W/m^2. The electrical generation per day for part 1 is computed as

$$\text{ElecF}_{day} = \frac{160\ \text{W}}{1000\ \text{W/m}^2}\mathbf{I}_F \tag{9.15}$$

This expression asserts that the electrical generation is directly proportional to the irradiation level. This assertion introduces some error in the calculations, but considering the uncertainties in the input values the error is acceptable. The monthly electricity produced E_t is found by multiplying the daily production by the number of days per month. The yearly total EtotF is obtained by adding the monthly values. The same procedure is followed for part 2, except that the average monthly data for a surface with two-axis tracking $\mathbf{I}_T$ is used. The yearly electricity produced by the BP 3160 module tilted at the latitude angle is 286 kWh, while the module with two-axis tracking produces 368 kWh. For the BP 3160 module placed at Meridian, MS, two-axis tracking significantly increase electricity production. The monthly generation is plotted in Figure 9.15 for both parts of the problem.

NREL provide an online calculator, PVWatts, for monthly/yearly photovoltaic performance estimates. The online calculator is available at http://pvwatts.nrel.gov/pvwatts.php, and a

ORIGIN≡ 1

Set up all input parameters on a monthly basis using the range variable i:

i := 1 .. 12

The monthly-average conditions from NREL are used to obtain solar and weather data for the location, Meridian, MS, in this case.

Define month in terms of days.

$$\text{month} := \begin{pmatrix} 31 \\ 28 \\ 31 \\ 30 \\ 31 \\ 30 \\ 31 \\ 31 \\ 30 \\ 31 \\ 30 \\ 31 \end{pmatrix} \cdot \text{day} \qquad \begin{pmatrix} \text{jan} \\ \text{feb} \\ \text{mar} \\ \text{apr} \\ \text{may} \\ \text{jun} \\ \text{jul} \\ \text{aug} \\ \text{sep} \\ \text{oct} \\ \text{nov} \\ \text{dec} \end{pmatrix}$$

$$I_F := \begin{pmatrix} 3.6 \\ 4.4 \\ 5.0 \\ 5.6 \\ 5.6 \\ 5.6 \\ 5.4 \\ 5.5 \\ 5.2 \\ 5.2 \\ 4.1 \\ 3.5 \end{pmatrix} \cdot \frac{\text{kW} \cdot \text{hr}}{\text{m}^2 \cdot \text{day}} \qquad I_T := \begin{pmatrix} 4.5 \\ 5.4 \\ 6.2 \\ 7.2 \\ 7.6 \\ 7.8 \\ 7.3 \\ 7.1 \\ 6.5 \\ 6.4 \\ 5.1 \\ 4.4 \end{pmatrix} \cdot \frac{\text{kW} \cdot \text{hr}}{\text{m}^2 \cdot \text{day}}$$

Nominal power generation is 160 W at an irradiation of 1000 W/m^2 irradiation.

$$E_{f_i} := 160 \cdot \text{W} \cdot I_{F_i} \cdot \frac{\text{month}_i}{1000 \cdot \frac{\text{W}}{\text{m}^2}} \qquad E_{t_i} := 160 \cdot \text{W} \cdot I_{T_i} \cdot \frac{\text{month}_i}{1000 \cdot \frac{\text{W}}{\text{m}^2}}$$

$$E_f = \begin{pmatrix} 17.856 \\ 19.712 \\ 24.8 \\ 26.88 \\ 27.776 \\ 26.88 \\ 26.784 \\ 27.28 \\ 24.96 \\ 25.792 \\ 19.68 \\ 17.36 \end{pmatrix} \cdot \text{kW} \cdot \text{hr} \qquad E_t = \begin{pmatrix} 22.32 \\ 24.192 \\ 30.752 \\ 34.56 \\ 37.696 \\ 37.44 \\ 36.208 \\ 35.216 \\ 31.2 \\ 31.744 \\ 24.48 \\ 21.824 \end{pmatrix} \cdot \text{kW} \cdot \text{hr}$$

$$\text{EtotF} := \sum_{i=1}^{12} E_{f_i} \qquad \text{EtotF} = 285.76\,\text{kW hr} \qquad \text{EtotT} := \sum_{i=1}^{12} E_{t_i} \qquad \text{EtotT} = 367.632\,\text{kW hr}$$

Figure 9.14 Mathcad worksheet for Example 9.3.

detailed manual is also available (Dobos, 2014). The results of Example 9.3 agree to within a few percentage points if inverter losses of 4% ($\eta_i = 0.96$) and systems losses of 14% ($\eta_t = 0.86$) are considered in Example 9.3. To account for these losses, Equation 9.15 is replaced by

$$\text{ElecF}_{\text{day}} = \frac{160\ \text{W}}{1000\ \text{W/m}^2} \mathbf{I}_F \times 0.96 \times 0.86 \tag{9.16}$$

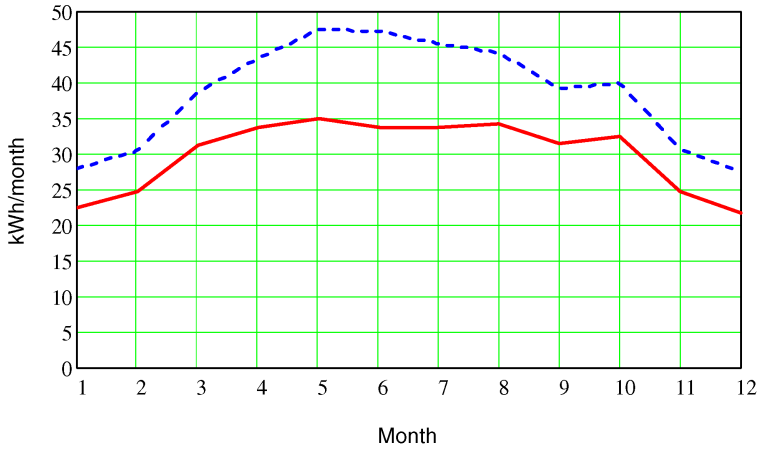

Figure 9.15 Monthly kilowatt-hour generation for Example 9.3.

Figure 9.16 A 49 kW photovoltaic array. *Source*: http://images.nrel.gov/viewphoto.php?imageId=6322492.

Modules, such as in Example 9.3, are assembled into arrays utilizing the series/parallel principles as for cells into modules. Figure 9.16 is an example of a photovoltaic array. The arrays are rated at 49 kW and were made by Solar Energy Systems and installed in Queens, New York.

9.4 Photovoltaic Systems

Photovoltaic systems come in a wide range of sizes and functions. The two principal classifications of photovoltaic systems are stand-alone and grid connected (or utility interactive). Stand-alone photovoltaic systems are not connected to the electric grid. Functional uses in an increasing hierarchy of complexity of photovoltaic systems are as follows:

1) direct coupled
2) systems with battery storage
3) systems with backup (generator) power

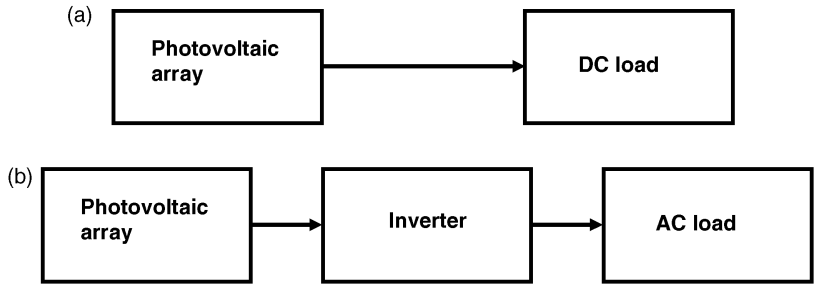

Figure 9.17 Direct-coupled photovoltaic system schematics: (a) DC load; (b) AC load.

4) hybrid power systems
5) systems connected to the electrical grid
6) systems for utility power production.

The first four in this list are generally stand-alone systems. The Florida Solar Energy Center (FSEC) presents schematics and some discussion on a variety of photovoltaic systems. Some of the schematics in this section are adaptations and modifications of the system schematics from the FSEC. The website is http://www.fsec.ucf.edu/en/consumer/solar_electricity/basics/types_of_pv.htm.

A direct-coupled photovoltaic system supplies DC power directly to the load or AC power, via an inverter, directly to the load. The schematics of direct-coupled systems (DC or AC) are presented in Figure 9.17. Such systems are frequently used for specific, usually low-kilowatt requirements – applications for which grid electricity is not available. With no grid connection, backup generation, or storage capability, stand-alone systems are completely dependent on solar irradiation for power generation and operation. Nonetheless, these are important "niche" applications for photovoltaics.

One of the disadvantages of direct-coupled photovoltaic systems is their inability to operate except when exposed to solar irradiation. A photovoltaic system with battery storage eliminates this disadvantage and permits operation during the night hours or when the solar irradiation is insufficient to meet the required electrical demand. Figure 9.18 schematically illustrates a photovoltaic system with battery storage. The charge controller, a key component, directs the

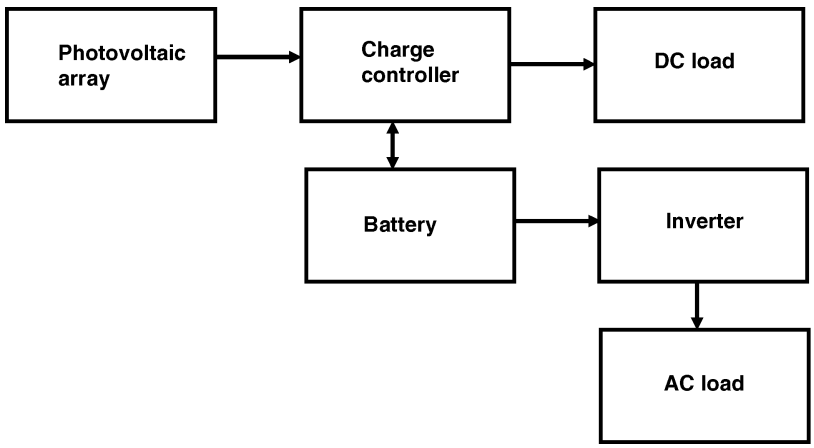

Figure 9.18 Stand-alone photovoltaic system with battery storage.

Table 9.3 Depth of discharge versus cycles (East Penn Deka)

Depth of discharge (%)	Cycles
10	5700
25	2100
50	1000
80	600
100	450

output of the photovoltaic array to the load and to battery recharging when electricity is being generated; when the array is not generating, it extracts electrical energy from the battery for the load. It also provides the capability to direct battery power to an inverter for AC loads. Conventional AC devices can be powered by a system with an inverter. In 2015, the installed cost of a nominal 5 kW, non-grid-connected system with battery backup (nominally 20 kWh) was about $35 000, depending on options exercised. Federal and state tax credits as well as utility rebates, depending on the location, can be used to offset installation costs for such systems. The internet contains a number of web sites offering a wide range of solar photovoltaic systems.

Battery characteristics and requirements for photovoltaic system applications are important and merit review. Typical battery metrics include the voltage, the charge capacity, the cycle capability, and the depth of discharge. The first two metrics, voltage and charge capacity, are used to specify the energy storage/retrieval potential of the battery. The voltage across the battery terminals is specified in volts, and the charge capacity of a battery is rated in the units of amp-hours. The product of the voltage and charge capacity yields the energy stored in the battery. For example, a 12 V battery with a charge capacity of 50 A h stores 600 V A h = 600 Wh = 0.6 kWh of energy.

Cycle capability refers to the number of charge/discharge cycles expected from the battery. The depth of discharge specifies how much (what percentage) of the stored energy at full capacity may be extracted without damaging the battery. Batteries for photovoltaic application require high cycle capacity as well as high depth of discharge capability. Automotive batteries require a large amount of power draw over a short period of time (engine cranking time) with a low depth of discharge. Thus, automotive batteries are not suitable for solar storage applications.

An example of a deep cycle set is the East Penn's MK Solar® 8G8D battery (www.eastpennmanufacturing.com, http://www.mkbattery.com/images/8G8D.pdf). Table 9.3 lists the depth of discharge versus the number of expected cycles for a Solar 8G8D battery. Each Solar 8G8D battery provides nominally 188–265 A h and weighs 166 lb. Thus, a six-cell pack capacity would be 1128–1590 A h, depending on the discharge rate. Prices (summer 2015) per battery vary from $500 to $700 on various websites or $3000 to $4200 for the stated capacity for six. Hence, the storage energy in a battery is relatively expensive as the set stores 1128–1590 A h for $3000–$4200.

As Table 9.3 indicates, depth of discharge significantly affects battery life. Most solar photovoltaic systems require long life from batteries.

Example 9.4

How many Solar 8G8D batteries would be needed to store and retrieve 10 kWh per day for 4 days (96 h) for a solar photovoltaic system.

Solution The battery system must store/retrieve

$$\text{EnergyStorage} = 10\frac{\text{kWh}}{\text{day}} \times 4\ \text{days} = 40\ \text{kWh} = 40\,000\ \text{Wh}$$

If the depth of charge is specified to be 50%, then the battery storage capacity must be 80 kWh. A single battery set stores 265 A h × 12 V = 3180 A h V = 3.1 kWh. So the number of sets is

$$\text{Number} = \frac{80\ \text{kW/battery}}{3.18\ \text{kW}} = 25\ \text{batteries}$$

Six battery pack sets of six batteries each would meet the requirement if the depth of discharge were increased to slightly more than 50%. An alternative solution would be to purchase 12 six-packs with the expectation of replacing them half as frequently. Table 9.3 shows that decreasing the depth of discharge from 50% to 25% results in slightly more than double the discharge cycles. The long-term costs of either option will be approximately the same.

Lazard, a financial advisory and asset management firm, in November 2015 released the results of a study to quantify the cost of storing and retrieving electricity (Lazard, 2015). The study showed wide variations in costs depending on the storage technology and usage, transmission system or photovoltaic system, for example. For photovoltaic systems, the cost estimates ranged from about $0.13/kWh to over $1.00/kWh, depending on the study parameters, technology, and assumptions. The variations in cost per kilowatt-hour are large for photovoltaic systems, but on a comparative basis the photovoltaic system costs are approaching the cost per kilowatt-hour of other storage technologies; pumped hydroelectric's low estimate was about $0.10/kWh. The results of the Lazard study are congruent with other cost estimates for storage and retrieval of electricity. Since the storage/retrieval cost per kilowatt-hour can be more than a grid kilowatt-hour would cost, photovoltaic systems with battery backup require a detailed economic analysis in order to establish economic feasibility.

A photovoltaic hybrid system results if a stand-alone system with battery storage is provided with a non-grid source of electricity (typically a generator driven by a prime mover). A schematic of a hybrid system is provided in Figure 9.19. The system schematic for a hybrid system is similar to a stand-alone system with battery storage with the addition of a non-grid source of electricity and a rectifier. The rectifier is used to convert AC from an AC generator to DC for battery charging. When photovoltaic output and/or the battery are insufficient to meet the loads

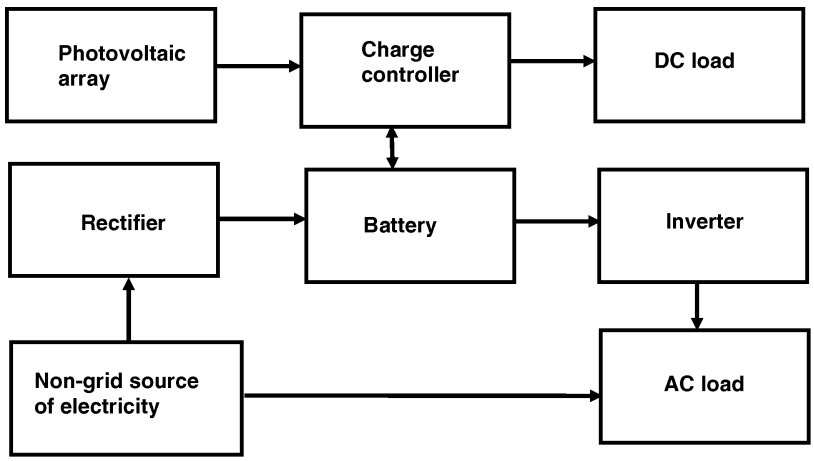

Figure 9.19 Photovoltaic hybrid system.

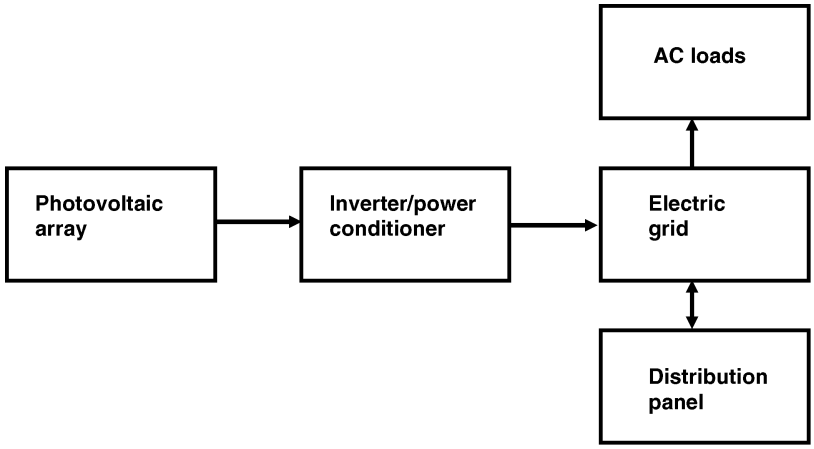

Figure 9.20 Schematic of a grid-connected photovoltaic system.

(AC and DC), the "other" source of electricity is then used to make up the difference. Such a system provides great flexibility, but for grid-connected systems the utility rate structure can be economically constraining. If large tariffs or penalties are exacted when grid power is used, the cost per kilowatt-hour of grid power can be excessive.

Photovoltaic systems can be used to supply electricity to the grid. A grid-connected photovoltaic system schematic is illustrated in Figure 9.20. In any photovoltaic system connected to the grid, the power from the solar arrays must be compatible with the voltage, frequency, and phase of the grid. IEEE Standard 1547 (Interconnecting Distributed Resources with Electric Power Systems) delineates the requirements for grid connectivity of photovoltaic systems. In 2015, the installed cost of a nominal 5 kW, grid-connected system was about $20 000, depending on options exercised. Federal and state tax credits as well as utility rebates may also apply. The internet is a good source of information and costs for a wide range of solar photovoltaic systems.

One issue with grid-connected systems is the price per kilowatt-hour paid by the utility to the system owner. Photovoltaic systems with high installed kilowatts may be owned by utilities, but low-kilowatt residential and commercial systems are likely to be privately owned. PURPA, the Public Utilities Regulatory Policies Act of 1978, delineates the federal regulatory requirements for most public utilities. Because of the complexity of PURPA, the US Department of Energy provides a web site (http://energy.gov/oe/services/electricity-policy-coordination-and-implementation/other-regulatory-efforts/public) with details and explanations of many PURPA features. Under PURPA a utility must purchase any kilowatt-hour offered by the owner of a photovoltaic system, but the utility is mandated to only pay its levelized cost of producing 1 kWh. In many instances the levelized cost is only 2–3¢/kW h. A much more advantageous arrangement for the seller is "net metering." In net metering, power drawn from the grid results in an increase in kilowatt-hour consumption, while power supplied to the grid results in a decrease in kilowatt-hour usage. The result is that the utility pays the same for a purchased kilowatt-hour as for a sold kilowatt-hour, a much better arrangement for a photovoltaic system owner than receiving the levelized cost for the purchase price of a kilowatt-hour. Since photovoltaic generating is considered as green power, many utilities are willing to participate in a net metering arrangement. The Energy Policy Act of 2005 requires utilities to consider net metering as well as other retail/wholesale, sale/purchase procedures; however, it does not require a utility to implement net metering, only to consider it. A formal agreement with the utility is needed by any owner contemplating selling power to the utility.

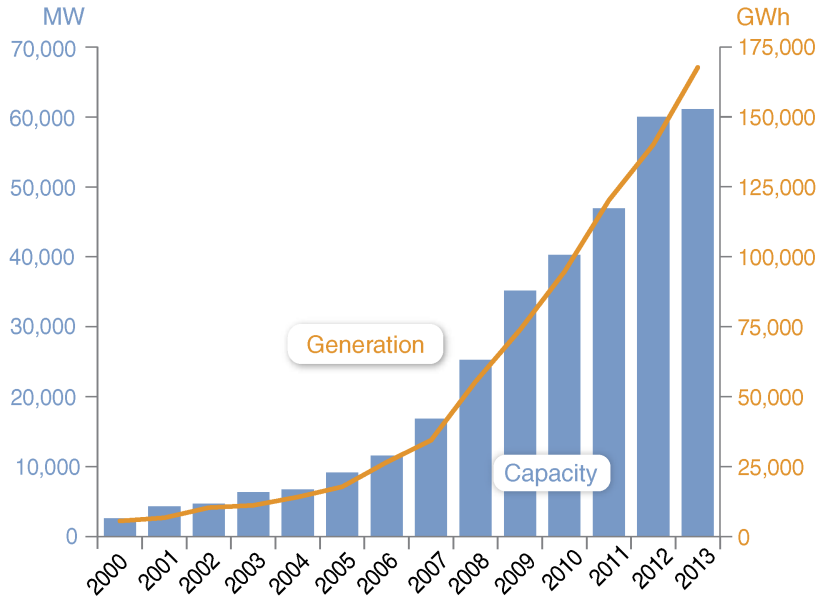

Figure 9.21 USA total installed photovoltaic capacity 2000 through 2013. *Source*: Esterly and Gelman (2014: 54).

9.5 Growth in Photovoltaic Capacity

Concerns over energy costs and environmental issues (greenhouse gas emissions and climate change) have made photovoltaic systems increasingly popular. As part of the Department of Energy's SunShot initiative, NREL monitors, analyzes, and reports statistics and costs relating to installed photovoltaic systems. Results through 2013, and projections through 2016, are reported by Feldman *et al.* (2014). Figure 9.21 presents the total installed peak kilowatt capacity for photovoltaic cells and the annual gigawatt-hour (1×10^6 kWh) generation from photovoltaic systems in the USA from 2000 through 2013. After being flat through the last years of the decade of the 1990s, photovoltaic system installed capacity after the millennium dramatically increased. From 1985 through 2000 (see Figure 1.14), the inflation-adjusted price per kilowatt-hour of residential electricity gradually decreased, but after 2000 the price gradually increased, providing more economic incentive for solar photovoltaic. Another reason is the dramatic decrease in the price per watt of installed photovoltaic. Figure 9.22 portrays the installed cost per watt of

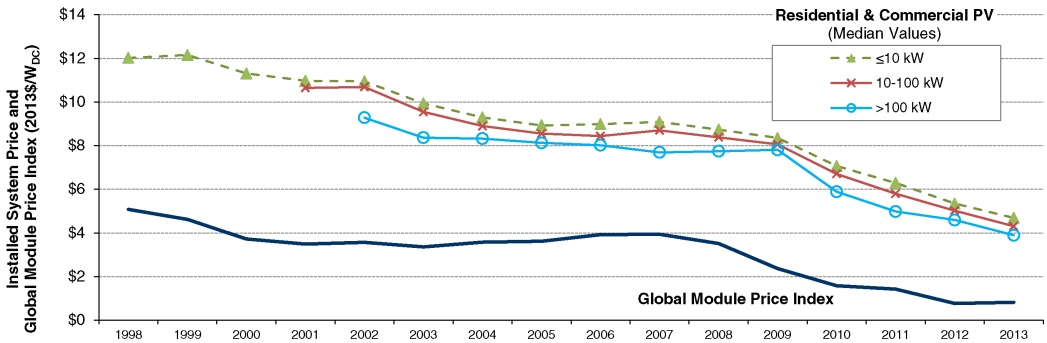

Figure 9.22 Installed costs per watt for photovoltaic systems for the USA and global module price index. *Source*: Feldman *et al.* (2014: 8).

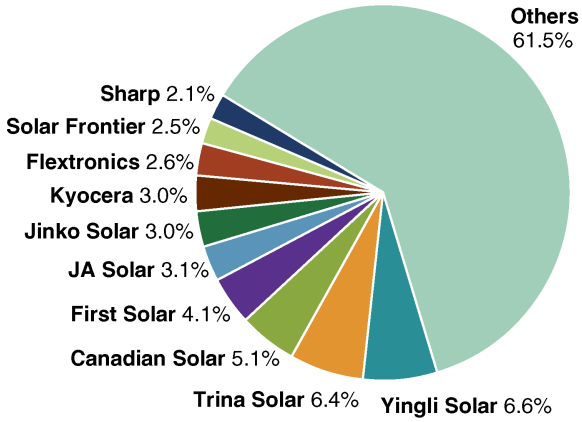

Figure 9.23 The 2013 photovoltaic module production percentages by manufacturer. *Source*: Esterly and Gelman (2014: 66).

photovoltaic capacity as a function of system size (<10 kW, 10–100 kW, and >100 kW) from 1998 until 2013. Also reported in the figure is the average module selling price per watt, the global module price index. Since 2001, the cost per watt has monotonically decreased (except for 2007), but since 2009 the decrease in cost has been more pronounced. Overall, the decrease has been quite dramatic from 2002 until 2013: about 50%! This cost decrease has made photovoltaic systems more attractive economically. The global module price index has fallen from about \$4/W in 2007 to about \$1/W in 2013 – a decrease of 75%! An interesting factoid is that while the installed price of residential photovoltaic systems in the USA was \$3.29/W in 2013, the installed price in Germany was \$2.05/W. Utility-scale projects (>100 kW) costs are more complex, depending on arrangement (fixed tilt, tracking, concentrating) as well as photovoltaic cell type (thin film, crystalline), but have exhibited installation cost decreases of about 50% since 2007 – see page 14 of Feldman *et al.* (2014).

Figure 9.23, from the *2013 Renewable Energy Data Book* (Esterly and Gelman, 2014), contains a breakdown, worldwide, of companies manufacturing photovoltaic cells. The figure provides an interesting contrast to Figure 4.30 that shows the production percentages by manufacturer for wind power in the USA. Whereas, at least in the USA, more than 70% of the wind turbines are supplied by GE, Siemens, and Vestas, for photovoltaic modules no individual company worldwide has more than a 7% share of the market. More than 60% of the worldwide market is supplied by companies with less than a 2% market share each. An interpretation is that significant consolation has already taken place in the wind power sector, but the photovoltaic manufacturing sector has experienced little consolation. In recent years, BP Solar has exited the solar photovoltaic arena to concentrate on other sectors. Two additional interesting metrics from Esterly and Gelman (2014) are (1) in 2013, China installed, at 25 610 MW, 64% of the capacity in the world and (2) 65% of the photovoltaic cells manufactured worldwide are multiple-junction silicon.

9.6 Closure

Although solar photovoltaics in the USA have not experienced the growth of wind energy, decreasing cost of solar photovoltaic systems is likely to impact the installation of such systems. As Figure 9.22 attests, costs for residential, commercial, and utility-scale photovoltaic systems have dramatically decreased in the last few years. These cost decreases have made solar photovoltaic more attractive economically, so that additional growth is anticipated.

The Solar Energy Industries Association (www.seia.org) provides an alphabetical listing of manufacturers of solar energy related items, including photovoltaic cells.

References

Dobos, A.P. (2014) *PVWatts Version 5 Manual.* Technical Report NREL/TP-6A20-62641. http://www.nrel.gov/docs/fy14osti/62641.pdf (accessed October 20, 2016).

Duffie, J.A., and Beckman, W.A. (2006) *Solar Engineering of Thermal Processes*, 3rd edn. John Wiley & Sons, Inc., New York.

Esterly, S. and Gelman, R. (2014) *2013 Renewable Energy Data Book*, Haas, K. (ed.). DOE/GO-102014-4491. http://www.nrel.gov/docs/fy15osti/62580.pdf (accessed October 20, 2016).

Feldman, D., Barbose, G., Margolis, R., *et al*. (2014) *Photovoltaic System Pricing Trends: Historical, Recent, and Near-Term Projections, 2014 Edition.* NREL/PR-6A20-62558. http://www.nrel.gov/docs/fy14osti/62558.pdf (accessed October 20, 2016)

Goswami, Y., Kreith, F., and Kreider, J.F. (2000) *Principles of Solar Engineering*, 2nd edn. Taylor and Francis, New York.

Kreith, F., and West, R.E. (1997) *CRC Handbook of Energy Efficiency*. CRC Press, Boca Raton, FL.

Lazard (2015) Lazard's Levelized Cost of Storage Analysis-Version 1. November. https://www.lazard.com/media/2391/lazards-levelized-cost-of-storage-analysis-10.pdf (accessed October 20, 2016).

Marion, W. and Wilcox, S. (1994) *Solar Radiation Data Manual for Flat-Plate and Concentrating Collectors*. NREL, Golden, CO.

Patel, M.R. (2005) *Wind and Solar Power Systems*, 2nd edn. Taylor & Francis, New York.

10

Fuel Cells

10.1 Introduction

In a conventional "fired" combustion system, a fuel (usually a hydrocarbon) reacts with an oxidizer (typically the oxygen in the air) to release the chemical energy stored in the fuel as heat. In a fuel cell, the chemical energy stored in the fuel is converted directly to useful work, electricity, without going through the process of combustion. For both combustion systems and fuel cells, the chemical equation describing the reaction is

$$\text{Fuel} + \text{Oxidizer} \rightarrow \text{Products} + \text{Chemical energy} \tag{10.1}$$

If the thermodynamic states of the fuel, oxidizer, and products are the same for both cases, then the heat released from combustion process and the work from the fuel cell's electrochemical reaction must be equal.

A fuel cell is not a heat engine, so the Carnot bound on efficiency does not apply. One of the reasons why fuel cells are of interest is that their efficiencies are higher than efficiencies of heat engines.

10.2 Fuel Cell Fundamentals

Fuel cells are similar to batteries in that both produce direct current (DC) via an electrochemical process in the absence of direct combustion of a fuel source. However, a battery can deliver power only from stored energy (a finite amount), but a fuel cell can operate as long as proper fuel and oxidizer sources are available. A fuel cell consists of an anode, an electrolyte, and a cathode. Weston (1992) presents a useful discussion of fuel cell components and thermodynamics. Figure 10.1 is a schematic of a typical hydrogen and oxygen fuel cell with a load. At the anode, a catalytic reaction splits the fuel into ions and electrons, and the ions pass from the anode, through an electrolyte, to the cathode.

The electrons pass through an external circuit to the load. At the anode, the hydrogen (H_2) dissociates into two hydrogen ions ($2H^+$) and two electrons ($2e^-$). The hydrogen ions pass through the electrolyte to the cathode where they combine with oxygen and the two electrons that have traversed the load to form water.

The fuel and the electrolyte determine the reactions at the anode and the cathode as well as the voltage produced by a single anode–cathode pair. Catalysts are generally needed at the anode and cathode to increase the reaction rates to acceptable levels. The catalysts required by some fuel cell types are precious metals, which increase the cost per kilowatt for a fuel cell. Section 10.3 examines the reactions produced by different electrolytes. Although a number of fuel–oxidant–electrolytes are available, the hydrogen–oxygen fuel cell is the most common.

Alternative Energy Systems and Applications, Second Edition. B. K. Hodge.

Companion website: www.wiley.com\go\Hodge\AESystemsandApplications2E

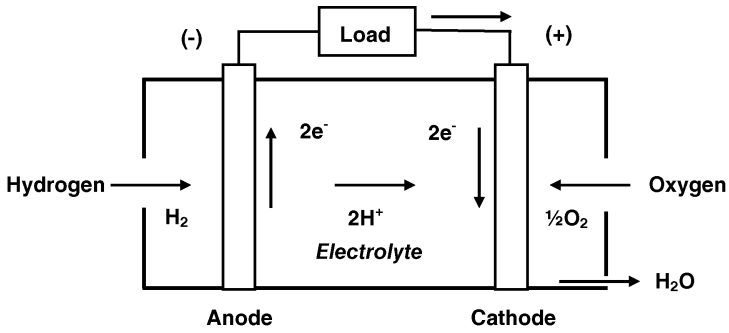

Figure 10.1 Schematic of a hydrogen/oxygen fuel cell.

Individual fuel cells produce between 0.5–0.9 V of DC electricity. Fuel cells are combined into "stacks" to obtain usable voltage and power output. The same rules apply for combining fuel cells in series and parallel as for combining photovoltaic cells in series and parallel (see Chapter 9). A fuel cell "stack" element is illustrated in Figure 10.2.

The repeating unit, a fuel cell stack element, is a single fuel cell and contains the anode, electrolyte, cathode, fuel flow channel, and oxidant flow channel. The stack is constructed by assembling the repeating units in series, with the result that the voltages of the units add to each other, while the transverse surface area determines the amperage.

A fuel cell system is composed of three major components: a fuel reformer (processor) that generates hydrogen-rich gas from fuel, a power section where the electrochemical process occurs, and a power conditioner (inverter) that converts the DC electricity generated in the fuel cell into alternating current (AC) electricity. If a fuel cell is to be connected to the grid, then the power conditioner must synchronize the electrical output to the grid in accordance with IEEE 1547. A simplified block diagram of a typical fuel cell system is illustrated in Figure 10.3.

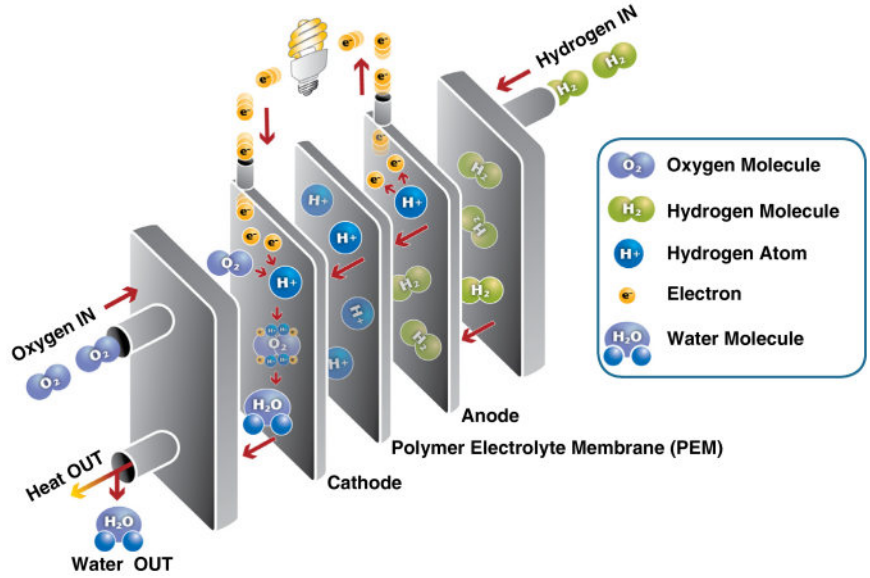

Figure 10.2 Fuel cell stack element. *Source:* http://energy.gov/sites/prod/files/2014/03/f10/fct_h2_fuelcell_factsheet.pdf.

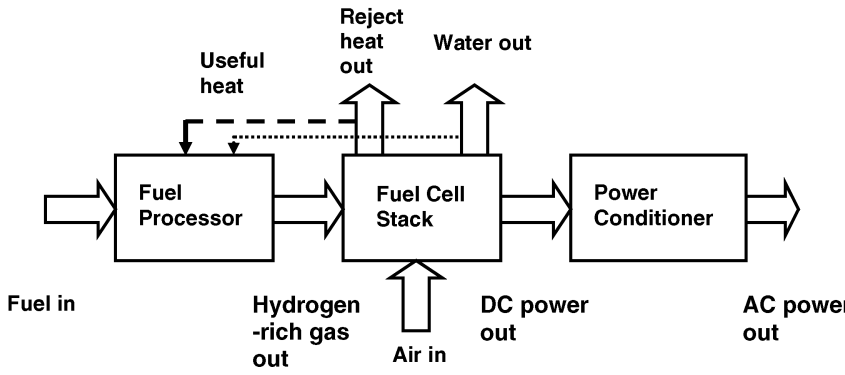

Figure 10.3 Fuel cell block diagram.

Natural gas, which is mostly methane, is readily available and is one of the cleanest fuels (next to hydrogen) for powering fuel cells. Much research is focused on natural-gas-powered fuel cells, but fuel cells can also be powered by propane, diesel fuel, fuel oil, and other fuels as well as bio-derived fuels.

For methane, the fuel processor utilizes steam reforming followed by a shift reaction. Reforming the fuel with steam concentrates the hydrogen and removes contaminants that could otherwise poison the catalyst in the cell. The chemical reaction for steam reforming is

$$CH_4 + H_2O \rightarrow CO + 3H_2 \tag{10.2}$$

The steam reforming reaction is an endothermic reaction with $\Delta H = 206\,\text{kJ/mol}$. The carbon monoxide (CO) in the mixture can be used to produce more hydrogen by the water-gas "shift" reaction:

$$CO + H_2O \rightarrow CO_2 + H_2 \tag{10.3}$$

The water-gas shift reaction is an exothermic reaction with $\Delta H = -41\,\text{kJ/mol}$. Taken together the two processes result in

$$CH_4 + 2H_2O \rightarrow CO_2 + 4H_2 \tag{10.4}$$

The output of the fuel processor is thus carbon dioxide and hydrogen. Hoogers (2002) contains a chapter on reforming techniques and procedures and comparisons of different reactions and is a good choice for additional information.

10.3 Fuel Cell Thermodynamics Fundamentals

Details of the thermodynamics of fuel cells are provided in references such as Appleby and Foulkes (1989), Kinoshita *et al.* (1988), and Li (2006). The energy released in a chemical reaction is equal to the change in the enthalpy of formation ΔH. ΔH is the sum of the enthalpies of formation for the products minus the sum of the enthalpies of formation of the reactants:

$$\Delta H = \sum \Delta H_{\text{products}} - \sum \Delta H_{\text{reactants}} \tag{10.5}$$

ΔH is negative for an exothermic reaction and positive for an endothermic reaction. If all the energy in the chemical reaction were converted into electrical energy, then

$$W_e = \Delta H \tag{10.6}$$

where W_e is the electrical generation per mole of fuel. However, some of the chemical energy is converted into internal thermal energy. The minimum amount of internal thermal energy, if the heat transfer process were reversible, would be equal to

$$Q_{te} = \int T\,ds \tag{10.7}$$

The fuel cell is essentially an isothermal device and

$$Q_{te} = \int T\,ds = T\int ds = T\Delta S \tag{10.8}$$

The maximum amount of electrical energy produced by an isothermal fuel cell then becomes

$$W_e \leq \Delta H - T\Delta S \tag{10.9}$$

where the equal sign is for a reversible reaction and the less-than sign for a fuel cell with irreversibilities. The Gibbs free energy is defined as

$$G = H - TS \tag{10.10}$$

which for an isothermal process can be cast as

$$\Delta G = \Delta H - T\Delta S \tag{10.11}$$

Hence, for a fuel cell:

$$W_e \leq \Delta G \tag{10.12}$$

Since ΔH and ΔG are usually expressed per mole, the above equations are on a per mole basis and W_e is the electrical energy of a mole of electrons passing through the circuit. A kilogram-mole of electrons contains 6.022×10^{26} electrons, each with a charge of 1.602×10^{-19} C. The charge contained in a kilogram-mole of electrons is thus 9.65×10^{7} C/kg-mol-electron, Faraday's constant F_c.

For a given reaction, ΔG becomes

$$\Delta G = \sum \Delta G_{\text{products}} - \sum \Delta G_{\text{reactants}} \tag{10.13}$$

The general thermodynamic relationship from the first law can be expressed as

$$V\,dp = dH - T\,ds \tag{10.14}$$

so that

$$dG = V\,dp \tag{10.15}$$

The thermal equation of state, in per mole form, is

$$V = \frac{R_g T}{p} \tag{10.16}$$

with R_g the universal gas constant, 8.314 kJ/(kg-mol K) or 1545 ft lbf/(lbm mol °R). Integrating Equation 10.15 between a reference state, designated by the superscript "o" at 1 atm pressure and a general state at p yields

$$\int_{G^\circ}^{G} dG = R_g T \int_{p^\circ}^{p} \frac{dp}{p} = G - G^\circ = R_g T \ln\left(\frac{p}{p^\circ}\right) \tag{10.17}$$

If the pressure is expressed in atmospheres, then $p^\circ = 1$ atm and

$$G = G^\circ + R_g T \ln p \tag{10.18}$$

The general chemical reaction for a fuel cell can be written as

$$a\mathrm{A} + b\mathrm{B} \rightarrow c\mathrm{C} + d\mathrm{D} \tag{10.19}$$

If the reactants and products are ideal gases with partial pressures of p_A, p_B, p_C, and p_D then application of Equation 10.19 to Equation 10.18 yields

$$\Delta G = \Delta G^\circ + R_g T \ln\left(\frac{p_A^a\, p_B^b}{p_C^c\, p_D^d}\right) \tag{10.20}$$

If n moles of electrons are released by the reaction and the internal cell voltage is E_c, then for a fuel cell with reversible reactions the electric power becomes

$$W_e = nF_c E_c \approx \Delta G \tag{10.21}$$

Since $E_c = \Delta G / nF_c$, Equation 10.20 for the reaction of Equation 10.19 takes the form (with the log term inverted)

$$E_g = E_g^\circ - \frac{R_g T}{nF_c} \ln\left(\frac{p_C^c\, p_D^d}{p_A^a\, p_B^b}\right) \tag{10.22}$$

which is a version (for ideal gases) of the Nernst equation. The Nernst equation provides the reversible, open-circuit potential across a fuel cell and is one of the fundamental expressions in fuel cell thermodynamics.

The maximum conversion efficiency is defined as

$$\eta_{\max} = \frac{W_e}{\Delta H^\circ} = \frac{\Delta G}{\Delta H^\circ} = 1 - \frac{T\Delta S}{\Delta H^\circ} \tag{10.23}$$

ΔH° and ΔG° must be known in order to apply the above equations. Thermodynamic properties are available from a number of sources, including a wide variety of software in thermodynamic and combustion textbooks. The JANAF tables are widely referenced for properties, and the NIST web site (http://kinetics.nist.gov/janaf/) contains a very inclusive set of thermodynamic properties. Care should be exercised to ensure that properties abstracted from different sources have unit compatibility. For example, results are expressed in gram-moles or kilogram-moles and in joules or kilojoules. A useful list of enthalpies of reaction at 25 °C and 1 atm pressure for a number of possible fuel cell reactants and products is found in Culp (1991).

However, the chemical equation for the most common fuel cell reaction, the production of water from hydrogen and oxygen, is

$$\mathrm{H_2} + \frac{1}{2}\mathrm{O_2} \rightarrow 2\mathrm{e^-} + 2\mathrm{H^+} + \mathrm{O} \rightarrow \mathrm{H_2O} \tag{10.24}$$

Values of ΔH° and ΔG° at 1 atm pressure and selected temperatures are provided in Table 10.1, which was adapted from Angrist (1982).

Example 10.1

Find the output voltage and theoretical conversion efficiency of an oxygen–hydrogen fuel cell operating at 298 K. Oxygen is supplied from air at 1 atm, and all other products and reactants are at 1 atm.

Table 10.1 $\Delta H°$ and $\Delta G°$ for H_2O at 1 atm pressure and selected temperatures.

T (K)	$\Delta H°$ (kJ/kg-mol)	$\Delta G°$ (kJ/kg-mol)
298	-2.42×10^5	-2.29×10^5
400	-2.43×10^5	-2.24×10^5
500	-2.44×10^5	-2.19×10^5
1000	-2.48×10^5	-1.93×10^5
2000	-2.52×10^5	-1.35×10^5

Solution At 1 atm, $E_g^\circ = \Delta G°/nF_c$. For the reaction of Equation 10.24, 2 kg-mol-electron are produced, so that $n = 2$ kg-mol-electron/kg-mol. From Table 10.1, $\Delta G° = -229\,000$ kJ/kg-mol. Using Faraday's constant, E_g° can then be calculated:

$$E_g^\circ = \frac{\Delta G°}{nF_c} = 229\,000\frac{\text{kJ}}{\text{kg-mol}}\times\frac{\text{kg-mol}}{2\text{ kg-mol-electron}}\times\frac{\text{kg-mol-electron}}{9.65\times10^7\text{ C}}$$
$$= 1.187\text{ V}$$

If air at 1 atm is used to supply the oxygen, the partial pressure of oxygen is 0.21 atm since oxygen is 20.95% by volume of air.

The reversible, open-circuit voltage then becomes

$$E_g = E_g^\circ - \frac{R_gT}{nF_c}\ln\left(\frac{p_C^c p_D^d}{p_A^a p_B^b}\right) = E_g^\circ - \frac{R_gT}{nF_c}\ln\left(\frac{p_{H_2O}^1}{p_{H_2}^1 p_{O_2}^{1/2}}\right)$$
$$= 1.187\text{ V} - 8.314\frac{\text{kJ}}{\text{kg-mol K}}\times298\text{ K}\times\frac{\text{kg-mol}}{2\text{ kg-mol-electron}}\times\frac{\text{kg-mol-electron}}{9.65\times10^7\text{ C}}$$
$$\times\ln\left(\frac{1^1}{1^1\times0.21^{1/2}}\right)$$
$$= 1.177\text{ V}$$

The efficiency is defined as $\eta_{max} = \Delta G/\Delta H°$, with ΔG provided by Equation 10.20. ΔG for the hydrogen–oxygen fuel cell at 298 K is

$$\Delta G = \Delta G° + R_gT\ln\left(\frac{p_{H_2}^1 p_{O_2}^1}{p_{H_2O}^{1/2}}\right)$$
$$= 229\,000\frac{\text{kJ}}{\text{kg-mol}} + 8.314\frac{\text{kJ}}{\text{kg-mol K}}\times298\text{ K}\times\ln\left(\frac{1^1\times0.21^{1/2}}{1^1}\right)$$
$$= 227\,100\frac{\text{kJ}}{\text{kg-mol}}$$

The efficiency can then be computed as

$$\eta_{max} = \frac{\Delta G}{\Delta H°} = \frac{\Delta G}{\text{LHV}} = \frac{227\,100\text{ kJ/kg-mol}}{242\,000\text{ kJ/kg-mol}} = 0.938$$

The efficiency in this expression is based on the product being water vapor when $\Delta H°$ is the lower heating value, LHV. If the efficiency is based on the product being liquid water, then the

higher heating value, HHV, is needed. The relationship between the two is

$$\text{HHV} = \text{LHV} + \Delta H_{\text{fg}} = 242\,000\ \text{kJ/kg-mol} + 44\,010\ \text{kJ/kg-mol}$$

where ΔH_{fg} is the heat of vaporization per kilogram-mole of water. The efficiency based on the HHV is

$$\eta = \frac{\Delta G}{\Delta H^\circ} = \frac{227\,100\ \text{kJ/kg-mol}}{286\,010\ \text{kJ/kg-mol}} = 0.794$$

Even though the energy required for reforming the fuel is not considered in the efficiency calculations, this example problem illustrates why fuel cells are generating so much interest. The conversion efficiency of fuel cells is significantly better than heat engine conversion efficiencies since the fuel cell is an isothermal device not constrained by the Carnot limit.

Example 10.2
Determine the effect of cell operating temperature on the fuel cell of Example 10.1. Present and discuss the appropriate results.

Solution The effect of cell operating temperature on the output voltage and LHV and HHV efficiencies are the characteristics of interest. Example 10.1 accomplished these calculations for an operating temperature of 298 K. The same procedure will be followed in this example, except the operating temperatures will be varied. The results of the sequence of calculations are presented in Table 10.2.

The cell output voltage and the LHV and HHV efficiencies are plotted as a function of temperature in Figure 10.4.

Although this is a simple thermodynamic model, Table 10.2 and Figure 10.4 capture much of the behavior of a "real" fuel cell. As the cell operating temperature increases, the cell voltage decreases and both the efficiencies (LHV and HHV) also decrease with cell operating temperature. Indeed, the effect of cell operating temperature on cell performance is quite pronounced.

The analysis presented in this section determines the salient features and limitations on the performance of a fuel cell. Fuel cell performance is limited by transport and chemical kinetics issues. Ramani (2006) and Brouwer (2001) specify and discuss the following 13 areas associated with losses in fuel cells:

1) reactant transport to gas–electrolyte interface;
2) reactant dissolution in the electrolyte;
3) reactant transport through the electrolyte to the electrode surface;
4) pre-electrochemical chemical reactions;
5) absorption of species onto the electrode;

Table 10.2 Summary of results from Example 10.2.

T (K)	ΔH° (kJ/kg-mol)	ΔG° (kJ/kg-mol)	E_g° (V)	E_g (V)	ΔG (kJ/kg-mol)	η_{LHV}	η_{HHV}
298	2.42×10^5	2.29×10^5	1.187	1.177	2.271×10^5	0.938	0.794
400	2.43×10^5	2.24×10^5	1.161	1.147	2.214×10^5	0.911	0.771
500	2.44×10^5	2.19×10^5	1.135	1.118	2.158×10^5	0.884	0.749
1000	2.46×10^5	1.93×10^5	1.000	0.966	1.865×10^5	0.758	0.643
2000	2.52×10^5	1.35×10^5	0.669	0.632	1.220×10^5	0.484	0.412

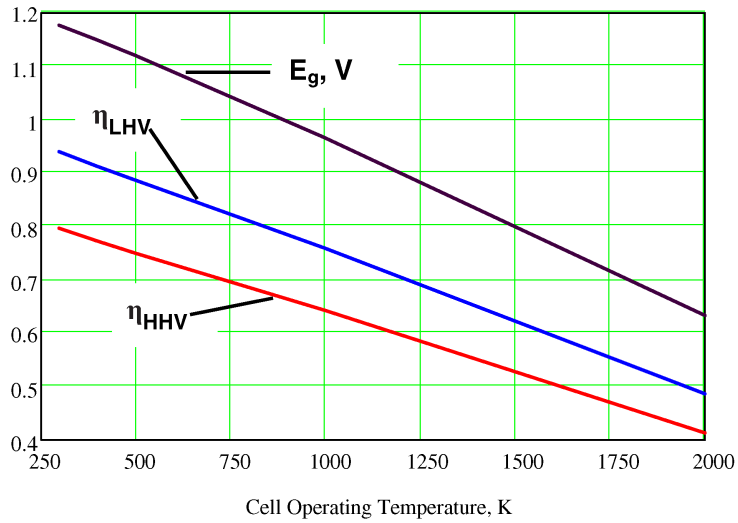

Figure 10.4 Cell voltage and efficiencies as a function of cell temperature.

6) surfaced migration of absorbed species;
7) electrochemical reaction involving electrically charged species;
8) post-electrochemical reactions;
9) desorption of products;
10) post-electrochemical surface migration;
11) product transport away from the electrode;
12) evolution of products from the electrolyte;
13) transport of gaseous products from the electrolyte.

These losses are generally grouped into three major categories:

1) activation polarization;
2) ohmic polarization;
3) concentration polarization.

The losses are irreversible and cause the cell voltage to be reduced from the ideal value. Activation overpotential is the result of chemical kinetics – slow chemical reactions. Ohmic polarization losses are due to the resistance in the cell to the flow of electricity. Concentration polarization losses are caused by lower concentrations of reactants at the electrode surface than in the bulk flow.

Figure 10.5 illustrates the effects and regions of dominance of each of the three major categories of losses as a function of current density. The theoretical voltage is indicated, and the various current density regimes for which each of the effects dominate are illustrated. The three add together for the total loss. Generally, the overall losses due to activation polarization, ohmic polarization, and concentration polarization are important and cannot be ignored. References such as Brouwer (2001), Larminie and Dicks (2003), Li (2006), Ramani (2006), and Hoogers (2002) treat in detail each of the loss categories.

In many thermal devices, economy of scale tends to demand systems with larger and larger capacities in order to attain near-maximum efficiencies. Fuel cells do not benefit for economy of scale; indeed, making them larger tends to exacerbate concentration polarization losses. Hence, fuel cells are individually likely to remain relatively small in size. Large power requirements for fuel cell installations will be met by assembling a number of fuel cells.

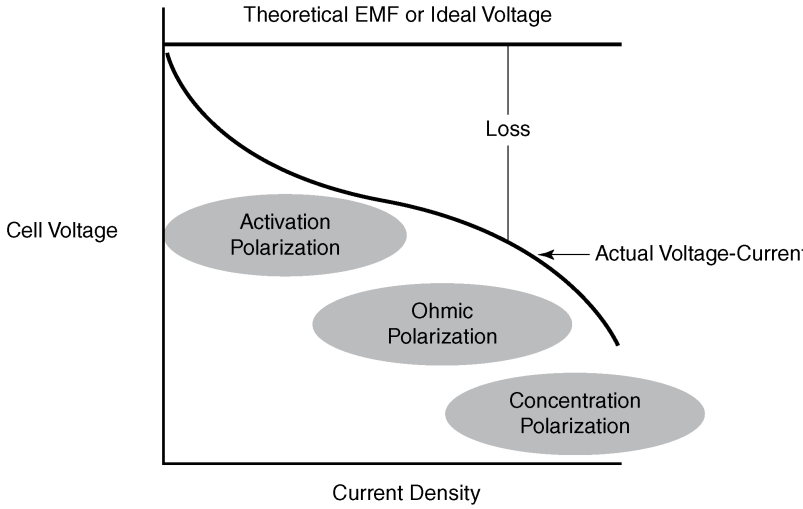

Figure 10.5 Fuel cell losses as a function of current density.

This section has examined the basic thermodynamics of fuel cells and briefly reviewed sources of losses in fuel cells. The examples were for a generic hydrogen–oxygen fuel cell. In actuality, the fuel cell operating characteristics and electrochemistry details depend on the oxidant, the fuel, and the electrolyte. The most common fuel cell types are explored next.

10.4 Fuel Cell Types

Most fuel cells are similar to the schematic illustrated in Figure 10.1, but differ with respect to the electrolyte used. The five main types of fuel cells, as distinguished by the electrolytes used, are as follows:

1) alkaline fuel cell (AFC);
2) phosphoric acid fuel cell (PAFC);
3) molten carbonate fuel cell (MCFC);
4) solid oxide fuel cell (SOFC);
5) proton exchange membrane fuel cell (PEMFC), including direct methanol fuel cells (DMFCs).

Each type will be examined in turn.

AFCs were the first type to be perfected and are used extensively in the space program to produce water and electricity on spacecraft. The electrolyte is potassium hydroxide in water. The catalyst at the anode and cathode is a non-precious metals, which is an advantage. Operating temperatures can range from 23 to 250 °C (74 to 482 °F), with about 70 °C being the most common, and efficiencies as high as 60%. But a disadvantage is that AFCs require pure hydrogen, which is difficult and expensive to produce. AFCs are easily poisoned by CO_2, as even a small amount can affect cell operation, requiring that the hydrogen and oxygen streams be purified. AFCs are not considered as a major contender for most applications, although their niche applications in the space program, along with limited commercial applications, are well documented.

The electrochemical reactions of the AFC are presented in Figure 10.6. At the cathode, water, electrons and oxygen combine to form the hydroxyl ion (OH^-). At the anode, hydrogen and the

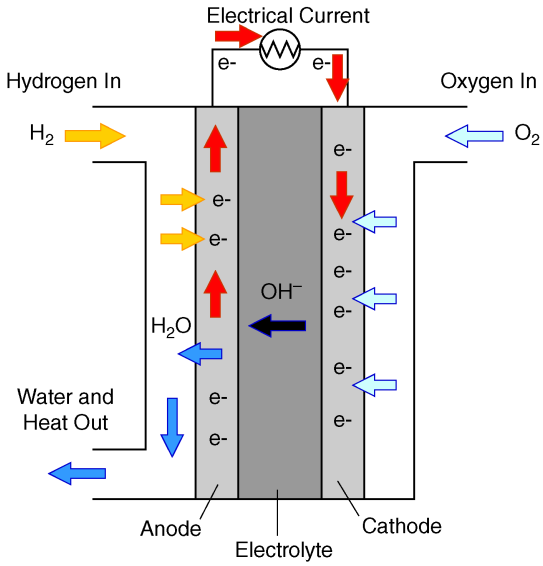

Figure 10.6 AFC electrochemistry. *Source*: EERE.

hydroxyl ion are combined to form water with the release of electrons (e^-). The hydroxyl ions pass through the electrolyte to the anode, and the electrons pass through the external circuit to the cathode. The reactions are as follows:

$$\begin{aligned} &\text{Anode reaction:} && 2H_2 + 4OH^- \rightarrow 4H_2O + 4e^- \\ &\text{Cathode reaction:} && O_2 + 2H_2O + 4e^- \rightarrow 4OH^- \end{aligned} \tag{10.25}$$

PAFCs use liquid phosphoric acid as an electrolyte and are generally considered "first-generation" fuel cell technology. The PAFCs use platinum as a catalyst and porous carbon electrodes for both the cathode and anode. The expensive catalyst is part of the cost of the PAFCs, $4000 to $4500 per installed kilowatt. These fuel cells operate at about 200 °C (400 °F) and achieve 37–42% fuel-to-electricity efficiencies, only slightly higher than simple-cycle combustion-based power plants. Thus, for a given power output, PAFCs are larger (more volume) and heavier than some other fuel cell types. However, the technology is mature, and PAFCs possess an impressive operation history.

The electrochemical reactions of PAFCs are presented in Figure 10.7. At the anode, hydrogen is split into two hydrogen ions (H^+) and two electrons (e^-). The hydrogen ions pass through the electrolyte to the cathode, and the electrons pass through the external circuit to the cathode. At the cathode, the hydrogen ions, electrons and oxygen combine to form water. The reactions are as follows:

$$\begin{aligned} &\text{Anode reaction:} && H_2 \rightarrow 2H^+ + 2e^- \\ &\text{Cathode reaction:} && \frac{1}{2}O_2 + 2H^+ + 2e^- \rightarrow H_2O \end{aligned} \tag{10.26}$$

MCFCs have the potential to reach 50–60% fuel-to-electricity efficiencies and can operate on hydrogen, carbon monoxide, natural gas, propane, landfill gas, marine diesel, and coal gasification products. The high operating temperatures, 650 °C (1200 °F), of MCFCs make direct operation (without a reformer) possible on gaseous hydrocarbon fuels, such as natural gas, possible, and dramatically increase the speed of the reaction kinetics, so expensive, precious-metal catalysts are not needed. MCFCs utilize molten carbonate salt mixtures as electrolytes. Electrolytes used include lithium carbonate, potassium carbonate, and sodium carbonate. The

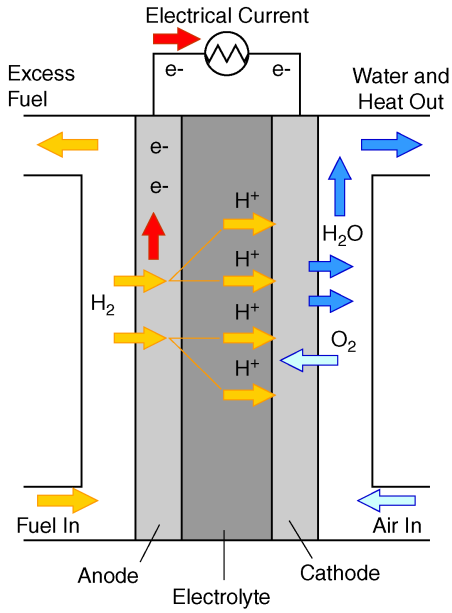

Figure 10.7 PAFC electrochemistry. *Source:* EERE.

high efficiencies and the ability to operate on a variety of fuels are significant advantages for MCFCs. However, the high operating temperatures and corrosive electrolyte exacerbate component breakdown and reduce cell life.

The electrochemical reactions of a molten carbonate fuel cell are presented in Figure 10.8. The MCFC reactions are as follows:

$$\begin{aligned} &\text{Anode reactions:} && H_2 + CO_3^{2-} \rightarrow H_2O + CO_2 + 2e^- \\ &&& CO + CO_3^{2-} \rightarrow 2CO_2 + 2e^- \\ &\text{Cathode reaction:} && O_2 + 2CO_2 + 4e^- \rightarrow 2CO_3^{2-} \end{aligned} \tag{10.27}$$

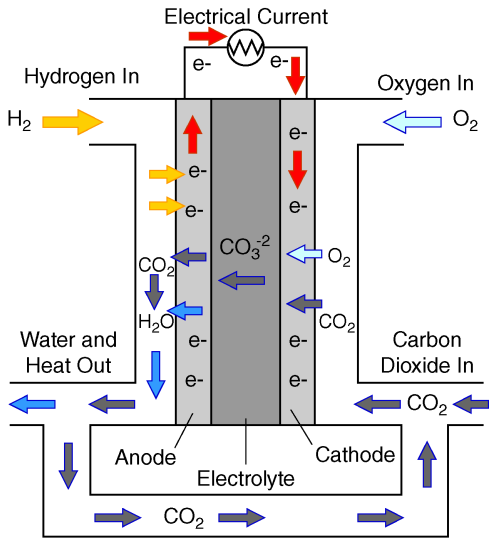

Figure 10.8 MCFC electrochemistry. *Source:* EERE.

An electrochemical reaction occurs at the anode between the hydrogen fuel and carbonate ions, CO_3^{2-}, from the electrolyte. This reaction produces water and carbon dioxide (CO_2) and releases electrons to the anode. At the cathode, oxygen and CO_2 are combined with electrons from the anode to produce carbonate ions, which enter the electrolyte. An added complexity for MCFCs is the requirement to inject CO_2 at the cathode since carbonate ions are consumed in the anode reaction. MCFCs are used for large stationary power generation. Megawatt-capacity fuel cell facilities almost always use MCFCs, as do large combined heat and power (CHP) installations (see Chapter 11 for discussions of such systems).

SOFCs operate at temperatures of 800–1000 °C (1400–1800 °F), thus permitting combined-cycle performance. As with other high-temperature fuel cell types, a fuel processor is not needed and the catalysts used are non-precious metals. Like MCFCs, the high operating temperatures of SOFCs mean that a wide variety of hydrocarbon fuels can be used. SOFCs have fuel-to-electricity conversion efficiencies of over 60%. Instead of a liquid electrolyte, solid oxide systems typically use a solid-ceramic material, such as zirconium–yttrium oxide. The solid ceramic construction provides a stable and reliable design, permits high temperatures, and enables flexibility in fuel choice. The SOFC is especially tolerant of sulfur compounds and carbon monoxide. Unlike other fuel cell types, SOFCs can use carbon monoxide as well as hydrogen as a fuel and are uniquely suited for fuels from coal gasification. SOFCs are used in large and small stationary power systems. SOFCs with outputs in the watt range are being developed for small portable chargers. The high operating temperatures also result in slow startup times and material durability problems. The electrochemical reactions of SOFCs are presented in Figure 10.9. The reactions occurring in an SOFC include

$$\begin{aligned} &\text{Anode reactions:} && H_2 + O^{2-} \rightarrow H_2O + 2e^- \\ &&& CO + O^{2-} \rightarrow CO_2 + 2e^- \\ &&& CH_4 + 4O^{2-} \rightarrow 2H_2O + CO_2 + 8e^- \\ &\text{Cathode reaction:} && O_2 + 4e^- \rightarrow 2O^{2-} \end{aligned} \tag{10.28}$$

In an SOFC, hydrogen or carbon monoxide (CO) in the fuel stream react with oxide ions (O^{2-}) from the electrolyte. These reactions produce water and CO_2 and provide electrons to the

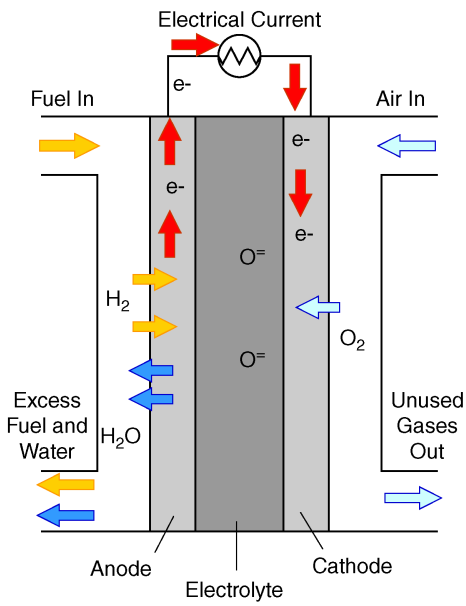

Figure 10.9 SOFC electrochemistry. *Source:* EERE.

anode. The electrons pass through the load. At the cathode, oxygen molecules (O_2) from the air receive electrons and are converted into oxide ions. The oxide ions are returned to electrolyte.

PEMFCs (also called polymer exchange membrane fuel cells) contain a thin plastic polymer membrane through which hydrogen ions can pass. The membrane is coated on both sides with metal alloy particles (mostly platinum) that act as catalysts. The use of precious-metal catalyst increases the system cost. Since the electrolyte in a PEMFC is a water-based solid polymer, electrolyte loss is not an issue and does not affect stack life. The use of a solid electrolyte also eliminates the safety concerns and corrosive effects associated with liquid electrolytes. PEMFCs operate at relatively low temperatures (below 100 °C). PEMFCs offer high power density and low weight and volume compared with other fuel cell types. The low operating temperatures mean that pure hydrogen is needed, but the low operating temperatures result in fast start up and enhanced component durability. The PEMFCs are the leading fuel cell type for use in light-duty and materials-handling vehicles, and to a lesser extent for stationary power applications. The electrochemistry for the PEMFC is shown in Figure 10.10. The reactions that occur in the PEMFC are as follows:

$$\begin{aligned} &\text{Anode reaction:} && H_2 \rightarrow 2H^+ + 2e^- \\ &\text{Cathode reaction:} && O_2 + 4H^+ + 4e^- \rightarrow 2H_2O \end{aligned} \tag{10.29}$$

Hydrogen ions and electrons are produced from the fuel at the anode. At the cathode, oxygen combines with electrons from the anode and hydrogen ions from the electrolyte to produce water. The solid electrolyte does not absorb the water; thus, the water is rejected from the back of the cathode into the oxidant gas stream.

High-temperature PEMFCs (HT PEMFCs) are a relatively recent (ca 2003) variant of PEMFCs that operate at temperatures up to 200 °C. The electrolyte in HT PEMFCs is mineral-acid based instead of water based for conventional PEMFCs. The increased operating temperature means that HT PEMFCs are more tolerant of fuel impurities such as CO (up to 5% by volume).

DMFCs are a relatively new type, development having been started about 1990. Similar to the PEMFC, a DMFC uses a polymer membrane as an electrolyte, but the platinum–ruthenium

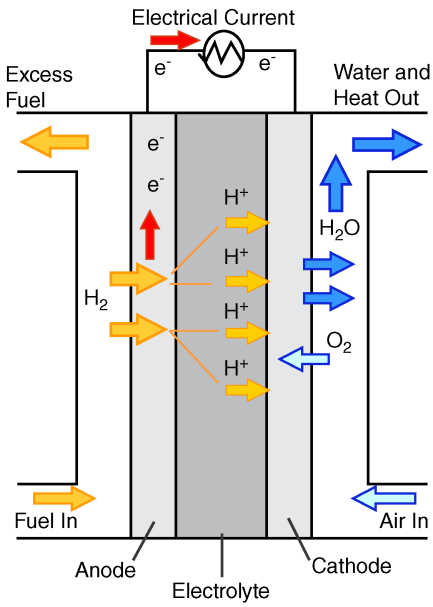

Figure 10.10 PEMFC electrochemistry. *Source:* EERE.

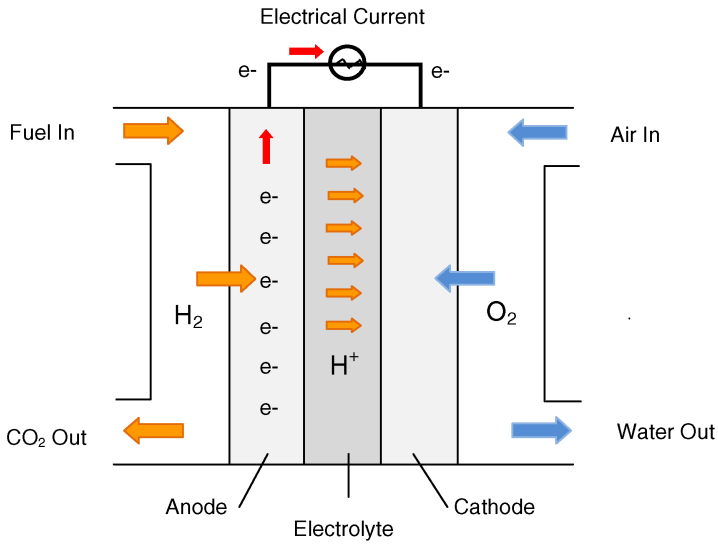

Figure 10.11 DMFC electrochemistry.

catalyst on the DMFC anode is able to extract hydrogen from methanol (CH_3OH) so that a reformer is not needed. Methanol (see Chapter 12) is an ideal fuel – an inexpensive liquid with a high energy density that can be easily stored, transported, and supplied to a fuel cell. DMFCs operate from 60 to 130 °C and are used in applications with modest power requirements such as mobile electronic devices, portable power packs, and materials handling vehicles. For the latter, DMFCs offer rapid refueling, rather than lengthy battery charging.

The electrochemistry for the DMFC is shown in Figure 10.11. The reactions that occur in the DMFC are as follows:

$$\begin{aligned} &\text{Anode reaction:} && CH_3OH + H_2O \rightarrow 6H^+ + 6e^- + CO_2 \\ &\text{Cathode reaction:} && \frac{3}{2}O_2 + 6H^+ + 6e^- \rightarrow 3H_2O \end{aligned} \tag{10.30}$$

At the anode, the hydrogen is extracted from the methanol, and hydrogen ions and electrons are produced. At the cathode, oxygen combines with electrons from the anode and hydrogen ions from the electrolyte to produce water. Carbon dioxide is formed at the anode, and water is formed at the cathode.

All fuel cells have the same function: the electrochemical generation of electricity from a fuel and an oxidant. The five types of fuel cells discussed have different electrolytes that result in different operating temperatures, efficiencies, suitable fuels, fuel processor requirements, and availability. Table 10.3 gives an overview of fuel cell characteristics for the AFC, PAFC, SOFC, MCFC, and PEMFC (including DMFC). The information contained in Table 10.3 was obtained from a variety of internet web sites, including manufacturers, national laboratories, academia, and industry technical organizations and is subject to change as significant research on most fuel cell types is ongoing.

Virtually all fuel cells have the advantages of quiet operation, low emissions, and high efficiency (compared with simple cycle thermal systems). The AFC and PAFC are relatively mature, proven technologies. All types of fuel cells are expensive when compared on a dollar per kilowatt basis with heat engines. The SOFC, MCFC, PEMFC, and DMFC types are just emerging into commercialization (quite limited for some types). Since 2010, commercialization of MCFC

Table 10.3 Overview of fuel cell characteristics.

	AFC	PAFC	SOFC	MCFC	PEMFC	DMFC
Commercial status	Available	Available	Available	Available	Available	Available
Size range	2–100 kW	100–400 kW	1 kW–10 MW	250 kW–10 MW	3 kW–1 MW	25 W–5 kW
Typical operating temperature (°F [°C])	480 [250]	400 [200]	1800 [1000]	1200 [650]	200 [90]	200 [90]
Fuel	Pure hydrogen	Natural gas, landfill gas, digester gas, propane	Natural gas, hydrogen, landfill gas, fuel oil	Natural gas, hydrogen	Natural gas, hydrogen, propane, diesel	Methanol
Efficiency (%)	50–60	40–45	50–60	50–60	35–60	20–30
Reforming		External	External/internal	External/internal	External	
Catalyst	Platinum/palladium	Platinum	Not required	Nickel/nickel oxide	Platinum/ruthenium	Platinum/ruthenium
Environmental	Nearly zero emissions	Nearly zero emissions	Nearly zero emissions	Nearly zero emissions	Nearly zero emissions	Nearly zero emissions

Source: California Energy Commission.

and PEMFC types has made great progress so that commercial offerings are much greater and more varied. The Office of Energy Efficiency & Renewable Energy (EERE) web-located documents http://energy.gov/eere/fuelcells/types-fuel-cells and http://energy.gov/sites/prod/files/2014/03/f10/fct_h2_fuelcell_factsheet.pdf offer good starting points for additional information on fuel cells, as does the E4Tech industry review (E4Tech, 2014). SOFCs have progressed from scant market penetration in 2009 to about 20% of the installed capacity in 2013. Section 10.5 examines some of the currently available fuel cells.

10.5 Fuel Cell Availability

From 1958 until 2013, UTC Power, a United Technologies Corporation company, marketed the PureCell™ series of fuel cells, the Model 200 rated at 200 kW and the Model 400 rated at 400 kW. By 2012, the PureCell™ Model 200 has amassed more than 9 million operating hours with 275 units in 19 countries. The PureCell™ Model 400, introduced in 2010, reached 1 million hours of operation in 2013. In February 2013, UTC Power was sold to ClearEdge Power, which eventually filed for bankruptcy protection in May 2014, and the Doosan Group, a large South Korean conglomerate, acquired ClearEdge Power and formed Doosan Fuel Cell America. In July 2015, Doosan Fuel Cell announced a major increase in fuel cell production at its South Windsor, CT, facility, the original UTC Power facility.

The PureCell™ Model 400, now built and marketed by Doosan Fuel Cell America, is a 400 kW PAFC and is one of the best-selling fuel cell systems. The Model 400 is especially suited for CHP applications – the subject of Chapter 11. Figure 10.12 contains a rendering of the fuel cell, and Table 10.4 lists salient metrics. Both the figure and the table are abstracted from the Doosan web site (http://www.doosanfuelcell.com/en/main.do). In Figure 10.12, the numbered components are as follows:

1) Fuel processor (reformer) – converts natural gas to a hydrogen-rich gas.
2) Fuel cell stack – hydrogen and air are combined electrochemically to produce electricity (DC), water, and heat. Part of the water (as steam) is used in the reformer.
3) Power conditioner – the DC power is converted to grid-acceptable AC power.
4) Integral heat recovery – heat is recovered for space heating, domestic hot water, and other process energy uses.

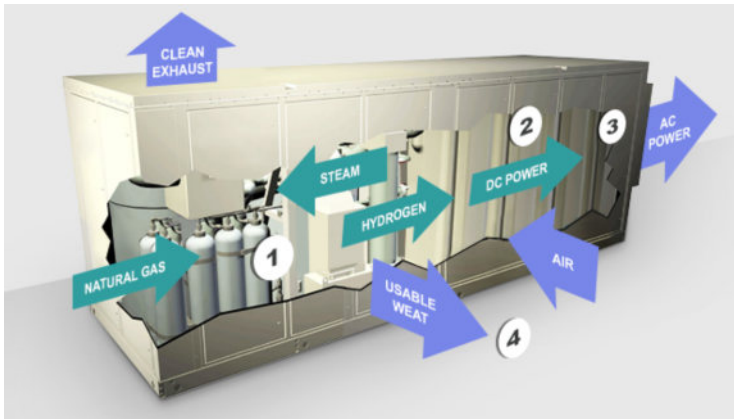

Figure 10.12 Cut-away illustration of the PureCell Model 400 PAFC. *Source:* http://www.doosanfuelcell.com/en/solutions/inside.do.

Table 10.4 Features of the Doosan PureCell™ Model 400.

Characteristic	Units	Operating mode	
		Maximum power	Baseload power
Electric power output	kW/kVA	440/440	400/471
Electrical efficiency	%, LHV	41	42
Gas consumption	MMBtu/h, HHV	4.06	3.60
High-grade heat output @ up to 250 °F	MMBtu/h (kW)	0.76 (223)	0.64 (188)
Low-grade heat output @ up to 140 °F	MMBtu/h (kW)	0.99 (290)	0.88 (258)
Ambient operating temperature	°F (°C)	−20 to 104 (−29 to 40)	
Fuel		Natural gas	

Source: http://www.doosanfuelcell.com/attach_files/link/PureCell%20Model%20400%20Datasheet.pdf.

As indicated by the figure, the system baseload output is 400 kW/471 kVA at 480 V, three-phase, 60 Hz power. Emissions are essentially negligible. The fuel cell dimensions are 100 in by 119 in by 344 in, and the PureCell™ Model 400 weighs 60 000 lb. At 33 ft from the cell, the noise is only 65 dB – verification that the fuel cell is amazingly quiet and can be located inside a structure. The life of the fuel cell stack is 10 years. The natural gas input (baseload) is 3.60 MMBtu/h, for which the electrical efficiency is quoted as 42%. The baseload heat recovery from the Model 400 is 0.88 MMBtu/h at 140 °F. The PureCell™ Model 400 is an example of a commercially available fuel cell, and the information presented is typical of what is found on web sites for various fuel cell manufacturers.

Research and Markets (2015), an international marketing research organization, in its publication *Fuel Cell Markets 2015–2019*, lists five primary North American companies and nine other firms that comprise most of the projected fuel activities. Table 10.5 was developed

Table 10.5 Companies developing/marketing fuel cells

Company	Web site	Fuel cell type	Fuel cell power
Ballard Power Systems	www.ballard.com	PEMFC	1.2–85 kW
Bloom Energy Corp.	www.bloomenergy.com	SOFC	50–250 kW
Doosan Fuel Cell	www.doosanfuelcell.com	PAFC	400 kW
FuelCell Energy	www.fuelcellenergy.com	MCFC	300 kW–2.4 MW
Hydrogenics	www.hydrogenics.com	PEMFC	4–12 kW
Acumetrics SOFC	www.acumentrics.com	SOFC	3 kW
Altergy Systems	www.altergy.com	PEMFC	500 W–7.5 kW
Delphi Automotive	www.delphi.com	SOFC	9 kW
Nuvera Fuel Cells	www.nuvera.com	PEMFC	10–100 kW
Oorja Protonics	www.oorjafuelcells.com	DMFC	1.1 kW
Plug Power	www.plugpower.com	PEMFC	Materials handling
Protonex Tech. Corp.	www.protonex.com	SOFC	20–200 W
Relion	See Plug Power	PEMFC	0.2–2.2 kW

from this list. A number of other companies are developing and/or marketing various sizes and types of fuel cells. As the industry is quite fluid, other companies may appear, and some listed in Table 10.5 may disappear. Fuel cell systems specifications are also likely to change. The companies listed in Table 10.5 all have web sites, and each web site contains information on the company's fuel cell endeavors. As is usual for the internet, much of the information is generally "non-technical," and detailed technical specifications may not be available except by contacting the company. Nonetheless, the table does provide an indication of what fuel cells are available in the marketplace and at least some indication of the power range and electrolyte types.

The fuel cell industry is in a state of flux and is undergoing consolidations and modifications – witness the divesture by UTC of UTC Power and the entry of the Doosan Group with Doosan Fuel Cell America. The years since 2009 have seen significant increases in installed megawatt fuel cell capacity, number of units sold, and commercialization of all electrolyte types. Figure 10.13 from the NREL's *2013 Renewable Energy Data Book* (Esterly and Gelman, 2014), illustrates the steady increases in installed fuel cell capacity from 2008 to 2013. Most of the growth is in stationary power applications. To some extent, automotive applications are still a research topic. Highlights, taken from the Esterly and Gelman (2014), indicate that global stationary fuel cell capacity increased threefold, reaching 160 MW in 2013, and fuel cell shipments increased by 25% from the previous year.

E4Tech (2014) reports the breakdown in installed megawatts by fuel-cell electrolyte type from 2009 to 2013. Figure 10.14, taken from that report, confirms a healthy increase in installed capacity (megawatts) as well as the strong emergence of SOFCs in the last few years.

Figure 10.15 provides a summary of stationary fuel cell installed capacity from 2001 through 2015. Since 2009, the installed capacity of stationary fuel cells has nearly doubled, and in 2015 it reached 178 MW. CHP (see Chapter 11) installed capacity has been essentially constant at 40 MW since 2010.

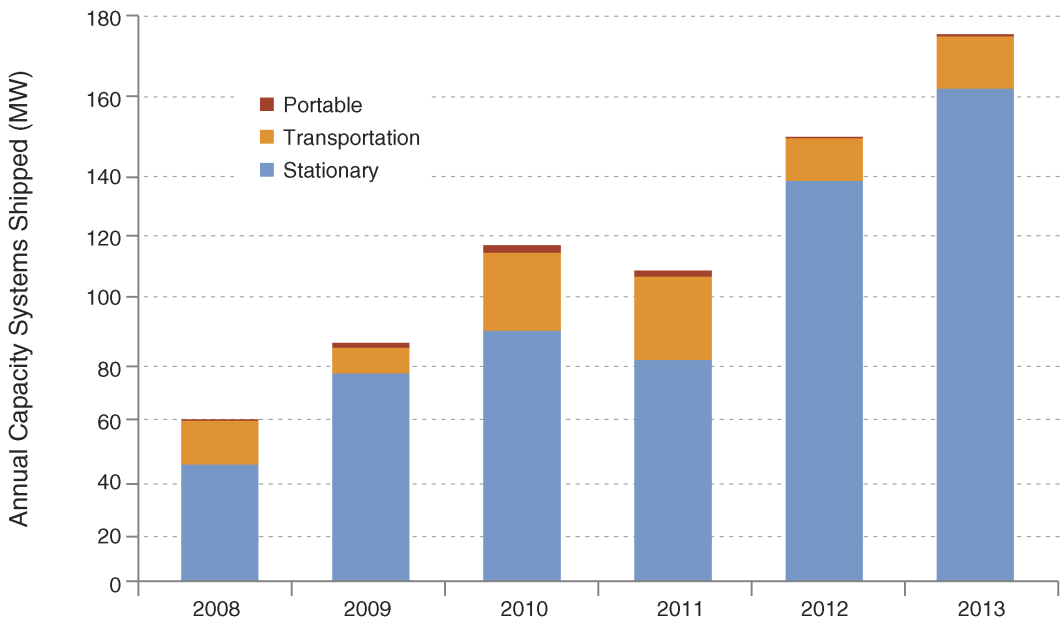

Figure 10.13 Installed megawatts of fuel cell capacity from 2008 to 2013. *Source:* http://www.nrel.gov/docs/fy15osti/62580.pdf (p. 91).

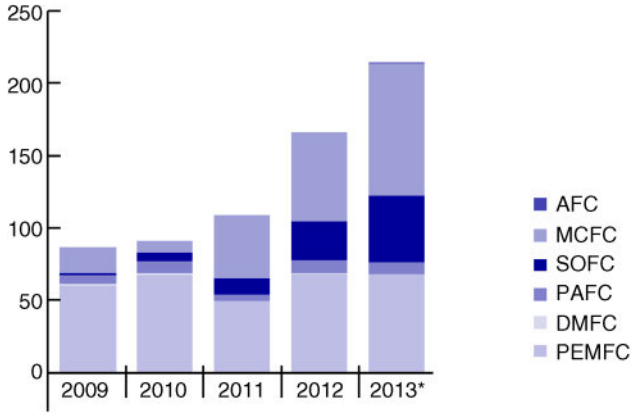

Figure 10.14 Installed megawatts of various electrolyte fuel cell types. *Source:* E4Tech (www.FuelCellIndustryReview.com).

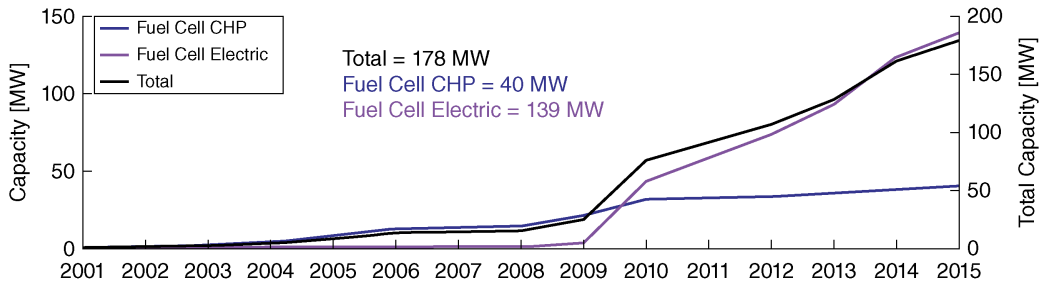

Figure 10.15 Installed capacity of stationary fuel cell from 2001 to 2015. *Source:* http://www.nrel.gov/hydrogen/images/cdp_stat_01.jpg.

10.6 Closure

AFCs have played an important role in the manned space program since its early days. But the relatively high cost per kilowatt of fuel cells, in spite of their high efficiencies and other advantages, has limited their use as an alternative energy system. However, as the cost per kilowatt decreases and as stable, pollution-free electric power becomes of more importance, fuel cells become more attractive from economic and "green" perspectives. Fuel cells are starting to play an increased role in scenarios ranging from baseload electricity, to emergency/backup power, to portable power solutions, and to electronic devices power, but widespread use of fuel cells in personal vehicles has yet to occur because of cost and hydrogen availability.

References

Angrist, S.W. (1982) *Direct Energy Conversion*, 4th edn. Allyn and Bacon, Boston, MA.
Appleby, A.J. and Foulkes, F.R. (1989) *Fuel Cell Handbook*. Van Nostrand Reinhold, New York.
Brouwer, J. (2001) Fuel cells. In *Distributed Generation: The Power Paradigm for the New Millennium*, A.-M. Borbely and J. F. Kreider (eds). CRC Press, Boca Raton, FL; pp. 151–184.
Culp, A.W. (1991) *Principles of Energy Conversion*, 2nd edn. McGraw-Hill, New York.

E4Tech (2014) *The Fuel Cell Industry Review 2014*. http://www.fuelcellindustryreview.com/archive/TheFuelCellIndustryReview2014.pdf (accessed October 21, 2016).

Esterly, S. and Gelman, R. (2014) *2013 Renewable Energy Data Book*, Haas, K. (ed.). DOE/GO-102014-4491. http://www.nrel.gov/docs/fy15osti/62580.pdf (accessed October 20, 2016).

Hoogers, G. (2002) *Fuel Cell Technology Handbook*. CRC Press, Boca Raton, FL.

Kinoshita, K., McLarnon, E.R., and Cairns, E.J. (1988) *Fuel Cells: A Handbook.* US DOE, DOE/METC-88/6096.

Larminie, J. and Dicks, A. (2003) *Fuel Cell Systems Explained*, 2nd edn. John Wiley & Sons, Inc., New York.

Li, X. (2006) *Principles of Fuel Cells*. Taylor and Francis, New York.

Ramani, V. (2006) Fuel cells. *The Electrochemical Society Interface*, **15**(1): 41–44.

Research and Markets (2015) *Global Fuel Cell Markets 2015–2019.* http://www.researchandmarkets.com/reports/3292488/global-fuel-cell-market-2015-2019#pos-0 (accessed October 21, 2016).

Weston, K.C. (1992) *Energy Conversion*. West Publishing Co., St. Paul, MN.

11

Combined Heat and Power Systems

11.1 Introduction

Combined heat and power (CHP) systems are characterized by the decentralized generation of electricity by a prime mover and the capture and use of reject thermal energy from the prime mover. The advantages for CHP systems are simple: increased overall system thermal efficiency, enhanced power quality, improved energy resiliency, and decreased greenhouse and other gases emissions.

The electrical grid is based on large, centrally located power plants. The transmission of power from such plants to the end users is accomplished through an electrical grid that consists of high-voltage transmission systems and low-voltage distribution systems. The high-voltage transmission system carries electricity from the power plants and transmits it to substations, where the high-voltage electricity is transformed into low voltages and distributed to individual customers.

The overall thermal efficiency of generation, transmission, and distribution is relatively low. Figures 11.1 and 11.2 illustrate the losses inherent to the generation and delivery of electric power in both traditional and combined-cycle power plants. Termuehler (2001) presents a lucid history of power plant developments, and Kehlhofer *et al*. (1999) discuss in detail combined-cycle power plants. Traditional power plants convert about >30% of the available energy of the fuel into end-user electric power, and highly efficient, combined-cycle power plants convert about 50% of the available energy into end-user electric power. The majority of the energy content of the fuel is lost at the power plant through the discharge or rejection of waste heat. Additional losses are incurred in the transmission and distribution of power to the end user.

Inefficiencies and emission issues associated with conventional power plants provide the impetus for new and revisited paradigms in "on-site and near-site" or "decentralized" generation. New developments in prime movers and power electronic technologies, along with restructuring and deregulation of the electrical utility industry, have enhanced the economics of decentralized electricity generation.

A technology consisting of power generation equipment coupled with thermally activated and/or thermal energy consuming components has evolved under the rubric of CHP. CHP has the potential to reduce carbon and other emissions and to increase thermal energy efficiency dramatically. CHP produces both electric or shaft power and useable thermal energy on-site or near-site, converting as much as 80% of the fuel into useable energy. A higher thermal efficiency means less fuel to meet an energy demand. Also, local power generation reduces the grid demand and provides better power quality and resilient (emergency) capability. Figure 11.3 illustrates the increase in efficiency of CHP systems over the conventional, centralized power plant efficiencies as in Figures 11.1 and 11.2.

A successful CHP system requires a need for both generated electricity/shaft power and thermal energy. An operation that does not have a need for both will not benefit from CHP. CHP is

Alternative Energy Systems and Applications, Second Edition. B. K. Hodge.

Companion website: www.wiley.com\go\Hodge\AESystemsandApplications2E

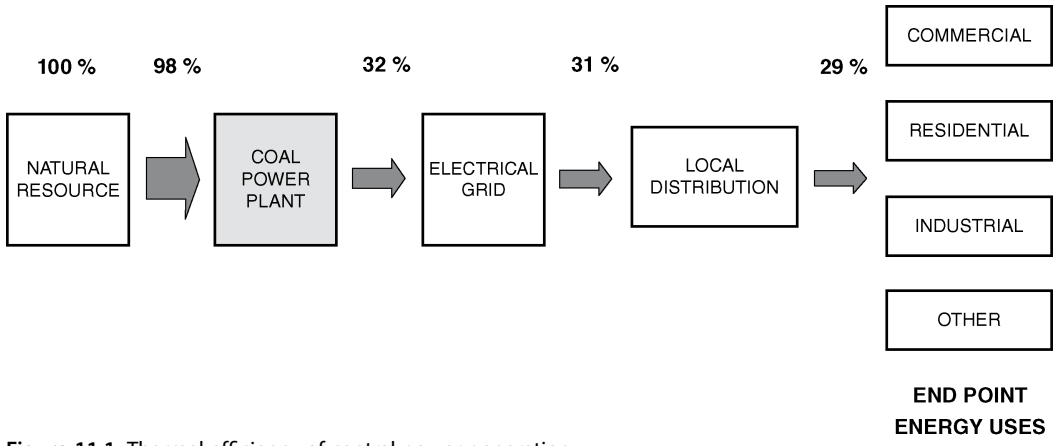

Figure 11.1 Thermal efficiency of central power generation.

especially beneficial to buildings or industrial processes, which typically use electric power and can have thermally activated heating, ventilation, and air conditioning system components or require thermal process energy.

CHP has become an emphasis for the US Department of Energy (USDOE). The CHP program resides in the Office of Energy Efficiency and Renewable Energy (EERE) of the USDOE. The EERE CHP Technical Assistance Partnerships (CHP TAPs) promote CHP and assist end-point energy users in implementing CHP systems by providing market opportunity analyses, education and outreach, and technical assistance. Contact information for the seven regional CHP TAPs, along with details of the program, is at http://energy.gov/eere/amo/chp-technical-assistance-partnerships-chp-taps. The DOE data base for CHP systems on a state-by-state basis is available at https://doe.icfwebservices.com/chpdb/.

Additionally, the US Environmental Protection Agency (EPA) has established the CHP Partnership initiative that seeks to promote the adoption of CHP technologies by involving government entities (national, state, and local), energy users, the CHP industry, and other clean-energy stakeholders. The EPA CHP Partnership publication *Catalog of CHP Technologies* (Darrow *et al*., 2015) provides a good overview. The US Combined Heat and Power Association

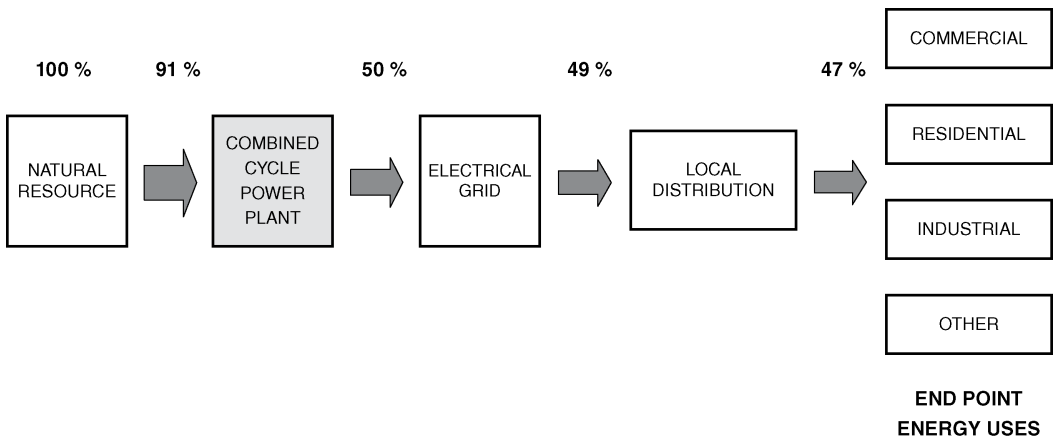

Figure 11.2 Thermal efficiency of central power combined cycle.

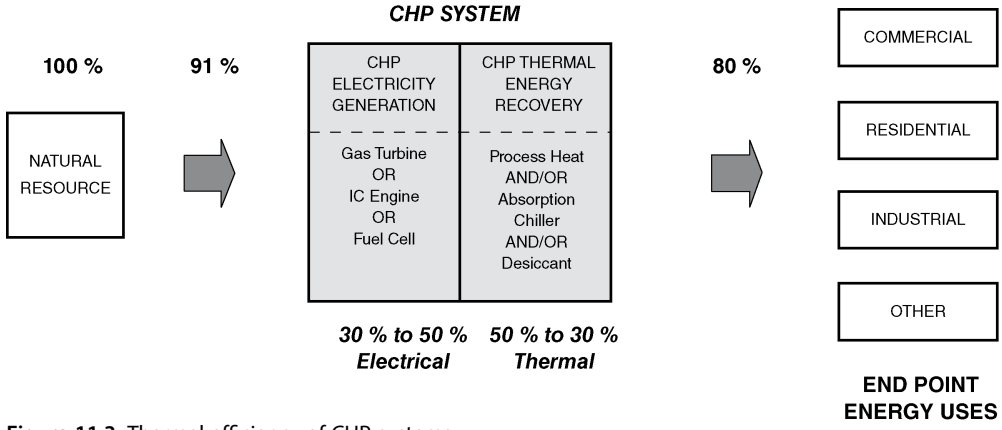

Figure 11.3 Thermal efficiency of CHP systems

(http://chpassociation.org/) also provides useful information. Books on CHP topics include those by ASHRAE (2015), Beith (2011), Boyce (2002), Horlock (1997), Kamm (1997), Kreith and West (1997), and Kolanowski (2000). The fundamentals of CHP systems are examined next.

11.2 Combined Heat and Power System Fundamentals

A CHP system combines distributed power generation with thermally activated components to meet the cooling, heating and power needs of buildings or with heat recovery devices (such as heat recovery steam generators, HRSGs) to meet process energy needs. Specific types of distributed power generation and thermally activated technologies will be introduced and briefly discussed.

A number of technologies are commercially available for generating electric power or mechanical shaft power on-site or near the site where the power is used. The major categories of prime movers for distributed generation (DG) are combustion (gas) turbines, internal combustion engines, and fuel cells, although steam turbines can also be used in CHP systems. Combustion turbines were examined in Chapter 5, and fuel cells were discussed in Chapter 10. Characteristics of these prime movers for DG technologies are contrasted in Table 11.1, from the *Catalog of CHP Technologies* (Darrow *et al.*, 2015). Additional cost information is also available from the *Distributed Generation Renewable Energy Estimate of Costs* (NREL, 2013).

The efficiency of electric power generation for combustion turbine systems, operating in a simple-cycle mode (i.e., without heat recovery in the turbine exhaust), ranges from 22 to 40%. Combustion turbines produce high-quality thermal energy that can be used to generate steam or hot water for thermal applications, including heating and cooling, or for process energy. Industrial gas turbines represent a well-established technology for power generation. These turbines also represent the "high-capacity" end of power generating equipment. Industrial gas turbines can provide 1 MW to more than 300 MW of electric power. Microturbines, with <1 MW electrical generating capability, represent the "low-capacity" end of power generating equipment but possess electrical efficiencies of 22–28%. Fuel source versatility of turbines allows their application in rural as well as urban areas.

A reciprocating engine, either four-cycle internal combustion or diesel, is frequently used as the prime mover in a CHP system. Internal combustion engines are a mature technology, and applications of reciprocating engines are well established and widespread. Engines can use

Table 11.1 Comparison of DG technologies (EPA).

Technology	Recip. engine	Steam turbine	Gas turbine	Microturbine	Fuel cell
Electric efficiency (HHV)	27–41%	5 to >40%[a)]	24–36%	22–28%	30–63%
Overall CHP efficiency (HHV)	77–80%	Near 80%	66–71%	63–70%	55–80%
Effective electrical efficiency	75–80%	75–77%	50–62%	49–57%	55–80%
Typical capacity (MW_e)	0.005–10	0.5 to several hundred MW	0.5–300	0.03–1.0	200–2.8 commercial CHP
Typical power to heat ratio	0.5–1.2	0.07–0.1	0.6–1.1	0.5–0.7	1–2
Part-load	OK	OK	Poor	OK	Good
CHP installed costs ($/$kW_e$)	1500–2900	$670–$1100	1200–3300 (5–40 MW)	2500–4300	5000–6500
Non-fuel O&M costs ($/kW h_e)	0.009–0.025	0.006–0.01	0.009–0.013	0.009–0.013	0.032–0.038
Availability	96–98%	72–99%	93–96%	98–99%	>95%
Hours to overhauls	30 000–60 000	>50 000	25 000–50 000	40 000–80 000	32 000–64 000
Start-up time	10 s	1 h–1 day	10 min–1 h	60 s	3 h–2 days
Fuel pressure (psig)	1–75	n/a	100–500 (compressor)	50–140 (compressor)	0.5–45
Fuels	Natural gas, biogas, LPG, sour gas, industrial waste gas, manufactured gas	All	Natural gas, synthetic gas, landfill gas, and fuel oils	Natural gas, sour gas, liquid fuels	Hydrogen, natural gas, propane, methanol
Uses for thermal output	Space heating, hot water, cooling, LP steam	Process steam, district heating, hot water, chilled water	Heat, hot water, LP–HP steam	Hot water, chiller, heating	Hot water, LP–HP steam
Power density (kW/m^2)	35–50	>100	20–500	5–70	5–20
NO_x ($lb/10^6$ Btu) (not including SCR)	0.013 rich burn 3-way cat. 0.17 lean burn	Gas 0.1–0.2, wood 0.2–0.5, coal 0.3–1.2	0.036–0.05	0.015–0.036	0.0025–0.0040
NO_x (lb/MW $h_{TotalOutput}$) (not including SCR)	0.06 rich burn 3-way cat. 0.8 lean burn	Gas 0.4–0.8, wood 0.9–1.4, coal 1.2–5.0	0.52–1.31	0.14–0.49	0.011–0.016

HHV: higher heating value; HP: high pressure; LP: low pressure; O&M: operation and maintenance; SCR: selective catalytic reduction.
a) Power efficiencies at the low end are for small backpressure turbines with boiler and for large supercritical condensing steam turbines for power generation at the high end.

natural gas, propane, or diesel fuel and are available in capacities ranging from 5 kW to 10 MW and possess electrical efficiencies of 27–41%. Reciprocating engines used for power generation have low capital cost, easy startup, proven reliability, good load-following characteristics, and significant heat recovery potential. Exhaust catalysts and better combustion design and control have significantly reduced internal combustion engine emissions over the past few years. Thermal energy is captured from both the engine exhaust gases and the engine cooling system.

Fuel cells produce electric power by electrochemical reactions, generally between hydrogen and oxygen, without the combustion processes. Like a battery, a fuel cell produces direct current. However, as discussed in Chapter 10, fuel cells come in a complete package in which the fuel cell stack is integrated with an inverter to convert the direct current to an alternating current and, if needed, a reformer to provide the hydrogen-rich fuel. Fuel cells have the highest electrical generating efficiency and lowest emissions of any CHP prime mover, but are the most expensive on an installed-kilowatt basis of any CHP prime mover.

In addition to on-site generation of electricity, an equally important consideration is the capture and use of reject heat. Energy recovery from any of the prime movers in a CHP system is accomplished by heat exchangers. Heat exchangers used to recover reject heat from a CHP prime mover are classified according to the fluid pairs handled and the temperatures of the fluids entering the heat exchangers. The input steams can be gas-to-gas, gas-to-liquid, or liquid-to-liquid, which are usually associated with high-, medium-, and low-temperature waste heat applications respectively.

Gas-to-gas heat exchangers are often used as recuperators for preheating combustion air for internal combustion engines or combustion turbines. A crossflow heat exchanger with flue gas flowing normal to a tube bundle containing air is called a convection recuperator. Such recuperators are used in low-temperature applications such as space heating, desiccant dehumidification systems, or direct-fired absorption chillers. Other types of heat exchangers used for gas-to-gas waste heat recovery include plate-fin, heat pipes, and rotary generators.

Gas-to-liquid heat exchangers include medium- to high-temperature heat recovery devices such as HRSGs, fluidized-bed heat exchangers, and heat pipes, as well as low- to medium-temperature heat exchangers used as economizers or fluid heaters. HRSGs, also called waste heat boilers, are used to generate steam from a prime mover, typically a gas turbine exhaust gas. HRSGs are very important in CHP applications and will be examined in a following paragraph. In a fluidized-bed heat exchanger, water or steam is heated by the exhaust gas (hot) stream that flows over a bed of finely divided solid particles. When the hot fluid reaches a critical velocity, the particles in the bed will float and act like a fluid, giving rise to an increase in the heat transfer coefficient. Fluidized-bed heat exchangers are often used for space or hot water heating, boiler feedwater heating, and process fluid heating. Gas-to-liquid heat pipes are similar to those used in gas-to-gas applications.

Economizers are crossflow heat exchangers in which water flows in individually finned tubes with hot gases flowing normal to the tubes. Economizers are often used with the boiler flue gases to preheat the boiler feedwater or to heat water or other process liquids or to superheat steam. Fluid heaters are double-pipe heat exchangers that use hot gases to heat a process heat transfer fluid that is circulated throughout a plant.

Liquid-to-liquid heat recovery exchangers are typically used in industrial applications that possess prime movers that use hot oil or other liquid coolants. Shell-and-tube heat exchangers are generally specified for this type of heat recovery.

HRSGs are frequently employed in processes that require steam for thermally activated components or for process energy use and are classified as unfired, partially fired, or fully fired. Unfired HRSGs use only the hot exhaust gases for steam generation. An HRSG that uses a duct burner upstream to increase the exhaust gas temperature is considered partially fired. If the exhaust gas is used as preheated air to the combustion process, the HRSG said to be fully fired.

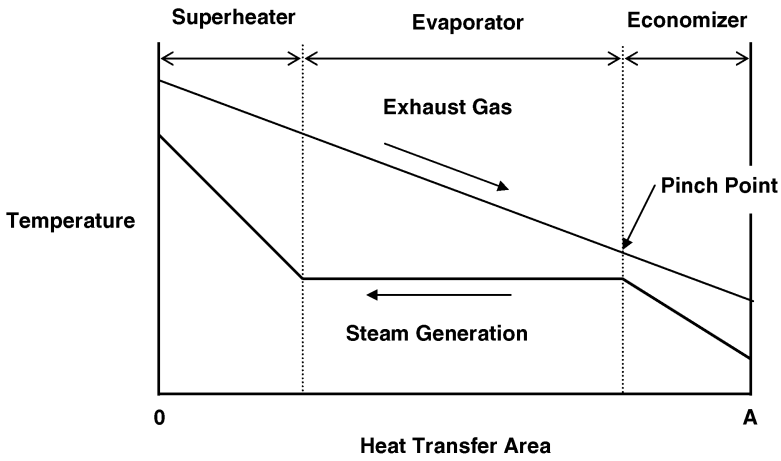

Figure 11.4 HRSG temperature–area diagram.

Figure 11.4 presents a temperature–area diagram of the temperature states in a HRSG. The hot exhaust gas enters at a high temperature and is cooled as it traverses the HRSG. The energy extracted from the hot gas is used to heat, vaporize (evaporate), and superheat the water. The flow arrangement shown in the figure is counterflow. An HRSG generally includes sections that are identified as an economizer, an evaporator, and a superheater. The water is heated to saturation conditions by the low-temperature exhaust as it exits the HRSG. In the evaporator, the water is vaporized into saturated steam, and the saturated steam is superheated by the inlet high-temperature exhaust in the superheater. The pinch point, where the water first starts to vaporize, is the smallest temperature difference in the HRSG and is the limiting factor in its overall performance. The hot and cold temperature–area distributions are especially critical in an HRSG as depicted in Figure 11.4. Poor design of such a device can result in a situation where the hot and cold exit enthalpies satisfy conservation of energy, but in the pinch-point region of the HRSG the local cold-fluid temperature can exceed the local hot-fluid temperature, resulting in a second law violation and invalidating the expected HRSG thermal performance. The HRSG must produce the pressure–temperature state of the steam required. To avoid condensation in the HRSG, the exit temperature of the exhaust gas must be above the condensation temperature of vapors in the exhaust.

In the majority of installations, a flapper damper or "diverter" valve is employed to vary the flow across the heat exchanger to maintain a specific design temperature of the hot water or a specific steam generation rate. A schematic of a typical combustion turbine, diverter valve, and HRSG arrangement is presented in Figure 11.5. The turbine-generator is contained in a sound-insulated enclosure to which inlet air is ducted. The diverter valve leads to a stack for venting unneeded exhaust gas. A duct burner is illustrated upstream of the HRSG. The steam from the HRSG is then directed to thermally activated devices or for process energy use.

Thermally activated devices use thermal energy instead of electric energy for providing heating, cooling, or humidity control for buildings. The two primary thermally activated devices used in CHP systems are absorption chillers and desiccant dehumidifiers.

Absorption chillers use heat as the primary source of energy for driving an absorption refrigeration cycle. These chillers require very little electric power (0.02 kW/ton) compared with electric chillers (0.47–0.88 kW/ton, depending upon the type of electric chiller). Absorption chillers have fewer and smaller moving parts and are quieter during operation than electric chillers. These chillers are also environmentally friendly in that they use non-chloro-fluorocarbon refrigerants.

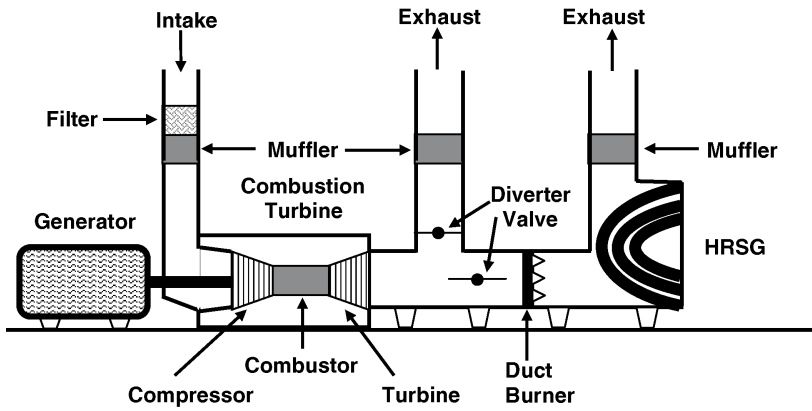

Figure 11.5 Typical CHP HRSG components.

Commercially available absorption chillers can utilize one of the following sources of heat: steam, hot water, exhaust gases, or direct combustion. Absorption chillers, except those that use direct combustion, are excellent candidates for providing cooling in a CHP system.

Two types of absorption chillers are commercially available: single effect and multiple effect. Compared with single-effect chillers, multiple-effect absorption chillers cost more (higher capital cost) but are more energy efficient and are thus less expensive to operate (lower energy cost). The overall economic attractiveness of each chiller depends on many factors, including the cost of capital and the cost of energy.

There are two separate aspects of space conditioning for comfort cooling:

- lowering the temperature of the air (sensible cooling), and
- reducing humidity in the air (latent cooling).

The humidity level should remain below 60% relative humidity to prevent growth of mold, bacteria and other harmful microorganisms in buildings and to prevent adverse health effects. Conventional air-conditioning systems reduce the air temperature below the air dew point temperature so that moisture in the incoming air condenses on the outside of a cooling coil over which the air passes. The cooled and dehumidified air is sent to the space being conditioned. Reducing humidity in the air by cooling often requires lowering the air temperature below a comfortable level and may necessitate reheating of the cooled dehumidified air if comfort is to be attained.

Desiccant dehumidifiers reduce humidity in the air by using solid or liquid desiccants to attract and hold moisture. Desiccant dehumidifiers operate independently of chiller operation. In CHP systems, thermal energy from the prime mover is used for regenerating desiccant material in these dehumidifiers. By reducing the moisture content of the air, desiccant dehumidifiers satisfy the latent cooling load and, thus, reduce the load of the chillers to only the sensible cooling (reducing the temperature). Desiccant components in effect permit the sensible and latent cooling functions to be separated and independently controlled.

11.3 Combined Heat and Power System Economics and Operation

CHP systems are attractive for a number of reasons, including economics, thermal efficiency, greenhouse gas emissions, power quality, and resiliency. However, in order for CHP to be viable for a given scenario, the following three attributes must be present:

1) a use for the electricity generated;
2) a use for the thermal energy recovered;
3) a sufficient "spark spread."

The spark spread refers to the difference, generally expressed in $\$/10^6$ Btu, between the costs of electricity and the prime mover fuel, typically natural gas. The accepted spark spread threshold for economically feasibility is $\$12/10^6$ Btu; that is, the more the spark spread exceeds that value, the more economically promising is CHP. Example 11.1 illustrates how the spark spread can be calculated.

Example 11.1
What is the spark spread if electricity cost \$0.12/kW h and natural gas is \$0.90/ccf (ccf: 100 cubic feet).

Solution As indicated in the problem statement, the energy charge for electricity is generally assessed as a cost per kilowatt-hour, and the cost of natural gas is expressed as the cost per cubic foot. Another common billing unit for natural gas is per 1000 cubic feet (mcf). The energy content of natural gas is nominally 100 000 Btu/ccf or 1 000 000 Btu/mcf. Thus:

$$\text{Cost of natural gas} = \frac{\$0.90}{\text{ccf}} \times \frac{\text{ccf}}{100\,000\ \text{Btu}} \times \frac{10}{10} = \frac{\$9.00}{1\,000\,000\ \text{Btu}} = \$9.00/10^6\ \text{Btu}$$

Recall from Chapter 1 that 1 kWh = 3412 Btu. Then

$$\text{Cost of electricity} = \frac{\$0.12}{\text{kWh}} \times \frac{\text{kWh}}{3412\ \text{Btu}} \times \frac{10^6}{10^6} = \frac{\$35.17}{1\,000\,000\ \text{Btu}} = \$35.17/10^6\ \text{Btu}$$

Thus, the spark spread becomes

$$\text{Spark spread} = \$35.16/10^6\ \text{Btu} - \$9.00/10^6\ \text{Btu} = \$26.16/10^6\ \text{Btu}$$

Hence, electricity is $\$26.16/10^6$ Btu more expensive than natural gas. A spark spread of this magnitude (much in excess of $\$12/10^6$ Btu) is very favorable for CHP if the first two conditions are met.

However, the determination of the economic feasibility of a CHP system is more involved than just calculating the spark spread. A first-order economic analysis of the feasibility of a CHP system requires consideration of the operating strategy of a candidate facility. Consider the five most common operating strategies (indicated as A through E) depicted in Figure 11.6. In the figure, the axes are the thermal energy and the electrical energy. The three dashed lines represent the characteristics of the prime mover. The larger the slope, the more electricity generated for a given amount of thermal energy recovered. Because of variations in the electricity and thermal energy needs, position A, which illustrates a perfect match between the thermal and electrical requirements, is virtually never met. Positions B–E, however, represents different but realistic strategies. For position B the electrical energy requirement is met but the thermal energy recovered is greater than required. Unless a neighboring facility can purchase the excess thermal energy, it must be rejected to the atmosphere, thus negating the economic effect of some of the energy recovered. Position C corresponds to meeting the thermal requirement but not meeting the electrical requirement. Electricity would have to be purchased from the grid. Condition C is a common operating strategy for a CHP system. In many instances connection to the grid provides power redundancy for a facility. For position D the electrical load is satisfied but the thermal needs are not met, so additional thermal energy must be provided. Condition D can be a useful operating strategy. Position E represents meeting the thermal needs but generating excess electricity that must be sold. Unless the excess power can

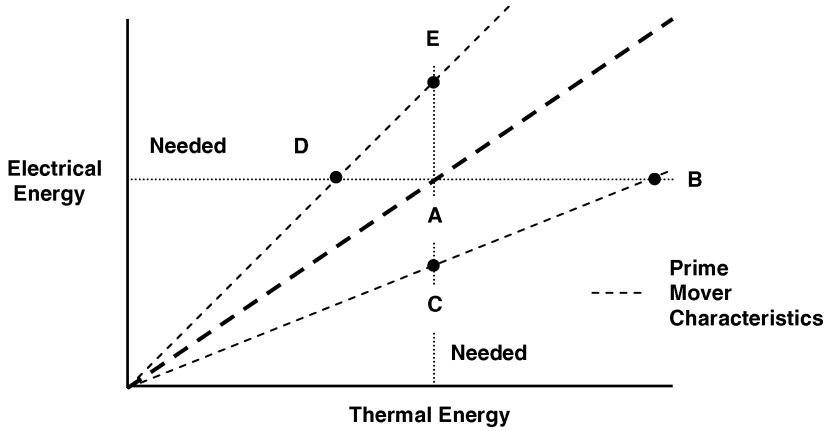

Figure 11.6 Operating strategies for a CHP system.

be sold at a sufficient price to pay the cost of generation, option E is not economically attractive and is infrequently specified.

Tables 11.2 and 11.3 present the utility bills for a year and the utility rate structures for a manufacturing facility. Consider the electric bill first (Table 11.2). Commercial and industrial electrical rate schedules usually involve energy and demand charges and can include items such as power factor charges and time-of-day or time-of-year tariffs. The electricity bill illustrated in Table 11.2 contains energy, demand, and power factor charges as well as industrial credits

Table 11.2 Example utility bill: electrical bill and rate structure.

Month	Energy usage (kWh)	Usage cost ($)	Peak demand (kW)	Billed demand (kW)	Demand cost ($)	Power factor charge ($)	Other charges ($)	TSI cost ($)	Total cost ($)
Aug	1 518 000	50 428	2 259	2 338	22 344	825	(4 641)	1 155	70 111
Sept	1 550 400	51 504	2 283	2 352	22 596	721	(4 719)	1 173	71 275
Oct	1 331 400	44 229	2 244	2 354	22 187	1 153	(4 252)	1 064	64 382
Nov	1 331 700	44 239	2 130	2 235	20 992	1 102	(4 177)	1 046	63 202
Dec	1 400 400	46 521	2 085	2 130	20 521	466	(4 258)	1 063	64 314
Jan	1 337 700	44 438	2 094	2 126	20 615	336	(4 122)	1 032	62 300
Feb	1 299 900	43 183	2 115	2 151	20 835	375	(4 056)	1 017	61 353
Mar	1 274 400	42 336	2 079	2 091	20 458	121	(3 964)	994	59 945
Apr	1 498 200	49 770	2 289	2 289	22 659	0	(4 568)	1 137	68 998
May	1 490 400	49 511	2 364	2 364	23 445	0	(4 598)	1 145	69 503
June	1 617 300	53 727	2 439	2 439	24 231	0	(4 917)	1 220	74 260
July	1 400 100	46 511	2 394	2 394	23 759	0	(4 424)	1 105	66 951
Total	17 049 900	566 398	26 775	27 262	264 642	5 099	(52.696)	13 151	796 593

TSI: tax, service charge, and industrial credit.
Electric rate schedule. Usage rate: $0.03322 kW h; demand rate: 9.15/kW for first 1000 kW of demand, 10.48 for all additional kilowatts; service charge: 50.0/month; tax rate: 1.5%.

Table 11.3 Example utility bill: gas bill and rates.

Month	Gas usage (ccf)	Usage cost ($)	Gas cost ($/ccf)	TSI cost ($)	Total cost ($)
Aug	191 467	48 699	0.254	742	49 441
Sept	163 219	36 252	0.222	552	36 804
Oct	177 653	47 262	0.266	720	47 982
Nov	193 294	51 088	0.264	778	51 866
Dec	193 791	53 686	0.277	818	54 503
Jan	181 893	43 480	0.239	662	44 142
Feb	168 669	40 632	0.241	619	41 251
Mar	192 318	43 080	0.224	656	43 736
Apr	187 298	47 046	0.251	716	47 763
May	193 764	60 660	0.313	924	61 584
June	190 402	54 399	0.286	828	55 227
July	180 018	52 418	0.291	798	53 216
Total	2 213 786	578 702	0.261	8 813	587 515

TSI: tax, service charge, and industrial credit.
Tax rate: 1.5%.

("Other charges"). The electrical energy is expressed in kilowatt-hours and is billed at some specified rate. The demand is the maximum sustained (usually for a 15 or 30 min period) power draw from the grid per billing period. Once set, the maximum demand is not reset until the start of the next billing period. The rate schedule shown in the table is relatively simple; rate schedules in many instances are more complex. Generally, natural gas is billed only as an energy charge. The usual billing units are per 100 or per 1000 cubic feet (as defined previously).

Plotting the electricity and gas usages on a monthly basis often reveals important trends in energy use and is the initial step in analyzing energy usage patterns. Figures 11.7 and 11.8 contain graphical representations of the energy usages from Tables 11.2 and 11.3.

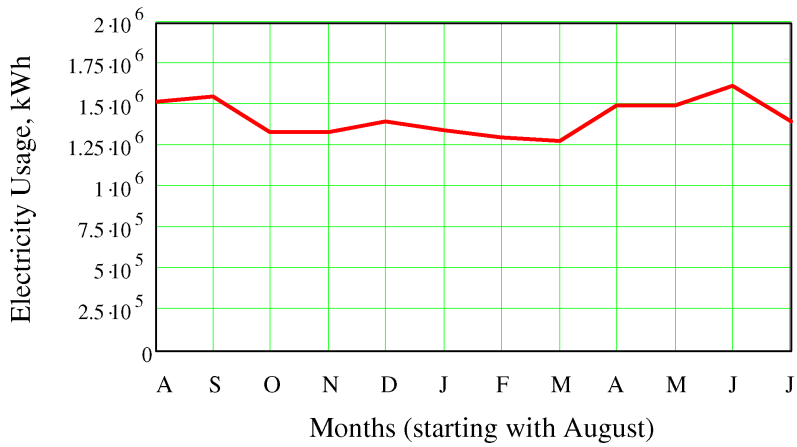

Figure 11.7 Electricity usage from Table 11.2.

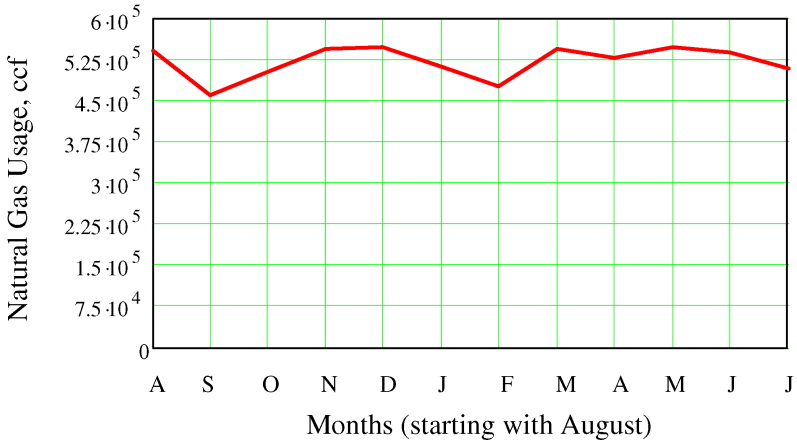

Figure 11.8 Natural gas usage from Table 11.3.

The trends indicated in Figures 11.7 and 11.8 are typical of manufacturing facilities with large electricity and large natural gas usages for process energy. The natural gas usage is essentially constant throughout the year with no dominant use in the winter months. This behavior means that only a small percentage of the natural gas is used for space heating; thus, most of the natural gas is used for the manufacturing process. Likewise, the near-constant monthly electricity usage, with about a 20% increase in the summer, implies that most of the electricity is also used for the process and not for space conditioning.

Another revealing metric is the usage factor of electricity. The usage factor is the percentage of time, for a given billing period, that the peak demand (kilowatts) must be used in order to account for the total energy usage (kilowatt-hours). The energy usage (kilowatt-hours) divided by the product of the peak demand (kilowatts) and the number of hours in the billing period yields the usage factor:

$$\text{Usage factor} = \frac{\text{Kilowatt-hour usage}}{\text{Peak kilowatts} \times \text{Days in billing period} \times 24\,\text{h/day}} \tag{11.1}$$

For the usage and demand represented by Tables 11.2 and 11.3, the monthly usage factor is presented in Figure 11.9.

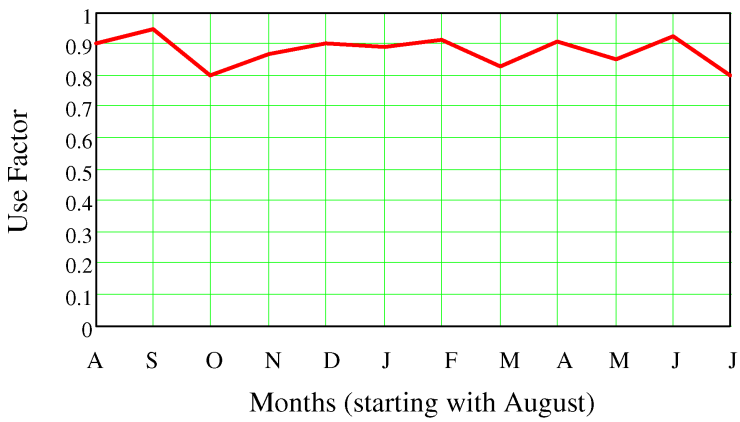

Figure 11.9 Usage factor per month.

As demonstrated in Figure 11.9, the usage factor varies between 0.8 and 0.95 and indicates that the facility runs most of the equipment most of the time. In a manufacturing scenario, the process must be run three shifts for 5 to 7 days a week in order to achieve such a high usage factor. Facilities with high electrical usage factors are good candidates for on-site generation since the prime mover/generator would be operating near peak load most of the time.

Example 11.2
Based on the three CHP attributes:

1) a use for the electricity generated,
2) a use for the thermal energy recovered, and
3) a sufficient "spark spread,"

is the facility whose bills are provided in Tables 11.2 and 11.3 a candidate for further investigation for a CHP system?

Solution Tables 11.2 and 11.3 and Figures 11.7, 11.8, and 11.9 contain information useful in analyzing the three questions. The kilowatt-hour and per 100 cubic feet usage by the facility certainly meet the first two conditions. The spark spread is calculated next. The average cost of 100 cubic feet is \$0.265, so the average cost per 10^6 Btu becomes

$$\text{Cost of natural gas} = \frac{\$0.265}{\text{ccf}} \times \frac{\text{ccf}}{100\,000\ \text{Btu}} \times \frac{10}{10} = \frac{\$2.65}{1\,000\,000\ \text{Btu}} = \$2.65/10^6\ \text{Btu}$$

The average cost of 1 kWh of electricity, including demand, service charges, and rebates, from Table 11.2 is

$$\text{Cost per kilowatt-hour} = \frac{\$796\,593}{17\,049\,900} = \$0.47/\text{kWh}$$

Then

$$\text{cost of electricity} = \frac{\$0.047}{\text{kWh}} \times \frac{\text{kWh}}{3412\ \text{Btu}} \times \frac{10^6}{10^6} = \frac{\$14.58}{1\,000\,000\ \text{Btu}} = \$14.58/10^6\ \text{Btu}$$

Thus, the spark spread becomes

$$\text{Spark spread} = \$14.58/10^6\ \text{Btu} - \$2.65/10^6\ \text{Btu} = \$11.93/10^6\ \text{Btu}$$

On a per 10^6 Btu basis, the cost of electricity is nearly \$12 more than the cost of natural gas. This magnitude of spark gap is usually taken as a positive indication for CHP. Hence, all three of the attributes are satisfied, so that this facility is a candidate for further investigation. This short analysis does not confirm that a CHP system is appropriate, only that further investigation is warranted.

If the "short" analysis of Example 11.2 indicates only that further investigation is appropriate, what is needed for the next level of feasibility study? Section 11.4 explores a more involved economic assessment of CHP suitability.

11.4 Economic Assessment of Combined Heat and Power Suitability

The economics and feasibility of a CHP system can be assessed on a first-order basis by considering the yearly utility bills. This technique uses the energy consumption information in

conjunction with industry-accepted efficiencies for both conventional and CHP components to estimate the savings, if any, from meeting the energy needs using CHP. Accepted values of component efficiencies and electrical and thermal energy production are assigned as follows:

Conventional	
Boiler	$\eta_{boiler} = 0.85$
Central power plant	$\eta_{cpp} = 0.35$
Central chiller	$COP_{cc} = 2.5$
CHP	
Electricity (gas turbine)	$\eta_e = 0.30$
Recovered thermal energy	$\eta_r = 0.35-0.50$
Absorption chiller	$COP_{abc} = 0.7-0.8$

The first-order assessment procedure is best described by considering a detailed example.

Example 11.3
Accomplish a first-order assessment for CHP suitability for the utility bills presented in Tables 11.2 and 11.3.

Solution The first step in the procedure is to establish the operating mode (conditions A–E of Figure 11.6) congruent with the energy usages. Insight into the appropriate operating mode can be gained by computing the ratio of the electrical energy (expressed in Btus) to the gas energy. The electrical energy is

$$\begin{aligned}\text{Electrical energy} &= \text{Kilowatt-hour usage} \times 3412\frac{\text{Btu}}{\text{kWh}}\\ &= 17\,049\,900\,\text{kWh} \times 3412\frac{\text{Btu}}{\text{kWh}}\\ &= 58\,170 \times 10^6\,\text{Btu}\end{aligned}$$

and

$$\begin{aligned}\text{Natural gas energy} &= 100\,\text{cubic feet usage} \times 100\,000\frac{\text{Btu}}{\text{ccf}}\\ &= 2\,213\,786\,\text{ccf} \times 100\,000\frac{\text{Btu}}{\text{ccf}}\\ &= 221\,400 \times 10^6\,\text{Btu}\end{aligned}$$

The ratio of electrical energy to gas energy then becomes

$$\text{Energy ratio} = \frac{\text{Electrical energy}}{\text{Natural gas energy}} = \frac{58\,170 \times 10^6\,\text{Btu}}{221\,400 \times 10^6\,\text{Btu}} = 0.263$$

Since the electrical energy required is much less than the gas energy required, a logical choice of the operating mode is case D of Figure 11.6. Mode D provides all the electricity required but does not meet the thermal requirements. The natural gas required for a gas turbine to generate the required kilowatt-hours can be calculated by dividing the electrical energy required by the gas turbine electrical generation efficiency η_e:

$$\begin{aligned}\text{Natural gas required} &= \frac{\text{Electrical energy required}}{\eta_e}\\ &= \frac{58\,170 \times 10^6\,\text{Btu}}{0.30}\frac{\text{ccf}}{100\,000\,\text{Btu}} = 1.939 \times 10^6\,\text{ccf}\end{aligned}$$

Thus, a gas turbine operating at an electrical efficiency of 30% will require 1.939×10^6 ccf to produce the required 17 049 900 kWh. The thermal energy recovered from the turbine is the natural gas required times the recovery efficiency η_r:

$$\begin{aligned}\text{Thermal energy recovered} &= \text{Natural gas recovered} \times \eta_e \\ &= 1.939 \times 10^6 \text{ ccf} \times 0.34 = 660\,000 \text{ ccf}\end{aligned}$$

However, to obtain the input energy content of the thermal energy recovered from boiler, the boiler efficiency η_{boiler} is needed:

$$\begin{aligned}\text{Thermal energy equivalent} &= \frac{\text{Thermal energy recovered}}{\eta_{\text{boiler}}} \\ &= \frac{660\,000 \text{ ccf}}{0.85} = 776\,000 \text{ ccf}\end{aligned}$$

The recovered thermal energy is equivalent to 776 000 ccf of natural gas. Since this amount is considerably less than the required thermal energy of 2 213 786 ccf, the thermal energy recovered does not exceed the thermal energy required. Operating mode D is confirmed as appropriate for the utility usage of Table 11.2. The total natural gas usage required would be the natural gas currently purchased to meet the thermal needs plus the additional natural gas required for the CHP system minus the thermal energy equivalent recovered from the turbine exhaust. For this example, the natural gas required is thus

$$\begin{aligned}\text{Natural gas required} &= \text{Currently purchased} + \text{CHP required} - \text{Equivalent recovered} \\ &= 2\,213\,786 \text{ ccf} + 1\,939\,000 \text{ ccf} - 776\,000 \text{ ccf} = 3.377 \times 10^6 \text{ ccf}\end{aligned}$$

At an average cost of \$0.265/ccf and a tax rate of 1.5%, the cost of natural gas to run the facility with a CHP system in mode D becomes

$$\text{Natural gas cost} = 3.377 \times 10^6 \text{ ccf} \times \frac{\$0.265}{\text{ccf}} \times 1.015 = \$908\,400$$

From Table 11.1 a reasonable operation and maintenance charge for a gas turbine is 1¢/kW h. The O&M cost is thus estimated as

$$\text{O\&M cost} = 17\,049\,900 \text{ kWh} \times \frac{\$0.01}{\text{kWh}} = \$170\,499$$

The total cost for operating the CHP system is the sum of the natural gas cost and the O&M cost:

$$\text{Total cost} = \$908\,000 + \$170\,499 = \$1\,078\,499$$

The cost of operating the current system, electricity and natural gas, is \$1 384 000. The savings for switching to a CHP system are thus

$$\text{CHP savings} = \$1.384 \times 10^6 - \$1.078 \times 10^6 = \$306\,000$$

The operation of a CHP system with a gas turbine would save \$306 000 per year over the existing, conventional system. For operating mode D, all of the electricity requirements are met, and the facility could be disconnected from the grid. However, for no grid reliance the facility would be without power during CHP system inspections or downtimes unless backup sources were provided. In many instances, the choice would be made to maintain a grid connection to ensure continued operation if the CHP system were down. The cost analysis will be done under the assumption of no grid connection charges.

If the turbine is take the full load of the facility, a turbine with an electrical output of at least 2439 kW (the maximum demand from Table 11.2) is needed. A nominal 2.5 MW turbine

would meet the existing needs but would provide little capability for expansion. A ballpark cost per kilowatt for an installed CHP system with a gas turbine is $1200, from Table 11.1. A CHP system with a 2.5 MW gas turbine is estimated to cost $3 000 000. The simple payback period, based on turbine cost only (no heat exchanger cost), becomes

$$\text{Simple payback} = \frac{\$3\,000\,000}{\$306\,000/\text{year}} = 9.8 \text{ years}$$

This is as far as this analysis can go without additional information on the facility, including management policies. In addition to economics examined in this example problem, other factors would enter into a decision to convert to a CHP system. These factors include, but are not limited to, power quality, CO_2 credits, company "green" policies, and energy security concerns.

The preceding example illustrates a first-order approach to assessing the economic feasibility of a CHP system. For systems operating in mode C a similar procedure would be used, except that electricity would have to be purchased from the grid. The cost of that power would be determined by the electrical rate schedule.

Example 11.3 contained a detailed explanation of the procedure used in the first-order assessment procedure, and the results were obtained "by hand." A more flexible approach is to use a computational system such as Mathcad to do the calculations. Example 11.4 is structured about the Mathcad approach to CHP economic assessment.

Example 11.4

Determine the cost savings and simple payback period for the facility discussed in Example 11.3 if 50% of the exhaust energy is recovered. This represents essentially the maximum that could reasonably be expected to be recovered. Use Mathcad.

Solution The same procedure would be followed as in Example 11.3 except that the recovered energy η_r would be 0.50 instead of 0.34. The Mathcad worksheet is contained in Figure 11.10. Variable names in the worksheet are similar to the names in Example 11.3 except that NG is used in place of "natural gas" and EE is the electrical energy. If more thermal energy is recovered, the savings increase to $403 400 and the simple payback period falls to 7.4 years.

$kWh := kW \cdot hr$ $\quad ccf := 100 \cdot ft^3$

$\eta_e := 0.30$ $\quad \eta_r := 0.50$ $\quad \eta_{boiler} := 0.85$

$EEy := 17049900 \cdot kWh$ $\quad Demandy := 26775 \cdot kW$ $\quad NGy := 2213786 \cdot ccf$

$$UFy := \frac{EEy \cdot 12}{Demandy \cdot 8760 \cdot hr} \qquad UFy = 0.872$$

At a generation efficiency of 30%, the natural gas required to generate the electricity is

$$NGelecy := \frac{EEy \cdot ccf}{\eta_e \cdot 100000 \cdot BTU} \qquad NGelecy = 1.939 \times 10^6 \text{ ccf} \qquad NGccfy := \frac{0.265}{ccf}$$

$$Erecy := NGelecy \cdot \frac{\eta_r}{\eta_{boiler}} \qquad Erec = 1.141 \times 10^6 \text{ ccf}$$

This is mode D of the narrative for which the electricity is supplied. The natural gas required is the old plus the new (electricity generation) minus the recovered.

NGreqy: = NGy + NGelecy − Erecy NGreqy = $3.012 \times 10^6 \cdot$ccf

NGcosty: = NGreqy·NGccfy·1.015 NGcosty = 8.102×10^5

$\text{OMcosty: = EEy}\cdot\frac{0.01}{\text{kWh}}$ OMcosty = 1.705×10^5

CHPcosty: = NGcosty + OMcosty CHPcosty = 9.807×10^5

ConvCost: = 796593 + 587515 ConvCost = 1.384×10^6

CHPsavingy: = ConvCost − CHPcosty CHPsavingy = 4.034×10^5

$\text{TurbineCost: = }\frac{1200}{\text{kW}}\cdot 2500\cdot\text{kW}$ TurbineCost = 3×10^6

$\text{Paybacky: = }\frac{\text{TurbineCost}}{\text{CHPsavingy}}$ Paybacky = 7.437

Figure 11.10 Mathcad solution for Example 11.4.

11.5 Thermal and Federal Energy Regulatory Commission Combined Heat and Power Metrics

The percentage metric used in Figures 11.1, 11.2, and 11.3 is the thermal efficiency; however, a Btu electrical equivalent is more "useful" than a heat energy Btu, especially at a low temperature. To account for the difference in usefulness of an electrical equivalent Btu versus a thermal Btu, the Federal Energy Regulatory Commission (FERC), established several modified efficiency definitions. If F is the fuel energy input, P is the useful power output (electricity equivalent in Btus), and Q is the thermal energy captured, the usual definition of thermal efficiency for a CHP system is

$$\eta_{\text{thermal}} = \frac{P+Q}{F} \tag{11.2}$$

To acknowledge the idea that an electrical equivalent Btu is more valuable than a thermal Btu, FERC discounts by 50% the thermal energy captured and defines a modified thermal efficiency as

$$\eta_{\text{FERC}} = \frac{P+(Q/2)}{F} \tag{11.3}$$

The fuel utilization efficiency (FUE or η_{FU}), also called the effective electrical efficiency, expresses the CHP efficiency as the ratio of electrical output to net fuel consumption, where the fuel consumption excludes that portion of the fuel that produces useful thermal energy and is defined to be

$$\eta_{\text{FU}} = \frac{P}{F-(Q/\eta_Q)} \tag{11.4}$$

where η_Q is the thermal efficiency of producing the thermal energy; $\eta_Q \approx 0.8$ for a boiler.

Since CHP fuel savings compared with separate power and thermal energy operations is appropriate when considering a CHP system, the fractional energy savings S becomes

$$S = 1 - \frac{F}{(P/\eta_P)+(Q/\eta_Q)} \tag{11.5}$$

where the denominator expresses the fuel required for separate production of power and thermal energy, with η_P and η_Q the thermal efficiencies of the power and thermal energy devices respectively.

Example 11.5 provides details of implementing the various definitions for the CHP example considered previously in this chapter.

Example 11.5

Determine η_{thermal}, η_{FERC}, η_{FU}, and S for the system of Example 11.4.

Solution From Example 11.4, the system is operating in mode D in which all the required electricity is generated but the recovered thermal energy is insufficient to meet the thermal needs. To generate 17.049×10^6 kWh, the fuel, natural gas, required ($\eta_e = 0.3$), is 1.939×10^6 ccf, and the recovered thermal energy is 9.699×10^{10} Btu $= 9.699 \times 10^5$ ccf. Converting the electric energy in kilowatt-hours to 100 cubic feet equivalent (for convenience):

$$17.049 \times 10^6 \text{ kWh} \times 3412 \times \frac{3412 \text{ Btu}}{\text{kWh}} \times \frac{\text{ccf}}{100\,000 \text{ Btu}} = 5.818 \times 10^5 \text{ ccf}$$

These values correspond to $P = 5.818 \times 10^5$ ccf, $F = 1.939 \times 10^6$ ccf, and $Q = 9.699 \times 10^5$ ccf. The thermal efficiency is

$$\eta_{\text{thermal}} = \frac{P + Q}{F} = \frac{5.818 \times 10^5 \text{ ccf} + 9.699 \times 10^5 \text{ ccf}}{1.939 \times 10^6 \text{ ccf}} = 0.80$$

This result should not be surprising, since for $\eta_e = 0.30$ and $\eta_r = 0.50$ the sum is 0.80 for a first-order analysis. However, consider η_{FERC}:

$$\eta_{\text{FERC}} = \frac{P + (Q/2)}{F} = \frac{5.818 \times 10^5 \text{ ccf} + \frac{1}{2} \times 9.699 \times 10^5 \text{ ccf}}{1.939 \times 10^6 \text{ ccf}} = 0.55$$

As expected, η_{FERC} is less than η_{thermal}; indeed, since Example 11.4 represents close to the maximum realistic performance for a CHP system, $\eta_{\text{FERC}} = 0.55$ represents close to the maximum FERC efficiency a CHP system can attain.

The fuel utilization efficiency η_{FU} becomes (with $\eta_Q = 0.85$)

$$\eta_{\text{FU}} = \frac{P}{F - (Q/\eta_Q)} = 0.729$$

And the energy savings S with $\eta_e = 0.350$ (consistent with the simple-cycle central generating plant) yields

$$S = 1 - \frac{F}{(P/\eta_P) + (Q/\eta_Q)} = 0.308$$

Hence, using CHP results in a fuel (natural gas) savings of 30% over a conventional system.

CHP offers thermal and economic advantages, as the following case study indicates.

11.6 Combined Heat and Power System Example

The Mississippi Baptist Medical Center (MBMC) in Jackson, MS, provides a good example of a CHP system that has a long history of economic success and reliability. Figure 11.11 is a photograph of the MBMC campus. The MBMC is a 624-bed, full-service hospital with a medical staff of 500 and 3000 employees. In 1990, in an effort to reduce utility costs, the hospital

Figure 11.11 MBMC campus.

investigated the possibility of installing a CHP system, at the time called a co-generation system. The energy profile in 1990 was as follows:

1) large electricity requirement;
2) large steam requirement;
3) significant price differential per Btu (spark spread) between electricity and gas;
4) centralized physical plant; and
5) small daily variations in energy requirements.

Thus, the MBMC possessed all the attributes to make CHP economically feasible. The results of a detailed engineering study resulted in the following specifications and costs estimates for a CHP system:

1) projected savings of $800 000/year;
2) initial system cost of $4.2 million;
3) simple payback of period of 6.3 years;
4) provide >70% of electricity requirement;
5) provide 95% of steam required; and
6) provide 75% of cooling load (via absorption chillers).

A system schematic is presented in Figure 11.12 and is similar to the layout discussed in conjunction with Figure 11.5. Since the system was planned to supply about 70% of the electricity, the facility is normally grid connected. The turbine exhaust is directed to an HRSG that provides steam for two absorption chillers and sterilization.

The diverter valve (DV), controlled by the HRSG, directs the exhaust gas to the HRSG or out of the bypass stack to maintain the required steam pressure. The HRSG contains a duct burner that can be operated in two modes: (1) with a heat addition up to 5.8×10^6 Btu/h to supplement the turbine exhaust or (2) with up to 41.5×10^6 Btu/h direct fire when the turbine is offline. The economizer utilizes the remaining waste heat to preheat boiler feedwater and to add water treatment chemicals to the feedwater.

Table 11.4 contains descriptive details of MBMC CHP system components.

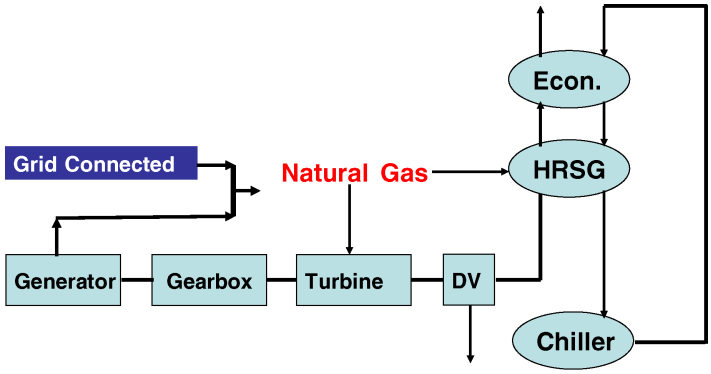

Figure 11.12 MBMC CHP system schematic.

The system went online in 1992 and has been in use since then. Table 11.5 provides a summary of savings and usage for several years of CHP operation.

The results contained in Table 11.5 demonstrate the expected savings during the initial years of operation. The system paid back in the projected 6 years. In subsequent years, the savings from the system were substantial. However, one unexpected benefit was the experience of MBMC during Hurricane Katrina. After landfall, Katrina's eye passed close to Jackson and severely damaged the city's electrical grid.

The MBMC's experience during Katrina is illustrated in Figure 11.13. About 1 h after Katrina impacted the area, the main power grid (MPG) failed. The switchgear shifted to the alternate electrical feed, and city water pressure was lost. The Jackson Fire Department placed a pumper truck near the MBMC CHP system and provided water for the duration of the emergency. The MPG was restored but proved to be unstable. At 5 h into the emergency a decision was made to shed sufficient load to enable it to disconnect totally from the grid and to use the CHP system as the only source of electricity. The hospital elevators were switched to the backup diesel generator, and magnetic resonance imaging use was discontinued. MBMC operated for 52 h on the CHP system and was literally an island of light and comfort during the emergency. Approximately 57 h after Hurricane Katrina hit the MPG was restored and normal operation was initiated. During this unforeseen event, the CHP system demonstrated its "islanding" capability and its power resiliency.

Table 11.4 MBMC CHP system component information

Component	Description	Performance
Turbine	Solar Centaur H	ISO 5600 hp/4.3 MW/13 800 V
		Natural gas fired
Controller	Allen Bradley PLC 5/20 microprocessor	
Diverter valve		
HRSG	ABCO	30 000 lb/h steam at 125 psi
Absorption chillers:	York Paraflow double effect	1250 tons
	Trane double effect	750 tons
Switch gear	Powell metal-clad 4-bay	Synchronizing controls
		2 s to secondary grid

Table 11.5 Yearly operation summary for several years

Year	Electricity saving ($)	Natural gas cost ($)	Maintenance cost ($)	Savings ($)
1994	1 250 000	402 000	159 000	686 000
1995	1 240 000	432 000	159 000	648 000
1996	1 400 000	468 000	163 000	770 000
Average cost avoidance				701 000
2001	1 415 770	708 549	174 000	533 225
2002	1 587 074	776 950	174 000	636 123
2003	1 823 494	743 852	174 000	905 643
2004	2 022 926	972 401	174 000	876 524
Average cost avoidance				737 879

Because of natural gas supply problems in the Gulf of Mexico due to Katrina, the price of natural gas spiked at about $\$15/10^6$ Btu in the months after Katrina. At this rate, electrical power purchased from the grid was cheaper than using the CHP system, so MBMC used economics to determine if the grid power or CHP-generated power would be used during periods of excessive natural gas costs. Once natural gas prices decreased from the post-Katrina high, normal CHP operation was resumed. However, MBMC continues to exercise its economic option when natural gas prices exceed an economic maximum. In this fashion, the CHP system provides fuel/energy diversity.

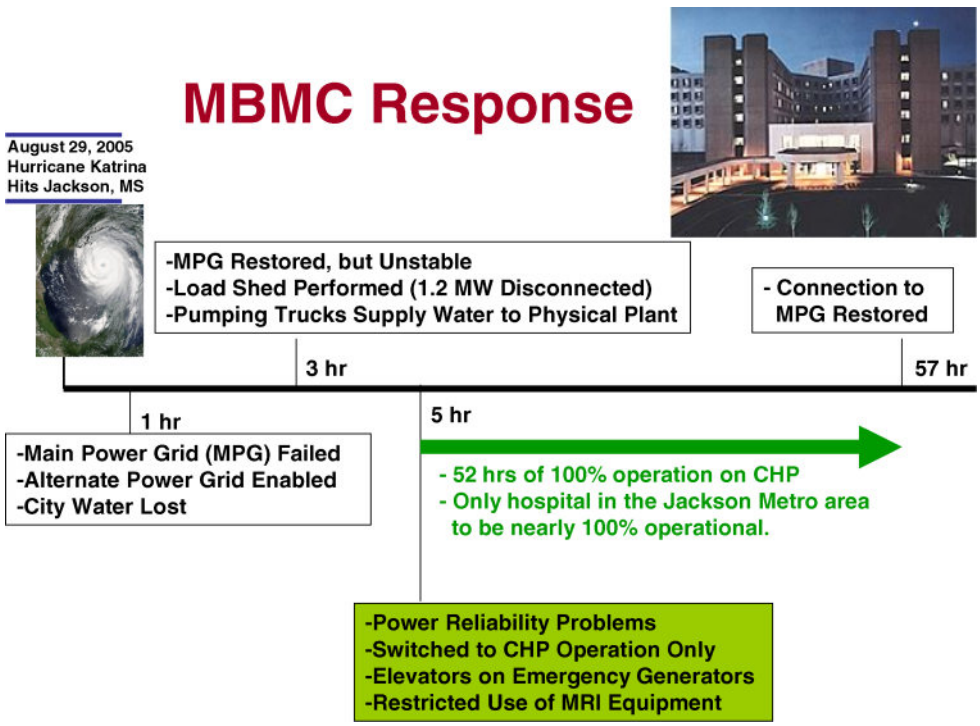

Figure 11.13 MBMC's response to Hurricane Katrina.

Table 11.6 Maintenance details and costs

Turbine gearbox overhaul	3.5 years
Oil change	As needed (years between)
Filter replacement	3 months
Routine inspections	8 weeks
Intermediate inspection	6 months
Annual inspection	
200 offline hours/year for inspections	
Monthly maintenance contract	$14 500

Two keys to the long-term successful operation of the MBMC CHP system have been attention to maintenance and staff expertise. Table 11.6 provides details of maintenance procedures and cost as of the summer of 2007. The monthly maintenance fee includes replacement components and scheduled inspections. Personnel under contract with Solar Turbines provide on-site expertise as required.

The lessons learned in the MBMC CHP operation can be summarized as follows:

1) necessity for accurate and consistent monitoring;
2) no-penalty switchover-to-grid electrical rate structure;
3) fuel/energy economic alternatives consideration;
4) comprehensive preventive maintenance program;
5) expertise of power house staff.

The MBMC CHP system is a success story and is an example of how effective CHP systems can be.

11.7 Closure

CHP is a new version of an old paradigm (co-generation) that offers many economic as well as other operational advantages. The internet provides considerable information beyond that presented here. Indications are that CHP will increase in importance in the coming years. CHP offers greatly improved thermal efficiencies and is an alternative use of existing fossil fuel resources.

Characteristics of installed CHP systems in the USA as of April 2014 were reported by the EPA in *Catalog of CHP Technologies* (Darrow *et al*., 2015). Table 11.7 was generated from those data. The results are interesting, with a total installed capacity of 83 317 MW in 4226 installations. However, by percentage, while 52% of the total CHP systems use reciprocating engines, their combined capacity (2288 MW) represents only 2.7% of the installed CHP capacity. The average capacity of reciprocating engine CHP systems is only 1 MW. Gas turbines account for 64% of the installed capacity, with an average installation size of 80 MW. Steam turbines provide 32% of the capacity, with an average size of 36 MW. Microturbines and fuel cells together provide only 0.2% of the installed capacity, with average capacities of less than 1 MW. CHP represents about 7% of the total US installed electrical generating capacity, but about 14% of the installed capacity devoted to manufacturing.

The USDOE has established a goal of an additional 40 GW of CHP capacity by 2020 (USDOE and US EPA, 2012). As Figure 11.14 demonstrates, the potential for significant additional CHP

Table 11.7 Characteristics of installed CHP systems in the USA

Prime mover	Number	Percentage of sites	Capacity (MW)	Average capacity (MW)	Percentage of capacity
Reciprocating engine	2 194	51.9	2 288	1.0	2.7
Gas turbine	667	15.8	53 320	80.0	64.0
Steam turbine	734	17.4	26 741	36.0	32.1
Microturbine	355	8.4	78	0.2	0.1
Fuel cell	155	3.7	84	0.5	0.1
Other	121	2.9	806	6.7	1.0
Total	4 226	100	83 317	19.7	100

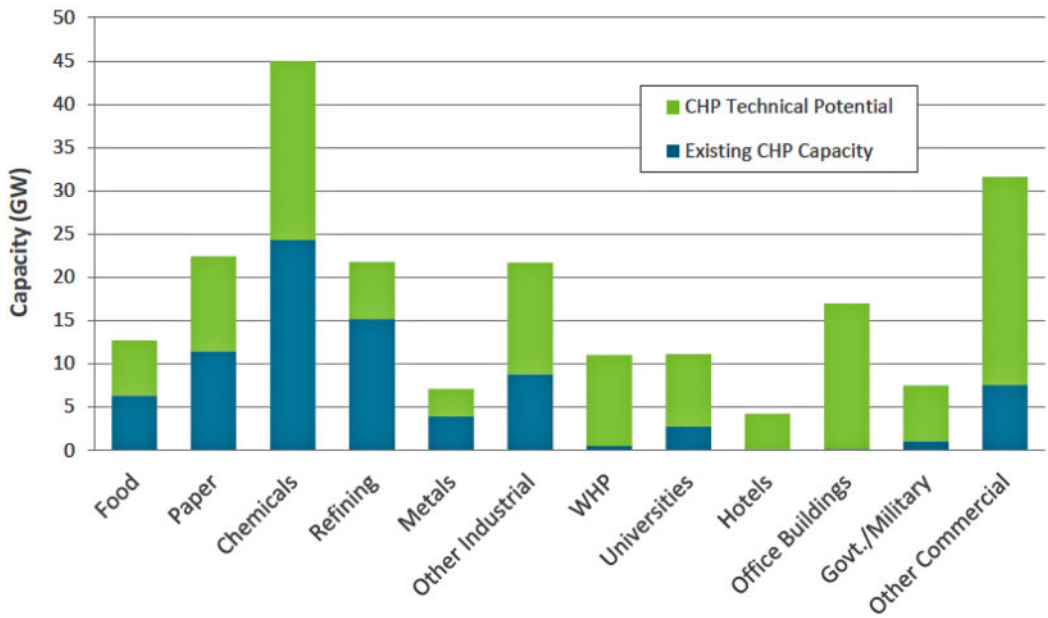

Figure 11.14 CHP potential in manufacturing. *Source*: http://energy.gov/sites/prod/files/2014/06/f17/CHP%20Deployment%20Program.pdf.

capacity in the manufacturing arena certainly exists. Indeed, for the last few years the yearly installed CHP capacity has been less than 1 GW per year in the USA (Pales *et al*., 2014). The general consensus is that restructuring of utility rate schedules and the volatility of energy costs, especially natural gas, have been primary causes of the small increase in installed capacity.

References

ASHRAE (2015) *Combined Heat and Power Design Guide*. ASHRAE, Atlanta, GA.
Beith, R. (2011) *Small and Micro Combined Heat and Power Systems Advanced Design, Performance, Materials and Applications*. Woodhead Publishing Limited, Cambridge, UK.

Boyce, M.P. (2010) *Handbook for Cogeneration and Combined Power Cycles*, 2nd edn. ASME Press, New York.

Darrow, K., Tidball, R., Wang, J., and Hampson, A. (2015) *Catalog of CHP Technologies.* US Environmental Protection Agency Combined Heat and Power Partnership. https://www.epa.gov/sites/production/files/2015-07/documents/catalog_of_chp_technologies.pdf (accessed October 21, 2016).

Horlock, J.H. (1997) *Cogeneration: Combined Heat and Power*. Krieger, Malabar, FL.

Kamm, F. (1997) *Heat and Power Thermodynamics*. Delmar, Albany, NY.

Kehlhofer, R, Bachman, R., Nielsen, H., and Warner, J. (1999) *Combined Cycle Gas and Steam Turbine Power Plants*. PennWell, Tulsa, OK.

Kolanowski, B.F. (2000) *Small-scale Cogeneration Handbook*. Prentice-Hall, Upper Saddle River, NJ.

Kreith, F. and West, R.E. (1997) *CRC Handbook of Energy Efficiency*, CRC Press, Boca Raton, FL.

NREL (2013) *Distributed Generation Renewable Energy Estimate of Costs.* http://www.nrel.gov/analysis/tech_lcoe_re_cost_est.html (accessed October 21, 2016).

Pales, A.F., Pielli, K., and Thornton, R. (2014) CHP/DHC Country Scorecard: United States. OECD/IEA, Paris http://www.iea.org/publications/insights/insightpublications/US_CountryScorecard_FINAL.pdf (accessed October 21, 2016).

Termuehler, H. (2001) *100 Years of Power Plant Development*. ASME Press, New York.

USDOE and US EPA (2012) *Combined Heat and Power: A Clean Energy Solution.* US Department of Energy and US Environmental Protection Agency. http://energy.gov/sites/prod/files/2013/11/f4/chp_clean_energy_solution.pdf (accessed October 21, 2016).

12

Biomass

12.1 Introduction

Biomass is defined as any material of recent biological origin. Examples include crops and forest products and residue associated with crops and forest products, as well as animal fat and food-processing waste.

In the pre-twentieth century era (see Figure 1.4), wood, a biomass, was the primary fuel used. Biomass as a solid has many disadvantages over liquids (such as petroleum) or gases (such as natural gas). The goal of many biomass processes is to convert solid fuel into more useful forms: gaseous or liquid fuels. Biomass has received much attention in the media and by political leaders, both in relation to alternative fuel sources and as a remedy for the USA's dependence on imported fossil fuels. Biomass is attractive as at least part of a strategy for reducing dependence on foreign oil imports because it is domestic, secure, and abundant. Books addressing biomass fuel issues include those by Brown (2011), Carareda (2014), Drapcho *et al.* (2008) and Speight (2008). However, Kreith and West (2007) emphatically point out that providing alternative fuel sources for transportation is not a long-term solution for fossil-fuel dependence. This chapter explores the salient features of biomass and biomass conversion processes.

Part of the economic impetus for biomass fuels has been the federal subsidies enacted supporting production and use of biomass-based fuels such as ethanol and biodiesel, both of which are discussed in this chapter. The website (http://www.afdc.energy.gov/laws/fed_summary) maintained by the Alternative Fuels Data Center of the Office of Energy Efficiency & Renewable Energy (EERE) provides a comprehensive compilation of current federal laws and incentives. Over the years, these subsidies have included different biofuels and have had a chaotic history of expirations, extensions, and retroactive extensions. A good example is the ethanol tax credit, first enacted more than 30 years ago and long considered to be immune to political pressure. However, the ethanol tax credit was allowed to expire on December 31, 2011, because of mounting pressures from a number of organizations, the belief that the expanding production of ethanol from corn had resulted in increased food prices, and the evidence that the ethanol industry had matured. For example, the volumetric ethanol excise tax credit was $0.51 per gallon of pure ethanol (minimum 190 proof) blended with gasoline and was available to those that produced, sold, or used ethanol in their trade or business. Qualified biodiesel producers or blenders are eligible for an income tax credit of $1.00 per gallon of biodiesel (B100) or renewable diesel produced or used in the blending process. The total amount of credits claimed by all biodiesel producers may not exceed the annual biodiesel tax credit cap of $10 million. For the purpose of this credit, biodiesel must meet ASTM specification D6751, and renewable diesel is defined as a renewable, biodegradable, non-ester combustible liquid derived from biomass resources that meets ASTM specification D975.

Biomass raw materials (feedstocks) exhibit considerable variations in chemical composition and cell structure. These features determine the products that can be obtained from biomass

Alternative Energy Systems and Applications, Second Edition. B. K. Hodge.

Companion website: www.wiley.com\go\Hodge\AESystemsandApplications2E

feedstocks as well as the processes and difficulties in obtaining useful fuel and other chemicals from biomass. Boundy *et al.* (2011) provides a comprehensive survey of biomass data from diverse sources. The statistics and information they present characterize the biomass industry from feedstocks to end use.

Biomass chemical compositions are broadly classed as cellulosic biomass or starch/sugar biomass. However, both biomass classes are based on photosynthesis using energy supplied by the sun. The basic photosynthesis process utilizes carbon dioxide (CO_2) and water (H_2O) to produce simple sugars in the presence of solar energy, chlorophyll, and other plant ingredients. A representative photosynthesis chemical reaction for the production of glucose ($C_6H_{12}O_6$) is

$$6C\,O_2 + 6H_2O \rightarrow C_6H_{12}O_6 + 6O_2 - 480\ \frac{kJ}{mol} \tag{12.1}$$

The detailed chemical path to glucose, as represented by Equation 12.1, is quite complicated, but the end products are glucose and oxygen. The energy comes from the sun, but as indicated in Table 1.3 and as confirmed by Decher (1994), while the local conversion efficiency may be as high as a few percentage points, the global efficiency of photosynthesis may be as low as 0.3%. The plants use the sugars of reactions, such as those represented by Equation 12.1, to produce the myriad of chemical substances needed for growth and life processes. One of the prime selling points of biomass is the potential use of CO_2, a greenhouse gas, to produce fuel (energy) and oxygen – a win–win situation.

Indeed, one of the great attractions for biomass is the concept that biomass may be CO_2 neutral. The central concept of a CO_2-neutral biomass fuel is that the CO_2 generated by combustion is balanced by the CO_2 incorporated by photosynthesis during the growth process. The implication is that the CO_2 produced by harvesting and combustion of the biomass is completely offset by growth of the biomass. But, as Schobert (2014) and others points out, this balance is difficult to achieve because of a myriad of reasons – the most important being the loss of CO_2 to the soil and the generation of CO_2 by fuels required to cultivate, harvest, and process biomass. Additionally, the timescale required for the biomass growth can be on the order of years to decades, depending on the particular biomass. Another environmental concern with burning biomass is that the combustion process produces emissions that may contain a diverse variety of pollutants, including carbon monoxide (CO), nitrogen oxides, and ash/soot particulate matter.

12.2 Biomass Availability

The US Department of Energy's (DOE's) EERE web site (www.eere.energy.gov) contains a wide variety of useful information relating to biomass and is a good source of additional, readily available, public-domain information on topics presented in this chapter. Oak Ridge National Laboratory (ORLN) provides an excellent source of data, updated periodically, in its *Biomass Energy Data Book*; the current version is the fourth edition (Boundy *et al.*, 2011). Following EERE, a delineation of biomass resources follows:

1) Agricultural crops – commodity products such as corn, soybeans, and wheat that yield sugar and oils.
2) Agricultural crop residues – residues (such as stalks and leaves) of agricultural crops that are not harvested for commercial use. Corn stover is the stalks, leaves, husks, and cobs of corn, for example.
3) Herbaceous energy crops – perennials that are harvested annually after reaching maturity. These are grasses such as switchgrass, miscanthus, bamboo, and fescue.

4) Woody energy crops – hardwood trees harvested within 5–7 years of planting. Examples are poplar, willow, maple, cottonwood, and sweetgum.
5) Forestry residues – biomass not harvested or removed during logging, and materials removed during forest management operations.
6) Aquatic crops – aquatic biomass such a kelp, seaweed, and algae.
7) Industrial crops – crops developed to produce specific chemicals or feedstocks. Kenaf is an example.
8) Animal waste – waste resulting from farm and processing operations.
9) Municipal waste – waste from residential, commercial, and industrial sectors contains significant biomass with energy content.

Figure 12.1 provides a breakdown of the sources of biomass. The sources include biomass from forest lands and agricultural lands as well as secondary sources from municipal solid waste, animal manure, and residues from food processing.

Much of the USA is well suited for the production of herbaceous and woody energy crops in addition to agricultural crops. Figure 12.2a illustrates by region the energy crops that are particularly suited for that region. Thus, most of the USA, except for the mountain and desert southwest, could produce biomass feedstock. Figure 12.2b indicates the biomass production potential for the USA. There are few surprises in Figure 12.2). The production potential tracks the agricultural production patterns in the USA. The question of availability of biomass was initially answered by a 2005 study jointly sponsored by the US Departments of Agriculture and Energy (Perlack *et al*., 2005). This report has become known as the "billion-ton report" because the authors conclude that land resources are sufficient to sustain a biomass budget of 1 billion tons/year – enough biomass to displace 30% of the fossil fuels used for transportation. Moreover, Perlack *et al*. (2005) suggest that an increase to more than 1.3 billion tons/year

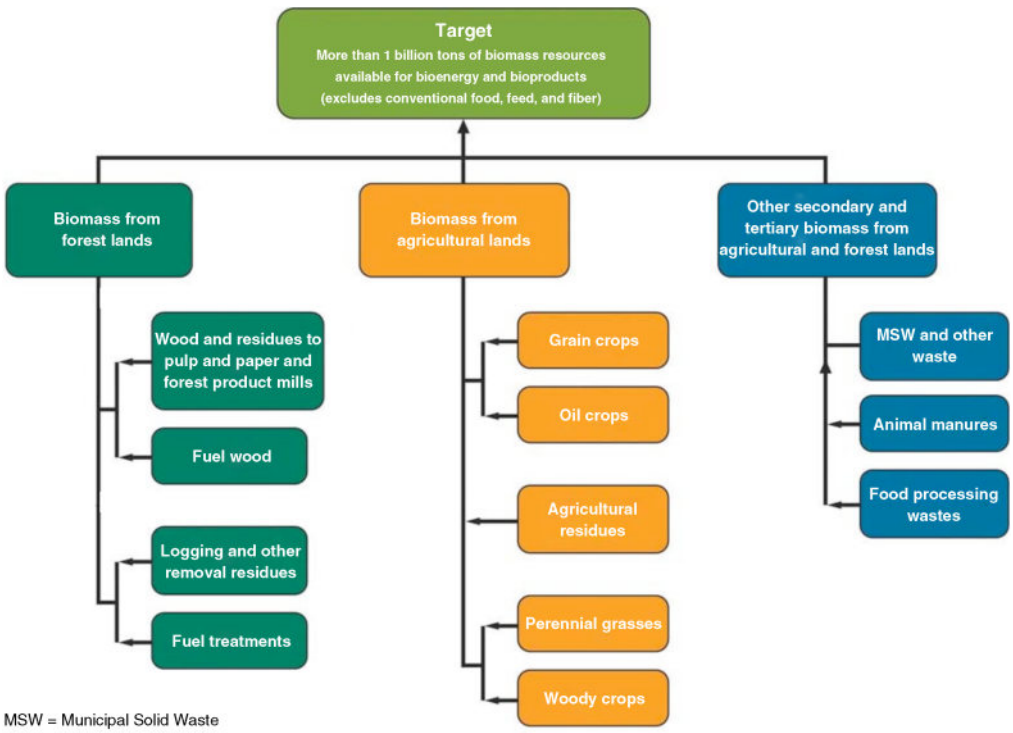

Figure 12.1 Biomass sources. *Source*: https://public.ornl.gov/site/gallery/originals/Biomass_Analysis_for_t.jpg.

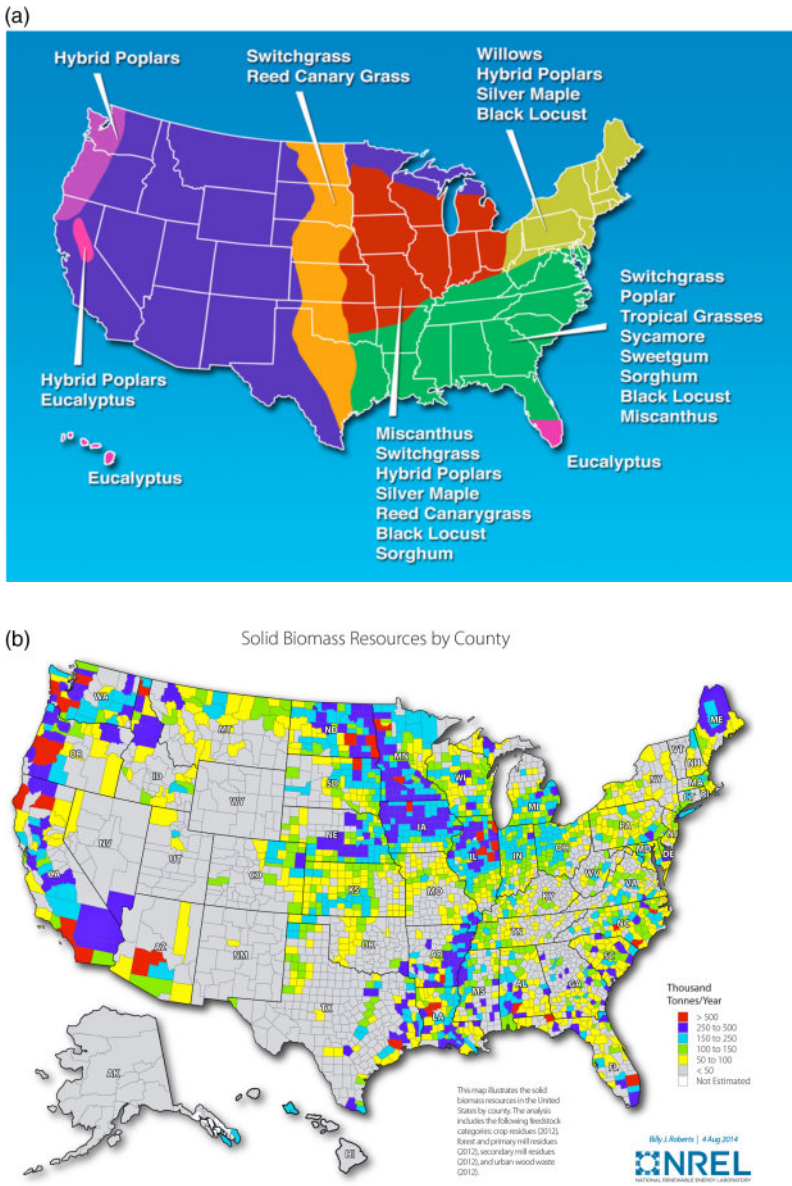

Figure 12.2 Biomass energy crops suitability and potential. (a) Crops suitability by region (ORNL 2000-00566A/abh). *Source*: http://web.ornl.gov/sci/ees/cbes/forums/Highlights%20of%2030%20years%20of%20Energy%20Crop%20Development.pdf. (b) Biomass production potential in the USA. *Source*: http://www.nrel.gov/gis/images/biomass_2014/national_biomass_solid_total_2014-01.jpg.

is possible with relatively modest changes in agricultural and forestry practices. They projected a total of 1.366 billion tons/year with 998 million tons/year from agricultural resources and 368 million tons/year from forestry resources. In 2011, the DOE issued an update to the "billion-ton report," *U.S. Billion-Ton Update: Biomass Supply for a Bioenergy and Bioproducts Industry* (Perlack and Stokes, 2011). The update is more comprehensive and rigorous than the 2005 version, and the focus is shifted from a strategic assessment to a comprehensive resource assessment. Nonetheless, the conclusions of the original and updated reports are congruent.

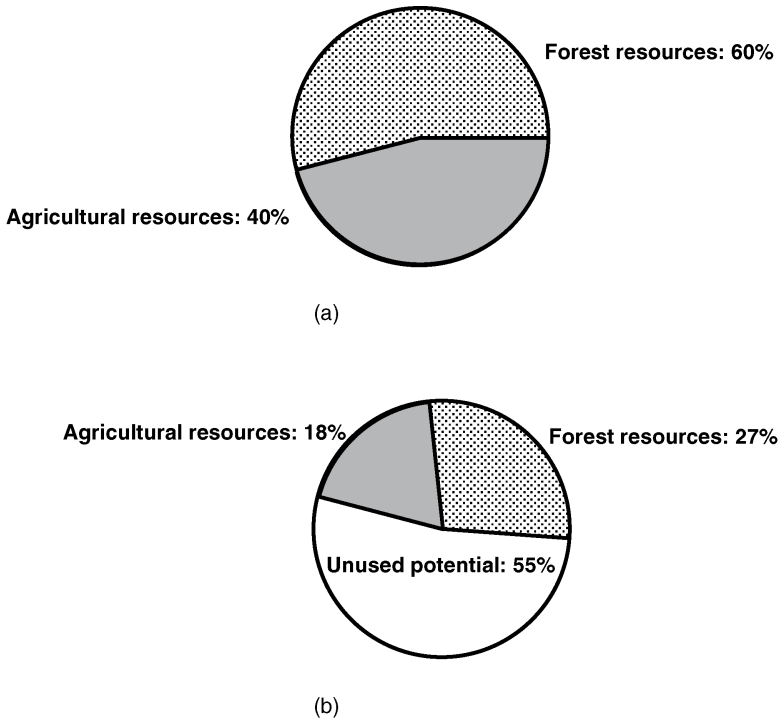

Figure 12.3 Biomass feedstock source distribution: (a) 2012 biomass usage; (b) 2012 biomass usage and potential.

The update confirms the baseline expectation of 1 billion tons biomass resource by 2020 is still valid, and a 2–4% high-yield option could result in as much as 1600 tons by 2020.

The results of data in the *Biomass Energy Data Book* (Boundy *et al.*, 2011) were used to construct Figure 12.3. In 2012, forest resources accounted for 60% of the actual usage with the remaining 40% supplied by agricultural resources. However, as Figure 12.3b demonstrates, 55% of biomass resources were not utilized.

12.3 Biomass Fundamentals

The primary products of interest from biomass processing are as follows:

1) Liquid fuels:
   a) ethanol – ethyl alcohol for use as a fuel;
   b) methanol – methyl alcohol produced as a by-product of gaseous fuels;
   c) biodiesel – chemically modified vegetable oils suitable for diesel fuel;
   d) vegetable oil – oils contained in grains and seed;
   e) pyrolysis oil – a liquid fuel with a heating value of 17–20 MJ/kg.
2) Gaseous fuels:
   a) biogas – a mixture of methane (CH_4) and CO_2, 55–70% CH_4 by volume;
   b) producer gas – flammable gas mixture containing carbon monoxide (CO), hydrogen (H_2), CH_4, nitrogen (N_2), CO_2, and higher hydrates;
   c) synthesis gas – a mixture of CO and H_2.

Each of the possible biomass fuels will be examined in Section 12.5.

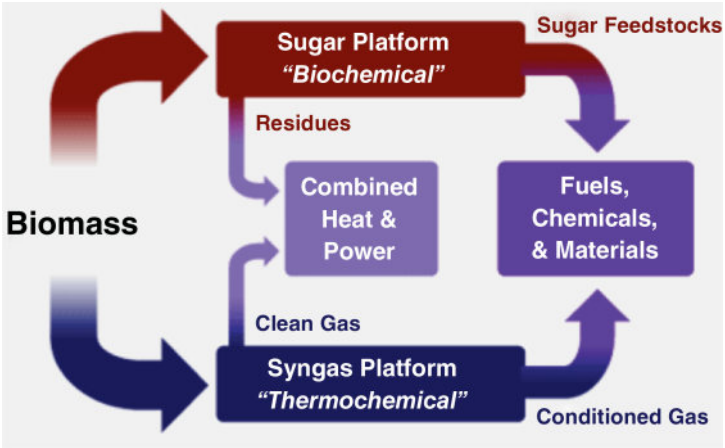

Figure 12.4 DOE biomass platforms. *Source*: http://www.nrel.gov/docs/gen/fy04/36831g.pdf.

The US DOE has classified biomass feedstock to fuels or other products in terms of platform. The two primary platforms for biomass and their relationships to feedstocks, processes, and fuels/products are illustrated in Figure 12.4. The primary platforms of interest for this discussion are the sugar (or biochemical) and the syngas (thermochemical) platforms. Biomass feedstocks are used in both platforms, with the primary output being fuels and chemicals. However, for both platforms fuels can be used in combined heat and power (CHP) applications. CHP systems are discussed in Chapter 11.

Biomass and biomass for fuel conversion are intimately involved with chemistry. To establish a uniform basis, the definitions listed in Tables 12.1 and 12.2 are introduced.

Table 12.1 Chemical formula and molecular masses.

Chemical formula	Molecular mass (g/g-mol)
Acetone, C_3H_6O	58.08
Ethane, C_2H_6	30.07
Ethanol (ethyl alcohol), C_2H_5OH	46.07
Ethylene, C_2H_4	28.05
Glycerol,[a] $C_3H_5(OH)_3$	92.094
Isopropanol, C_3H_8O	60.09
Methane, CH_4	16.0425
Methanol (methyl alcohol), CH_3OH	32.04
Phenol (hydroxybenzene), C_6H_5OH	94.11
Sucrose, $C_{12}H_{22}O_{11}$	342.30

a) Clear, colorless, viscous, sweet-tasting liquid belonging to the alcohol family of organic compounds.

Table 12.2 Definitions of terms used.

Acetate	Man-made textile fiber produced from the plant substance cellulose.
Ash	The powdery residue of matter that remains after burning.
Carbohydrates	Compounds that include sugars, starches, cellulose, and a wide variety of other cellular products. The name carbohydrates arose because many of these compounds have the formula $C_n(H_2O)_m$ (where m and n are integers) – apparently making them a "hydrate of carbon," although this description was later found to be inaccurate.
Cellulose	$(C_6H_{10}O_5)_x$, the chief constituent of cell walls of plants.
Ester	Any of a class of organic compounds that react with water to produce alcohols and organic or inorganic acids.
Hemicellulose	Complex carbohydrates that surround the cellulosefibers of a plant cell.
Hydrolysis	The breaking of hydrogen bonds in long-chained organic molecules.
Lignin	Complex oxygen-containing organic substance that, with cellulose, forms the chief constituent of wood.
Protein	Any group of nitrogenous organic compounds of high molecular weight that are synthesized by plants and animals that are required for life processes.
Starch	$(C_6H_{10}O_5)_n$, a white, granular, organic chemical that is produced by all green plants.
Sugar	Any of numerous sweet, colorless, water-soluble compounds present in the sap of seed plants and the milk of mammals and making up the simplest group of carbohydrates.
Triglycerides	Esters in which three molecules of one or more different fatty acids are linked to the alcohol glycerol.

12.4 Biomass Characteristics

Three types of chemical descriptions are used to describe the attributes of biomass: biochemical, proximate, and ultimate. Biochemical analysis describes an organic compound in terms of proteins, oils, sugars, and fiber (lignocellulose). For cellulosic materials, the breakdown of lignocellulose into cellulose, hemicellulose, and lignin is important in formulating specific processes for extracting useful fuel and other products. Proximate analysis breaks a compound into its constituents of volatiles, ash, and fixed carbon. Volatile material is the faction that can be decomposed by heat (~400 °C) in a nonoxidizing surrounding. Ultimate analysis, as its name implies, yields components including the elements (C, H, O, N, S, and Cl), moisture, and ash. All three are useful in understanding biomass processes. Table 12.3 illustrates biochemical analysis of some common biomass feedstocks. The feedstocks are divided into those that are food based and those that are lignocellulose based. Table 12.4 shows proximate analysis of feedstocks, and Table 12.5 presents results of ultimate analyses for most of the feedstocks listed in Table 12.4.

A wide range of liquid and gaseous fuels can be obtained from biomass. Biomass-derived fuels may be used directly in some internal combustion engines, may be used for process energy, or may be further processed into more desirable fuels or chemical feedstocks. Section 12.5 examines the characteristics of a number of biomass-based fuels and products.

12.5 Biomass-Based Fuels and Products

12.5.1 Ethanol

Ethanol (C_2H_5OH), also called ethyl alcohol or grain alcohol, is the alcohol in "alcoholic" beverages and can be used as a fuel in modified internal combustion engines. The nominal

Table 12.3 Biochemical composition of biomass feedstocks (rounded to integer percentages).

	Protein	Oil	Starch	Sugar	Fiber	Cellulose	Hemicellulose	Lignin	Other
Food-based									
Corn (grain)	10	5	72	<1	12				
Wheat (grain)	14	<1	80	<1	5				
Artichoke	<1	<1	<1	75	25				
Sugar cane	<1	<1	<1	50	50				
Sorghum	<1	<1	<1	50	50				
Cellulosic									
Bagasse						35	25	20	20
Corn stover						53	15	16	16
Corn cobs						32	44	13	11
Wheat straw						38	36	16	10
Woody crops						50	23	22	5
Herbaceous crops						45	30	25	10
Waste paper						76	13	11	0

Source: Adapted from Goswami *et al.* (2000).

Table 12.4 Proximate analysis of common biomass feedstocks.

Feedstock	HHV (MJ/kg)	Volatile (%)	Ash (%)	Fixed carbon (%)
Alfalfa	18.45	73	7	20
Black locust	19.71	81	1	18
Black oak	18.65	86	1	13
Cedar	20.56	87	~0	13
Corn cobs	18.77	80	1	19
Corn stover	17.65	75	6	19
Corn grain	17.20	87	1	12
Douglas fir	20.37	87	~0	13
Pine, ponderosa	20.02	83	~0	17
Poplar	19.38	82	1	16
Redwood	20.72	80	~0	20
Rice, hulls	16.14	65	18	17
Rice, straw	14.56	62	24	13
Sudan grass	17.39	73	9	19
Sugarcane bagasse	17.33	74	11	15
Switchgrass	18.64	81	4	15
Wheat straw	17.51	71	9	20

Source: adapted from Goswami *et al.* (2000).
HHV: higher heating value.
Percentages rounded to integer values.

Table 12.5 Ultimate analysis of common biomass feedstocks.

Feedstock	C (%)	H (%)	O (%)	N (%)	S (%)	Cl (%)	Ash (%)
Black locust	51	6	42	1	—	—	1
Black oak	49	6	43	—	—	—	1
Corn cobs	47	6	45	—	—	—	1
Corn stover	44	6	43	1	—	1	6
Corn grain	44	6	47	1	—	—	1
Douglas fir	51	6	43	—	—	—	—
Pine, ponderosa	49	6	44	—	—	—	—
Poplar	48	6	44	—	—	—	1
Redwood	51	6	43	—	—	—	—
Rice, hulls	41	4	36	—	—	—	18
Rice, straw	35	4	36	1	—	—	25
Sugarcane bagasse	45	5	40	—	—	—	10
Switchgrass	47	6	42	1	—	—	—
Wheat straw	43	5	39	1	—	—	11

Source: adapted from Goswami *et al.* (2000).
Percentages rounded to integer values.

heating value of ethanol as a fuel is typically quoted as 101 000 Btu/gal, about three-fourths of the value of gasoline (on a volumetric basis). Thus, a motor vehicle that possesses a gas mileage of 24 miles/gal of gasoline would likely have an ethanol mileage of 18 miles/gal.

Ethanol is used to improve the octane rating and emission characteristics of gasoline and is commonly used as a 10% blend in "gasohol" called E10 (10% ethanol and 90% gasoline). The highest blend, E85, contains 85% ethanol and is used in flex fuel vehicles. Most (about 90%) of the ethanol in the USA is produced by fermentation of corn or other biomass feedstocks. The remaining, called synthetic ethanol, is produced from ethylene, a petroleum by-product, and is used mostly in industrial applications. Ethylene is one of the most highly produced organic chemical and is important as an industrial feedstock. However, the extensive production of ethanol from petroleum-based ethylene would not alleviate the dependence on imported fossil fuels.

The feedstock for fermentation to produce ethanol must be high in sugars. Sugar cane, sugar beets, and sorghum all contain high levels of suitable sugars. Sugar beets are the basis for the fuel ethanol industry in Brazil. A variety of carbohydrates (starches, hemicellulose, and cellulose) can also serve as feedstock if the carbohydrates can be broken down into sugars capable of undergoing fermentation. Corn, which is high in starches, has been the basis of the US ethanol industry for more than two decades. Cellulose and hemicellulose can be converted to fermentable sugar compounds, but the process is more difficult than for starches.

Ethanol produced from grains, such as corn, starts as a water-based slurry. After the starches are converted into sugars, the sugars are fermented into ethanol. In the fermentation process, the enzymes produced by yeast or other microorganisms decompose the sugars into ethanol and CO_2. For the production of ethanol from glucose, $C_6H_{12}O_6$, the chemical reaction is

$$C_6H_{12}O_6 \rightarrow 2C_2H_5OH + 2CO_2 \tag{12.2}$$

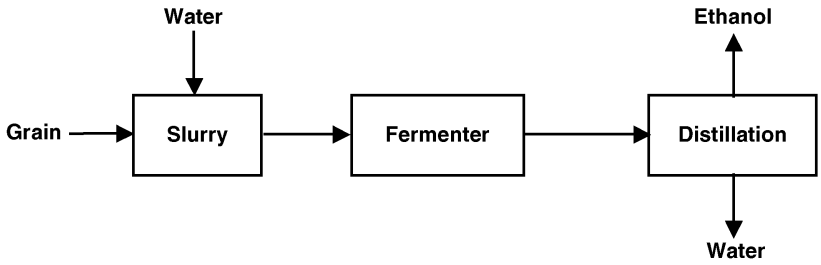

Figure 12.5 Principal steps in ethanol production from grain.

After fermentation, distillation is necessary to separate the ethanol from the water. The primary steps are illustrated in Figure 12.5.

Example 12.1
How much ethanol can be produced from a ton of sucrose?

Solution Fermentation of sucrose, $C_{12}H_{22}O_{11}$, with water results in ethanol and CO_2; the chemical equation is

$$C_{12}H_{22}O_{11} + H_2O \rightarrow 4C_2H_5OH + 4CO_2$$

The molecular masses (expressed in kilograms per kilogram-mole) of C, H, O, and OH are as follows:

$$C_{mm} 12.01 \frac{kg}{kg\text{-}mol}, \qquad H_{mm} = 1.008 \frac{kg}{kg\text{-}mol}, \qquad O_{mm} = 16.00 \frac{kg}{kg\text{-}mol}$$

$$OH_{mm} = O_{mm} + H_{mm} = 17.008 \frac{kg}{kg\text{-}mol}$$

Sucrose, SUC, possesses a molecular mass of

$$SUC_{mm} = 12C_{mm} + 22H_{mm} + 11O_{mm} = 342.30 \frac{kg}{kg\text{-}mol}$$

And for water (WAT), ethanol (ETH), and carbon dioxide (CO2), the molecular masses become

$$WAT_{mm} = 2H_{mm} + O_{mm} = 18.016 \frac{kg}{kg\text{-}mol}$$

$$ETH_{mm} = 2C_{mm} + 5H_{mm} + OH_{mm} = 46.068 \frac{kg}{kg\text{-}mol}$$

$$CO2_{mm} = C_{mm} + 2O_{mm} = 44.01 \frac{kg}{kg\text{-}mol}$$

For 1 ton of sucrose, the water required for the reaction and the ethanol and carbon dioxide formed become

$$WAT = \frac{WAT_{mm}}{SUC_{mm}} \times 1 \text{ ton} = 0.053 \text{ ton} = 105.3 \text{ lb}$$

$$ETH = \frac{4ETH_{mm}}{SUC_{mm}} \times 1 \text{ ton} = 0.538 \text{ ton} = 1077 \text{ lb}$$

$$CO2 = \frac{4CO2_{mm}}{SUC_{mm}} \times 1 \text{ ton} = 0.514 \text{ ton} = 1029 \text{ lb}$$

Although grain is the leading feedstock for ethanol production in the USA, significant replacement of gasoline by grain-based ethanol poses severe problems. Availability is a primary limitation. If all the corn in the USA were used to produce ethanol, the ethanol produced would only replace about 10% of the gasoline (Schobert, 2014). Hence, for close to 100% replacement of gasoline by ethanol, the production of corn would have to increase 10-fold. Given the amount of cultivatable land in the USA, such an increase is not possible. Moreover, widespread utilization of corn grain for ethanol would mean diverting a primary food stock to a nonfood use. Because of these limitations, ethanol from corn cannot be viewed as a solution to foreign oil dependence. However, the use of other biomass feedstocks for ethanol production, especially the use of cellulosic feedstock, offers significant long-term potential. Indeed, the US DOE has announced a biofuels initiative with the goal of reducing the cost of cellulosic-based ethanol. Because of this potential, further examination of cellulosic ethanol is warranted.

The conversion of cellulosic biomass to ethanol involves the three primary polymers (cellulose, hemicellulose, and lignin) that make up the cell walls of a plant. Depending on the plant, a cell wall typically consists of 35–50% cellulose, 20–25% hemicellulose, and 10–25% lignin. Cellulose is the most abundant biomass on Earth (http://genomicscience.energy.gov/research/DOEUSDA/)! From a biochemical standpoint, cellulose is a linear polymer of glucose residues. Hemicellulose is a branched sugar polymer formed mostly of five-carbon sugars (pentose) with some six-carbon sugars (hexose). Lignin is complex, cross-linked polymer that is covalently bonded to hemicellulose. These three polymers impart strength to mature cell walls, and this strength is part of the reason cellulosic biomass is difficult to break down into its component sugar compounds. The process of breaking down the cellulosic biomass in order to extract the sugars is called hydrolysis. The long-term, conventional process is acid hydrolysis, but the biochemical hydrolysis process is thought to have the potential to convert cellulosic biomass in quantities sufficient to replace a significant amount of gasoline with ethanol.

The biochemical hydrolysis of cellulosic biomass is a complex process requiring a detailed understanding of the roles of various enzymes in degrading the cell structure into sugars. The web site http://www.doegenomestolife.org/biofuels/ and Himmel (2008) are excellent sources of additional information and details on cellulosic biomass. Fundamentally, the enzymatic biochemical conversion of cellulosic biomass consists of three steps: (1) pretreatment to make the complex polymers more accessible to enzymatic breakdown, (2) the use of appropriate enzymes to hydrolyze the plant cell walls polymers (cellulose, hemicellulose, and lignin) into sugars, and (3) fermentation to convert the sugars into ethanol. Figure 12.6, taken from the Oak Ridge National Laboratory web site, provides a block diagram for the production of ethanol from cellulosic biomass and is indicative of the relative complexity of the process. Figure 12.7 illustrates how a cellulosic ethanol facility, with the three steps indicated, might appear.

An issue of concern with grain-based ethanol is the ratio of the energy per gallon of ethanol to the energy required to produce a gallon of ethanol – the energy balance. If the ratio is greater than unity, then the ethanol saves energy; if the ratio is less than unity, then ethanol production consumes more energy than is available in the final product. Not surprisingly, various groups, agencies, and individuals are arrayed on opposite sides of the question. The US DOE, for example, is a strong advocate that ethanol does save energy. Kreith (2007) accepts that the ratio of ethanol energy content (higher heating value) to the nonrenewable energy input for production is 1.25, but he is a strong advocate of cellulosic-based ethanol with a ratio of about 5. Tidwell and Weir (1986) also concur with Kreith, especially if the fuel used for distillation is part of a waste stream. Schobert (2014) recognizes that the energy balance for ethanol might be negative. Pimental, in a series of paper, articles, and interviews (e.g., Pimental, 2003), has maintained that the ethanol takes more energy to produce than it provides. A 2010 report from the US DOE (Shapouri *et al*., 2010), based on 2008 data from a number of ethanol facilities,

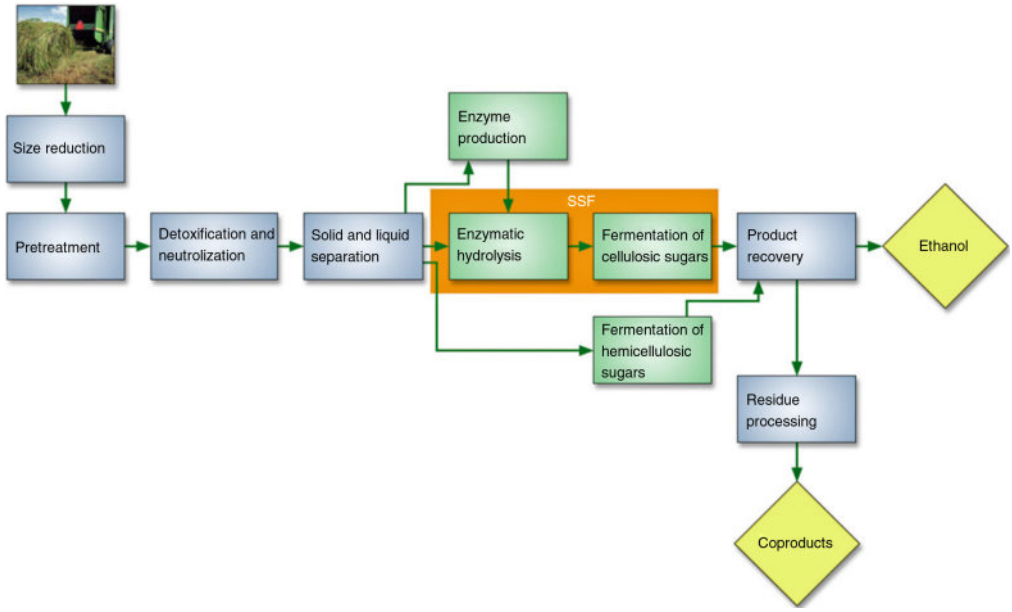

Figure 12.6 Enzymatic biochemical process to produce ethanol from cellulosic biomass. *Source*: https://public.ornl.gov/site/gallery/originals/Traditional_Cellulosic.jpg.

concludes that the ethanol energy ratio (energy from a gallon of ethanol/energy required to produce a gallon of ethanol) is significantly greater than unity in energy-efficient facilities. They state that ethanol production has made the transition from an energy sink, to a moderate energy ratio in the 1990s, to a substantial energy ratio at the present. One of the great attractions for cellulosic-based ethanol is that cellulosic ethanol requires much less hydrocarbon energy in the

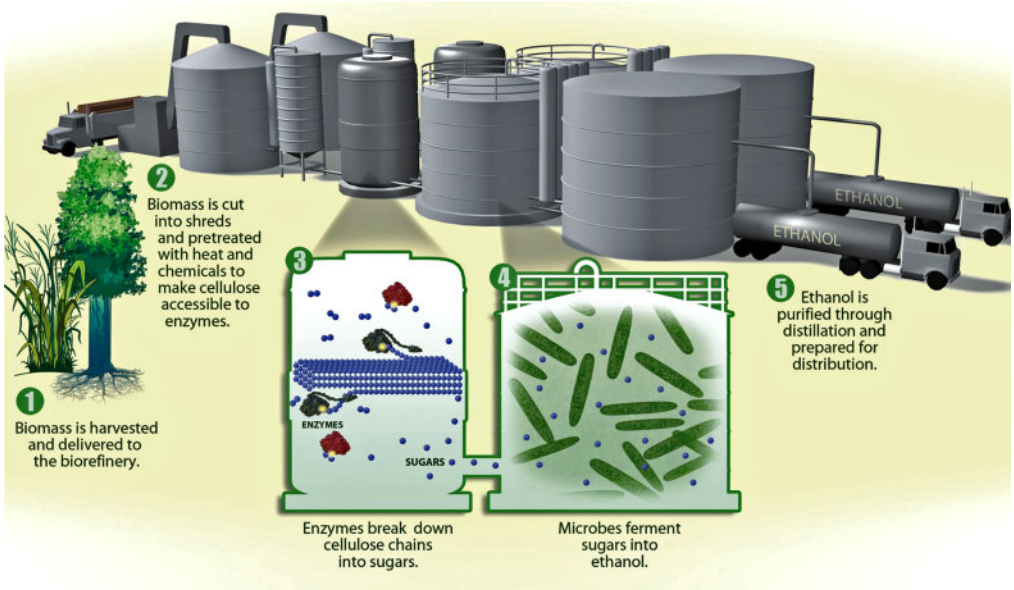

Figure 12.7 Pictorial representation of a cellulosic biomass facility. *Source*: https://public.ornl.gov/site/gallery/detail.cfm?id=252&topic=&citation=&general=&restsection.

growing, harvesting, and producing. In comparison with conventional gasoline, ethanol produces less emissions (NO_x, SO_x, soot, and CO_2).

12.5.2 Methanol

Methanol (CH_3OH), also called wood alcohol, can be used as a fuel in modified internal combustion engines. The heating value of methanol as a fuel is nominally taken as 76 000 Btu/gal, only about 58% of the value of gasoline (on a volumetric basis). Thus, a motor vehicle that possesses a gas mileage of 24 miles/gal of gasoline would likely have a methanol mileage of about 14 miles/gal. Direct methanol fuel cells (DMFC), that use methanol without reforming, were discussed in Chapter 10.

Most methanol produced in the USA is based on natural gas as the feedstock. The production of methanol from natural gas involves three chemical processes. First, natural gas (primarily CH_4) reacts with steam to produce synthesis gas (CO and H_2) according to

$$CH_4 + H_2O \rightarrow CO + 3H_2 \tag{12.3}$$

In the second step, the synthesis gas is combined with CO_2 to alter the ratio of H_2 and CO in the fashion

$$H_2 + CO_2 \rightarrow H_2O + CO \tag{12.4}$$

For the third step of the process, CO and water, in the presence of a catalyst, is used to produce methanol:

$$CO + 2H_2O \rightarrow CH_3OH \tag{12.5}$$

While production of methanol from natural gas only increases the need for natural gas, an important observation of the three-step process is that only step 1, the production of synthesis gas, involves natural gas. Synthesis gas can also be produced from a variety of carbonaceous biomass feedstocks, as well as coal. Thus, large-scale production of methanol does not have to be dependent on natural gas. Because of its importance, synthesis gas is covered as a separate topic in Section 12.5.7.

Methanol has many advantages over conventional gasoline: the methanol–air flame temperature is lower than that for gasoline, so that NO_x production would be decreased; methanol produces no SO_x, and methanol would limit soot and CO_2 emissions. As for drawbacks, in addition to the lower energy density, methanol presents severe health hazards if ingested or absorbed, and it is soluble in water. Also, since methanol burns with a nearly colorless flame, accidental ignitions could be hard to see.

12.5.3 Biodiesel/Vegetable Oil

By definition, biodiesel is a fuel composed of fatty acid alkyl esters and is made from feedstocks such as vegetable oils or animal fats. This is not a particularly useful definition for non-chemical engineers, so additional discussion is needed. A plethora of oils can be extracted from seeds, nuts, and other plant parts. Additionally, recycled cooking oil and animal fats are sources of biodiesel feedstocks. Examples include corn oil, linseed oil, olive oil, soybean oil, and sunflower oil. Although these, and similar, plant oils can be used as a fuel in diesel engines, the direct use of plant oils in diesel engines shortens operating life and leads to engine maintenance issues. Additionally, plant oils have a higher viscosity (by a factor as much as 20) than diesel fuel and have a lower cetane number, which is a performance metric. Schobert (2014) states that the expected 10 000 h between engine overhauls can be reduced to as little as 600 h for sunflower oil operation or 100 h for operation on linseed oil. If, however, plant oil is reacted with methanol,

the resulting methyl ester product is a generic biodiesel. The generic chemical reaction is

$$\underset{\text{(plant oil)}}{\text{triglyceride}} + \text{methanol} \rightarrow \text{methyl ester} + \text{glycerol} \tag{12.6}$$

A specific example for a slightly simplified composition for olive oil, from Schobert (2014), is

$$(C_{17}H_{33}CO_2)_3C_3H_5 + 3CH_3OH \rightarrow 3C_{17}H_{33}CO_2CH_3 + C_3H_5(OH)_3 \tag{12.7}$$

where $C_{17}H_{33}CO_2$ is the fatty acid component of olive oil. This chemical procedure is called transesterification. The resulting methyl ester is a biodiesel fuel that possesses characteristics much closer to those of conventional diesel fuel than the original plant oil. As van Gerpen *et al.* (2004) point out, 100 lb of oil and 10 lb of methanol input into a transesterification reaction will yield about 100 lb of biodiesel and 10 lb of glycerol.

Example 12.2
Verify that the transesterification reaction of olive oil agrees with the assertion of van Gerpen *et al.* (2004) about biodiesel yields.

Solution Equation 12.7 represents the reaction. The molecular masses for C, H, O, and OH are given in the solution to Example 12.1.

The fatty acid component, $(C_{17}H_{33}CO_2)_3$, of olive oil has a molecular mass of

$$FA_{mm} = 3(17C_{mm} + 33H_{mm} + C_{mm} + 2O_{mm}) = 844.332\frac{\text{kg}}{\text{kg-mol}}$$

The molecular mass of olive oil is thus

$$PO_{mm} = FA_{mm} + 3C_{mm} + 5H_{mm} = 885.402\frac{\text{kg}}{\text{kg-mol}}$$

For methanol (MET), biodiesel (BD), and glycerol (GLY), the molecular masses are

$$MET_{mm} = 3(C_{mm} + 3H_{mm} + OH_{mm}) = 96.126\frac{\text{kg}}{\text{kg-mol}}$$

$$BD_{mm} = FA_{mm} + 3(C_{mm} + 3H_{mm}) = 889.434\frac{\text{kg}}{\text{kg-mol}}$$

$$GLY_{mm} = 3C_{mm} + 5H_{mm} + 3OH_{mm} = 92.094\frac{\text{kg}}{\text{kg-mol}}$$

For 100 lb of olive oil feedstock, the methanol required and the biodiesel and glycerol formed are thus

$$MET = \frac{MET_{mm}}{PO_{mm}} \times 100\text{ lbs} = 10.85\text{ lb}$$

$$BD = \frac{BD_{mm}}{PO_{mm}} \times 100\text{ lbs} = 100.45\text{ lb}$$

$$GLY = \frac{GLY_{mm}}{PO_{mm}} \times 100\text{ lbs} = 10.40\text{ lb}$$

Thus, the assertion is substantially correct. Moreover, since most plant oils have similar (large) molecular masses and since the transesterification process involves changes of a few atoms, the generalization of van Gerpen *et al.* (2004) is likely to be an appropriate rule of thumb for most biodiesel transesterification reactions.

Biodiesel has a viscosity comparable to that of conventional diesel fuel and cetane number of about 50. Moreover, operating experience with biodiesel suggests that biodiesel provides for a much longer time between overhauls than operating with plant oils. It also burns cleaner than conventional diesel fuel and significantly reduces emissions of CO, unburned and aromatic hydrocarbons, and sulfates as well as particulate matter. Biodiesel is compatible with most emission control technologies. Blends of up to 20% biodiesel with conventional fuel can be used without any engine or infrastructure (storage and distribution) modifications. Similar to the practice for ethanol, biodiesel blends are labeled with a B followed by the percentage of biodiesel; B20, a commonly used blend, consists of 20% biodiesel. B5, B10, and B20 are the usual biodiesel blends. Tyson *et al*. (2004) estimate that sufficient biomass feedstock exists to supply 1.9 billion barrels of biodiesel, about 5% of the on-road use of conventional diesel fuel. Biodiesel that is classified as fuel grade must be produced in compliance with ASTM D6751. Unprocessed vegetable oil does not meet biodiesel specifications and is not a legal motor fuel (www.eere.energy.gov/RE/bio_fuels.html).

The three basic process for producing biodiesel are

1) base-catalyzed transesterification;
2) direct acid-catalyzed transesterification;
3) conversion of the oil to its fatty acids and then to biodiesel.

Base-catalyzed transesterification, is the most prevalent and possesses the following advantages:

1) The process occurs at low temperature and pressure.
2) The conversion efficiency is high (98%).
3) The process involves minimal side reactions.
4) The conversion to biodiesel is direct with no intermediate compounds.
5) No special materials are needed in the reactor.

Since biodiesel can be made from a wide variety of plant oils and animal fats, the physical properties of biodiesel have some variation. Generally accepted values (http://biodiesel.org/docs/using-hotline/nrel-handling-and-use.pdf?sfvrsn=4) are presented in Table 12.6.

12.5.4 Pyrolysis liquids

Pyrolysis is defined as the thermal decomposition of organic compounds in the absence of oxygen. Charcoal is a simple example of pyrolysis that results when wood is heated to about 250 °C and the moisture and volatile products are driven off by the heat. The resulting product has a very high carbon content. Pyrolysis is an endothermic reaction that results in the degradation of solid fuels into a variety of gases, organic vapors, and liquids. In contrast, combustion is an exothermic reaction that involves the rapid oxidation of fuel with a large release of heat.

The product stream from pyrolysis depends on the rate and duration of heating. In the production of oil using fast pyrolysis, cellulosic biomass feedstock is ground to a fine power that

Table 12.6 Characteristics of biodiesel fuels.

Specific gravity	0.87–0.89
Cetane number	48–65
Higher heating value (Btu/gal)	127 042

is heated for a short period of time (<0.5 s) to 400–600 °C and then rapidly quenched. Rapid quenching is necessary in order to prevent high-molecular-weight liquids from decomposing into lower-molecular-weight gases. Liquids from fast pyrolysis processes have a low viscosity and are dark brown in appearance. Pyrolysis liquids are highly oxygenated, complex mixtures of hydrocarbons that contain significant amounts of water. Such liquids are highly unstable and highly corrosive (low pH). Because of the corrosive nature of pyrolysis liquids, storage is difficult, and the high oxygen and water content makes them incompatible with conventional hydrocarbon fuels. Hence, conversion of pyrolysis liquids into more conventional hydrocarbon fuels is desirable, although pyrolysis liquids can be used in place of heavy fuel oils such as bunker C.

12.5.5 Biogas

Biogas is a mixture of CH_4 and CO_2, typically 50–80% CH_4 and 50–20% CO_2 by volume, with traces of H_2, CO, and N_2. The International Energy Agency offers a compact examination of biogas production and utilization (IEA Bioenergy, 2005). Biogas is the final product of anaerobic digestion of organic waste, such as animal manure and food processing waste. Anaerobic digestion is the decomposition of such wastes into gaseous fuels by the action of bacteria in an oxygen-free environment. A detailed presentation of anaerobic digestion topics is offered by Chynoweth and Isaacson (2004). Biogas differs from natural gas in that natural gas is composed of more than 70% CH_4, with the remaining constituents being other hydrocarbons. Biogas is also called swamp gas, landfill gas, or digester gas. Although the biological processes that result in biogas are relatively complex, anaerobic digestion systems are relatively simple. Biogas is produced in stages by different types of bacteria that break down the complex organic compounds. The following four stages, with the associated bacteria function, form the generally accepted path from organic waste to biogas: (1) hydrolytic bacteria break down the waste into sugars and amino acids; (2) fermentative bacteria convert the sugars and amino acids into organic acids; (3) acidogenic bacteria convert the organic acids into H_2, CO_2, and acetate; and (4) methanogenic (CH_4-forming) bacteria produce biogas from the acetic acid, H_2, and CO_2.

Anaerobic digestion takes place in an airtight chamber called a digester. Digesters may operate in batch mode or in continuous mode. Continuous digesters produce a steady stream of biogas and are typically associated with large-scale operation. The digestion process is temperature sensitive; a temperature of at least 68 °F is required, but temperatures as high as 150 °F are possible. The higher the temperature, the shorter the process time and smaller the digester volume, but high-temperature digesters are more difficult to operate and maintain and require close monitoring. Boyle (2004) states that a typical anaerobic digester can produce 200–400 m^3 of biogas, with a 50–75% CH_4 content, per tonne of feedstock. A typical anaerobic digester consists of a pre-mixing tank, a digester vessel, a system that uses the biogas, and a means of spreading or distributing the digested effluent. Figure 12.8 presents a schematic of a typical batch anaerobic digester. In many instances the "system" is an engine–generator set. The dotted line from the system to the digester represents an energy stream directed from the system to the digester to maintain digester temperature.

The Alberta (Canada) Agriculture and Rural Development Agency is heavily involved in promoting anaerobic digesters for agricultural waste. Figure 12.9, taken from the agency's website, is an example of an anaerobic digester system that utilizes manure and provides the potential for biogas use on-site in a cogeneration arrangement as well as for upgrading to natural gas for pipeline connection. Additionally, concentrated nutrients and water from the effluents are provided. The CO_2 and water must be removed, leaving mostly CH_4, if biogas is to be upgraded to natural gas and fed to the pipeline.

The US Environmental Protection Agency Landfill Methane Outreach Program provides assistance for landfill issues; details are available at https://www.epa.gov/lmop. The Tillamook

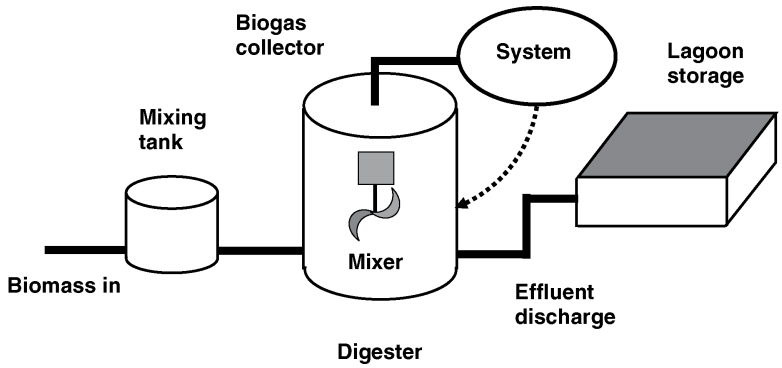

Figure 12.8 Batch anaerobic digester schematic.

Digester Facility (http://www.potb.org/hooley-digester/) located in Tillamook, Oregon, makes use of manure from the extensive dairy farms that support the famous Tillamook cheese industry in the area. The Tillamook Facility has two 400 000 gal digester cells that produce biogas, which is used to run two grid-connected 200 kW engine-driven generators.

12.5.6 Producer Gas

Producer gas is a low to medium British thermal unit flammable gas mixture containing CO, H_2, CH_4, N_2, CO_2, and higher hydrates and is made from gasification of wood or coal. Producer gas

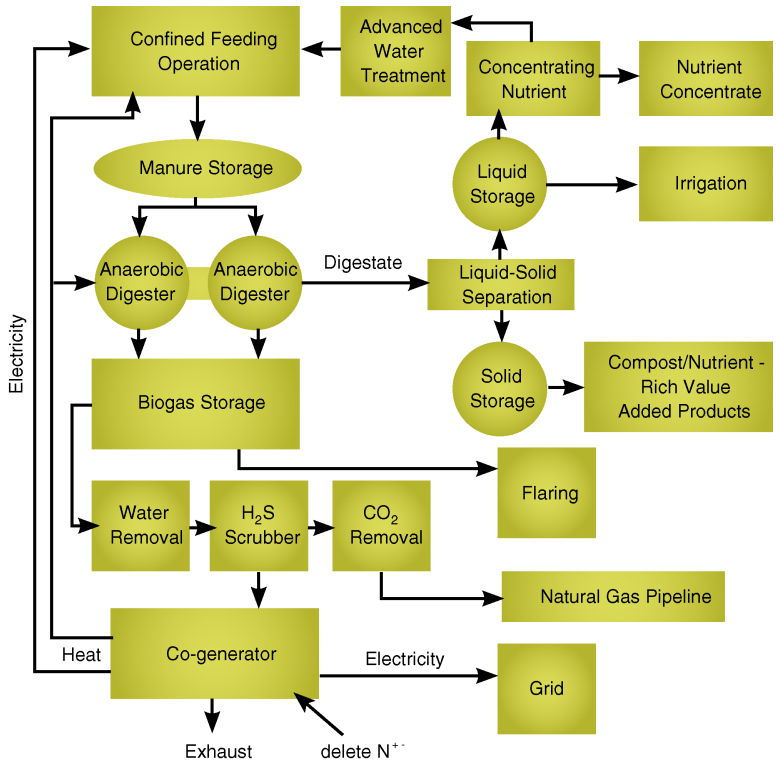

Figure 12.9 Anaerobic digester schematic with diverse products (Alberta Agriculture and Rural Development Agency). *Source*: http://www1.agric.gov.ab.ca/$Department/deptdocs.nsf/all/agdex13088/$FILE/400_28-2.pdf.

Table 12.7 Producer gas composition variation.

H_2 (vol.%)	9–31
CO (vol.%)	14–48
CO_2 (vol.%)	20–0
CH_4 (vol.%)	7–21
N_2 (vol.%)	50–0
Heating value (HHV, MJ/m^3)	5.4–17.4

Source: adapted from Goswami *et al.* (2000).

can be burned directly or used as a feedstock for liquid fuels. The conversion of biomass to producer gas is often called thermal gasification. Thermal gasification is the partial oxidation of a solid fuel, such as a solid biomass, at elevated temperatures into a flammable gas mixture called producer gas. As Boyle (2004) points out, all gasification processes involve interacting steam and oxygen with a solid feedstock. The producer gas contains varying percentages of H_2, CO, CH_4, and CO_2 as well as smaller quantities of higher hydrates; the specific chemical constituents are determined by the temperature to which the biomass is heated, the composition of the biomass feedstock, and the gasifier layout. Table 12.7 shows the varying composition of producer gas.

Brown (2011) presents a compact, lucid description of thermochemical biomass technologies, including gasification. He describes thermal gasification as a multistep process involving heating and drying, pyrolysis, solid–gas reactions that consume char, and gas-phase reactions that determine the final composition of the producer gas. At about 100 °C, moisture is driven out by heating and drying. Other authors (e.g., Goswami *et al.*, 2000) view thermal gasification as a combination of combustion and pyrolysis. (The distinction between combustion and pyrolysis were discussed previously in Section 12.5.4.) Since pyrolysis is an endothermic process, energy is required for pyrolysis to proceed, and combustion (by means of the addition of oxygen or air to the gasifier) is only to the extent necessary to produce energy for pyrolysis. At about 400 °C, the biomass begins to break down into gases, vapors, and liquids. Only char, a porous solid containing carbon and ash, remains. Some idea of the percentage composition of products from pyrolysis can be obtained from the proximate analysis of the biomass feedstock (see Table 12.4). The volatile content is approximately equal to the pyrolysis yield, and the carbon and ash percentages are roughly equal to the char. At about 700 °C, the char begins to react with any oxygen as well as CO_2 and water vapor to produce additional flammable gases. Gasification involves a number of different chemical reactions. Table 12.8 presents a summary of the important reactions associated with biomass gasification.

Table 12.8 Gasification reactions.

Name	Chemical reaction	Comment
Carbon–water	$C + H_2O \leftrightarrow H_2 + CO$	Endothermic →
Water-gas shift	$CO + H_2O \leftrightarrow H_2 + CO_2$	
Hydrogenation	$C + 2H_2 \leftrightarrow CH_4$	
Carbon–oxygen	$2C + O_2 \leftrightarrow 2CO$	
Boudouard	$C + CO_2 \leftrightarrow 2CO$	
Methanation	$CO + 3H_2 \leftrightarrow H_2O + CH_4$	Exothermic →

Source: adapted from Goswami *et al.* (2000) and Tester *et al.* (2005).

The arrows in the reactions of Table 12.8 indicate that the gasification reactions can proceed in either direction depending on the fuel, oxygen, and steam added to the gasifier as well as the temperature and pressure. Low temperatures and high pressures favor the formation of CH_4, while high temperatures and low pressures favor the formation of H_2 and CO.

In addition to producer gas, tars (viscous, liquid high-molecular-weight compounds) and particulate matter are likely to be in the gasifier output streams. Thus, most gasifiers include processes for gas cleaning. The thermodynamic efficiency of gasifiers varies widely depending on the type and operating conditions. Gasifiers that can harvest more than 90% of the chemical energy of the biomass feedstock are possible but are expensive. Most gasifiers harvest between 70 and 80% of the available energy in the feedstock.

12.5.7 Synthesis Gas

Synthesis gas, or syngas, is a mixture of CO and H_2 and can be produced by a gasification process using oxygen rather than air. The oxygen requirement for syngas production is about one-third of the oxygen required for complete combustion. Synthesis gas is so named because, in addition to being a useful, high-energy fuel, it can also be used as the feedstock for synthesis of many useful chemicals. The chemistry of the production and use of syngas from natural gas, coal, and heavy oil fractions has been well known for more than a century. Reyes *et al.* (2003) provide a historical perspective on the production of syngas from non-biomass sources and review technological advances in the production of syngas from traditional feedstocks. In recent years, the production of syngas from biomass resources has received much attention as at least a partial solution to the energy needs of the many countries, including the USA. Spath and Dayton (2003) assess the potential for biomass-derived syngas in the USA, and Cobb (2007) includes a survey of biomass gasification facilities in the USA. The National Energy Technology Laboratory provides a database of gasification plants in the USA at http://www.netl.doe.gov/research/coal/energy-systems/gasification/gasification-plant-databases. Worley and Yale (2012) summarize the equipment, general arrangement of the equipment, operating characteristics and operating severity for each gasification technology.

Syngas is used via the Fischer–Tropsch process to produce a wide range of hydrocarbon products, typically in liquid form. Documents related to the history and development of the Fischer–Tropsch process are archived in electronic form at www.fischer-tropsch.org. This web site is unusual, but its existence points out the importance of the process in hydrocarbon chemical engineering. De Klerk (2011) has been well received as a book devoted to details of the Fischer–Tropsch process. Fischer–Tropsch synthesis takes place at low temperature (200–240 °C) or high temperature (300–350 °C) with iron or cobalt serving as catalyst in reactors that operate at pressures ranging from 10 to 40 atm (Spath and Dayton, 2003). The most common hydrocarbons synthesized using the Fischer–Tropsch process are listed in Table 12.9. In the first reaction in Table 12.9, —CH_2— indicates methyl species that can serve as initiators for chain growth via sequential addition of —CH_2—. Depending on the ratio of CO to H_2, a wide range of hydrocarbons can result from the Fischer–Tropsch synthesis. Paraffins are alkane hydrocarbons and have the general chemical formula C_nH_{2n+2}. For $20 < n < 40$ paraffins are solid and waxy, as suggested by the name. Octane, C_8H_{18}, is an example of a paraffin. Olefins are alkene hydrocarbons; an example is propene, C_3H_6. Two characteristics of such syntheses are (1) the unavoidable production of a wide range of hydrocarbon products and (2) the liberation of significant amounts of heat from the exothermic synthesis reactions. The distribution of the products is determined by temperature, pressure, CO/H_2 ratio, and catalyst (type and composition). Products generated by the Fischer–Tropsch process must generally undergo upgrading procedures that result in product separation, concentration, and tailoring. The upgrading procedures generally involve further chemical reactions.

Table 12.9 Fischer–Tropsch synthesis examples.

Reaction	Product
$CO + 2H_2 \rightarrow -CH_2- + H_2O$	Methyl species
$CO + 3H_2 \rightarrow CH_4 + H_2O$	CH_4
$nCO + (2n+1)H_2 \rightarrow C_nH_{2n+2} + nH_2O$	Paraffins
$nCO + 2nH_2 \rightarrow C_nH_{2n} + nH_2O$	Olefins
$nCO + 2nH_2 \rightarrow C_nH_{2n+1}OH + (n-1)H_2O$	Alcohols

Source: adapted from Spath and Dayton (2003).

The extensive Fischer–Tropsch literature should be consulted for additional details. For biomass syngas, Spath and Dayton (2003) is a comprehensive reference.

Example 12.3
For 1 kg of CO, calculate the hydrogen required and the products produced for CH_4, ethanol, octane, and propene for Fischer–Tropsch synthesis.

Solution The molecular masses for CO, H_2, CH_4, H_2O, ethanol, octane, and propene are as follows:

$$CO_{mm} = 28.01\frac{kg}{kg\text{-}mol} \qquad H2_{mm} = 2.016\frac{kg}{kg\text{-}mol}$$

$$CH4_{mm} = 16.042\frac{kg}{kg\text{-}mol} \qquad H2O_{mm} = 18.016\frac{kg}{kg\text{-}mol}$$

$$ETHANOL_{mm} = 46.068\frac{kg}{kg\text{-}mol} \qquad OCTANE_{mm} = 114.224\frac{kg}{kg\text{-}mol}$$

$$PROPENE_{mm} = 42.078\frac{kg}{kg\text{-}mol}$$

For **CH_4** the reaction is

$$CO + 3H_2 \rightarrow CH_4 + H_2O$$

For 1 kg of CO, the H_2 required and the CH_4 and H_2O formed become

$$H_2 = \frac{3 \times H2_{mm}}{CO_{mm}} \times 1\,kg = 0.216\,kg \qquad CH_4 = \frac{CH4_{mm}}{CO_{mm}} \times 1\,kg = 0.573\,kg$$

$$H_2O = \frac{H2O_{mm}}{CO_{mm}} \times 1\,kg = 0.643\,kg$$

For **ethanol** (C_2H_5OH), an alcohol, the general alcohol reaction from Table 12.9 with $n = 2$ can be used:

$$nCO + 2nH_2 \rightarrow C_nH_{2n+1}OH + (n-1)H_2O$$

For 1 kg of CO, the H_2 required and the ethanol and H_2O formed become

$$H_2 = \frac{4 \times H2_{mm}}{2 \times CO_{mm}} \times 1\,kg = 0.144\,kg \qquad ethanol = \frac{ETHANOL_{mm}}{2 \times CO_{mm}} \times 1\,kg = 0.822\,kg$$

$$H_2O = \frac{H2O_{mm}}{2 \times CO_{mm}} \times 1\,kg = 0.322\,kg$$

For **methanol** (CH_3OH), also an alcohol, the general alcohol reaction with $n = 1$ is required. No water is produced. For 1 kg of CO, the H_2 required and the methanol and H_2O formed become

$$H_2 = \frac{4 \times H2_{mm}}{CO_{mm}} \times 1\,kg = 0.144\,kg \quad \text{methanol} = \frac{METHANOL_{mm}}{CO_{mm}} \times 1\,kg = 1.144\,kg$$
$$H_2O = 0.0\,kg$$

For **octane** (C_8H_{18}), the general paraffin reaction with $n = 8$ is used:

$$nCO + (2n + 1)H_2 \rightarrow C_nH_{2n+2} + nH_2O$$

For 1 kg of CO, the H_2 required and the octane and H_2O formed become

$$H_2 = \frac{17 \times H2_{mm}}{8 \times CO_{mm}} \times 1\,kg = 0.153\,kg \qquad \text{octane} = \frac{OCTANE_{mm}}{8 \times CO_{mm}} \times 1\,kg = 0.51\,kg$$
$$H_2O = \frac{8 \times H2O_{mm}}{8 \times CO_{mm}} \times 1\,kg = 0.643\,kg$$

For **propene** (C_3H_6), the general olefin reaction with $n = 3$ is used:

$$nCO + 2nH_2 \rightarrow C_nH_{2n} + nH_2O$$

For 1 kg of CO, the H_2 required and the propene and H_2O formed become

$$H_2 = \frac{6 \times H2_{mm}}{3 \times CO_{mm}} \times 1\,kg = 0.144\,kg \qquad \text{propene} = \frac{PROPENE_{mm}}{3 \times CO_{mm}} \times 1\,kg = 0.501\,kg$$
$$H_2O = \frac{3 \times H2O_{mm}}{3 \times CO_{mm}} \times 1\,kg = 0.643\,kg$$

A summary of the reactants and products for each of the reactions is presented is Table 12.10. The variety of Fischer–Tropsch possible products is illustrated by these results. The ratio of CO to H_2 is the same for some reactions, but the products are different. The products are different for reactions with different CO to H_2 ratios – hence the first characteristic of Fischer–Tropsch synthesis, relating to the unavoidable production of a wide range of hydrocarbon products.

Although not strictly a process with biomass feedstock, a proposal by Uhrig *et al.* (2007) utilizes CO_2 from fossil-fuel-fired power plants in conjunction with hydrogen from non-fossil fuel sources and the Frischer–Tropsch process to produce synthetic fuels for motor vehicles. In this process the feedstocks are CO_2 and water; electrolysis is used to produce hydrogen from the water. The "reverse" water shift reaction (Table 12.8) is used for production of CO from CO_2 and water, followed by the Fischer–Tropsch reaction to produce CH_2 – the fundamental building block for hydrocarbon synthetic fuels.

Table 12.10 Summary of Fischer–Tropsch synthesis reactions for Example 12.3.

Reaction	CO (kg)	H_2 (kg)	H_2O (kg)	Product (kg)
Methane (CH_4)	1	0.216	0.643	0.573
Ethanol (C_2H_5OH)	1	0.144	0.322	0.822
Methanol (CH_3OH)	1	0.144	0.0	1.144
Octane (C_8H_{18})	1	0.153	0.643	0.510
Propene (C_3H_6)	1	0.144	0.643	0.501

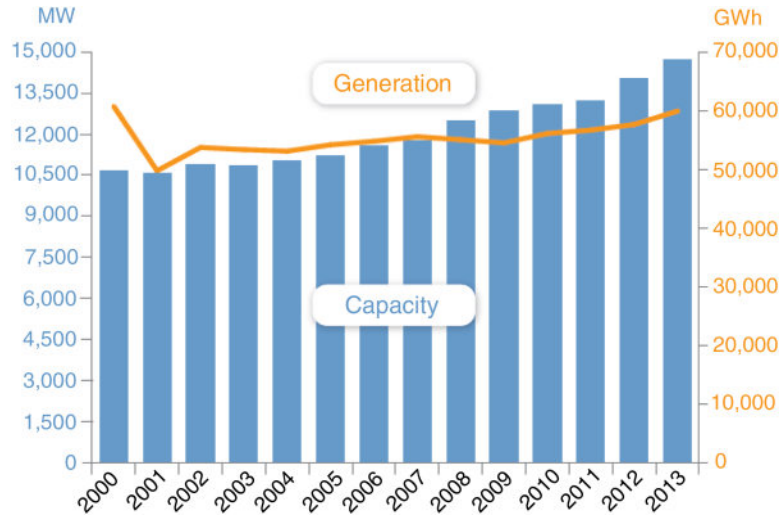

Figure 12.10 Biopower installed capacity and generation rate (2000–2013). *Source*: Esterly and Gelman (2014).

12.5.8 Biopower and Biofuels Statistics

The *2013 Renewable Energy Data Book* (Esterly and Gelman, 2014) provides some interesting data on biopower and biofuels for 2013. The biopower data will be examined first. The *Data Book* summarizes three important facts about 2013: (1) biopower electricity generation accounted for 11% of all renewable energy generated in the USA, (2) biopower electricity comes primarily from wood and agricultural residues that are burned as fuel in the industrial sector, and (3) the installed biopower electricity capacity grew at an annual growth rate of 3.8% from 2007 to 2013. Figure 12.10 shows the annual generation in gigawatt-hours and installed megawatt capacity from 2000 to 2013. The growth in installed capacity is steady, if not spectacular.

Ethanol and biodiesel statistics will be examined next. For ethanol, NREL *Data Book* (Esterly and Gelman, 2014) provides the following 2013 highlights: (1) ethanol production was $13\,300 \times 10^6$ gal, (2) between 2000 and 2013 corn-based ethanol production increased by a factor of 8, (3) the USA produced 57% of the world's ethanol (Brazil produced 27%), and (4) the first commercial cellulosic plant in the USA started operation. The 2013 highlights for biodiesel are (1) USA biodiesel production was 1.8×10^9 gal (up 63% from 2012) or 360 times biodiesel production in 2000, (2) the USA led the world in biodiesel production, and (3) worldwide biodiesel production increased by 17% from 2012. A useful approach is to display ethanol prices and production side by side with biodiesel prices and production. Table 12.11 is such an arrangement; for both ethanol and biodiesel, the prices are "gasoline gallon equivalent basis," since the heating values for ethanol and biodiesel on a per gallon basis are different from gasoline. Using the gasoline gallon equivalent basis accounts for the differences in the heating values. On an energy basis, both ethanol and biodiesel are more expensive than gasoline. In recent years, on a gasoline equivalent basis, biodiesel is marginally cheaper than ethanol. In 2013, seven times as much ethanol was produced than biodiesel.

12.6 Municipal Solid Waste

Because of its high percentage content of organic materials, municipal solid waste (MSW) is often classed as a biomass feedstock source. MSW is trash or garbage that is usually thrown away

Table 12.11 Ethanol and biodiesel production and costs.

		Ethanol		Biodiesel	
	Gasoline price[a] ($/gal)	Price[b] ($/gal)	Production (10^6 gal/year)	Price[b] ($/gal)	Total US production (10^6 gal)
2000	1.56	2.16	1 622		
2001	1.50	2.38	1 765	1.80	5
2002	1.38	1.97	2 140	1.70	15
2003	1.54	2.27	2 810	1.80	20
2004	1.76	2.86	3 404	2.20	25
2005	2.07	3.40	3 904	3.40	75
2006	2.27	2.98	4 884	3.30	250
2007	2.76	3.39	6 521	3.40	450
2008	1.86	2.56	9 309	2.68	700
2009	2.65	3.36	10 938	3.28	545
2010	3.08	3.89	13 298	3.59	315
2011	3.37	4.44	13 929	3.88	1 100
2012	3.29	4.48	13 218	4.04	1 100
2013	3.34	4.29	13 300	3.92	1 800

a) Average retail price.
b) Gasoline gallon equivalent basis.

from households, and does not include industrial, hazardous, or construction waste. The Environmental Protection Agency (EPA) provides a yearly compilation of MSW information that addresses MSW generation, composition, and disposal. Prior to 2015, the yearly compilations were titled *Municipal Solid Waste Generation, Recycling, and Disposal in the United States: Facts and Figures*; in 2015 the series was renamed *Advancing Sustainable Materials Management: Facts and Figures*. Additionally, historical data on MSW are presented in the reports so that trends can be ascertained. Most of the first portion of this section was abstracted from the *Advancing Sustainable Materials Management: Facts and Figures 2013* (EPA, 2015). Consider the following statistics.

Figure 12.11 presents the US total MSW (in millions of tons) generated per year and the per capita generation (pounds per person per day) from 1960 through 2013. In the 53 years represented by Figure 12.11, the total MSW generation rate increased by 188% while the population increased by 73%! On a per capita basis, the increase was 64%. About the only positive comment that can be made about the information in the figure is that since 2000 the per capita generation rate has decreased slightly to 4.40 lb/(person day). Figure 12.11 illustrates in a rather dramatic fashion the "disposal" nature of the economy of the USAs.

Two questions are germane: (1) What is the composition of MSW? (2)What happens to MSW? Figure 12.12 is a pie chart showing the composition of MSW for 2013. The EPA defines MSW as being composed of yard trimmings, wood, plastics, metals, glass, paper, food scraps, rubber/leather/textiles, and other. Paper at 27% (by weight) is by far the largest category, followed by food scraps, yard trimmings, and plastics, each at 12–14%. The remaining categories are between 5 and 9%. Plastics, glass, and metals are non-biomass components in MSW. Later in this section, the biomass versus non-biomass composition of MSW is examined in more detail.

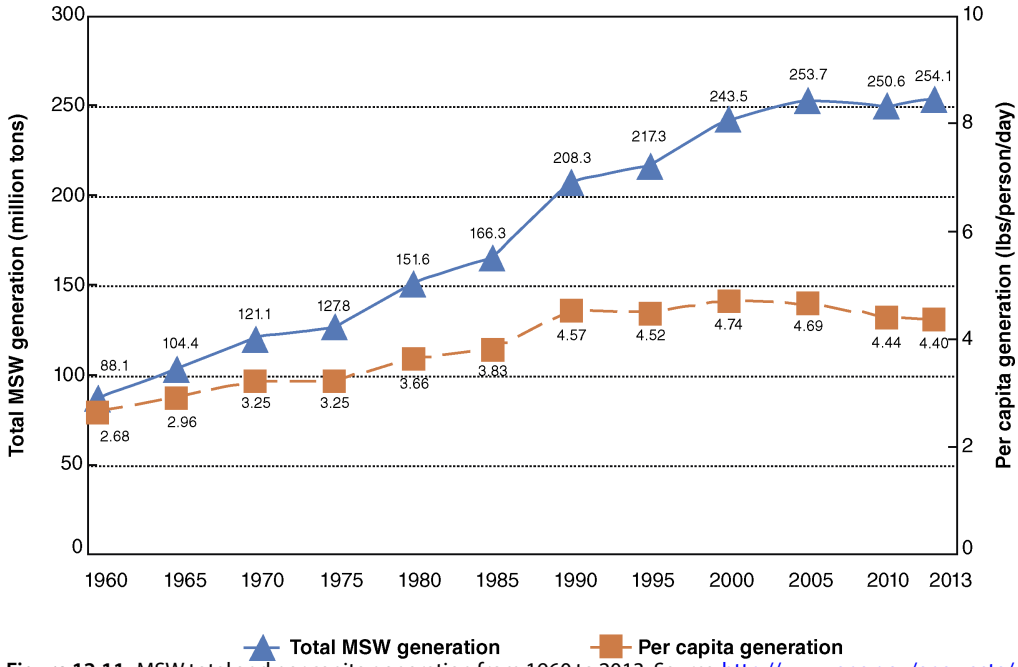

Figure 12.11 MSW total and per capita generation from 1960 to 2013. *Source*: http://www.epa.gov/epawaste/nonhaz/municipal/index.htm.

Table 12.12, with the results expressed in millions of tons, addresses the second question: what happens to MSW? The EPA compiles information on MSW recovered for recycling, recovered for composting, combusted with energy recovery, and discarded to landfills. The good news is that while the generation rate has remained nearly constant since 2000, the amount recovered for recycling, the total composted, and the amount of materials recovered have all

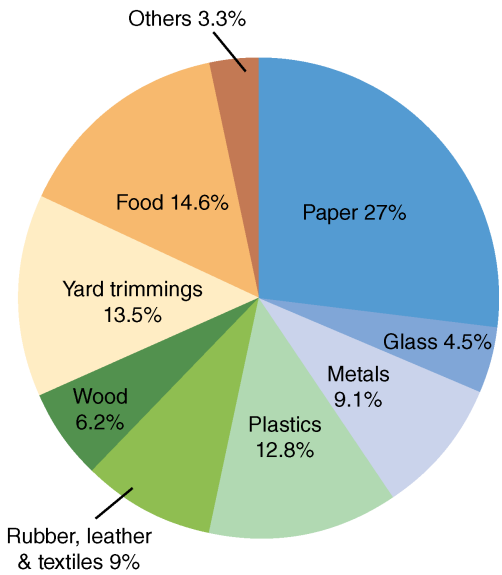

Figure 12.12 MSW composition in 2013. *Source*: http://www.epa.gov/epawaste/nonhaz/municipal/index.htm.

Table 12.12 Generation, recovery, composting, combustion with energy recovery, and discards of MSW (millions of tons) from 1960 to 2013.

Activity	1960	1970	1980	1990	2000	2005	2009	2011	2012	2013
Generation	88.1	121.1	151.6	208.3	243.5	253.7	244.6	250.5	251.0	254.1
Recovery for recycling	5.6	8.0	14.5	29.0	53.0	59.2	61.9	66.4	65.3	64.7
Recovery for composting[a)]	Negligible[b)]	Negligible[b)]	Negligible[b)]	4.2	16.5	20.6	20.7	20.6	21.3	22.4
Total materials recovery	5.6	8.0	14.5	33.2	69.5	79.8	82.6	87.0	86.6	87.2
Discards after recovery	82.5	113.0	137.1	175.0	174.0	173.9	162.0	163.5	164.4	167.0
Combustion with energy recovery[c)]	0.0	0.4	2.7	29.7	33.7	31.6	29.0	31.8	32.2	32.7
Discards to landfill, other disposal[d)]	82.5	112.6	134.4	145.3	140.3	142.3	133.0	131.7	132.2	134.3

Source: www.epa.gov.

a) Composting of yard trimmings, food waste, and other MSW organic material. Does not include backyard composting.
b) Negligible equals less than 5000 tons or 0.05%.
c) Includes combustion of MSW in mass burn or refuse-derived fuel form, and combustion with energy recovery of source separated materials in MSW (e.g, wood pallets, tire-derived fuel).
d) Discards after recovery minus combustion with energy recovery. Discards include combustion without energy recovery. Details might not add to totals due to rounding.

increased. The MSW combusted in facilities producing energy has increased slightly since 1990, reflecting the increasing cost of such facilities, the more stringent emissions requirements, and the increase in permitting difficulties.

While landfilling has long been the usual solution for disposal of MSW, landfilling possesses difficulties such as availability, siting, costs, transportation, effluent generation, and capacity. The number of available landfills in the USA has decreased from 7924 in 1988 to 1967 in 2000 to 1908 in 2013 (EPA, 2015). One way to reduce the landfill volume is incineration – burning MSW at high temperatures. Incineration decreases the volume of MSW to 10–12% of the original for "typical" MSW, allowing existing landfills to last longer.

The discussion focuses on facilities that combust MSW and produce useful energy – waste-to-energy (WTE) facilities. Such facilities use the energy from the MSW to make steam that is used in district heating and cooling systems or to power a generator to produce electricity for the grid. In 2013, the EPA identified 86 WTEs in the USA with a waste handling capacity of 95 253 tons/day. *The 2016 ERC Directory of Waste-to-Energy Facilities* (Michaels and Shiang, 2016) contains a list and characteristics of all WTE facilities in the USA, along with extensive statistical information relating to WTE technologies. Many of the developed countries make more extensive use of MSW than the USA. Most of the countries of western Europe, for example, have extensive WTE facilities and programs. The internet is an excellent source of detailed information about WTE facilities. The primary purpose of a WTE facility is to reduce the volume of solid waste with minimum adverse impact on the environment. The energy captured is secondary, but important especially as a selling point for local governments with both solid waste disposal and energy concerns.

WTE facilities are broadly classed as mass-burn systems or refuse-derived fuel (RDF) systems. Mass-burn WTE facilities combust, with excess air, the MSW as received and usually have only a single combustion chamber. A moving, sloping grate is used to ensure that the MSW is well mixed with air; the grate also provides a path for ash to enter an ash collection system. For RDF systems, the MSW is processed to a more homogeneous mix than the as-received MSW for the mass-burn system. Mass-burn WTEs are the most common, with the MSW being used in the same fashion as other biomass fuels in direct combustion technologies. The mechanical processing for RDF can include grinding/shredding as well as pelletization and removal of metals and other bulky items. RDFs can be used as the primary fuel or co-fired with fossil fuels in conventional utility boilers.

The Energy Recovery Council (ERC) (http://energyrecoverycouncil.org/page/21/) is a national organization representing companies and local governments involved with waste-to energy endeavors. ERC, formed in 1991 as the Institute for Resource Recovery, operated as the Integrated Waste Services Association until 2008, when it became the ERC. The *2016 ERC Directory of Waste-to-Energy Facilities* (Michaels and Shiang, 2016) provides a comprehensive overview of waste-to-energy activities in the USA. Included in the *2016 ERC Directory* are details of each US WTE, a list of WTE members (owners/operators, municipal members, and associate members), WTE performance metrics (daily MSW throughput, generating capacity, WTE facility characterizations and number, and waste-to energy production). The *2016 ERC Directory* lists 77 WTE facilities with a 2014 MSW throughput of nearly 30×10^6 tons from which 14×10^6 MW h was generated. Additionally, yearly MSW throughput and electricity generated from 2001 to 2014 are provided. Over the long term, a ton of MSW generated nearly 500 kW h. Of the 77 WTE facilities, 60 are mass burn, 13 are RDF, and 4 are modular. In an independent assessment, Stringfellow (2014) concludes that mass burn and RDF WTE facilities cost ranges from \$7000 to \$10 000 per installed kilowatt.

The Pinellas County (Florida) Utilities WTE facility is an example of a facility that burns MSW and uses the energy to generate electricity, which is supplied to the grid. Information is available at http://www.pinellascounty.org/solidwaste/wte.htm and in Michaels and Shiang (2016).

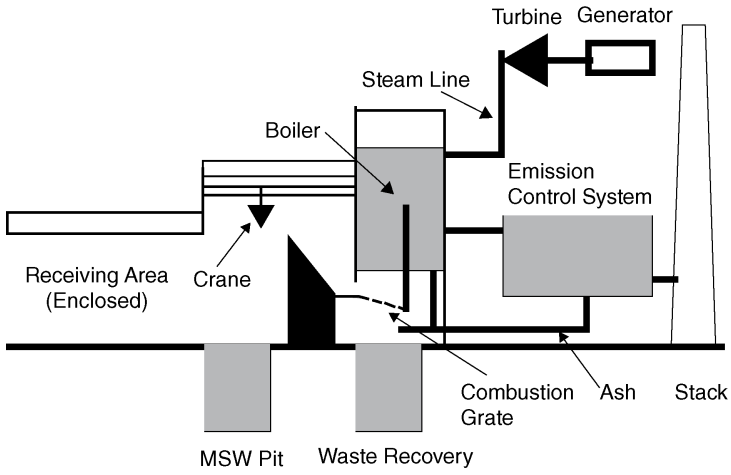

Figure 12.13 WTE facility schematic.

Figure 12.13 is a schematic illustrating the primary features of a WTE facility. MSW arrives at the facility by truck and is dumped into a receiving pit. A crane feeds the MSW into the combustion section of the boiler; ash falls through the combustion grate and is routed for post-combustion treatment. Steam is produced in the boiler and directed to a turbine-generator that is grid connected. Young (2010) contains an overview of municipal solid WTE technologies with some emphasis on plasma incineration.

The Pinellas County WTE facility processes about 1 million tons annually, although the capacity is 3150 tons of MSW per day. The nominal output is 75 MW, of which 60 MW is routed to the electrical grid and 15 MW is used internally. The Pinellas County WTE uses modern pollution control technology to ensure emissions are within EPA standards. The metals in the ash resulting from the combustion of the MSW are recovered and sold for recycling. The remaining ash, after being size-separated, is used for landfill cover, interior berms fill, and roadways. WTE facilities are quite complex and only a brief overview has been presented here; however, Kreith and West (1997) present a detailed discussion of most aspects of WTE technology. Many local governments with WTE facilities have web sites with statistics and operational details. A web search with "WTE" as the key word yields many hits. Many of these web sites contain technical information and operational experiences; however, a non-negligible number of web sites report details of litigation involving solid waste disposal or counterclaims by individuals or citizen interests groups. WTE facilities thus generate some controversy.

Many state and federal programs classify MSW-derived as renewable, thus making MSW a part of the renewable portfolio standard program. The federal Energy Policy Act of 2005 explicitly includes MSW-derived electricity as a form of renewable energy that meets federal renewable energy purchase requirements. Although MSW consists mainly of renewable resources such as food, paper, and wood products, nonrenewable materials such as tires and plastics are also included. The Energy Information Administration (EIA) has developed a procedure for classifying MSW as being composed of biogenic material or non-biogenic material. Formal definitions of these terms for the EPA (EPA Glossary available at www.epa.gov) are as follows:

Biogenic: Produced by biological processes of living organisms. (Note: EIA uses the term "biogenic" to refer only to organic nonfossil material of biological origin.)

Non-biomass (non-biogenic) waste: Material of nonbiological origin that is a by-product or a discarded product. "Non-biomass waste" includes municipal solid waste from non-biogenic sources, such as plastics, and tire-derived fuels.

Depending on state and federal regulations, renewable-energy credit for using MSW could be portioned on the basis of biogenic and non-biogenic contributions. Table 12.13 presents the time history of MSW in terms of biogenic and non-biogenic energy content.

The trend indicated in Table 12.13 and Figure 12.14 is a decrease in MSW biogenic content and an increase in non-biogenic content through the years shown. Indeed, by 2010, biogenic and non-biogenic waste contents became equal. Because the non-biogenic material generally has a higher heating value than the biogenic portion, the energy content per ton has also increased over time. The heating value of MSW is important in determining the output of a WTE facility. In 2011, the EIA reported the average heating value of MSW as 11.1×10^6 Btu/ton (http://www.eia.gov/todayinenergy/detail.cfm?id=8010), which is close to the 2005 value from Table 12.13.

Example 12.4

Using the average of 500 kW h/ton from Michaels and Shiang (2016), find the electrical efficiency using the EIA value of 11.1×10^6 Btu/ton (http://www.eia.gov/todayinenergy/detail.cfm?id=8010) for MSW in 2011. If 50% of the MSW were to be used in WTEs, estimate the base-load power that could be supplied to the electrical grid.

Table 12.13 MSW biogenic and non-biogenic heat content from 1989 to 2005.

		Share of total MSW energy	
Year	Heat content (10^6 Btu/ton)	Biogenic	Non-biogenic
1989	10.08	0.67	0.33
1990	10.21	0.66	0.34
1991	10.40	0.65	0.35
1992	10.61	0.64	0.36
1993	10.94	0.64	0.36
1994	11.15	0.63	0.37
1995	11.11	0.62	0.38
1996	10.94	0.61	0.39
1997	11.17	0.60	0.40
1998	11.06	0.60	0.40
1999	10.95	0.60	0.40
2000	11.33	0.58	0.42
2001	11.21	0.57	0.43
2002	11.19	0.56	0.44
2003	11.17	0.55	0.45
2004	11.45	0.55	0.45
2005	11.73	0.56	0.44

Source: https://www.eia.gov/totalenergy/data/monthly/pdf/historical/msw.pdf.
Years in bold are EPA data collection years. Non-bold years have been linearly interpolated at the materials group level between immediately surrounding bolded years.

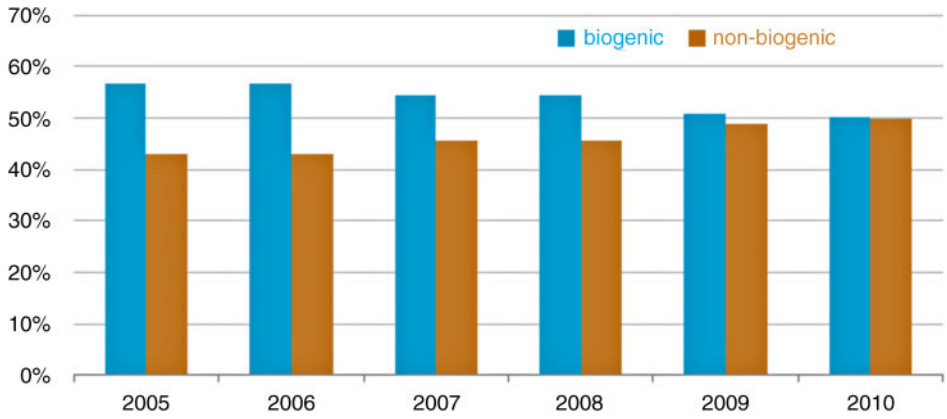

Figure 12.14 Biogenic and non-biogenic MSW content from 2005 to 2010. *Source*: http://www.eia.gov/todayinenergy/detail.cfm?id=8010.

Solution If 500 kW h (ERC average) could be supplied to the grid, then the electrical efficiency becomes

$$\eta = \frac{500\ \text{kW h/ton} \times 3412\ \text{Btu/kW h}}{11.1 \times 10^6\ \text{Btu/ton}} = 0.15$$

Thus, a WTE can harvest and supply to the grid about 15% of the energy content of average MSW. If this seems small, remember that additionally the MSW volume has been reduced by 88–90% in the WTE and that much of the remaining ash might have other uses.

The electricity that might be generated from using 50% of the MSW in the USA in 2013 can be estimated using the ERC information. Consider

$$E_{\text{generated}} = 0.5 \times 254.1 \times 10^6\ \text{tons} \times 500\ \frac{\text{kW h}}{\text{ton}} = 6.35 \times 10^{10}\ \text{kW h}$$

The only viable strategy for WTE usage is as a base-load supply to the electrical grid. For a base-load situation, the total kilowatt-hours generated would be constant with respect to time. Since a year contains 8760 h, the power supplied is estimated as

$$\text{Power} = \frac{6.35 \times 10^{10}\ \text{kW h}}{8760\ \text{h}} = 7.25 \times 10^6\ \text{kW} = 7200\ \text{MW}$$

Used in a uniform manner as a base load to the grid, 50% of the MSW could supply nearly 7200 MW of baseline power to the grid.

The estimates made in Example 12.4 contain significant uncertainties since they are based on "average" energy content, expected electrical harvesting, and yearly data. Nonetheless, the electrical efficiency, the kilowatt-hours generated, and the average power available are reasonable first-order estimates.

Crawford (2013) provides some interesting comparisons and statistics on WTE endeavors. In the USA, 54% of MSW is land filled, 33% is recycled, and 13% used in WTEs. In Denmark, by comparison, 7% is land filled, 69% is recycled, and 24% is used in WTEs. In many instances, WTEs have been rejected as too unpopular to be considered, but Crawford points out that new technologies have alleviated many environmental problems – but getting the word out is difficult. One of the interesting observations made by him is that since New York City rejected WTE, they have been sending 10 000 tons/day out of the city at a cost of $100/ton at a cost of more than $300 million/year!

Table 12.14 Biomass summary (developed from Oregon Department of Energy Biomass Program).

Technology	Conversion process type	Major biomass feedstock	Energy or fuel produced
Direct combustion	Thermochemical	Wood Agricultural waste MSW	Heat Steam Electricity
Gasification	Thermochemical	Wood Agricultural waste MSW	Producer gas
Pyrolysis	Thermochemical	Wood Agricultural waste MSW	Synthetic fuel oil (biocrude) Charcoal
Anaerobic digestion	Biochemical (anaerobic)	Animal manure agricultural waste Landfills/wastewater	Methane
Ethanol production	Biochemical (aerobic)	Sugar or starch crops Wood waste Pulp sludge	Ethanol
Biodiesel production	Chemical	Seed oils Waste vegetable oil Animal fats	Biodiesel
Methanol production	Thermochemical	Wood Agricultural waste MSW	Methanol

12.7 Closure

As is true for many alternate energy sources, the energy content and potential for biomass is staggering, but the technical and economic challenges are also imposing. Table 12.14 provides a convenient summary of biomass technologies, processes, feedstocks, and end-point uses. Biomass is certainly going to be an increasingly important source of energy in the USA.

The outlook for the widespread use of biomass feedstock for fuels and chemical is summarized in a quote from Tester *et al.* (2005):

> As a raw material we can think of biomass as a nearly "universal feedstock" for producing energy and a plethora of energy intensive fuels and chemicals. Because of this versatility and the renewability of biomass, is it then the preferred solution" for a sustainable planet? . . . a variety of challenges must first be surmounted to push biomass beyond it current 5% contribution to energy needs in the developed world.

References

Boundy, B., Diegel, S., Wright, L., and Davis, S. (2011) *Biomass Energy Data Book: Edition 4.* ORNL/TM-2011-446. ONRL, Oak Ridge, TN. http://info.ornl.gov/sites/publications/Files/Pub33120.pdf (accessed October 24, 2016).

Boyle, G. (ed.) (2013) *Renewable Energy: Power for a Sustainable Future*, 3rd edn. Oxford University Press, Oxford.
Brown, R.C. (2011) *Thermochemical Processing of Biomass: Conversion into Fuels, Chemicals and Power*. John Wiley & Sons, Inc., New York.
Carareda, S. (2014) *Introduction to Biomass Energy Conversions*. CRC Press, Boca Raton, FL.
Chynoweth, D.P. and Isaacson, R.E. (eds) (2004) *Anaerobic Digestion of Biomass*. Springer-Verlag, New York.
Cobb, J.T. (2007) Production of synthesis gas by biomass gasification. In Proceedings of the 2007 Spring National AIChE Meeting, Houston, TX.
Crawford, M. (2013) Turning trash into treasure. *Mechanical Engineering*, (May): 43–47.
Decher, R. (1994) *Energy Conversion*. Oxford University Press, New York.
De Klerk, A. (2011) *Fischer–Tropsch Refining*. John Wiley & Sons, Inc., New York.
Drapcho, C., Nghiem, J., and Walker, T. (2008) *Biofuels Engineering Process Technology*. McGraw-Hill, New York.
EPA (2015) *Advancing Sustainable Materials Management: Facts and Figures 2013*. US Environmental Protection Agency. https://www.epa.gov/smm/advancing-sustainable-materials-management-facts-and-figures-report (accessed October 24, 2016).
Esterly, S. and Gelman, R. (2014) *2013 Renewable Energy Data Book*, Haas, K. (ed.). DOE/GO-102014-4491. http://www.nrel.gov/docs/fy15osti/62580.pdf (accessed October 20, 2016).
Goswami, Y., Kreith, F., and Kreider, J.F. (2000) *Principles of Solar Engineering*, 2nd edn. Taylor and Francis, New York.
Himmel, M. (ed.) (2008) *Biomass Recalcitrance: Deconstructing the Plant Cell Wall for Bioenergy*. Wiley-Blackwell, Hoboken, NJ.
IEA Bioenergy (2005). *Biogas Production and Utilisation*. T37:2005-01. http://www.cti2000.it/Bionett/BioG-2005010%20IEA%20T37%20biogas%20brochure.pdf (accessed October 24, 2016).
Kreith, F. (2007) Cellulosic ethanol: answer to the biofuels challenges? *Solar Today*, **21** (3): 42.
Kreith, F. and West, R. (1997) *CRC Handbook of Energy Efficiency*. CRC Press, Boca Raton, FL.
Kreith, F. and West, R. (2007) The road not yet taken: to end our dependence on rapidly dwindling oil supplies, switching to hybrid vehicles and ethanol fuel from corn simply isn't enough. *Mechanical Engineering*, **129** (4): 24.
Michaels, T. and Shiang, I. (2016) *2016 ERC Directory of Waste-to-Energy Facilities*. Energy Recovery Council. http://energyrecoverycouncil.org/wp-content/uploads/2016/06/ERC-2016-directory.pdf (accessed November 15, 2016).
Perlack. R.D. and Stokes, B.J. (leads) (2011) *U.S. Billion-Ton Update: Biomass Supply for a Bioenergy and Bioproducts Industry*. DOE/EE-0363. Oak Ridge National Laboratory, Oak Ridge, TN. http://www1.eere.energy.gov/bioenergy/pdfs/billion_ton_update.pdf (accessed October 24, 2016).
Perlack, R.D., Wright, L.L., Turhollow, A.F., *et al*. (2005) *Biomass as Feedstock for a Bioenergy and Bioproducts Industry: The Technical Feasibility of a Billion-Ton Annual Supply*. DOE/GO-102005-2136, ORNL/TM-2005/66. https://www1.eere.energy.gov/bioenergy/pdfs/final_billionton_vision_report2.pdf (accessed October 24, 2016).
Pimentel, D. (2003) Ethanol fuels: energy balance, economics, and environmental impacts are negative. *Natural Resources Research*, **12** (2): 127–134.
Reyes, S.C., Sinfelt, J.H., and Feeley, J.S. (2003) Evolution of processes for synthesis gas production: recent developments in an old technology. *Industrial and Engineering Chemistry Research*, **42**: 1588–1597.
Schobert, H.H. (2014) *Energy and Society*, 2nd edn. CRC Press, Boca Raton, FL.
Shapouri, H., Gallagher, P.W., Nefstead, W., *et al*. (2010) *2008 Energy Balance for the Corn-ethanol Industry*. Department of Agriculture, Agricultural Economic Report Number 846, June.

Spath, P.L. and Dayton, D.C. (2003) *Preliminary Screening – Technical and Economic Assessment of Synthesis Gas to Fuels and Chemicals with Emphasis on the Potential for Biomass-Derived Syngas*. NREL/TP-510-34929. NREL, Golden, CO. http://www.nrel.gov/docs/fy04osti/34929.pdf (accessed October 24, 2016).

Speight, J. (2008) *Synthetic Fuels Handbook: Properties, Process, and Performance*. McGraw-Hill, New York.

Stringfellow, T. (2014) An Independent engineering evaluation of waste-to-energy technologies. *Renewable Energy World*, **17**. (1). http://www.renewableenergyworld.com/articles/2014/01/an-independent-engineering-evaluation-of-waste-to-energy-technologies.html (accessed November 15, 2016).

Tester, J.W., Drake, E.M., Driscoll, M.J., *et al*. (2005) *Sustainable Energy*. MIT Press, Cambridge, MA.

Tidwell, J.W. and Weir, A.D. (1986) *Renewable Energy Resources*. Taylor & Francis, New York.

Tyson, K.S., Bozell, J., Wallace, R., *et al*. (2004) Biomass oil analysis: research needs and recommendations. NREL/TP-510-34796. NREL, Golden CO.

Uhrig, R.E., Schultz, K.R., and Bogart, S.L. (2007) Implementing the "hydrogen economy" with synfuels. *The BENT of Tau Beta Pi*, **XCVII** (3): 18–22.

Van Gerpen, J., Shanks, B., Pruszko, R., *et al*. (2004) Biodiesel production technology. NREL/SR-510-36244. NREL, Golden, CO.

Worley, M. and Yale, J. (2012) *Biomass Gasification Technology Assessment: Consolidated Report*. NREL/SR-5100-57085. http://www.nrel.gov/docs/fy13osti/57085.pdf (accessed October 24, 2016).

Young, G.C. (2010) *Municipal Solid Waste to Energy Conversion Processes: Economic, Technical, and Renewable Comparisons*. John Wiley & Sons, Inc., New York.

Further Reading

Haynie, D.T. (2008) *Biological Thermodynamics*, 2nd edn. Cambridge University Press, Cambridge.

Klass, D.L. (1998) *Biomass for Renewable Energy, Fuels, and Chemicals*. Academic Press, San Diego, CA.

Kruger, P. (2006) *Alternative Energy Resources: The Quest for Sustainable Energy*. John Wiley & Sons, Inc., Hoboken, NJ.

Van Loo, S., and Koppejan, J. (2008) *The Handbook of Biomass, Combustion, & Co-firing*. Earthscan, London.

13

Geothermal Energy

13.1 Introduction

Geothermal energy is energy from the Earth. Traditionally, geothermal energy has been thought of in terms of harvesting energy whose sources originate deep with the Earth. In recent years, the use of the ground-source heat pumps (GSHPs), which use soil as a reservoir, has become common; see www.geokiss.com and Section 13.5 for more information. In Figure 13.1 is a telling statement about the pervasiveness of geothermal energy. But harvesting this energy poses problems in both access and technology. One of the goals of this chapter is to understand the challenges associated with geothermal energy systems.

The geological structure of the Earth is a good starting point for examining geothermal energy. Consider the cut-away view of the Earth's composition as schematically illustrated in Figure 13.2. At the center is a molten inner core, surrounded by an outer core. An inner mantle surrounds the outer core. The lithosphere is a thin, rigid crust that serves as the outmost mantle. The lithosphere is fractured into tectonic plates – twelve large and a number of smaller ones. These plates move relative to each other driven by gravitational and convection forces in the mantle. This geological process, known as plate tectonics, creates fault lines where the plates meet and produces volcanic and seismic activity. Figure 13.3 illustrates the major plates and their boundaries. Where the plates move apart, pools of molten rock (magma) rise, leading to volcanic activity. Where the plates collide, one plate typically moves underneath the other, a process called subduction. In the subduction zone, temperatures become high enough to melt rock, and earthquake and volcanic activities are common. Much of the geothermal energy is inaccessible at great depths, but along the plate boundaries geothermal activity is close enough to the surface to be accessible. The active geothermal zones are indicated in Figure 13.3. The United States Geological Survey (USGS) web site http://pubs.usgs.gov/gip/dynamic/dynamic.html contains a good description of the relationship between plate tectonics and volcanic activity. The active geothermal zones are, not surprisingly, the regions with the most geothermal energy activities.

Section 13.2 examines the estimated geothermal energy resources and provides an introduction to the harvesting procedures appropriate for geothermal energy.

13.2 Geothermal Resources

As can be inferred from Figure 13.1, geothermal resources are extensive, but the real issues are accessibility and technology. Gupta and Roy (2007) provide a contemporary assessment of geothermal resources and geothermal energy outlook for the Earth. Green and Nix (2006) present a similar assessment for the USA. Kruger (1976) contains an earlier discussion of geothermal energy, and Mock *et al*. (1997) examine geothermal energy as an environmentally

Alternative Energy Systems and Applications, Second Edition. B. K. Hodge.

Companion website: www.wiley.com\go\Hodge\AESystemsandApplications2E

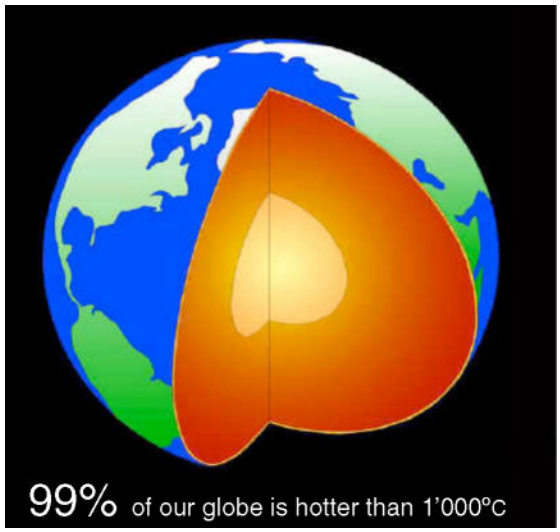

Figure 13.1 A geothermal energy factoid. *Source*: Haring GeoProject.

sustainable resource. Energy harvesting procedures for geothermal energy vary widely and depend on the local geology. Geothermal resources are characterized by their thermal and compositional characteristics as follows:

1) hydrothermal or geohydrothermal;
2) geopressurized;
3) magma;
4) enhanced geothermal systems (EGS) – formerly, hot, dry rock (HDR).

Different harvesting strategies are required for the different classes of geothermal resources. But before exploring the harvesting strategies, we will examine general characteristics of each class.

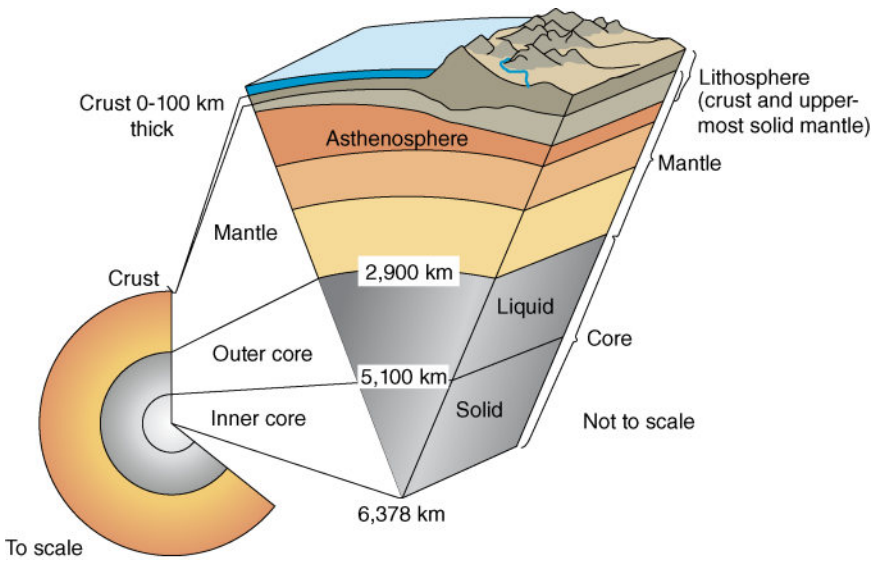

Figure 13.2 Schematic of the structure of the Earth. *Source*: http://pubs.usgs.gov/gip/dynamic/inside.html.

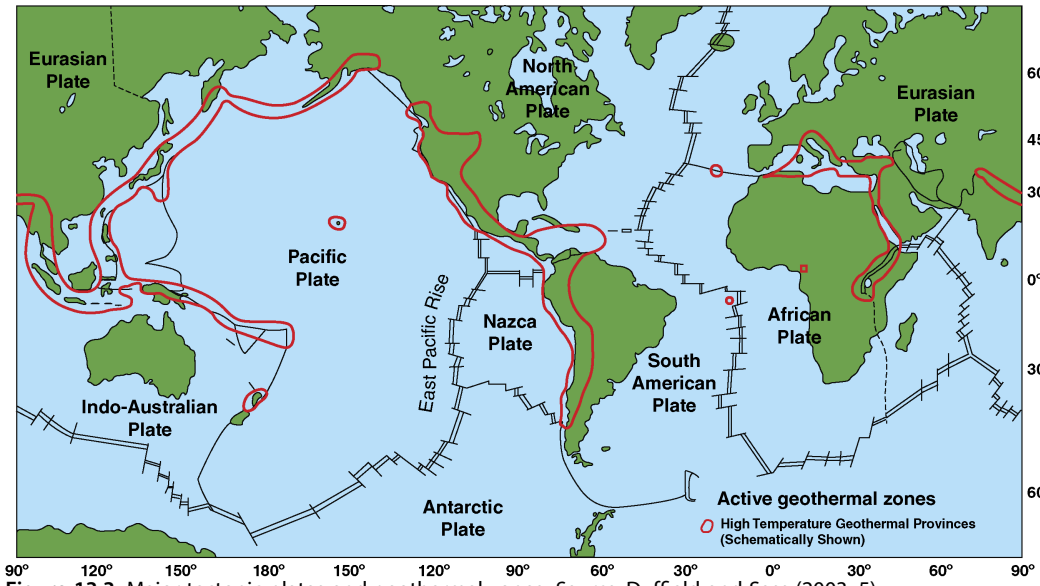

Figure 13.3 Major tectonic plates and geothermal zones. *Source*: Duffield and Sass (2003: 5).

"Hydrothermal" refers to conditions in which water is heated and/or evaporated by direct contact with hot porous rock. The porous or permeable rock in a hydrothermal site is contained (bounded) by rock strata of low permeability. Water, provided by aquifers, trickles through the porous rock and is heated and perhaps vaporized (to form steam), and is discharged at the surface. Hydrothermal systems that produce steam are labeled as vapor dominated, while hydrothermal systems that produce hot water or a mixture of hot water and steam are called liquid dominated. Energy from hydrothermal sources can be harvested relatively easily. Many existing geothermal power plants are associated with hydrothermal systems. But rock formations with hydrothermal characteristics are rare, and hydrothermal resources are the most limited of the four categories.

Geopressurized resources are associated with sediment-filled reservoirs that contain hot water confined under pressures much greater than hydrostatic. The fluids contained in geopressurized systems are in the temperature range 150–180 °C and may be pressurized up to 600 bar (~9000 psi). In many geopressurized systems, the hot water may also contain methane in solution, as well as very high levels of dissolved solids – up to 100 000 ppm. These brine solutions are both highly corrosive and difficult to handle.

Magma, molten rock, at accessible depths is contained in pools under active volcanoes. Magma temperatures are typically in excess of 650 °C, making magma attractive from a resource standpoint. Although the energy density of molten rock is quite large, proposed ways of harvesting magma energy are at best speculative.

HDR suitable as a geothermal resource is characterized by temperatures in excess of 200 °C, but, as the name implies, has little in the way of naturally contained liquids. Recently, HDR systems have been referred to as enhanced geothermal systems (EGS), and the US Department of Energy has adopted the EGS classification. The basic idea for harvesting energy from EGS resources is to inject water under pressure to fracture the rock, and to use the steam formed from the injected water to drive a turbine to generate electricity.

Table 13.1 presents estimates of the accessible geothermal resources in terms of the aforementioned classifications. The values in the table are order-of-magnitude estimates

Table 13.1 Geothermal resources estimates.

Resource classification	Geothermal resources (1000 quad)	
	USA	World
Hydrothermal	10	130
Geopressurized	170	540
Magma	1 000	5 000
EGS (formerly HDR)	30 000	105 000

Source: adapted from Tester *et al.* (2005).

and are listed in order of increasing availability of geothermal resources: hydrothermal, geopressurized, magma, and EGS (HDR). The energy economy of the USA is about 100 quad (see Chapter 1) and that of the world about 400 quad. Thus, at the current usage rates, hydrothermal resources in the USA could last about 100 years, but the other geothermal resource classifications offer an essentially unlimited quantity of energy. The problem is, of course, how to harvest and use all of these resources.

The usefulness of geothermal energy is closely associated with the temperature of a geothermal resource. A convenient graphic for displaying the applications of geothermal energy and system configurations as a function of temperature is the Lindal diagram (Figure 13.4), named for Baldur Lindal, a pioneer in geothermal energy development.

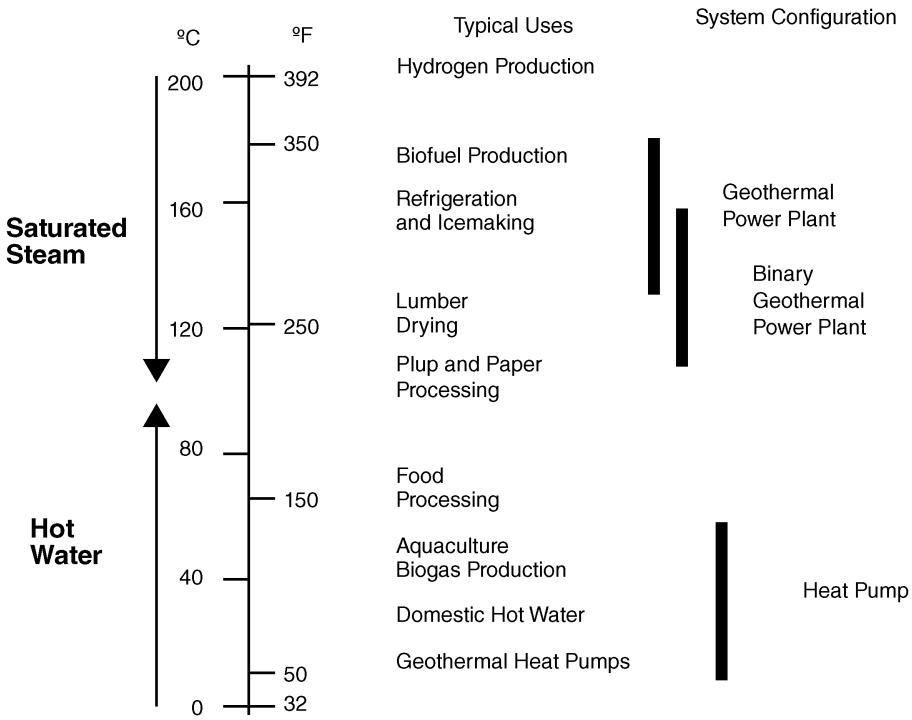

Figure 13.4 Lindal diagram for geothermal energy.

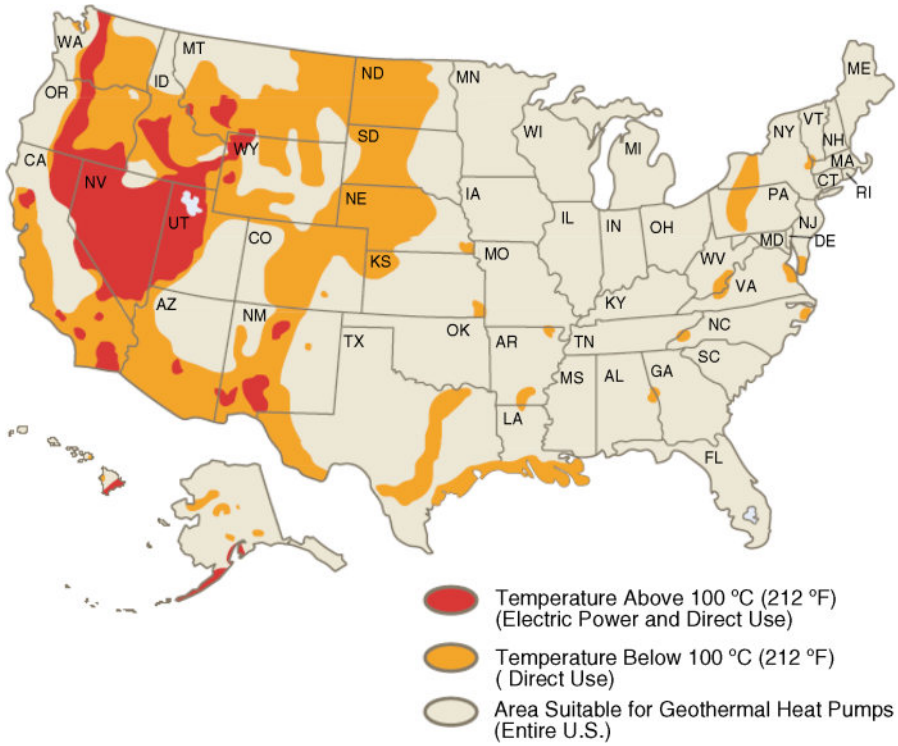

Figure 13.5 Geothermal resources in the USA. *Source*: Geo-heat Center.

In 2008 the USGS completed an assessment of US geothermal energy (USGS, 2008). The electric power generation potential from identified geothermal resources is 9057 MW. The estimated power production potential from undiscovered geothermal resources is an additional 30 033 MW. However, an estimated 517 800 MW could be generated through implementation of advanced technology for low-permeability, but high-temperature rock formations. This is an enormous power generation capacity considering that 1000 GW (1 000 000 MW) exceeds the nominal US electrical grid capacity. For geothermal utilization of this magnitude to occur, a massive shift in infrastructure and technology development would be required.

Figure 13.5 illustrates regions in the USA with accessible geothermal resources. In this figure, geothermal resources are expressed in terms of end-use capability. Resources above 100 °C have the potential to be utilized for electric power generation, while resources below 100 °C can be used for direct thermal energy – congruent with the Lindal diagram (Figure 13.4). Most of these geothermal resources are located in the mountain and coastal areas of the west that conform generally to the active geothermal zones of Figure 13.3. As briefly mentioned in Section 13.1, GSHPs are also considered users of geothermal energy – albeit it at low temperatures with shallow (meters rather than kilometers) access. The entire continental USA offers the possibility of geothermal energy for GSHP applications.

A slightly different view is provided by the National Renewable Energy Laboratory (NREL) in Figure 13.6. This figure illustrates the deep enhanced EGS resources as well as indicates locations of identified hydrothermal sites. The figures are generally congruent, but Figure 13.6 identifies more EGS availability.

Different geothermal resource classifications require different harvesting technologies. Geothermal systems details are examined next.

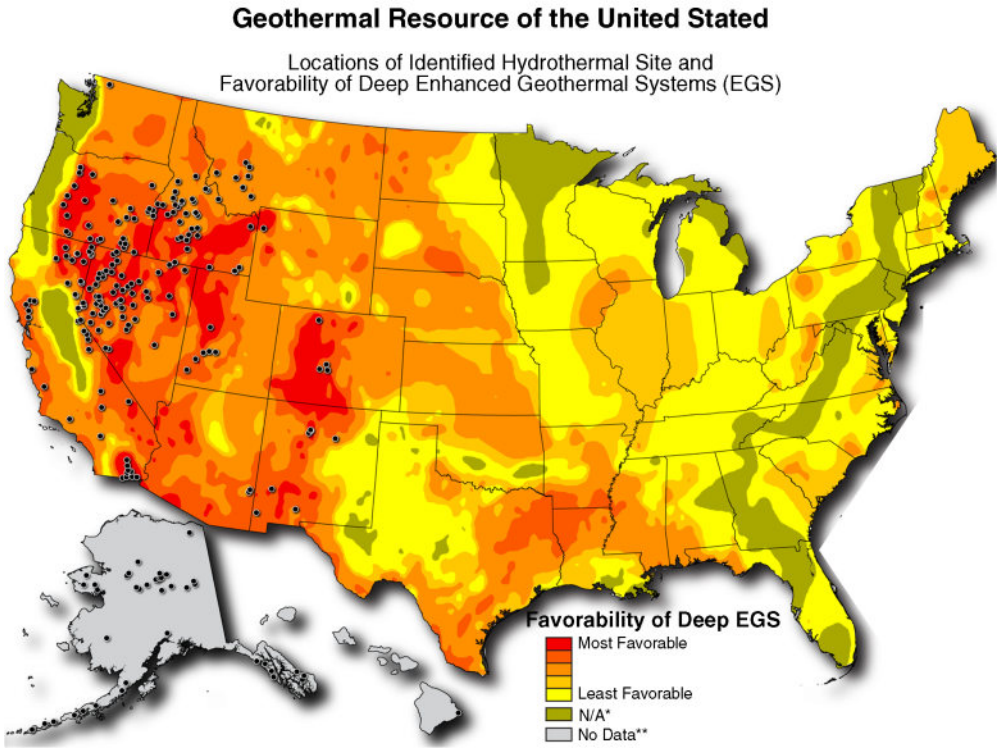

Figure 13.6 NREL geothermal resources in the USA. *Source*: http://www.nrel.gov/gis/images/geothermal_resource2009-final.jpg.

13.3 Geothermal Energy Systems

Different system configurations have been proposed and investigated for harvesting geothermal energy resources according to the different classifications. DiPippo (2012) provides the seminal presentation and case studies for geothermal energy and is recommended reading for engineering aspects of geothermal energy. Several geothermal systems will be examined in detail next.

13.3.1 Hydrothermal

Hydrothermal sources have either hot water or steam available and represent the easiest geothermal sources to harvest. Dissolved solids, entrained solid particles, and noncondensable gases are problems with most geothermal resources. The entrained solids are generally removed by centrifugal separators at the well head, but filters are placed in the system to ensure solid particles are removed. Non-condensable gases abound in some locations and pose many problems for geothermal systems. Many of the noncondensable gases form acids under wet conditions, necessitating the use of stainless steel or other expensive materials. Additionally, these gases pose environmental hazards if released to the atmosphere. Hydrothermal sources are usually considered in terms of being vapor dominated or liquid dominated.

Vapor-dominated hydrothermal sources are the most suitable for generation of electricity, but are the rarest source of geothermal energy. As the name implies, steam is the available resource in vapor-dominated systems. Vapor-dominated systems require steam at temperatures >175 °C (Kutscher, 2000). Conditions at the surface seldom exceed 205 °C and 8 bar (El-Wakil, 1984). A system schematic for vapor-dominated systems is presented in Figure 13.7. The steam from

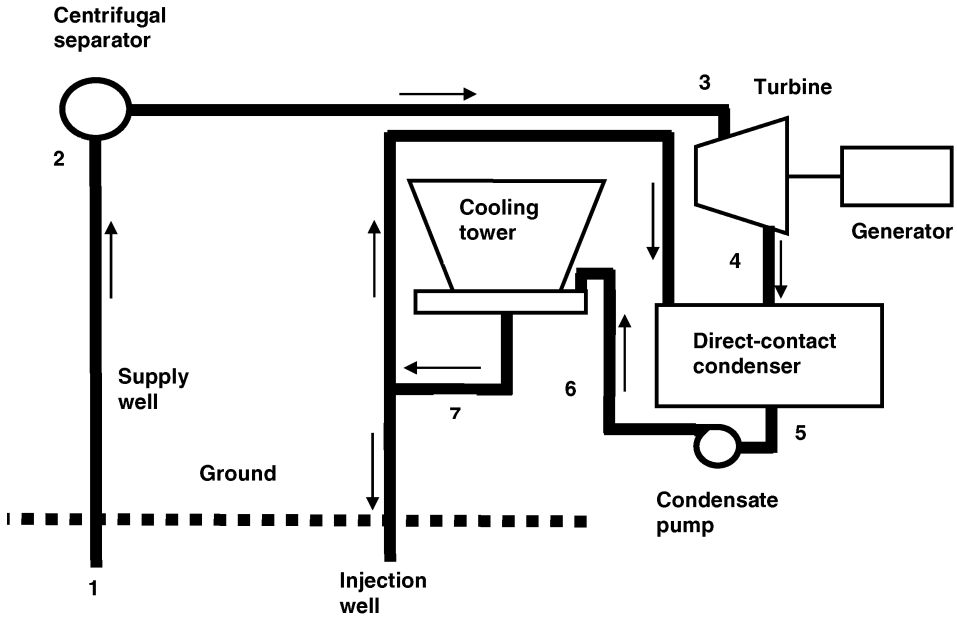

Figure 13.7 Vapor dominated geothermal system schematic.

the well passes through a centrifugal separator and enters the turbine. After exiting the turbine, the steam is condensed, cooled in a cooling tower, and reinjected. In the figure, the thermodynamics states are indicated as 1–7. The process path is shown on the *T*–*s* diagram presented as Figure 13.8. State 1 is saturated vapor (steam) at the well bottom. The vapor goes through a centrifugal separator (state 2) for removal of solid particles and enters the turbine (state 3) as a superheated vapor. Processes 1–2 and 2–3 are essentially constant-enthalpy (throttling) processes. In the turbine, some condensation takes place and the mixture exits at state 4. State 4s represents the exit state if the turbine expansion process were isentropic. State 5 is the exit from the condenser, and state 6 is the state after the condensate pump at the cooling tower. The fluid leaves the cooling tower at state 7 and is either reinjected or used in the direct-contact

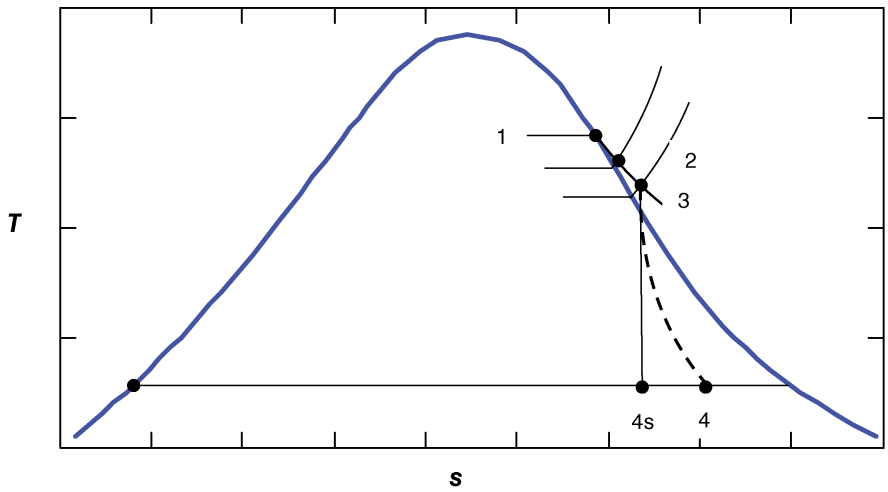

Figure 13.8 *T*–*s* diagram for vapor-dominated systems.

condenser. Details of the thermodynamics of vapor-dominated systems are presented in Example 13.1.

Example 13.1

A vapor-dominated geothermal systems is supplied with saturated steam at 3 MPa. The steam enters the turbine at 0.5 MPa and exits at 15 kPa. The turbine isentropic efficiency is 82%, and the electrical generator is 90% efficient. If reinjection occurs to the cooling tower, analyze the system performance (thermal efficiency and heat rate). What flow rate of steam is required for a power generation of 10 MW?

Solution Saturated vapor at 3 MPa possesses the following properties:

$$h_1 = 2804.2\frac{\text{kJ}}{\text{kg}} \text{ and } T_1 = 233.9\ \text{K}$$

The processes from states 1 to 3 are constant enthalpy, so

$$h_1 = h_2 = h_3$$

As illustrated in Figure 13.8, a constant-enthalpy process from 1 to 3 results in superheated vapor. At 0.5 MPa ($T_{\text{sat}} = 151.9\ ^\circ\text{C}$) and $h_3 = 2804.2$ kJ/kg, the remaining properties of interest are

$$T_3 = 176.7\ ^\circ\text{C} \text{ and } s_3 = 6.945\frac{\text{kJ}}{\text{kg K}}$$

with 25 °C of superheat. The process path 3–4s is isentropic, so that

$$s_{4s} = s_3 = 6.945\frac{\text{kJ}}{\text{kg K}} \text{ and } P_4 = 15\ \text{kPa}$$

with state 3 in the superheated region and 4s "under the dome." At 15 kPa:

$$s_f = 0.7549\frac{\text{kJ}}{\text{kg K}}, \qquad s_{fg} = 7.2536\frac{\text{kJ}}{\text{kg K}}, \qquad h_f = 225.94\frac{\text{kJ}}{\text{kg}}, \qquad h_{fg} = 2373.1\frac{\text{kJ}}{\text{kg}}$$

The quality at state 4s can be found as

$$s_{4s} = 6.945\frac{\text{kJ}}{\text{kg K}} = 0.7549\frac{\text{kJ}}{\text{kg K}} + x \times 7.2536\frac{\text{kJ}}{\text{kg K}}$$

$$x = 0.853$$

With the quality known, the enthalpy can be obtained by

$$h_{4s} = 225.94\frac{\text{kJ}}{\text{kg}} + 0.853 \times 2373.1\frac{\text{kJ}}{\text{kg}} = 2251\frac{\text{kJ}}{\text{kg}}$$

Then the ideal (isentropic) work extracted becomes

$$W_{\text{ideal}} = h_3 - h_{4s} = 2804.2\frac{\text{kJ}}{\text{kg}} - 2251\frac{\text{kJ}}{\text{kg}} = 553\frac{\text{kJ}}{\text{kg}}$$

and the actual work is

$$W_{\text{act}} = \eta_e W_{\text{ideal}} = 0.82 \times 553\frac{\text{kJ}}{\text{kg}} = 454\frac{\text{kJ}}{\text{kg}}$$

At 20 °C (taken as ambient), the enthalpy of the liquid is

$$h_{\text{amb}} = 83.96 \frac{\text{kJ}}{\text{kg}}$$

The thermal efficiency of the electricity production is the electrical energy produced per kilogram divided by the available energy of the liquid (well to ambient):

$$\eta_{\text{thermal}} = \frac{\eta_{\text{elec}} W_{\text{act}}}{h_1 - h_{\text{amb}}} = \frac{0.9 \cdot 454\,\text{kJ/kg}}{2804.2\,\text{kJ/kg} - 83.96\,\text{kJ/kg}} = 0.15$$

from which the heat rate can be computed as

$$\text{Heat rate} = \frac{3412}{\eta_{\text{thermal}}} \frac{\text{Btu}}{\text{kW h}} = 22\,730 \frac{\text{Btu}}{\text{kW h}}$$

Because the thermal efficiency is so small, the heat rate is significantly higher than those associated with the prime movers examined in Chapter 12.

The mass flow rate of steam required for 10 MW of electricity production is

$$\dot{m}_{\text{steam}} = \frac{10\,\text{MW}}{\eta_{\text{elec}} W_{\text{act}}} = \frac{10\,\text{MW}}{0.9 \times 454\,\text{kJ/kg}} = 24.5 \frac{\text{kg}}{\text{s}}$$

The thermal efficiency of only 15% does not include losses and pumping requirements. Indeed, the accepted thermal efficiency of vapor-dominated geothermal systems is about 10%. One ramification of low thermal efficiencies is that system mass flow rates and sizes must be large to generate significant power.

Liquid-dominated geothermal resources are more abundant than vapor-dominated sources. In liquid-dominated systems, water is available at 150–315 °C. If the pressure is reduced, the water will flash into a two-phase mixture of relatively low quality – hence the name, "liquid dominated." Three system configurations are possible with liquid-dominated systems: flash, binary, and total. Each will be examined in turn.

In flash systems, hot brine from a geothermal well is brought to the surface, where the pressure is reduced and some of the liquid is flashed into vapor. The vapor is expanded through a turbine to produce electricity, and the liquid is reinjected through another bore. A system schematic of a flash liquid-dominated system is presented in Figure 13.9, and a *T*–*s* diagram of the process is provided in Figure 13.10.

Water from the well bore is supplied at state 1 and enters the flash separator at state 2 after a constant-enthalpy process. In the flash separator, vapor at state 3g is directed into the turbine, and liquid at state 3f is reinjected. State 3g is expanded to state 4 in the turbine. The isentropic expansion process to state 4s is also indicated in Figure 13.10. The mixture is condensed in the direct-contact condenser to state 5,6. Part of the condensate is reinjected, and part is directed to the cooling tower and subsequently used in the direct-contact condenser as the cooling fluid. One of the disadvantages of the flash system is that the brine (state 3f), which contains significant energy, is reinjected. Energy is extracted only from the vapor phase. Example 13.2 addresses flash liquid-dominated geothermal systems.

Example 13.2

A geothermal power plant is supplied with water at a well-bottom temperature of 225 °C and a pressure of 8 MPa. The fluid flows into a flash separator maintained at 40 kPa. The turbine

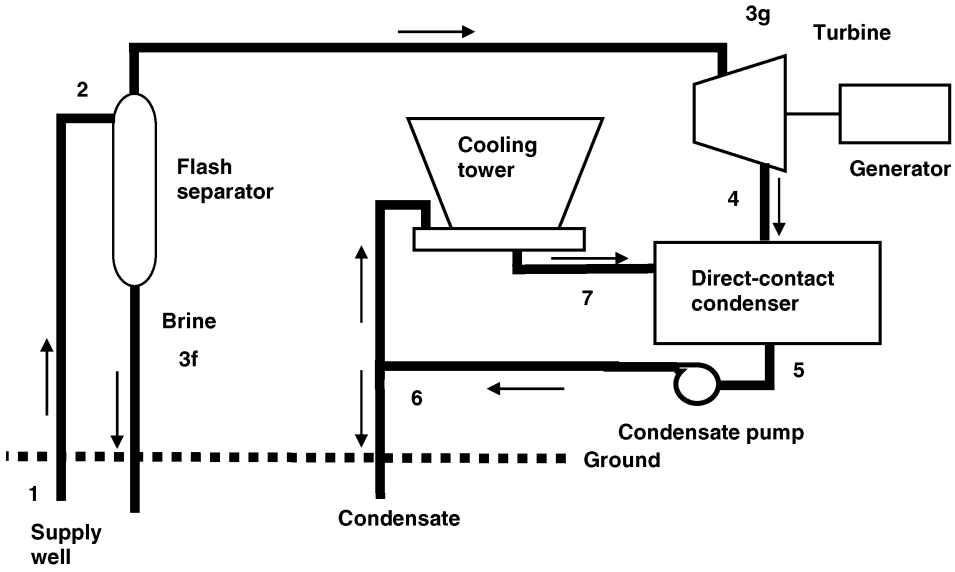

Figure 13.9 Flash liquid-dominated geothermal system schematic.

exit pressure is 10 kPa. The overall efficiency of the turbine is 0.83. Calculate the thermal efficiency, the heat rate, and the steam and water mass flow rates required for an output of 10 MW.

Solution Properties for this example were computed using the IAPWS Industrial Formulation 1997 for the thermodynamic properties of water and steam (Palmer *et al.*, 2004). At 8 MPa and 225 °C the well-bottom fluid possesses an enthalpy of

$$h_1 = 968.18 \frac{\text{kJ}}{\text{kg}}$$

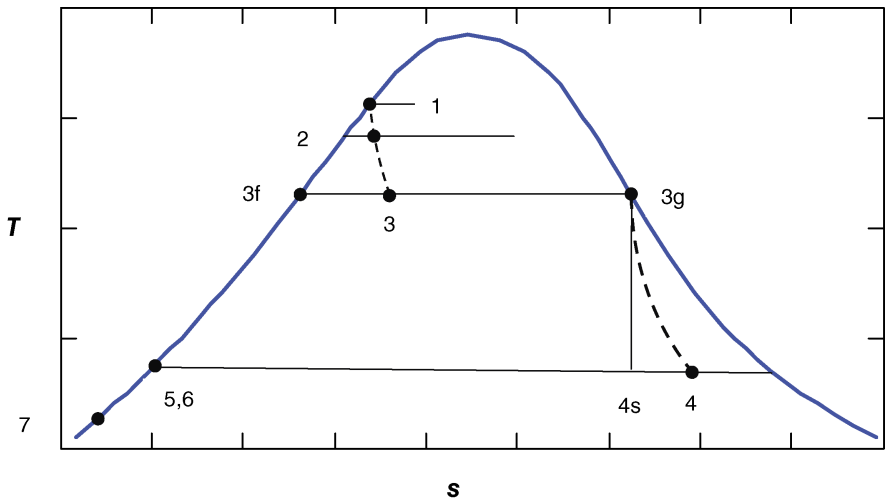

Figure 13.10 *T–s* diagram for flash liquid-dominated systems.

The processes from 1 to 3 are constant enthalpy, so

$$h_1 = h_2 = h_3$$

As illustrated in Figure 13.10, a constant-enthalpy process from 1 to 3 results in a mixture of liquid and vapor. At 40 kPa:

$$h_f = 317.62\frac{kJ}{kg}, \qquad h_{fg} = 2318.5\frac{kJ}{kg}, \qquad h_g = 2636.1\frac{kJ}{kg}, \qquad s_g = 7.667\frac{kJ}{kg\,K}$$

The quality at state 3 can be found as

$$\begin{aligned} h_3 &= 968.18\frac{kJ}{kg} = 317.62\frac{kJ}{kg} + x \times 2318.5\frac{kJ}{kg} \\ x &= 0.281 \end{aligned}$$

Since only vapor ($x = 1$) enters the turbine, $h_{3g} = 2636.1$ kJ/kg and $s_{3g} = 7.667$ kJ/(kg K). At the turbine exit, $P_4 = 10$ kPa, and the remaining properties of interest are

$$s_f = 0.6492\frac{kJ}{kg\,K}, \qquad s_{fg} = 7.4998\frac{kJ}{kg\,K}, \qquad h_f = 191.81\frac{kJ}{kg}, \qquad h_{fg} = 2392.1\frac{kJ}{kg}$$

The isentropic process, 3–4s, has $s_{3g} = s_{4s} = 7.667$ kJ/(kg K), so that the quality at state 4s becomes

$$\begin{aligned} s_{4s} &= 7.667\frac{kJ}{kg\,K} = 0.6492\frac{kJ}{kg\,K} + x \times 7.4998\frac{kJ}{kg\,K} \\ x &= 0.936 \end{aligned}$$

And the enthalpy at state 4s is

$$h_{4s} = 191.81\frac{kJ}{kg} + 0.936 \times 2392.1\frac{kJ}{kg} = 2431\frac{kJ}{kg}$$

The ideal (isentropic) work extracted becomes

$$W_{ideal} = h_{3g} - h_{4s} = 2636\frac{kJ}{kg} - 2431\frac{kJ}{kg} = 205\frac{kJ}{kg}$$

and the actual work is

$$W_{act} = \eta_e W_{ideal} = 0.83 \times 205\frac{kJ}{kg} = 170\frac{kJ}{kg}$$

At 20 °C, the enthalpy of the liquid is $h_{amb} = 83.91$ kJ/kg.

The mass flow rate of steam required for 10 MW of electricity production is

$$\dot{m}_{steam} = \frac{10\,MW}{W_{act}} = \frac{10\,MW}{170\,kJ/kg} = 58.69\frac{kg}{s}$$

and the water required from the geothermal well is

$$\dot{m}_{water} = \frac{\dot{m}_{steam}}{x} = \frac{58.670}{0.281}\frac{kg}{s} = 209.2\frac{kg}{s}$$

Because of the low quality of the working fluid at the steam separator, the required water mass flow rate from the geothermal well is large for the amount of power produced.

The thermal efficiency of the electricity production is the electrical energy produced per kilogram of steam divided by the available energy (enthalpy) of the liquid (well to ambient):

$$\eta_{\text{thermal}} = \frac{W_{\text{act}}}{h_1 - h_{\text{amb}}} = \frac{170\ \text{kJ/kg}}{968.18\ \text{kJ/kg} - 83.91\ \text{kJ/kg}} = 0.193$$

from which the heat rate can be computed as

$$\text{Heat rate} = \frac{3412}{\eta_{\text{thermal}}} \frac{\text{Btu}}{\text{kW h}} = 17\,710 \frac{\text{Btu}}{\text{kW h}}$$

Compared with most other systems examined in the textbook, the heat rate is quite large since the thermal efficiency is low. However, the thermal efficiency calculated using only the steam does not consider the energy of the reinjected water. The "well-bottom" thermal efficiency of the electricity production is the electrical energy produced by the steam divided by the available energy (enthalpy) of the liquid extracted from the well bottom:

$$\eta_{\text{well bottom}} = \frac{\dot{m}_{\text{steam}} W_{\text{act}}}{\dot{m}_{\text{water}}(h_1 - h_{\text{amb}})} = \frac{x W_{\text{act}}}{h_1 - h_{\text{amb}}} = x\eta_{\text{thermal}} = 0.281 \times 0.193 = 0.054$$

As with the thermal efficiency, the efficiency based on the well-bottom water flow rate does not consider losses and the auxiliary equipment energy required to operate the facility. Thus, in the flash separator system the electrical energy generation per kilogram of extracted water from the well bottom is quite low.

As demonstrated in Example 13.2, the flash liquid-dominated geothermal system has a low well-bottom efficiency since so much energy is reinjected back into the site. A proposed solution is the total-flow concept for liquid-dominated systems, in which the turbine is replaced by a mixed-flow expander that extracts energy from the vapor-liquid mixture – thus permitting the total well-head flow to be expanded to the condenser pressure. A suggested schematic and *T*–*s* diagram are presented in Figures 13.11 and 13.12.

Instead of undergoing the flash process, the fluid from the supply well enters a mixed-flow expander at state 2 and exits the expander at state 3. All of the fluid from the well is directed to the expander. In principle the process is simple; however, most geothermal fluids contain

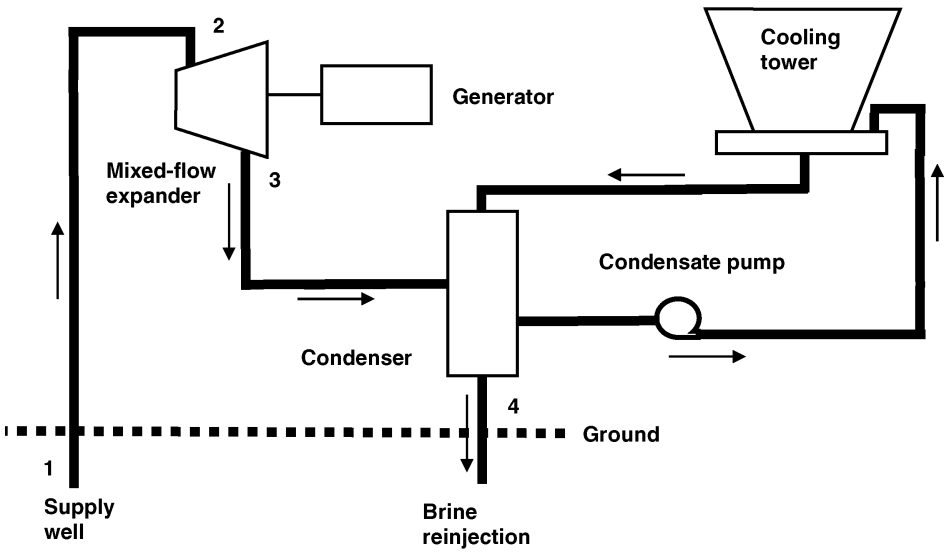

Figure 13.11 Total-flow liquid-dominated geothermal system schematic.

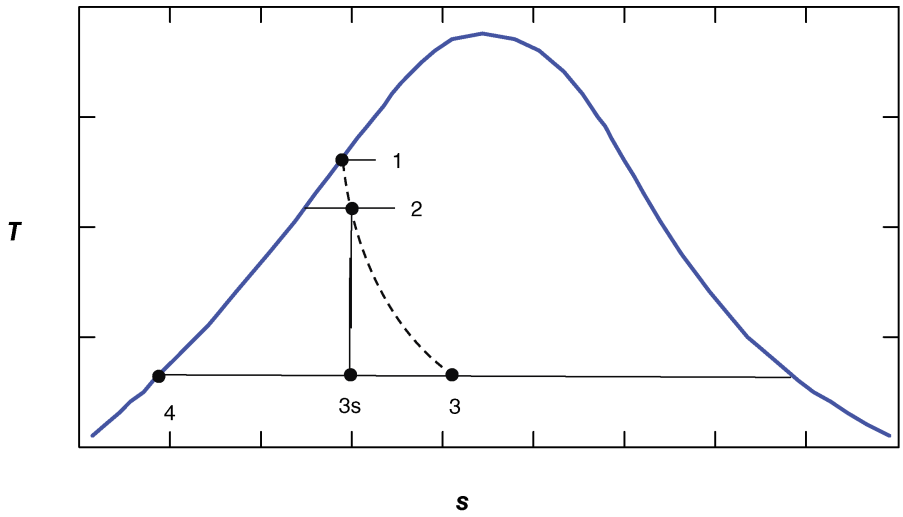

Figure 13.12 *T–s* diagram for total-flow liquid-dominated system.

significant concentrations of corrosive solid and dissolved gases, and the design of turbines expanding from a near-saturated liquid to two-phase flow is difficult. Indeed, an examination of the literature shows much interest in mixed-flow expanders for geothermal operation in the 1970s and 1980s, with waning interest after that, to be followed by increased interest currently. Isentropic efficiencies for mixed-flow expanders are not anticipated to be as high as for conventional single-phase working fluid turbines. DiPippo (2012) concludes that, for appropriate circumstances for single-flash and total-flow systems, a mixed-flow expander would need to possess an isentropic efficiency of about 50% to be competitive. Example 13.3 is a variation of Example 13.2, but uses a mixed-flow expander.

Example 13.3
Consider a total-flow geothermal system using the same well-bottom conditions as Example 13.2. The fluid enters the expander as a saturated liquid and is discharged at 10 kPa. Determine the thermal efficiency, the heat rate, and the flow rate for a 10 MW system if the mixed-flow expander possesses an isentropic efficiency of 0.50.

Solution Thermodynamic properties for this example are taken from Cengel and Boles (1998). For the prescribed conditions, state 2 is the saturated state; hence, in Figure 13.12, states 1 and 2 occur on the saturation line and are the same. The saturation pressure for a saturation temperature of 225 °C is 2.548 MPa. Thus, at state 2

$$h_f = 966.78\frac{\text{kJ}}{\text{kg}}, \qquad h_{fg} = 1836.5\frac{\text{kJ}}{\text{kg}}, \qquad s_{f2} = 2.5639\frac{\text{kJ}}{\text{kg K}}, \qquad s_{fg2} = 3.6863\frac{\text{kJ}}{\text{kg K}}$$

The process 2–3s is isentropic, so that

$$s_{3s} = s_{f2} = 2.5369\frac{\text{kJ}}{\text{kg K}}$$

The mixture exits the expander at 10 kPa. The corresponding properties for state 3 are

$$s_f = 0.6493\frac{\text{kJ}}{\text{kg K}}, \qquad s_{fg} = 7.5009\frac{\text{kJ}}{\text{kg K}}, \qquad h_f = 191.83\frac{\text{kJ}}{\text{kg}}, \qquad h_{fg} = 2392.8\frac{\text{kJ}}{\text{kg}}$$

The quality at the exit of the expander becomes

$$s_{3s} = 2.5369\frac{\text{kJ}}{\text{kg K}} = 0.6493\frac{\text{kJ}}{\text{kg K}} + x \times 7.5009\frac{\text{kJ}}{\text{kg K}}$$
$$x = 0.255$$

And the enthalpy at state 3s is

$$h_{3s} = 191.83\frac{\text{kJ}}{\text{kg}} + 0.255 \times 2392.8\frac{\text{kJ}}{\text{kg}} = 802.6\frac{\text{kJ}}{\text{kg}}$$

The ideal (isentropic) work extracted becomes

$$W_{\text{ideal}} = h_2 - h_{3s} = 966.78\frac{\text{kJ}}{\text{kg}} - 802.6\frac{\text{kJ}}{\text{kg}} = 164.2\frac{\text{kJ}}{\text{kg}}$$

and the actual work is

$$W_{\text{act}} = \eta_e W_{\text{ideal}} = 0.50 \times 164.2\frac{\text{kJ}}{\text{kg}} = 82.1\frac{\text{kJ}}{\text{kg}}$$

At 20 °C, the enthalpy of the liquid is $h_{\text{amb}} = 83.96$ kJ/kg.

The mass flow rate required for 10 MW of electricity production is

$$\dot{m} = \frac{10\text{ MW}}{W_{\text{act}}} = \frac{10\text{ MW}}{82.1\text{ kJ/kg}} = 121.8\frac{\text{kg}}{\text{s}}$$

The thermal efficiency of the electricity production is the electrical energy produced divided by the available energy (enthalpy) from the well:

$$\eta_{\text{thermal}} = \frac{W_{\text{act}}}{h_2 - h_{\text{amb}}} = \frac{82.1\text{ kJ/kg}}{967\text{ kJ/kg} - 83.96\text{ kJ/kg}} = 0.093$$

From which the heat rate can be computed as

$$\text{Heat rate} = \frac{3412}{\eta_{\text{thermal}}}\frac{\text{Btu}}{\text{kW h}} = 36\,690\frac{\text{Btu}}{\text{kW h}}$$

The heat rate is higher than for the flashed system, but the mass flow rate is significantly reduced since all of the extracted fluid traverses the mixed-flow expander. This example glosses over the many problems associated with a mixed-flow expander for the total-flow geothermal system, but it does illustrate why such an arrangement is advantageous and attractive.

The other common system for liquid-dominated geothermal applications is the binary system. A number of existing geothermal power plants utilize such systems. A schematic illustrating the important components of a binary liquid-dominated system is provided in Figure 13.13.

In a binary geothermal system, two fluids are involved: the hot brine from the geothermal well and a working fluid (generally a hydrocarbon) that circulates in the closed portion of the system containing the turbine, condenser, and heat exchangers. In the binary system, the hot brine for the well supplies the hot fluid to the heat exchanger in which the organic fluid undergoes evaporation. The organic vapor is expanded through the turbine and condensed in the condenser and, hence, is in a closed system. The cooling tower is used as the cold medium in the condenser. Strictly speaking, the only geothermal components of the binary system are the supply/reinjection process with the well and the heat exchanger. The working fluids used in binary geothermal systems include propane (C_3H_8), isobutene (2-methyl propane, C_4H_{10}),

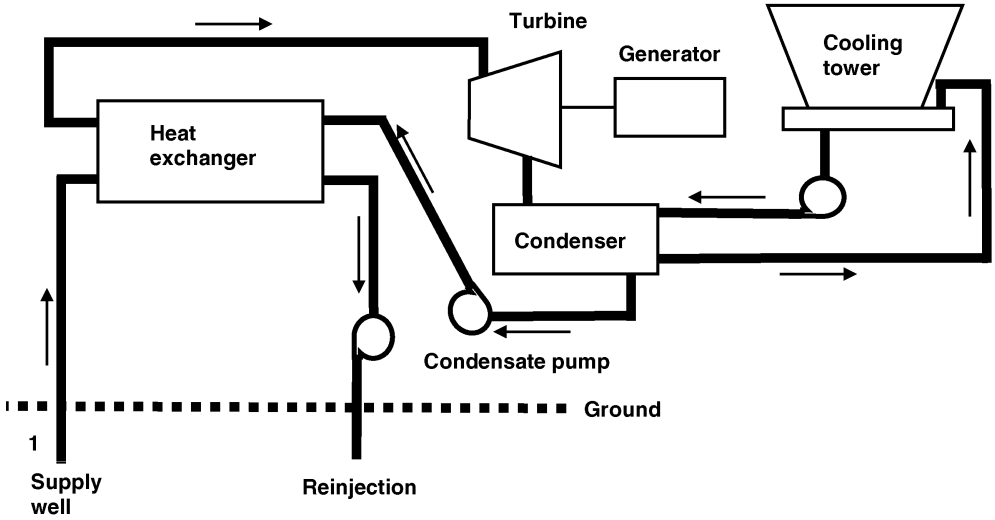

Figure 13.13 Binary liquid-dominated geothermal system schematic.

isopentane (2-methyl butane, C_5H_{12}), and water–ammonia. The working fluids all have boiling points lower than that of water. Binary systems have advantages over flash liquid-dominated systems – not the least of which is that only the heat exchanger and hot brine transport components are exposed to the generally harsh and corrosive brine conditions.

13.3.2 Geopressurized

Geopressurized resources may be pressurized up to 1000 bar (~15 000 psi), pressures that are much greater (as much as a factor of 2) than hydrostatic, and are in the temperature range 150–180 °C. In the USA the primary location of such resources is in the Gulf Coast region in Texas and Louisiana. Figure 13.14 shows, in the cross-hatched regions, the geopressurized resource locations. Geopressurized sites are 2000–9000 m in depth. Common features of many geopressurized resources are the high content of dissolved methane and the high levels of dissolved solids – up to 100 000 ppm. Geopressurized brine typically contains 30–80 ft^3/barrel of methane. Indeed, Smil (2003) estimates that the global resources of geopressurized brine gas could be more than 100 times the current proven natural gas reserves and that the Gulf of Mexico region may contain more brine-gas methane than the current natural gas reserves.

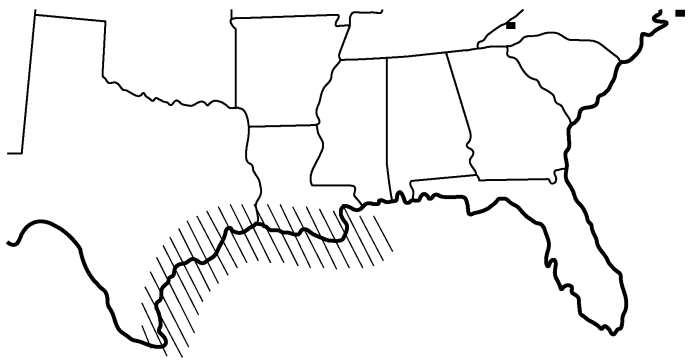

Figure 13.14 Geopressurized resource locations.

These brine solutions are both highly corrosive and difficult to handle. Most proposed schemes for harvesting geopressurized resources involve the recovery of both energy and methane. The combination of depth and the content of geopressurized brine makes harvesting energy and methane for this resource difficult and capital intensive. A number of feasibility studies of geopressurized systems, some with economics components, have been accomplished over the years, but the technical problems and high costs have precluded anything but pilot studies.

13.3.3 Magma

Magma is molten rock (with temperatures typically in excess of 650 °C) contained in pools 3–10 km below active volcanoes and in other geologic formations. Although the energy density of molten rock is large and the estimated resources quite significant (see Table 13.1), methods for harvesting magma energy are at best speculative. The most referenced studies for magma energy extraction were those sponsored by Sandia National Laboratory in the 1980s. Dunn (1987) and Boehm *et al.* (1989) are good examples of the Sandia efforts. The good news is that, in addition to producing energy, the high temperature and pressure associated with magma pools also produces desirable gaseous fuels, such as hydrogen, carbon monoxide, and methane. The bad news is the high-temperature environment and the high concentration of corrosive gases and solid exacerbate material compatibility and longevity problems.

At 600 °C iron oxide reacts with water to produce hydrogen according to

$$2FeO + H_2O \rightarrow 2FeO_{1.5} + H_2 \tag{13.1}$$

The quantity of hydrogen produced can be enhanced by introducing biomass into the injected water. In a chemical process similar to gasification, appreciable quantities of carbon monoxide, carbon dioxide, and methane along with steam and hydrogen result.

Figure 13.15 is a sketch of how a magma power/fuel plant might appear. In addition to utilizing the steam produced for generating electrical power, gaseous fuels would also be recovered. As indicated in the figure, magma pools are quite large, with a single magma pool capable of providing energy and fuel for many years. Although the potential is great, the technological problems are immense, and the general consensus is that deep magma-based power/fuel plants are years away. Recently, two events have enhanced interest in magma energy: (1) the mapping of a very large magma pool under Yellowstone National Park; (2) the

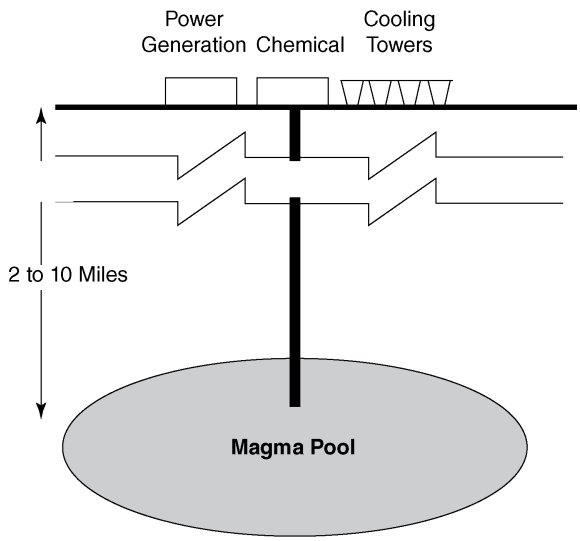

Figure 13.15 Magma power plant visualization.

serendipitous generation of electricity using shallow magma in Iceland. Both are discussed in the next paragraph.

Haung *et al.* (2015) at the University of Utah identified and mapped an enormous lava (magma) pool beneath Yellowstone National Park. The magma structure is composed of two segments: a shallow "whale-shaped" magma chamber, oriented with the tail toward the surface, 2–10 km deep, with the shallow end composed of hydrothermal fluids and the deeper end composed of magma. The volume of this upper chamber is estimated to be of the order of 10 000 km^3 (2.5 times the Grand Canyon volume). The magma is spongy and is composed of about 9% liquid phase. The deeper chamber is 20 to 50–60 km below the surface and is connected to the upper chamber. The volume of the lower chamber is about 45 000 km^3 (11.2 times the Grand Canyon volume) and is about 2% liquid phase. A super eruption event would be climatologically catastrophic, but the University of Utah researchers pose those odds at 1 in 700 000 on a yearly basis. In 2009, the Iceland Deep Drilling Project (IDDP) (Elders *et al.*, 2014), in search of conventional geothermal energy, encountered a magma pool at a depth of 2.1 km. A steel casing, perforated at the bottom, was cemented into the bore hole. Steam at more than 450 °C from the magma was used to generate about 36 kW of power. This effort is a milestone as it was a successful demonstration that energy could be extracted from magma in a controlled fashion and used to generate electricity, although from a shallow, not a deep magma pool. Ultimately, the site was shut down due to equipment failure. Iceland is pursuing further generation of electricity from magma.

13.3.4 Enhanced Geothermal Systems

Proposed harvesting procedures for EGS (or HDR) systems involve injecting water into the resource, circulating the water through the rock as the energy capture mechanism, and bringing the heated water to the surface for use. Because of the low thermal conductivity of the rock, large surface areas are needed in order to extract meaningful amounts of energy. Thus, a major problem in EGS systems is how to attain the large surface areas in the hot rock required for effective harvesting of thermal energy. Most proposed procedures for the use of the EGS resource advocate hydrofracturing the rock by injecting water at very high pressures (200 atm) into the strata. In EGS systems with sufficient surface area, the use of techniques developed for enhanced oil recovery may be employed. For an interesting tidbit of EGS history, search for the topic, "Project Plowshare" on the internet.

EGS facilities require both injection bores and production bores. A proposed schematic for an EGS site is provided in Figure 13.16. In the figure, the fractured hot rock is illustrated, as are the injection and production bores. El-Wakil (1984) reported a Los Alamos National Laboratory study as stating that that water would be pumped in at 1600 psia and 65 °C and retrieved at 2000 psia and 280 °C. In 2008, the US Department of Energy completed an 8 month assessment of the technology developments needed for EGS to become commercially viable. The results are available in Geothermal Technologies Program (2008). Pacing technology requirements include site selection and characterization, reservoir creation, wellfield development, system operation, and drilling and power conversion technologies. As with some other geothermal resources, economical and safe implementation of EGS will require significant development and capital.

13.4 Geothermal Examples

The previous sections of this chapter have examined various aspects of geothermal energy systems, so some examples are in order. The US geothermal electrical generating capacity was 3792 MW in 2012 (Esterly and Gelman, 2014; Matek, 2014), with California, Nevada, Utah, Oregon, and Idaho obtaining significant energy from geothermal resources. Matek (2014)

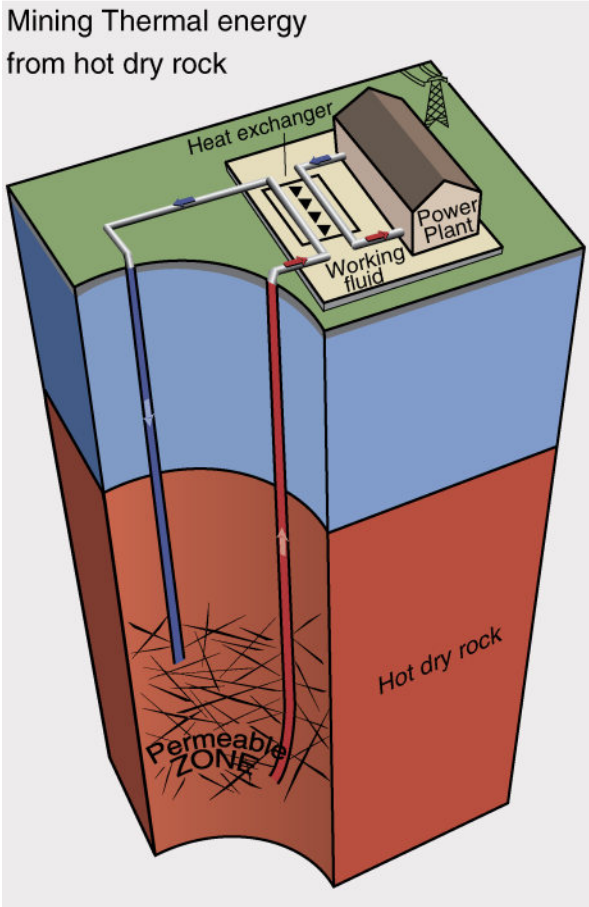

Figure 13.16 Schematic of an EGS power plant. *Source*: Duffield and Sass (2003: 22).

contains a listing and some details of geothermal power plants and projects in the USA. Although somewhat dated, a detailed compilation of geothermal energy use in the USA is provided by Lund *et al*. (2005). The geothermal plants in the USA are dry steam (hydrothermal), binary, or flash (some are double flash).

The Geysers Geothermal Area, north of San Francisco, contains 17 dry steam geothermal power plants. Figure 13.17 is a photograph of the Big Geysers 75 MW hydrothermal power plant. The facility has been in operation since 1980.

The Mammoth Pacific Power Plants, in the Sierra Nevada Mountains, utilize brine from the Casa Diablo Hot Springs. Mammoth Pacific I, shown in Figure 13.18, was built in 1984. It generates10 MW and is a binary geothermal plant.

Figure 13.19 shows an 85 MW double-flash geothermal power plant located at Coso Junction, CA. In a double-flash geothermal power plant, the liquid exiting the flash separator is flashed to produce low-pressure steam that can be utilized by a second low-pressure turbine or injected at an appropriate stage of the main turbine. Navy I has been online since 1987.

Geothermal energy has exhibited a slow, but steady growth in the USA. Table 13.2 depicts the growth in installed capacity as well as the gigawatt-hours generated from 2000 until 2013. Over that timeframe the growth was 12%, although six of those years show zero or less than 1% growth. The USA leads the world in installed geothermal capacity (3.8 GW) followed by the Philippines with 1.9 GW, Indonesia with 1.3 GW, and Mexico with 1 GW.

Figure 13.17 One of the Geysers hydrothermal power plants (NREL 17270). *Source*: http://images.nrel.gov/viewphoto.php?imageId=6318101.

Figure 13.18 Mammoth Pacific I, a binary geothermal power plant. *Source*: EERE.

Figure 13.19 Navy I double-flash geothermal power plant (NREL 07667). *Source*: http://images.nrel.gov/viewphoto.php?imageId=6312443.

Table 13.2 Growth in geothermal energy in the USA.

	US geothermal electricity		
	Generation (GW h)	**Capacity (MW)**	**Annual capacity increase (%)**
2000	14 093	2798	2.2
2001	13 741	2798	0.0
2002	14 491	2798	0.0
2003	14 424	2798	0.0
2004	14 811	2798	0.0
2005	14 692	2828	1.1
2006	14 568	2831	0.1
2007	14 637	2936	3.7
2008	14 840	3039	3.5
2009	15 009	3085	1.5
2010	15 219	3100	0.5
2011	15 316	3238	4.4
2012	15 562	3385	4.5
2013[a]	16 517	3792[a]	12.0[a]

Source: Esterly and Gelman (2014).

a) The increase in capacity in 2013 is partially due to a change in data sources from the Geothermal Energy Association to the Energy Information Administration, which account for capacity differently.

The primary focus of this chapter to this point has been geothermal power systems using steam and/or hot brine to produce electric power. As alluded to in the Section 13.1, geothermal heat pumps or GSHPs can also be considered users of geothermal energy. GSHPs are covered next.

13.5 Ground-Source Heat Pumps

GSHPs or geothermal heat pumps utilize the ground (soil) for heat rejection in summer and as a heat source in winter. Conventional heat pumps reject heat to the atmosphere in summer and extract energy from the atmosphere in winter. A few feet below the surface, the ground temperature remains nearly constant throughout the year. If the ground is used as a heat source/sink for a heat pump, the performance of the heat pump is enhanced when compared with a heat pump using the atmosphere as a heat source/sink. The Carnot efficiency is the maximum possible thermal efficiency for a heat engine operating between two temperatures and producing work and is stated as

$$\eta_{\text{Carnot}} = \frac{T_{\text{H}} - T_{\text{C}}}{T_{\text{H}}} \tag{13.2}$$

where T_{H} and T_{C} are the absolute temperatures of the high-temperature and low-temperature reservoirs respectively. Refrigerators, air conditioners, and heat pumps are heat engines operating in reverse – transferring energy from a low-temperature reservoir to a high-temperature reservoir by the addition of work. For heat engines operating in reverse, the coefficient of performance (COP) is the usual performance metric. For a heat pump the desired

energy result is the addition of heat to the hot reservoir, and the COP is defined as the heat added to the high-temperature reservoir divided by the work input required. The COP for a Carnot heat pump is

$$\mathrm{COP}_{\text{heat pump}} = \frac{\text{Heat addition to high-temperature reservoir}}{\text{Work input}} = \frac{T_H}{T_H - T_C} \tag{13.3}$$

In a similar fashion, the COP for a Carnot refrigerator or air conditioner is the heat removed from the low-temperature reservoir divided by the work input:

$$\mathrm{COP}_{\text{refrig}} = \frac{\text{Heat removed from low-temperature reservoir}}{\text{Work input}} = \frac{T_L}{T_H - T_C} \tag{13.4}$$

The reason from the difference is the desired outcome – heat addition for the heat pump and heat removal for the refrigerator. The two COPs are related as

$$\mathrm{COP}_{\text{heat pump}} = \mathrm{COP}_{\text{refrig}} + 1 \tag{13.5}$$

Since $\mathrm{COP}_{\text{refrig}}$ is always positive, $\mathrm{COP}_{\text{heat pump}}$ is always greater than one. Although an actual heat pump is significantly different from a reversed Carnot engine, the thermodynamic implications of Equations 13.3 and 13.5 to a heat pump are valid – namely, the smaller the temperature difference between the high- and low-temperature reservoirs, the higher the COP.

In the winter, heat is extracted from the ground instead of the air, so that T_C is the temperature of the ground instead of the outside-air temperature, thus significantly increasing the $\mathrm{COP}_{\text{heat pump}}$. Conventional (air-source) heat pumps possess COP values of near 3, while GSHPs have COP values approaching 4. In the summer, heat is rejected to the ground, not the outside air, such that the $\mathrm{COP}_{\text{refrig}}$ is increased. The use of the ground as a source/sink is thus advantageous for the GSHP. The general configuration of a GSHP is featured in Figure 13.20. The heat exchanger transfers energy between the compressor refrigerant and the ground via a circulating pump in the ground loop.

The ground can be utilized as a heat sink/source for GSHPs in several different configurations: (a) closed loop, horizontal, (b) closed loop, vertical, (c) closed loop, lake/pond, and (d) open loop. Figure 13.21 presents an example of configuration.

The most common configuration for residences is the closed loop, horizontal (Figure 13.21a). The pipes are arranged in a helical coil shape and buried 4–6 ft deep in a trench 2 ft wide. A disadvantage of this method is the amount of soil that must be moved/disturbed. Closed-loop, vertical arrangements (Figure 13.21b) are quite common in government/commercial/industrial sites and are becoming more common for residences. In vertical systems, holes 4 in in diameter are drilled about 20 ft apart and 100–400 ft deep. In each vertical hole, two pipes are connected at the bottom to form a "U" shape. The pipes are manifolded together and connected to the heat pump in the conditioned space of the building. If a body of water, such as a lake or a large pond, is available, the water can be used as the heat source/sink, as in Figure 13.21c. A helical or slinky arrangement is again used, but the pipe must be coiled at least 8 ft under the surface for freeze protection. Finally, an open-loop system, as in Figure 13.21d, can be utilized. Water from a well or a pond is circulated through the GSHP and then returned to the ground via a recharge well. The discharge must conform to local codes and regulations for groundwater discharge.

Since the ground temperature is an important consideration for GSHPs, some discussion is warranted. Depending on the location, at 6 ft underground the near-constant temperature ranges from 45 to 75 °F. Figure 13.22 illustrates the "yearly average" ground temperature distribution in the USA. Not surprisingly, the ground temperatures correlates reasonably well with the "heating degree-days" representations presented in Figure 8.6 – that is, the lower the heating degree-days, the higher the ground temperature.

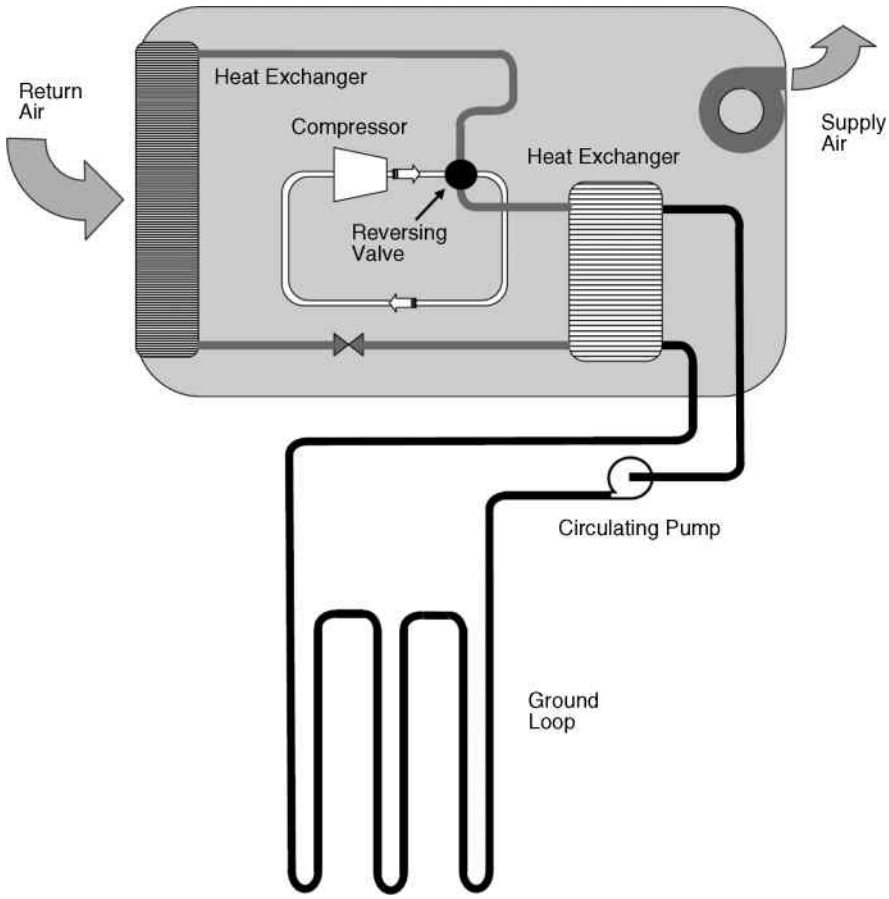

Figure 13.20 GSHP system schematic.

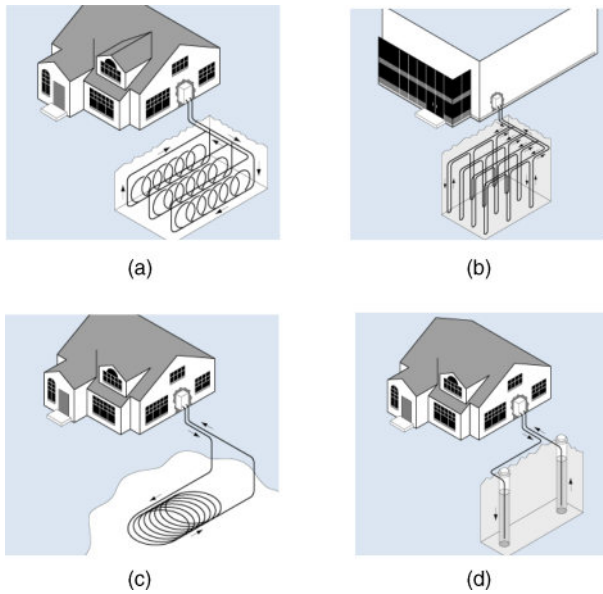

Figure 13.21 GSHP ground-loop configurations: (a) closed loop, horizontal; (b) closed loop, vertical; (c) closed loop, lake/pond; (d) open loop. *Source*: EERE.

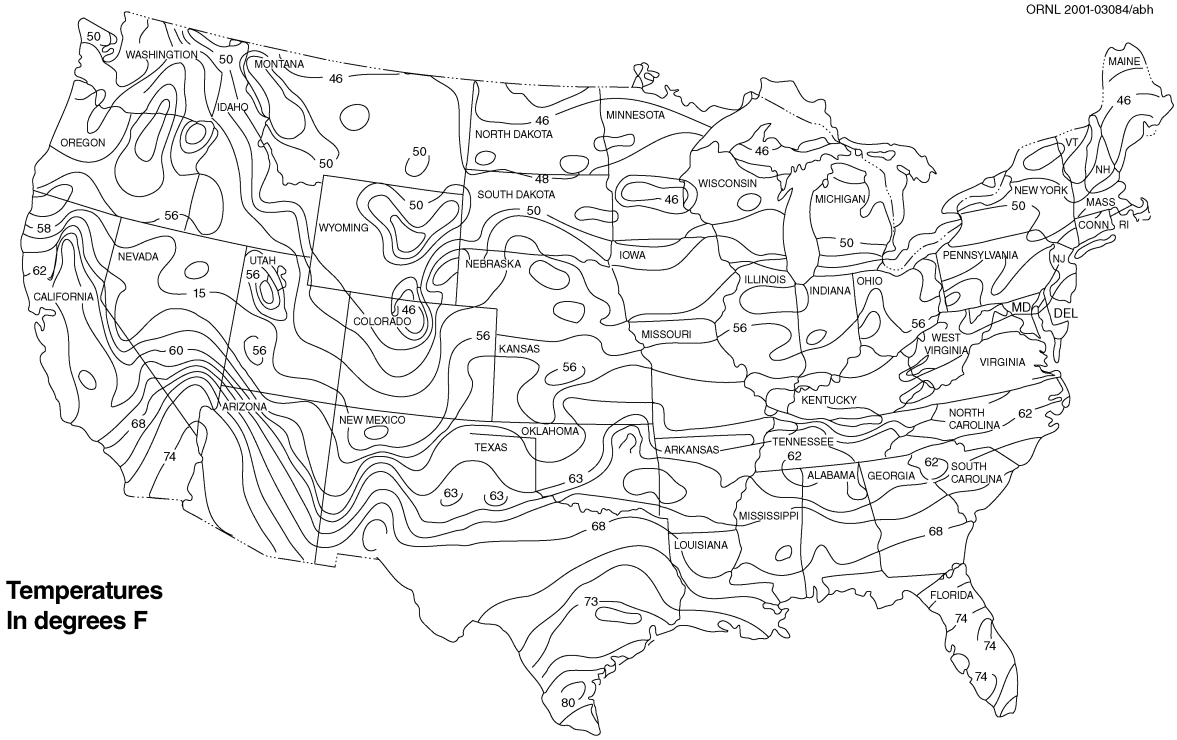

Figure 13.22 Average ground temperature distribution in the USA. *Source*: Oak Ridge National Laboratory.

Table 13.3 Energy for cooling, heating, and domestic hot water for GSHP and conventional systems.

System	Energy (kWh)		
	Atlanta	Spokane	Portland
Air-source heat pump	14 925	16 458	11 299
Air-source heat pump with variable-speed drive	12 159	13 850	9 111
Standard GSHP	9 455	9 163	7 354
High-efficiency GSHP	8 098		

Corrosion-inhibited fluids with antifreeze are used as heat transfer fluids. The general recommendation is that antifreeze sufficient for protection to 10 °F below the minimum expected temperature be used. The fluids should be biodegradable and nontoxic and possess relatively low viscosities. The two most commonly used fluids are ethylene or propylene glycols or an alcohol–water mixture. Methyl, ethyl, or isopropyl alcohols have all been used in GSHP applications. Bio-inhibited water may be used in climates where freezing is not a problem.

Residential systems can be equipped with a "desuperheater" for heating domestic hot water. In the summer, heat that is taken from the house and rejected into the ground loop is used to heat the water. In the winter, the desuperheater can reduce water-heating costs by about half, with a conventional water heater meeting the rest of the hot water needs.

Obviously, GSHP systems are more expensive than conventional systems. The question then becomes, how much energy can be saved by using a GSHP. US Department of Energy studies suggest that approximately 70% of the energy used in a GSHP system comes from the ground. The US Environmental Protection Agency now designates GSHPs as an EnergyStar®-rated product. Rafferty (2001) reports the results of Kavanaugh of energy usage by the same residence in three different climates. The results are summarized in Table 13.3. Four systems were studied: air-source heat pump, air-source heat pump with variable-speed drive, standard GSHP, and high-efficiency GSHP. The total kilowatt-hour usages for cooling, heating, and domestic hot water are presented. The savings for the GSHP options are significant compared with either conventional system. The GSHP systems demonstrate significant electrical savings.

The general rule-of-thumb cost for GSHP systems is $2500/ton installed. This price is about twice what a conventional residential system would cost. Thus, the energy cost savings and possible incentives offered by utilities make GSHPs economically attractive with a reasonable payback period. The web site www.geokiss.com contains extensive information on GSHPs and is recommended for additional information.

GSHPs are also extensively used for commercial, industrial, and government buildings, where they offer the same savings and advantages as for residences. Details, information, and case studies are available from the US Department of Energy (http://energy.gov/search/site/ground%20source%20heat%20pumps) from the Geothermal Heat Pump Consortium (www.geoexchange.org) and the International Ground Source Heat Pump Association (www.igshpa.okstate.edu).

13.6 Closure

This chapter has previewed geothermal energy, primarily as a source of heat for power generation, but also for use in GSHP systems. Figure 13.23 is a good summary of the geothermal applications in the USA. Essentially the entire country is suitable for GSHPs, and in much of the

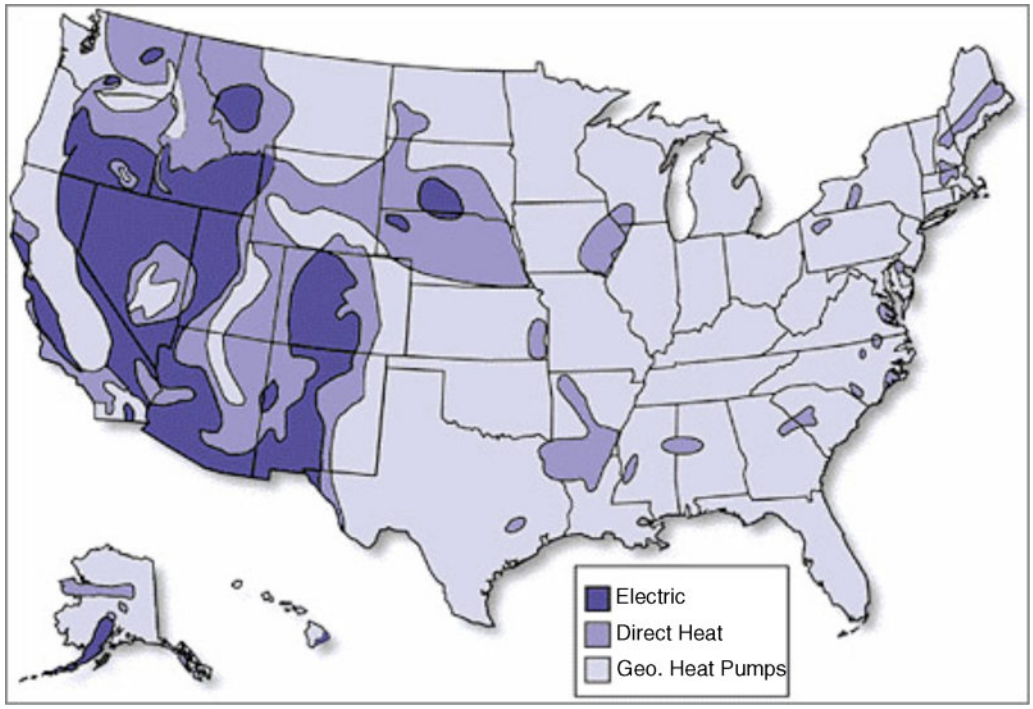

Figure 13.23 Geothermal application summary for the USA. *Source*: https://web.archive.org/web/20150907183014/http://www1.eere.energy.gov/tribalenergy/guide/geothermal_resources.html.

country geothermal can be used for heating. Regions where the geothermal resource temperature is useful for electricity generation are limited, but still surprisingly large. As with many of the energy sources reviewed in this textbook, geothermal has much potential, but research and development issues need to be resolved and significant capital will be required to fully realize this potential.

References

Boehm, R.F., Borg, D.L., and Ortega, A. (1987) Modeling of a magma energy geothermal open cycle power plant. *Journal of Energy Resources Technology*, **111** (4): 239–245.

Cengel, Y.A. and Boles, M.A. (2015) *Thermodynamics*, 8th edn. McGraw-Hill, New York.

DiPippo, R. (2012) *Geothermal Power Plants: Principles, Applications and Case Studies*, 3rd edn. Elsevier, Oxford.

Duffield, W.A. and Sass, J.H. (2003) Geothermal Energy – Clean Power from the Earth's Heat. USGS Circular 1249. US Geological Survey, Reston, VA. http://pubs.usgs.gov/circ/2004/c1249/c1249.pdf (accessed October 25, 2016).

Dunn, J.C. (1987) *Status of the magma energy project*. SAND 87–2560C. Sandia National Laboratories, Albuquerque, NM.

Elders, W.A., Fridleifsson, G.O., and Pálsson, B. (eds), (2014) Iceland Deep Drilling Project: the first well, IDDP-1, drilled into magma. *Geothermics*, **49**: 1–128.

El-Wakil, M.M. (1984) *Powerplant Technology*. McGraw-Hill, New York.

Esterly, S. and Gelman, R. (2014) *2013 Renewable Energy Data Book*, Haas, K. (ed.). DOE/GO-102014-4491. http://www.nrel.gov/docs/fy15osti/62580.pdf (accessed October 20, 2016).

Matek, B. (2014) *2014 Annual U.S. & Global Geothermal Power Production Report*. Geothermal Energy Association. http://geo-energy.org/events/2014%20Annual%20US%20&%20Global%20Geothermal%20Power%20Production%20Report%20Final.pdf (accessed October 25, 2016).

Geothermal Technologies Program (2008) *An Evaluation of Enhanced Geothermal Systems Technology*. US Department of Energy. https://www1.eere.energy.gov/geothermal/pdfs/evaluation_egs_tech_2008.pdf (accessed October 25, 2016).

Green, B.D. and Nix, R.G. (2006) *Geothermal – The Energy Under Our Feet: Geothermal Resource Estimates for the United States*. NREL/TP-840-40665. NREL, Golden, CO.

Gupta, H. and Roy, H. (2007) *Geothermal Energy: An Alternative Resource for the 21st Century*. Elsevier, Amsterdam.

Huang, H.-H., Lin, F.-C., Schmandt, B., *et al*. (2015) The Yellowstone magmatic system from the mantle plume to the upper crust, *Science*, **348** (6236): 773–776.

Kruger, P. (1976) Geothermal energy. *Annual Review of Energy*, **1**: 159–180.

Kutscher, C.F. (2000) *The Status and Future of Geothermal Electric Power*. NREL/CP-550-28204. NREL, Golden, CO.

Lund, J.W., Bloomquist, R.G., Boyd, T.L., and Renner, J. (2005) The United States of America country update. In Proceedings of the World Geothermal Congress, 2005, Anatalya, Turkey.

Mock, J.E., Tester, J.W., and Wright, P.M. (1997) Geothermal energy from the Earth: its potential impact as an environmentally sustainable resource. *Annual Review of Energy and the Environment*, **22**: 305–356.

Palmer, D.A., Fernandez-Prini, R., and Harvey, A.H. (eds), (2004) *Aqueous Systems at Elevated Temperatures and Pressures*. Elsevier, Amsterdam.

Rafferty, K. (2001) *An Information Survival Kit for the Prospective Geothermal Heat Pump Owner*. Geo-Heat Institute, Kalmath Falls, OR.

Smil, V. (2003) *Energy at the Crossroads: Global Perspectives and Uncertainties*. MIT Press, Boston, MA.

Tester, J.W., Drake, E.M., Driscoll, M.J., *et al*. (2012) *Sustainable Energy*, 2nd edn. MIT Press, Cambridge, MA.

USGS (2008) Assessment of Moderate- and High-Temperature Geothermal Resources of the United States. USGS Fact Sheet 2008–3082. US Geological Survey, Reston, VA. http://pubs.usgs.gov/fs/2008/3082/pdf/fs2008-3082.pdf (accessed October 25, 2016).

Further Reading

The following web sites contain information on geothermal topics.
http://energy.gov/search/site/ground%20source%20heat%20pumps
www.energyquest.ca.gov
http://www.oit.edu/orec/geo-heat-center
www.geothermal.org
www.geo-energy.org
www.geokiss.com
http://www.smu.edu/dedman/academics/programs/geothermallab

14

Ocean Energy

14.1 Introduction

The oceans house an enormous amount of thermal and mechanical energy. The thermal energy comes from the mass and temperature of the oceans, and the mechanical energy from the waves and tidal actions of the oceans. The oceans can be viewed as a very large solar thermal collector. The solar irradiation is incident on the surface, where the solar energy is absorbed and the surface layer of the water heated. Over the years a number of proposals have been made for harvesting energy resulting from the temperature difference between the solar-heated surface and the deep ocean water – a general concept called ocean thermal energy conversion (OTEC). The actions of waves, currents, and tides have long been of interest, and various systems have been proposed, built, and/or operated to harvest wave, current, and tidal energy. Tidal energy is often separated into energy harvested by the tidal inflow–outflow from a captured volume via a turbine and energy harvested by utilizing the kinetic energy of waves and currents. The latter is referred to as marine and hydrokinetic (MHK) technology. This chapter will explore OTEC, tidal, and MHK concepts for ocean energy capture.

14.2 Ocean Thermal Energy Conversion

The solar irradiation incident on the surface of the oceans heats the layer of water near the surface, but deep ocean convective currents transport cooler water to the lower depths of the equatorial regions. On a typical day, the energy equivalent of 250 billion barrels of oil (http://www1.eere.energy.gov/education/pdfs/ocean_power.pdf) is absorbed! The net result is temperature stratification with hot surface water and cooler water at depths greater than about 1 km. Surface temperatures can be in excess of 27 °C, and the temperature at depths greater than 1 km can be as low as 4 °C. Thus, between the surface and the deep water, a temperature difference of 23 °C or more can exist. If the surface is viewed as a hot reservoir and the deep water a cold reservoir, then a heat engine can extract useful work. OTEC systems exploit this temperature difference to produce useful work. Depending on the OTEC system configuration, other useful products and processes may also result. Avery and Berl (1997) and Avery and Wu (1994) provide additional discussion of OTEC energy harvesting.

As shown, the temperature difference is an important metric in determining the feasibility of an OTEC system. Generally, OTEC systems are deemed economically feasible if the surface-to-depth temperature difference is greater than 20 °C. Figure 14.1 illustrates the distribution of surface-to-depth (1 km) temperature differences in the oceans. The western equatorial Pacific Ocean region contains a large area with temperature differences in excess of 24 °C. Much of the ocean between ±20° latitude and the equator possess surface-to-depth temperature differences

Alternative Energy Systems and Applications, Second Edition. B. K. Hodge.

Companion website: www.wiley.com\go\Hodge\AESystemsandApplications2E

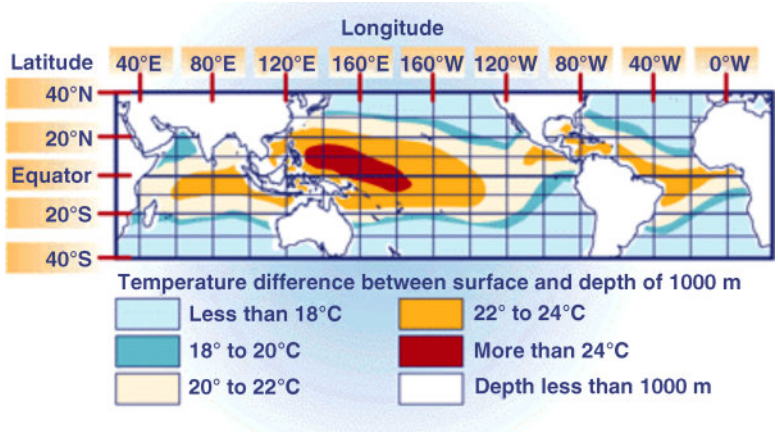

Figure 14.1 Temperature difference distribution between the surface and 1 km depth. *Source*: US Department of Energy.

of 20–24 °C. However, much of the OTEC-applicable areas are in mid ocean and/or are far removed from both population centers and high energy-consumption locations. Thermodynamic considerations, examined next, also place limits on the feasibility of OTEC systems.

Since an OTEC system is essentially a heat engine, the Carnot efficiency represents an upper bound on the thermal efficiency. Consider the thermal efficiency of an OTEC system operating with a surface temperature of 27 °C and a temperature difference of 20 °C. The Carnot efficiency can be computed as

$$\eta_{\text{Carnot}} = \frac{T_{\text{H}} - T_{\text{cold}}}{T_{\text{hot}}} = \frac{\Delta T}{T_{\text{hot}}} = \frac{20\ \text{K}}{(27 + 273)\ \text{K}} = 0.067 \tag{14.1}$$

Hence, the maximum possible efficiency is only 6.7%. In reality, the efficiency projected or obtained for most OTEC facilities is around 3%. The implications of such a low efficiency are at least twofold: (1) high flow rates and large components are required for significant power extraction, and (2) OTEC economics are very sensitive to irreversibilities and losses in components. OTEC systems with high flow rates and large component sizes lead to very large capital expenditures for construction and operation. If losses are underestimated, an OTEC system may be subject to deficit economics or may require more energy to operate than is extracted. These realities have, to a large extent, limited OTEC research and the availability of funds for construction and operation of OTEC systems. However, as energy costs escalate and energy availability becomes an increasing political issue, OTEC will represent a more attractive opportunity. OTEC configurations are generally classed as open-flow or closed-flow systems. Each will be examined in turn.

14.2.1 Open Ocean Thermal Energy Conversion Systems

Open OTEC systems operate using the Claude cycle. An open OTEC system is illustrated in Figure 14.2. Warm water from the surface (state 1) is admitted to a low-pressure evaporator. A vacuum pump maintains the low pressure in the evaporator, where the warm surface water is flashed into a low-quality mixture. The warm liquid is discharged, and the vapor is directed to the turbine. Energy is extracted in the turbine, and the resulting liquid–vapor mixture is discharged at state 3. In the direct-contact condenser, cold water at state 5 is used to condense the mixture from the turbine. State 4 is the state at the condenser exit. Because of the low quality

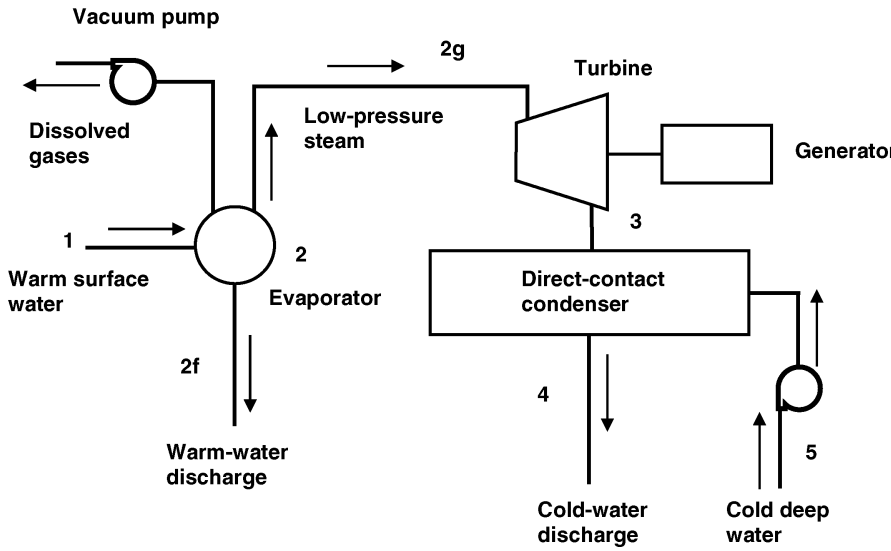

Figure 14.2 Open (Claude Cycle) OTEC system configuration.

of the mixture in the evaporator, most of the most of the warm surface water entering the evaporator is discharged.

The *T*–*s* diagram corresponding to the schematic of Figure 14.2 is presented in Figure 14.3. The warm water enters the evaporator at state 1 and is flashed to state 2 with 2f the liquid state and 2g the vapor state. The warm liquid is discharged, and the vapor (quality equals 1) enters the turbine at 2g and exits at state 3 as a mixture. State 3s represents the exit state if the turbine process were isentropic. Cold water at state 5 is used in the direct-contact condenser. The condenser water exits at state 4. Because the quality at state 2 is low and the quality at state 3 is near unity, the mass flow rate through the turbine differs significantly from the warm-water discharge and the cold-water intake. Example 14.1 examines an open OTEC system performance metrics.

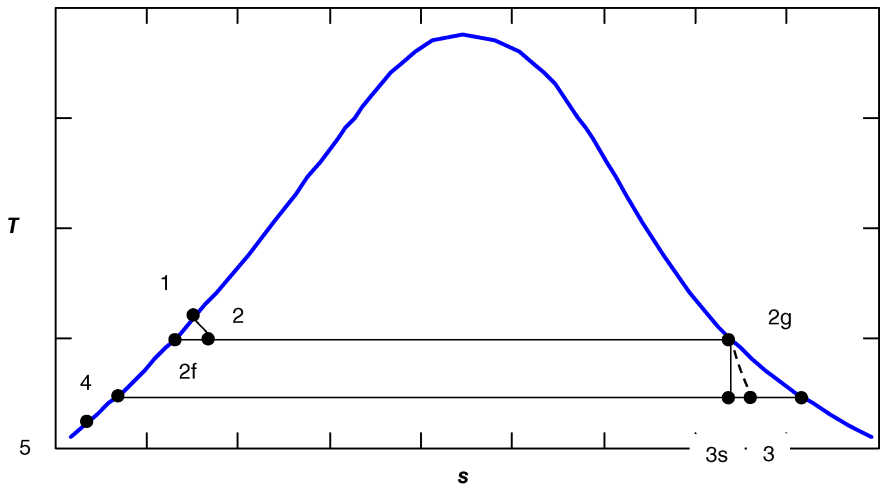

Figure 14.3 *T*–*s* diagram for open-cycle OTEC system.

Example 14.1
An open-cycle OTEC system operates with warm surface water at 27 °C and surface condenser water of 13 °C from the deep cold water at 11 °C. The evaporator pressure is 0.0317 bar, which corresponds to a saturation temperature of 25 °C; the condenser pressure and temperature are 0.017 bar and 15 °C respectively. The turbine efficiency is 0.80. If the turbine is to extract 100 kW, determine the system efficiency and the warm water, cold water, and turbine mass flow rates.

Solution Properties for this example were computed using the IAPWS Industrial Formulation 1997 for the thermodynamic properties of water and steam (Palmer *et al.*, 2004). At 27 °C, the warm surface water possesses an enthalpy of

$$h_1 = 113.19\ \frac{\text{kJ}}{\text{kg}}$$

The process from states 1 to 2 is constant enthalpy, so that

$$h_1 = h_2 = 113.19\ \frac{\text{kJ}}{\text{kg}}$$

As illustrated in Figure 14.3, a constant enthalpy process from states 1 to 2 results in a mixture of liquid and vapor. At 25 °C

$$h_\text{f} = 104.83\ \frac{\text{kJ}}{\text{kg}}, \qquad h_\text{fg} = 2441.9\ \frac{\text{kJ}}{\text{kg}}, \qquad h_\text{g} = 2546.72\ \frac{\text{kJ}}{\text{kg}}, \qquad s_\text{g} = 8.5573\ \frac{\text{kJ}}{\text{kg K}}$$

The quality at state 2 can be found as

$$h_2 = 113.19\frac{\text{kJ}}{\text{kg}} = 104.83\frac{\text{kJ}}{\text{kg}} + x_2 \times 2441.9\frac{\text{kJ}}{\text{kg}}$$

$$x_2 = 0.003\,424$$

Since only vapor ($x = 1$) enters the turbine, $h_{3\text{g}} = 2546.72$ kJ/kg and $s_{3\text{g}} = 8.5573$ kJ/(kg K). At the turbine exit, $T_4 = 15$ °C, and the remaining properties of interest are

$$s_\text{f} = 0.2245\frac{\text{kJ}}{\text{kg K}}, \qquad s_\text{fg} = 8.5565\frac{\text{kJ}}{\text{kg K}}, \qquad h_\text{f} = 62.98\frac{\text{kJ}}{\text{kg}}, \qquad h_\text{fg} = 2465.6\frac{\text{kJ}}{\text{kg}}$$

The isentropic process, 2g–3s, has $s_2 = s_{3\text{s}} = 8.5573$ kJ/(kg K), so that the quality at state 3s becomes

$$s_{3\text{s}} = 8.5573\frac{\text{kJ}}{\text{kg K}} = 0.22454\frac{\text{kJ}}{\text{kg K}} + x \times 8.5565\frac{\text{kJ}}{\text{kg K}}$$

$$x = 0.974$$

and the enthalpy at state 3s is

$$h_{3\text{s}} = 62.98\frac{\text{kJ}}{\text{kg}} + 0.974 \times 2465.6\frac{\text{kJ}}{\text{kg}} = 2464\frac{\text{kJ}}{\text{kg}}$$

The ideal (isentropic) work extracted can be calculated as

$$W_{\text{ideal}} = h_{2g} - h_{3s} = 2546.72\frac{\text{kJ}}{\text{kg}} - 2464\frac{\text{kJ}}{\text{kg}} = 82.6\frac{\text{kJ}}{\text{kg}}$$

and the actual work is

$$W_{\text{act}} = \eta_e W_{\text{ideal}} = 0.80 \times 82.6\frac{\text{kJ}}{\text{kg}} = 66.08\frac{\text{kJ}}{\text{kg}}$$

The enthalpy at state 3 is thus

$$h_3 = h_{2g} - W_{\text{act}} = 2546.72\frac{\text{kJ}}{\text{kg}} - 66.08\frac{\text{kJ}}{\text{kg}} = 2481\frac{\text{kJ}}{\text{kg}}$$

The turbine mass flow rate required to extract 100 kW from the turbine is

$$\dot{m}_{\text{turbine}} = \frac{100\,\text{kW}}{W_{\text{act}}} = \frac{100\,\text{kW}}{66.08\,\text{kJ/kg}} = 1.513\frac{\text{kg}}{\text{s}}$$

The thermal efficiency of the system is the energy produced per kilogram of turbine flow divided by the enthalpy difference between the steam entering the system and exiting the condenser:

$$\eta_{\text{thermal}} = \frac{W_{\text{act}}}{h_3 - h_4} = \frac{W_{\text{act}}}{h_3 - h_{3f}} = \frac{66.08\,\text{kJ/kg}}{2481\,\text{kJ/kg} - 62.98\,\text{kJ/kg}} = 0.027$$

The warm water flow rate required is the turbine mass flow rate divided by the quality at state 2:

$$\dot{m}_{\text{warm water}} = \frac{\dot{m}_{\text{turbine}}}{x_2} = \frac{1.513}{0.003\,424}\ \frac{\text{kg}}{\text{s}} = 442.03\frac{\text{kg}}{\text{s}}$$

In the direct-contact condenser, cold water at state 5 (13 °C) is used to condense the vapor at state 3. At state 5, the enthalpy is $h_5 = 54.60$ kJ/kg. An energy balance yields

$$\dot{m}_{\text{turbine}}(h_3 - h_4) = \dot{m}_{\text{cold water}}(h_4 - h_5)$$

The cold water mass flow rate then becomes

$$\dot{m}_{\text{cold water}} = \dot{m}_{\text{turbine}}\frac{h_3 - h_4}{h_4 - h_5} = 1.513\frac{\text{kg}}{\text{s}}\frac{2481\,\text{kJ/kg} - 62.98\,\text{kJ/kg}}{62.98\,\text{kJ/kg} - 54.60\,\text{kJ/kg}} = 436.596\frac{\text{kg}}{\text{s}}$$

The low quality in the evaporator results in a large warm water flow rate compared with the turbine mass flow rate, and the quality near unity at the turbine exit results in a high cold water flow rate.

The efficiency and flow rates represented in Example 14.1 are realistic for OTEC systems and explain, in part, the thermodynamic difficulties of open OTEC systems. The high specific volume of the turbine working fluid, 43.40 m^3/kg for Example 14.1, is startlingly different from that of modern steam power plants at 0.021 m^3/kg. Thus, the mature technology of steam turbines is not generally applicable to open-cycle OTEC turbines. El-Wakil (1984) discusses turbine requirements and difficulties for application in open-cycle OTEC systems. In a 1979 Westinghouse study (http://arc.aiaa.org/doi/abs/10.2514/6.1981-2595), a turbine 43.6 m in diameter operating at 200 rpm was proposed for a 100 MW OTEC system.

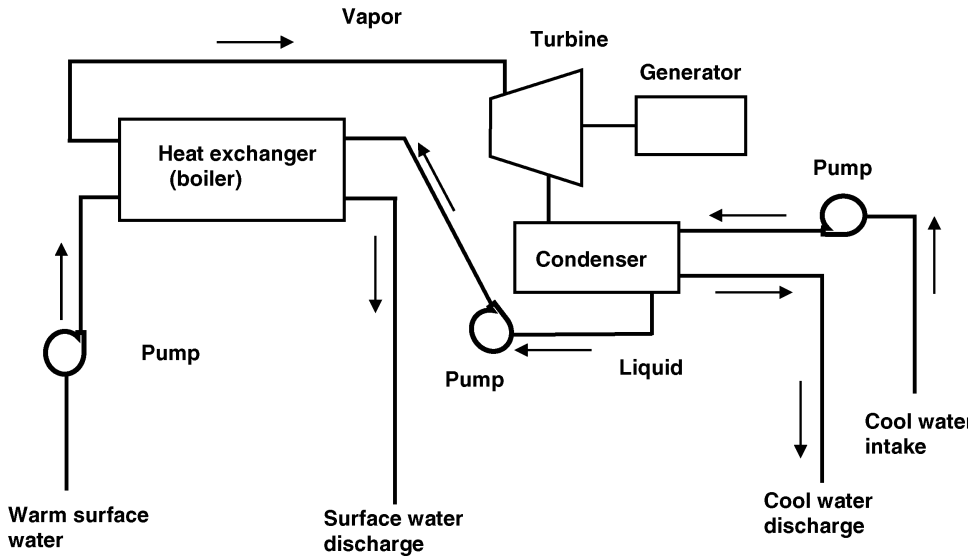

Figure 14.4 Closed (Anderson cycle) OTEC system configuration.

14.2.2 Closed Ocean Thermal Energy Conversion Systems

One way to avoid turbine issues in OTEC systems is to use a binary system with a working fluid other than water. Closed-cycle OTEC (Anderson cycle) systems using working fluids such as ammonia and propane have been proposed. Figure 14.4 presents a schematic of a closed-cycle binary OTEC system. The warm surface water provides the energy to vaporize the working fluid that is directed to the turbine. After exiting the turbine, the cold water is used to condense the working fluid.

Example 14.2

A closed-cycle OTEC system uses propane as the working fluid. The warm surface water enters and leaves the evaporator at 28 °C and 25 °C respectively. The cold water enters and leaves the condenser at 5 °C and 8 °C respectively. The propane evaporating temperature is 22 °C, and the condensing temperature is 11 °C. The plant output is 125 MW, and the turbine efficiency is 0.90. The overall heat transfer coefficient for both the evaporator and the condenser is 1400 W/(m^2 K). Determine the propane flow rate, the evaporator and condenser surface areas, the warm- and cold-water mass flow rates, and the overall thermal efficiency.

Solution Propane properties were obtained from Perry and Chilton (1973). The evaporator operates at 22 °C, and the condenser operates at 11 °C. Table 14.1 shows the saturation properties at these temperatures.

Table 14.1 Propane properties at 22 °C and 11 °C.

T (°C)	P (kPa)	h_f (kJ/kg)	h_{fg} (kJ/kg)	h_g (kJ/kg)	s_f (kJ/kg K)	s_{fg} (kJ/kg K)	s_g (kJ/kg K)
11	649.9	546.2	361.7	907.9	4.359	1.273	5.633
22	877.4	573.8	344.4	918.2	4.456	1.165	5.621

In the evaporator the warm fluid vaporizes the propane to a saturated vapor at 22 °C. The vapor enters the turbine at 22 °C with $h_g = 918.2\,\text{kJ/kg}$ and $s_g = 5.621\,\text{kJ/(kg K)}$. At the turbine exit, the propane temperature is 11 °C, and for an isentropic expansion through the turbine the entropy of the liquid–vapor mixture at the exit would be 5.621 kJ/(kg K). The quality at the turbine exit for an isentropic expansion becomes

$$s_{\text{turbine exit}} = 5.621\frac{\text{kJ}}{\text{kg K}} = 4.359\frac{\text{kJ}}{\text{kg K}} + x \times 1.273\frac{\text{kJ}}{\text{kg K}}$$
$$x = 0.991$$

and the enthalpy for the isentropic expansion is

$$h_{\text{isentropic}} = 546.2\frac{\text{kJ}}{\text{kg}} + 0.991 \times 361.7\frac{\text{kJ}}{\text{kg}} = 904.5\frac{\text{kJ}}{\text{kg}}$$

The ideal (isentropic) work extracted is the change in enthalpy across the turbine:

$$W_{\text{ideal}} = h_{\text{entrance}} - h_{\text{exit}} = 918.2\frac{\text{kJ}}{\text{kg}} - 904.5\frac{\text{kJ}}{\text{kg}} = 13.7\frac{\text{kJ}}{\text{kg}}$$

and the actual work is

$$W_{\text{act}} = \eta_{\text{turbine}} W_{\text{ideal}} = 0.9 \times 13.7\frac{\text{kJ}}{\text{kg}} = 12.31\frac{\text{kJ}}{\text{kg}}$$

The enthalpy at the exit of the turbine is thus

$$h_{\text{exit}} = h_{\text{entrance}} - W_{\text{act}} = 918.2\frac{\text{kJ}}{\text{kg}} - 12.31\frac{\text{kJ}}{\text{kg}} = 905.9\frac{\text{kJ}}{\text{kg}}$$

The propane mass flow rate can be calculated as

$$\dot{m}_{\text{propane}} = \frac{\text{Power}_{\text{extracted}}}{W_{\text{act}}} = \frac{125\,\text{MW}}{12.31\,\text{kJ/kg}} = 10150\frac{\text{kg}}{\text{s}}$$

Propane enters the evaporator as a saturated liquid at 11 °C and exits the evaporator as a saturated vapor at 22 °C. The energy required is thus

$$\dot{Q}_{\text{evap}} = \dot{m}_{\text{propane}}\left\{h[(22°\text{C})_g - h(11°\text{C})_f]\right\}$$
$$= 10150\frac{\text{kg}}{\text{s}} \times \left(918.2\frac{\text{kJ}}{\text{kg}} - 546.2\frac{\text{kJ}}{\text{kg}}\right) = 3.78 \times 10^6\,\text{kW}$$

Since most of the energy transfer is required for the phase change, which occurs at 22 °C, the log mean temperature difference (LMTD) for the evaporator becomes

$$\text{LMTD}_{\text{evap}} = \frac{\Delta T_2 - \Delta T_1}{\ln(\Delta T_2/\Delta T_1)}$$
$$= \frac{(28°\text{C} - 22°\text{C}) - (25°\text{C} - 22°\text{C})}{\ln\left(\frac{28°\text{C} - 22°\text{C}}{25°\text{C} - 22°\text{C}}\right)} = \frac{6°\text{C} - 3°\text{C}}{\ln\left(\frac{6°\text{C}}{3°\text{C}}\right)} = 4.33°\text{C}$$

For a heat exchanger:

$$\dot{Q}_{\text{evap}} = UA_{\text{evap}} \times \text{LMTD}_{\text{evap}}$$

from which the evaporator surface area can be computed as

$$A_{\text{evap}} = \frac{\dot{Q}_{\text{evap}}}{U \times \text{LMTD}_{\text{evap}}}$$
$$= \frac{3.78 \times 10^6 \text{ kW}}{1400 \text{ W/(m}^2\text{°C)} \times 4.33\text{°C}} = 6.234 \times 10^5 \text{ m}^2$$

The saturated liquid water enthalpies for 28 °C and 25 °C are 117.35 kJ/kg and 104.81 kJ/kg respectively. An energy balance then yields the warm water mass flow rate:

$$\dot{m}_{\text{warm water}} = \frac{\dot{Q}_{\text{evap}}}{h(28\text{°C})_{\text{f}} - h(25\text{°C})_{\text{f}}}$$
$$= \frac{3.78 \times 10^6 \text{ kW}}{117.35 \text{ kJ/kg} - 104.81 \text{ kJ/kg}} = 3.01 \times 10^5 \frac{\text{kg}}{\text{s}}$$

Propane enters the condenser as a mixture at 11 °C and exits the condenser as a saturated liquid at 11 °C. The energy required to condense the vapor is thus

$$\dot{Q}_{\text{cond}} = \dot{m}_{\text{propane}}[h_{\text{exit}} - h(11\text{°C})]$$
$$= 10150 \frac{\text{kg}}{\text{s}} \left(905.9 \frac{\text{kJ}}{\text{kg}} - 546.2 \frac{\text{kJ}}{\text{kg}}\right) = 3.65 \times 10^6 \text{ kW}$$

The LMTD for the condenser becomes

$$\text{LMTD}_{\text{cond}} = \frac{\Delta T_2 - \Delta T_1}{\ln(\Delta T_2 / \Delta T_1)}$$
$$= \frac{(11\text{°C} - 5\text{°C}) - (11\text{°C} - 8\text{°C})}{\ln\left(\frac{11\text{°C} - 5\text{°C}}{11\text{°C} - 8\text{°C}}\right)} = \frac{6\text{°C} - 3\text{°C}}{\ln\left(\frac{6\text{°C}}{3\text{°C}}\right)} = 4.33\text{°C}$$

For the condenser:

$$\dot{Q}_{\text{cond}} = UA_{\text{cond}} \times \text{LMTD}_{\text{cond}}$$

from which the condenser surface area can be computed as

$$A_{\text{cond}} = \frac{\dot{Q}_{\text{cond}}}{U \times \text{LMTD}_{\text{cond}}}$$
$$= \frac{3.65 \times 10^6 \text{ kW}}{1400 \text{ W/(m}^2 \text{ °C)} \times 4.33\text{°C}} = 6.03 \times 10^5 \text{ m}^2$$

The saturated liquid water enthalpies for 8 °C and 5 °C are 21.05 kJ/kg and 33.55 kJ/kg respectively. An energy balance then yields the cold-water mass flow rate:

$$\dot{m}_{\text{cold water}} = \frac{\dot{Q}_{\text{cond}}}{h(8\text{°C})_{\text{f}} - h(5\text{°C})_{\text{f}}}$$
$$= \frac{3.65 \times 10^6 \text{ kW}}{33.55 \text{ kJ/kg} - 21.05 \text{ kJ/kg}} = 2.92 \times 10^5 \frac{\text{kg}}{\text{s}}$$

The thermal efficiency is the turbine power output divided by the energy transferred in the evaporator:

$$\eta_{\text{thermal}} = \frac{\text{Power}_{\text{out}}}{\dot{Q}_{\text{evap}}} = \frac{125\ \text{MW}}{3.78 \times 10^6\ \text{kW}} = 0.033$$

As would be expected because of the small temperature differences involved in this closed-cycle OTEC system, the thermal efficiency is low. The thermodynamic disadvantages of small temperature differences in heat engines are real for both OTEC configurations. Although the closed-cycle does not have the turbine availability (or suitability) problem of the open-cycle OTEC system, the closed-cycle system requires very large heat exchangers. The surface areas required for both evaporator and condenser are in excess of 600 000 m^2!

14.2.3 Hybrid Ocean Thermal Energy Conversion Systems

A hybrid OTEC system possesses features of both the open-cycle and closed-cycle OTEC arrangements. In a hybrid OTEC system, the warm surface water is flashed into steam in a process similar to the open-cycle OTEC configuration. The steam is then used to vaporize the working fluid, typically ammonia, in a closed loop containing a turbine. Desalinated water is provided by condensing the steam.

14.2.4 Ocean Thermal Energy Conversion System Outputs

In addition to the generation of electricity, OTEC systems can provide useful outputs, such as:

1) *Desalinated water.* The condensation of steam as in proposed hybrid OTEC systems can provide potable water.
2) *Nutrients for mariculture applications.* The cold-water stream for an OTEC system contains abundant nutrients (and is relatively free of pathogens) that can be used in commercial mariculture applications.
3) *Air conditioning for buildings and moderate-temperature refrigeration.* The cold water stream (5 °C or 41 °F) can be used in conjunction with heat exchangers to provide conditioned air for cooling or chilled water for moderate-temperature refrigeration applications.
4) *Mineral extraction.* Since OTEC systems possess large flow rate, the extraction of minerals dissolved in the ocean water has been proposed as an additional OTEC application.

14.2.5 Ocean Thermal Energy Conversion Assessment

Examples 14.1 and 14.2 demonstrate the size/efficiency problems associated with OTEC systems. Indeed, except for a few pilot plants, no commercial OTEC facility has been built and operated. To date the biggest success has been the pilot plant in Hawaii that operated from 1993 to 1998 (Vega, 2002). The facility produced a net power of 103 kW with 255 kW of gross power extracted. The warm surface water was 26 °C, and the cold deep water was 6 °C. Vega (2002) provides a contemporary assessment of OTEC and makes several suggestions for future OTEC development.

Since the 1970s, a number of large OTEC systems have been proposed and a few have reached the detailed engineering stage. Most of these systems are quite large and are to be moored in deep ocean waters. Figure 14.5, a concept sketch of how a large OTEC facility might appear, was a TRW design reported in 1976 and appears in Kayton (1981). An interesting feature of the TRW design is that the expelled sea water is used to provide a thrust in a dynamic positioning strategy that helps the facility to hold station (position and alignment). Additional representations of 1970s-era OTEC concepts are presented by Rudiger and Smith (1977), Baker (2006), and Takahashi (2000).

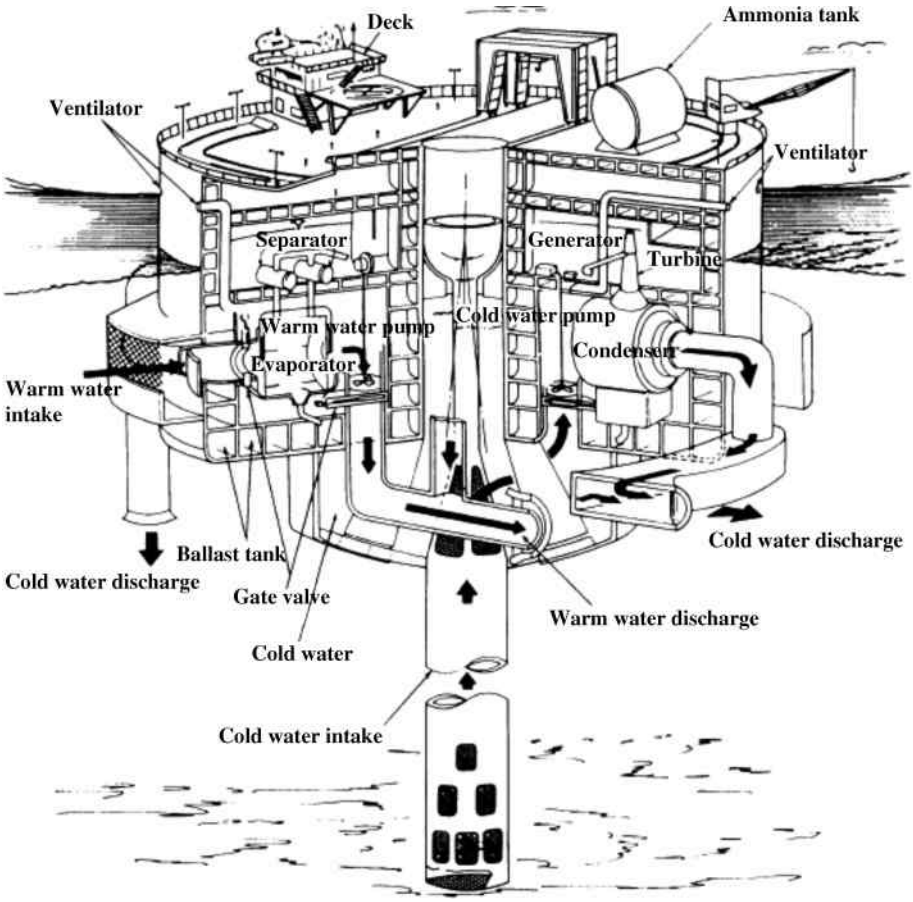

Figure 14.5 TRW proposed OTEC facility. *Source*: Kayton (1981).

For a number of years, the US Department of Energy (USDOE) did not support significant OTEC research, but in recent years that has changed and the USDOE has renewed their support of OTEC. The USDOE web site for OTEC is http://energy.gov/eere/energybasics/articles/ocean-energy-technology-basics. In conjunction with the National Oceanic and Atmospheric Administration, the University of New Hampshire in 2009 hosted a workshop devoted to assessing the technical readiness of OTEC technologies required for commercialization (Coastal Response Research Center, 2010). The workshop explicitly addressed (1) platforms, (2) mooring, (3) interface, (4) heat exchangers, (5) turbines, (6) cable, and (7) pipe. Teams composed of technical experts were charged with determining required technological advances needed for OTEC implementation.

Areas especially suited for initial OTEC system applications include the small island nations in the south Pacific Ocean, American territories (such as Guam) in the Pacific, and the state of Hawaii. All of these locations use diesel-powered generators for electricity and have water potability issues.

OTEC plant ships have been proposed (e.g., Vega, 2002). These ocean-going ships would contain OTEC systems and would move slowly in OTEC-favorable regions to harvest energy and minerals. The electric power from the harvested energy would be used in on-board manufacturing and fuel (such as hydrogen) production. Figure 14.6, from Vega (2002), presents the layout of a proposed pilot facility with a 5 MW electrical output.

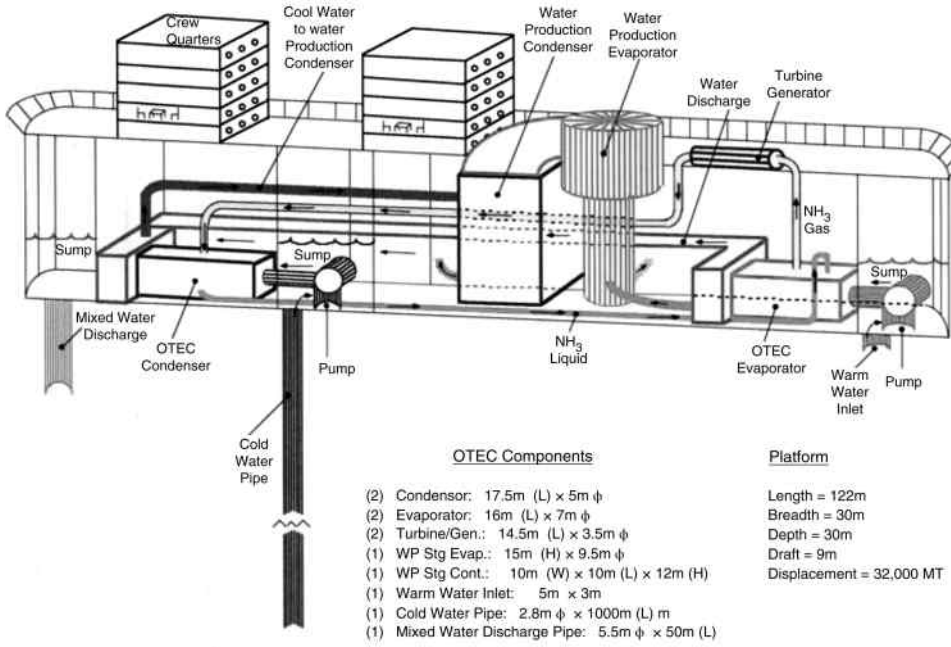

Figure 14.6 Proposed 5 MW OTEC plant-ship layout. *Source*: Vega (2002).

A comprehensive assessment of OTEC worldwide electric generation potential was funded by the USDOE, conducted by Lockheed Martin, and published in 2012. The Ocean Thermal Extractable Energy Visualization (OTEEV) project (Ascari *et al.*, 2012) focused on the maximum practicably extractable energy (MPEE) from ocean thermal resources. They defined MPEE as being sustainable and technically feasible, using state-of-the-art ocean energy technology. The analysis used detailed ocean and climatological data and a validated nominal 100 MW OTEC system to estimate the MPEE. The OTEC system used was a conventional single-stage closed cycle, much like the cycle in Example 14.2, except that ammonia was used as the working fluid. The report presents a detailed explanation of the methodology used as well as extensive presentations of results. Within the Exclusive Economic Zones of US interest, the estimated annual average OTEC net power was 529 GW with an estimated generation of 4636 TW h/year. The average annual net power is the mean of the summer and winter values. The next nine countries have a combined average annual capacity of 1019 GW with 8923 TW h/year of electricity generation. The total global estimate is 55 000 TW h/year! Hence, in terms of capacity and energy, the global potential for OTEC is quite large. Economics were not considered in the study, only the MPEE.

To obtain the capacity referenced in the previous paragraph, Ascari *et al.* (2012) developed a model to permit ocean thermal resources to be used to estimate the electrical generating capacity. They devised, using data from existing OTEC test facilities and pilot plants, a model for a nominal 100 MW OTEC facility. The model development and validation are explained in detail in the report. However, we will use the model to determine and understand the relationship between the temperature difference (surface to depth), the depth for the deep temperature, and the power output – thus permitting parametric studies to be made. The model baseline conditions are in Table 14.2.

The OTEEV study expressed the net power output as the difference between the gross energy extracted and the fixed and variable losses:

$$\text{Power}_{\text{net}} = \text{Power}_{\text{gross}} - \text{Loss}_{\text{fixed}} - \text{Loss}_{\text{variable}} \tag{14.2}$$

Table 14.2 The 100 MW OTEEV OTEC system baseline values.

Surface (warm) water temperature T_S (°C)	25.7
Warm water flow rate (kg/s)	460 000
Deep (cold) water temperature T_D (°C)	4.1
Cold water flow rate (kg/s)	366 000
Cold water pipe depth d (m)	1000
Ammonia mass flow rate (kg/s)	4060
Turbine efficiency (%)	86
Ammonia pump efficiency (%)	75
Seawater pump efficiency (%)	80
Generator efficiency (%)	97.5
Evaporator UA (MW/°C)	1410
Condenser UA (MW/°C)	1350

The $\text{Power}_{\text{gross}}$ relationship was developed using the values in Table 14.2 and is

$$\text{Power}_{\text{gross}} = 13.89\Delta T - 149.71 \tag{14.3}$$

where the $\text{Power}_{\text{gross}}$ is in megawatts and ΔT is the temperature difference in Celsius. The fixed loss $\text{Loss}_{\text{fixed}}$ is composed of the cold water intake power loss, condenser and distribution pumping loss, evaporator and distribution pumping loss, and ammonia pumping loss and is 42.7 MW. The variable loss $\text{Loss}_{\text{variable}}$ is the sum of pipe friction and static head losses and is a function of the pipe depth, the temperature difference, and the surface temperature. The $\text{Loss}_{\text{variable}}$ is developed in detail in the OTEEV report and has the form

$$\begin{aligned}\text{Loss}_{\text{variable}} = {} & 0.0038d + 4.488d(5.234 \times 10^{-10}d^3 - 1.378 \times 10^{-6}d^2 + 1.313 \times 10^{-3}d \\ & - 0.6541)\left[\frac{-0.00599T_S^2 + 0.031T_S + 1025}{-0.00599(T_S - \Delta T)^2 + 0.031(T_S - \Delta T) + 1025} - 1\right]\end{aligned} \tag{14.4}$$

where $\text{Loss}_{\text{variable}}$ is in megawatts, d is the depth in meters, and the temperatures are in Celsius. An example is useful.

Example 14.3
Determine the $\text{Power}_{\text{gross}}$, $\text{Power}_{\text{net}}$, and $\text{Loss}_{\text{variable}}$ for the baseline values of Table 14.2.

Solution Mathcad is used for the solution, with the results displayed in Figure 14.7. The values of T_S, T_D, and the depth d are input. The gross power is computed to be 150.3 MW. To simplify the variable loss calculations, two functions are defined and are used to compute the variable loss value of 2.718 MW. The net power is 104.9 MW. Thus, for the baseline case, the losses (fixed and variable) are 45.4 MW or 30% of the power extracted. The variable losses are nonlinear with length; for example, if the depth in this example were changed to 500 m, the variable losses become 1.924 MW, which corresponds to a reduction of 30% in the variable loss for a 50% change in the depth. An interactive visualization tool is available to view the results of the OTEEV study. Details are available in Ascari *et al.* (2012).

Thus far in this chapter, OTEC has been examined, but ocean energy harvesting from tides and waves is also possible. Sections 14.3 and 14.4 investigate these concepts.

$C := K$ Define °C to be K (for ease of use)

Input values of T_S, T_D, and d

$T_S := 25.7 \cdot C$ $T_D := 4.1 \cdot C$ $\Delta T := T_S - T_D$ $\Delta T = 21.6K$ $d := 1000 \cdot m$

Calculate the gross power extracted

$$Power_{gross} := \left(13.89 \cdot \frac{\Delta T}{C} - 149.71\right) \cdot MW \qquad Power_{gross} = 150.314 \cdot MW$$

Define the fixed loss value

$$Loss_{fixed} := 42.7 \cdot MW$$

Define functions for the variable losses

$$LVT1\left(d, T_S, \Delta T\right) := \frac{-0.00599 T_S^{\,2} + 0.031 \cdot T_S + 1025}{-0.00599\left(T_S - \Delta T\right)^2 + 0.031 \cdot \left(T_S - \Delta T\right) + 1025} - 1$$

$$LVT2(d) := 0.0038 \cdot d + 4.488 \cdot d \cdot \left(5.234 \cdot 10^{-10} \cdot d^3 - 1.378 \cdot 10^{-6} \cdot d^2 + 1.313 \cdot 10^{-3} \cdot d - 0.6541\right)$$

Calculate the variable losses using the defined functions

$$Loss_{variable} := \left(LVT2\left(\frac{d}{m}\right) \cdot LVT1\left(\frac{d}{m}, \frac{T_S}{C}, \frac{\Delta T}{C}\right)\right) \cdot MW \qquad Loss_{variable} = 2.718 \cdot MW$$

Calculate the net power produced

$$Power_{net} := Power_{gross} - Loss_{fixed} - Loss_{variable} \qquad Power_{net} = 104.896 \cdot MW$$

$$TotalLosses := Loss_{fixed} + Loss_{variable} = 45.418MW \qquad \frac{TotalLosses}{Power_{gross}} = 30.216\%$$

Figure 14.7 Solution to Example 14.3 using Mathcad.

14.3 Tidal energy

Tidal energy uses the rise and fall of the tides to indirectly generate electricity. In principle, the harvesting of energy from the tides is similar to hydroelectric power. At high tide a reservoir is charged, and at low tide the reservoir is discharged. In both the charging and discharging process, a turbine can be used to generate electricity, as in other hydroelectric facilities. However, the temporal aspects of the tides add other considerations. The simplest tidal power system is called the ebb generating system and uses a dam, usually called a barrage, across an estuary. Sluice gates open and close to regulate the flow into and out of the reservoir. Two-way tidal energy systems generate electricity with flow into and out of the reservoir, but are more complex and costly than "single-direction" generation since the turbine and supporting structure must be more robust and complex.

The tides are periodic but not constant, since tides are governed by the moon, and to some extent by the sun. Tides are described based on their schedule and range. The range is the elevation difference between high and low tide, and the schedule includes the times of

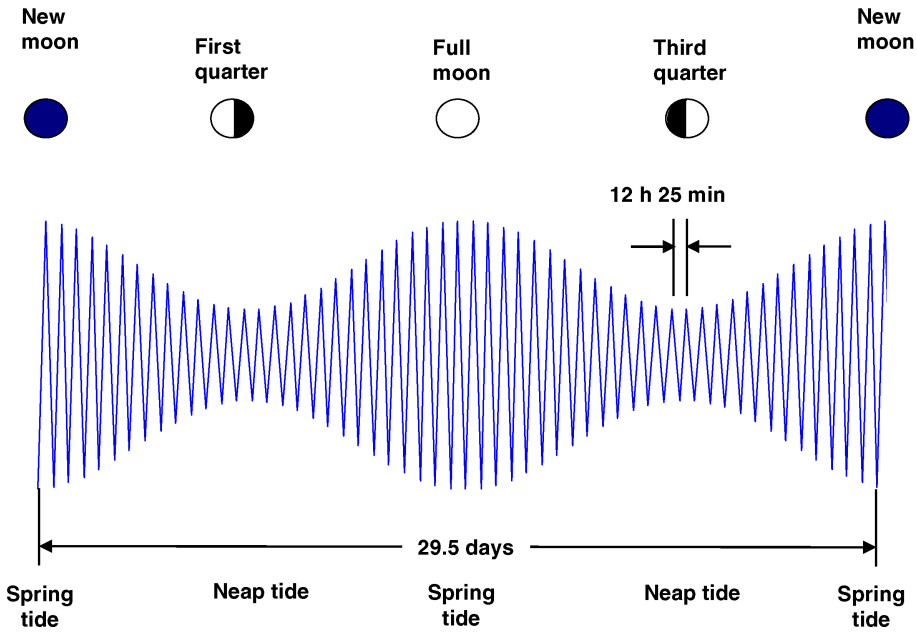

Figure 14.8 Typical monthly tidal ranges.

occurrence of the high and low tides. A "lunar month" is 29.5 days, so that a lunar day is 24 h 50 min. During a lunar day, the tides rise and fall twice– a tidal cycle is thus 12 h 25 min. This means that high and low tides do not occur at the same time every day, but progress 25 min per cycle, or 50 min per lunar day. Moreover, the range is not constant but varies during the lunar month, with the maximum range occurring at the time of the new and full moons and the minimum range occurring at the first and third quarter moons. At a given location, the average ranges are complicated but predictable. The maximum range is called the spring tide, and the minimum range the neap tide. A graphical representation, such as Figure 14.8, is a good way to understand the details of tidal motions. The figure shows the daily tidal cycle, the monthly tidal cycles, the tidal range variations, and the relationship of the phases of the moon with the spring and neap tides.

The observation that the high and low tides occur at different times during different days and that the range varies from day to day (spring to neap to spring tides) means that control strategies to maximize tidal energy benefits (typically power produced) are more involved than strategies for hydroelectric facilities. The consideration of how to distribute the generating time based on the tidal range for a given day impacts the size (output) of the turbine and the system total output. A typical arrangement for a tidal pool to generate power is illustrated in Figure 14.9. The difference in elevation due to the tidal range determines the energy stored in the pool. The energy stored in a differential element of height dh located above the low-level tide is

$$\mathrm{d}W = g\,\mathrm{d}m\,h \tag{14.5}$$

where dm is the mass in differential element and $\mathrm{d}m = \rho A\,\mathrm{d}h$, where A is the horizontal area, so that

$$\mathrm{d}W = g\rho A h\,\mathrm{d}h \tag{14.6}$$

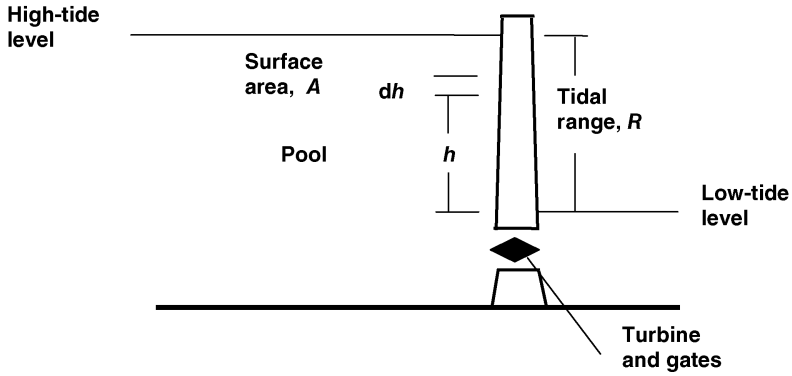

Figure 14.9 Tidal pool schematic.

Then for the tidal pool

$$W = \int_0^R \mathrm{d}W = \int_0^R g\rho A\, h\, \mathrm{d}h \tag{14.7}$$

If the surface area variation with elevation in the tidal pool is small, then A is sensibly constant and

$$W = \frac{1}{2} g\rho A R^2 \tag{14.8}$$

Equation 14.8 demonstrates that the available energy in a tidal pool, referenced to the low-tide datum, is proportional to the surface area and the square of the tidal range. Hence, the tidal range is an important metric in assessing tidal energy potential.

The energy indicated by Equation 14.8 is based on the low-tide datum; hence, the energy is attainable only when discharged to that datum. This observation raises the question of how a tidal energy system might be operated to maximize the usefulness of the energy harvested. Consider the conditions illustrated in Figure 14.9; namely, the tidal pool at its maximum height and the low-tide datum at its minimum. If all the tidal pool were discharged rapidly, then the energy attainable would be the maximum; however, if the pool were gradually discharged, then the low-tide datum would increase and the high-tide elevation would decrease, and the available energy would be decreased. Two protocols are thus associated with tidal discharge strategies: (1) a simple tidal pool, in which the discharge is rapid and the conditions of Equation 14.8 are fulfilled; and (2) the modulated simple tidal pool, in which the flow is varied over time and the energy recovered is reduced from the maximum. Although protocol 2 results in less energy available than protocol 1, protocol 2 has major advantages. Protocol 2 requires smaller turbines and results in a more uniform power level applied to the grid or for local use. Protocol 1 results in large "spikes" of electrical power that occur at high and low tides.

El-Wakil (1984) investigates protocol 2, as illustrated in Figure 14.10, which is adapted from his book. A single tidal cycle with a period of 6.2083 h is indicated. Generation is initiated at time t_1, when the elevation difference between the pool and the tide is sufficient for efficient generation, and is stopped at time t_2, when elevation difference becomes too small for efficient generation. The determination of the times is facility dependent, but to reduce the "spikiness" of the generation, the generation time should be an appreciable portion of the tidal

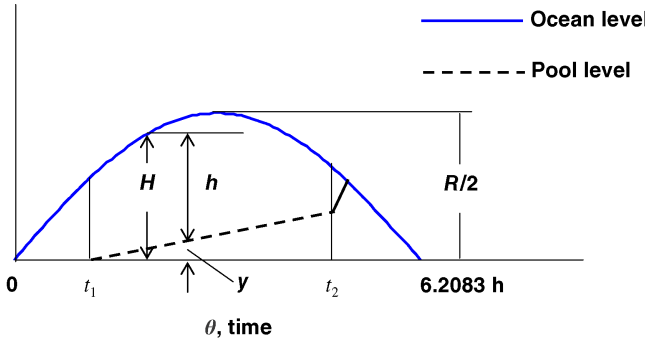

Figure 14.10 Nomenclature for modulated single-pool tidal system.

cycle. During generation, the gates to the pool are controlled in such a fashion that the pool fills linearly with time, as indicated by the dashed line in Figure 14.10. The tide is represented by a sine function:

$$H = \frac{R}{2}\sin\left(\frac{\pi t}{6.2083\,\text{h}}\right) \tag{14.9}$$

and the pool depth as a linear function of time:

$$y = aR(t - t_1) \tag{14.10}$$

where a controls the slope of the tidal pool filling and R is the tidal range. Over a tidal cycle, El-Wakil determined the energy available for harvesting to be

$$W = g\rho AR^2\left\{0.988a\left[\cos\left(\frac{\pi t_1}{6.2083}\right) - \cos\left(\frac{\pi t_2}{6.2083}\right)\right] - \frac{a^2}{2}(t_2^2 - t_1^2)\right\} \tag{14.11}$$

Example 14.4 answers the question of how much protocol 2 reduces the energy.

Example 14.4

Investigate the energy available from protocol 1 and protocol 2 per square kilometer of surface area if the tidal range is 12 m, a is 0.0625 h^{-1}, and energy is harvested between $t_1 = 1$ h and $t_2 = 4$ h. How does a influence the energy harvested?

Solution The nominal density of sea water is 1025 kg/m^3. For protocol 1, Equation 14.8 represents the energy available and has the value

$$W_1 = \frac{1}{2}g\rho AR^2 = \frac{1}{2}\times 9.807\frac{\text{m}}{\text{s}^2}\times 1025\frac{\text{kg}}{\text{m}^3}\times 1\,\text{km}^2\times(12\,\text{m})^2 = 201040\,\text{kW h}$$

Equation 14.11 represents the energy availability with modulated flow, and appears as

$$\begin{aligned} W_2 &= g\rho AR^2\left\{0.988a\left[\cos\left(\frac{\pi t_1}{6.2083}\right) - \cos\left(\frac{\pi t_2}{6.2083}\right)\right] - \frac{a^2}{2}(t_2^2 - t_1^2)\right\} \\ &= 9.807\frac{\text{m}}{\text{s}^2}\times 1025\frac{\text{kg}}{\text{m}^3}\times 1\,\text{km}^2\times(12\,\text{m})^2 \\ &\quad\times\left\{0.988\,\text{h}\times 0.0625\,\text{h}^{-1}\left[\cos\left(\frac{\pi\times 1\,\text{h}}{6.2083\,\text{h}}\right) - \cos\left(\frac{\pi\times 4\,\text{h}}{6.2083\,\text{h}}\right)\right] - \frac{(0.0625\,\text{h}^{-1})^2}{2}\left[(4\,\text{h})^2 - (1\,\text{h})^2\right]\right\} \\ &= 20811\,\text{kW h} \end{aligned}$$

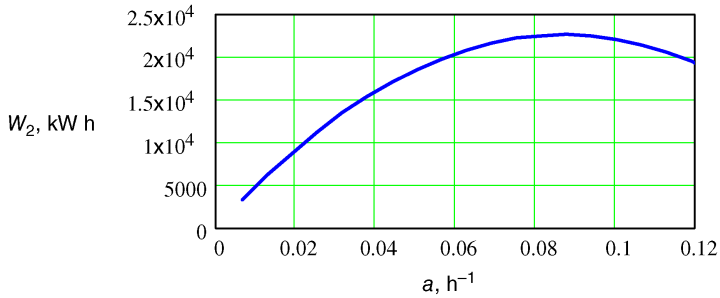

Figure 14.11 Energy availability as a function of a.

Hence, the modulated flow, protocol 2, has the potential to produce only about one-tenth of the energy that protocol 1 can. This is a dramatic decrease in the energy available for harvesting, but energy harvested is spread over a 4 h time period instead of a very brief generating interval, and the turbine size (power output) required is dramatically smaller. The primary control variable in the modulated scenario is the value of a. Hence, a legitimate question is, how does the energy harvest availability depend on a? If the calculation for W_2 is repeated for a range of values of a and the results plotted, Figure 14.11 results. As a is increased for a small value, the energy availability increases, reaches a maximum, and then gradually decreases. The value of a for maximum energy availability is near 0.09 h^{-1}, and the value of $a = 0.0625\ h^{-1}$ prescribed in the problem statement results in nearly as much possible energy recovery.

In Example 14.4 and in Equations 14.8 and 14.11, the energy harvested is just the energy extracted from the flow and not the net energy output of the tidal system. Turbine efficiency as well as losses in the system need to be considered to obtain the net output. El-Wakil (1984) suggests that the overall efficiency may be as small as 30%.

Equations 14.8 and 14.11 have R^2 in the leading term, demonstrating the importance of the tidal range in determining energy harvesting potential for tidal systems. Tidal systems are attractive in regions where the tidal range is high and the coastal geometry permits the development of large-surface-area tidal pools. Gorlov (2001) provides a list of regions with high tidal ranges, from which Table 14.3 is adapted. Locations with large tidal ranges are limited in number, and the total available tidal resources are very limited compared with most of the alternative energy sources considered in this textbook.

Table 14.3 presents a list of locations with large tidal ranges. As of 2015 only five tidal energy systems were operational; however, a number are in the planning/constructions stages.

Table 14.3 Locations with large tidal ranges.

Site	Country	Tidal range R (m)
Bay of Fundy	Canada	16.2
Severn Estuary	UK	15.4
Port of Granville	France	14.0
La Rance	France	13.5
Puerto Rio Gallegos	Argentina	13.3
Bay of Mezen	Russia	10.0
Sea of Okhotsk	Russia	13.4

Table 14.4 Existing tidal energy facilities.

Site	Country	Power (MW)	Basin area (km^2)	Mean tide (m)
Annapolis	Canada	20.0	15.0	6.4
Jiangxia	China	3.9	1.4	5.1
Kislaya Guba	Russia	1.2	1.1	2.3
La Rance	France	240.0	22.0	8.6
Sihwa Lake	South Korea	254.0	30.0	5.6

Table 14.4 contains details of the five operating tidal systems. Only two, La Rance and Sihwa Lake, generate large quantities of electricity and involve appreciable surface areas. Tidal systems under planning/construction include Ganghwa Island (South Kores) with 812 MW and Incheon (South Korea) with 1320 MW.

The La Rance Tidal Power Plant, near Saint-Michel in Brittany (de LaLeu, 2009) is clearly the most outstanding example of such facilities. La Rance became operational in 1967, and it has operated without any major breakdowns and annually generates more than 600×10^6 kW h. The facility has 24 turbines, each producing 10 MW. The dam, the barrage, is 750 m long and 13 m high, and, as indicated in Table 14.4, the pool has an area of 22 km^2. La Rance has operated more than 160 000 h and produced electricity that is economically competitive. Électricité de France has carried out a general overhaul of all the equipment, including installation of three new turbines per year until the originals have all been replaced.

The Sihwa Tidal Power Plant (Schmid, 2005), with an output of 254 MW, is larger than La Rance. The facility utilizes 10 bulb-type turbines, each with an output of 10 MW, and uses the elevation difference between high tide and a reservoir to generate the 260 MW of electricity. Sihwa generates power in one flow direction, from the ocean to the Sihwa Lake, with up to 60 billion tons of seawater being circulated annually.

In addition to large capital costs, tidal energy systems raise significant environmental and ecological questions. Effects on the local area are site specific and difficult to quantify. These effects include aquatic and shoreline ecosystems impacts, silting, and water-quality issues.

14.4 Marine and hydrokinetic energy

The final topic examined in this chapter, in "old" terminology, is wave energy, but is now called marine and hydrokinetic (MHK) energy. The source of the energy is still currents and waves. Ocean waves are caused by wind, which is an indirect effect of uneven solar heating, and by the motion of the Earth. As with other alternative energy resources, the quantity of energy available is enormous, but the techniques for harvesting the energy are still under development. McCormick (2007) and Cruz (2008) are good introductions. Figure 14.12, from Thresher (2014), shows an estimate of tidal current and wave energy and power for the USA. The power available is in megawatts, and the energy harvested is in terawatt-hours per year. The power for Alaska is separated into 47 MW and 437 MW.

Even moderate wave motion possesses an energy density in excess of the incident solar energy density. However, before exploring the energy content of waves, we will consider the usual description of a traveling wave:

$$y = a \sin\left(\frac{2\pi}{\lambda}x - \frac{2\pi}{\tau}t\right) \tag{14.12}$$

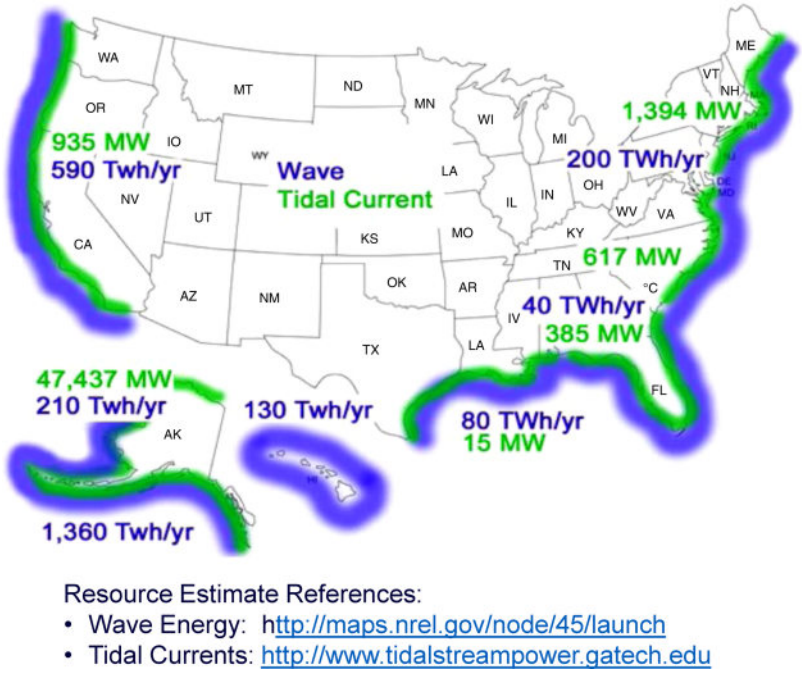

Figure 14.12 Estimated US tidal current and wave energy resources. *Source*: Thresher (2014).

where a is the amplitude, λ is the wavelength, and τ is the period; y is the height above mean sea level, t is the time, and x is the horizontal coordinate. Traveling wave nomenclature is presented in Figure 14.13. The wavelength λ, the distance of a complete cycle in the x direction, and the crest a are illustrated in the figure. Since the wave is periodic, when $t = \tau$ the wave shape is identical to the shape at $t = 0$.

Although the wave motion is in the x direction, with a speed of $c = \lambda/\tau$, the motion of the water is not the same as the motion of the wave. The water rotates in place with an elliptical path in the plane of the wave propagation (El-Wakil, 1984).

The total energy of a wave is the sum of the potential and kinetic energies (El-Wakil, 1984). The potential energy density per unit area is

$$\frac{\mathrm{PE}}{A} = \frac{1}{4}\rho a^2 g \tag{14.13}$$

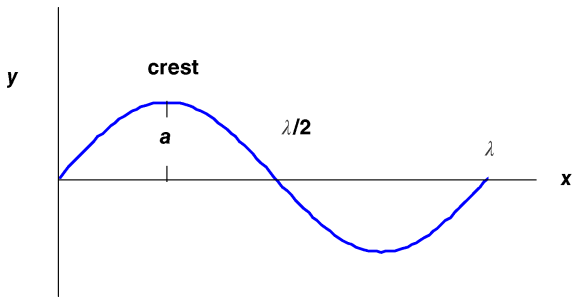

Figure 14.13 Traveling wave nomenclature.

and the kinetic energy density per unit area is also

$$\frac{\text{KE}}{A} = \frac{1}{4}\rho a^2 g \tag{14.14}$$

so that the total energy is the sum of the potential and kinetic or

$$\frac{\text{TE}}{A} = \frac{1}{2}\rho a^2 g \tag{14.15}$$

The power density is the energy density times the frequency f:

$$\frac{\text{PD}}{A} = \frac{1}{2}\rho f a^2 g \tag{14.16}$$

El-Wakil (1984) approximates the relationship between the wavelength and period of ocean wave to be

$$\lambda = 1.56\tau^2 \text{ m} = 5.12\tau^2 \text{ ft} \tag{14.17}$$

with τ in seconds. Example 14.5 illustrates how to use the preceding definitions.

Example 14.5
A 2 m ocean wave has a period of 5s. Find the wavelength, the wave velocity, and the energy and power densities for this wave.

Solution With a wave height of 2 m, the amplitude is one-half of the wave height, or $a = 1$ m. The relationship between the period and wavelength is provided by Equation 14.17 and the wavelength becomes

$$\lambda = 1.56\,\tau^2 \text{ m} = 1.56\left(\frac{5\text{ s}}{\text{s}}\right)^2 = 39\text{ m}$$

The wave speed is calculated as

$$c = \frac{\lambda}{\tau} = \frac{39\text{ m}}{5\text{ s}} = 7.8\frac{\text{m}}{\text{s}}$$

and the frequency is the reciprocal of the period, or

$$f = \frac{1}{\tau} = \frac{1}{5\text{ s}} = 0.2\frac{1}{\text{s}}$$

The total energy (TE) and power (PD) densities are calculated using Equations 14.15 and 14.16 respectively:

$$\frac{\text{TE}}{A} = \frac{1}{2}\rho a^2 g = \frac{1}{2}\times 1025\frac{\text{kg}}{\text{m}^3}\times(1\text{ m})^2\times 9.807\frac{\text{m}}{\text{s}^2} = 5030\frac{\text{J}}{\text{m}^2}$$

and

$$\frac{\text{PD}}{A} = \frac{1}{2}\rho a^2 f g = \frac{1}{2}\times 1025\frac{\text{kg}}{\text{m}^3}\times(1\text{ m})^2\times 0.2\frac{1}{\text{s}}\times 9.807\frac{\text{m}}{\text{s}^2} = 1005\frac{\text{W}}{\text{m}^2}$$

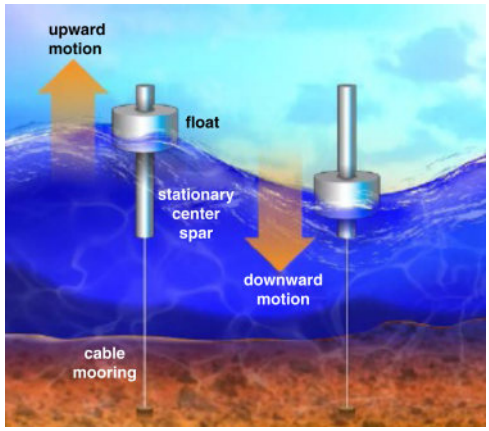

Figure 14.14 Point absorber schematic. *Source*: Thresher (2014).

For these wave conditions, the power density of 1005 W/m^2 is high – greater than the solar irradiation absorbed by the water or incident on the water surface.

Example 14.5 illustrates that a reasonable wave possesses a higher power density than might be absorbed by the ocean. Considering the extent of the oceans and the wave conditions present at any given time, the energy available from waves is enormous. The questions then become: (1) How can wave energy be harvested? (2) Why are MHK devices not in widespread use?

Most of the proposed and demonstrated MHK machines harvest kinetic rather than thermal energy. MHK devices are often grouped as (1) point absorbers, (2) attenuators, (3) oscillating water columns, or (4) overtopping devices. Each category will be reviewed.

1) *Point absorbers.* Point absorbers harvest energy at a single point by using the vertical motion of waves (from all directions) to pressurize sea water (or another working fluid) that drives a turbine. Figure 14.14 is a schematic of a point absorber system. The system is anchored to the sea floor, and the float moves up and down the stationary center spar. An example is the PowerBuoy® by Ocean Power Technologies that has been deployed at several test sites. Figure 14.15 shows the above-surface portion. In 2014 Ocean Power Technologies focused

Figure 14.15 PowerBuoy point absorber above-surface portion. *Source*: http://images.nrel.gov/viewphoto.php?imageId=6471938.

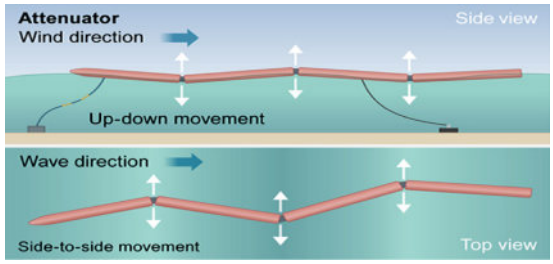

Figure 14.16 Attenuator schematic.
Source: Thresher (2014).

its research and development and marketing efforts on a smaller, stand-alone PowerBuoy primarily used for oceanographic data reporting.

2) *Attenuators.* Attenuators are long, articulated floating devices that are aligned parallel to the wave direction. The articulated joints contain piston–cylinder arrangements whose relative movements pressurize hydraulic fluid that drives a motor connected to a generator. Figure 14.16 illustrates how the wave motion and wind cause the articulated joints to flex.

   A good example of an attenuator device was deployed by Pelamis Wave Power, formerly Ocean Power Delivery, several years ago. Unfortunately, the company declared bankruptcy in 2014. Nonetheless, the Pelamis device, a semi-submerged, articulated system composed of cylindrical sections connected by hinged joints, is an example of an attenuator device. The wave-induced motion drives hydraulic rams that pump high-pressure fluid through hydraulic motors that drive electrical generators. The power is fed via an umbilical cord to shore. Several devices can be linked to form a wave-energy farm. The Pelamis P-750 is 140 m long, 3.5 m in diameter, and is rated at 750 kW. Specifications for the P-750 are given in Table 14.5. A Pelamis P-750 produces a yearly average of 25–40% of the rated power. Figure 14.17 is a photograph of the P-750. The articulated nature of the design is perhaps the salient feature.

3) *Oscillating water columns.* In an oscillating water column, waves cause the sea water level inside a confined container, the chamber, to move up and down. Figure 14.18 shows the operating features of an oscillating water column device. The inclined side of the chamber is

Table 14.5 P-750 specifications.

Overall length	150 m
Diameter	3.5 m
Displacement	700 t (metric tonne = 1000 kg)
Nose	5 m long, drooped conical
Power take off	Three power conversion units
	Hydraulic rams (2 in heave, 2 in sway)
Ram speed	0–0.2 m/s
Working pressure	100–350 bar
Power conversion	Two variable-displacement motors
Generator	Two 157 kVA/125 kW
Speed	1500 rpm
Power	750 kW
Energy	2.7 GWh/year
Wave power	Nominal 55 kW/m

Source: Pelamis brochure.

Figure 14.17 Pelamis P-750 articulated wave energy converter. *Source*: Pelamis.

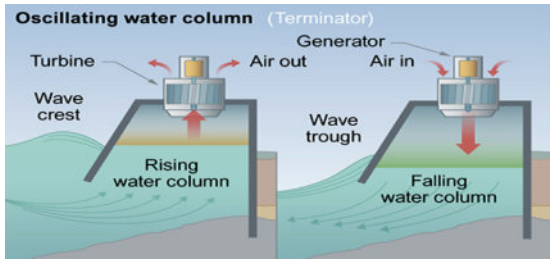

Figure 14.18 Oscillating water column operation. *Source*: Thresher (2014).

a dominant feature. As the water level rises, the air trapped in the chamber is forced through a turbine that extracts energy to drive an electrical generator. When the wave recedes, air enters the chamber through a turbine, again extracting energy. The process is repeated with the next wave. In order to harvest significant energy, the wave machines must be large and there must be many of them. For example, Wavegen®, a Voith and Siemens company, installed the first grid-connected commercial-scale wave energy plant off the coast of western Scotland. The plant uses an inclined oscillating water column system and serves as a full-scale test bed for component validation and development.

4) *Overtopping devices.* An overtopping device is a reservoir that is filled as waves break over its walls. Since the free surface inside the reservoir is above the sea level outside the reservoir, the liquid inside the reservoir flows through a turbine into the sea – generating electricity in the process. Figure 14.19 illustrates the important features of an overtopping device.

Other configurations for extracting energy from waves are also under consideration. These four are the most common. A web search will yield a number of "hits," if MHK devices is entered. Wave energy devices are under active development by governmental agencies and private companies; significant technological advances are likely.

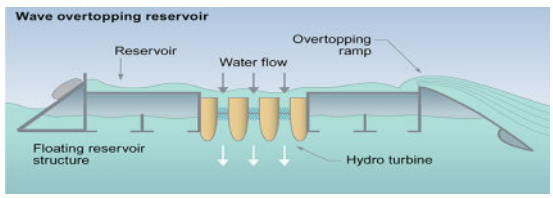

Figure 14.19 Overtopping device features. *Source*: Thresher (2014).

14.4.1 Rotating devices

Section 14.3 examined tidal energy using barrages. But tidal energy is also contained in tidal currents in non-barrage systems. Turbines placed in tidal currents with appreciable power density (and kinetic energy) can also harvest energy from tidal currents. In the general MHK nomenclature, these machines are called rotating devices. The operating principle is the same as for wind turbines (see Chapter 4). However, since the density of water is nearly two orders of magnitude greater than that of air, the tidal current velocity does not need to be nearly as large as the wind velocity for the same power density, $\rho V^3/2$. Consider

$$\frac{1}{2}\rho_{\text{water}} V_{\text{water}}^3 = \frac{1}{2}\rho_{\text{air}} V_{\text{air}}^3 \tag{14.18}$$

where ρ_{water} is the density of sea water. V_{water} becomes for the same power density

$$V_{\text{water}} = \sqrt[3]{\frac{\rho_{\text{air}}}{\rho_{\text{water}}} V_{\text{air}}} \tag{14.19}$$

If the densities of the two fluids are taken at a reasonable temperature with the wind velocity of 10 m/s (effective for most wind turbines), then

$$V_{\text{water}} = \sqrt[3]{\frac{1.204\ \text{kg/m}^3}{1027\ \text{kg/m}^3}} \times 10\frac{\text{m}}{\text{s}} = 1.05\frac{\text{m}}{\text{s}} \tag{14.20}$$

Thus, a tidal current velocity of 1.05 m/s contains the same power density as a wind speed of 10 m/s.

A wide range of turbine configurations have been proposed for use in tidal currents. A web search will generate a large number of hits for tidal current turbines. Rotational devices used in tidal currents are conceptually similar to wind turbines, which has helped to speed up the development and acceptance of the rotating devices for water-based applications. Although subject to change as new developments emerge, the most common rotating device configuration is the vertical-axis turbine, as illustrated in Figure 14.20.

In the last few years, tidal current devices and technologies have become of increasing interest. The Jindo Uldolmok Tidal Power Plant in South Korea was commissioned in 2009 and expanded to 90 MW in 2013. The Uldolmok Strait experiences tidal water speeds in excess of 6.5 m/s! In Scotland, a tidal farm, when completed, will have 269 turbines of 1.5 MW each. The first phase, 90 MW, is scheduled for completion in 2020.

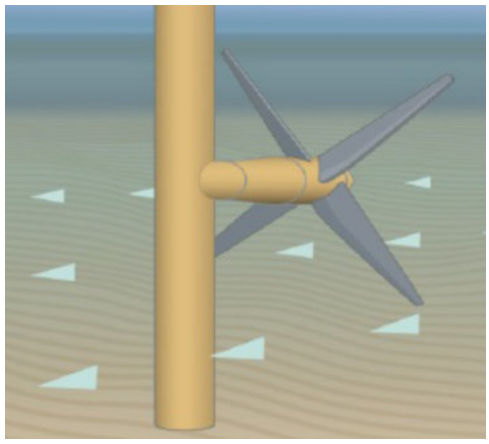

Figure 14.20 Vertical-axis rotating device (turbine) illustration. *Source*: Thresher (2014).

Table 14.6 DOE estimates of theoretical and technical MHK energy potentials.

Source	Energy potential (TWh/year)	
	Theoretical	Technical
Waves	1594–2640	898–1229
Tidal streams	445	222–334
Ocean currents	200	45–163
River currents	1381	120

The Marine and Hydrokinetic Technology Database at OpenEI (http://en.openei.org/wiki/Marine_and_Hydrokinetic_Technology_Database) is especially useful for MHK as it contains a searchable, rather complete, database for MHK. The EERE site (http://energy.gov/sites/prod/files/2015/01/f19/MHK_DBsystems1pager.pdf) provides information on MHK databases and systems. Thresher (2014) also previews several wave energy devices and installations, and on page 25 presents in tabular format, on a country basis, the development status of ocean energy. The earlier *Ocean Energy Technology Overview* (EERE, 2009) still provides useful information. The *2014 Water Power Program Peer Review* (EERE, 2014), at 791 pages, is perhaps the most exhaustive review of water power energy technologies, needs, and assessment ever untaken. USDOE funding for MHK has grown from zero funding in 2007 to $42 million in 2014 with a 2007–2014 funding total of near $200 million. A summary of the DOE role in MHK from EERE (2014) is

> . . . Establish the viability of a nascent MHK industry to attract private investment. Maximize sharing of knowledge and support device technologies that can accelerate and grow the industry as a whole. Research and reduce the risk of technologies ahead of industry adoption.

The USDOE at http://energy.gov/eere/water/marine-and-hydrokinetic-resource-assessment-and-characterization provides a summary of MHK potential for the USA. Table 14.6 lists the theoretical energy available in terawatt-hours per year as well as the energy that might be harvested from a technical standpoint. Four categories are examined: (1) waves, (2) tidal streams, (3) ocean currents, and (4) river currents. Since the USA uses about 4000 TW h of electricity per year, the potential resources available from MHK devices are not trivial and could, if developed, provide at least 10% of the annual electricity usage. However, significant technical challenges as well as infrastructure development issues are present if the MHK potential is to be realized.

14.5 Closure

OTEC, tidal, and MHK have been explored in this chapter. The energy potential is enormous for OTEC, and for MKT in particular, but the technical, operational, and financial problems are daunting. Ocean energy devices must cope with large size, high capital costs, corrosive environments, and uncertain and severe weather conditions. The potential is present, however, and as greenhouse gas and climate change issues and uncertainties in energy costs continue to be of concern, more resources are being directed to ocean energy as at least part of the energy solution.

References

Ascari, M., Hanson, H.P., Rauchenstein, L., *et al*. (2012) *Ocean Thermal Extraction Visualization.* http://energy.gov/sites/prod/files/2013/12/f5/1055457.pdf (accessed October 2, 2016).

Avery, W.H. and Berl, W.G. (1997) Solar energy from tropical oceans. *Issues in Science and Technology*, **XIV**. (2). http://issues.org/14-2/avery-2/ (accessed October 25, 2016).

Avery, W.H. and Wu, C. (1994) *Renewable Energy from the Ocean: A Guide to OTEC*. Oxford University Press, New York.

Baker, J.B. (2006) Energy from the sea. *Technology Review*, **109** (3): 96.

Coastal Response Research Center (2010) *Technical Readiness of Ocean Thermal Energy Conversion (OTEC)* University of New Hampshire, Durham, NH. http://coast.noaa.gov/czm/media/otec_nov09_tech.pdf (accessed October 25, 2016).

Cruz, J. (ed.) (2008) *Ocean Wave Energy*. Springer-Verlag, Berlin.

De LaLeu, V. (2009) La Rance Tidal Power Plant 40-year operation feedback – lessons learnt. In *BHA Annual Conference*, Liverpool, UK, October. http://www.british-hydro.org/downloads/La%20Rance-BHA-Oct%202009.pdf (accessed October 25, 2016).

EERE (2009) *Ocean Energy Technology Overview*. DOE/G0-102009-2823, July. http://large.stanford.edu/courses/2013/ph240/lim2/docs/44200.pdf (accessed October 25, 2016).

EERE (2014) *2014 Water Power Program Peer Review*. PR-5A00-61854. http://energy.gov/sites/prod/files/2014/09/f18/00_mhk_peer_review_presentations_2014_0.pdf (accessed October 25, 2016).

El-Wakil, M.M. (1984) *Powerplant Technology*. McGraw-Hill, New York.

Gorlov, A.M. (2001) Tidal energy. In *Encyclopedia of Ocean Sciences*, J.H. Steele, K.K. Turekian, and S.A. Thorpe (eds). Elsevier, pp. 2955–2960.

Kayton, M. (1981) Steady-state and dynamic performance of an OTEC plant. *IEEE Transactions on Power Apparatus and Systems*, **PAS-100** (3): 1148–1153.

McCormick, M.E. (2007) *Ocean Wave Energy Conversion*. Dover Publications, Mineola, NY.

Palmer, D.A., Fernandez-Prini, R., and Harvey, A.H. (2004) *Aqueous Systems at Elevated Temperatures and Pressures: Physical Chemistry in Water, Steam and Hydrothermal Solutions*. Academic Press, New York.

Perry, R.H. and Chilton, C.H. (1973) *Chemical Engineer's Handbook*, 5th edn. McGraw-Hill, New York.

Rudiger, C.E. and Smith, L.O. (1977) OTEC – an emerging program of significance to the marine community. In *Proceedings of the 3rd Oceans '77 Annual Combined Conference*, Los Angeles, October, vol. 2, pp. 41C-1–41C-7.

Schmid, H. (2005) Sihwa in the mix. *Power Engineering International*, **13**. (9). http://www.powerengineeringint.com/articles/print/volume-13/issue-9/renewable-energy-review/tidal-power/sihwa-in-the-mix.html (accessed October 25, 2016).

Takahashi, M.M. (2000) *DOW: Deep Ocean Water as Our Next Natural Resource*. Terra Scientific Publishing Co., Tokyo.

Thresher, R. (2014) Ocean wave energy technology. In *BOEM Offshore Renewable Energy Workshops*, Sacramento, CA, July. http://www.boem.gov/NREL-Ocean-Wave-Energy-Technology/ (accessed October 25, 2016).

Vega, L.A. (2002) Ocean thermal energy conversion primer. *Marine Technology Society Journal*, **6** (4): 25–35. http://www.uprm.edu/aceer/pdfs/MTSOTECPublished.pdf (accessed October 25, 2016).

15

Nuclear Energy

15.1 Introduction

In the USA, nuclear power has been a controversial issue for more than a generation. It was controversial before the Three Mile Island incident in 1979, with legal barriers and maneuvers effectively halting additional penetration into the electric utility industry. After Three Mile Island, construction of new nuclear power plant in the USA essentially ceased. Internationally, nuclear power has achieved greater acceptance, with western Europe and Japan generating much of their electricity from nuclear energy. Poor design choices and operational procedures in the former USSR led to the 1986 Chernobyl disaster, with further clouded nuclear power generation safety issues. However, with increasing concern over greenhouse-gas-driven climate change, as well as energy independence, nuclear power was under active consideration in the USA, and for the first time in almost 30 years plans were ongoing for new nuclear power plant construction. Then, in 2011, disaster struck in the aftermath of an earthquake-induced tsunami at Fukushima Daiichi, a Japanese nuclear plant with six reactors. World reaction was swift and devastating, and the favorable outlook for nuclear power diminished significantly. However, several years after Fukushima, the outlook for increased use of nuclear power is becoming more positive as a number of nuclear power plants are now under construction or being planned.

An interesting graphic on nuclear power is provided by the World Nuclear Association (WNA) on their web site (www.world-nuclear.org) and is reproduced as Figure 15.1. In 2013, the electricity generated by nuclear power was about 2300 TWh/year. Nuclear power produced about 19% (Table 1.2) of the electricity in the USA in 2014. Even after the moratorium on construction of nuclear power plants in the USA, electricity generation by nuclear power is significant. By any measure, nuclear power is important and vital to the production of electricity and is hardly an "alternative energy" source in the generally accepted connotation of the phrase. However, nuclear was included in this textbook because of the important role it currently plays and because the growing interest in nuclear power, even after Fukushima, especially in China, India, and Russia, portends that it is likely to become more important, not less important. In the USA, new nuclear plants are under construction or in the planning stages. Indeed, many individuals in the electric power industry believe nuclear power will become more important in this century. Both the WNA (www.world-nuclear.org) and the International Atomic Energy Agency (IAEA, www.iaea.org) are advocates for nuclear power and provide lists for operating and shut-down nuclear reactors as well as for those under construction. Currently, 438 nuclear reactors are in operation, with an additional 67 under construction. The US Nuclear Regulatory Commission (NRC, www.nrc.gov) is the US government agency charged with overseeing all aspects of nuclear energy. In 2015, the NRC stated that 99 reactors were in operation in the USA. *Nuclear Engineering International* (NEI) is a monthly print magazine that includes feature and technical articles on the civil nuclear power industry (http://www.neimagazine.com/). NEI also publishes a yearly *Nuclear Engineering International Handbook*.

Alternative Energy Systems and Applications, Second Edition. B. K. Hodge.

Companion website: www.wiley.com\go\Hodge\AESystemsandApplications2E

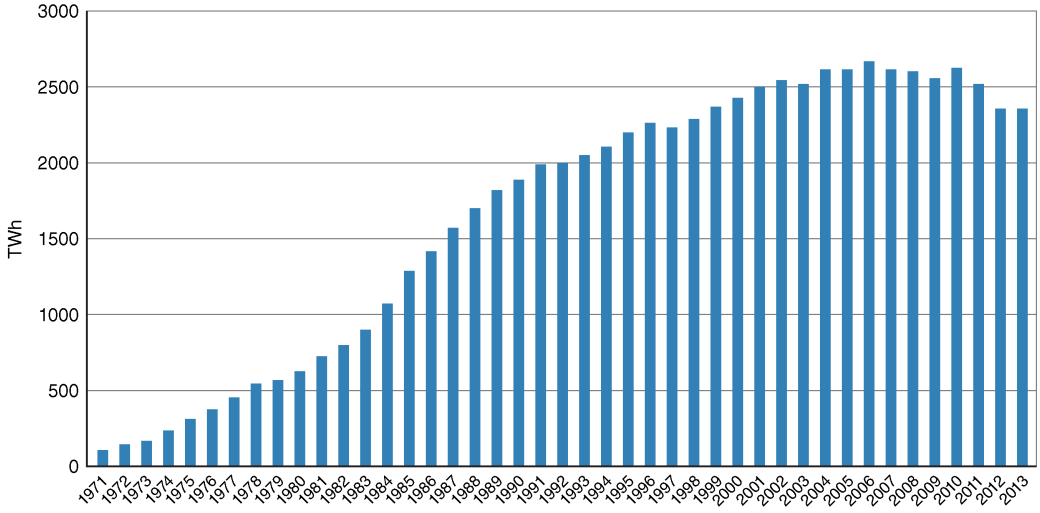

Figure 15.1 Worldwide nuclear electricity generation. *Source*: http://www.world-nuclear.org/info/Current-and-Future-Generation/Nuclear-Power-in-the-World-Today/

This chapter discusses the fundamentals and basics of nuclear energy, examines the various configurations of nuclear power plants, and reviews the potential and technical problems of fusion-power production.

15.2 Fundamentals of Nuclear Energy

An atom consists of a heavy, positively charged nucleus with much lighter electrons in orbits about the nucleus (see Chapter 9). The nucleus is composed of electrically neutral neutrons and positively charged protons. The charge on the proton is equal to, but opposite, to the charge on the electron. Since an atom is electrically neutral, the number of protons is equal to the number of electrons. The three primary subatomic particles are the electron, the neutron, and the proton. The masses of these particles, expressed in atomic mass units, or amu (1 amu = $1.660\,539 \times 10^{-27}$ kg), are as follows (Shultis and Faw, 2008):

- neutron mass, $m_n = 1.008\,665$ amu
- proton mass, $m_p = 1.007\,276$ amu
- electron mass, $m_e = 0.000\,548\,6$ amu.

The proton and neutron, particles that make up the nucleus, are called nucleons. By convention, the number of protons in the nucleus defines the atomic number Z of an element, and the sum of the neutrons and protons in the nucleus defines the mass number A. The usual notation for an atom of element X is ${}^{A}_{Z}\mathrm{X}$, so that the atomic number and mass number are easily tracked. Most of the mass of an atom is in the nucleus. Isotopes of an element have the same number of protons but a different number of neutrons and, thus, different mass numbers. For example, uranium has three common isotopes: ${}^{238}_{92}\mathrm{U}$, ${}^{235}_{92}\mathrm{U}$, and ${}^{234}_{92}\mathrm{U}$. In this protocol, "ordinary" hydrogen appears as ${}^{1}_{1}\mathrm{H}$, and because the hydrogen nucleus contains a single proton and no neutrons, ${}^{1}_{1}\mathrm{H}$ is also a proton. The nucleus of deuterium contains a proton and a neutron and appears as ${}^{2}_{1}\mathrm{H}$ and is sometimes written as ${}^{2}_{1}\mathrm{D}$. The helium nucleus contains a pair of neutrons and protons and is cast as ${}^{4}_{2}\mathrm{He}$. Since the electron mass is quite small compared with the mass of a neutron or a proton, an electron is often represented as ${}^{0}_{-1}\mathrm{e}$. A neutron, which carries no charge, then becomes ${}^{1}_{0}\mathrm{n}$.

In a chemical reaction whole atoms are involved, as in the hydrogenation reaction

$$C + 2H_2 \rightarrow CH_4 \tag{15.1}$$

In this reaction, atoms of carbon and hydrogen combine to form methane, but the atoms retain their identity; indeed, the number of carbon and hydrogen atoms on the left (reactant) and right (product) sides of the equation must be equal. In a nuclear reaction the reactant nuclei do not show up in the products, but other nuclei or different isotopes of the reactants are present. Consider a nuclear reaction involving elements A, B, C, and D:

$${}^{A_1}_{Z_1}\mathrm{A} + {}^{A_2}_{Z_2}\mathrm{B} \rightarrow {}^{A_3}_{Z_3}\mathrm{C} + {}^{A_4}_{Z_4}\mathrm{D} \tag{15.2}$$

Conservation of mass number and conservation of atomic number (protons) demand

$$A_1 + A_2 = A_3 + A_4 \quad \text{and} \quad Z_1 + Z_2 = Z_3 + Z_4 \tag{15.3}$$

An example is ordinary aluminum capturing in its nucleus a helium nucleus, ${}^4_2\mathrm{He}$. The aluminum nucleus with the addition of a helium nucleus is unstable and decays:

$${}^{27}_{13}\mathrm{Al} + {}^4_2\mathrm{He} \rightarrow {}^{30}_{14}\mathrm{Si} + {}^1_1\mathrm{H} \tag{15.4}$$

The result of the nuclear reaction is silicon and a proton (hydrogen nucleus). The sums of the mass numbers (31) and the atomic numbers (15) are the same on both sides of the equation.

Each isotope of each element has a specific mass that is dependent on the mass number and the atomic number. The atomic mass unit is defined to be one-twelfth the mass of a neutral ground-state atom of ${}^{12}_6\mathrm{C}$. All other isotopes are referenced to this standard. The atomic mass units of all 3200 isotopes are provided in atomic mass tables. Atomic mass tables are available in textbooks on nuclear engineering or nuclear physics and on a number of web sites; http://physics.nist.gov/cgi-bin/Compositions/stand_alone.pl is an especially useful site. In this chapter, the atomic mass table presented in Shultis and Faw (2008) is used. From this table, the following were abstracted:

- mass of ${}^{27}_{13}\mathrm{Al} = 26.981\,538$ amu
- mass of ${}^4_2\mathrm{He} = 4.002\,603$ amu
- mass of ${}^{30}_{14}\mathrm{Si} = 29.973\,770$ amu
- mass of ${}^1_1\mathrm{H} = 1.007\,825$ amu

For the nuclear reaction of Equation 15.4 the mass of the reactants is

$$26.981\,538 \text{ amu} + 4.002\,603 \text{ amu} = 30.984\,141 \text{ amu}$$

and the mass of the products is

$$29.973\,770 \text{ amu} + 1.007\,825 \text{ amu} = 30.981\,595 \text{ amu}$$

Mass is not conserved! The product mass is less than the reactant mass. The difference, $\Delta m = -0.002\,546$ amu, represents the mass converted to energy via Einstein's famous expression

$$\Delta E = \Delta m c^2 \tag{15.5}$$

where c is the speed of light, 3×10^8 m/s. Thus, the energy is

$$\begin{aligned} \Delta E = \Delta m c^2 &= -0.002\,546 \text{ amu} \times \left(3 \times 10^8 \frac{\text{m}}{\text{s}}\right)^2 = -2.2914 \times 10^{14} \text{ amu} \frac{\text{m}^2}{\text{s}^2} \\ &= -2.2914 \times 10^{14} \text{ amu} \frac{\text{m}^2}{\text{s}^2} \times \frac{1.660\,539 \times 10^{-27} \text{ kg}}{\text{amu}} \times \frac{\text{N s}^2}{\text{kg m}} \times \frac{\text{J}}{\text{N m}} \\ &= -3.8053 \times 10^{-13} \text{ J} \times \frac{\text{eV}}{1.602\,176 \times 10^{-19} \text{ J}} \times \frac{\text{MeV}}{10^6 \text{ eV}} = -2.375 \text{ MeV} \end{aligned} \tag{15.6}$$

Hence, the nuclear reaction of Equation 15.4 produces 2.375 MeV of energy by the conversion of mass into energy. Were the energy produced by a chemical reaction to be examined, the energy produced would have been orders of magnitude less – hence the interest in nuclear reactions as an energy source.

When Z protons and $(A - Z)$ neutrons come together to form a nucleus, energy is emitted. This energy, called the binding energy, comes from the conversion of some of the mass of the neutrons and protons. The mass of the resulting nucleus is reduced from the mass of the individual neutrons and protons by the mass equivalent (Equation 15.5) of the binding energy.

Three types of nuclear reactions are important in the production of energy: fission, fusion, and radioactivity. Each will be examined in turn. In fission, a "heavy" element (one with a high atomic number) is split into two or more lighter nuclei; in fusion, two or more light nuclei are fused to form a heavier nucleus. Radioactivity occurs when an isotope spontaneously undergoes decay or disintegration into a different nucleus, usually by emission of one or more smaller particles. Currently, all large, commercial nuclear reactors utilize fission, so fission is of great interest in this chapter.

El-Wakil (1984) points out that neutrons are the only particles that can be practically used in fission reactors, and only a few isotopes are fissionable by neutrons: ${}^{235}_{92}\mathrm{U}$, ${}^{239}_{94}\mathrm{Pu}$, ${}^{233}_{92}\mathrm{U}$, ${}^{238}_{92}\mathrm{U}$, ${}^{232}_{90}\mathrm{Th}$, and ${}^{240}_{94}\mathrm{Pu}$. Nuclides that fission when a neutron is absorbed by the nucleus are called fissile. Consider two fission reactions involving ${}^{235}_{92}\mathrm{U}$:

$$\begin{aligned} {}^{235}_{92}\mathrm{U} + {}^{1}_{0}\mathrm{n} &\rightarrow {}^{140}_{54}\mathrm{Xe} + {}^{94}_{38}\mathrm{Sr} + 2{}^{1}_{0}\mathrm{n} \\ {}^{235}_{92}\mathrm{U} + {}^{1}_{0}\mathrm{n} &\rightarrow {}^{137}_{56}\mathrm{Ba} + {}^{97}_{36}\mathrm{Sr} + 2{}^{1}_{0}\mathrm{n} \end{aligned} \tag{15.7}$$

These reactions result in two nuclei different from uranium and the emission of two neutrons. If a reaction is to be sustained, then more neutrons must be emitted than absorbed. Example 15.1 examines the energy release from the first of the nuclear reactions in Equation 15.7.

Example 15.1
Compute the energy resulting from the ${}^{235}_{92}\mathrm{U} + {}^{1}_{0}\mathrm{n} \rightarrow {}^{140}_{54}\mathrm{Xe} + {}^{94}_{38}\mathrm{Sr} + 2{}^{1}_{0}\mathrm{n}$ nuclear reaction.

Solution The atomic mass tables (Shultis and Faw, 2008) provide the atomic mass unit values for the reactants and products of the reaction:

- mass of ${}^{235}_{92}\mathrm{U} = 235.043\,923$ amu
- mass of ${}^{1}_{0}\mathrm{n} = 1.008\,665$ amu
- mass of ${}^{140}_{54}\mathrm{Xe} = 139.921\,640$ amu
- mass of ${}^{94}_{36}\mathrm{Sr} = 93.915\,360$ amu.

The masses of the reactants and products are

$$\begin{aligned} \text{Reactants} &= 235.043\,923 \text{ amu} + 1.008\,665 \text{ amu} = 236.053 \text{ amu} \\ \text{Products} &= 139.921\,640 \text{ amu} + 93.915\,360 \text{ amu} + 2 \times 1.008\,665 \text{ amu} = 235.854 \text{ amu} \end{aligned}$$

The change in mass is

$$\Delta m = 235.854 \text{ amu} - 236.053 \text{ amu} = -0.198 \text{ amu}$$

And the energy released is

$$\Delta E = \Delta m c^2 = -0.198 \text{ amu} \times \left(3 \times 10^8 \frac{\text{m}}{\text{s}}\right)^2 = -2.963 \times 10^{-11} \text{ J} = -184.93 \text{ MeV}$$

Nuclides that are not themselves fissile but which can be converted to fissile nuclides upon adsorption of a neutron are called fertile. For example, when ${}^{238}_{92}\mathrm{U}$, a non-fissile isotope, absorbs a neutron it eventually becomes ${}^{239}_{94}\mathrm{Pu}$, a fertile isotope.

In fusion, two or more light nuclei are combined to form a heavier nucleus. Such reactions are possible only if the nuclei possess sufficient kinetic energy to overcome the repulsive forces and are able to reach each other. This topic will be examined in detail in Section 15.4. A typical fusion reaction and the energy released are as follows:

$$ {}_1^2\mathrm{H} + {}_1^2\mathrm{H} \rightarrow {}_1^3\mathrm{H} + {}_1^1\mathrm{H} + 4.03\ \mathrm{MeV} \tag{15.8} $$

As with fission reactions, fusion reaction energy release results from the conversion of mass to energy.

Radioactivity, the spontaneous decay of a nucleus by emission of one or more smaller particles, is the last of the three nuclear reactions to be examined. A key word in this definition is "spontaneous," since, unlike fission and fusion reactions, the instability of the nucleus of a radioactive isotope is the causative effect. Isotopes that occur naturally are stable in most elements, but elements with atomic numbers greater than 84 have no stable isotopes, and a few isotopes of elements with atomic numbers less than 84 are also unstable. Isotopes artificially produced in particle accelerators and nuclear reactors are all unstable and number in the thousands. The time required for a single unstable nucleus to decay is indeterminate, but among a large cohort of the same unstable nuclei there is a statistical probability that a certain fraction will decay within a specified time. If N is the number of radioactive isotopes present at time t, then the rate of decay is proportional to N. Mathematically, this is expressed as

$$ \frac{\mathrm{d}N}{\mathrm{d}t} = -\lambda N \tag{15.9} $$

where λ is the decay constant. Equation 15.9 is variable separable; if N_o isotopes are present at $t = 0$, then

$$ \int_{N_\mathrm{o}}^{N} \frac{\mathrm{d}N}{N} = -\int_0^t \lambda\, \mathrm{d}t \qquad \text{or} \qquad \ln\frac{N}{N_\mathrm{o}} = -\lambda t \qquad \text{or} \qquad \frac{N}{N_\mathrm{o}} = \exp(-\lambda t) \tag{15.10} $$

Decay is thus exponential in time. An important metric in radioactive decay is the half-life. By definition, the half-life is the time required for one-half of the radioactive nuclei to decay. Using Equation 15.10, the half-life can be expressed as

$$ \frac{N_\mathrm{o}/2}{N} = \exp(-\lambda t_{\text{half-life}}) \qquad \text{or} \qquad t_{\text{half-life}} = \frac{\ln(1/2)}{-\lambda} = \frac{0.693\,15}{\lambda} \qquad \text{or} \qquad \lambda = \frac{0.693\,15}{t_{\text{half-life}}} \tag{15.11} $$

Equation 15.10 can be cast as

$$ \frac{N}{N_\mathrm{o}} = \exp\left(-0.693\,15\frac{t}{t_{\text{half-life}}}\right) \tag{15.12} $$

Equation 15.12 is plotted in Figure 15.2; the abscissa is $t/t_{\text{half-life}}$, the number of half-lives. The exponential decay is rapid, such that by slightly over three half-lives the number of nuclei has diminished to only 10%; by 10 half-lives, the number of nuclei has been reduced to less than 0.1%.

The half-lives of different isotopes differ by many orders of magnitude. For example, the half-life of ${}_{84}^{212}\mathrm{Po}$ is only 0.298×10^{-6} s, while the half-life of ${}_{92}^{238}\mathrm{U}$ is 4.51×10^9 years. Most textbooks on nuclear engineering contain abbreviated tables of radionuclides that include half-life and other useful data. However, a number of web sites provide extensive listings; http://nucleardata.nuclear.lu.se/toi/nucSearch.asp is especially user friendly and is a partial implementation of the contents of the eighth edition of *Table of Isotopes* (Firestone and Shirley, 1999).

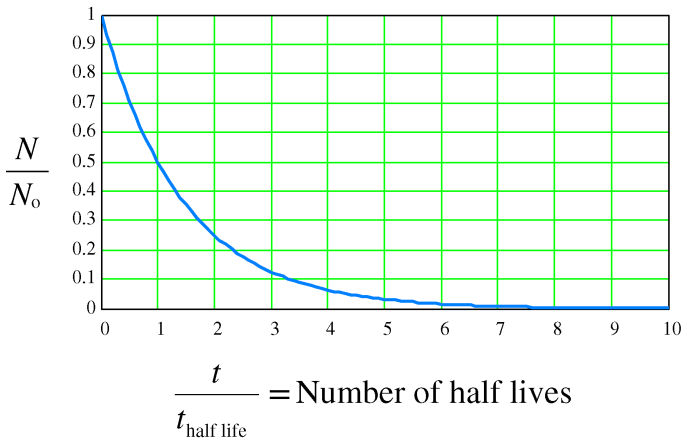

Figure 15.2 Exponential decay as a function of half-lives.

Shultis and Faw (2008) identify four mechanisms that result in the decay of a natural (*not* man-made) isotope: alpha decay, beta decay, positron decay, and gamma decay. Consider each of the four.

1) *Alpha decay.* An alpha (α) particle is the nucleus of a helium atom and is written as ${}^{4}_{2}\mathrm{He}$. Alpha decay occurs when an alpha particle is ejected. An example is

$$ {}^{226}_{88}\mathrm{Ra} \rightarrow {}^{222}_{86}\mathrm{Rn} + {}^{4}_{2}\mathrm{He} \tag{15.13} $$

In alpha decay, the Z is reduced by 2 and A by 4; in the reaction of Equation 15.13, Ra is the parent and Rn is the daughter. Alpha particles give up their kinetic energy by ionizing the matter through which they pass. Most of the energy is dissipated close to the emitting nucleus. Alpha particles possess limited penetrating ability – a few centimeters in air and a much shorter distance (about the thickness of a sheet of paper) in solids. Unless alpha emitters are ingested, they pose little health danger.

2) *Beta decay.* Beta (β) decay is the transformation of a neutron in the nucleus into a proton and an electron, which results in the emission of the electron in order to maintain the charge balance of the nucleus. Beta particles are thus electrons, ${}^{0}_{-1}\mathrm{e}^{-1}$. An example of beta decay is

$$ {}^{214}_{82}\mathrm{Pb} \rightarrow {}^{214}_{83}\mathrm{Bi} + {}^{0}_{-1}\mathrm{e}^{-1} + \nu \tag{15.14} $$

where ν represents the neutrino, a small neutrally charged particle that carries about 5% of the energy of the reaction. In many cases, the neutrino in Equation 15.14 is ignored. The beta particle has more penetrating ability than the alpha particle. In beta decay, the atomic number is increased by 1, while the mass number is unchanged.

3) *Positron decay.* In positron decay, the nucleus is unstable because of an excess of protons, and a proton is converted into a neutron by the emission of a positron, a subatomic particle with the mass of an electron but with a positive charge; the symbol is ${}^{0}_{+1}\mathrm{e}^{+1}$. An example is

$$ {}^{22}_{11}\mathrm{Na} \rightarrow {}^{22}_{10}\mathrm{Ne} + {}^{0}_{+1}\mathrm{e}^{+1} + \nu \tag{15.15} $$

As with the beta decay, a neutrino is also emitted. Shortly after emission, the positron will capture an electron, and the mass of the positron–electron pair will be completely converted to energy, with the result being two photons traveling in opposite directions, each with an energy of 0.511 MeV.

4) *Gamma decay.* Gamma radiation is electromagnetic radiation of extremely short wavelengths and very high frequencies – implying significant energy content. As Table 6.1 delineates, gamma rays have wavelengths λ of less than 10^{-4} μm. Gamma decay does not change either the mass number or the atomic number, but represents a reduction in the energy level of the nucleus. In gamma decay, a high-energy photon is emitted from the nucleus. Gamma rays have much more penetrating ability than either alpha or beta particles, and external exposure to γ-rays can be very hazardous.

Example 15.2
The radioactive isotope $^{135}_{53}\mathrm{I}$ decays by beta emission into $^{135}_{54}\mathrm{Xe}$. Determine the time required for the number of $^{135}_{53}\mathrm{I}$ atoms to be reduced by 90%.

Solution From the *Table of Isotopes* (Firestone and Shirle, 1999), the half-life of $^{135}_{53}\mathrm{I}$ is 6.57 h. If the number of nuclides is to be reduced by 90%, then only 10% of the original number will remain, or

$$\frac{N}{N_\mathrm{o}} = 0.10$$

From which

$$\frac{N}{N_\mathrm{o}} = 0.1 = \exp\left(-0.693\,15\frac{t}{t_{\text{half-life}}}\right) = \exp\left(-0.693\,15\frac{t}{6.57\,\mathrm{h}}\right)$$

Solving for t yields

$$t = -\frac{t_{\text{half-life}}}{0.693\,15}\ln\left(\frac{N}{N_\mathrm{o}}\right) = -\frac{6.57\,\mathrm{h}}{0.693\,15}\ln(0.1) = 21.82\,\mathrm{h}$$

15.3 Nuclear Power

In the context of this textbook, the discussion of nuclear power is limited to the generation of electricity. However, the US Navy has a long and rich history of using nuclear power for shipboard operations, including propulsion as well as onboard electricity distribution. The Navy has designed, built, operated, and decommissioned nuclear reactors, maintaining an astonishing safety and performance record and thus representing a significant repository of US nuclear engineering expertise. This section will examine nuclear reactors used for the generation of electricity.

Worldwide as of 2015, 438 nuclear power plants with a generating capacity of 376 000 MW (376 GW) were in commercial operation (IAEA, 2015). The US NRC provides a list of domestic operating nuclear power units at http://www.nrc.gov/reactors/operating/list-power-reactor-units.html. In addition, several hundred nuclear reactors are used in the naval vessels of various countries. A general rule of thumb is that the fission of 1 g of uranium provides the energy equivalent of 10 tons of oil. An overview of nuclear reactors is thus appropriate.

In any discussion of nuclear reactors, the concept of the neutron economy is central. Section 15.2 reviewed several aspects of fission reactions, including the energy released by such reactions. The fundamental idea of a nuclear reactor is to provide radioactive fuel in an environment such that nuclear reactions can proceed in a safe and dependable manner to provide power to generate electricity. For that to occur, enough neutrons must be produced to sustain controlled nuclear reactions sufficient to provide the power required. Uranium, for example, is a common fuel for many reactors and will fission in many different ways, resulting in

variations in the fission products. A general nuclear reaction for a large cohort of ${}^{235}_{92}\mathrm{U}$ atoms would result in the "average" reaction (Murray, 1961)

$$ {}^{235}_{92}\mathrm{U} + {}^{1}_{0}\mathrm{n} \rightarrow {}^{236}_{92}\mathrm{U} \rightarrow {}^{A_1}_{Z_1}\mathrm{FF} + {}^{A2}_{Z_2}\mathrm{FF} + 2.43\,{}^{1}_{0}\mathrm{n} \tag{15.16} $$

where ${}^{A_1}_{Z_1}\mathrm{FF}$ and ${}^{A_2}_{Z_2}\mathrm{FF}$ are the fission fragments of the reaction. The mass numbers of the fission fragments and the neutrons emitted must sum to 236. On average, 2.43 neutrons are produced. If the reaction is to be sustained, then at least one of the 2.43 neutrons must be absorbed and result in the fission of the nucleus of another ${}^{235}_{92}\mathrm{U}$ atom.

The nuclear reaction presented in Equation 15.16 yields on average about 200 MeV per fission. An important consideration for any power-producing machine, such as a nuclear reactor, is how much fuel is used to produce a specified amount of energy. A convenient metric is 1 MW day = 24 000 kW h. So a reasonable question is how much ${}^{235}_{92}\mathrm{U}$ is required to produce 1 MW day? Example 15.3 addresses this question.

Example 15.3

How much ${}^{235}_{92}\mathrm{U}$ is required to produce 1 MW day if the average energy yield is 200 MeV per fission and the electrical conversion efficiency is 35%?

Solution Since the energy yield per fission is 200 MeV, the number of fissions per second for 1 MW can be calculated as

$$ 1\ \mathrm{MW} = 1\,000\,000\ \mathrm{W} = 1\,000\,000\ \frac{\mathrm{J}}{\mathrm{s}} \times \frac{\mathrm{MeV}}{1.602 \times 10^{-13}\ \mathrm{J}} \times \frac{\text{fissions}}{200\ \mathrm{MeV}} = 3.121 \times 10^{16}\ \frac{\text{fissions}}{\mathrm{s}} $$

The mass of one atom of ${}^{235}_{92}\mathrm{U}$ can be computed since 235 g of ${}^{235}_{92}\mathrm{U}$ contains 6.023×10^{23} atoms/g-mol; so:

$$ m_{\mathrm{atom}} = \frac{235\ \text{g-mol}}{6.023 \times 10^{23}\ \text{atom-mol}} = 3.902 \times 10^{-22}\ \frac{\mathrm{g}}{\text{atom}} $$

The amount of uranium required to produce 1 MW day of energy then becomes

$$ 1\ \mathrm{MW\ day} = 3.212 \times 10^{16}\ \frac{\text{fissions}}{\mathrm{s}} \times \frac{86\,400\ \mathrm{s}}{\text{day}} \times \frac{3.902 \times 10^{-22}\ \mathrm{g}}{\text{atom}} \times \frac{1\ \text{atom}}{\text{fission}} = 1.083\ \frac{\mathrm{g}}{\text{day}} $$

Shultis and Faw (2008) state that about 15% of the neutrons absorbed by ${}^{235}_{92}\mathrm{U}$ result in something other than fission. The mass per day for 1 MW day at an electrical conversion efficiency of 35% is thus

$$ m_{\mathrm{U}} = 1.083\ \frac{\mathrm{g}}{\text{day}} \times \frac{1}{0.85 \times 0.35} = 3.640\ \frac{\mathrm{g}}{\text{day}} $$

Hence, in a day 3.64 g of ${}^{235}_{92}U$ would be consumed to produce 1 MW day (24 000 kW h).

Most neutrons resulting from the reactions such as indicated by Equation 15.16 are fast neutrons – indicating large kinetic energies (~2 MeV) and, hence, high speeds. A fast neutron is difficult for a ${}^{235}_{92}\mathrm{U}$ nucleus to absorb, and unless it is absorbed it will not initiate another nuclear reaction. A slow (or thermal) neutron has a much higher probability of being absorbed than a fast neutron. A thermal neutron is one that is in thermal equilibrium with its surroundings. Thus, fast neutrons need to be slowed down to become thermal neutrons to enhance their chances of capture so that nuclear reactions can be sustained. Fast neutrons that are slowed down are said to be scattered. The material in a nuclear reactor that is used to slow down or thermalize the fast neutrons is called the moderator. A moderator should have small nuclei with

high neutron scattering and low potential for neutrons absorption (or capture). Materials that fit these specifications include light water (containing ${}_{1}^{1}\mathrm{H}$), heavy water (containing deuterium, ${}_{1}^{2}\mathrm{H}$), graphite (C), and beryllium (Be or BeO). The moderator material also plays a role in the fuel requirement of a nuclear reactor.

As mined and processed, natural uranium is composed of 99.2% ${}_{92}^{238}\mathrm{U}$ and 0.7% ${}_{92}^{235}\mathrm{U}$. If the moderator is graphite or heavy water, then natural uranium can be used as a fuel. However, if light water is the moderator, then the amount of ${}_{92}^{235}\mathrm{U}$ in the fuel must be increased to from 0.7% to 3.5–5%. Enriching uranium is an expensive and energy-consuming process; Shultis and Faw (2008) discuss enrichment procedures.

The neutron economy is also a factor in reactor control. For a steady-state reactor operation an increase in neutron production results in an increase in the fission rate and in the power output. If neutron production were to continue to increase, the reactor core would eventually meltdown. To change the power level of a reactor, neutron production must be altered (increased or decreased) until the required new power level is reached. The neutron production in a reactor can be altered by control rods or chemical shims. Control rods are made of materials that absorb neutrons and thus reduce the neutrons that can be absorbed by fissile nuclei. Control rods can be moved in or out to affect the neutron economy. Materials that absorb neutrons include boron, cadmium, and indium. A chemical shim involves the use of a soluble neutron absorber, usually boron, in the coolant of a reactor. Chemical shims allow intermediate time control and help to reduce the movement of control rods.

Control rods or chemical shims alter the production of neutrons from one fission generation to the next. The effective neutron multiplication factor k_{eff} is defined as the ratio of the neutrons produced from one fission generation to the next fission generation:

$$k_{\mathrm{eff}} = \frac{\text{neutrons produced in generation } n+1}{\text{neutrons produced in generation } n} = \frac{n_{n+1}}{n_n} \tag{15.17}$$

where n is the number of neutrons. Since $k_{\mathrm{eff}} = 1$ represents steady-state operation, the excess of k_{eff} is used to define the reactivity ρ:

$$\rho = \frac{k_{\mathrm{eff}} - 1}{k_{\mathrm{eff}}} \tag{15.18}$$

If n_n are the neutrons produced in generation n and n_{n+1} the neutrons produced in generation $n+1$, then $n_{n+1} = k_{\mathrm{eff}} n_n$ and $\Delta n = n_{n+1} - n_n = n_n(k_{\mathrm{eff}} - 1)$. If the time between successive generations is t_{avg}, then (Murray, 1961; Sorensen, 1983)

$$\frac{\mathrm{d}n}{\mathrm{d}t} \approx \frac{\Delta n}{\Delta t} = \frac{n(k_{\mathrm{eff}} - 1)}{t_{\mathrm{avg}}} = \frac{n\rho k_{\mathrm{eff}}}{t_{\mathrm{avg}}} \tag{15.19}$$

Integrating Equation 15.19 with $n = n_{\mathrm{o}}$ at $t = 0$ yields

$$\ln \frac{n}{n_{\mathrm{o}}} = \frac{\rho k_{\mathrm{eff}}}{t_{\mathrm{avg}}} t \quad \text{or} \quad n = n_{\mathrm{o}} \exp\left(\frac{\rho k_{\mathrm{eff}}}{t_{\mathrm{avg}}} t\right) \tag{15.20}$$

Hence, the number of neutrons experience exponential growth with time. Example 15.4 illustrates how rapid power can increase in a nuclear reactor with $k_{\mathrm{eff}} > 1$.

Example 15.4

At $t = 0$ in a reactor, $k_{\mathrm{eff}} = 1.001$ with $t_{\mathrm{avg}} = 0.0001$ s. How much has the power increased at $t = 1$ s?

Solution With $k_{\text{eff}} = 1.001$ the reactivity is

$$\rho = \frac{k_{\text{eff}} - 1}{k_{\text{eff}}} = \frac{1.001 - 1}{1.001} = 0.000\,999$$

The ratio of neutrons produced is n/n_{o}:

$$\frac{n}{n_{\text{o}}} = \exp\left(\frac{\rho k_{\text{eff}}}{t_{\text{avg}}} t\right) = \exp\left(\frac{0.000\,999 \times 1.001}{0.0001\ \text{s}} \times 1\ \text{s}\right) = 22\,024$$

In 1 s, the number of neutrons increases by a factor of 22 024, and since the power is proportional to the number of neutrons, the power increases by the same factor. With such a small neutron magnification factor, the power increase in a single second is astonishingly large – the implication being that, under these circumstances, control would be virtually impossible. However, control is possible because of delayed neutrons.

Delayed neutrons are produced in the radioactive decay of some products from the fission of $^{235}_{92}$U. Out of the ~2.43 neutrons produced in fission reaction of Equation 15.16, about 0.65% comes from the decay of fission products such as Br and I. The times for the emission of the delayed neutrons are very long compared with the conventional fission cycle time. The net result is that t_{avg} is much longer than for the 99.35% of the neutrons released at the time of the reaction, the prompt neutrons. Murray (1961) states that the average life of a delayed neutron is 12.7 s. Instead of the $t_{\text{avg}} = 0.0001$ s for the prompt neutrons, when the delayed neutrons are considered in conjunction with prompt neutrons t_{avg}~0.1 s. For Example 15.4, if $t_{\text{avg}} = 0.1$ s, after 1 s the ratio of neutrons produced is 1.01 – quite a contrast to 22 024 for $t_{\text{avg}} = 0.0001$ s, and a more rational number for nuclear reactor control.

As with many energy systems, different configurations of nuclear reactors have different advantages and disadvantages, and for various reasons one configuration is preferred over another. Nuclear reactor configurations are based on the following considerations: (1) fuel, (2) moderator, (3) coolant, (4) control rods, (5) cost, and (6) containment. Table 15.1 provides a convenient summary of the most prevalent reactor configurations. The salient features of each type will be reviewed next. The NRC web site (http://www.nrc.gov/reactors/power.html), Nero (1979), Weston (1992), and Fay and Golomb (2002) contain a variety of schematics and explanations for the various reactor types and are good sources for qualitative information about nuclear reactors and subsystems.

Table 15.1 Nuclear reactor types and characteristics.

Type	Number	Power (GW)	Fuel	Coolant	Moderator
Pressurized water (PWR)	277	257	Enriched UO_2	Water	Water
Boiling water (BWR)	80	75	Enriched UO_2	Water	Water
Pressurized heavy water (PHWR) "CANDU"	40	25	Natural UO_2	Heavy water	Heavy water
Gas-cooled	15	8	Natural U, enriched UO_2	CO_2	Graphite
Light water graphite	15	10	Enriched UO_2	Water	Graphite
Fast neutron (FBR)	1	1	PuO_2, UO_2	Liquid sodium	None

Source: adapted from IAEA (2015) and WNA (2015).

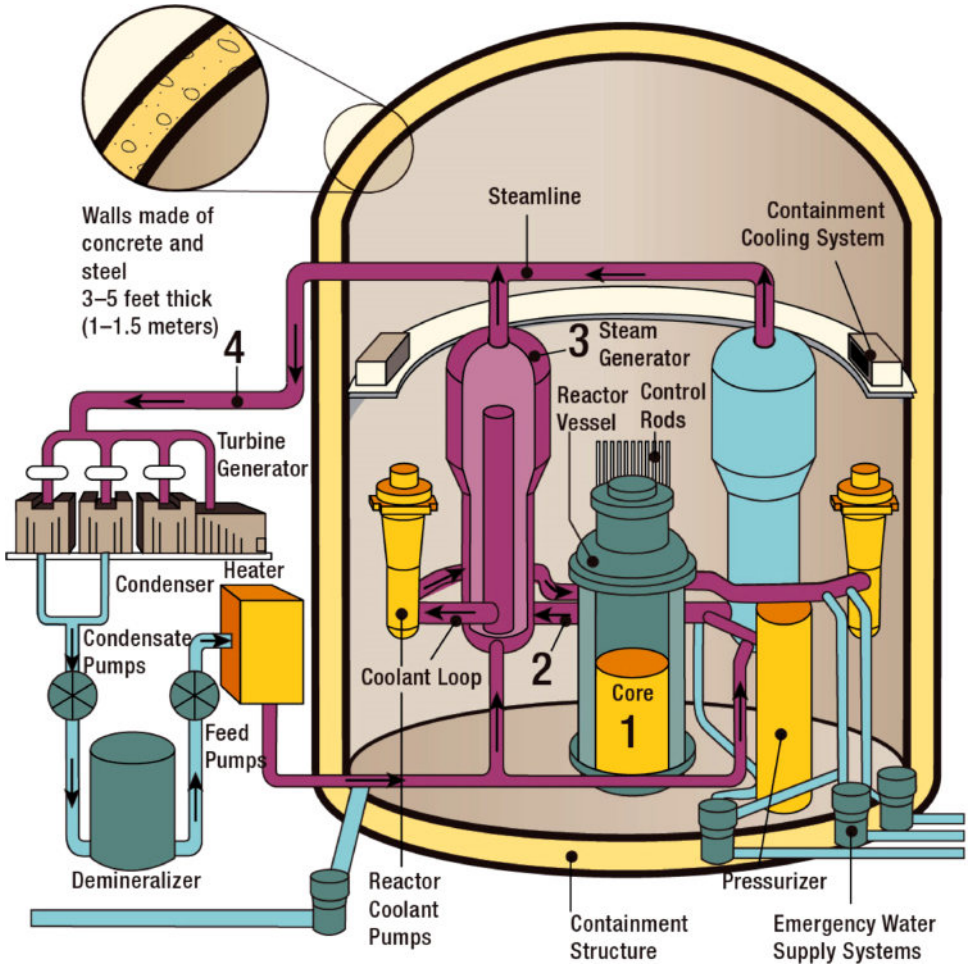

Figure 15.3 Schematic of a PWR, where "1" is the core, "2" is the pressurized water coolant loop, "3" is the steam generator, and "4" is the turbine/generator. *Source*: US Nuclear Regulatory Commission (http://www.nrc.gov/reactors/pwrs.html).

1) *Pressurized-water reactors* (PWRs). These constitute the largest number of reactors, with an estimated 278 (www.euronuclear.org) for commercial power and about 200 in service as naval propulsion systems. A simplified schematic of a PWR is given in Figure 15.3 where the containment vessel and the reactor vessel are shown. The concept behind PWRs is that the reactor vessel is pressurized to a high enough pressure so that the coolant (and moderator) is maintained in a liquid state. Typically, PWRs operate at about 300–325 °C and are pressurized to 15 or 16 MPa. The reactor core is located in the lower portion of the reactor vessel. In addition to the high operating pressure of the reactor vessel, a primary feature of a PWR is the pair of fluid loops. The high-pressure coolant loop circulates fluid within the reactor core and to a steam generator. In the steam generator the hot, high-pressure fluid is used to make steam at a pressure much lower (6 MPa) compared with the reactor coolant loop that is circulated outside the containment structure to the turbine and generator. The steam exiting the turbine is condensed in the cooling tower and returned to the steam generator. Because the steam to the turbine is not exposed to the reactor core, the turbine does not need to be shielded.

Westinghouse, Babcock and Wilcox, and Combustion Engineering are the designers of many of the existing PWR systems. After these reactors were built, Westinghouse and Combustion Engineering combined their nuclear assets with those of British Nuclear Fuels Limited to form Westinghouse BNFL. The French–German owned firm Framatome ANP acquired much of the nuclear technology of Babcock and Wilcox.

2) *Boiling-water reactor* (BWR). This is the second most popular reactor type. A simplified schematic of a BWR is provided in Figure 15.4. In the schematic, the containment vessel and the reactor vessel are shown. A BWR differs from a PWR in several important features: (1) the pressure in the reactor vessel is much lower (7 MPa) since steam is the desired fluid; (2) a BWR essentially contains only a single fluid loop; and (3) steam is generated in the reactor vessel and directed outside the containment structure to the turbine. BWRs operate at about 285 °C. Details of a General Electric BRW/6 reactor vessel are presented in Figure 15.5. A steam–water mixture leaves the top of the core and flows into the separator, where the water droplets are removed and the steam is directed to the turbine. The steam separator assembly is in the upper portion of the vessel. Any steam remaining after exit from the turbine is condensed and the liquid is returned to the reactor vessel. The recirculation pumps permit the coolant flow rate to be varied in the core to change the power output of the reactor.

   A comparison of Figures 15.3 and 15.5 illustrates the significant differences between a PWR and a BWR vessel. The steam (vaporized coolant) in a BWR is radioactive since it is in direct contact with the reactor core; thus, the turbine and piping must be shielded.

3) *Pressurized heavy-water reactor* (PHWR). A number (15 in 2015) of PHWRs are presently in use. As the name implies, heavy water is used as the moderator. The reactor temperature of PHWRs is about 290 °C. The most prevalent of this type is called the CANDU after its country of origin, Canada. The PHWR offers the following advantages over the PWR and BWR: (1) since heavy water is used as the moderator, the uranium fuel does not have to be enriched; (2) they can be refueled without shutting down; and (3) they are not as expensive to build and operate as some reactor types. A schematic of a PHWR is presented in Figure 15.6. The reactor vessel is often called a calandria. The PHWR type shares many characteristics with a PWR. However, a large amount of heavy water is required, and heavy water is expensive. But since the uranium fuel does not have to be enriched, fuel costs are lower. An issue of concern is that the spent fuel contains $^{239}_{94}\mathrm{Pu}$, an isotope that can be used in nuclear weapons.

4) *Gas-cooled reactor* (GCR). These reactors use carbon dioxide as the coolant and graphite as a moderator. GCRs allow the use of natural uranium as a fuel. A schematic of a GCR is presented in Figure 15.7. Carbon dioxide is an effective coolant and does not absorb neutrons. The CO_2 reaches 650 °C in the reactor core. Gases are not good moderators, so graphite is used. Graphite is inexpensive, relatively widely available, and possesses good high-temperature properties.

Issues of concern for nuclear power have traditionally been safety, nuclear weapon proliferation, and disposal of nuclear waste. Dorf (2001) examines issues concerned with nuclear power. Arguably, the dominant issues concerning nuclear power have been radioactive waste and safety.

The handling/storage/disposal of radioactive waste from nuclear power reactors (and military programs) has been an issue of great concern in the USA for many decades. Nuclear fuel removed from power reactors exhibits high levels of radioactivity since the spent fuel contains radioactive fission products and other neutron-activated isotopes. The extracted fuel, generally in the form of rods, is stored on the reactor site in secure water ponds or dry casts. Permanent storage in a nuclear waste repository is the long-term goal, but in the USA the designation and

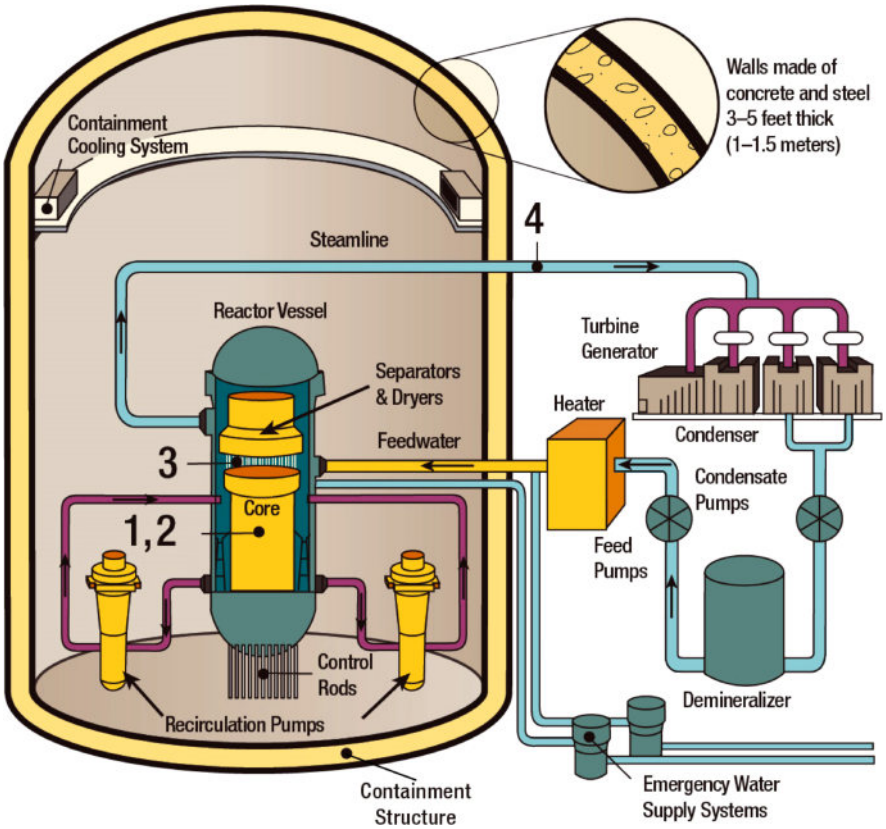

Figure 15.4 Schematic of a BWR, where "1" is the core, "2" is the steam–water mixture from the core, "3" is the moisture separator, and "4" is the turbine/generator. *Source:* US Nuclear Regulatory Commission (http://www.nrc.gov/reactors/bwrs.html).

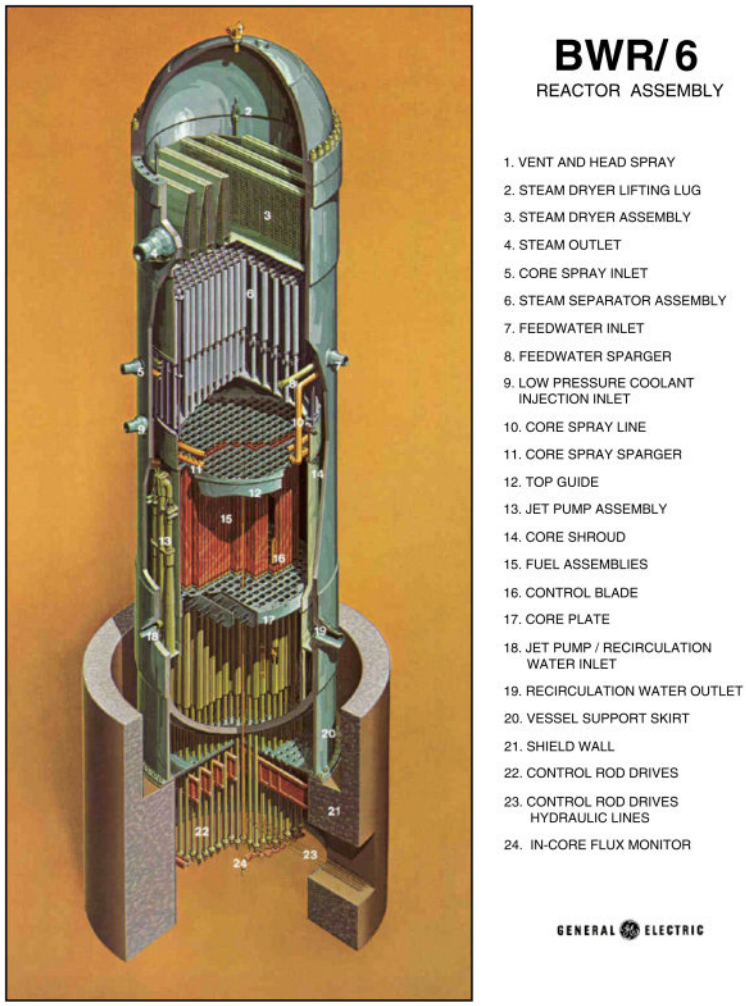

Figure 15.5 Details of a BWR reactor vessel. *Source:* General Electric.

licensing of a long-term nuclear repository has been an emotional political issue. In 1985 Congress mandated a permanent storage site in 1985 in the Yucca Mountains, 130 km north of Los Vega, NV, and reaffirmed that site in 2002. However, since 2008 a bizarre series of events surrounding the site have occurred. In 2011, federal funding was terminated with the concurrence of the Secretary of Energy. The Government Accountability Office stated that the termination was for political, not technical or safety reasons. The Secretary of Energy then established a commission to make recommendations for a repository. The commission's final report was released in January 2012, expressing urgency in finding a repository site. Moreover, the commission recommended that any future repository facility plans should be made by an independent organization (with direct access to the Nuclear Waste Fund), not subject to political and financial control like the DOE! One problem associated with spent fuel is that reprocessing is prohibited in the USA; in other countries, spent nuclear fuel is reprocessed and the recovered uranium is sent back for enrichment and reuse, significantly reducing the volume and half-life of spent fuel nuclear waste. One technique for long-term storage of radioactive waste is to mix the waste with pulverized glass and solidify the glass mixture. The resulting

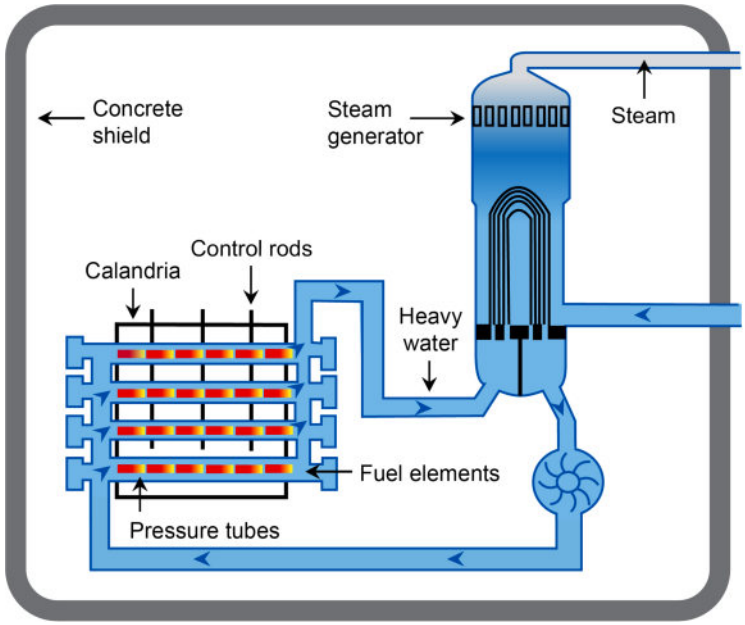

Figure 15.6 Schematic of a PHWR. *Source:* World Nuclear Association (http://world-nuclear.org/Gallery/?galleryId=4455%20&ImageId=36525).

canisters leach only about 0.1% (volume basis) per 10 000 years and are considered environmentally benign.

Although Three Mile Island generated much adverse publicity and resulted in an unbelievably expensive clean-up effort, very little radiation was released to the atmosphere and no public health issues have ever been raised. The disasters at Chernobyl and Fukushima, however, caused significant release to the atmosphere and are worth examining.

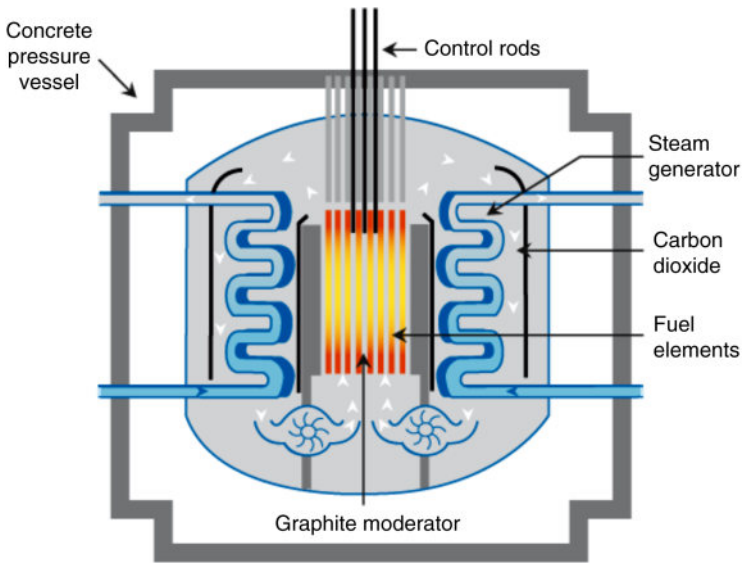

Figure 15.7 Schematic of a GCR. *Source*: World Nuclear Association.

15.3.1 Chernobyl

The Chernobyl nuclear reactor disaster of 1986 is infamous as a catastrophe to both people and the environment. The causes of Chernobyl serve as a litany of how *not* to do things. Details are provided in Deutch and Lester (2004) and at the web sites www.world-nuclear.org/info/chernobyl/inf07.html and https://www.iaea.org/newscenter/focus/chernobyl. The location of Chernobyl is indicated in Figure 15.8.

The reactor was a light-water graphite reactor, a type extensively used by the counties of the former USSR. The general consensus is that the accident was the result of a flawed reactor design coupled with serious operator mistakes in a system characterized by minimal training, nonexistent safety culture, and Cold War isolation. The Chernobyl reactor was a 1000 MW reactor of the RBMK (Reaktor Bolshoy Moshchnosti Kanalnyy) type, a boiling-water-cooled, graphite-moderated design that was the workhorse of the USSR nuclear reactor program. A schematic of the RBMK nuclear reactor is shown in Figure 15.9. The RBMK 1000 uses uranium enriched to about 2% $^{235}_{92}$U. The enriched uranium is contained in 1700 individual pressure tubes, each about 7 m long, through which cooling water flows and steam is generated.

Since graphite is the moderator, excessive boiling reduces the cooling (and neutron absorption by the coolant) without inhibiting neutron absorption since the moderator is unaltered by the excessive boiling. This positive-feedback behavior, termed a positive void coefficient, is one of the problems with the RBMK nuclear reactors, with the effect that at low power levels an increase in steam results in an increase in the reactivity. Conventional BWRs have a negative void coefficient – a decline in reactivity with an increase in boiling since water is the also the moderator in BWRs.

In addition to the inherent stability problems of a positive void coefficient, the Chernobyl accident occurred during a test of a safety system. As part of this test, the flow of cooling water through the core was interrupted, resulting in the reactivity ρ becoming greater than unity. The power started to increase and was estimated to have reached 100 times the nominal full-power output within 4 s! The rapid increase in power meant that not enough time was available to insert the control rods. In any case, by 4 s the enormous power surge had destroyed the fuel channels, effectively blocking any further insertion of the control rods. The fuel then overheated, melted, and fragmented. When steam came into contact with the fragmented fuel, a steam explosion occurred that literally lifted the 1000 ton reactor upper plate. Unlike most reactors

Figure 15.8 The location of Chernobyl. *Source:* World Nuclear Association (www.world-nuclear.org/info/Safety-and-Security/Safety-of-Plants/Chernobyl-Accident/).

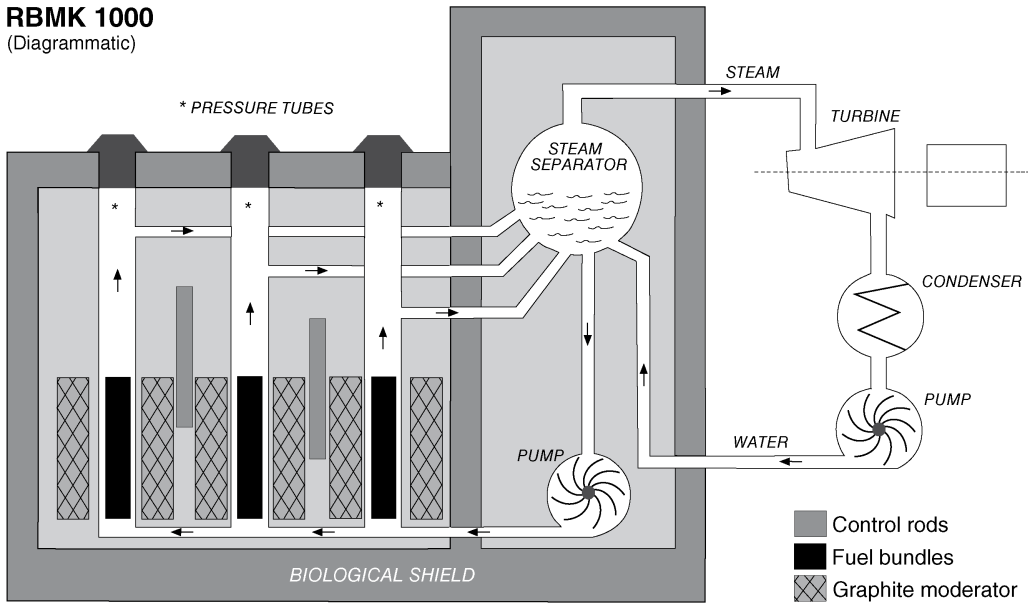

Figure 15.9 RBMK reactor schematic. *Source*: https://www.oecd-nea.org/rp/chernobyl/chernobyl-figure2.pdf.

(especially in the Western nations), the RBMK reactor was not surrounded by a containment structure, so that when the explosion occurred and lifted the upper cover plate, the reactor core was open to the atmosphere. Hydrogen, produced by reactions between the steam, the fuel, and the graphite, then caused a second explosion that resulted in significant amounts of radioactive material being discharged into the atmosphere. To exacerbate matters, the hot graphite ignited and fission continued, producing additional heat and releasing even more radioactive material into the atmosphere. A number of emergency response workers attempting to stabilize the situation and put out the fire eventually died of radiation poisoning. Figure 15.10 depicts the current state of the reactor at Chernobyl. About 5000 t of boron, dolomite, sand, clay, and lead were dropped onto the burning core by helicopters to control the burning and limit the release of radioactive materials to the atmosphere.

The adverse effects of Chernobyl were many. So far, more than 50 deaths have been directly attributed to the disaster. At least 5% of the radioactive core ultimately found its way into the atmosphere. The USSR nuclear program was not cancelled, but no new RBMK reactors were constructed, and the existing RBMK reactors have been retrofitted to make them safer. Safety and training for nuclear reactor personnel have become more important in the former USSR states. Some adjacent towns were permanently evacuated, and long-term health effects on a large number of citizens continue to be of great concern. Indeed, some early estimates place the ultimate death toll in the tens of thousands (Deutch and Lester, 2004). However, more recent studies have concluded that long-term radiation-related health issues are not nearly as significant as early projections indicated (www.world-nuclear.org).

15.3.2 Fukashima Daiichi

The sequence of events and aftermath of the nuclear disaster at Fukushima Daiichi, a Japanese nuclear plant with six reactors, are well known and have been documented, and perhaps

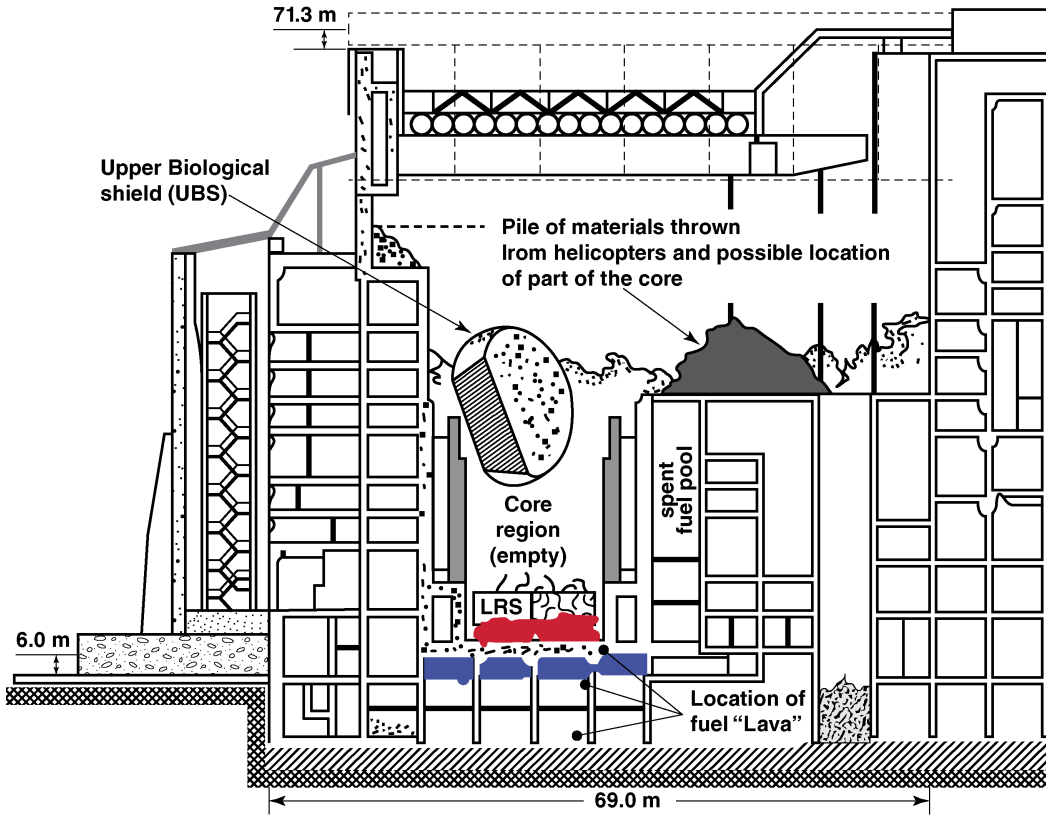

Figure 15.10 Chernobyl reactor after the accident. *Source*: http://chernobylfoundation.org/chernobyl/.

sensationalized, by a number of organizations and media. Consistent explanations and sequences are provided by the WNA (http://www.world-nuclear.org/info/Safety-and-Security/Safety-of-Plants/Fukushima-Accident/), the IAEA (https://www.iaea.org/newscenter/focus/fukushima), the Organisation for Economic Co-operation and Development Nuclear Energy Agency (http://www.oecd-nea.org/press/press-kits/fukushima.html), and Hayes (http://www.academia.edu/1708583/Fukushima_and_the_Politics_of_Nuclear_Energy). The US NRC developed a number of studies related to the event and the lessons learned. Information in the following paragraph was abstracted for these web sites.

On March 11, 2011, Japan experienced a magnitude 9.0 earthquake (centered 130 km offshore the city of Sendai in Miyagi Prefecture), and the resulting tsunami that impacted the Fukushima Daiichi Nuclear Power Station was at least 14 m (45 ft) high. The Fukushima sea wall was 5.7 m high. The earthquake and tsunami resulted in a high death toll and widespread property damage on the eastern coast of Japan. Of the six reactors in the facility, three (Units 1, 2, and 3) were running and three (Units 4, 5, and 6) were shut down for maintenance.

The tsunami destroyed primary and secondary electrical power sources, so that instrumentation, lights, and/or coolant circulating pumps were down. Fortunately, when the earthquake was detected, control rods were inserted in Units 1, 2, and 3. The reactor cores and the stored spent fuel rods continued to generate heat that could not be removed. The pressures in the containment structures eventually became so high that they were vented to the atmosphere,

resulting in the discharge of radioactive gases. The radiation release was about 10% of that of Chernobyl, and the primary isotope released was $^{131}_{53}$I (half-life 8.04 days), with $^{137}_{55}$Cs (half-life 30 years), and $^{134}_{55}$Cs (half-life 2.06 years) also being released. Radioactive release peaked on September 15, mostly from Unit 2. The evidence indicated core meltdowns in Units 1, 2, and 3 also resulted in contamination to the surroundings. At 1–3 days into the disaster, hydrogen explosions occurred in Units 1 and 3. Fire pumps with seawater were in use 1–3 days after the tsunami in an attempt to cool the facility. The offsite electrical supply was restored 11–15 days after the event, and fresh water cooling was available 14–15 days after the event. Mandatory evacuations were ordered (in excess of 100 000 people), and consumption of food from the affected areas was prohibited. Although health issues directly attributed to radiation were small, a number of deaths among those evacuated resulted from stress and other causes. All-in-all, the Japanese handled the Fukushima nuclear crisis more effectively than the USSR handled Chernobyl. What about the aftermath of Fukushima?

By the summer of 2011, all Japanese nuclear power plants were shut down, and the governing political party publicly abandoned nuclear power as a partial solution for Japan's energy needs. However, at the next election, that party was soundly defeated, and the new government moved rapidly to reintroduce nuclear power as part of Japan's energy solution. While the projected percentage of nuclear-supplied electricity in Japan is down from pre-Fukushima estimates, nuclear power has been affirmed as part of the base-load electricity solution for Japan. Many of the existing nuclear power plants in Japan are either online or scheduled to come online, while some of the older ones (and smaller ones) will be decommissioned. Additionally, a number of advanced design nuclear power plants are under construction or planned for construction. Initial world reaction included some countries deciding to eliminate nuclear power. Section 15.3.3 examines recent developments in commercial nuclear reactors.

15.3.3 Nuclear Power in the Twenty-First Century

A convenient concept that aids in understanding the evolution of power nuclear reactors is to refer to technological innovations in terms of reactor "generations." An excellent summary is provided by Goldberg and Rosner (2011). Four generations are identified, spanning the time period from 1950 through to about 2030. Salient features and characteristics of each generation are as follows:

Generation I. The power reactors that initiated commercial nuclear power in the 1950s and 1960s. This generation of reactors typically ran at power levels considered as proof of concept. A well-known example is the Shippingport Reactor in service from 1957 to 1982. All Generation I reactors have been decommissioned.

Generation II. This generation of reactors was designed to be economical and reliable with operating lifetimes of >40 years and includes PWRs, CANDUs, and BWRs. Generation II reactors began operation in the late 1960s and comprise the bulk of the commercial operating power reactors in use today. Most of this generation's reactors (in the West) were manufactured by Westinghouse, General Electric, or AREVA. Generation II reactor designs have been upgraded and modified, especially in Korea and China. Many Generation II operating reactors have had their operating lifetimes extended to well beyond 40 years. This generation of reactors produces significant quantities of spent fuel, which require long-term storage in high-level waste repositories or reprocessing. The Fukushima experience will undoubtedly impact the future evolutions of nuclear reactors.

Generation III. These reactors evolved from Generation II reactors with improvements in fuel technology, thermal efficiency, construction techniques, and standardized designs. Generation

III reactors are expected to have operating lifetimes in excess of 60 years and include the AP-600 by Westinghouse, the advanced BWR (ABWR) by General Electric, the Enhanced CANDU 6 by Atomic Energy of Canada Limited, and the System 80+ by Combustion Engineering. No Generation III reactors are in service in the USA. However, a General Electric–Hitachi ABWR was constructed in only 4 years in Japan!

Generation III+. This generation of reactors represents important evolutionary developments from Generation III reactors and offers significant safety improvements via passive safety features that utilize natural convection and do not require operator interventions. A number of Generation III+ reactors are under development; a partial list includes the AP1000 (based on the AP600), the economic simplified BWR (ESBWR), which is based on the ABWR, and an advanced PWR design (based on the System 80+). Although somewhat dated, *A Technology Roadmap for Generation IV Nuclear Energy Systems* (US DOE Nuclear Energy Research Advisory Committee and the Generation IV International Forum, 2002), is still frequently cited as a source of information on the evolution and future directions of nuclear power. Figure 15.11 was taken from the aforementioned document, and effectively and succinctly delineates both the history and expectations for technology advances in nuclear power.

The US NRC, the Energy Information Administration, and the WNA provide data on advances in nuclear reactor technology and periodically update information on the number, type, and status of new nuclear power installations. The NRC compilation is focused on the USA and is available at http://www.nrc.gov/reactors/new-reactors/design-cert/apr1400.html. The WNA contains similar information, except on a worldwide basis, and is available at http://www.world-nuclear.org/information-library/nuclear-fuel-cycle/nuclear-power-reactors/advanced-nuclear-power-reactors.aspx. The IAEA also publishes extensive information on nuclear power. Table 15.2 was abstracted from these sources and lists pertinent information about advanced nuclear power reactors (especially in the USA).

The status of new nuclear technology and new power plant construction is addressed in detail by the US NRC, the IAEA, and the WNA. The NRC considers mostly activities in the USA, but the others deal on a worldwide basis. In 2015 the WNA stated that 467 nuclear power reactors were in service worldwide with 67 under construction, 166 planned, and 322 proposed. Were all

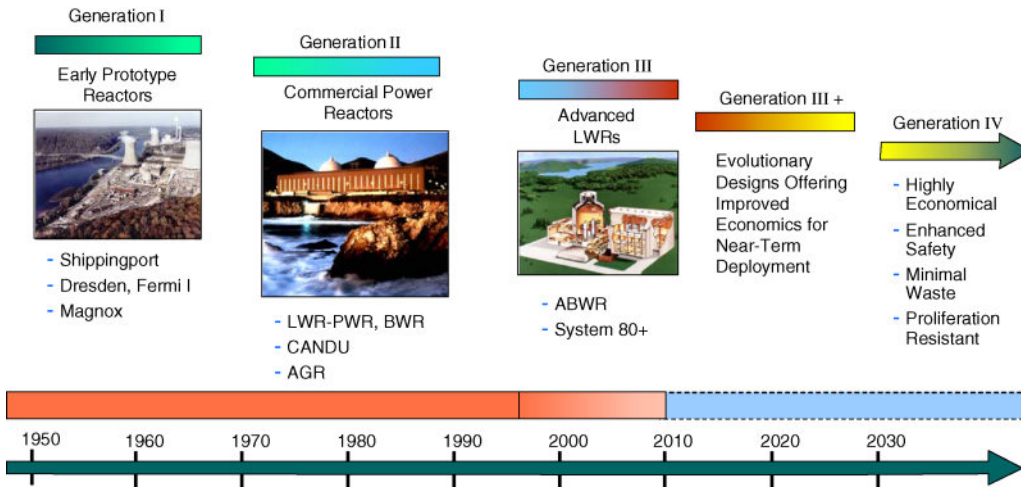

Figure 15.11 Generation IV International Forum Nuclear Power Time line. *Source*: US DOE Nuclear Energy Research Advisory Committee and the Generation IV International Forum (2002).

Table 15.2 Status of selected new nuclear reactor designs.

Name	Manufacturer	Power (MW)	Type	Certification date or status
Generation III				
ABWR	General Electric	1400	BWR	1997
				2010 renew request
AP600	Westinghouse	600	PWR	1999
System 80+	Westinghouse	1300+	PWR	1997
Generation III+				
AP1000	Westinghouse	1000	PWR	2005
				2011 revision
ESBWR	GE-Hitachi	1500	BWR	2014
US EPR	AREVA NP	1750	PWR	Suspended 2015
US-APWR	Mitsubishi	1700	PWR	Expected 2016
APR1400	Korea Electric	1400	PWR	Initiated 2014
EC6	Candu Energy	750	PHWR	2013 (Canada)
ATMEA I	AREVA/Mitsubishi	1150	PWR	2012 (France)
WER-TO1	Atomenergoproekt	1300	PWR	2015 application
Hualong I	China General	1150	PWR	In use (China)

of the proposed and planned to be constructed, the nuclear generating capacity would be 1000 GW, up from the current 379 GW. Most of the proposed and planned reactors are in China, India, and Russia. However, how many of the planned and proposed will actually be constructed is speculative.

In the USA, 5 are under construction, 5 are in the planning stage, and 17 are proposed; were all to be realized, an additional 38 GW capacity would be added to the existing (2015) 99 GW of nuclear capacity. Of the five under construction, four are AP1000s, and the other is an ESBWR. Of the 17 proposed, 10 are AP1000s, 2 are EPRs, 1 is an ESBWR, and 4 are ABWRs.

In addition to the Generation III+ and eneration IV reactors, much activity is being devoted to small light-water reactors (LWRs), also called small modular reactors (SMRs). SMRs are defined as reactors with 300 MW or less output and designed to be fabricated using factory modular production techniques to capture manufacturing economy of scale and to promote shorter construction times. Design characteristics for SMRs include high levels of passive safety features (for malfunctions). Many are to be placed below ground level, providing a high resistance to terrorist threats. SMRs using water as a moderator mostly use <5% enriched uranium and possess refueling intervals of 6 years or less. Indeed, SMRs offer longer fuel cycles (time between refueling) than larger, conventional designs. They are similar in technology to most power and naval reactors.

SMRs can be used for generating electricity (in isolated areas) or for producing high-temperature thermal energy, although some utilities are investigating using LWRs in their capacity suites. SMRs are often viewed as complementing large nuclear power units by giving utilities more power plant options by (1) reducing capital costs and project risks, (2) improving passive safety technology, and (3) providing replacements for aging fossil-fuel generating

Table 15.3 Status of selected SMRs.

Name	Manufacturer	Power (MW)	Type	Certification date or status
NuScale	NuScale Power	150	PWR	Under review
B&W mPower	mPower LLC	180	PWR	Under review
SMR-160	Holtec	160	PWR	Under review
Westinghouse SMR		225	PWR	Under review
SMART	KAERI	100	PWR	Licensed
KLT-40S	OKBM (Russia)	2×32	PWR	In use (icebreakers)

plants. Table 15.3, from the NRC and WNA, delineates SMR activities. The WNA (http://www.world-nuclear.org/information-library/nuclear-fuel-cycle/nuclear-power-reactors/small-nuclear-power-reactors.aspx) contains a discussion of SMRs and an extensive list of current/proposed SMRs as well as a summary of deployed units. IAEA (2014) presents a detailed description of SMRs from many countries.

The increasing activity and interest in fission nuclear power plants is reflected in books on the subject. White (2005) and Sweet (2006) advocate nuclear power as an alternative to fossil-fuel electrical generation, and Shultis and Faw (2008) and LaMarsh and Baratta (2001) are editions of classical nuclear engineering textbooks.

Adams (2005) provides a lucid, documented assessment of the use of fission power in a sustainable scenario and concludes that fission power has the potential to provide a large fraction of the world's energy for many years. He recommends the use of high-conversion reactors, reactors in which the production of fissile isotopes exceeds the consumption of fissile isotopes (breeder nuclear reactors), and the reprocessing of spent and "reburning" nuclear fuel. If a majority of the heavy isotopes can be made to fission, then most of the remaining radioactive waste would decay to a radioactive level less than the original ore in 300 years. Adams points out that significant technical and political challenges must be met in order for this minimum-waste, sustainable scenario to be realized.

15.4 Fusion Power

Fusion power has long been viewed as the panacea of the world's energy problems, and much effort and research over an extended period of time has been devoted to fusion power. A number of books (Harms *et al.*, 2000; Freidberg, 2007; McCracken and Stott, 2012) and research projects demonstrate the optimism about eventual fusion power. A brief overview of fusion is thus appropriate here.

Fusion was briefly mentioned in Section 15.2 as one of three categories of nuclear reactions, and Equation 15.8 was presented as an example of a fusion reaction. Indeed, the primary source of energy from the sun is the fusion of ordinary hydrogen ${}_1^1\mathrm{H}$ into helium ${}_2^4\mathrm{He}$ through a series of fusion reactions;, the results can be summarized as

$$4\,{}_1^1\mathrm{H} \rightarrow {}_2^4\mathrm{He} + 2\,{}_{+1}^0\mathrm{e} + 2\gamma + 2\nu \tag{15.21}$$

which occurs at the sun's core temperature of 15×10^6 K.

A number of reactions are candidates for power production from fusion reactors. The most likely ones and their energy releases are summarized as follows:

$$
\begin{aligned}
&{}^{2}_{1}\mathrm{H} + {}^{2}_{1}\mathrm{H} \rightarrow {}^{3}_{1}\mathrm{H} + {}^{1}_{1}\mathrm{H} + 4.03\ \mathrm{MeV}\\
&{}^{2}_{1}\mathrm{H} + {}^{2}_{1}\mathrm{H} \rightarrow {}^{3}_{2}\mathrm{He} + {}^{1}_{0}\mathrm{n} + 3.27\ \mathrm{MeV}\\
&{}^{2}_{1}\mathrm{H} + {}^{3}_{1}\mathrm{H} \rightarrow {}^{4}_{2}\mathrm{He} + {}^{1}_{0}\mathrm{n} + 17.59\ \mathrm{MeV}\\
&{}^{2}_{1}\mathrm{H} + {}^{3}_{2}\mathrm{He} \rightarrow {}^{4}_{2}\mathrm{He} + {}^{1}_{1}\mathrm{H} + 18.35\ \mathrm{MeV}\\
&{}^{3}_{1}\mathrm{H} + {}^{3}_{1}\mathrm{H} \rightarrow {}^{4}_{2}\mathrm{He} + 2{}^{1}_{0}\mathrm{n} + 11.33\ \mathrm{MeV}
\end{aligned}
\tag{15.22}
$$

As indicated in the fusion reactions in Equation 15.22, energy is released. The energy release results from the difference in the masses of the reactants and products as with fission nuclear reactions. Consider an example, which is based on the second of the reactions listed in Equation 15.22.

Example 15.5
Compute the energy resulting from ${}^{2}_{1}\mathrm{H} + {}^{2}_{1}\mathrm{H} \rightarrow {}^{3}_{2}\mathrm{He} + {}^{1}_{0}\mathrm{n}$, a fusion reaction.

Solution The atomic mass tables (Shultis and Faw, 2008) provide the atomic mass unit values for the reactants and products of the fusion reaction:

- mass of ${}^{2}_{1}\mathrm{H} = 2.014\,102$ amu
- mass of ${}^{1}_{0}\mathrm{n} = 1.008\,665$ amu
- mass of ${}^{3}_{2}\mathrm{He} = 3.016\,029$ amu.

The masses of the reactants and products are

$$\text{Reactants} = 2 \times 2.014\,102\ \text{amu} = 4.028\,204\ \text{amu}$$

$$\text{Products} = 3.016\,029\ \text{amu} + 1.008\,665\ \text{amu} = 4.024\,695\ \text{amu}$$

The change in mass is

$$\Delta m = 4.024\,695\ \text{amu} - 4.028\,204\ \text{amu} = -0.003\,51\ \text{amu}$$

And the energy released is

$$\Delta E = \Delta m c^2 = -0.003\,51\ \text{amu} \times \left(3 \times 10^8 \frac{\text{m}}{\text{s}}\right)^2 = -5.246 \times 10^{-13}\ \text{J} = -3.274\ \text{MeV}$$

Fusion has the great advantages over fission of not requiring high mass number radioactive isotopes as a fuel and not yielding radioactive products (thus alleviating the spent fuel storage/reprocessing problem). Moreover, as the fusion reactions of Equation 15.22 demonstrate, the "fuel" is deuterium (${}^{2}_{1}\mathrm{H}$) and tritium (${}^{3}_{1}\mathrm{H}$), isotopes of hydrogen in which the nucleus contains two and three protons respectively. Although the individual fission of an atom of ${}^{235}_{92}\mathrm{U}$ releases more energy (~200 MeV) than a single fusion reaction (3–18 MeV), on a mass basis the energy release ratio (fusion to fission) is about seven to one (Sorensen, 1983). The great appeal of fusion over fission and fission over chemical reactions (burning) is well summarized on the Princeton Plasma Physics Laboratory web site (www.pppl.gov), from which Table 15.4 is adapted. Table 15.4 delineates the fuel requirements for a 1000 MW power plant operating continuously for a year using coal (black or brown), nuclear fission, and nuclear fusion. While the fuel consumption of coal-fired power plants is measured in millions of tonnes and the fuel consumption of nuclear fission plants in tonnes, the fuel consumption of a fusion plant is

Table 15.4 Fuel consumption for various power plant types.

Plant type	Quantity of fuel used
Coal-fired	4.4×10^6 t (metric tonne) of black coal
Coal-fired	10.8×10^6 t of brown coal
Fission	1.3 t of $^{235}_{92}$U
Fusion	150 kg of deuterium and 500 kg of lithium

measured in kilograms! The deuterium part of the fusion fuel requirement poses little problem since about 1 part in 5000 of sea water is deuterium. Since the oceans contain $\sim 10^{15}$ tons of deuterium, the deuterium supply for fusion is essentially unbounded. The lithium requirement is more problematic, but, compared with other energy sources (coal and uranium), is also plentiful.

Why, then, with all the possibilities, has fusion power not been realized? The requirements for fusion are very difficult to attain and sustain. Any of the fusion reactions listed in Equation 15.22 requires the individual fuel nuclei to come together and then fuse. But all nuclei have positive charges; thus, the nuclei will repel each other unless the kinetic energy of each nucleus is sufficient to overcome the Coulomb repulsive force. For fusion to occur, the speed of each nucleus must be very high, and very high kinetic energies corresponds to very high temperature, since on average (Shultis and Faw 2008)

$$E_{\text{avg}} = kT \tag{15.23}$$

Depending on the fusion reaction, E_{avg} values of from a few to several hundred kilo-electronvolts are needed in order to ensure that the Coulomb force is overcome and the fuel nuclei can be in position to fuse. The resulting temperatures range is $(10\text{–}300) \times 10^6$ K. At these elevated temperature, the reactants have been ionized, with all electrons stripped from their orbits about the nucleus, and a plasma results. The plasma consists of electrons and the positively charged nuclei. The basic problems for a fusion reactor are threefold: (1) how to generate the high temperatures required (basically solved), (2) how to contain the hot plasma (in progress), and (3) how to achieve the required density of the plasma so that fusion takes place (in progress).

Of the fusion reactions listed in Equation 15.22, the one of most interest is the deuterium–tritium reaction:

$$^2_1\text{H} + {}^3_1\text{H} \rightarrow {}^4_2\text{He} + {}^1_0\text{n} + 17.59\ \text{MeV} \tag{15.24}$$

The individual energy release per fusion reaction is high (17.59 MeV). The minimum temperature required for deuterium–tritium fusion is 45×10^6 K; however, the generally accepted temperature for a deuterium–tritium fusion power plant is about 100×10^6 K. The deuterium–deuterium fusion reaction, with only 4.03 MeV energy release, requires 500×10^6 K – a factor of five higher than the deuterium–tritium fusion reaction. Since tritium, $^3_1$H, has a half-life of only 12.33 years, none occurs in nature. Thus, part of the problem with a fusion reactor using the deuterium–tritium reaction is providing the tritium. Fortunately, tritium is relatively easy to produce by means of neutron capture by lithium. The fission reactions of the two isotopes of lithium are as follows:

$$\begin{aligned} {}^6_3\text{Li} + {}^1_0\text{n} &\rightarrow {}^3_1\text{H} + {}^4_2\text{He} + 4.78\ \text{MeV} \\ {}^7_3\text{Li} + {}^1_0\text{n} &\rightarrow {}^3_1\text{H} + {}^4_2\text{He} + {}^1_0\text{n} - 2.47\ \text{MeV} \end{aligned} \tag{15.25}$$

But how is a plasma at 100×10^6 K contained? Two methods have been proposed and extensively researched: (1) magnetic containment and (2) inertial containment. Since the electrons and ions are charged, the plasma can be confined by a magnetic field. In magnetic containment, the magnetic field forces the particles to follow spiral paths. Consequently, the charged particles in the plasma are confined by the magnetic field and do not strike the fusion reactor walls. Inertial confinement is based on using high-energy lasers to vaporize, ionize, and ignite the fusion reaction in such a short period of time ($\sim 10^{-10}$ s) that the fuel does not have an opportunity to expand – hence it is confined by its own inertia. Extensive research has been accomplished using both techniques, but magnetic confinement is the more promising of the two. The production of electricity from fusion has been a dream for more than 70 years, but the technical problems are daunting. Nonetheless, significant progress has been made in attaining fusion, but much work is still required before a fusion power plant becomes a reality.

In what form might a fusion power plant appear? Figure 15.12 is a schematic of a fusion power plant. The overall shape of the fusion reactor is toroidal, a requirement that results from the magnetic containment and the helical path the charged nuclei must traverse. In fusion research projects, toroidal fusion vessels are called "tokamaks." Tokamaks at the Princeton Plasma Physics Laboratory and the Joint European Torus (JET) are perhaps the best known of these research vessels, but tokamaks are being used for fusion research in a number of countries.

The neutrons (14 MeV) are absorbed in the lithium-containing breeding blanket that surrounds the fusion chamber. Neutron capture by the lithium nucleus results in fission nuclear reactions that generate (or breed) tritium, a required fuel (see Equation 15.25). The tritium is separated and fed back into the fusion reactor for use as a fuel. As is evident from Figure 15.12, a fusion power plant is much more involved than a fission power plant. If a deuterium–tritium reaction is to occur, then lithium must be injected into the breeding blanket so that tritium results. Unburned deuterium, tritium, and helium are recovered from the reactor; the helium, which has commercial value, is removed and sold, and the deuterium and tritium are reinjected. Energy is recovered from the reactor vessel and used to generate electricity.

But, the germane question is, "When will fusion power be a reality?" The most realistic (and likely) answer is provided by a roadmap report from EUROfusion (EFDA, 2012). The plans required to achieve power production at the few hundred MW level by the 2050 are detailed in

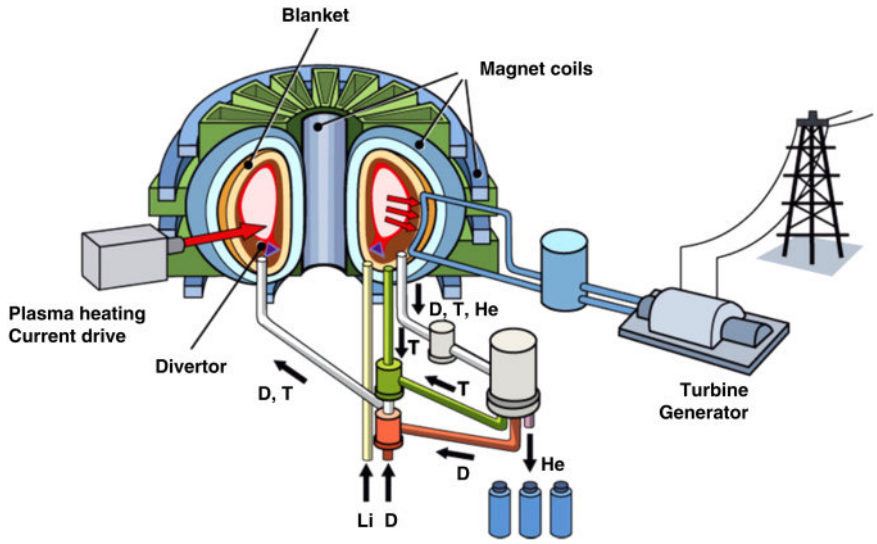

Figure 15.12 Schematic of a fusion power plant. *Source*: Maisonnier *et al.* (2005).

the report. Widespread commercial generation of electricity by fusion would take place after that time. The roadmap report is quite candid about the technical challenges remaining, and the possibility of unforeseen problems that could delay commercialization, and presents a realistic assessment of the needed technology for commercial fusion power. The International Thermonuclear Experimental Reactor (ITER) program, a part of EUROfusion, involves using the next-generation tokamak (discussed in the next paragraph) to resolve technical issues needed for the production of fusion power. The ITER assessment of fusion progress (from www.iter.org) is

> Fusion research has increased key fusion plasma performance parameters by a factor of 10,000 over 50 years; research is now less than a factor of 10 away from producing the core of a fusion power plant.

Although other organization and countries are at work on realizing fusion power, EUROfusion is arguably the leader. EUROfusion evolved from the European Fusion Development Agreement (EFDA) organization. EFDA, now, EUROfusion, oversees the JET facility and is charged with constructing the ITER, the next-generation research tokamak.

JET is currently one of the largest tokamaks in operation and has been known as the world's foremost tokamak machine for 20 years. In 1997 it successfully produced a peak power of 16 MW with 10 MW being sustained over a 0.5 s period (Wesson, 2000). The most significant fusion research project of the next few decades is the ITER program, a joint project funded by many countries, including the USA and many European countries. The ITER project (www.iter.org) has as its goals the development of equipment, techniques, and procedures required for commercial fusion power generation, and is viewed as perhaps the last step before the realization of commercial fusion power. Specifically, the ITER goals lie in the development of plasma regimes of operation and in developing techniques to manage the plasma exhaust heat. A second issue is concerned with the area of the tokamak wall that is exposed to the highest heat and particle fluxes: the divertor. ITER investigations will include divertor configurations which could reduce the heat loads. Specifically, the ITER goals are fourfold (https://www.eurofusion.org/): (1) to produce more power than it consumes; (2) to maintain fusion plasma for up to 8 min; (3) to test technologies needed for fusion power plants; and (4) to test and develop concepts for breeding tritium from a blanket surrounding the plasma. Figure 15.13 is a cut-away, same-scale rendering of the JET and ITER fusion reactor vessels. The ITER fusion reactor is under construction at Cadarache, France. US participation and contributions for the ITER program are detailed at www.science.energy.gov, https://burningplasma.org/, and www.usiter.org.

The ITER program will be followed by the DEMO (Demonstration Fusion Power Reactor) program, also by EUROfusion, that is viewed as the last step before commercialization of fusion power. An excerpt from EUROfusion's statement about DEMO is

> The central requirements for DEMO lie in its capability to generate several 100 Megawatt of net electricity to the grid and to operate with a closed fuel-cycle (i.e., to produce and burn tritium in a closed cycle). A number of outstanding technology and physics integration issues must be resolved before a DEMO plant concept selection is made. Each of them has very strong interdependencies . . .

Were fusion power to become a reality, the energy economy of the world would be dramatically changed. But, even barring unforeseen technical problems, fusion power is not likely to be a reality for about 50 years. Thus, the concepts in this book retain their importance for many years – perhaps even after fusion power is a reality.

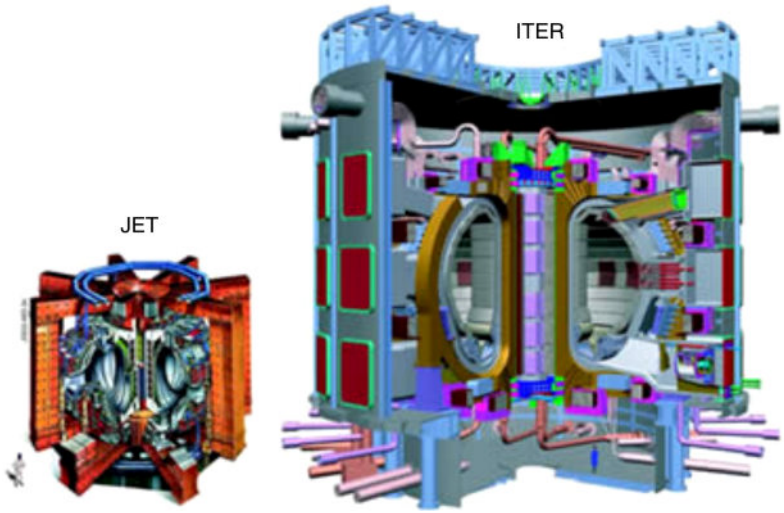

Figure 15.13 JET and ITER fusion vessel cut-away sketch.

15.5 Closure

Electricity from nuclear fission power plants represents a significant percentage of the electricity generated. Fission power plant technology is relatively mature, but questions about safety issues, nuclear proliferation, and long-term radioactive waste disposal along with a generally adverse political climate have clouded the future of fission power. Nonetheless, energy security and greenhouse gas emission concerns have provided the impetus for renewed consideration of new nuclear fission power plant construction, and many in the electric power industry believe nuclear power will increase in importance and acceptance in the next few decades.

Fusion power represents a solution to the world's energy crisis and offers many advantages over both nuclear fission and conventional fuel for electricity and power generation. However, the technical problems are daunting, and even optimists in the fusion community suggest that 2050 may be as soon as fusion can be commercially exploited for power generation.

References

Adams, M.L. (2005) Sustainable energy from nuclear fission power. *The Bridge*, **32**. (4). https://www.nae.edu/Publications/Bridge/ExpandingFrontiersofEngineering7308/SustainableEnergyfromNuclearFissionPower.aspx (accessed October 27, 2016).

Maisonnier, D., Cook, I., Sardain, P., *et al.* (2005) *A Conceptual Study of Commercial Fusion Power Plants*. EFDA-RP-RE-5.0, European Fusion Development Agreement. https://www.euro-fusion.org/wpcms/wp-content/uploads/2012/01/PPCS_overall_report_final.pdf (accessed October 27, 2016).

Deutch, J.M. and Lester, R.K. (2004) *Making Technology Work: Applications in Energy and the Environment*. Cambridge University Press, Cambridge.

Dorf, R.C. (2001) *Technology, Humans, and Society: Toward a Sustainable World*. Academic Press, San Diego, CA.

El-Wakil, M.M. (1984) *Powerplant Technology*. McGraw-Hill, New York.

EFDA (2012) *Fusion Electricity: A Roadmap to the Realisation of Fusion Energy*. European Fusion Development Agreement. https://www.euro-fusion.org/wpcms/wp-content/uploads/2013/01/JG12.356-web.pdf (accessed October 27, 2016).

Fay, J.A. and Golomb, D.S. (2012) *Energy and the Environment*, 2nd edn. Oxford University Press, Oxford.

Firestone, R.V. and Shirley, V.S. (eds) (1999) *Table of Isotopes*. John Wiley & Sons, Inc., New York.

Freidberg, J.P. (2007) *Plasma Physics and Fusion Energy*. Cambridge University Press, Cambridge.

Goldberg, S.M. and Rosner, R. (2011) *Nuclear Reactors: Generation to Generation*. American Academy of Arts and Sciences, Cambridge, MA. https://www.amacad.org/pdfs/nuclearReactors.pdf (accessed October 27, 2016).

Harms, A.A., Kingdon, D.R., and Schoepf, K.F. (2000) *Principles of Fusion Energy*. World Scientific Publishing, Singapore.

IAEA (2014) *Advances in Small Modular Reactor Technology Development*. International Atomic Energy Agency, Vienna. https://www.iaea.org/NuclearPower/Downloadable/SMR/files/IAEA_SMR_Booklet_2014.pdf (accessed October 27, 2016).

IAEA (2015) *Nuclear Power Reactors in the World*. International Atomic Energy Agency, Vienna. http://www-pub.iaea.org/MTCD/Publications/PDF/rds2-35web-85937611.pdf (accessed October 27, 2016).

LaMarsh, J.R. and Baratta, A.J. (2001) *Introduction to Nuclear Engineering*, 3rd edn. Addison-Wesley, New York.

McCracken, G. and Stott, P. (2012) *Fusion: The Energy of the Universe*, 2nd edn. Elsevier, Amsterdam.

Murray, R.L. (1961) *Introduction to Nuclear Engineering*, 2nd edn. Prentice-Hall, Englewood Cliffs, NJ.

Nero, A.V. (1979) *A Guidebook to Nuclear Reactors*. University of California Press, Berkeley, CA.

Shultis, J.K. and Faw, R.E. (2008) *Fundamentals of Nuclear Science and Engineering*, 2nd edn. CRC Press, Boca Raton, FL.

Sorensen, H.A. (1983) *Energy Conversion Systems*. John Wiley & Sons, Inc., New York.

Sweet, W. (2008) *Kicking the Habit: Global Warming and the Case for Renewable and Nuclear Energy*. Columbia University Press, New York.

US DOE Nuclear Energy Research Advisory Committee and the Generation IV International Forum (2002) *A Technology Roadmap for Generation IV Nuclear Energy Systems*. https://www.gen-4.org/gif/upload/docs/application/pdf/2013-09/genivroadmap2002.pdf (accessed October 27, 2016).

Wesson, J. (2000) *The Science of JET*. JET Joint Undertaking, Abingdon, UK. http://www.euro-fusionscipub.org/archives/jet-archive/the-science-of-jet (accessed October 27, 2016).

Weston, K.C. (1992) *Energy Conversion*. West, St. Paul, MN.

White, R.S. (2005) *Energy for the Public: The Case for Increased Nuclear Fission Energy*. Santa Barbara, CA.

WNA (2015) Nuclear Power Reactor Characteristics Pocket Guide. World Nuclear Association. http://www.world-nuclear.org/uploadedFiles/org/WNA/Publications/Nuclear_Information/Pocket%20Guide%20Reactors.pdf (accessed October 27, 2016).

16

Transportation and Hybrid and Electric Vehicles

16.1 Transportation Energy Usage Alternatives to Internal Combustion Engines

Figure 1.10 presents the end-point energy usages for the USA in 2014. Transportation accounted for 28% of the energy used in the USA – more than the residential or commercial energy used. Figure 16.1 shows the breakdown of transportation energy as a function of energy use by vehicle type. Light trucks, cars and motorcycles, and other trucks account for 80% of the 2014 transportation energy usage in the USA. Aviation represents an additional 7% and has special needs and standards. Boats and ships, trains and buses, military uses, pipeline fuel, and lubricants make up for the remainder. Thus, cars, trucks, and motorcycles represent the greatest potential for significant energy savings. This chapter examines how that potential might be realized.

Internal combustion engines (ICEs) were the dominant power source for motor vehicles for most of the twentieth century. As automobiles were being developed in the late nineteenth century, a number of power sources, including steam and electricity as well as ICEs, were explored. Steam was too cumbersome, and electricity, with storage and control issues, was beyond the technology of the day for mass-produced and mass-used vehicles. The ICE "won" out because hydrocarbon fuels of high energy density could be supplied locally and because the ICE technology matured rapidly enough to displace the other options. Kirsch (2000) contains an interesting discussion of how electric vehicle usage might have been different had some circumstances changed. However, the operating characteristics of ICEs and the Carnot efficiency limitation of heat engines limit their overall operating efficiency. In the days of cheap gas and little concern for greenhouse gas emissions, few economic or environmental incentives existed for alternative power sources for vehicles. However, that started changing in the 1970s, and alternatives to ICEs have been under serious consideration for a number of years.

Ehsani *et al*. (2010), Fuhs (2009), and Mi *et al*. (2011) are good textbooks devoted to hybrid and electric vehicles. Additionally, a number of web sites contain useful information, although care must be taken to ensure the accuracy of the information. A good place to start is to consider what characteristics of ICEs, other than the Carnot limitation, result in inefficiencies. Figure 16.2 presents ideal torque and power functional forms for a power source in a motor vehicle. The abscissa is the motor speed. The ideal performance is for constant power over a wide range of motor speeds, ensuring that the engine operates at its best efficiency point. The torque then becomes a decreasing function of speed (and is nearly hyperbolic with speed). At low speeds, torque must be constant in order to avoid tire and road slippage and to provide the power needed for vehicle acceleration, climbing, and towing.

Figure 16.3 illustrates the typical torque and power performance of an internal combustion engine. The ideal and ICE performance curves are not very congruent. Because of these mismatches, ICE vehicles have transmissions with different gear ratios and operate much of the

Alternative Energy Systems and Applications, Second Edition. B. K. Hodge.

Companion website: www.wiley.com\go\Hodge\AESystemsandApplications2E

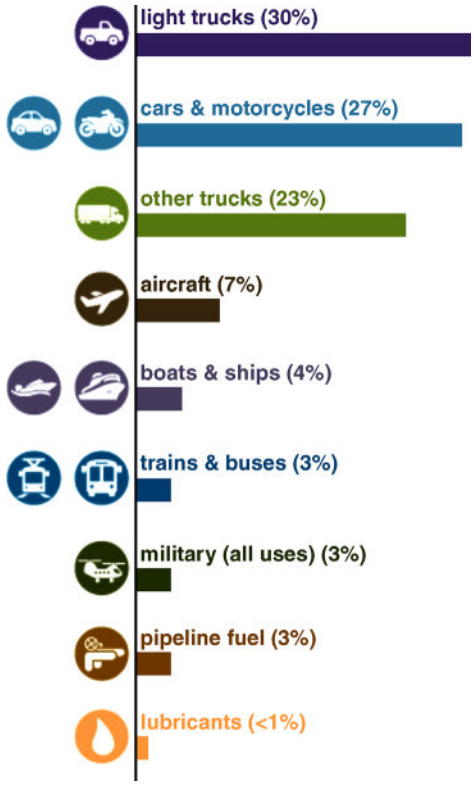

Figure 16.1 Transportation energy use for 2014 by type. *Source*: http://www.eia.gov/Energyexplained/?page=us_energy_transportation#tab2.

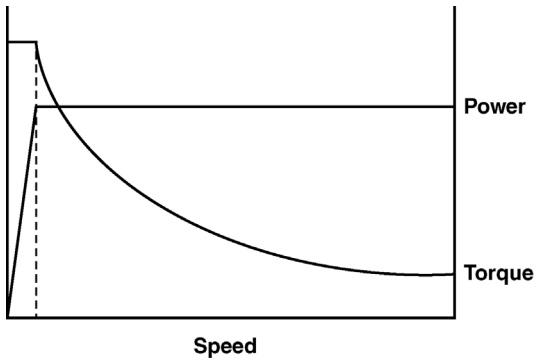

Figure 16.2 Ideal power and torque relationships for a motor vehicle power source.

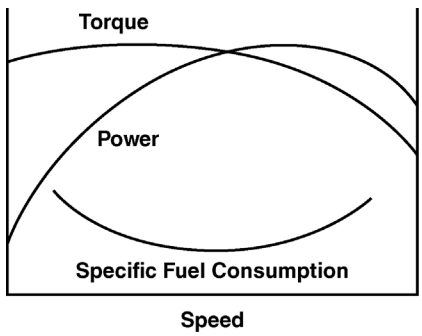

Figure 16.3 Power and torque characteristics for an ICE.

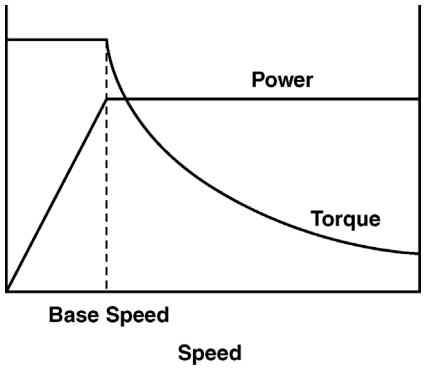

Figure 16.4 Power and torque characteristics for an electric motor.

time with high specific fuel consumptions. Consider the power and torque characteristics of an electric motor as illustrated in Figure 16.4. The electric motor power and torque characteristics as a function of motor speed mimic those of the ideal in Figure 16.2. Electric motor torque and power are well matched to the ideal torque and power. Up to a base speed, electric motors provide constant torque; beyond the base speed, the power is constant and torque decreases nearly hyperbolically with motor speed – in the same fashion as the ideal. Since electric motor characteristics match those of the ideal, a transmission (gearing) is not needed.

Given the discussion in the previous paragraphs, three tactics emerge as candidates to improve the overall energy efficiencies of motor vehicles: (1) change the engine to a non-heat engine with characteristics closer to the ideal, (2) remove the engine and use only an electric motor, and (3) combine the best features of an ICE and an electric motor in a hybrid system. Each of these will be examined in Section 16.2, but before that some additional considerations are appropriate.

A hybrid-electric vehicle is defined as a vehicle that contains an ICE and an electric motor and, depending on the system configuration (examined in Section 16.2), is capable of operating on either or both. In a hybrid, the ICE is downsized from a conventional (ICE-only) vehicle in such a fashion as to result in the ICE operating near it best efficiency point and being supplemented as needed by the electric motor. A hybrid's miles per gallon (mpg) is increased over that of a conventional vehicle's. Following Fuhs (2009), a conventional vehicle with a usage of M miles per year and a gas mileage (in miles per gallon) of $\mathrm{MPG_C}$ requires G_C gallons per year

$$G_C = \frac{M}{\mathrm{MPG_C}} \tag{16.1}$$

And a hybrid with a gas mileage of $\mathrm{MPG_H}$ requires G_H gallons per year:

$$G_H = \frac{M}{\mathrm{MPG_H}} \tag{16.2}$$

If f is the fractional increase in miles per gallon by the hybrid, then

$$\mathrm{MPG_H} = \mathrm{MPG_C}(1+f) \tag{16.3}$$

And the savings G_S in gallons per year by using a hybrid becomes

$$\begin{aligned} G_S &= G_C - G_H = \frac{M}{\mathrm{MPG_C}} - \frac{M}{\mathrm{MPG_H}} = M\frac{\mathrm{MPG_H} - \mathrm{MPG_C}}{\mathrm{MPG_C} \times \mathrm{MPG_H}} \\ &= M\frac{\mathrm{MPG_C}(1+f) - \mathrm{MPG_C}}{\mathrm{MPG_C} \times \mathrm{MPG_C} \times (1+f)} = M\frac{\mathrm{MPG_C} \times f}{\mathrm{MPG_C^2} \times (1+f)} \\ &= \frac{M}{\mathrm{MPG_C}}\frac{f}{1+f} \end{aligned} \tag{16.4}$$

Consider an example using typical conditions for an SUV or pickup truck and a small, fuel-efficient vehicle.

Example 16.1
An SUV or pickup truck has a gas mileage of 20 mpg, and a small, fuel-efficient vehicle possesses a gas mileage of 32 mpg. Both are driven 15 000 miles per year. If the hybrid versions have $f = 0.2$, how many gallons of gasoline per year are saved? What are the miles per gallon for each hybrid vehicle?

Solution For the SUV vehicle

$$(G_S)_{SUV} = \frac{M}{MPG_C}\frac{f}{1+f} = \frac{15\,000\ \text{miles/year}}{20\ \text{mpg}}\frac{0.2}{1+0.2} = 125\frac{\text{gal}}{\text{year}}$$

And for the small, fuel-efficient vehicle we have

$$(G_S)_{SmallEE} = \frac{M}{MPG_C}\frac{f}{1+f} = \frac{15\,000\ \text{miles/year}}{32\ \text{mpg}}\frac{0.2}{1+0.2} = 78\frac{\text{gal}}{\text{year}}$$

Both exhibit the same percentage gas savings, but since the SUV has a lower gas miles per gallon, its savings are larger than the small, fuel-efficient vehicle. The miles per gallon of the hybrid versions of the two vehicles become

$$(MPG_H)_{SUV} = (1+f)(MPG_C)_{SUV} = (1+0.2)\times 20\ \text{mpg} = 24\ \text{mpg}$$
$$(MPG_H)_{SmallEE} = (1+f)(MPG_C)_{SmallEEE} = (1+0.2)\times 32\ \text{mpg} = 38.4\ \text{mpg}$$

This simple example points out that an $f = 0.2$, a mild hybrid modification (see Section 16.2) to a conventional vehicle, can lead to significant fuel savings. Section 16.2 examines characteristics of hybrid and electric vehicles.

16.2 Hybrid and Electric Vehicles

The US Energy Information Administration (EIA) provides definitions of a hybrid-electric vehicle and an electric-motor vehicle; the following definitions were modified from the EIA versions.

- *Hybrid-electric vehicle.* An electric vehicle that either (1) operates solely on electricity, but contains an internal combustion motor that generates additional electricity or (2) contains an electric system and an internal combustion system and is capable of operating on either system.
- *Electric-motor vehicle.* A motor vehicle powered by an electric motor that draws current from rechargeable storage batteries or other sources of electric power.

ICE technology is mature and well understood, with only incremental increases in efficiency expected from technological innovations. Hybrid and electric vehicles are more complex than ICE stand-alone vehicles. Depending on the configuration, hybrid and electric vehicles can feature ICEs, large battery capacities, electric motor-generators, regenerative braking accommodations, a myriad of energy-saving/–harvesting systems, and external electrical plug-in ports. A striking feature of hybrid and electric vehicles is the extent and sophistication of the control systems required to monitor/supervise/troubleshoot all the features. The increased number of components, as well as the control protocols, required for hybrid and electric vehicles mean that initial costs are higher, maintenance issues are more varied and complex, and component-replacement costs are larger (and perhaps more frequent).

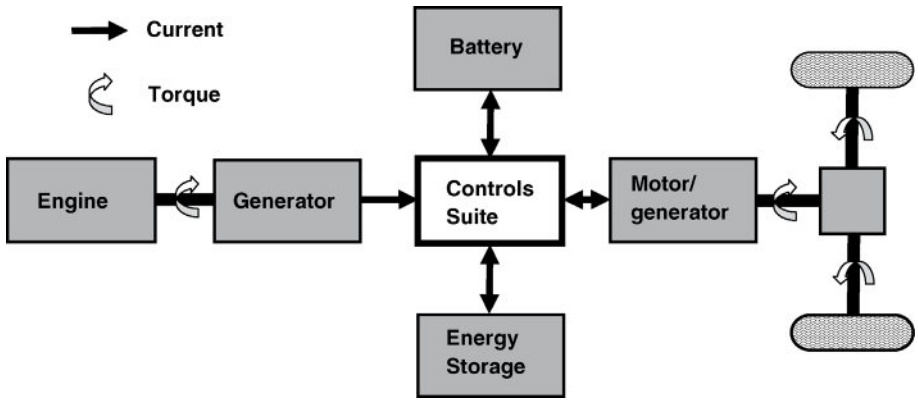

Figure 16.5 Series hybrid system schematic.

Hybrid-electric vehicles will be considered first. A hybrid contains an ICE (or a fuel cell) and an electrical storage device, typically a battery, but a capacitor or a flywheel can also be used. Fuhs (2009) contains a particularly good discussion of many aspects of hybrid vehicles. A characteristic of hybrids is the ability to harvest some of the energy used in accelerating the vehicle by using regenerative braking – transforming kinetic energy to electrical energy by using the "motor" as a generator. In addition to the regenerative braking feature, hybrids often possess fuel-saving features such as engine-off during stops, electric-only propulsion, downsized engines, and electric-motor vehicle launch since ICEs have low starting torque. An operating-design philosophy for hybrid-electric vehicles has the following tenets:

1) To operate the electric motor when possible (minimizes emissions/fuel required).
2) To use the ICE only when needed and, if possible, only at the best efficiency point (minimum fuel consumption).

Hybrid systems may be configured as series, parallel, or compound; a vital component of a hybrid system is the control interface between the engine and electric motor that permits efficient operation to be maintained.

A schematic for a typical series system is illustrated in Figure 16.5. The series system places the ICE and the electric motor in series with the drive train. Additional elements are required to generate electricity, to charge the battery, to provide the myriad control functions needed, and to store recovered energy from options such as regenerative braking. These functions are schematically indicated in Figure 16.5; in a specific vehicle the sequences/layout/interconnectivities may differ. In a series hybrid, the ICE drives a generator, rather than drive shaft; the electric motor is the only means of powering the wheels. Because the electric motor is directly connected to the drive shaft, and is generally well matched in terms of power, torque, and speed, a transmission is not required. The generator provides power to charge the battery as well as to power the electric motor. If needed for acceleration or climbing, the motor can draw electricity from both the generator and the battery. In regenerative braking, the motor acts as a generator with energy recovered going either to the battery or to another energy storage device. A controls suite, including electronics, is an integral part of any hybrid and is much more complex than for a conventional vehicle. The more complex the hybrid's operating options, the more complicated the controls suite. The Chevrolet Volt is essentially a series hybrid, as are almost all diesel-electric railroad engines.

Another common type of hybrid vehicle is the parallel. Figure 16.6 contains a schematic of a typical parallel hybrid system. The key feature of a parallel hybrid is that both the electric motor and the ICE are connected to the drive shaft. The same system elements are present as in the

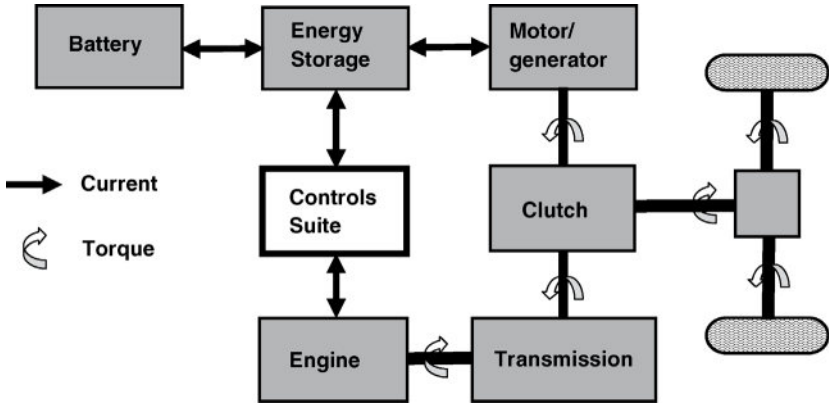

Figure 16.6 Parallel hybrid system schematic.

series hybrid, including the controls function, but the interconnections are different. The motor and a large generator are often combined into a single unit. The battery can be recharged when the ICE power output is larger than that required for vehicle motion and during regenerative braking. Most parallel hybrids have a mechanical link between the ICE and the electric motor, so that the battery cannot be recharged when the vehicle is stationary. When only the electric motor is being used, or during regenerative braking, the ICE is either not running or idling. The flexibility of a parallel-hybrid vehicle permits the following operating regimes:

1) City driving – electric motor only.
2) Road operation, low speed – ICE only.
3) Road operation, higher speed or acceleration – ICE plus electric motor in parallel.
4) Battery recharging – if ICE power output is higher than required for the vehicle speed, the excess can be used for battery recharging.
5) Regenerative braking – when decelerating or braking, the motor acts as a generator and harvests kinetic energy.

The Honda Accord and Civic hybrids are parallel hybrids, but, due to poor sales, 2015 was the last year the Civic hybrid was manufactured. The Honda Accord hybrid was completely redesigned for 2016.

More common than either the series or parallel hybrid is the combined series and parallel hybrid, also called the power-split hybrid. Figure 16.7 illustrates a schematic of a combined

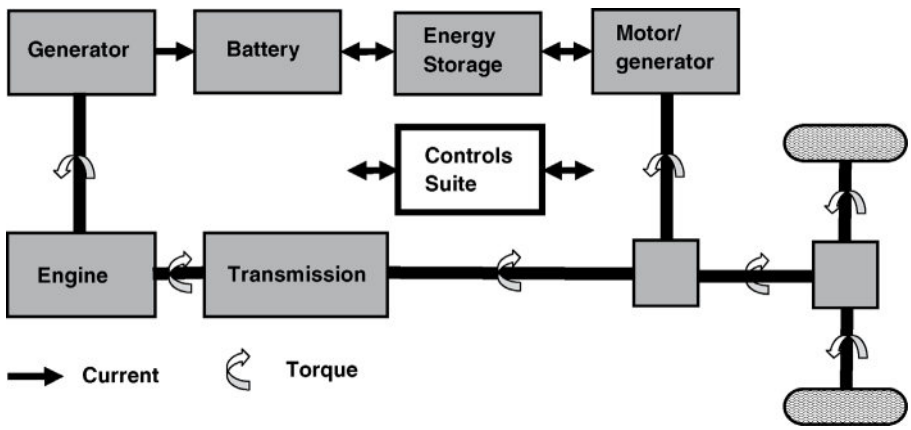

Figure 16.7 Combined series and parallel (or power-split) hybrid schematic.

hybrid. As might be expected, combined hybrids possess both series and parallel systems architecture. The most significant feature of a combined hybrid is that the ICE and the electric motor both have direct connections to the drive shaft. In Figure 16.7, the connections for the block "Control Suite" are not shown to avoid clutter in the schematic. Because of the increased complexity of a combined hybrid, the system is more expensive and the control protocols are more complex than for a parallel hybrid. This arrangement effectively decouples the power supplied by the ICE from the power required to propel the vehicle. A combined hybrid utilizes a smaller, more efficient ICE since the electric motor can directly assist when high starting torque is needed. The Toyoda Prius II, the best-selling hybrid in the USA (see Section 16.3), is a combined series–parallel hybrid vehicle.

While series, parallel, and combined hybrid configurations are used to distinguish between characteristics of hybrids, the concept of hybridness or hybridization is also used to distinguish hybrid characteristics. Hybridness is defined as the ratio of the total power of the electric motors divided by the sum of the power of the electric motors and the power of the ICE:

$$H = \frac{\text{Power of all electric motors}}{\text{Power of all electric motors} + \text{ICE power}} \tag{16.5}$$

The dominator value of Equation (16.5) is not necessarily the total power available to the hybrid vehicle as the peak power for the electric motor and the ICE may not coincide at the same vehicle speed. A small value of H correspond to "mild" hybridness, while a value near 0.50 is described as "full" hybridness. A value of $H = 1$ signifies the vehicle has only an electric motor (no ICE). An $H = 0.75$ means large electrical power compared with the ICE power with a large (and heavy) battery.

Example 16.2
Using information from the Toyota web site on the Pruis, estimate the hybridness of the Toyota Prius.

Solution A convenient web address is http://www.toyota.com/prius/features/mechanical_performance/1223/1225/1227/1229, from which the ICE engine specifications are1.8-liter 4-cylinder DOHC 16-valve with variable valve timing; 73 kW, 5200 rpm

And the electric motor specifications arePermanent magnet AC synchronous motor; 60 kW

The hybridness is

$$H = \frac{\text{Power of all electric motors}}{\text{Power of all electric motors} + \text{ICE power}} = \frac{60\,\text{kW}}{60\,\text{kW} + 73\,\text{kW}} = 0.45$$

Not surprisingly, the Toyota Prius is considered a full hybrid.

Hybridness is a continuum from $H = 0$ for a conventional vehicle to $H = 1$ for an electric-motor vehicle. Figure 16.8 delineates the nature of that continuum. A "mild" hybrid is dominated by the ICE, while in "full" hybrids the ICE and electric motor outputs are balanced. A hybridness much greater than 0.5 is typically designated as a "plug-in hybrid vehicle" (PHEV), meaning that the ICE power is much less than the electric motor power. As the hybridness increases from $H \approx 0.5$, a series configuration is generally used; while as the hybridness decreases from $H \approx 0.5$, a parallel configuration is likely. The "heights" of the shaded triangles depict the relative values of the power contributions from the ICE and the electric motor. Figure 16.8 is useful not only for distinguishing between hybrid configurations, but also to introduce the PHEV and electric vehicle concepts.

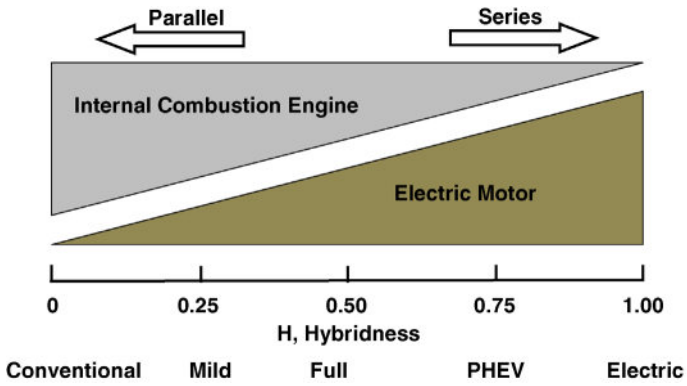

Figure 16.8 The hybridness continuum.

An electric-motor vehicle must contain an onboard source of electricity, typically a battery or a fuel cell, as well as an electric motor (or motors). A schematic of an electric vehicle with a battery is presented in Figure 16.9. Although a battery is illustrated in the figure, the battery could be replaced by another energy storage device such as a flywheel or capacitor bank. As with hybrids, the complexity of the controls function is determined by the features exploited for energy recovery. External power must be available to recharge the storage device. Part of the appeal of an electric vehicle is that the external power can be supplied by a number of sources, including renewable resources such as wind and solar. The Nissan Leaf, with more than 150 000 units sold by fall 2015, is the world's best-selling electric-motor vehicle. The Leaf comes with an 80 kW electric motor and a 24 kW h battery. For electric vehicles, a miles per gallon equivalent (mpge), based on the external energy source is often stated; the Leaf mpge is 126. The Department of Energy Alternative Fuels Data Center (AFDC) listed 43 electric motor vehicles available in the USA in the fall of 2015. In addition to mostly small cars, a few buses and small trucks were included. The *Transportation Energy Data Book* (Davis *et al*., 2015) contains an itemized list of specific models, along with their salient features, from each manufacturer.

The PHEV is the remaining category from Figure 16.8. A PHEV is often called a range extender because its primary purpose is to extend the range of an electric-motor vehicle. A PHEV, typically a series hybrid, has a hybridness value greater than 0.5, with 0.75 or larger likely. Figure 16.5, with an external charging connection, is appropriate for a PHEV schematic. Since the H values are large, the ICE power is small compared with the battery power. Fuhs (2009)

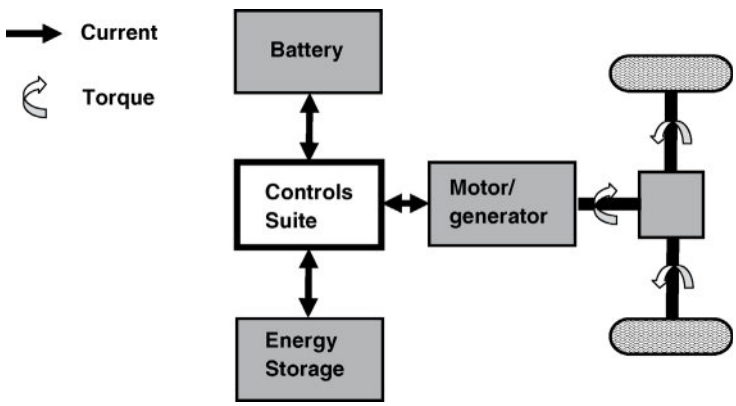

Figure 16.9 Electric vehicle schematic.

derives a relation (Equation (16.6)) between the hybridness H, the battery-only range R_o, and the extended range R_e:

$$R_e = \frac{R_o}{H} \tag{16.6}$$

The increase in range, $R_e - R_o$, can be expressed as

$$\Delta R = R_e - R_o = R_o \frac{1 - H}{H} \tag{16.7}$$

Consider an example.

Example 16.3
A PHEV possesses a 110 kW electric motor and a 55 kW ICE. If the electric-only distance traveled is 35 miles, estimate the extended range when the ICE is used.

Solution The hybridness is

$$H = \frac{110\,\text{kW}}{110\,\text{kW} + 55\,\text{kW}} = 0.67$$

and the extended range and the increase in range becomes

$$R_e = \frac{R_o}{H} = \frac{35\ \text{miles}}{0.67} = 52\ \text{miles}$$

$$\Delta R = R_o \frac{1 - H}{H} = 35\ \text{miles} \times \frac{1 - 0.67}{0.67} = 17\ \text{miles}$$

Care should be exercised in interpreting this result. This is the per trip increase in distanced traveled, indicating the added distance traveled by the addition of the ICE on a single battery charge. Many PHEV advertisements show several hundreds of miles between fuel tank refills, but the number of miles traveled between fuel tank fill-ups involve many trips.

The Department of Energy AFDC listed 24 PHEVs available in the USA in the fall of 2015; all are passenger cars. Additionally, the *Transportation Energy Data Book* (Davis *et al.*, 2015) contains an itemized list of specific models, along with their salient features, from each manufacturer.

By the usual definition, a hybrid vehicle is one that utilizes more than one form of onboard energy for propulsion. On that basis, a fuel cell vehicle can be a hybrid since electricity can be supplied to the motor by both the fuel cell and the battery. A fuel cell vehicle, however, is always an electric-motor vehicle. Figure 16.10 presents a modification of Figure 16.5 (series ICE

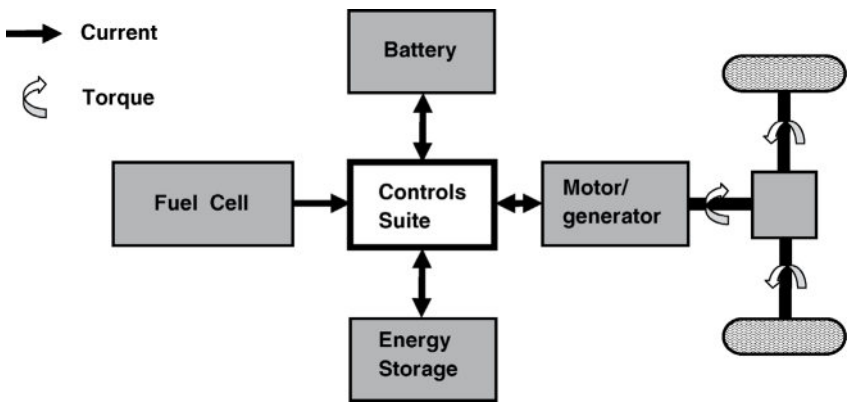

Figure 16.10 Fuel cell electric vehicle system schematic.

configuration) for a fuel cell electric vehicle. Since the fuel cell produces electrical power, prospective fuel cell hybrids are all expected to use series configurations with the ICE-generator replaced by a fuel cell. An issue with fuel-cell-powered vehicles is the availability of hydrogen refueling stations, so fuel cell vehicles are viable only in regions where a hydrogen refueling infrastructure exists. About 50 hydrogen refueling stations were available nationwide as of 2015; most are located in California. The proton exchange membrane fuel cell (see Chapter 10) is the likely fuel cell type to be used for such vehicles. Because of the limitation on hydrogen availability, cost, reliability, and other issues, commercially available, fuel-cell-powered conventional and hybrid vehicles are few. The AFDC listed 12 fuel-cell-powered vehicles in the fall of 2015. Included in the list were several buses, trucks, and passenger vehicles.

16.3 Hybrid and Electric Vehicles Past, Present, and Future

The ICE has been the prevalent form of power for most road vehicles for many decades. However, because of energy, environmental, and sustainability concerns, the last few decades, individuals, corporations, and government agencies (local, state, and federal) have increasingly become proponents of alternatives to ICEs. Personal beliefs, corporate policies, governmental policies, and governmental incentives have resulted in a significant, and increasing, market penetration of alternative fuel vehicles. This trend is examined next.

The *Transportation Energy Data Book* (Davis *et al*., 2015) contains tabular data showing the history of hybrid and electric vehicles sales and compares them with conventional vehicle sales. Table 16.1, taken from Davis *et al*. (2015), presents the data in a useful format. The table

Table 16.1 Hybrid and plug-in vehicles sales history.[a]

	Vehicle sales (thousands)			Share of all light vehicles (%)	
Calendar year	Hybrid	Plug-in	All light vehicles	Hybrid	Plug-in
1999	0.0	0.0	16 711	0.0	0.0
2000	9.4	0.0	17 164	0.1	0.0
2001	20.3	0.0	16 950	0.1	0.0
2002	36.0	0.0	16 675	0.2	0.0
2003	47.6	0.0	16 494	0.3	0.0
2004	84.2	0.0	16 737	0.5	0.0
2005	205.9	0.0	16 774	1.2	0.0
2006	251.9	0.0	16 336	1.5	0.0
2007	351.1	0.0	15 867	2.2	0.0
2008	315.8	0.0	13 015	2.4	0.0
2009	290.3	0.0	10 236	2.8	0.0
2010	274.6	0.3	11 394	2.4	0.0
2011	266.5	17.8	12 539	2.1	0.1
2012	434.6	53.2	14 219	3.1	0.4
2013	495.5	97.1	15 278	3.2	0.6
2014	452.2	118.9	16 171	2.8	0.7

a) Plug-in vehicle sales include only those vehicles certified for highway use. Small electric carts and neighborhood electric vehicles are excluded.

Source: Davis *et al*. (2014: 6–9).

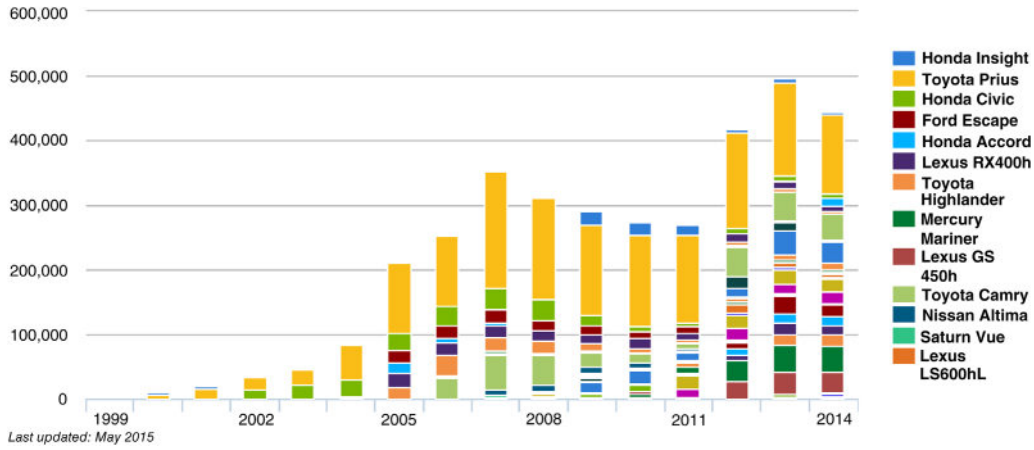

Figure 16.11 Hybrid vehicle sales history and manufacturers. *Source*: http://www.afdc.energy.gov/data/10301.

considers only "light" vehicles; the EIA defines a light vehicle as one weighing less than 8500 lbs. Starting in 1999, the general trend for hybrid and plug-in vehicles sales has been increasing, although a few years exhibit decreases (2008–2011 and 2014). The 2008–2011 decreases in hybrid sales are attributed to economics; the 2014 decrease is likely due to falling gasoline prices (see Chapter 17). Plug-in vehicle sales have monotonically increased.

The AFDC (http://www.afdc.energy.gov/data/) provides comprehensive data on all aspects of alternative fuels, including hybrid and electric vehicle information. One interesting aspect that AFDC compiles is hybrid and electric vehicles sales parsed by manufacturer. Figure 16.11 illustrates the history of hybrid vehicles sales by manufacturer. Several items are of interest in the figure: (1) the number totals agree substantially with Table 16.1, (2) the consistent best seller, by a significant margin every year, has been the Toyota Prius, and (3) the number of manufacturers offering hybrid vehicles is substantial and increasing.

Figure 16.12 provides essentially the same information for plug-in vehicles as does Figure 16.9 for hybrid vehicles. The number of plug-in electric vehicles sold is about an order of magnitude less than hybrid vehicles, but on a year-to-year basis, the trends for plug-in vehicle sales track the sales of hybrid vehicles. The number of manufacturers offering plug-in electric vehicles has increased since 2010, but unlike the sales of hybrids, no single manufacturer has been as dominant as the Toyota Prius has for the hybrid vehicles.

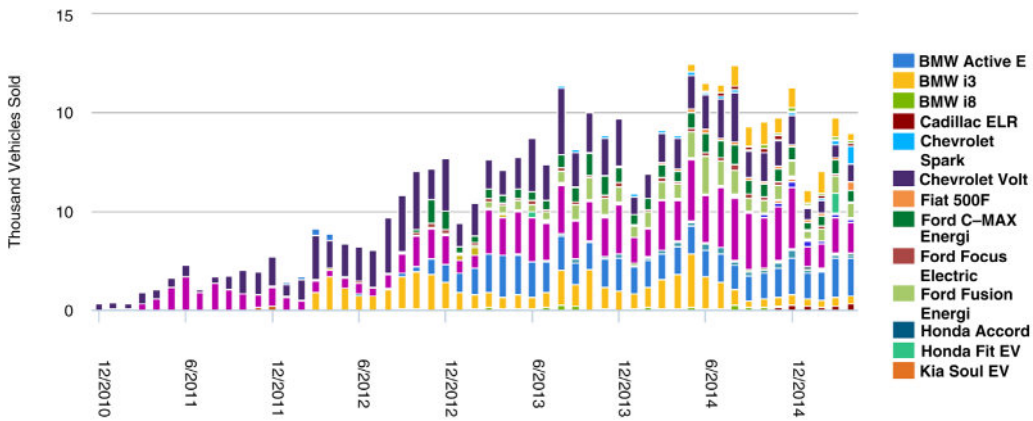

Figure 16.12 Plug-in electric vehicle sales history and manufacturers. *Source*: http://www.afdc.energy.gov/data/10567.

Between the AFDC web site and the *Transportation Energy Data Book* (Davis *et al*., 2015), a rather complete listing of individual hybrid and electric vehicle models can be obtained. However, the AFDC web site offers interactive features that enhance the information available. Some features of the web site are examined in the next paragraph.

One useful interactive feature of the AFDC web site is the capability to identify specific manufacturers and models by category. The AFDC web site for finding specific vehicles is http://www.afdc.energy.gov/vehicles/electric_availability.html. Selecting either "Hybrid electric vehicles," Plug-in hybrid electric vehicles," All-electric vehicles," or "Electric drive vehicles" will open a page containing a list of Fuel/Technology options and Class/Type options as well as pull-down menus for "Manufacturer-Light Duty" and "Manufacturer-Med & Heavy Duty." The Fuel/Technology options and Class/Type options have the following selections available:

Fuel/Technology	Class/Type
All Fuels	All Classes/Types
Biodiesel (B20)	Sedan/Wagon
Ethanol (E85)	Truck
Hydrogen Fuel Cell	SUV
LNG-Liquified Natural Gas	Van
CNG-Compressed Natural Gas	Step Van
CNG-Bi-Fuel	Vocational/Cab Chassis
Propane	Street Sweeper
Electric	Refuse
Plug-in Hybrid Electric	Tractor
Hybrid Electric	Shuttle Bus
Hybrid-Hydraulic	Transit Bus
Hybrid-CNG	School Bus

The options of interest are selected, and the resulting vehicles that meet the options are indicated as a total and then a photograph and a short description of salient features of each of the selected vehicles is presented. For example, if "Plug-in Hybrid Electric" is selected as the Fuel/Technology option and "All Classes/Types" is selected from the Class/Type option, then 24 vehicles are returned as the available vehicles matching the selection criteria. The Chevrolet Volt information returned is

Chevrolet Volt (2015)
Plug-in Hybrid Electric
Sedan/Wagon
Fuel Economy: 98 Mpge combined electricity city
Emission Certification: Tier 2 Bin 3, LEV III SULEV30
Engine: 1.4 L I4, 111 kW electric motor
Transmission: Auto

A photograph from company literature accompanies each vehicle. As Figures 16.9 and 16.10 indicate, hybrid and electric vehicle commercial availability is continually changing, so that a web site that is updated frequently is a valuable source for information on alternative fuel vehicles.

What is the future for hybrid and electric vehicles? In 2012 the Department of Energy initiated *EV Everywhere*, an umbrella effort to increase the adoption and use of plug-in vehicles with the

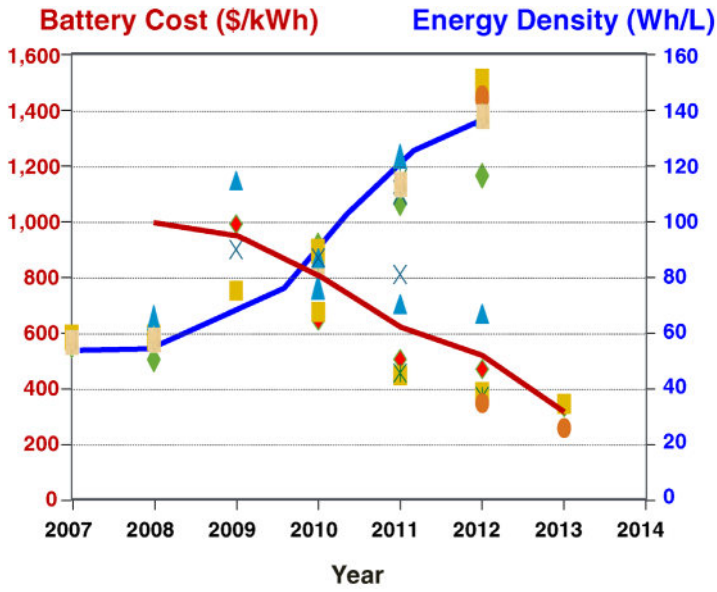

Figure 16.13 Progress in PHEV and EV battery costs and energy densities. *Source*: Howell (2014).

technical goal of having the USA by 2020 becoming the first nation to produce electric vehicles that are as affordable as conventional vehicles were in 2012. Details are available on the *EV Everywhere* website at http://energy.gov/eere/eveverywhere/about-ev-everywhere and in "EV Everywhere Grand Challenge Road to Success" (DOE, 2014). *EV Everywhere* research focuses on advanced batteries, electric drive systems, and lightweight materials with the following goals:

1) *Vehicle weight reduction* – reduce vehicle weight by nearly 30% (includes body, chassis, interior, and electric drive components).
2) *Electric drive system* – reduce cost from \$30/kW in 2012 to \$8/kW in 2020 (1.4 kW/kg, 4 kW/L, and 95% efficiency).
3) *Battery* – reduce cost from \$500/kW h in 2012 to \$125/kW h in 2020 (250 W h/kg, 400 W h/L, and 2 kW/kg).

Storage and retrieval of electrical energy is difficult to accomplish economically; indeed, the storage and retrieval of a kilowatt-hour of electricity is one of the most expensive endeavors in energy engineering. Refer to the battery discussion in Section 9.4 for additional information relating to storage-retrieval issues. The *EV Everywhere* battery goals are daunting; nonetheless, significant progress has been made. Figure 16.13, taken from the EERE overview of the advanced battery program in 2014 (Howell, 2014), demonstrates that progress in terms of cost and energy density. The symbols represent different size and capacity (14 kW h, PHEV, to 40 kW h, EV) batteries under development, and the costs were estimated based on 100 000 battery packs per year production.

The economics of plug-in and electric vehicles is determined almost entirely by the battery cost, initial and replacement. Battery storage energy density is low, meaning that a large (and heavy) battery network is needed to store a meaningful quantity of electrical energy. Batteries also have a finite life in terms of discharge–recharge cycles, so that replacements are needed. Muller (2012) concludes that while full hybrids make economic sense, pure electric vehicles do not. Indeed, he estimates that the battery purchase-replacement cost, on a per mile basis, exceeds the cost, on a per mile basis, of electricity required to recharge the battery. Muller's

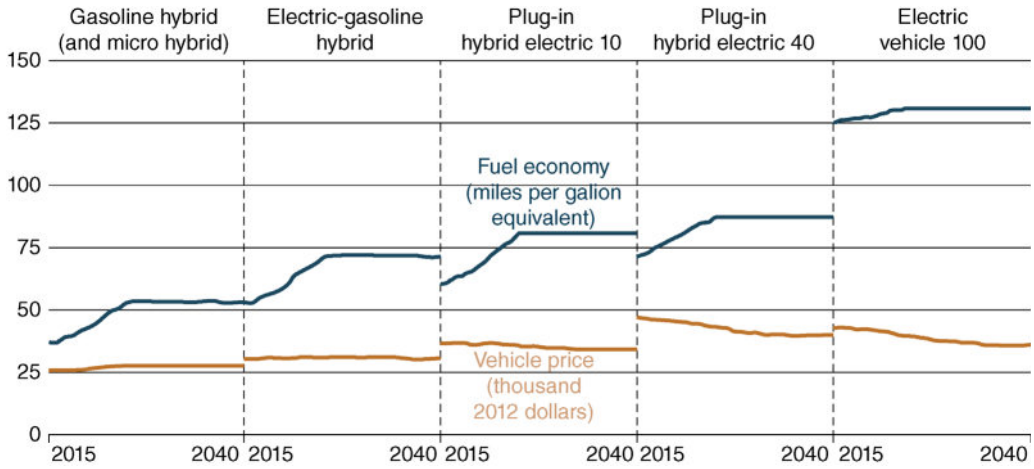

Figure 16.14 EIA hybrid and plug-in vehicle projections to 2040. *Source*: EIA (2015).

numbers can be juggled, but the results will be the same: battery storage expense is a pacing economic consideration for electric vehicles.

The EIA *Annual Energy Outlook 2015* (EIA, 2015) examines scenarios and makes projections for future energy use and likely technological improvements. One of the topics considered is hybrid and electric vehicles. Vehicle price and fuel economy are delineated in Figure 16.14 from 2015 to 2040 for five different alternative fuel vehicles. The gasoline hybrid is a mild hybrid with the ICE power larger than the electric motor, while the electric–gasoline hybrid is a full hybrid. The PHEV10 and PHEV40 are for vehicles with a 10 mile range and a 40 mile range respectively, and the electric vehicle (EV100) range is 100 miles. All five different vehicle types are projected to have improvements in fuel economy (expressed as miles per gallon) from 2015 until about 2025 when miles-per-gallon values essentially plateau. The EV100 is expected to have the least improvement in fuel economy. For the plug-in types, the fuel economy improves as the electric-only mileage values increase, with more than 125 mpg (equivalent) for the EV100. The costs of the gasoline–electric and electric–gasoline types are projected to exhibit only modest increases (constant dollar) from 2015 to 2040. The plug-in vehicles (PHEV10, PHEV40, and electric) are expected to cost more than the non-plug-in types, but to decline in costs from 2015 to 2040. The PHEV40 is anticipated to cost more than the PHEV10, primarily because of the larger battery required for the PHEV40. The EV10 estimated cost is somewhat less than the PHEV40 over the timeframe examined; even though a larger battery is required, the EV100 does not have an ICE, and the controls requirements are simplified.

However, the EIA notes that fuel-efficient technologies will enable vehicle manufacturers to meet miles-per-gallon and emissions standards with vehicles that are predominantly gasoline powered. Even though the prices of some vehicles using electric motors are projected to decline, their relative cost-effectiveness does not improve. The EIA acknowledges that while the reasons for vehicle purchases vary, not always on an economic basis, wider market acceptance would require more favorable fuel economics. Based on the EIA 2040 projections (using the reference or most likely fuel price scenario), a full hybrid would have a payback period of 13 years, a PHEV10 a payback period of 27 years, a PHEV40 a payback period of 46 years, and a EV100 a payback period of 19 years. However, were gasoline prices to increase significantly from 2015 to 2040, then the payback periods decrease and the economics of hybrids and plug-in vehicles greatly improve. Details are given in EIA (2015: 11).

Considering the preceding discussions based on the *EV Everywhere* initiative and the EIA projections, where does that leave hybrid and electric vehicles? Muller (2012) makes a very

cogent argument that full hybrids make sense, but that plug-in and electric vehicles do not make economic, and perhaps environmental, sense. He points out that, thus far, the US use of gasoline in automobiles has contributed only about 1/40 °C of the temperature rise, and that if the EIA anticipated 60% increase in automobiles were to occur, the contribution for the next 50 years would be only 1/25 °C, perhaps less if more stringent mileage mandates are adopted. Hence, the environmental reason to displace gasoline is small. Moreover, if plug-in and electric vehicles use electricity generated by fossil fuels, any overall reductions in emissions and greenhouse gases are negated.

Prentiss (2015), who reaches some different conclusions than Muller (2012), argues that by infrastructure changes and much more reliance on renewable resources (wind, solar, and biomass especially), the USA could have achieve a sustainable energy economy with little reliance on petroleum. Prentiss acknowledges the importance and difficulty of energy storage, but expects technology to solve energy storage issues. With that assertion, electric vehicles then become her recommended choice for personal transportation, with hybrids becoming her choice for driving in urban traffic.

All major automobiles manufacturers are preparing for futures that are heavily involved with hybrid and electric vehicles. Ford, for example, announced in December 2015 that it was investing $4.5 billion in electrified (hybrid and electric) vehicles. The Ford web site (https://media.ford.com/content/fordmedia/fna/us/en/news/2015/12/10/ford-investing-4-5-billion-in-electrified-vehicle-solutions.html) presents the details. Key elements include: (1) $4.5 billion invested by 2020, (2) a new Ford Focus electric with a 100 mile range and 30 min recharging (80%), (3) adding 13 new electrified vehicles to their product portfolio by 2020, and (4) expanding their electrified vehicle offering internationally. Ford also announced that 120 new engineers would be added to their electrified powertrain engineering program. Other major automotive manufacturers, in the USA and worldwide, have announced similar plans and are heavily invested in hybrid and electric vehicles.

16.4 Closure

Hybrid and electric vehicles have been examined and discussed. The degree of displacement of gasoline-only powered vehicles by plug-in and electric vehicles is uncertain as of the fall 2016. The *EV Everywhere* initiative has as its primary goal the development of technology that would result in plug-in and electric vehicles being economically competitive with gasoline vehicles. This is a daunting task. The full hybrid is likely to continue to increase its market share. Overall, the future price and availability of gasoline as well as federal mandates will determine the depth of market penetration of hybrids, and especially plug-in and stand-alone electric vehicles.

References

Davis, S.C., Diegel, S.W., and Boundy, R.G. (2015) *Transportation Energy Data Book, Edition 34*. Oak Ridge National Laboratory, Oak Ridge, TN. http://cta.ornl.gov/data/index.shtml (accessed October 26, 2016).

DOE (2014) *EV Everywhere Grand Challenge: Road to Success.* DOE/EE-1024. http://energy.gov/sites/prod/files/2014/02/f8/eveverywhere_road_to_success.pdf (accessed October 26, 2016).

Ehsani, M., Gao, Y., and Elmadi, A. (2010) *Modern Electric, Hybrid Electric, and Fuel Cell Vehicles Fundamentals, Theory, and Design*, 2nd edn. CRC Press, Boca Raton, FL.

EIA (2015) *Annual Energy Outlook 2015 with Projections to 2040*. DOE/EIA-0383(2015). http://www.eia.gov/forecasts/aeo/pdf/0383(2015).pdf (accessed October 26, 2016).

Fuhs, A.E. (2009) *Hybrid Vehicles and the Future of Personal Transportation*. CRC Press, Boca Raton, FL.

Howell, D. (2014) *Overview of the DOE Advanced Battery R&D Program.* http://energy.gov/sites/prod/files/2014/09/f18/battery_rd_amr_plenary_june_2014_final.pdf (accessed October 26, 2016).

Kirsch, D.A. (2000) *The Electric Vehicle and the Burden of History*. Rutgers University Press, Piscataway, NJ.

Mi, C., Abul Masrur, M., and Gao, D.W. (2011) *Hybrid Electric Vehicles Principle and Applications with Practical Perspectives*. John Wiley & Sons, Inc., New York.

Muller, R.A. (2012) *Energy for Future Presidents: The Science behind the Headlines*. Norton, New York.

Prentiss, M. (2015) *Energy Revolution: the Physics and the Promise of Efficient Technology*. Harvard University Press, Cambridge, MA.

17

Hydraulic Fracturing, Oil, Natural Gas, and the New Reality

17.1 Introduction

The US Energy Information Administration (EIA) defines *hydraulic fracturing* (http://www.eia.gov/tools/glossary/index.cfm?id=H) as "the fracturing of rock at depth with fluid pressure. Hydraulic fracturing at depth may be accomplished by pumping water into a well at very high pressures."

In the oil and gas industry, the usual abbreviation for hydraulic fracturing is "fracing." In the media, hydraulic fracturing is usually called "fracking" and generally connotes all steps involved with enhanced or stimulated oil/gas recovery which involve hydraulic fracturing. The practice of hydraulic fracturing has generated a significant amount of controversy, and the "pro" and "con" sides vehemently and emotionally defend their positions. Many in the oil and gas industry believe fracking to be a pejorative term and prefer fracing for the hydraulic fracturing step of stimulating reservoirs. Books and papers often avoid the controversy by simply using fracturing. In Ahmed and Meehan (2012), one of the most respected textbooks on reservoir engineering, neither fracing nor fracking is listed in the index, and they typically use fracturing – although in a few instances (not in the index) frac is used.

When the preface to the first edition of this textbook was written in the summer of 2009, retail gas prices (87 octane) were approaching $4.00/gal. As this is being written, spring of 2016, retail gas prices are less than $2.00/gal. What happened to cause this unforeseen price reduction? The short answer is enhanced-stimulated oil/gas recovery using hydraulic fracturing and the identification of significant natural gas resources, including those made available by fracturing, in the USA. Figures 17.1 and 17.2 demonstrate how fracturing has resulted in the identification of crude oil and natural gas proved reserves well beyond what was expected near the end of the twentieth century. The proved oil reserves in 2013 were close to the proved reserves in 1973. For natural gas, the proved reserves in 2013 were 40% higher than in 1973. Webber (2013) discusses the recent dramatic increase in proved reserves and enhanced oil and natural gas recovery and concludes that market forces, government policy, and technological innovations came together to provide the unexpected results. Indeed, in a perhaps optimistic view of fossil fuel reserves, BP (British Petroleum) recently stated that the world is not likely to run out of oil anytime soon (Reuters, 2015). The goals of this chapter are to examine the circumstances which led to the additional proved reserves, to understand what hydraulic fracturing is in stimulated oil and natural gas recovery, and to delineate the energy futures that are possible.

17.2 Unconventional Oil and Gas

This section begins with a few definitions used by the oil and gas industry. The following definitions were adapted from the EIA glossary (http://www.eia.gov/tools/glossary/index.cfm):

Alternative Energy Systems and Applications, Second Edition. B. K. Hodge.

Companion website: www.wiley.com\go\Hodge\AESystemsandApplications2E

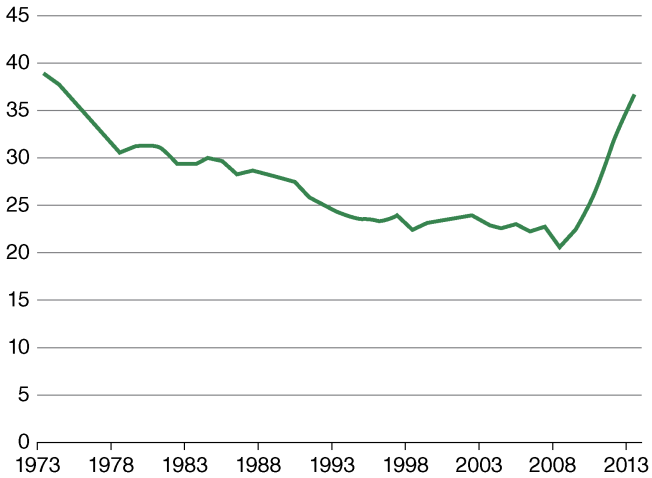

Figure 17.1 History of US proved oil reserves (10^9 barrels). *Source*: http://www.eia.gov/naturalgas/crudeoilreserves/.

- *Conventional oil and natural gas.* Crude oil and natural gas that is produced by a well drilled into a geologic formation in which the reservoir and fluid characteristics permit the oil and natural gas to readily flow to the wellbore.
- *Unconventional oil and gas.* An umbrella term for oil and natural gas that is produced by means that do not meet the criteria for conventional production. "UOG" often appears in the literature to represent unconventional oil and gas. Note: what has qualified as "unconventional" at any particular time is a complex interactive function of resource characteristics, the available exploration and production technologies, the current economic environment, and the scale, frequency, and duration of production from the resource.
- *Play.* A set of oil and gas accumulations sharing similar geologic, geographic, and temporal properties, such as source rock, migration pathway, timing, trapping mechanism, and

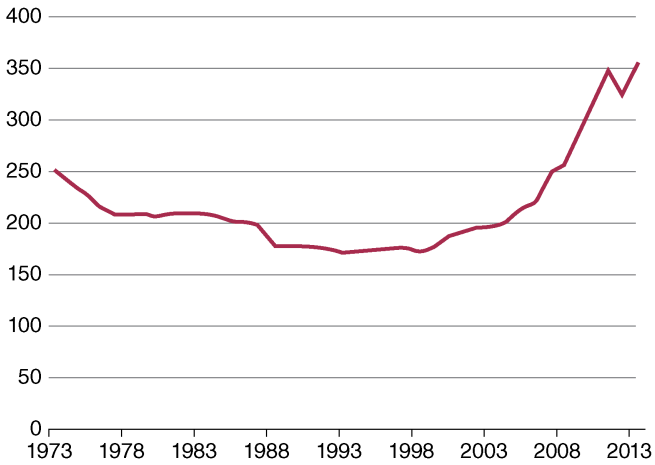

Figure 17.2 History of US proved natural gas reserves (10^{12} cubic feet). *Source*: http://www.eia.gov/naturalgas/crudeoilreserves/.

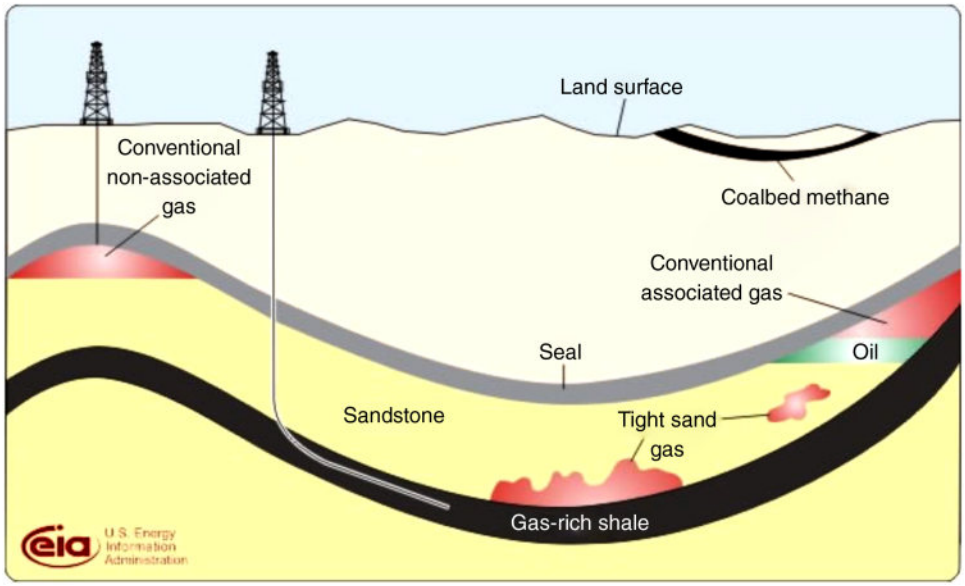

Figure 17.3 Conventional and unconventional gas illustrations. *Source*: http://www.eia.gov/oil_gas/natural_gas/special/ngresources/ngresources.html.

hydrocarbon type. A play is often used to refer to a natural gas accumulation – a natural gas shale play.

- *Tight oil.* Oil produced from petroleum-bearing formations with low permeability that must be hydraulically fractured to produce oil at commercial rates. Shale oil is a subset of tight oil.

Figure 17.3 is a help in understanding the conventional and unconventional oil and gas distinctions. Conventional is extracted by drilling into geologic formations which have sufficiently large permeabilities that the gas can be obtained using conventional techniques. Unconventional gas is extracted from reservoirs of very low permeability by hydraulic fracturing and recovery using unconventional techniques. Section 17.3 will examine unconventional hydraulic fracturing. Gas extracted by conventional means and not associated with a low-permeability reservoir, as in the upper left-hand corner of Figure 17.3, is called conventional, non-associated gas. Depending on the geologic structure, as in the middle, left-hand side of Figure 17.3, gas may be extracted using conventional techniques from high-permeability regions of an otherwise low-permeability formation (e.g., shale); such gas is called conventional, associated gas to distinguish it from conventional, non-associated gas.

Although shale plays are not necessary for unconventional oil/gas extraction, the majority of such extractions are expected to occur in shale formations. The availablity of shale plays is likely to determine the potential for unconventional oil/gas recovery using hydraulic fracturing. Figure 17.4 illustrates the prevalence of shale plays in the continential USA and shows current as well as prospective locations amenable for hydraulic fracturing. The natural gas production from different shale plays, identified in Figure 17.4, in the USA since 2000 is summarized in Figure 17.5. The increase in shale gas production since 2000 is startling and is responsible for the increase in natural gas production in the USA.

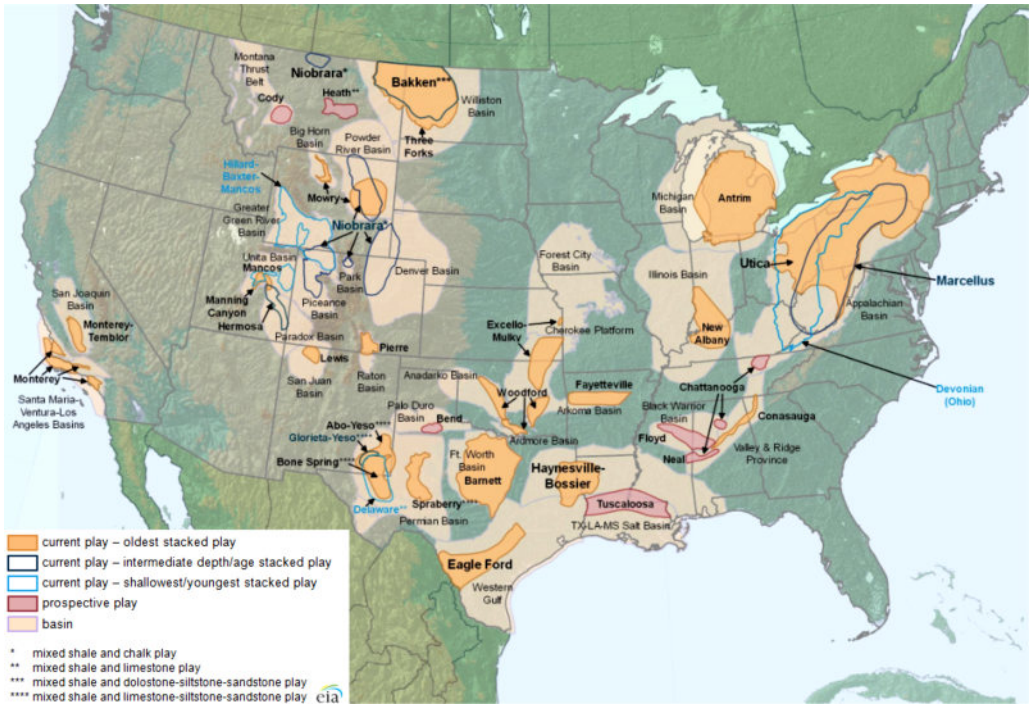

Figure 17.4 Shale plays in the continental USA. *Source*: http://www.eia.gov/todayinenergy/detail.cfm?id=20852.

Shale plays in the world, including the USA, are highlighted in Figure 17.6. The estimates of proved tight gas and oil reserves are quite large, and such reserves are mostly responsible for the unexpected fossil-fuel reserves outlook. We next consider reservoir engineering concepts and examine hydraulic fracturing.

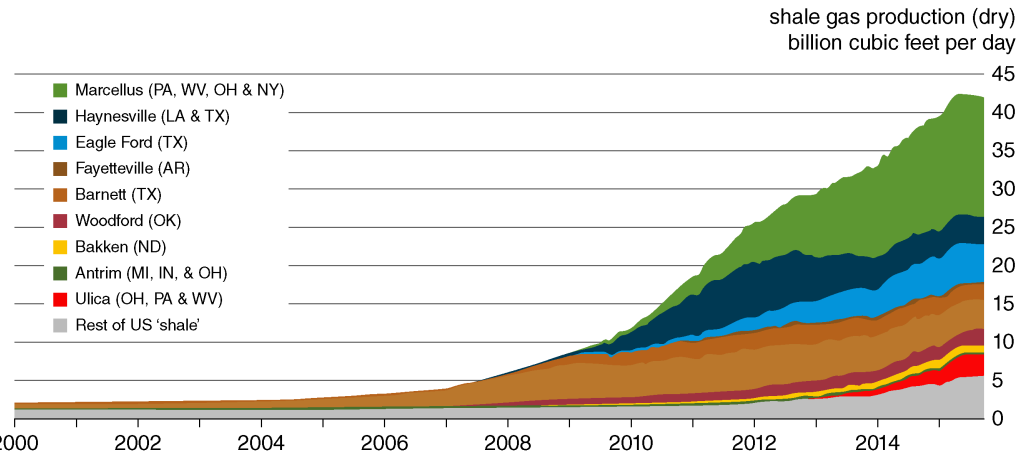

Figure 17.5 History of shale gas production from different plays in the USA. *Source*: http://www.eia.gov/energy_in_brief/article/shale_in_the_united_states.cfm.

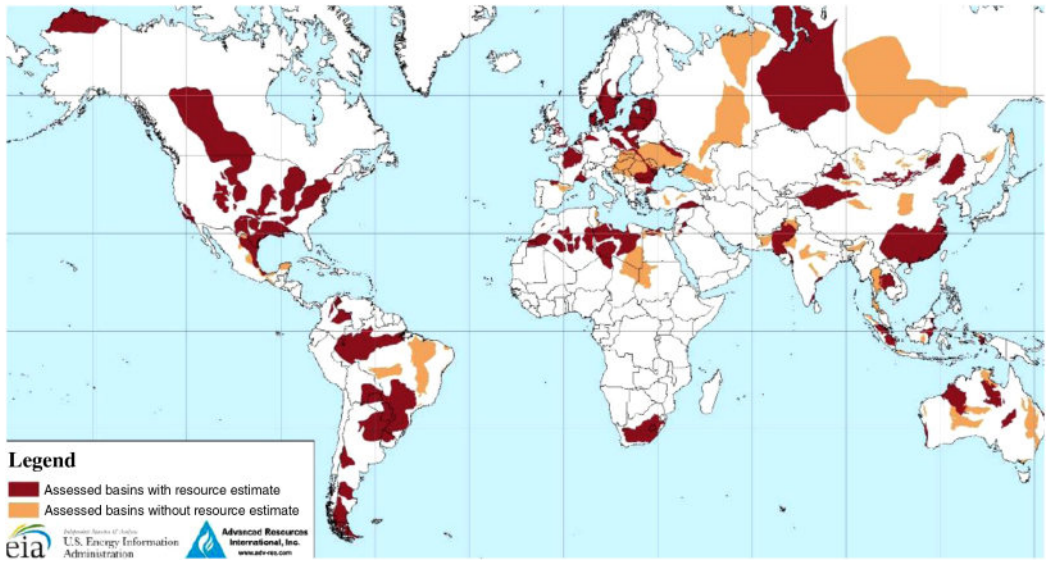

Figure 17.6 Shale deposits in the world. *Source*: EIA (2013: 5).

17.3 Reservoir Engineering Concepts

Prior to discussing hydraulic fracturing, some important features of reservoir engineering are needed. Reservoir engineering has become very sophisticated, very technical, and very effective, especially when coupled with horizontal drilling and hydraulic fracturing technologies. A number of excellent reservoir engineering textbooks are available, as are a number of web sites. Ahmed and Meehan (2012) and Economides *et al.* (2013) are frequently referenced; an examination of either will confirm the complexity of reservoir engineering. Since most oil and gas production involves porous geologic formations, a good place to start is with the expression of Darcy (in 1856), often called Darcy's law, for flow through porous media:

$$Q = -A\frac{k}{\mu}\frac{\mathrm{d}p}{\mathrm{d}x} \tag{17.1}$$

where Q is the volumetric flow rate, A the cross-sectional flow area, k the permeability, μ the viscosity, and $\mathrm{d}p/\mathrm{d}x$ the pressure gradient. Equation (17.1) is valid for laminar, steady-state, incompressible, and homogeneous flow in a porous medium. Figure 17.7 illustrates the relationship between the variables and the sign convention in a Cartesian coordinate system.

Dimensional homogeneity requires the units of permeability be *length squared*; the SI SI unit for permeability is square meter, but a more practical unit is the darcy. By definition, a darcy is

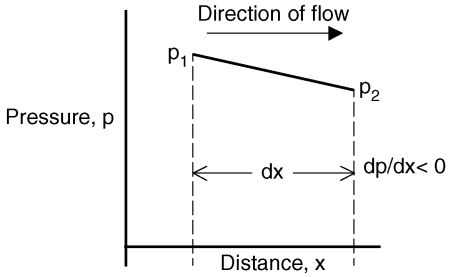

Figure 17.7 Darcy's law interpretation.

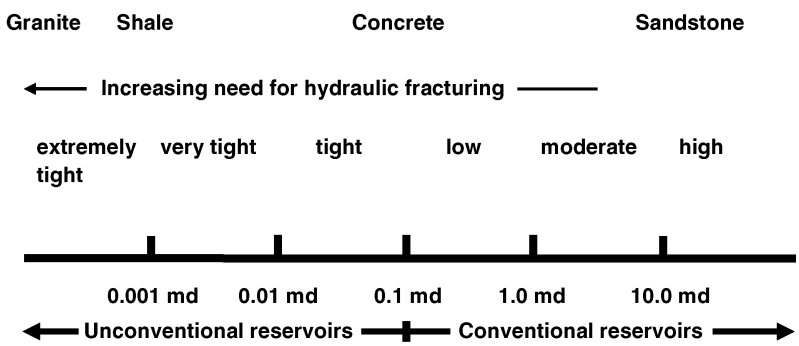

Figure 17.8 Relative permeability scale.

the permeability that results in a volumetric flow rate of 1 cm^3 across an area of 1 cm^2 with a pressure gradient of 1 atm/cm and a viscosity of 1 cP. The *millidarcy* (md) (1 d = 1000 md) is the commonly used unit for permeability, especially in the oil and gas industry, and the conversion factor from the SI units to the darcy is 1 d = 9.869×10^{-13} m^2. Interestingly, the plural of darcy is darcys. *A Guide to Shale Gas* (Energy Institute, 2015) provides a cogent overview of permeability values as related to hydraulic fracturing. Figure 17.8 is adapted from their approach. The permeability can be as high as 100 000 d for gravel to as low as 0.0001 md for granite. The flow rate as predicted by Darcy s law (Equation (17.1)) is directly proportional to the permeability k. Going from a 1.0 md play to a 0.01 md play means that the flow rate is reduced by 99%. Thus, the need for hydraulic fracturing for low-permeability plays.

Reservoir engineering is a complex topic. Ahmed and Meehan (2012) categorize the complexity of reservoir flows by considering four attributes: (1) types of flow, (2) flow regimes, (3) reservoir geometry, and (4) fluid phases. Each attribute is further subdivided as follows:

1) Types of fluids in a reservoir
   a) incompressible
   b) slightly compressible
   c) compressible
2) Flow regimes
   a) steady state
   b) unsteady state
   c) pseudosteady
3) Reservoir geometry
   a) radial flows
   b) linear flows
   c) spherical and hemispherical flows
4) Number of fluids in a reservoir
   a) single phase
   b) two phase
   c) three phase.

In Ahmed and Meehan (2012) and Economides *et al.* (2013), several hundred pages are devoted to details of the preceding as applied to reservoir engineering. These details are well beyond the scope of this book; however, an examination of two examples is useful both to capture an understanding of some flows and to discuss the units commonly used in the oil and gas industry.

Consider the radial flow of an incompressible fluid; the geometry is illustrated in Figure 17.9. Ahmed and Meehan (2012) develop, starting with Darcy's law, the following expression for the

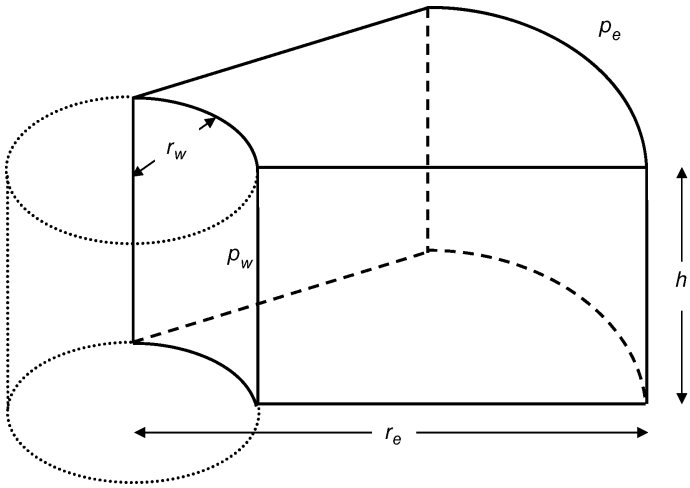

Figure 17.9 Geometry variables for radial flow scenario.

volumetric flow rate for the radial flow of an incompressible fluid:

$$Q_o = \frac{0.007\,080\,kh}{\mu_o B_o} \frac{p_e - p_w}{\ln(r_e/r_w)} \tag{17.2}$$

where the 0.007 080 is needed to reconcile the "field units" with conventional units. The variables in Equation (17.2) with the associated field units are as follows:

Q_o oil flow rate (STB/day – Stock Tank Barrel is 42 US gallons, liquid)
B_o oil formation factor (bbl/STB) – the oil formation factor is the ratio of volume of oil at reservoir conditions to the volume at surface (stock tank) conditions
k permeability (md)
μ_o oil viscosity (cP)
h thickness of reservoir (ft)
p_e pressure at the boundary of the drainage area (psi)
p_w wellbore pressure (psi)
r_e drainage radius (ft)
r_w wellbore radius (ft).

The drainage radius r_e is determined by the well spacing area A such that

$$r_e = \sqrt{\frac{43\,560A}{\pi}} \tag{17.3}$$

where A is the well spacing in acres. An example is in order.

Example 17.1
An oil well has the following properties:

$k = 100$ md $\quad h = 15$ ft $\quad \mu_o = 2.5$ cP $\quad A = 50$ acres
$B_o = 1.25$ bbl/STB $\quad p_e = 2500$ psi $\quad r_w = 3$ in $= 0.25$ ft $\quad p_w = 1800$ psi

Estimate the oil flow rate.

Solution The drainage radius is computed as

$$r_e = \sqrt{\frac{43\,560A}{\pi}} = \sqrt{\frac{43\,560 \times 50}{\pi}} = 832.6 \text{ ft}$$

The estimated flow rate becomes

$$Q_o = \frac{0.007\,080kh}{\mu_o B_o}\frac{(p_e - p_w)}{\ln(r_e/r_w)} = \frac{0.007\,080 \times 100 \times 15}{2.5 \times 1.25} \times \frac{2500 - 1800}{\ln(0.25/832.6)}$$
$$= 294.3 \frac{\text{STB}}{\text{day}}$$

The values used in this example are typical of reservoir conditions and represent reasonable results. Of special note is the use of "field units" in the expressions.

Example 17.1 represented conditions typical of oil recovery. But also of interest is the recovery of gas. The volumetric gas flow rate for radial flow of a compressible fluid, using the "pressure-squared method," is developed from Darcy's law in Ahmed and Meehan (2012) and appears as

$$Q = \frac{kh}{1422T(\mu_g Z)_{avg}}\frac{p_e^2 - p_w^2}{\ln(r_e/r_w)} \tag{17.4}$$

where the 1422 is needed to reconcile the "field units" with conventional units. The variables in Equation (17.4) with the associated field units are as follows:

Q gas flow rate (Mscf/day)
k permeability (md)
h thickness of reservoir (ft)
p_e pressure at the boundary of the drainage area (psi)
p_w wellbore pressure (psi)
μ_s gas viscosity (cP)
Z gas compressibility factor (dimensionless)
T temperature (°R)
r_e drainage radius (ft)
r_w wellbore radius (ft).

Z is the compressibility factor and is needed for high pressures in the equation of state, $p = Z\rho RT$. The variable $(\mu_g Z)_{avg}$ is evaluated at an average pressure defined by $\overline{p} = [(p_w^2 + p_e^2)/2]^{1/2}$; hence the designation pressure-squared method.

Example 17.2, adapted from Ahmed and Meehan (2012), is presented to illustrate the use of Equation (17.4) in a typical reservoir calculation using field units and to provide a sense of numeracy for the magnitudes involved.

Example 17.2
Estimate the flow rate from a gas reservoir with the following characteristics:

$k = 65$ md $\quad h = 15$ ft $\quad T = 600$ °R
$r_e = 1000$ ft $\quad p_e = 4400$ psi $\quad r_w = 3$ in $= 0.25$ ft $\quad p_w = 3600$ psi

Ahmed and Meehan (2012) provide viscosity and compressibility factor characteristics for the reservoir gas at 600 °R; see Table 17.1.

Table 17.1 Viscosity and compressibility factor.

p (psi)	μ (cP)	Z
0	0.012 70	1.000
400	0.012 86	0.937
800	0.013 90	0.882
1200	0.015 30	0.832
1600	0.016 80	0.794
2000	0.018 40	0.770
2400	0.020 10	0.763
2800	0.021 70	0.775
3200	0.023 40	0.797
3600	0.025 00	0.827
4000	0.026 60	0.860
4400	0.028 31	0.896

Solution The average pressure is

$$\overline{p} = \sqrt{\frac{p_w^2 + p_e^2}{2}} = \sqrt{\frac{(3600\ \text{psi})^2 + (4400\ \text{psi})^2}{2}} = 4020\ \text{psi}$$

The product $(\mu_g Z)_{avg}$ at 4020 psi is found by interpolating the values of μ and Z from Table 17.1. At 4020 psi, $\mu = 0.026\,67$ cP and $Z = 0.8618$, so that

$$(\mu_g Z)_{avg} = 0.026\,67\ \text{cP} \times 0.8618 = 0.022\,98\ \text{cP}$$

The flow rate calculation is

$$Q = \frac{kh}{1422T(\mu_g Z)_{avg}} \frac{p_e^2 - p_w^2}{\ln(r_e/r_w)} = \frac{65 \times 15}{1422 \times 600 \times 0.02298} \times \frac{4400^2 - 3600^2}{\ln(1000/0.25)}$$
$$= 38\,372\ \frac{\text{Mscf}}{\text{day}}$$

The pressure-squared approach as presented in Equation (17.2) is generally considered to be accurate for pressures less than 2000 psia, but the results of this example are within about 2% of the much more involved exact solution. Equations (17.2) and (17.4) serve well for illustrative purposes. A number of observations are pertinent for Examples 17.1 and 17.2: (1) units of individual quantities are not carried in the calculation since the "0.007 080" and "1422" implicitly account for the field units; (2) the units for all quantities must be the field units consistent with the original development; (3) magnitudes can be large; (4) significant information (e.g., μ, Z, k, B_o) specific to a given site must be available; and (5) assumptions are important.

From Figure 17.8, permeabilities of 100 md and 65 md would be considered "large" and be congruent with reservoirs for which conventional recovery procedures would be appropriate. However, in Example 17.2, if the permeability were 0.065 md, a thousand time less, then the production from such a tight reservoir would be only 38 Mfsc/day (all other parameters being the same), a number that is so small as to be economically unfeasible. Hydraulic fracturing would be needed to economically recover gas from such a tight reservoir. Hydraulic

fracturing essentially increases (dramatically) the effective permeability of a reservoir, rendering it feasible for oil/gas recovery.

17.4 Oil and Gas Recovery from Tight Plays

Hydraulic fracturing is only part of the reason why recovery of oil/gas from tight plays has become economically feasible. Webber (2013) identified technological innovation, market forces, and government policy as components of the recent increase in oil and gas production and proved reserves. Perhaps the most important technological innovation was made by oilmen George P. Mitchell (Crawford, 2013), in the 1980s, when he combined two existing technologies, horizontal drilling and hydraulic fracturing, to make oil and gas recovery economically feasible from tight plays.

Horizontal drilling is important because instead of drilling multiple wells into a relatively shallow play that will "pay," horizontal drilling permits one well to be drilled and multiple, horizontal bores to extend for thousands of feet, opening up much more of the play for oil/gas recovery from a single well. Hydraulic fracturing was developed shortly after World War II as a technique to "stimulate" the production of oil from conventional oil reservoirs. Typically in hydraulic fracturing, water (with some additives) is pumped at pressures sufficiently high to fracture oil-bearing formations, resulting in additional production. How does the combination of horizontal drilling and hydraulic fracturing produce oil/gas from tight plays?

A number of governmental agencies, companies, and associations discuss the stages or sequences needed to produce oil/gas from tight plays. The Energy Institute (2015), NETL (2011), Turcotte *et al*. (2014), Crawford (2013), Graves (2012), and Bell (2013), as well as a number of web sites, have been consulted in the development of the follow discussion. Various stages are cited by different sources, but all encompass the same procedures, just with some procedures in different stages. Six stages are common; a six-stage procedure for extracting oil/gas from tight plays includes:

1) well construction
2) horizontal drilling
3) well completion and stimulation
4) flow testing
5) long-term production
6) project completion and reclamation.

Each of these topics will be discussed. Figure 17.10 provides an illustration with important features associated with a typical hydraulically fractured well with a horizontal trace in a tight geologic formation.

Starting at the top of the figure, representing the surface, are indications of a private water well and a municipal water well, both designated as "USDW" (underground source of drinking water). A USDW must contain less than 10 000 mg/L of dissolved solids. The initial vertical wellbore is illustrated and transitions to a horizontal bore in the play of interest. Separating the surface and the horizontal bore are several geologic layers (extending over many thousands of feet depth), many of very low permeability, which effectively blocks any migration of fluids from the play to the surface. In the wellbore near the surface, steel casings, cemented in place, line the bore and prevent any migration of fracturing fluids from contaminating the USDW. The wellbore is also lined with steel casings. The horizontal segment of the wellbore illustrates the results of hydraulic fracturing by showing the fractures in the shale play in this illustration.

1) *Well construction.* A well site requires about 5 acres and an access road that is likely to have heavy traffic. The well is drilled in stages, with each diameter smaller and deeper than the preceding one, forming a drill string. During the drilling process, drilling "mud" is circulated

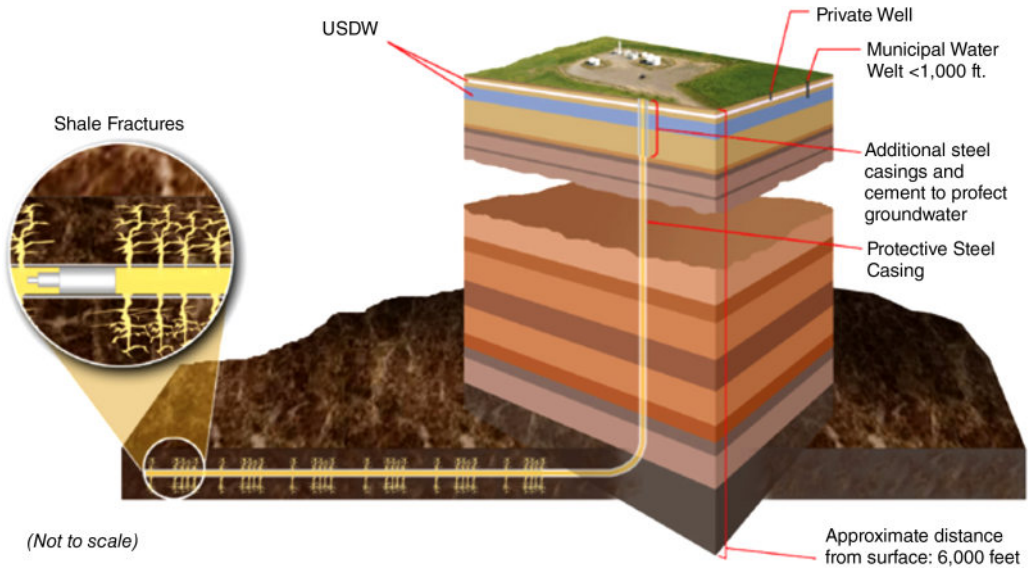

Figure 17.10 Features associated with a typical hydraulically fractured well with a horizontal trace. *Source*: NETL (2011).

through the drill string back to surface; the mud carries drill cuttings back to surface and cools the drill bit. At each stage a casing, run to the drill location, composed of steel pipe is hung from the wellhead. Cement is pumped down the casing to form a protective barrier, and the integrity of the barrier tested. Portions of the wellbore near the surface may have two or more layers of cement and steel casings. Figure 17.11 illustrates the general layout for a three-casing arrangement. The intermediate casings may extend several thousands of feet from the surface. The casing and cement provide a barrier to prevent drilling fluids from contaminating the USDW and other water sources.

2) *Horizontal drilling.* As illustrated in Figure 17.10, as the play is approached, the drilling direction is directed from the vertical to the horizontal as the wellbore enters the play. Although sharp turns are possible, they exacerbate drilling issues, so gradual turns are the usual. Once horizontal and into the "pay" part of the play, the wellbore may extend several thousands of feet – generally much longer than the play is deep. The horizontal length in the play determines the oil or gas recovery potential. Depending on the geology, a single surface well may have two or more horizontal wellbores extending in different directions. Use of multiple horizontal bores from a single wellhead minimizes the surface footprint.

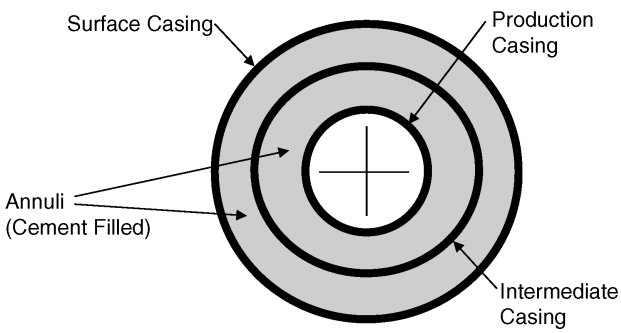

Figure 17.11 Wellbore with multiple casings.

3) *Well completion and stimulation.* This step begins with the wellbore and involves hydraulic fracturing to achieve oil/gas flow from a tight play. Starting at the end of a horizontal wellbore, the "toe," segments of the bore are isolated into fracture stages with each stage containing a number of perforation clusters. Within a stage, at each cluster location, the casing is perforated, typically by explosives charges in a "gun," until all clusters are perforated. This phase is called "plug and perf," and is the dual process of perforating the casing and plugging the wellbore until the entire segment is ready for fluid flow. The plug and perf process moves to the next fracture stage, where it is repeated at the next clusters. When the plug and perf process is completed for a stage, hydraulic fracturing is initiated. The gun is removed from the stage, the debris washed out, and hydraulic fracturing initiated. This sequence is repeated for each stage until the sector of interest has been completed. Hydraulic fracturing involves pumping under high pressure (thousands of pounds per square inch) a series of fracturing fluids, each formulated to accomplish a specific task in the fracturing process. The fracturing fluid, typically water with additives, is pumped through the casing perforations, initiating cracks that create one or more fractures that extend into the surrounding rock. A fracture may propagate for hundreds of feet until the high-pressure pumping ceases.

Several fluids are sequentially used to prepare and fracture the rock. Each is essentially a dilute mixture of water with specific additives. The exact blends and additives vary as functions of the site characteristics. The first fluid used is often acetic, a dilute mixture of hydrochloric or muriatic acid, used to clear cement debris from the wellbore and dissolve minerals from the open fractures near the wellbore. That is often followed by a low viscosity water mixture called "slickwater." Traditional hydraulic fracturing uses relatively low flow rates of high-viscosity fluids; however, large flow rates of slickwater have become the norm for many fracturing applications. Both traditional and slickwater fracturing require high pressures to accomplish fracturing of the rock. However, when fracturing takes place and the pressure is reduced in preparation for oil/gas recovery, the fractures often collapse, rendering the fracturing less effective. To avoid this, fracturing fluids after the initial fracturing has been accomplished are formulated with solid "proppants" that "prop" open the fractures. Proppants are usually spherical, fine-grained sand or ceramic materials of uniform size. The proppant material is mixed with water and other additives and injected into the fractured rock. The proppant load in the water varies depending on the characteristics of the fractured rock. In addition to proppants, hydraulic fracturing fluids can also contain biocides (to control bacteria growth), scale inhibitors (to control precipitation of minerals), iron-stabilizing agents (to maintain ferrous compounds in soluble form), and corrosion inhibitors (to protect casing walls).When the hydraulic fracture is complete, fresh water is used to flush the excess proppant from the wellbore and prepare the fracture stage for production. Shale wells may have as many as 25 fracture stages. Since each stage may require up to 500 000 gal of water; a single sector can require more than 10 000 000 gal. When the fracturing process is completed, a portion of the water flows out of the well and can be recycled after processing to remove harmful compounds.

Decisions about the details of any well stimulation, stages and fractures or fluids, are not arbitrarily made. Most companies have well-established procedures to ascertain what decisions to make in order to maximize the benefit-to-cost ratio. Ajayi *et al.* (2013) and Crawford (2013) provide interesting insight into the effort and level of sophistication of details of well stimulation. Crawford (2013) points out that Halliburton, one of the largest companies involved in fracturing activities, has a number of PhD-level technical experts engaged in making decisions and improving techniques to ensure that each hydraulically fractured well returns its maximum economic potential. In an insightful paper, Ajayi *et al.* (2013) describe Schlumberger's (another large company in the fracturing business) efforts to

optimize the stage and perforation cluster distributions for maximum return. They reference a computer program, *Mangrove Completion Advisor*, which has been validated as significantly improving stage and cluster distributions. The complexity of a play undergoing hydraulic fracture is best described by a quote from Ajayi *et al*. (2013):

> Hydraulic fracture growth is governed by the rock fabric and geomechanical properties of the reservoir, the preexisting fracture network and prevailing in situ stress magnitudes, and anisotropy.

The approach is not just to punch a hole and plug and perf, but to understand the completion process and to take advantage of that understanding. Site preparation is complicated, with many different functions required. Figure 17.12 provides a drawing of a typical site during the fracture procedure. The wellhead occupies the center position; around the wellhead are positioned the pumps required for the fracturing process, a blender for the fracturing fluids, and a control van. Storage is provided for fluid storage, the proppant, and any additives used. Figure 17.12 was drawn by DOE artist Joe Lindley. He drew a number of line drawings illustrating different enhanced oil recovery (EOR) procedures and was active in last part of the twentieth century: they are available on the NETL website at http://netl.doe.gov/research/oil-and-gas/enhanced-oil-recovery/eor-process-drawings. Although Figure 17.12 shows the hydraulic fracturing to be in the vertical as opposed to the now more common horizontal, the details and the relationships of the components at the surface are still valid. Figure 17.13 is a photograph of a site with multiple wellheads. The congestion is apparent, but the photograph is essentially congruent with the schematic of Figure 17.12.

An interesting question is how long does the process of drilling, plugging and perforating, and readying a well for production take? The general answer is that a typical well might take 3 or 4 weeks for site preparation, 4–6 weeks for drilling, 5–10 days for hydraulic fracturing, and 2 or 3 weeks for completion after fracturing.

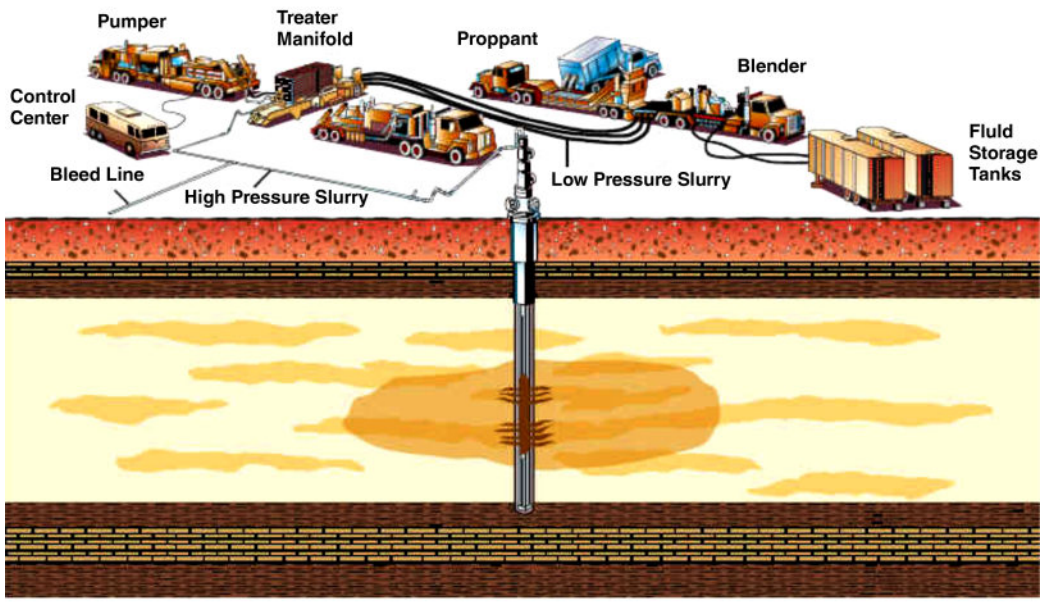

Figure 17.12 Well site during hydraulic fracturing procedure. *Source*: http://netl.doe.gov/file%20library/research/oil-gas/enhanced%20oil%20recovery/other/colhf.pdf.

Figure 17.13 Photograph of hydraulic fracturing site with two wellheads. *Source*: NETL (2011).

4) *Flow testing.* As might be expected, once the well is ready for production, flow testing to verify the flow rate and product characteristics are needed. A temporary separator vessel is used to determine characteristics and flow rates of the gas/oil recovered as well as the fracturing fluid that flows back up the well. Oil recovered is delivered to a refinery for further processing, and natural gas is either harvested or flared, depending on the purpose of the well.
5) *Long-term production.* When testing is complete, production starts and continues as long as the economics are favorable. In many instance (Graves, 2012) the initial recovery rate declines significantly after a few years to 10–20% of the initial recovery rate. But a well may produce at 10–20% of the initial rate for a number of years. Industry expectation is for production runs of up to 20 years. Some wells may be restimulated after about 5 years to increase production.
6) *Shutdown and recovery.* When production decreases to a noneconomic level and if restimulation is not warranted, the site is shut down and the land returned to near predrilling conditions.

The preceding has provided an introduction to the processes involved in extracting oil/gas for tight shale plays. As discussed in Section 17.1, while the use of hydraulic fracturing in tight plays is an undeniable economic success, environmental issues and other concerns have resulted in the process becoming quite controversial. The internet contains a plethora of pro and con web sites and articles. The issues and concerns include: (1) fracturing fluids and other contaminants finding their way into the water supply; (2) fracturing within geological plays resulting in increased seismic activity; (3) the water required for hydraulic fracturing, perhaps as much as 10 million gallons per well, causing water shortages,; and (4) overburdening of local infrastructures. There are other concerns, but these are frequently mentioned and have creditable responses. Each will be examining separately.

1) *Fracturing fluids and other contaminants finding their way into the water supply.* The US Environmental Protection Agency has been assigned responsibility to assess this issue. A draft report was issued in June 2015 (EPA, 2015). The following quote was taken from the Executive Summary of this report:

> Through this national-level assessment, we have identified potential mechanisms by which hydraulic fracturing could affect drinking water resources. Above ground

mechanisms can affect surface and ground water resources and include water withdrawals at times or in locations of low water availability, spills of hydraulic fracturing fluid and chemicals or produced water, and inadequate treatment and discharge of hydraulic fracturing wastewater. Below ground mechanisms include movement of liquids and gases via the production well into underground drinking water resources and movement of liquids and gases from the fracture zone to these resources via pathways in subsurface rock formations. We did not find evidence that these mechanisms have led to widespread, systemic impacts on drinking water resources in the United States . . . The number of identified cases where drinking water resources were impacted are small relative to the number of hydraulically fractured wells.

2) *Fracturing within geological plays resulting in increased seismic activity.* Hydraulic fracturing undoubtedly leads to an increase in seismic activity; however, virtually all are classified as micro-seismic events, Richter scale values of less than −1, and are not detectable on the surface. Turcotte et *al*. (2015) examined this concern and concluded that most micro-seismic events caused by hydraulic fracturing are in the range −3 to −2 on the Richter scale. Moreover, they assessed the probability of a Richter scale 4 seismic event as being 10^{-15} to 10^{-9}.
3) *The water required for hydraulic fracturing, perhaps as much as 10 million gallons per well, causing water shortages.* Although the water used in hydraulic fracturing is significant, the overall quantity of water used for fracturing is small compared with the water use for other purposes. The EPA (2015) draft report provides a cogent assessment:

> Water is a major component of nearly all hydraulic fracturing operations. It typically makes up almost 90% or more of the fluid volume injected into a well, and each hydraulically fractured well requires thousands to millions of gallons of water. Cumulatively, hydraulic fracturing activities in the United States used on average 44 billion gal of water a year in 2011 and 2012, according to the EPA's analysis . . . Although this represents less than 1% of total annual water use and consumption at this scale, water withdrawals could potentially impact the quantity and quality of drinking water resources at more local scales . . .
>
> The potential for impacts to drinking water resources from hydraulic fracturing water withdrawals is highest in areas with relatively high fracturing water use and low water availability. Southern and western Texas are two locations where hydraulic fracturing water use, low water availability, drought, and reliance on declining ground water has the potential to affect the quantity of drinking water resources. Any impacts are likely to be realized locally within these areas . . .
>
> The potential for impacts to drinking water quantity due to hydraulic fracturing water use appears to be lower – but not eliminated – in other areas of the United States. Future problems could arise if hydraulic fracturing increases substantially in areas with low water availability, or in times of water shortages.

Testa (2013) provides examples of hydraulically fractured water-availability issues in Texas and presents interesting examples of how local residents assess EOR.

4) *Overburdening of local infrastructures*. Extensive EOR activities in an area can overwhelm local and state governmental services. Williston, ND, is often cited as a modern boom town because of the EOR activities in the Bakken shale play. Anyone passing through the town sees the widespread evidence of effects of the increased EOR activities. The Williston experience has even been a Smithsonian Channel subject. A typical well site requires many 18-wheeler

loads over likely two-lane, farm-to-market roads. Not only are the roads impacted, but safety issues are compounded.

Other issues and concerns are also mentioned in conjunction with EOR in a region. Fundamentally, issues and concerns with EOR activities are ongoing. The final conclusions, and attendant regulations, could significantly impact EOR activities in the USA. This is not a closed issue by any means.

17.5 The New Reality

On a yearly basis, the EIA provides an *Annual Energy Outlook* (AEO) that makes energy consumption and production predictions for 25 years by examining six scenarios: (1) a reference case, (2) low economic growth, (3) high economic growth, (4) low oil price, (5) high oil price, and (6) high oil and gas resource. Table 17.2 summarizes the six scenarios. The 2015 AEO (EIA, 2015) *reference case* provides an overview of the expected energy future from 2015 until 2040 for the USA. Figure 17.14 presents the reference case projections as well as the energy history from

Table 17.2 EIA AEO cases.

Case name	GDP (%)	Crude oil ($/bbl)[a)]	Resource recovery
Reference	2.4	to 141 in 2040	
Low growth	1.8	to 141 in 2040	
High growth	2.9	to 141 in 2040	
Low oil price	2.4	to 76 in 2040	
High oil prices	2.4	to 252 in 2040	
High oil/gas resources	2.4		50% higher than reference case with additional resources identified.

GDP: gross domestic product.
a) 2013 dollars.

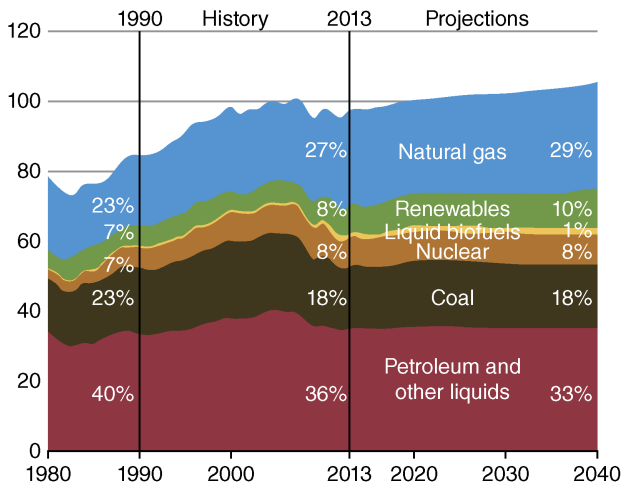

Figure 17.14 Primary energy consumption (quads) by fuel type from 2013 to 2040 (reference case). *Source*: EIA (2015).

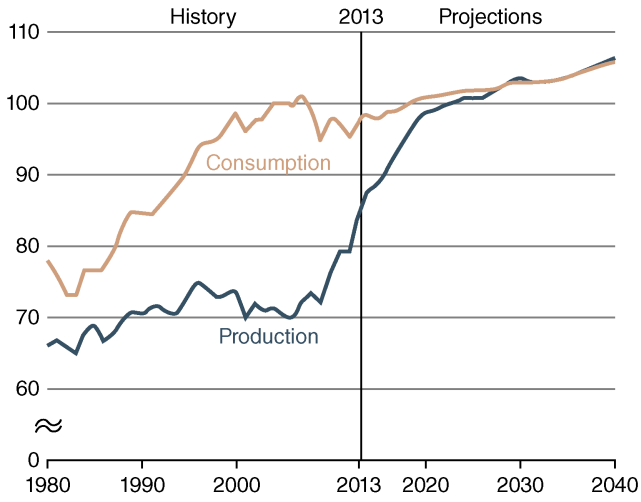

Figure 17.15 Reference case total energy production and consumption (quads) 1980–2040 (reference case). *Source*: EIA (2015).

1980 through 2013. The energy usage is in quads. The actual energy usage data are congruent with the details in Chapter 1. Perhaps the most noteworthy aspects of the energy projections are the lack of significant changes in either total consumption or the constituent contributors. The total estimated energy use increases from slightly under 100 quad to slightly more than 100 quad through 2040, and the percentage contributions shift by a maximum of 3%.

A prime concern in the USA has been the dependence on petroleum imports and its impact on economic and political issues. Figure 17.15 illustrates the actual (history, 1980–2013) and projected production and consumption (to 2040) for the reference case. From the mid-1980s through about 2005, the difference between consumption and production widened; however, from 2005 onwards the gap between the two narrowed. For the reference case, consumption and production become equal by about 2030 with little difference between the two by 2020. Considering that the gap between consumption and production by 2013 had narrowed to about 10 quad/year, the effects of enhanced oil and natural gas recovery in the USA have been pronounced.

Figures 17.14 and 17.15 are for the reference case, perhaps the most likely scenario, but the chaotic history of "energy" teaches us that unforeseen events can have dramatic effects on energy cost and availability. The other five cases in the EIA AEO review alternate energy scenarios. Since net energy imports are the difference between consumption and production, the history and projections of net energy imports for the six cases are an effective gauge of the importance of the six different energy scenarios. Figure 17.16 delineates the dramatic differences between energy consumption and production for the various cases considered. The "history" portion of the figure unequivocally demonstrates the effects of enhanced oil and gas production since 2005. Except for the *low oil price* case, imports are projected to continue to decrease through 2040. If the *high oil price* or the *high oil and gas resource* cases are followed, the USA would become an energy exporting nation – quite a change from the 1980s dependence on foreign energy imports.

Figure 17.17 contains similar information on natural gas imports (10^{12} cubic feet) for four cases (reference case, low oil price, high oil price, high oil and gas resource). For all four cases, natural gas imports decline through 2040. Indeed, for all cases considered, by 2015–2020, the USA would become a natural gas exporting nation! Figure 17.18, which illustrates USs natural gas production, is a companion figure to Figure 17.17. From 2005 to 2013, natural gas

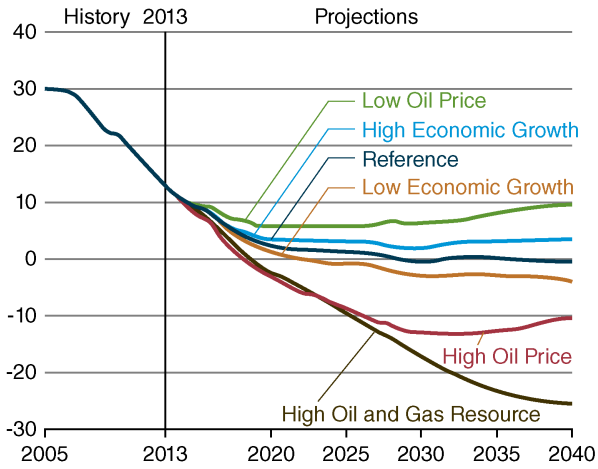

Figure 17.16 History and projections of energy imports (quads) for the six cases considered. *Source*: EIA (2015).

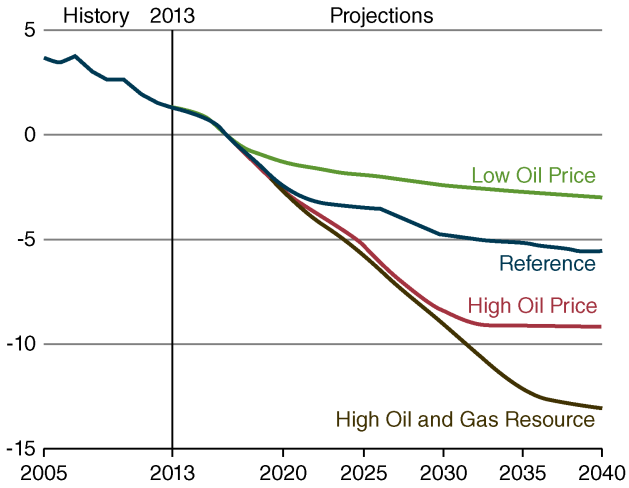

Figure 17.17 Natural gas imports (10^{12} cubic feet) for four cases. *Source*: EIA (2015).

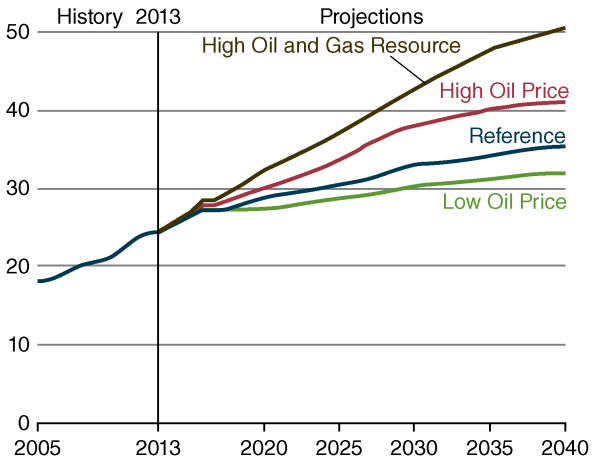

Figure 17.18 US natural gas production (10^{12} cubic feet) for four cases. *Source*: EIA (2015).

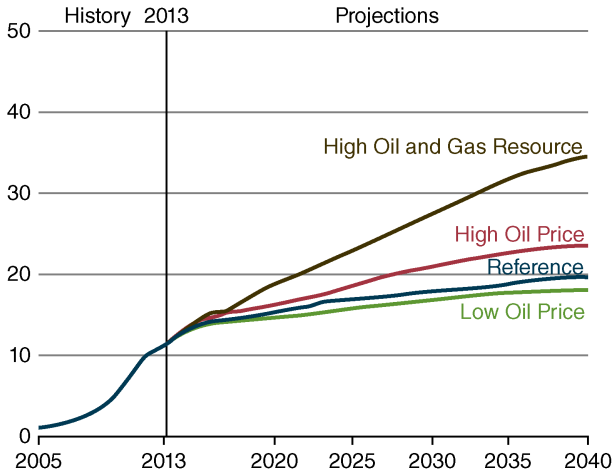

Figure 17.19 US shale gas production (10^{12} cubic feet) for four cases. *Source*: EIA (2015).

production in the USA increased by 35%. The growth in production was driven by the development of shale gas resources. In the reference case, shale natural gas production is projected to increase by close to 59% by 2040. Natural gas is an attractive energy source because, compared with many other fuels, it has relatively lower CO_2 generation and a lower cost on a per million British thermal unit basis. Figure 17.19 presents history and projections for shale gas production. Comparing Figures 17.18 and 17.19 reveals that much of the future production is attributable to shale gas. As evidenced by Figure 17.20, since 2005 natural gas cost per million British thermal units has declined by nearly two-thirds. Projections of cost per million British thermal units for the four cases from 2013 to 2040 show moderate price increases, except for the high oil price case, and even in that case, in 2013 dollars, the price of natural gas does not reach the 2005 level until about 2035. As in Chapter 1, the use of dollars cast in terms of a single year (2013 for EIA AEO 2015) implicitly accounts for inflation by considering constant or chained dollars. For the high oil and gas resource case, the price, in 2013 dollars, remains nearly through 2040.

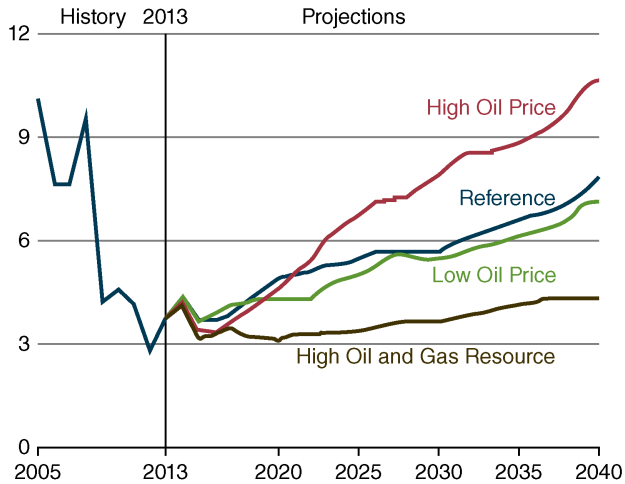

Figure 17.20 US natural gas costs (2013 dollars/million Btu) for four cases. *Source*: EIA (2015).

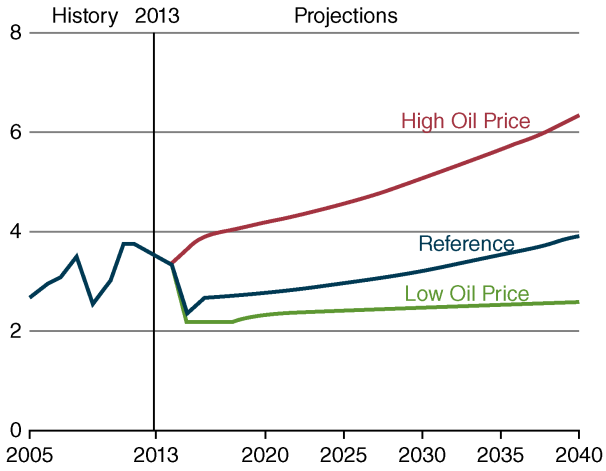

Figure 17.21 History and projections of motor gasoline prices (2013 dollars/gal). *Source*: EIA (2015).

Recent (since 2012) decreases in motor gasoline prices have been dramatic, as is evidenced by Figure 17.21. For the reference case, gasoline prices (2013 dollars) do not reach the 2010 value until 2037, and in the low oil price case, prices per gallon (2013 dollars) stay below the 2013 level. The high oil price case monotonically increases. For the reference and low oil price cases the USA is being given another chance, as in the 1980s, to utilize technology and conservation to mitigate future energy "crises." Perhaps the results will be better than earlier. The continued importance of oil from fracturing endeavors ("tight" oil) is illustrated by Figure 17.22. The production of tight oil has increased since 2005 and is currently about 5 million barrels per day. The EIA predicts substantial continued contributions of tight oil from hydraulic fracturing, with the reference case production reaching a plateau by about 2020. The high oil and gas case monotonically increases through 2040.

Although coal is an abundant resource in the USA, politics, public perceptions, and emission-control economics have significantly impacted coal production since 2005. Figure 17.23 presents the history and projections for coal production for the six cases. Except for the high oil and gas resource case, coal production for the other cases is predicted to rebound. Indeed, for the high oil price case, coal production may well exceed the 2005 level by 2035.

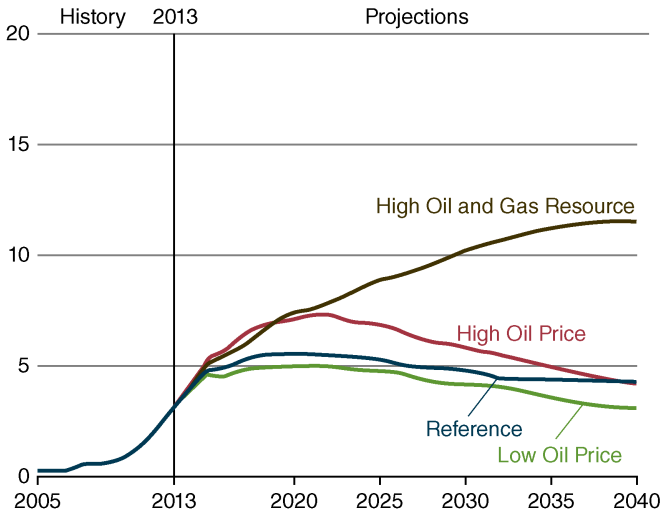

Figure 17.22 US tight oil production (10^6 barrels/day) for four cases. *Source*: EIA (2015).

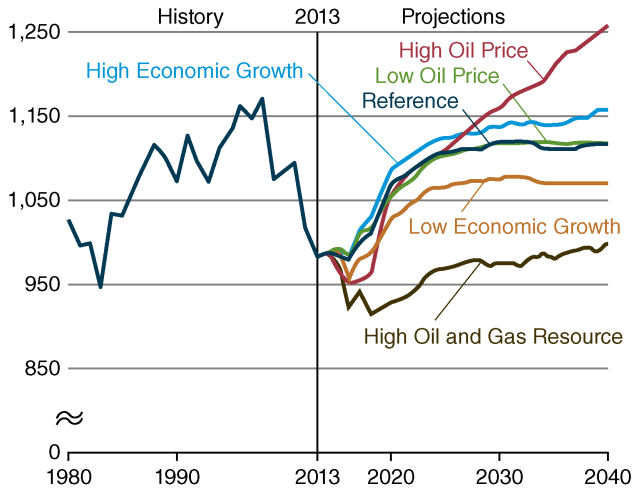

Figure 17.23 History and projections of coal production (10^6 short tons) for the six cases considered. *Source*: EIA (2015).

Figure 1.16, the US coal flow diagram (2014), shows that 92% of coal is used for electricity generation. Considering the emissions issues for coal, increased natural gas reserves, and enhanced oil and gas production, what mix of fuel sources will be likely in the future? Figures 17.24 and 17.25 help to answer that question. The history portion of Figure 17.24, the reference case, is congruent with the details presented in Chapter 1. From 2013 to 2040, electricity production is predicted to increase about 40% for the reference case; coal's portion is decreased from 39% to 34%, nuclear is reduced by 3%, renewable energy is increased by 5%, and natural gas increased by 4%. None of the reference case's predictions are startling. Figure 17.25 examines the breakdown of fuel types for electricity generation in 2013 and projected in 2040. Except for hydroelectric power, the electricity generation from other renewable sources is expected to increase – the amounts depending on the specific case scenarios.

The projected price of electricity (2013 cents per kilowatt-hour) from 2013 through 2040 is provided in Figure 17.26 for the six cases. The high oil and gas resource case electricity costs are

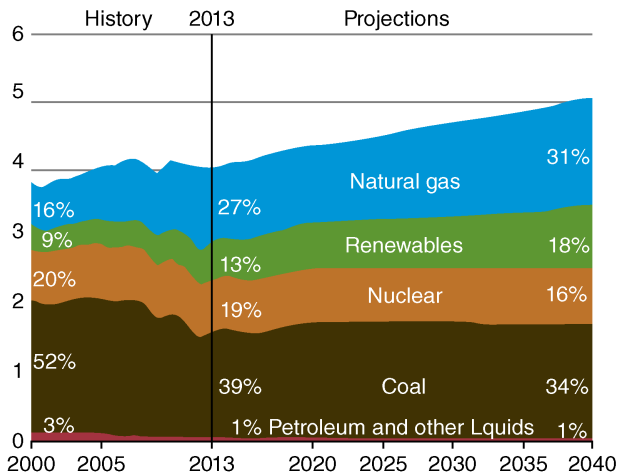

Figure 17.24 Electricity generation (10^{12} kWh) by fuel type from 2013 to 2040 (reference case). *Source*: EIA (2015).

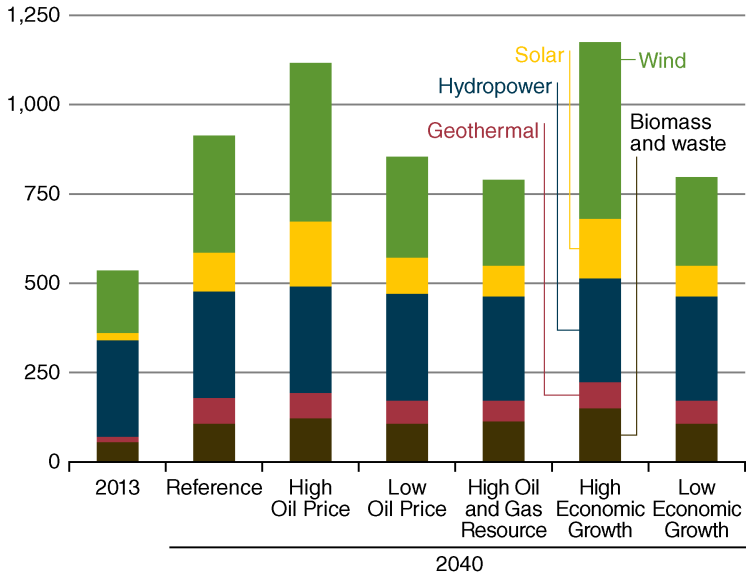

Figure 17.25 Renewable electricity generation (10^9 kWh) for the six cases for 2013 and 2040. *Source*: EIA (2015).

expected to be nearly constant through 2040, while the other five cases are projected to have varying levels of price increases. But even for the high oil price case, the increase per kilowatt-hour is only from 10¢ to 13¢. Hence, in terms of 2013 dollars, electricity is not expected to dramatically increase in price.

As Figure 17.24 indicates, in 2013 fossil fuels provided 67% of the energy used in electricity production. By 2040, for the reference case, the percentage of electricity generated by fossil fuels is projected to be 66%, a decrease of only 1%. However, since electricity usage is expected to increase by about 20% from 2013 to 2040, the quantity of fossil fuels used for electricity generation increases significantly. Thus, fossil fuel combustion product emissions attributable to electricity generation will also increase accordingly, unless measures are taken to reduce/capture/sequester/control the emissions. In late 2016, the National Academies released the report *The Power of Change* that delineated findings and made recommendations in three

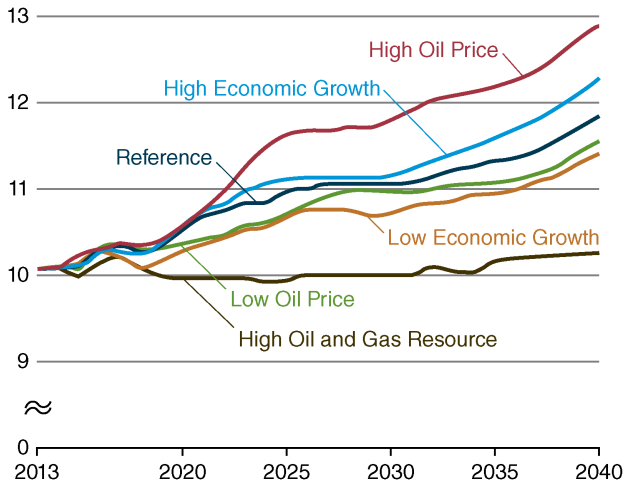

Figure 17.26 Average retail electricity price (2013 dollars/kWh) for the six cases. *Source*: EIA (2015).

prioritized categories: overarching, key, and other (National Academies of Sciences, Engineering, and Medicine, 2016). In the first category (overarching) are two recommendations that are more important than all the others. Also included are 10 key recommendations and eight key findings. Twelve additional recommendations are made in the "other" category. The findings and recommendations are presented in the Summary section of the report and are discussed in detail in the remainder of the report. Essentially, *The Power of Change* findings and recommendations address economic, legal, legislative, and technology issues whose resolution would markedly enhance the production of "clean" electricity.

This section has examined the future of energy as projected by the EIA from 2013 through 2040. The impact of hydraulic fracturing and increased natural gas resources-reserves are significant and are examined in terms of the six cases (scenarios) delineated at the start of the section. Because of enhanced oil and natural gas recovery, the energy future of the USA is markedly different from what might have been expected in the late twentieth century.

17.6 Closure

However, even though hydraulic fracturing has alleviated some energy concerns, many issues, problems, and concerns still exist. Fossil fuels are still finite, nonrenewable resources whose combustion still produces CO_2, a greenhouse gas. Hence, the topics of this textbook are very germane for the future. *The identification of additional fossil fuel resources has essentially provided more time to discover, implement, and develop other, more sustainable and more greenhouse gas friendly energy resources*.

References

Ahmed, T. and Meehan, D.N. (2012) *Advanced Reservoir Management and Engineering*, 2nd edn. Elsevier, Waltham. MA.

Ajayi, B., Aso, I.I., Terr, I.J., Jr. *et al.* (2013) Stimulation design for unconventional resources. *Oilfield Review*, **25** (2): 34–46.

Bell, T. (2013) 'There's gas in them thar shales!" Shale gas recovery 101. *The Bent of Tau Beta Pi*, (Summer): 22–27 61.

Crawford, M. (2013) Fracturing rock to unlock new oil. *Mechanical Engineering*, **135** (12): 24–29.

Economides, M.J., Hill, A.D., Ehlig-Economides, C., and Zhu, D. (2013) *Petroleum Production Systems*, 2nd edn. Prentice-Hall, Upper Saddle River, NJ.

EIA (2013) Technically Recoverable Shale Oil and Shale Gas Resources: An Assessment of 137 Shale Formations in 41 Countries outside the United States. http://www.eia.gov/analysis/studies/worldshalegas/archive/2013/pdf/fullreport_2013.pdf (accessed October 27, 2016).

EIA (2015) *Annual Energy Outlook 2015 with Projections to 2040*. DOE/EIA-0383(2015). www.eia.gov/forecasts/aeo/pdf/0383(2015).pdf (accessed October 26, 2016).

Energy Institute (2015) *A Guide to Shale Gas*. Energy Institute, London.

EPA (2015) Assessment of the Potential Impacts of Hydraulic Fracturing for Oil and Gas on Drinking Water Resources. EPA/600/R-15/047a. www.epa.gov/hfstudy (accessed October 27, 2016).

Graves, J. (2012) *Fracking: America's Alternative Energy Revolution*. Safe Harbor International Publishing, Ventura, CA.

National Academies of Sciences, Engineering, and Medicine (2016) The Power of Change: Innovation for Development and Deployment of Increasingly Clean Electric Power

Technologies. The National Academies Press, Washington, DC. https://www.nap.edu/catalog/21712/the-power-of-change-innovation-for-development-and-deployment-of (accessed November 2, 2016).
NETL (2011) Shale Gas: Applying Technology to Solve America's Energy Challenges. National Energy Technology Laboratory. http://www.netl.doe.gov/file%20library/research/oil-gas/Shale_Gas_March_2011.pdf (Accessed October 27, 2016).
Reuters (2015) The Earth is not running out of oil and gas, BP says. *The Telegraph*, November 2. http://www.telegraph.co.uk/finance/newsbysector/energy/oilandgas/11971280/The-Earth-is-not-running-out-of-oil-and-gas-BP-says.html (accessed October 27, 2016).
Testa, B.M. (2013) Home on the shales. *Mechanical Engineering*, **135** (12): 30–35.
Turcotte, D.L., Moores, E.M., and Rundle, J.B. (2014) Super fracking. *Physics Today*, **67** (8): 34–39.
Webber, M.E. (2013) Lessons from the shale revolution. *Mechanical Engineering*, **135** (10): 20.

Further Reading

Hefley, W.E. and Wang, Y. (eds.) (2015) *Economics of Unconventional Shale Gas Development*. Springer, New York.
Holloway, M.D. and Rudd, O. (2013) *Fracking: The Operations and Environmental Consequences of Hydraulic Fracking*. Scrivener Publishing/John Wiley & Sons, Inc., Salem, MA/Hoboken, NJ.

Appendix A

Reproduced from Goswami, Y., Kreith, F., and Kreider, J.F. (2000) *Principles of Solar Engineering*, 2nd edn. Taylor and Francis, New York.

Alternative Energy Systems and Applications, Second Edition. B. K. Hodge.

Companion website: www.wiley.com\go\Hodge\AESystemsandApplications2E

Table A.1 Solar position and insolation values for 24°N latitude.

Date	Solar time		Solar position		BTUH/sq. ft. total insolation on surface[b]						
	AM	PM	Alt	Azm			South facing surface angle with horiz.				
					Normal[c]	Horiz.	14	24	34	44	90
Jan 21	7	5	4.8	65.6	71	10	17	21	25	28	31
	8	4	16.9	58.3	239	83	110	126	137	145	127
	9	3	27.9	48.8	288	151	188	207	221	228	176
	10	2	37.2	36.1	308	204	246	268	282	287	207
	11	1	43.6	19.6	317	237	283	306	319	324	226
	12		46.0	0.0	320	249	296	319	332	336	232
	Surface daily totals				2766	1622	1984	2174	2300	2360	1766
Feb 21	7	5	9.3	74.6	158	35	44	49	53	56	46
	8	4	22.3	67.2	263	116	135	145	150	151	102
	9	3	34.4	57.6	298	187	213	225	230	228	141
	10	2	45.1	44.2	314	241	273	286	291	287	168
	11	1	53.0	25.0	321	276	310	324	328	323	185
	12		56.0	0.0	324	288	323	337	341	335	191
	Surface daily totals				3036	1998	2276	2396	2436	2424	1476
Mar 21	7	5	13.7	83.3	194	60	63	64	62	59	27
	8	4	27.2	76.8	267	141	150	152	149	142	64
	9	3	40.2	67.9	295	212	226	229	225	214	95
	10	2	52.3	54.8	309	266	285	288	283	270	120
	11	1	61.9	33.4	315	300	322	326	320	305	135
	12		66.0	0.0	317	312	334	339	333	317	140
	Surface daily totals				3078	2270	2428	2456	2412	2298	1022
Apr 21	6	6	4.7	100.6	40	7	5	4	4	3	2
	7	5	18.3	94.9	203	83	77	70	62	51	10
	8	4	32.0	89.0	256	160	157	149	137	122	16
	9	3	45.6	81.9	280	227	227	220	206	186	46
	10	2	59.0	71.8	292	278	282	275	259	237	61
	11	1	71.1	51.6	298	310	316	309	293	269	74
	12		77.6	0.0	299	321	328	321	305	280	79
	Surface daily totals				3036	2454	2458	2374	2228	2016	488
May 21	6	6	8.0	108.4	86	22	15	10	9	9	5
	7	5	21.2	103.2	203	98	85	73	59	44	12
	8	4	34.6	98.5	248	171	159	145	127	106	15
	9	3	48.3	93.6	269	233	224	210	190	165	16
	10	2	62.0	87.7	280	281	275	261	239	211	22
	11	1	75.5	76.9	286	311	307	293	270	240	34
	12		86.0	0.0	288	322	317	304	281	250	37
	Surface daily totals				3032	2556	2447	2286	2072	1800	246
Jun 21	6	6	9.3	111.6	97	29	20	12	12	11	7
	7	5	22.3	106.8	201	103	87	73	58	41	13
	8	4	35.5	102.6	242	173	158	142	122	99	16
	9	3	49.0	98.7	263	234	221	204	182	155	18
	10	2	62.6	95.0	274	280	269	253	229	199	18
	11	1	76.3	90.8	279	309	300	283	259	227	19
	12		89.4	0.0	281	319	310	294	269	236	22
	Surface daily totals				2994	2574	2422	2230	1992	1700	204

Table A.1 (*Continued*)

Date	Solar time		Solar position		BTUH/sq. ft. total insolation on surface[b]						
							South facing surface angle with horiz.				
	AM	PM	Alt	Azm	Normal[c]	Horiz.	14	24	34	44	90
Jul 21	6	6	8.2	109.0	81	23	16	11	10	9	6
	7	5	21.4	103.8	195	98	85	73	59	44	13
	8	4	34.8	99.2	239	169	157	143	125	104	16
	9	3	48.4	94.5	261	231	221	207	187	161	18
	10	2	62.1	89.0	272	278	270	256	235	206	21
	11	1	75.7	79.2	278	307	302	287	265	235	32
	12		86.6	0.0	280	317	312	298	275	245	36
	Surface daily totals				2932	2526	2412	2250	2036	1766	246
Aug 21	6	6	5.0	101.3	35	7	5	4	4	4	2
	7	5	18.5	95.6	186	82	76	69	60	50	11
	8	4	32.2	89.7	241	158	154	146	134	118	16
	9	3	45.9	82.9	265	223	222	214	200	181	39
	10	2	59.3	73.0	278	273	275	268	252	230	58
	11	1	71.6	53.2	284	304	309	301	285	261	71
	12		78.3	0.0	286	315	320	313	296	272	75
	Surface daily totals				2864	2408	2402	2316	2168	1958	470
Sep 21	7	5	13.7	83.8	173	57	60	60	59	56	26
	8	4	27.2	76.8	248	136	144	146	143	136	62
	9	3	40.2	67.9	278	205	218	221	217	206	93
	10	2	52.3	54.8	292	258	275	278	273	261	116
	11	1	61.9	33.4	299	291	311	315	309	295	131
	12		66.0	0.0	301	302	323	327	321	306	136
	Surface daily totals				2878	2194	2342	2366	2322	2212	992
Oct 21	7	5	9.1	74.1	138	32	40	45	48	50	42
	8	4	22.0	66.7	247	111	129	139	144	145	99
	9	3	34.1	57.1	284	180	206	217	223	221	138
	10	2	44.7	43.8	301	234	265	277	282	279	165
	11	1	52.5	24.7	309	268	301	315	319	314	182
	12		55.5	0.0	311	279	314	328	332	327	188
	Surface daily totals				2868	1928	2198	2314	2364	2346	1442
Nov 21	7	5	4.9	65.8	67	10	16	20	24	27	29
	8	4	17.0	58.4	232	82	108	123	135	142	124
	9	3	28.0	48.9	282	150	186	205	217	224	172
	10	2	37.3	36.3	303	203	244	265	278	283	204
	11	1	43.8	19.7	312	236	280	302	316	320	222
	12		46.2	0.0	315	247	293	315	328	332	228
	Surface daily totals				2706	1610	1962	2146	2268	2324	1730
Dec 21	7	5	3.2	62.6	30	3	7	9	11	12	14
	8	4	14.9	55.3	225	71	99	116	129	139	130
	9	3	25.5	46.0	281	137	176	198	214	223	184
	10	2	34.3	33.7	304	189	234	258	275	283	217
	11	1	40.4	18.2	314	221	270	295	312	320	236
	12		42.6	0.0	317	232	282	308	325	332	243
	Surface daily totals				2624	1474	1852	2058	2204	2286	1808

Table A.2 Solar position and insolation values for 32°N latitude.

Date	Solar time		Solar position		BTUH/sq. ft. total insolation on surfaces[b]						
							South facing surface angle with horiz.				
	AM	PM	Alt	Azm	Normal[c]	Horiz.	22	32	42	52	90
Jan 21	7	5	1.4	65.2	1	0	0	0	0	1	1
	8	4	12.5	56.5	203	56	93	106	116	123	115
	9	3	22.5	46.0	269	118	175	193	206	212	181
	10	2	30.6	33.1	295	167	235	256	269	274	221
	11	1	36.1	17.5	306	198	273	295	308	312	245
	12		38.0	0.0	310	209	285	308	321	324	253
	Surface daily totals				2458	1288	1839	2008	2118	2166	1779
Feb 21	7	5	7.1	73.5	121	22	34	37	40	42	38
	8	4	19.0	64.4	247	95	127	136	140	141	108
	9	3	29.9	53.4	288	161	206	217	222	220	158
	10	2	39.1	39.4	306	212	266	278	283	279	193
	11	1	45.6	21.4	315	244	304	317	321	315	214
	12		48.0	0.0	317	255	316	330	334	328	222
	Surface daily totals				2872	1724	2188	2300	2345	2322	1644
Mar 21	7	5	12.7	81.9	185	54	60	60	59	56	32
	8	4	25.1	73.0	260	129	146	147	144	137	78
	9	3	36.8	62.1	290	194	222	224	220	209	119
	10	2	47.3	47.5	304	245	280	283	278	265	150
	11	1	55.0	26.8	311	277	317	321	315	300	170
	12		58.0	0.0	313	287	329	333	327	312	177
	Surface daily totals				3012	2084	2378	2403	2358	2246	1276
Apr 21	6	6	6.1	99.9	66	14	9	6	6	5	3
	7	5	18.8	92.2	206	86	78	71	62	51	10
	8	4	31.5	84.0	255	158	156	148	136	120	35
	9	3	43.9	74.2	278	220	225	217	203	183	68
	10	2	55.7	60.3	290	267	279	272	256	234	95
	11	1	65.4	37.5	295	297	313	306	290	265	112
	12		69.6	0.0	297	307	325	318	301	276	118
	Surface daily totals				3076	2390	2444	2356	2206	1994	764
May 21	6	6	10.4	107.2	119	36	21	13	13	12	7
	7	5	22.8	100.1	211	107	88	75	60	44	13
	8	4	35.4	92.9	250	175	159	145	127	105	15
	9	3	48.1	84.7	269	233	223	209	188	163	33
	10	2	60.6	73.3	280	277	273	259	237	208	56
	11	1	72.0	51.9	285	305	305	290	268	237	72
	12		78.0	0.0	286	315	315	301	278	247	77
	Surface daily totals				3112	2582	2454	2284	2064	1788	469
Jun 21	6	6	12.2	110.2	131	45	26	16	15	14	9
	7	5	24.3	103.4	210	115	91	76	59	41	14
	8	4	36.9	96.8	245	180	159	143	122	99	16
	9	3	49.6	89.4	264	236	221	204	181	153	19
	10	2	62.2	79.7	274	279	268	251	227	197	41
	11	1	74.2	60.9	279	306	299	282	257	224	56
	12		81.5	0.0	280	315	309	292	267	234	60
	Surface daily totals				3084	2634	2436	2234	1990	1690	370

Table A.2 *(Continued)*

Date	Solar time		Solar position		BTUH/sq. ft. total insolation on surfaces[b]						
							South facing surface angle with horiz.				
	AM	PM	Alt	Azm	Normal[c]	Horiz.	22	32	42	52	90
Jul 21	6	6	10.7	107.7	113	37	22	14	13	12	8
	7	5	23.1	100.6	203	107	87	75	60	44	14
	8	4	35.7	93.6	241	174	158	143	125	104	16
	9	3	48.4	85.5	261	231	220	205	185	159	31
	10	2	60.9	74.3	271	274	269	254	232	204	54
	11	1	72.4	53.3	277	302	300	285	262	232	69
	12		78.6	0.0	279	311	310	296	273	242	74
	Surface daily totals				3012	2558	2422	2250	2030	1754	458
Aug 21	6	6	6.5	100.5	59	14	9	7	6	6	4
	7	5	19.1	92.8	190	85	77	69	60	50	12
	8	4	31.8	84.7	240	156	152	144	132	116	33
	9	3	44.3	75.0	263	216	220	212	197	178	65
	10	2	56.1	61.3	276	262	272	264	249	226	91
	11	1	66.0	38.4	282	292	305	298	281	257	107
	12		70.3	0.0	284	302	317	309	292	268	113
	Surface daily totals				2902	2352	2388	2296	2144	1934	736
Sep 21	7	5	12.7	81.9	163	51	56	56	55	52	30
	8	4	25.1	73.0	240	124	140	141	138	131	75
	9	3	36.8	62.1	272	188	213	215	211	201	114
	10	2	47.3	47.5	287	237	270	273	268	255	145
	11	1	55.0	26.8	294	268	306	309	303	289	164
	12		58.0	0.0	296	278	318	321	315	300	171
	Surface daily totals				2808	2014	2288	2308	2264	2154	1226
Oct 21	7	5	6.8	73.1	99	19	29	32	34	36	32
	8	4	18.7	64.0	229	90	120	128	133	134	104
	9	3	29.5	53.0	273	155	198	208	213	212	153
	10	2	38.7	39.1	293	204	257	269	273	270	188
	11	1	45.1	21.1	302	236	294	307	311	306	209
	12		47.5	0.0	304	247	306	320	324	318	217
	Surface daily totals				2696	1654	2100	2208	2252	2232	1588
Nov 21	7	5	1.5	65.4	2	0	0	0	1	1	1
	8	4	12.7	56.6	196	55	91	104	113	119	111
	9	3	22.6	46.1	263	118	173	190	202	208	176
	10	2	30.8	33.2	289	166	233	252	265	270	217
	11	1	36.2	17.6	301	197	270	291	303	307	241
	12		38.2	0.0	304	207	282	304	316	320	249
	Surface daily totals				2406	1280	1816	1980	2084	2130	1742
Dec 21	8	4	10.3	53.8	176	41	77	90	101	108	107
	9	3	19.8	43.6	257	102	161	180	195	204	183
	10	2	27.6	31.2	288	150	221	244	259	267	226
	11	1	32.7	16.4	301	180	258	282	298	305	251
	12		34.6	0.0	304	190	271	295	311	318	259
	Surface daily totals				2348	1136	1704	1888	2016	2086	1794

Table A.3 Solar position and insolation values for 40°N latitude.

Date	Solar time		Solar position		BTUH/sq. ft. total insolation on surface[b]						
							South facing surface angle with horiz.				
	AM	PM	Alt	Azm	Normal[c]	Horiz.	30	40	50	60	90
Jan 21	8	4	8.1	55.3	142	28	65	74	81	85	84
	9	3	16.8	44.0	239	83	155	171	182	187	171
	10	2	23.8	30.9	274	127	218	237	249	254	223
	11	1	28.4	16.0	289	154	257	277	290	293	253
	12		30.0	0.0	294	164	270	291	303	306	263
	Surface daily totals				2182	948	1660	1810	1906	1944	1726
Feb 21	7	5	4.8	72.7	69	10	19	21	23	24	22
	8	4	15.4	62.2	224	73	114	122	126	127	107
	9	3	25.0	50.2	274	132	195	205	209	208	167
	10	2	32.8	35.9	295	178	256	267	271	267	210
	11	1	38.1	18.9	305	206	293	306	310	304	236
	12		40.0	0.0	308	216	306	319	323	317	245
	Surface daily totals				2640	1414	2060	2162	2202	2176	1730
Mar 21	7	5	11.4	80.2	171	46	55	55	54	51	35
	8	4	22.5	69.6	250	114	140	141	138	131	89
	9	3	32.8	57.3	282	173	215	217	213	202	138
	10	2	41.6	41.9	297	218	273	276	271	258	176
	11	1	47.7	22.6	305	247	310	313	307	293	200
	12		50.0	0.0	307	257	322	326	320	305	208
	Surface daily totals				2916	1852	2308	2330	2284	2174	1484
Apr 21	6	6	7.4	98.9	89	20	11	8	7	7	4
	7	5	18.9	89.5	206	87	77	70	61	50	12
	8	4	30.3	79.3	252	152	153	145	133	117	53
	9	3	41.3	67.2	274	207	221	213	199	179	93
	10	2	51.2	51.4	286	250	275	267	252	229	126
	11	1	58.7	29.2	292	277	308	301	285	260	147
	12		61.6	0.0	293	287	320	313	296	271	154
	Surface daily totals				3092	2274	2412	2320	2168	1956	1022
May 21	5	7	1.9	114.7	1	0	0	0	0	0	0
	6	6	12.7	105.6	144	49	25	15	14	13	9
	7	5	24.0	96.6	216	214	89	76	60	44	13
	8	4	35.4	87.2	250	175	158	144	125	104	25
	9	3	46.8	76.0	267	227	221	206	186	160	60
	10	2	57.5	60.9	277	267	270	255	233	205	89
	11	1	66.2	37.1	283	293	301	287	264	234	108
	12		70.0	0.0	284	301	312	297	274	243	114
	Surface daily totals				3160	2552	2442	2264	2040	1760	724
Jun 21	5	7	4.2	117.3	22	4	3	3	2	2	1
	6	6	14.8	108.4	155	60	30	18	17	16	10
	7	5	26.0	99.7	216	123	92	77	59	41	14
	8	4	37.4	90.7	246	182	159	142	121	97	16
	9	3	48.8	80.2	263	233	219	202	179	151	47
	10	2	59.8	65.8	272	272	266	248	224	194	74
	11	1	69.2	41.9	277	296	296	278	253	221	92
	12		73.5	0.0	279	304	306	289	263	230	98
	Surface daily totals				3180	2648	2434	2224	1974	1670	610

Table A.3 (*Continued*)

Date	Solar time		Solar position		BTUH/sq. ft. total insolation on surface[b]						
	AM	PM	Alt	Azm	Normal[c]	Horiz.	South facing surface angle with horiz. 30	40	50	60	90
Jul 21	5	7	2.3	115.2	2	0	0	0	0	0	0
	6	6	13.1	106.1	138	50	26	17	15	14	9
	7	5	24.3	97.2	208	114	89	75	60	44	14
	8	4	35.8	87.8	241	174	157	142	124	102	24
	9	3	47.2	76.7	259	225	218	203	182	157	58
	10	2	57.9	61.7	269	265	266	251	229	200	86
	11	1	66.7	37.9	275	290	296	281	258	228	104
	12		70.6	0.0	276	298	307	292	269	238	111
	Surface daily totals				3062	2534	2409	2230	2006	1728	702
Aug 21	6	6	7.9	99.5	81	21	12	9	8	7	5
	7	5	19.3	90.9	191	87	76	69	60	49	12
	8	4	30.7	79.9	237	150	150	141	129	113	50
	9	3	41.8	67.9	260	205	216	207	193	173	89
	10	2	51.7	52.1	272	246	267	259	244	221	120
	11	1	59.3	29.7	278	273	300	292	276	252	140
	12		62.3	0.0	280	282	311	303	287	262	147
	Surface daily totals				2916	2244	2354	2258	2104	1894	978
Sep 21	7	5	11.4	80.2	149	43	51	51	49	47	32
	8	4	22.5	69.6	230	109	133	134	131	124	84
	9	3	32.8	57.3	263	167	206	208	203	193	132
	10	2	41.6	41.9	280	211	262	265	260	247	168
	11	1	47.7	22.6	287	239	298	301	295	281	192
	12		50.0	0.0	290	249	310	313	307	292	200
	Surface daily totals				2708	1788	2210	2228	2182	2074	1416
Oct 21	7	5	4.5	72.3	48	7	14	15	17	17	16
	8	4	15.0	61.9	204	68	106	113	117	118	100
	9	3	24.5	49.8	257	126	185	195	200	198	160
	10	2	32.4	35.6	280	170	245	257	261	257	203
	11	1	37.6	18.7	291	199	283	295	299	294	229
	12		39.5	0.0	294	208	295	308	312	306	238
	Surface daily totals				2454	1348	1962	2060	2098	2074	1654
Nov 21	8	4	8.2	55.4	136	28	63	72	78	82	81
	9	3	17.0	44.1	232	82	152	167	178	183	167
	10	2	24.0	31.0	268	126	215	233	245	249	219
	11	1	28.6	16.1	283	153	254	273	285	288	248
	12		30.2	0.0	288	163	267	287	298	301	258
	Surface daily totals				2128	942	1636	1778	1870	1908	1686
Dec 21	8	4	5.5	53.0	89	14	39	45	50	54	56
	9	3	14.0	41.9	217	65	135	152	164	171	163
	10	2	20.,	29.4	261	107	200	221	235	242	221
	11	1	25.0	15.2	280	134	239	262	276	283	252
	12		26.6	0.0	285	143	253	275	290	296	263
	Surface daily totals				1978	782	1480	1634	1740	1796	1646

Table A.4 Solar position and insolation values for 48°N latitude.

Date	Solar time		Solar position		BTUH/sq. ft. total insolation on surfaces[b]						
							South facing surface angle with horiz.				
	AM	PM	Alt	Azm	Normal[c]	Horiz.	38	48	58	68	90
Jan 21	8	4	3.5	54.6	37	4	17	19	21	22	22
	9	3	11.0	42.6	185	46	120	132	140	145	139
	10	2	16.9	29.4	239	83	190	206	216	220	206
	11	1	20.7	15.1	261	107	231	249	260	263	243
	12		22.0	0.0	267	115	245	264	275	278	255
	Surface daily totals				1710	596	1360	1478	1550	1578	1478
Feb 21	7	5	2.4	72.2	12	1	3	4	4	4	4
	8	4	11.6	60.5	188	49	95	102	105	106	96
	9	3	19.7	47.7	251	100	178	187	191	190	167
	10	2	26.2	33.3	278	139	240	251	255	251	217
	11	1	30.5	17.2	290	165	278	290	294	288	247
	12		32.0	0.0	293	173	291	304	307	301	258
	Surface daily totals				2330	1080	1880	1972	2024	1978	1720
Mar 21	7	5	10.0	78.7	153	37	49	49	47	45	35
	8	4	19.5	66.8	236	96	131	132	129	122	96
	9	3	28.2	53.4	270	147	205	207	203	193	152
	10	2	35.4	37.8	287	187	263	266	261	248	195
	11	1	40.3	19.8	295	212	300	303	297	283	223
	12		42.0	0.0	298	220	312	315	309	294	232
	Surface daily totals				2780	1578	2208	2228	2182	2074	1632
Apr 21	6	6	8.6	97.8	108	27	13	9	8	7	5
	7	5	18.6	86.7	205	85	76	69	59	48	21
	8	4	28.5	74.9	247	142	149	141	129	113	69
	9	3	37.8	61.2	268	191	216	208	194	174	115
	10	2	45.8	44.6	280	228	268	260	245	223	152
	11	1	51.5	24.0	286	252	301	294	278	254	177
	12		53.6	0.0	288	260	313	305	289	264	185
	Surface daily totals				3076	2106	2358	2266	2114	1902	1262
May 21	5	7	5.2	114.3	41	9	4	4	4	3	2
	6	6	14.7	103.7	162	61	27	16	15	13	10
	7	5	24.6	93.0	219	118	89	75	60	43	13
	8	4	34.7	81.6	248	171	156	142	123	101	45
	9	3	44.3	68.3	264	217	217	202	182	156	86
	10	2	53.0	51.3	274	252	265	251	229	200	120
	11	1	59.5	28.6	279	274	296	281	258	228	141
	12		62.0	0.0	280	281	306	292	269	238	149
	Surface daily totals				3254	2482	2418	2234	2010	1728	982
Jun 21	5	7	7.9	116.5	77	21	9	9	8	7	5
	6	6	17.2	106.2	172	74	33	19	18	16	12
	7	5	27.0	95.8	220	129	93	77	59	39	15
	8	4	37.1	84.6	246	181	157	140	119	95	35
	9	3	46.9	71.6	261	225	216	198	175	147	74
	10	2	55.8	54.8	269	259	262	244	220	189	105
	11	1	62.7	31.2	274	280	291	273	248	216	126
	12		65.5	0.0	275	287	301	283	258	225	133
	Surface daily totals				3312	2626	2420	2204	1950	1644	874

Table A.4 *(Continued)*

Date	Solar time		Solar position		BTUH/sq. ft. total insolation on surfaces[b]						
	AM	PM	Alt	Azm	Normal[c]	Horiz.	South facing surface angle with horiz. 38	48	58	68	90
Jul 21	5	7	5.7	114.7	43	10	5	5	4	4	3
	6	6	15.2	104.1	156	62	28	18	16	15	11
	7	5	25.1	93.5	211	118	89	75	59	42	14
	8	4	35.1	82.1	240	171	154	140	121	99	43
	9	3	44.8	68.8	256	215	214	199	178	153	83
	10	2	53.5	51.9	266	250	261	246	224	195	116
	11	1	60.1	29.0	271	272	291	276	253	223	137
	12		62.6	0.0	272	279	301	286	263	232	144
	Surface daily totals				3158	2474	2386	2200	1974	1694	956
Aug 21	6	6	9.1	98.3	99	28	14	10	9	8	6
	7	5	19.1	87.2	190	85	75	67	58	47	20
	8	4	29.0	75.4	232	141	145	137	125	109	65
	9	3	38.4	61.8	254	189	210	201	187	168	110
	10	2	46.4	45.1	266	225	260	252	237	214	146
	11	1	52.2	24.3	272	248	293	285	268	244	169
	12		54.3	0.0	274	256	304	296	279	255	177
	Surface daily totals				2898	2086	2300	2200	2046	1836	1208
Sep 21	7	5	10.0	78.7	131	35	44	44	43	40	31
	8	4	19.5	66.8	215	92	124	124	121	115	90
	9	3	28.2	53.4	251	142	196	197	193	183	143
	10	2	35.4	37.8	269	181	251	254	248	236	185
	11	1	40.3	19.8	278	205	287	289	284	269	212
	12		42.0	0.0	280	213	299	302	296	281	221
	Surface daily totals				2568	1522	2102	2118	2070	1966	1546
Oct 21	7	5	2.0	71.9	4	0	1	1	1	1	1
	8	4	11.2	60.2	165	44	86	91	95	95	87
	9	3	19.3	47.4	233	94	167	176	180	178	157
	10	2	25.7	33.1	262	133	228	239	242	239	207
	11	1	30.0	17.1	274	157	266	277	281	276	237
	12		31.5	0.0	278	166	279	291	294	288	247
	Surface daily totals				2154	1022	1774	1860	1890	1866	1626
Nov 21	8	4	3.6	54.7	36	5	17	19	21	22	22
	9	3	11.2	42.7	179	46	117	129	137	141	135
	10	2	17.1	29.5	233	83	186	202	212	215	201
	11	1	20.9	15.1	255	107	227	245	255	258	238
	12		22.2	0.0	261	115	241	259	270	272	250
	Surface daily totals				1668	596	1336	1448	1518	1544	1442
Dec 21	9	3	8.0	40.9	140	27	87	98	105	110	109
	10	2	13.6	28.2	214	63	164	180	192	197	190
	11	1	17.3	14.4	242	86	207	226	239	244	231
	12		18.6	0.0	250	94	222	241	254	260	244
	Surface daily totals				1444	446	1136	1250	1326	1364	1304

Table A.5 Solar position and insolation values for 56°N latitude.

Date	Solar time		Solar position		BTUH/sq. ft. total insolation on surfaces[b]						
							South facing surface angle with horiz.				
	AM	PM	Alt	Azm	Normal[c]	Horiz.	46	56	66	76	90
Jan 21	9	3	5.0	41.8	78	11	50	55	59	60	60
	10	2	9.9	28.5	170	39	135	146	154	156	153
	11	1	12.9	14.5	207	58	183	197	206	208	201
	12		14.0	0.0	217	65	198	214	222	225	217
	Surface daily totals				1126	282	934	1010	1058	1074	1044
Feb 21	8	4	7.6	59.4	129	25	65	69	72	72	69
	9	3	14.2	45.9	214	65	151	159	162	161	151
	10	2	19.4	31.5	250	98	215	225	228	224	208
	11	1	22.8	16.1	266	119	254	265	268	263	243
	12		24.0	0.0	270	126	268	279	282	276	255
	Surface daily totals				1986	740	1640	1716	1742	1716	1598
Mar 21	7	5	8.3	77.5	128	28	40	40	39	37	32
	8	4	16.2	64.4	215	75	119	120	117	111	97
	9	3	23.3	50.3	253	118	192	193	189	180	154
	10	2	29.0	34.9	272	151	249	251	246	234	205
	11	1	32.7	17.9	282	172	285	288	282	268	236
	12		34.0	0.0	284	179	297	300	294	280	246
	Surface daily totals				2586	1268	2066	2084	2040	1938	1700
Apr 21	5	7	1.4	108.8	0	0	0	0	0	0	0
	6	6	9.6	96.5	122	32	14	9	8	7	6
	7	5	18.0	84.1	201	81	74	66	57	46	29
	8	4	26.1	70.9	239	129	143	135	123	108	82
	9	3	33.6	56.3	260	169	208	200	186	167	133
	10	2	39.9	39.7	272	201	259	251	236	214	174
	11	1	44.1	20.7	278	220	292	284	268	245	200
	12		45.6	0.0	280	227	303	295	279	255	209
	Surface daily totals				3024	1892	2282	2186	2038	1830	1458
May 21	4	8	1.2	125.5	0	0	0	0	0	0	0
	5	7	8.5	113.4	93	25	10	9	8	7	6
	6	6	16.5	101.5	175	71	28	17	15	13	11
	7	5	24.8	89.3	219	119	88	74	58	41	16
	8	4	33.1	76.3	244	163	153	138	119	98	63
	9	3	40.9	61.6	259	201	212	197	176	151	109
	10	2	47.6	44.2	268	231	259	244	222	194	146
	11	1	52.3	23.4	273	249	288	274	251	222	170
	12		54.0	0.0	275	255	299	284	261	231	178
	Surface daily totals				3340	2374	2374	2188	1962	1682	1218
Jun 21	4	8	4.2	127.2	21	4	2	2	2	2	1
	5	7	11.4	115.3	122	40	14	13	11	10	8
	6	6	19.3	103.6	185	86	34	19	17	15	12
	7	5	27.6	91.7	222	132	92	76	57	38	15
	8	4	35.9	78.8	243	175	154	137	116	92	55
	9	3	43.8	64.1	257	212	211	193	170	143	98
	10	2	50.7	46.4	265	240	255	238	214	184	133
	11	1	55.6	24.9	269	258	284	267	242	210	156
	12		57.5	0.0	271	264	294	276	251	219	164
	Surface daily totals				3438	2526	2388	2166	1910	1606	1120

Table A.5 *(Continued)*

Date	Solar time		Solar position		BTUH/sq. ft. total insolation on surfaces[b]						
	AM	PM	Alt	Azm	Normal[c]	Horiz.	South facing surface angle with horiz. 46	56	66	76	90
Jul 21	4	8	1.7	125.8	0	0	0	0	0	0	0
	5	7	9.0	113.7	91	27	11	10	9	8	6
	6	6	17.0	101.9	169	72	30	18	16	14	12
	7	5	25.3	89.7	212	119	88	74	58	41	15
	8	4	33.6	76.7	237	163	151	136	117	96	61
	9	3	41.4	62.0	252	201	208	193	173	147	106
	10	2	48.2	44.6	261	230	254	239	217	189	142
	11	1	52.9	23.7	265	248	283	268	245	216	165
	12		54.6	0.0	267	254	293	278	255	225	173
	Surface daily totals				3240	2372	2342	2152	1926	1646	1186
Aug 21	5	7	2.0	109.2	1	0	0	0	0	0	0
	6	6	10.2	97.0	112	34	16	11	10	9	7
	7	5	18.5	84.5	187	82	73	65	56	45	28
	8	4	26.7	71.3	225	128	140	131	119	104	78
	9	3	34.3	56.7	246	168	202	193	179	160	126
	10	2	40.5	40.0	258	199	251	242	227	206	166
	11	1	44.8	20.9	264	218	282	274	258	235	191
	12		46.3	0.0	266	225	293	285	269	245	200
	Surface daily totals				2850	1884	2218	2118	1966	1760	1392
Sep 21	7	5	8.3	77.5	107	25	36	36	34	32	28
	8	4	16.2	64.4	194	72	111	111	108	102	89
	9	3	23.3	50.3	233	114	181	182	178	168	147
	10	2	29.0	34.9	253	146	236	237	232	221	193
	11	1	32.7	17.9	263	166	271	273	267	254	223
	12		34.0	0.0	266	173	283	285	279	265	233
	Surface daily totals				2368	1220	1950	1962	1918	1820	1594
Oct 21	8	4	7.1	59.1	104	20	53	57	59	59	57
	9	3	13.8	45.7	193	60	138	145	148	147	138
	10	2	19.0	31.3	231	92	201	210	213	210	195
	11	1	22.3	16.0	248	112	240	250	253	248	230
	12		23.5	0.0	253	119	253	263	266	261	241
	Surface daily totals				1804	688	1516	1586	1612	1588	1480
Nov 21	9	3	5.2	41.9	76	12	49	54	57	59	58
	10	2	10.0	28.5	165	39	132	143	149	152	148
	11	1	13.1	14.5	201	58	179	193	201	203	196
	12		14.2	0.0	211	65	194	209	217	219	211
	Surface daily totals				1094	284	914	986	1032	1046	1016
Dec 21	9	3	1.9	40.5	5	0	3	4	4	4	4
	10	2	6.6	27.5	113	19	86	95	101	104	103
	11	1	9.5	13.9	166	37	141	154	163	167	164
	12		10.6	0.0	180	43	159	173	182	186	182
	Surface daily totals				748	156	620	678	716	734	722

Table A.6 Solar position and insolation values for 64°N latitude.

Date	Solar time		Solar position		BTUH/sq. ft. total insolation on surfaces[b]						
							South facing surface angle with horiz.				
	AM	PM	Alt	Azm	Normal[c]	Horiz.	54	64	74	84	90
Jan 21	10	2	2.8	28.1	22	2	17	19	20	20	20
	11	1	5.2	14.1	81	12	72	77	80	81	81
	12		6.0	0.0	100	16	91	98	102	103	103
	Surface daily totals				306	45	268	290	302	306	304
Feb 21	8	4	3.4	58.7	35	4	17	19	19	19	19
	9	3	8.6	44.8	147	31	103	108	111	110	107
	10	2	12.6	30.3	199	55	170	178	181	178	173
	11	1	15.1	15.3	222	71	212	220	223	219	213
	12		16.0	0.0	228	77	225	235	237	232	226
	Surface daily totals				1432	400	1230	1286	1302	1282	1252
Mar 21	7	5	6.5	76.5	95	18	30	29	29	27	25
	8	4	20.7	62.6	185	54	101	102	99	94	89
	9	3	18.1	48.1	227	87	171	172	169	160	153
	10	2	22.3	32.7	249	112	227	229	224	213	203
	11	1	25.1	16.6	260	129	262	265	259	246	235
	12		26.0	0.0	263	134	274	277	271	258	246
	Surface daily totals				2296	932	1856	1870	1830	1736	1656
Apr 21	5	7	4.0	108.5	27	5	2	2	2	1	1
	6	6	10.4	95.1	133	37	15	9	8	7	6
	7	5	17.0	81.6	194	76	70	63	54	43	37
	8	4	23.3	67.5	228	112	136	128	116	102	91
	9	3	29.0	52.3	248	144	197	189	176	158	145
	10	2	33.5	36.0	260	169	246	239	224	203	188
	11	1	36.5	18.4	266	184	278	270	255	233	216
	12		97.6	0.0	268	190	289	281	266	243	225
	Surface daily totals				2982	1644	2176	2082	1936	1736	1594
May 21	4	8	5.8	125.1	51	11	5	4	4	3	3
	5	7	11.6	112.1	132	42	13	11	10	9	8
	6	6	17.9	99.1	185	79	29	16	14	12	11
	7	5	24.5	85.7	218	117	86	72	56	39	28
	8	4	30.9	71.5	239	152	148	133	115	94	80
	9	3	36.8	56.1	252	182	204	190	170	145	128
	10	2	41.6	38.9	261	205	249	235	213	186	167
	11	1	44.9	20.1	265	219	278	264	242	213	193
	12		46.0	0.0	267	224	228	274	251	222	201
	Surface daily totals				3470	2236	2312	2124	1898	1624	1436
Jun 21	3	9	4.2	139.4	21	4	2	2	2	2	1
	4	8	9.0	126.4	93	27	10	9	8	7	6
	5	7	14.7	113.6	154	60	16	15	13	11	10
	6	6	21.0	100.8	194	96	34	19	17	14	13
	7	5	27.5	87.5	221	132	91	74	55	36	23
	8	4	34.0	73.3	239	166	150	133	112	88	73
	9	3	39.9	57.8	251	195	204	187	164	137	119
	10	2	44.9	40.4	258	217	247	230	206	177	157
	11	1	48.3	20.9	262	231	275	258	233	202	181
	12		49.5	0.0	263	235	284	267	242	211	189
	Surface daily totals				3650	2488	2342	2118	1862	1558	1356

Table A.6 (*Continued*)

Date	Solar time		Solar position		BTUH/sq. ft. total insolation on surfaces[b]						
							South facing surface angle with horiz.				
	AM	PM	Alt	Azm	Normal[c]	Horiz.	54	64	74	84	90
Jul 21	4	8	6.4	125.3	53	13	6	5	5	4	4
	5	7	12.1	112.4	128	44	14	13	11	10	9
	6	6	18.4	99.4	179	81	30	17	16	13	12
	7	5	25.0	86.0	211	118	86	72	56	38	28
	8	4	31.4	71.8	231	152	146	131	113	91	77
	9	3	37.3	56.3	245	182	201	186	166	141	124
	10	2	42.2	39.2	253	204	245	230	208	181	162
	11	1	45.4	20.2	257	218	273	258	236	207	187
	12		46.6	0.0	259	223	282	267	245	216	195
	Surface daily totals				3372	2248	2280	2090	1864	1588	1400
Aug 21	5	7	4.6	108.8	29	6	3	3	2	2	2
	6	6	11.0	95.5	123	39	16	11	10	8	7
	7	5	17.6	81.9	181	77	69	61	52	42	35
	8	4	23.9	67.8	214	113	132	123	112	97	87
	9	3	29.6	52.6	234	144	190	182	169	150	138
	10	2	34.2	36.2	246	168	237	229	215	194	179
	11	1	37.2	18.5	252	183	268	260	244	222	205
	12		38.3	0.0	254	188	278	270	255	232	215
	Surface daily totals				2808	1646	2108	1008	1860	1662	1522
Sep 21	7	5	6.5	76.5	77	16	25	25	24	23	21
	8	4	12.7	72.6	163	51	92	92	90	85	81
	9	3	18.1	48.1	206	83	159	159	156	147	141
	10	2	22.3	32.7	229	108	212	213	209	198	189
	11	1	25.1	16.6	240	124	246	248	243	230	220
	12		26.0	0.0	244	129	258	260	254	241	230
	Surface daily totals				2074	892	1726	1736	1696	1608	1532
Oct 21	8	4	3.0	58.5	17	2	9	9	10	10	10
	9	3	8.1	44.6	122	26	86	91	93	92	90
	10	2	12.1	30.2	176	50	152	159	161	159	155
	11	1	14.6	15.2	201	65	193	201	203	200	195
	12		15.5	0.0	208	71	207	215	217	213	208
	Surface daily totals				1238	358	1088	1136	1152	1134	1106
Nov 21	10	2	3.0	28.1	23	3	18	20	21	21	21
	11	1	5.4	14.2	79	12	70	76	79	80	79
	12		6.2	0.0	97	17	89	96	100	101	100
	Surface daily totals				302	46	266	286	298	302	300
Dec 21	11	1	1.8	13.7	4	0	3	4	4	4	4
	12		2.6	0.0	16	2	14	15	16	17	17
	Surface daily totals				24	2	20	22	24	24	24

Appendix B

Reproduced from Goswami, Y., Kreith, F., and Kreider, J.F. (2000) *Principles of Solar Engineering*, 2nd edn. Taylor and Francis, New York.

Table B.1 Designation and characteristics for 94 referenced passive systems.

(a) Overall System Characteristics	
Masonry properties	
thermal conductivity (k)	
sunspace floor	0.5 Btu/hr/ft/°F
all other masonry	1.0 Btu/hr/ft/°F
density (Q)	150 lb/ft^3
specific heat (c)	0.2 Btu/lb/°F
infrared emittance of normal surface	0.9
infrared emittance of selective surface	0.1
Solar absorptances	
waterwall	1.0
masonry, Trombe wall	1.0
direct gain and sunspace	0.8
sunspace: water containers	0.9
lightweight common wall	0.7
other lightweight surfaces	0.3
Glazing properties	
transmission characteristics	diffuse
orientation	due south
index of refraction	1.526
extinction coefficient	0.5 inch^{-1}
thickness of each pane	one-eighth inch
gap between panes	one-half inch
ared emittance	0.9
Control range	
room temperature	65 to 75°F
sunspace temperature	45 to 95°F
internal heat generation	0

(*continued*)

Alternative Energy Systems and Applications, Second Edition. B. K. Hodge.

Companion website: www.wiley.com\go\Hodge\AESystemsandApplications2E

Table B.1 (*Continued*)

(a) Overall System Characteristics

Thermocirculation vents (when used)	
vent area/projected area (sum of both upper and lower vents)	0.06
height between vents	8 ft
reverse flow	none
Nighttime insulation (when used)	
thermal resistance	R9
in place, solar time	5:30 P.M. to 7:30 A.M.
Solar radiation assumptions	
shading	none
ground diffuse reflectance	0.3

(b) Direct-Gain (DG) System Types

Designation	Thermal Storage Capacity* (in Btu/ft²/°F)	Mass Thickness* (inches)	Mass-Area-to-Glazing-Area Ratio	No. of Glazings	Nighttime Insulation
A1	30	2	6	2	no
A2	30	2	6	3	no
A3	30	2	6	2	yes
B1	45	6	3	2	no
B2	45	6	3	3	no
B3	45	6	3	2	yes
C1	60	4	6	2	no
C2	60	4	6	3	no
C3	60	4	6	2	yes

(c) Vented Trombe-Wall (TW) System Types

Designation	Thermal Storage Capacity* (Btu/ft²/°F)	Wall Thickness* (inches)	*pck* Btu²/hr/ft⁴/°F²)	No. of Glazings	Wall Surface	Nighttime Insulation
A1	15	6	30	2	normal	no
A2	22.5	9	30	2	normal	no
A3	30	12	30	2	normal	no
A4	45	18	30	2	normal	no
B1	15	6	15	2	normal	no
B2	22.5	9	15	2	normal	no
B3	30	12	15	2	normal	no
B4	45	18	15	2	normal	no
C1	15	6	7.5	2	normal	no
C2	22.5	9	7.5	2	normal	no
C3	30	12	7.5	2	normal	no
C4	45	18	7.5	2	normal	no

Table B.1 (*Continued*)

(c) Vented Trombe-Wall (TW) System Types

D1	30	12	30	1	normal	no
D2	30	12	30	3	normal	no
D3	30	12	30	1	normal	yes
D4	30	12	30	2	normal	yes
D5	30	12	30	3	normal	yes
E1	30	12	30	1	selective	no
E2	30	12	30	2	selective	no
E3	30	12	30	1	selective	yes
E4	30	12	30	2	selective	yes

(d) Unvented Trombe-Wall (TW) System Types

Designation	Thermal Storage Capacity* (Btu/ft²/°F)	Wall Thickness* (inches)	ρck Btu²/hr/ft⁴/°F²)	No. of Glazings	Wall Surface	Nighttime Insulation
F1	15	6	30	2	normal	no
F2	22.5	9	30	2	normal	no
F3	30	12	30	2	normal	no
F4	45	18	30	2	normal	no
G1	15	6	15	2	normal	no
G2	22.5	9	15	2	normal	no
G3	30	12	15	2	normal	no
G4	45	18	15	2	normal	no
H1	15	6	7.5	2	normal	no
H2	22.5	9	7.5	2	normal	no
H3	30	12	7.5	2	normal	no
H4	45	18	7.5	2	normal	no
I1	30	12	30	1	normal	no
I2	30	12	30	3	normal	no
I3	30	12	30	1	normal	yes
I4	30	12	30	2	normal	yes
I5	30	12	30	3	normal	yes
J1	30	12	30	1	selective	no
J2	30	12	30	2	selective	no
J3	30	12	30	1	selective	yes
J4	30	12	30	2	selective	yes

(e) Waterwall (WW) System Types

Designation	Thermal Storage Capacity* (in Btu/ft²/°F)	Wall Thickness (inches)	No. of Glazings	Wall Surface	Nighttime Insulation
A1	15.6	3	2	normal	no
A2	31.2	6	2	normal	no
A3	46.8	9	2	normal	no
A4	62.4	12	2	normal	no

(*continued*)

Table B.1 (*Continued*)

(e) Waterwall (WW) System Types

A5	93.6	18	2	normal	no
A6	124.8	24	2	normal	no
B1	46.8	9	1	normal	no
B2	46.8	9	3	normal	no
B3	46.8	9	1	normal	yes
B4	46.8	9	2	normal	yes
B5	46.8	9	3	normal	yes
C1	46.8	9	1	selective	no
C2	46.8	9	2	selective	no
C3	46.8	9	1	selective	yes
C4	46.8	9	2	selective	yes

(f) Sunspace (SS) System Types

Designation	Type	Tilt (degrees)	Common Wall	End Walls	Nighttime Insulation
A1	attached	50	masonry	opaque	no
A2	attached	50	masonry	opaque	yes
A3	attached	50	masonry	glazed	no
A4	attached	50	masonry	glazed	yes
A5	attached	50	insulated	opaque	no
A6	attached	50	insulated	opaque	yes
A7	attached	50	insulated	glazed	no
A8	attached	50	insulated	glazed	yes
B1	attached	90/30	masonry	opaque	no
B2	attached	90/30	masonry	opaque	yes
B3	attached	90/30	masonry	glazed	no
B4	attached	90/30	masonry	glazed	yes
B5	attached	90/30	insulated	opaque	no
B6	attached	90/30	insulated	opaque	yes
B7	attached	90/30	insulated	glazed	no
B8	attached	90/30	insulated	glazed	yes
C1	semienclosed	90	masonry	common	no
C2	semienclosed	90	masonry	common	yes
C3	semienclosed	90	insulated	common	no
C4	semienclosed	90	insulated	common	yes
D1	semienclosed	50	masonry	common	no
D2	semienclosed	50	masonry	common	yes
D3	semienclosed	50	insulated	common	no
D4	semienclosed	50	insulated	common	yes
E1	semienclosed	90/30	masonry	common	no
E2	semienclosed	90/30	masonry	common	yes
E3	semienclosed	90/30	insulated	common	no
E4	semienclosed	90/30	insulated	common	yes

Table B.2 Load collector ratio table for Santa Maria, CA.

SSF	.10	.20	.30	.40	.50	.60	.70	.80	.90
Santa Maria, California									3053 DD
WW A1	1776	240	119	73	50	35	25	18	12
WW A2	617	259	154	103	74	54	39	28	19
WW A3	523	261	164	114	82	61	45	33	22
WW A4	482	260	169	119	87	65	48	35	24
WW A5	461	263	175	125	92	69	52	38	26
WW A6	447	263	177	128	95	72	54	40	27
WW B1	556	220	128	85	60	43	32	23	15
WW B2	462	256	168	119	88	66	49	36	25
WW B3	542	315	211	151	112	85	64	47	32
WW B4	455	283	197	144	109	83	63	47	32
WW B5	414	263	184	136	103	79	60	45	31
WW C1	569	330	221	159	118	89	67	49	33
WW C2	478	288	197	143	107	81	61	45	31
WW C3	483	318	228	170	130	100	77	57	40
WW C4	426	280	200	149	114	88	68	51	35
TW A1	1515	227	113	70	48	34	24	17	11
TW A2	625	234	134	89	63	46	33	24	16
TW A3	508	231	140	95	68	50	37	27	18
TW A4	431	217	137	95	69	51	38	28	19
TW B1	859	212	112	71	49	35	25	18	12
TW B2	502	209	124	83	59	43	32	23	15
TW B3	438	201	123	84	60	44	33	24	16
TW B4	400	184	112	76	55	40	30	22	14
TW C1	568	188	105	69	48	35	25	18	12
TW C2	435	178	105	70	50	36	27	19	13
TW C3	413	165	97	64	46	33	25	18	12
TW C4	426	146	82	54	38	27	20	14	10
TW D1	403	170	101	67	48	35	25	18	12
TW D2	488	242	152	105	76	57	42	31	21
TW D3	509	271	175	123	90	67	50	36	25
TW D4	464	266	177	127	94	71	53	39	27
TW D5	425	250	169	122	91	69	52	38	26
TW E1	581	309	199	140	102	76	57	42	28
TW E2	512	283	186	132	97	73	55	40	27
TW E3	537	328	225	164	123	94	71	53	36
TW E4	466	287	199	145	109	83	63	47	32
TW F1	713	198	107	68	47	34	25	18	12
TW F2	455	199	120	81	58	42	31	22	15
TW F3	378	190	120	83	60	45	33	24	16
TW F4	311	169	110	77	57	42	32	23	16
TW G1	450	170	98	65	46	33	24	17	12
TW G2	331	163	102	70	51	38	28	20	14
TW G3	278	147	94	66	48	36	27	20	13
TW G4	222	120	78	55	40	30	22	16	11
TW H1	295	137	84	57	41	30	22	16	11
TW H2	226	118	75	52	38	28	21	15	10
TW H3	187	99	64	44	33	24	18	13	9

(*continued*)

Table B.2 (*Continued*)

SSF	.10	.20	.30	.40	.50	.60	.70	.80	.90
TW H4	143	75	48	33	24	18	14	10	7
TW I1	318	144	88	59	42	31	23	16	11
TW I2	377	203	132	93	68	51	38	28	19
TW I3	404	226	149	106	78	58	44	32	22
TW I4	387	230	156	113	84	64	48	36	24
TW I5	370	226	155	113	85	65	49	36	25
TW J1	483	271	179	127	94	71	53	39	26
TW J2	422	246	165	119	88	67	50	37	25
TW J3	446	283	199	146	111	85	65	48	33
TW J4	400	254	178	132	100	77	58	43	30
DG A1	392	188	117	79	55	38	26	16	7
DG A2	389	190	121	85	61	45	32	22	14
DG A3	443	220	142	102	77	58	44	31	19
DG B1	384	191	122	86	64	48	35	24	13
DG B2	394	196	127	91	69	53	40	29	19
DG B3	445	222	145	105	80	62	49	37	25
DG C1	451	225	146	104	78	61	47	34	21
DG C2	453	226	148	106	80	63	49	37	25
DG C3	509	254	167	121	92	73	58	45	31
SS A1	1171	396	220	142	98	69	49	34	22
SS A2	1028	468	283	190	135	98	71	50	33
SS A3	1174	380	209	133	91	64	45	31	20
SS A4	1077	481	289	193	136	98	71	50	32
SS A5	1896	400	204	127	86	60	42	29	18
SS A6	1030	468	283	190	135	97	71	50	32
SS A7	2199	359	178	109	72	50	35	24	15
SS A8	1089	478	285	190	133	96	69	48	31
SS B1	802	298	170	111	77	55	40	28	18
SS B2	785	366	224	152	108	79	57	41	27
SS B3	770	287	163	106	74	52	37	26	17
SS B4	790	368	224	152	108	78	57	40	26
SS B5	1022	271	144	91	62	44	31	22	14
SS B6	750	356	219	149	106	77	56	40	26
SS B7	937	242	127	80	54	38	27	19	12
SS B8	750	352	215	146	103	75	55	39	25
SS C1	481	232	144	99	71	52	39	28	19
SS C2	482	262	170	120	88	66	49	36	24
SS C3	487	185	107	71	50	36	27	19	13
SS C4	473	235	147	102	74	55	41	30	20
SS D1	1107	477	282	188	132	95	68	48	31
SS D2	928	511	332	232	169	125	92	66	43
SS D3	1353	449	248	160	110	78	56	39	25
SS D4	946	500	319	222	160	117	86	61	40
SS E1	838	378	227	153	108	78	56	40	26
SS E2	766	419	272	190	138	102	75	54	36
SS E3	973	322	178	115	79	56	40	28	18
SS E4	780	393	247	170	122	89	65	47	31

Table B.3 Load collector ratio table for Albuquerque, NM.

SSF	.10	.20	.30	.40	.50	.60	.70	.80	.90
Albuquerque, New Mexico									4292 DD
WW A1	1052	130	62	38	25	18	13	9	6
WW A2	354	144	84	56	39	29	21	15	10
WW A3	300	146	90	62	45	33	24	18	12
WW A4	276	146	93	65	47	35	26	19	13
WW A5	264	148	97	69	50	38	28	21	14
WW A6	256	148	99	70	52	39	30	22	15
WW B1	293	111	63	41	28	20	15	11	7
WW B2	270	147	96	67	49	37	28	20	14
WW B3	314	179	119	84	62	47	35	26	18
WW B4	275	169	116	85	64	49	37	28	19
WW B5	252	159	110	81	61	47	36	27	19
WW C1	333	190	126	89	66	50	38	28	19
WW C2	287	171	115	83	62	47	36	27	18
WW C3	293	191	136	101	77	59	46	34	24
WW C4	264	172	122	91	69	54	41	31	22
TW A1	900	124	60	37	25	17	12	9	6
TW A2	361	130	73	48	33	24	18	13	8
TW A3	293	129	77	52	37	27	20	15	10
TW A4	249	123	76	52	38	28	21	15	10
TW B1	502	117	60	38	26	18	13	9	6
TW B2	291	118	68	45	32	23	17	12	8
TW B3	254	114	68	46	33	24	18	13	9
TW B4	233	104	63	42	30	22	16	12	8
TW C1	332	106	58	37	26	19	14	10	6
TW C2	255	101	58	39	27	20	15	11	7
TW C3	243	94	54	36	25	18	13	10	7
TW C4	254	84	46	30	21	15	11	8	5
TW D1	213	86	50	33	23	17	12	9	6
TW D2	287	139	86	59	43	32	24	17	12
TW D3	294	153	97	68	49	37	27	20	14
TW D4	281	158	104	74	55	41	31	23	16
TW D5	260	151	101	73	54	41	31	23	16
TW E1	339	177	113	78	57	43	32	23	16
TW E2	308	168	109	77	56	42	32	23	16
TW E3	323	195	133	96	72	55	42	31	21
TW E4	287	175	120	88	66	50	38	28	20
TW F1	409	108	57	36	24	17	13	9	6
TW F2	260	110	65	43	31	22	17	12	8
TW F3	216	106	66	45	33	24	10	13	9
TW F4	178	95	61	42	31	23	17	13	9
TW G1	256	93	53	34	24	17	13	9	6
TW G2	189	91	56	38	27	20	15	11	7
TW G3	159	82	52	36	26	20	15	11	7
TW G4	128	68	43	30	22	16	12	9	6
TW H1	168	76	45	31	22	16	12	9	6
TW H2	130	66	41	29	21	15	11	8	6

(*continued*)

Table B.3 (*Continued*)

SSF	.10	.20	.30	.40	.50	.60	.70	.80	.90
TW H3	108	56	35	25	8	13	10	7	5
TW H4	83	42	27	19	13	10	7	5	4
TW I1	166	73	43	29	20	15	11	8	5
TW I2	221	117	75	52	30	28	21	16	11
TW I3	234	128	83	59	43	32	24	10	12
TW I4	234	137	92	66	49	37	28	21	14
TW I5	226	136	93	67	50	38	29	22	15
TW J1	282	156	102	72	53	40	30	22	15
TW J2	254	146	97	69	51	39	29	22	15
TW J3	269	169	118	86	65	50	38	29	20
TW J4	247	155	106	80	60	46	35	26	18
DG A1	211	97	57	36	22	13	5	—	—
DG A2	227	107	67	46	32	23	16	10	5
DG A3	274	131	83	59	44	34	25	18	10
DG B1	210	97	60	42	30	21	13	6	—
DG B2	232	110	69	49	37	28	21	14	8
DG B3	277	134	85	61	47	37	28	21	14
DG C1	253	120	74	53	39	30	22	14	—
DG C2	271	130	82	59	45	35	26	19	12
DG C3	318	155	96	71	54	43	34	26	18
SS A1	591	187	101	64	44	31	22	16	10
SS A2	531	232	137	92	65	47	34	25	16
SS A3	566	170	90	56	38	27	19	13	8
SS A4	537	230	135	89	63	45	33	23	15
SS A5	980	187	92	56	37	26	18	13	8
SS A6	529	231	136	91	64	47	34	24	16
SS A7	1103	158	74	44	29	20	14	10	6
SS A8	540	226	131	87	61	44	32	23	15
SS B1	403	141	78	50	35	25	18	13	8
SS B2	412	186	111	75	53	39	28	20	14
SS B3	372	130	71	46	31	22	16	11	7
SS B4	403	181	106	72	51	37	27	20	13
SS B5	518	127	65	40	27	19	13	9	6
SS B6	390	179	106	73	52	38	28	20	13
SS B7	457	108	54	33	22	16	11	8	5
SS B8	379	171	102	69	49	35	26	19	12
SS C1	270	126	77	52	37	27	20	15	10
SS C2	282	150	97	68	49	37	28	20	14
SS C3	276	101	57	37	26	19	14	10	7
SS C4	277	135	83	57	41	31	23	17	11
SS D1	548	225	130	85	59	43	31	22	14
SS D2	474	253	162	113	82	61	45	33	22
SS D3	683	212	113	72	49	35	25	17	11
SS D4	484	248	156	107	77	57	42	30	20
SS E1	410	176	103	68	48	35	25	18	12
SS E2	390	208	133	92	67	50	37	27	18
SS E3	487	151	80	51	35	25	18	12	8
SS E4	400	195	120	82	59	43	32	23	15

Table B.4 Load collector ratio table for Nashville, TN.

SSF	.10	.20	.30	.40	.50	.60	.70	.80	.90
Nashville, Tennessee									3696 DD
WW A1	588	60	24	13	8	5	3	2	1
WW A2	192	70	38	23	15	11	7	5	3
WW A3	161	72	42	27	18	13	9	6	4
WW A4	148	72	43	29	20	14	10	7	5
WW A5	141	74	46	31	22	16	11	8	5
WW A6	137	74	47	32	22	16	12	8	5
WW B1	135	41	19	10	6	3	2	—	—
WW B2	152	78	48	33	23	17	12	9	6
WW B3	179	97	61	42	30	22	16	12	8
WW B4	164	97	65	46	34	25	19	14	9
WW B5	153	93	63	45	33	25	19	14	9
WW C1	193	105	67	46	33	24	18	13	8
WW C2	169	97	63	44	32	24	18	13	8
WW C3	181	115	79	58	43	33	25	18	12
WW C4	164	104	72	53	39	30	23	17	11
TW A1	509	59	25	13	8	5	3	2	1
TW A2	199	64	33	20	13	9	6	4	3
TW A3	160	65	36	23	15	11	8	5	3
TW A4	136	62	36	23	16	11	8	6	4
TW B1	282	57	26	15	9	6	4	3	2
TW B2	161	59	32	20	13	9	6	4	3
TW B3	141	58	32	21	14	10	7	5	3
TW B4	131	54	30	19	13	9	7	5	3
TW C1	188	53	27	16	10	7	5	3	2
TW C2	144	52	28	18	12	8	6	4	2
TW C3	139	49	27	17	11	8	5	4	2
TW C4	149	45	23	14	9	7	5	3	2
TW D1	99	33	16	9	5	3	2	1	—
TW D2	164	75	44	29	20	14	10	7	5
TW D3	167	82	49	33	23	17	12	8	5
TW D4	168	91	58	40	29	21	15	11	7
TW D5	160	89	58	40	29	22	16	12	8
TW E1	198	98	59	40	28	20	15	10	7
TW E2	182	95	59	40	29	21	15	11	7
TW E3	197	115	76	54	39	29	22	16	11
TW E4	178	105	70	50	37	27	20	15	10
TW F1	221	50	23	13	8	5	4	2	1
TW F2	139	53	29	18	12	8	6	4	2
TW F3	116	52	30	19	13	9	7	5	3
TW F4	96	47	28	19	13	9	7	5	3
TW G1	137	44	22	13	9	6	4	3	2
TW G2	101	44	25	16	11	8	5	4	2
TW G3	86	41	24	16	11	8	6	4	2
TW G4	69	34	21	14	10	7	5	3	2
TW H1	89	36	20	13	8	6	4	3	2
TW H2	69	33	19	12	9	6	4	3	2
TW H3	59	28	17	11	8	5	4	3	2

(*continued*)

Table B.4 (*Continued*)

SSF	.10	.20	.30	.40	.50	.60	.70	.80	.90
TW H4	46	22	13	9	6	4	3	2	1
TW I1	74	26	13	7	4	2	1	—	—
TW I2	125	62	38	25	18	13	9	7	4
TW I3	133	69	43	29	20	15	11	8	5
TW I4	139	78	51	35	26	19	14	10	7
TW I5	137	80	53	37	27	20	15	11	7
TW J1	164	86	54	36	26	19	14	10	6
TW J2	150	82	53	36	26	19	14	10	7
TW J3	165	101	68	49	36	27	20	15	10
TW J4	153	93	63	46	34	25	19	14	10
DG A1	98	34	—	—	—	—	—	—	—
DG A2	130	55	31	19	11	6	—	—	—
DG A3	173	78	47	32	23	16	11	7	2
DG B1	100	36	17	—	—	—	—	—	—
DG B2	134	58	33	22	15	10	6	—	—
DG B3	177	81	49	33	24	18	14	10	6
DG C1	131	52	28	17	9	—	—	—	—
DG C2	161	71	42	28	20	14	10	6	—
DG C3	205	94	57	39	29	22	17	12	8
SS A1	351	100	50	29	19	13	9	6	4
SS A2	328	135	76	49	33	24	17	12	8
SS A3	330	87	41	24	15	10	6	4	2
SS A4	331	133	74	47	32	22	16	11	7
SS A5	595	98	43	24	15	10	7	4	2
SS A6	324	132	75	48	32	23	16	11	7
SS A7	668	79	32	17	10	6	4	2	1
SS A8	330	129	71	45	30	21	15	10	6
SS B1	236	74	38	23	15	10	7	5	3
SS B2	258	110	63	41	28	20	14	10	6
SS B3	212	65	32	19	12	8	5	3	2
SS B4	251	105	60	39	27	19	13	9	6
SS B5	307	65	30	17	10	7	4	3	2
SS B6	241	104	60	39	27	19	14	10	6
SS B7	264	52	23	12	7	5	3	2	—
SS B8	233	98	56	36	25	17	12	9	5
SS C1	141	60	33	21	14	10	7	5	3
SS C2	161	81	50	33	23	17	12	9	6
SS C3	149	48	25	15	10	7	4	3	2
SS C4	160	73	43	28	19	14	10	7	5
SS D1	317	119	64	39	26	18	13	8	5
SS D2	287	147	90	61	43	31	23	16	10
SS D3	405	113	55	33	21	14	10	6	4
SS D4	295	144	87	58	40	29	21	15	10
SS E1	229	89	48	29	19	13	9	6	4
SS E2	233	118	72	48	34	24	18	12	8
SS E3	283	77	37	22	14	9	6	4	2
SS E4	242	111	65	43	29	21	15	11	7

Table B.5 Load collector ratio table for Medford, OR.

SSF	.10	.20	.30	.40	.50	.60	.70	.80	.90
Medford, Oregon									4930 DD
WW A1	708	64	24	11	—	—	—	—	—
WW A2	212	73	38	22	13	7	3	—	—
WW A3	174	75	41	25	16	9	5	2	—
WW A4	158	74	43	27	17	11	6	3	1
WW A5	149	75	45	29	19	12	7	4	2
WW A6	144	75	46	30	20	13	8	4	2
WW B1	154	43	16	—	—	—	—	—	—
WW B2	162	80	48	31	21	14	9	6	3
WW B3	190	100	62	41	28	19	13	8	5
WW B4	171	99	65	45	32	23	16	11	7
WW B5	160	95	63	45	32	23	17	12	7
WW C1	205	108	67	45	31	21	15	10	6
WW C2	178	99	63	43	30	22	15	10	6
WW C3	189	117	80	57	42	31	23	16	10
WW C4	170	106	72	52	38	28	21	15	9
TW A1	607	63	25	12	5	—	—	—	—
TW A2	222	68	33	19	11	6	2	—	—
TW A3	175	67	36	21	13	8	4	2	—
TW A4	147	64	36	22	14	9	5	3	1
TW B1	327	61	27	14	7	3	—	—	—
TW B2	178	62	32	19	12	7	4	2	—
TW B3	154	60	33	20	12	8	4	2	1
TW B4	143	56	31	19	12	8	5	2	1
TW C1	212	56	27	15	9	5	2	—	—
TW C2	159	55	28	17	11	7	4	2	—
TW C3	154	52	27	16	10	6	4	2	1
TW C4	167	48	24	14	9	5	3	2	—
TW D1	112	34	14	—	—	—	—	—	—
TW D2	177	77	44	28	18	12	8	5	3
TW D3	180	85	50	32	21	14	9	6	3
TW D4	177	93	58	39	27	19	13	9	5
TW D5	168	92	58	40	28	20	14	10	6
TW E1	213	101	60	39	26	18	12	8	4
TW E2	194	98	59	39	27	19	13	9	5
TW E3	208	118	77	53	38	27	20	13	8
TW E4	186	108	71	49	36	26	19	13	8
TW F1	256	53	23	12	5	—	—	—	—
TW F2	153	56	29	17	10	5	2	—	—
TW F3	125	54	30	18	11	7	3	1	—
TW F4	102	48	28	18	11	7	4	2	1
TW G1	153	46	22	12	7	—	—	—	—
TW G2	109	46	25	15	9	5	3	1	—
TW G3	92	42	24	15	9	6	3	2	—
TW G4	74	35	20	13	8	5	3	2	—
TW H1	97	38	20	12	7	4	1	—	—
TW H2	75	34	19	12	7	5	3	1	—

(*continued*)

Table B.5 (*Continued*)

SSF	.10	.20	.30	.40	.50	.60	.70	.80	.90
TW H3	63	29	17	10	7	4	3	1	—
TW H4	49	23	13	8	5	3	2	1	—
TW I1	83	27	10	—	—	—	—	—	—
TW I2	133	64	38	24	16	11	7	4	2
TW I3	142	71	43	28	19	13	9	5	3
TW I4	146	80	51	35	25	17	12	8	5
TW I5	144	82	53	37	26	19	13	9	6
TW J1	175	89	54	36	24	17	11	7	4
TW J2	158	85	53	36	25	18	12	8	5
TW J3	173	103	69	48	35	26	18	13	8
TW J4	160	96	64	45	33	24	17	12	8
DG A1	110	35	—	—	—	—	—	—	—
DG A2	142	58	32	18	9	—	—	—	—
DG A3	187	82	48	32	22	15	9	5	—
DG B1	110	40	15	—	—	—	—	—	—
DG B2	146	61	35	21	13	7	—	—	—
DG B3	193	84	51	34	24	17	12	7	3
DG C1	144	57	29	13	—	—	—	—	—
DG C2	177	75	44	28	19	12	6	—	—
DG C3	224	98	60	41	29	21	14	10	5
SS A1	415	110	51	28	16	9	4	2	—
SS A2	372	146	79	48	31	21	14	8	5
SS A3	397	96	42	21	10	—	—	—	—
SS A4	379	144	76	46	29	19	12	7	4
SS A5	732	111	45	23	12	5	—	—	—
SS A6	368	143	77	47	30	20	13	8	4
SS A7	846	90	33	14	—	—	—	—	—
SS A8	379	140	73	44	27	17	11	6	3
SS B1	274	81	38	21	12	6	3	—	—
SS B2	288	117	65	40	26	18	12	7	4
SS B3	249	71	33	17	8	—	—	—	—
SS B4	282	113	62	38	25	16	11	7	4
SS B5	368	72	30	15	7	—	—	—	—
SS B6	269	111	62	30	25	17	11	7	4
SS B7	323	58	23	10	—	—	—	—	—
SS B8	262	106	57	35	23	15	9	6	3
SS C1	153	62	33	19	11	5	—	—	—
SS C2	172	83	50	32	22	15	10	6	3
SS C3	166	51	24	13	7	3	—	—	—
SS C4	173	76	43	27	18	12	8	5	3
SS D1	367	129	65	37	22	13	7	3	1
SS D2	318	156	92	60	40	27	18	12	7
SS D3	480	124	57	31	18	10	5	2	—
SS D4	328	153	89	57	38	26	17	11	6
SS E1	262	95	48	27	15	7	—	—	—
SS E2	257	124	73	47	31	21	14	9	5
SS E3	334	84	38	20	10	4	—	—	—
SS E4	269	118	67	42	27	18	12	7	4

Table B.6 Load collector ratio table for Boston, MA.

SSF	.10	.20	.30	.40	.50	.60	.70	.80	.90
Boston, Massachusetts									5621 DD
WW A1	368	28	9	—	—	—	—	—	—
WW A2	119	41	20	12	7	5	3	2	—
WW A3	101	43	24	15	10	6	4	3	1
WW A4	93	44	26	16	11	7	5	3	2
WW A5	89	45	27	18	12	8	6	4	2
WW A6	87	46	28	19	13	9	6	4	3
WW B1	59	—	—	—	—	—	—	—	—
WW B2	103	52	31	21	15	10	7	5	3
WW B3	123	66	41	28	20	14	10	7	5
WW B4	118	70	46	33	24	18	13	9	6
WW B5	113	69	46	33	25	18	14	10	7
WW C1	135	72	46	31	22	16	12	8	5
WW C2	121	68	44	31	22	16	12	9	6
WW C3	136	86	60	44	33	25	19	14	9
WW C4	124	78	54	40	30	23	17	12	8
TW A1	324	30	11	4	—	—	—	—	—
TW A2	126	37	18	10	6	4	2	1	—
TW A3	102	39	21	13	8	5	3	2	1
TW A4	88	38	22	14	9	6	4	3	2
TW B1	180	32	13	7	4	2	—	—	—
TW B2	104	36	19	11	7	5	3	2	1
TW B3	92	36	19	12	8	5	3	2	1
TW B4	86	34	19	12	8	5	4	2	1
TW C1	122	32	15	9	5	3	2	1	—
TW C2	95	33	17	10	7	4	3	2	1
TW C3	93	31	16	10	6	4	3	2	1
TW C4	102	29	15	9	6	4	3	2	1
TW D1	45	—	—	—	—	—	—	—	—
TW D2	112	49	28	18	12	9	6	4	3
TW D3	113	54	32	21	15	10	7	5	3
TW D4	121	64	41	28	20	15	11	8	5
TW D5	118	66	42	30	21	16	12	8	6
TW E1	138	67	40	27	18	13	9	7	4
TW E2	130	66	41	28	20	14	10	7	5
TW E3	146	84	56	39	29	21	16	11	8
TW E4	133	78	52	37	27	20	15	11	7
TW F1	134	25	10	4	—	—	—	—	—
TW F2	86	30	16	9	5	3	2	1	—
TW F3	72	31	17	11	7	4	3	2	1
TW F4	61	29	17	11	7	5	3	2	1
TW G1	83	24	11	6	3	2	—	—	—
TW G2	63	26	14	9	5	4	2	1	—
TW G3	54	25	14	9	6	4	3	2	1
TW G4	45	21	12	8	5	4	3	2	1
TW H1	54	21	11	6	4	2	1	—	—
TW H2	44	20	11	7	5	3	2	1	—
TW H3	38	17	10	6	4	3	2	1	—

(*continued*)

Table B.6 (*Continued*)

SSF	.10	.20	.30	.40	.50	.60	.70	.80	.90
TW H4	30	14	8	5	3	2	2	1	—
TW I1	30	—	—	—	—	—	—	—	—
TW I2	84	41	24	16	11	8	6	4	2
TW I3	91	46	28	19	13	9	7	5	3
TW I4	100	56	36	25	18	13	10	7	5
TW I5	101	58	38	27	20	15	11	8	5
TW J1	114	59	37	25	17	12	9	6	4
TW J2	107	58	37	25	18	13	10	7	4
TW J3	123	75	51	36	27	20	15	11	7
TW J4	115	70	47	34	25	19	14	10	7
DG A1	43	—	—	—	—	—	—	—	—
DG A2	85	34	18	9	—	—	—	—	—
DG A3	125	56	33	22	16	11	7	4	—
DG B1	44	—	—	—	—	—	—	—	—
DG B2	87	36	20	12	7	—	—	—	—
DG B3	129	58	35	24	17	13	9	6	3
DG C1	71	23	—	—	—	—	—	—	—
DG C2	109	47	27	17	12	8	4	—	—
DG C3	151	68	41	28	21	16	12	8	5
SS A1	230	61	29	16	10	6	4	2	1
SS A2	231	93	52	33	22	15	11	7	5
SS A3	205	48	20	10	4	—	—	—	—
SS A4	229	90	49	31	20	14	9	6	4
SS A5	389	58	23	11	6	3	—	—	—
SS A6	226	91	50	32	21	15	10	7	4
SS A7	420	40	12	—	—	—	—	—	—
SS A8	226	86	46	28	19	12	8	6	3
SS B1	151	44	21	12	7	4	2	1	—
SS B2	183	77	43	28	19	13	9	6	4
SS B3	129	36	16	8	3	—	—	—	—
SS B4	176	73	41	26	17	12	8	6	4
SS B5	193	36	15	7	3	—	—	—	—
SS B6	169	72	41	26	18	12	9	6	4
SS B7	157	25	7	—	—	—	—	—	—
SS B8	160	66	37	23	16	11	7	5	3
SS C1	84	33	17	10	6	4	2	1	—
SS C2	110	54	33	22	15	11	8	5	3
SS C3	91	26	12	7	4	2	—	—	—
SS C4	109	48	28	18	12	9	6	4	3
SS D1	206	73	38	22	14	9	5	3	2
SS D2	203	103	63	42	29	21	15	10	6
SS D3	264	69	32	18	10	6	4	2	1
SS D4	208	100	60	39	27	19	14	9	6
SS E1	140	51	25	14	8	4	2	—	—
SS E2	161	80	48	32	22	15	11	7	5
SS E3	177	44	19	10	5	2	—	—	—
SS E4	166	75	43	28	19	13	9	6	4

Table B.7 Load collector ratio table for Madison, WI.

SSF	.10	.20	.30	.40	.50	.60	.70	.80	.90
Madison, Wisconsin									7730 DD
WW A1	278	—	—	—	—	—	—	—	—
WW A2	91	27	12	—	—	—	—	—	—
WW A3	77	30	15	8	3	—	—	—	—
WW A4	72	32	17	10	5	—	—	—	—
WW A5	69	33	19	11	7	4	—	—	—
WW A6	67	34	19	12	7	4	2	—	—
WW B1	—	—	—	—	—	—	—	—	—
WW B2	84	41	24	15	10	7	5	3	2
WW B3	102	53	32	21	15	10	7	5	3
WW B4	101	59	39	27	19	14	10	7	5
WW B5	98	59	39	28	20	15	11	8	5
WW C1	113	59	37	25	17	12	8	6	3
WW C2	103	57	37	25	18	13	9	6	4
WW C3	119	75	51	37	28	21	15	11	7
WW C4	109	68	47	34	25	19	14	10	7
TW A1	249	16	—	—	—	—	—	—	—
TW A2	97	26	11	4	—	—	—	—	—
TW A3	79	28	13	7	3	—	—	—	—
TW A4	69	28	15	9	5	3	—	—	—
TW B1	139	20	5	—	—	—	—	—	—
TW B2	81	26	12	6	3	—	—	—	—
TW B3	72	27	13	7	4	2	—	—	—
TW B4	69	26	13	8	5	3	1	—	—
TW C1	96	23	10	4	—	—	—	—	—
TW C2	76	25	12	7	4	2	—	—	—
TW C3	75	24	12	7	4	2	1	—	—
TW C4	84	23	11	6	4	2	1	—	—
TW D1	—	—	—	—	—	—	—	—	—
TW D2	91	39	22	13	9	6	4	2	1
TW D3	93	43	25	16	10	7	5	3	1
TW D4	103	54	34	23	16	12	8	6	4
TW D5	102	56	36	25	18	13	10	7	4
TW E1	115	54	32	21	14	10	7	4	3
TW E2	110	55	34	22	16	11	8	5	3
TW E3	126	72	47	33	24	18	13	9	6
TW E4	116	68	45	32	23	17	13	9	6
TW F1	99	13	—	—	—	—	—	—	—
TW F2	65	20	8	—	—	—	—	—	—
TW F3	55	22	11	5	—	—	—	—	—
TW F4	47	21	11	7	4	2	—	—	—
TW G1	61	14	—	—	—	—	—	—	—
TW G2	47	18	8	4	—	—	—	—	—
TW G3	42	18	9	5	3	—	—	—	—
TW G4	35	16	9	5	3	2	—	—	—
TW H1	41	13	6	—	—	—	—	—	—
TW H2	34	14	7	4	2	—	—	—	—

(*continued*)

Table B.7 (*Continued*)

SSF	.10	.20	.30	.40	.50	.60	.70	.80	.90
TW H3	29	13	7	4	2	1	—	—	—
TW H4	24	10	6	3	2	1	—	—	—
TW I1	—	—	—	—	—	—	—	—	—
TW I2	68	32	18	12	8	5	3	2	1
TW I3	75	37	22	14	10	7	4	3	2
TW I4	85	47	30	21	15	11	8	5	3
TW I5	87	50	33	23	16	12	9	6	4
TW J1	95	48	29	19	13	9	6	4	3
TW J2	91	48	30	21	14	10	7	5	3
TW J3	106	65	43	31	23	17	12	9	6
TW J4	100	61	41	29	21	16	12	9	6
DG A1	—	—	—	—	—	—	—	—	—
DG A2	68	25	11	—	—	—	—	—	—
DG A3	109	47	28	18	12	8	5	—	—
DG B1	—	—	—	—	—	—	—	—	—
DG B2	70	27	14	6	—	—	—	—	—
DG B3	114	50	30	20	14	10	7	4	—
DG C1	47	—	—	—	—	—	—	—	—
DG C2	91	37	21	13	7	—	—	—	—
DG C3	133	59	35	24	17	13	9	6	3
SS A1	192	47	20	9	3	—	—	—	—
SS A2	200	78	42	26	17	12	8	5	3
SS A3	166	32	—	—	—	—	—	—	—
SS A4	197	74	39	23	15	10	6	4	2
SS A5	329	42	13	—	—	—	—	—	—
SS A6	195	75	40	25	16	11	7	5	3
SS A7	349	22	—	—	—	—	—	—	—
SS A8	192	69	36	21	13	8	5	3	2
SS B1	122	32	13	5	—	—	—	—	—
SS B2	158	64	36	22	15	10	7	5	3
SS B3	100	22	—	—	—	—	—	—	—
SS B4	150	60	33	29	13	9	6	4	2
SS B5	156	24	—	—	—	—	—	—	—
SS B6	145	59	33	20	13	9	6	4	2
SS B7	122	—	—	—	—	—	—	—	—
SS B8	136	54	29	18	11	7	5	3	2
SS C1	61	20	7	—	—	—	—	—	—
SS C2	90	43	25	16	11	7	5	3	2
SS C3	67	16	—	—	—	—	—	—	—
SS C4	90	38	22	13	9	6	4	2	1
SS D1	169	56	26	13	6	—	—	—	—
SS D2	175	86	51	34	23	16	11	7	5
SS D3	221	52	21	10	—	—	—	—	—
SS D4	179	84	49	32	21	15	10	7	4
SS E1	108	34	12	—	—	—	—	—	—
SS E2	135	65	38	24	16	11	7	5	3
SS E3	141	29	8	—	—	—	—	—	—
SS E4	140	61	34	21	14	9	6	4	2

Index

Alternative Energy Systems and Applications, Second Edition. B. K. Hodge.

Companion website: www.wiley.com\go\Hodge\AESystemsandApplications2E